THE PERFORMANCE STABILITY OF A HOMOGENEOUS CHARGE LEAN-BURN SPARK-IGNITION ENGINE.

Thesis submitted in accordance with the requirements of the University of Liverpool for the degree of Doctor of Philosophy by Jeremy Gidney.

September 1990.

ERRATA.

"Kg" should read "kg".

"KW" should read "kW".

"Davis and Fisher" should read "Davies and Fisher".

<><><><>

CONTENTS

Figures Index		v
Tables Index		xvii
Abstract		xix
Chapter 1	**Introduction**	
1.1	Lean-burn in the context of spark-ignition engine development.	1
1.2	Pollution generation and control.	2
1.3	Cycle efficiency considerations.	4
1.4	Flame speed restoration and operating stability.	6
1.5	In-cylinder gas motion structure and history.	8
1.6	In-cylinder turbulence analysis.	11
1.7	Flame development history and cyclic variation.	14
1.8	Experimental objectives and overview.	16
1.9	Summary.	19
Chapter 2	**In-Cylinder Gas Velocity Measurement**	
2.1	Introduction.	20
2.2	Calculation of a heat transfer rate between a filament and a gas of fluctuating properties.	25
2.3	Introduction to motored engine data processing.	32
2.4	Design of anemometer probes.	34
2.5	Anemometer signal interpretation and processing	39
2.6	Resistance thermometer signal interpretation and processing.	45
2.7	Motored pressure record evaluation	49
2.8	Summary	50

Chapter 3	**High Speed Logging Equipment, Sensor Calibration and Data Processing**	
3.1	Introduction.	51
3.2	The high speed logging equipment.	52
3.3	Wire calibration to evaluate a heat transfer relationship (hot wire calibration).	58
3.4	Resistance thermometer calibration.	65
3.5	Pressure transducer calibration.	66
3.6	In-cylinder data acquisition and signal processing.	66
3.7	Summary.	73
Chapter 4	**Engine Performance Analysis, Firing Engine Data Acquisition and Processing**	
4.1	Introduction.	74
4.2	Non-transient data acquisition.	75
4.3	Brake load measurement and BMEP calculations.	76
4.4	Air mass flow rate measurement.	78
4.5	Fuel flow measurement and air-fuel ratio evaluation.	80
4.6	Temperature and crankshaft speed measurement.	82
4.7	Engine performance monitoring and data acquisition programme.	84
4.8	Fitting discrete performance data.	90
4.9	Detailed pressure record evaluation.	91
4.10	Fuel mass and volume fraction burnt analysis.	92
4.11	Summary.	102
Chapter 5	**An Overview of the Motored Engine Anemometric Measurements and the Firing Engine performance**	
5.1	Introduction.	103

5.2	Experimental design.	104
5.3	Motored engine results.	106
5.4	Firing engine results.	113
5.5	Summary.	119
Chapter 6	**Motored Engine Data Smoothing and Cycle-by-Cycle Analysis**	
6.1	Introduction.	121
6.2	Ensemble mean velocity and RMS turbulence data smoothing.	122
6.3	A cycle-by-cycle resolution of mean velocity and turbulence intensity.	129
6.4	A cycle-by-cycle estimation of spatial velocity gradient intensity.	141
6.5	Summary.	146
Chapter 7	**Possible Anemometric Influences on the Firing Engine Performance in the Context of the In-Cylinder Flame Development**	
7.1	Introduction.	147
7.2	The correlation between early and total burn times	148
7.3	The relative duration and variability of the early, remaining and total burn times.	155
7.4	Combustion rate enhancement and flame propagation modelling.	157
7.5	Summary.	167
Chapter 8	**Overall Summary and Suggestions for Future Work**	
8.1	Introduction and experimental overview.	169

8.2	Motored engine anemometric measurements.	172
8.3	The firing engine performance maps, combustion histories and correlations with the motored engine experiments.	177
8.4	Conclusions.	182
8.5	Suggestions for future work	185
References		189
Acknowledgements		198
Appendix A	**Proof of the End-Loss Equations for Fine Wire Anemometers**	A1
Appendix B	**Parabolic Error Minimisation**	B1
Appendix C	**Data Fitting by the Method of Least Squares**	C1
Appendix D	**The Programming and Polling of the Microlink Transient Capture System**	D1
Appendix E	**Apricot Specific Programming of Non-Transient Data Logger MEE12030**	E1
Appendix F	**Smoothing by a Finite Fourier Series**	F1
Appendix G	**Smoothing by Cubic Splines**	G1
Appendix H	**Data File Formats, Contents and Locations**	H1
Appendix I	**Idealised Flame Geometry Modelling**	I1
Appendix J	**Averaged Peak Burning Velocity Ratios and Associated Anemometric and Combustion Data**	J1

FIGURES

1.1	Emissions, power and fuel consumption against air to fuel ratio.	200
1.2	Anticipated intake stroke air flow patterns for 2 valve designs (swirl, non-swirl).	201
1.3	Further modes of gas motion generation (squish, barrelling).	202
1.4	Photographic view of the E6 engine test bed.	203
1.5	Cross sectional arrangement of the variable compression research engine.	204
1.6	Assembly drawing showing shrouded valve location details.	205
1.7	Sketch to illustrate the degree of intake valve shrouding.	206
1.8	Photographic view of the test bed instrumentation.	207
1.9	Instrumentation identification schematic.	208
2.1	Split-sectional view of the E6 cylinder head illustrating spark plug and indicator ports.	209
2.2	Plug cavity and flush probe details.	210
2.3	Flush probe wire orientation sketches.	211
2.4	Side view to illustrate the relative location of the hot wires.	212
2.5	Photographs illustrating the assembly sequence of the hot wire probes.	213
2.6	Circuit diagram schematic of the constant temperature hot wire anemometer bridge.	214
2.7	Resistance thermometer quarter bridge.	215
2.8	Piezio-electric pressure transducer and holder.	216

3.1	Block diagram of Microlink data logger.	217
3.2	MEE13007 schematic (encoder interface).	218
3.3	Module layout of Prosser anemometer.	219
3.4	Basic description of resistance thermometer circuit and bridge modifications.	220
3.5	Oven door bracket used to find wire temperature coefficient of resistance.	221
3.6	Resistance-temperature plot for 9 micro-metre platinum-plated tungsten wire.	222
3.7	Resistance-temperature plot for 10 micro-metre platinum-rhodium wire.	223
3.8	Steady flow hot wire calibration rig.	224
3.9	Hot wire calibration rig test section.	225
3.10	Twin hot wire steady-state logging programme (flow chart).	226
3.11	Programme to process hot wire calibration raw data (flow chart).	227
3.12	Nu-Re hot wire calibration plot.	228
3.13	Log-log hot wire calibration plot.	229
3.14	Piezio-electric transducer calibration routine (flow chart).	230
3.15	Pressure transducer calibration plot.	231
3.16	High speed data acquisition programme (flow chart)	232
3.17	In-cylinder gas velocity, temperature and pressure calculation flow chart.	233
3.18	Twin anemometer in-cylinder velocity evaluation programme flow chart.	234
3.19	In-cylinder data logging, transfer and processing summary.	235
4.1	Schematic of MEE12030 (Apricot computer interface).	236

4.2	Schematic of engine dynamometer load cell arrangement.	237
4.3	Basic description of complete bridge circuit for load cell and air flow meter transducer.	238
4.4	Load cell calibration plot.	239
4.5	Schematic of the air flow meter and pressure transducer arrangement.	240
4.6	Air flow meter calibration plot.	241
4.7	Fuel pipette photo-detector mounting block details.	242
4.8	Schematic of buffer volume volumetric fuel flow measurement system.	243
4.9	Schematic of float chamber volumetric fuel flow measurement system.	244
4.10	Block diagram of performance mapping data acquisition procedure.	245
4.11	Performance data acquisition: Main programme (flow chart).	246
4.12	Performance data acquisition: Monitoring routine (flow chart).	247
4.13	Performance data acquisition: Testing routine (flow chart).	248
4.14	Example of data output from an engine performance test.	249
4.15	(B)MEP versus AFR polynomial fitting routine for separate ignition advances.	250
4.16	Third order BMEP/AFR curve fit.	251
4.17	Block diagram of firing engine data acquisition procedure.	252
4.18	Mass fraction burnt calculation for one cycle (heat transfer too low).	253
4.19	Mass fraction burnt calculation for one cycle (heat transfer too high).	254

4.20 Mass fraction burnt calculation for one cycle (heat transfer 'correct'). 255

5.1 Raw data logged from one cycle (standard valve) 256

5.2 Processed gas velocity and temperature from one cycle (standard valve). 257

5.3 Processed gas velocity and temperature from one cycle (shrouded valve). 258

5.4 Temperature comparison plot (experiment and theory). 259

5.5 Ensembled gas temperatures (standard valve, increasing speed). 260

5.6 Ensembled gas temperatures (standard valve, increasing compression ratio). 261

5.7 Temperature variations (standard valve, standard deviations for increasing compression ratio). 262

5.8 Sensitivity analysis on calculated velocity (at TDC and BDC). 263

5.9 The effect of wire orientation (standard valve, ensembled mean velocities). 264

5.10 The effect of wire orientation (standard valve, RMS turbulence). 265

5.11 One cycle of 'shifted window' velocities (vertical wire, standard valve). 266

5.12 Radial wire ensembled mean velocities (standard valve, twin hot wires, increasing speed). 267

5.13 Circumferential wire ensembled mean velocities (standard valve, twin hot wires, increasing speed). 268

5.14 Plug cavity wires ensembled mean velocities (standard valve, twin hot wires, increasing speed). 269

5.15 Radial wires RMS turbulence (standard valve, twin hot wires, increasing speed). 270

5.16 Circumferential wires RMS turbulence (standard valve, twin hot wires, increasing speed). 271

5.17 Plug cavity wires RMS turbulence (standard valve, twin hot wires, increasing speed). 272

5.18 Radial wires ensembled mean velocities (standard valve, twin hot wires, increasing compression ratio). 273

5.19 Radial wires RMS turbulence (standard valve, twin hot wires, increasing compression ratio). 274

5.20 Radial wires ensembled mean velocities (shrouded valve, twin hot wires, increasing speed). 275

5.21 Circumferential wires ensembled mean velocities (shrouded valve, twin hot wires, increasing speed). 276

5.22 Plug cavity wires ensembled mean velocities (shrouded valve, twin hot wires, increasing speed). 277

5.23 Radial wires RMS turbulence (shrouded valve, twin hot wires, increasing speed). 278

5.24 Circumferential wires RMS turbulence (shrouded valve, twin hot wires, increasing speed). 279

5.25 Plug cavity wires RMS turbulence (shrouded valve, twin hot wires increasing speed). 280

5.26 BMEP contour maps (standard valve, 1000 and 1250 rpm, 8:1 compression ratio). 281

5.27 BMEP contour maps (standard valve, 1500 and 1750 rpm, 8:1 compression ratio) 282

5.28 IMEP and BMEP contour maps (standard valve, 2000 rpm, 8:1 compression ratio). 283

5.29 BMEP contour maps (standard valve, 1500 rpm, 7:1 and 9:1 compression ratios). 284

5.30 Variation in the coefficient of drivability (Cpi) for fixed ignition advances (standard valve, 2000 rpm, 8:1 compression ratio). 285

5.31 BMEP contour maps (shrouded valve, 1000 and 1250 rpm, 8:1 compression ratio) 286

5.32 BMEP contour maps (shrouded valve, 1500 and 1750 rpm, 8:1 compression ratio). 287

5.33 BMEP contour map (shrouded valve, 2000 rpm, 8:1 compression ratio). 288

5.34 Variation in the coefficient of drivability (Cpi) for fixed ignition advances (shrouded valve, 2000 rpm, 8:1 compression ratio). 289

5.35 Volumetric efficiency as a function of engine speed 290

5.36 Pressure records from 10 firing cycles (standard valve). 291

5.37 Pressure records from 10 firing cycles (shrouded valve). 292

6.1 Comparison between phase averaged and spline smoothed ensembled mean velocity plots. 293

6.2 Comparison between phase averaged and spline smoothed RMS turbulence intensity plots. 294

6.3 Smoothed ensemble mean velocity plots (radial wires). 295

6.4 Smoothed ensemble mean velocity plots (circumferential wires). 296

6.5 Smoothed ensemble mean velocity plots (plug cavity wires). 297

6.6 Smoothed RMS turbulence intensity plots (radial wires). 298

6.7 Smoothed RMS turbulence intensity plots (circumferential wires). 299

6.8 Smoothed RMS turbulence intensity plots (plug cavity wires). 300

6.9 A comparison between single cycle and ensemble mean velocity plots. 301

6.10 Fourier coefficients from ensembled mean velocity DFT curve fits (standard valve). 302

6.11 Fourier coefficients from ensembled mean velocity DFT curve fits (shrouded valve). 303

6.12 12-coefficient Fourier fits (standard valve). 304

6.13 12-coefficient Fourier fits (shrouded valve). 305

6.14 25-coefficient Fourier fits (standard valve). 306

6.15 25-coefficient Fourier fits (shrouded valve). 307

6.16 A comparison between ensemble and averaged CBC mean velocity plots (maximum smoothing). 308

6.17 A comparison between ensemble and averaged CBC mean velocity plots (medium smoothing). 309

6.18 A comparison between ensemble and averaged CBC mean velocity plots (minimum smoothing). 310

6.19 Single cycle spline fit (shrouded valve, radial wires, too much smoothing). 311

6.20 Single cycle spline fit (standard valve, radial wires). 312

6.21 Single cycle spline fit (standard valve, circumferential wires). 313

6.22 Single wire spline fit (standard valve, plug cavity wires) 314

6.23 Single wire spline fit (shrouded valve, radial wires). 315

6.24 Single wire spline fit (shrouded valve, circumferential wires). 316

6.25 Single cycle spline fit (shrouded valve, plug cavity wires). 317

6.26 Phase averaged CBC turbulence intensity plots (standard valve). 318

6.27 Phase averaged CBC turbulence intensity plots (shrouded valve). 319

6.28 Phase averaged CBC mean velocity variation (standard valve). 320

6.29 Phase averaged CBC mean velocity variation (shrouded valve). 321

6.30 Time averaged CBC turbulence intensities as a function of window size 322

6.31 Fourier analysis of CBC turbulence frequencies 323

6.32 A comparison between phase averaged and averaged window CBC turbulence intensity plots. 324

6.33 Averaged window CBC turbulence intensity plots (radial wires). 325

6.34 Averaged window CBC turbulence intensity plots circumferential wires). 326

6.35 Averaged window CBC turbulence intensity plots (plug cavity wires). 327

6.36 A comparison between phase averaged and averaged window CBC velocity gradient plots. 328

6.37 Averaged window CBC velocity gradient plots (radial wires) 329

6.38 Averaged window CBC velocity gradient plots (circumferential wires). 330

6.39 Averaged window CBC velocity gradient plots (plug cavity wires). 331

6.40 A direct estimate of velocity gradients. 332

7.1 Mass fraction burnt calculations for 182 consequetive cycles (standard valve, Cpi=5%). 333

7.2 Mass fraction burnt calculations for 182 consequetive cycles (standard valve, Cpi=20%). 334

7.3 Delay to burn a 2% mass fraction against the total burn time (standard valve). 335

7.4 Delay to burn a 5% mass fraction against the total burn time (standard valve). 336

7.5 Delay to burn a 10% mass fraction against the total burn time (standard valve). 337

7.6 Delay-total burn time correlation (standard valve, delay defined by increasing product mass fractions). 338

7.7 Delay-total burn time correlation (standard valve, delay defined by increasing product volume fractions). 339

7.8 Delay-total burn time correlation (standard valve, delay defined by increasing product volume values). 340

7.9 Delay-total burn time correlation (standard valve, delay defined by increasing mass fractions, different speeds). 341

7.10 Mass fraction burnt calculations for 182 consequetive cycles (shrouded valve, Cpi=5%). 342

7.11 Delay to burn a 5% mass fraction against the total burn time (shrouded valve). 343

7.12 Delay-total burn time correlations (shrouded valve, delay defined by increasing product mass fractions). 344

7.13 Distributions of 0-6% mass fraction burnt times 345

7.14 Distributions of instantaneous velocities (at the time of sparking). 346

7.15 Distributions of CBC turbulence intensities (at the time of sparking). 347

7.16 Distributions of CBC mean velocities (at the time of sparking). 348

7.17 Distributions of CBC mean velocity gradient intensities (at the time of sparking). 349

7.18 Ratios of average standard/shrouded valve mass fraction burnt times. 350

7.19 Averaged mass fraction burnt times for changing air/fuel ratios. 351

7.20 Averaged 0-6% mass fraction burnt times. 352

7.21 Averaged 6-90% mass fraction burnt times. 353

7.22 Averaged 0-90% mass fraction burnt times. 354

7.23 Distributions of 6-90% mass fraction burnt times. 355

7.24 Distributions of 0-90% mass fraction burnt times. 356

7.25 Averaged Model 1 burning velocity ratios as a function of crank-angle (increasing speed). 357

7.26 Averaged Model 2 burning velocity ratios as a function of crank-angle (increasing speed). 358

7.27 Averaged Model 2 burning velocity ratios as a function of smoothed flame radius (increasing speed). 359

7.28 Averaged Model 2 burning velocity ratios as a function of crank-angle (increasing air/fuel ratio). 360

7.29 Averaged Model 2 burning velocity ratios as a function of smoothed flame radius (increasing air/fuel ratio). 361

7.30 Averaged Model 2 flame speeds as a function of smoothed flame radius (increasing speed). 362

7.31 Model 1 peak burning velocity ratio against radial wire CBC turbulence intensity correlation. 363

7.32 Model 1 peak burning velocity ratio against circumferential wire CBC turbulence intensity correlation. 364

7.33 Model 1 peak burning velocity ratio against radial wire CBC velocity gradient intensity correlation. 365

7.34 Model 1 peak burning velocity ratio against circumferential wire CBC velocity gradient correlation. 366

7.35 Model 2 peak burning velocity ratio against radial wire CBC turbulence intensity correlation. 367

7.36 Model 2 peak burning velocity ratio against circumferential wire CBC turbulence intensity correlation. 368

7.37 Model 2 peak burning velocity ratio against radial wire CBC velocity gradient intensity correlation. 369

7.38 Model 2 peak burning velocity ratio against circumferential wire CBC velocity gradient correlation. 370

7.39 Models 1 and 2 peak burning velocity ratios against radial wire CBC turbulence intensity correlation. 371

7.40 Models 1 and 2 peak burning velocity ratios against circumferential wire CBC turbulence intensity correlation. 372

7.41 Models 1 and 2 peak burning velocity ratios against radial wire CBC velocity gradient intensity correlation. 373

7.42 Models 1 and 2 peak burning velocity ratio against circumferential wire CBC velocity gradient correlation. 374

A1 Temperature distribution along hot wire filament. A5

B1	Possible error versus coefficient plots.	B4
E1	Assembler code routine and parameter stack positions.	E7
G1	Fit of sin(x) and input data.	G9
G2	Fit of cos(x) and original data.	G10
G3	Fit of -sin(x) and original data.	G11
G4	Fit of -cos(x) and original data.	G12
I1	Cylinder centre-line based idealised flame geometries.	I7
I2	Spark-plug based idealised flame geometries.	I8

TABLES

2.1	Wire temperature coefficients of resistance and possible operating temperatures.	37
2.2	Further wire material properties.	38
2.3	A comparison of empirical air viscosity values.	42
2.4	A comparison of empirical air thermal conductivity values.	43
3.1	Experimentally determined wire properties.	60
4.1	The resolution of the MEE12030 interface modules.	76
4.2	The channel allocation of the 'Type T' thermocouples.	83
4.3	Polynomial coefficients G(j,k).	94
7.1	Possible "delay" criteria.	151
7.2	0-6% mass fraction burnt times and angles.	156
7.3	0-90% mass fraction burnt times and angles.	156
D1	CH12 module programming codes.	D3
D2	TB module programming codes.	D3
D3	CH12 module polling codes.	D4
E1	MEE12030 A-D gain codes.	E3
E2	MEE12030 thermocouple programming codes.	E4
H1	Motored test results tape files.	H6
H2	Probe cold resistances and calibration constants A and B.	H10
H3	Velocity and spline fit tape files.	H11
H4	Further velocity and spline fit tape files.	H13

H5	Standard valve firing engine pressure records.	H14
H7	Shrouded valve firing engine pressure records.	H15
I1	Analytical relationships linking volume, radius and surface area for the idealised models 1a-d.	I6
J0	The tabulated parameter names, symbols, units and angles.	J2
J1	Peak burning speed ratios and the corresponding crank-angles (standard inlet valve).	J3
J2	Peak burning speed ratios and the corresponding crank-angles (shrouded inlet valve).	J4
J3	Averaged CBC turbulence intensity corresponding to the crank-angles in Table J1 (standard valve).	J5
J4	Averaged CBC spatial velocity gradient intensity corresponding to the crank-angles in Table J1 (standard valve).	J6
J5	Averaged CBC turbulence intensity corresponding to the crank-angles in Table J2 (shrouded valve).	J7
J6	Averaged CBC spatial velocity gradient intensity corresponding to the crank-angles in Table J2 (shrouded valve).	J8
J7	Further combustion parameters corresponding to the crank-angles in Table J1 (standard valve).	J9
J8	Further combustion parameters corresponding to the crank-angles in Table J2 (shrouded valve).	J10

ABSTRACT

Improved efficiency and reduced exhaust emissions are possible by fuelling a four stroke spark-ignition engine with a lean homogeneous air/fuel mixture. However cyclic variations in the initial flame development and a reduced laminar burning velocity in quiescent combustion chambers lead to a deterioration in drivability. Enhancing the overall combustion rate by turbulent or velocity gradient flame wrinkling mechanisms is identified as a route to restoring the engine performance stability. A Ricardo E6 engine, fitted with and without a shrouded inlet valve, has been used to study in-cylinder gas motion and lean combustion histories at a range of speeds and compression ratios. The gas motion intensity is measured by hot wire anemometry, which has dictated that separate motored and firing engine experiments are performed. Micro-computer based data acquisition systems have been developed to take a large number of measurements from the two cases and simple statistical comparisons are used to correlate the results obtained.

Parallel wired probes are used to take measurements of the gas velocity and temperature in the spark plug region and the main combustion chamber of the motored engine. A cubic spline curve-fitting procedure is adopted to smooth the ensembled results and resolve between bulk flow variations and a 'true turbulence' intensity on a cycle-by-cycle basis. A simple method to determine the degree of over-smoothing is presented. Parallel hot wires are used to seek a direct estimate of spatial velocity gradient intensities but inconsistencies in the ensembled results have led to the introduction of an alternative approach based upon single wire measurements and the

spline resolved mean velocities. Marked differences in the flow patterns obtained with the two inlet valve geometries are observed and the velocity gradient intensity emerges as a parameter which clearly increases with engine speed.

The general performance of the firing engine is summarised by plotting BMEP and IMEP contour maps between the bounds of knock and poor drivability. Based upon these results detailed pressure records are logged and a two-zone model is used to calculate the combustion histories. A correlation coefficient and least-squares analysis indicates a cause-and-effect relationship between the 'delay' to burn the first 6% mass fraction of the reactants and the total burn time. A comparison of cycle-by-cycle distributions suggests that the prevailing velocity gradient intensity determines the success of the initial stages of combustion. However a review of the results also indicates that the developing flame kernel may be cooled or even extinguished by high intensities at the time of sparking. A degree of wrinkling for the developed flame is calculated by considering the laminar burning velocity and idealised flame propagation models. The result is found to be a function of the flame radius and a possible relationship with its peak value and the spline-based turbulence and velocity gradient intensities is suggested. The velocity gradient intensity gives the strongest correlation which may encompass the effect of both the local wrinkling and bulk smearing distortions which act to enhance the flame surface area and promote rapid combustion.

CHAPTER 1

INTRODUCTION

1.1 Lean-Burn in the Context of Spark-Ignition Engine Development

Following the patent of the original Otto engine in 1876 and the first car in 1885, the four-stroke spark-ignition engine has evolved in accord to consumer, economic and legislative influences. Initially the response to driver demand, or "drivability", became the primary concern. With the onset of World War I a quest for a greater power-to-weight ratio emerged, which has been followed by a need to reduce exhaust emissions in the 1960's and to increase fuel economy since the 1970's [5]. Modern European engines burn a near stoichiometric, homogeneous charge with a combustion chamber and ignition advance settings suitable for these cumulative objectives.

Legislation to be introduced by the E.E.C. requiring a further reduction of the environmental impact of vehicle exhausts, coupled with more realistic road testing cycles [54] has encouraged a further reappraisal of spark-ignition engine design. It has long been established that operating with a higher than stoichrometric, or "lean", air-to-fuel mass ratio offers both an increase in economy and a reduction in exhaust emissions [33]. However a decrease in engine power with erratic performance and misfire, combined with a lack of understanding of the internal combustion process, has dampened interest in this area until recently.

1.2 Pollution Generation and Control

The currently regulated emissions generated by a fossil fuelled spark-ignition engine are carbon monoxide (CO), nitrous oxides (NO_x) and unburned hydrocarbons (HC). The latter two are accredited to the photochemical smog in the Los Angeles region [13,15] and they all cause environmental damage.

Carbon monoxide is generated by the incomplete oxidation of fuel rich mixtures and by dissociation reactions [15]. The latter is "rate controlled" in that the forward formation process is faster than the reverse oxidation to carbon dioxide, giving higher than equilibrium concentrations in the exhaust stroke. Nitrous oxide is also formed by rate controlled dissociation, the levels emitted being a function of peak temperature and flame speed. Increases in the former and latter encourage forward and reverse reactions respectively. Unburned hydrocarbons remain in the exhaust gas as a result of incomplete combustion. Possible causes include poor mixture homogeneity and distribution in multi-cylinder engines [32], misfires, combustion chamber flame quenching and crevices [15,40], and possibly fuel centrifuging in strongly swirling in-cylinder gas flows [10].

Reductions in NO_x concentration can be achieved by using slightly rich air to fuel ratios, or by retarding the ignition timing from M.B.T. ("minimum advance-best torque") [13,15,16,55]. The aim of both approaches is to lower the peak combustion temperatures with little risk of performance instability, but at a cost in efficiency, and an increase in the exhaust temperature serves to encourage late HC oxidation.

Stratified charge engines [10,15] or exhaust gas recirculation [13,32,48] by overall charge dilution, are other routes to the same end. Post combustion gas treatment methods include exhaust gas rectors to oxidise CO and HC emissions [32] and "three way" catalytic converters to reduce NO_x as well [33,54]. The latter two options prefer the use of stoichiometric mixtures, although insulation can extend the leanness range of reactors, and all represent a cost in manufacturing or efficiency.

The sketch presented in Figure 1.1 illustrates the effect of using a homogeneous lean charge alone, as a route to emission control, and the consequent effects on fuel economy and power [10,32,33]. The CO levels decrease in the presence of excess air and NO_x concentrations react in response to peak combustion temperatures, the maximum level occurring at an air-to-fuel ratio slightly weak of stoichiometric (15:1). The proportion of HC remaining initially falls in response to an increased oxygen availability. However a point of "hydrocarbon turn-up" [32] is reached as the leanness is further increased. This is associated with poor mixture uniformity and distribution (in multi-cylinder engines), incomplete combustion and ultimately misfire. The dashed line indicates the levels, in terms of HC concentration and fuel economy, that are attainable if these problems are tackled. Failing this an exhaust gas reactor or a catalytic converter may still be required.

1.3 Cycle Efficiency Considerations

The efficiency of the ideal Otto cycle is given by:

$$\eta = 1 - \frac{1}{R^{\gamma-1}} \qquad (1.1)$$

where η = thermal efficiency

R = compression ratio

γ = ratio of specific heat capacities (= Cp/Cv)

Cp = specific heat capacity of working fluid at constant pressure (J/KgK)

Cv = specific heat capacity of working fluid at constant volume (J/Kg K)

Ignoring for a moment the deviations of the real cycle from the ideal, it is seen that the only governing factors in the equation are R and γ. The compression ratio in a spark-ignition engine is "knock limited" [16], one cause of which is the spontaneous ignition of the charge ahead of the flame front ("end gas"), with a consequential high heat transfer rate eroding the piston crown and cylinder walls [26,55]. This tendency to "auto-ignite" is a function of fuel quality (octane number) and concentration, the reactant temperature and burn time history. It is usually discouraged by retarding the ignition timing. However in combusting lean mixtures, an increase in compression ratio is permitted [16,33,79] provided that the flame arrival time to the end gas region and the associated charge temperatures are not excessive. Fast burning is desirable therefore in further extending the knock tolerance [55,79].

The value of the specific heat ratio increases as the average charge composition becomes more diatomic. In the range of 0-600°F the value for air is approximately 1.4-1.38, whereas that for 2-2-4 trimethyl pentane (iso-octane) lies between 1.055 and 1.02 [33]. Thus reducing the charge fuel concentration increases the theoretical efficiency.

Deviations from the ideal include pumping loop and valve overlap losses, which are outside the scope of this study. Other factors which are important, however, are listed below [16]:

(i) Non constant volume heat addition.

(ii) Heat transfer losses in the compression and expansion stroke.

(iii) Dissociation losses.

(iv) Specific heat capacity increases.

(v) Non-unity molar yield.

The non-unity molar yield is a small beneficial effect which deteriorates slightly with an increasing air to fuel ratio. The associated temperature fall when burning lean mixtures will reduce the energy absorption of dissociation reactions and the disproportionate rises in the gas specific heat capacity. The heat transfer losses are a function of the gas temperature and motion intensity [4], indicating a route towards a further increase in efficiency in quiescent combustion chambers. However any benefits gained may be outweighed by a rise in the total burn time, which also deleteriously effects the rate of heat addition to the cycle.

1.4 Flame Speed Restoration and Operating Stability

The ideal Otto efficiency discussed in Section 1.3 indicates a tendency towards optimum output with an infinitely lean mixture of air and fuel. Ignoring the obvious conclusion that no power would actually be generated in this situation, two principle limits are reached long before this condition is attained [33]:-

(i) The Lean Ignition Limit

This is the energy which must be supplied to a critical volume to raise the mixture to its minimum ignition temperature. It is a function of fuel type and the local gas velocity, temperature and pressure at the point of spark discharge.

(ii) The Lean Flamability Limit

This is the weakest air to fuel ratio mixture which will sustain flame propagation, and is a function of temperature, pressure and fuel type.

The lean ignition limit should be independent of the source and combustion chamber details. However in an engine the effects of mixture motion and wall quenching cannot be ignored [33]. Given an optimised ignition system, local mixture inhomogeneity and convective cooling at the spark will determine the acceptable degree of leanness, which in an ideal situation should converge for the two criteria. This is further discussed in Section 1.7.

The variation in peak cylinder pressure generated by fast burning is small, because a large fraction of the combustion energy release is timed to occur near to the compression stroke

TDC (top dead centre). At this point the piston induced cylinder volume changes are low [10,33,55,79]. Increasing the spark timing advance angle to compensate for the slower flame speeds in lean mixtures, encourages cycle-by-cycle power variations because ignition takes place at low reactant temperatures and pressures. Conversely retarding the ignition causes fluctuations because combustion is occurring when the cylinder volume is rapidly changing.

An increase in the compression ratio serves to beneficially aid the ignition and flame propagation processes by an overall increase in reactant temperature and pressure, and by improved scavenging reducing the degree of residual exhaust gas dilution [33]. Although an overall amelioration may have been achieved, depending upon the spark timing an inconsistency in ignition is still capable of yielding occasional knocking or misfire cycles. The former coupled with the rise in peak temperatures will increase NO_x levels, while the latter in conjunction with a higher degree of heat transfer will encourage HC emissions. Therefore in aiming to improve the engine efficiency and restore operating stability, changes in ignition advance and compression ratio must be used judiciously.

A third route is to increase the gas motion intensity within the engine cylinder [54]. The aim is to "wrinkle" the flame front and hence by virtue of an increased surface area the overall combustion rate is increased. This wrinkling may be in the form of small corrugations, deep peninsulas or ultimately of islands of gas in the reactant and product zones. The resulting reduction in the total burn period and its

proportional variations permits an improved synchronisataion of the peak heat release rate. Also a further increase in compression ratio is possible because the time available for the auto ignition process is smaller [79].

The mechanisms for surface area enhancement are variously accredited to the reactant gas flow turbulence, velocity gradients and bulk motions. This is further discussed in the context of the flame development process in Section 1.7.

1.5 In-Cylinder Gas Motion Structure and History

The turbulence and velocity gradient intensities sought late in the compression and early in the expansion strokes to promote rapid burning generally stem from bulk gas motions that develop during induction. By increasing the engine speed or modifying the intake or combustion chamber geometry to amplify these flow structures, the levels generated can be enhanced. Figures 1.2 and 1.3 illustrate possible routes to this end.

The non-swirl case represents a "quiet" chamber with no explicit mechanism for bulk flow motion generation. Swirl is an axial rotation that can be induced by the use of directed, tangential or helical intake ports [40], upstream guide vanes [83] or a shrouded inlet valve [88]. Barrelling is usually a consequence of valve location and intake port geometry rather than the shrouding illustrated, and results in a rotating motion that is perpendicular to the cylinder axis.

Computational predictions and flow mapping experiments using low speed, single (central) valve model engines have been used to quantify the averaged flow structure histories, as a route towards understanding the mechanisms of in-cylinder

turbulence and shear generation. The general conclusions reached can be summarised as follows:

(i) Non-Swirl

During the induction stroke a hollow cone jet separates on both sides to produce a ring vortex on the cylinder head-wall junction, and a main toroidal vortex in the bulk of the chamber [1,6,40]. In the early stages the dominance and strength of each structure is a function of the lift and seat angle of the inlet valve [6,7,76] and the compression ratio [1], which influence the impingement of the jet on the piston crown and the cylinder wall. As the chamber volume increases, the main vortex grows by entrainment of the intake jet and through stretching by the piston, filling the bulk of the cylinder [1,40]. Turbulence is generated by shear layers in the jet, and levels are high at this stage [1,40,76]. As bottom dead centre is approached, a reduction in intake velocity removes the major sources of momentum and turbulent energy production, and consequently both begin to decay [1].

During the compression stroke the velocity field is dominated by the diminishing main vortex [1,40] and as TDC is approached the turbulence tends towards homogeneity (no spatial intensity gradients) and isotrophy (no preferred direction). Vortex disintegration is enhanced by an increase in compression ratio [1] and conversely a large clearance volume promotes turbulence decay [76]. The geometrical effects of the inlet system diminish and those of the head dominate at this stage [6]. Early in the stroke the remaining bulk flow structures collapse and the motion tends to one dimensionality, following the descending piston.

(ii) **Swirl**

During the induction stroke the intake jet interacts with the valve wake to perform a helical or spiralling motion in the axial plane [6], the details of which are a strong function of the valve geometry [7,83]. In the tangential plane a double vortex structure is produced as the jet impinges on the cylinder wall. The strength of each is dependent upon the valve lift, flow asymmetry and the axial distance from the cylinder head [6]. As bottom dead centre is approached axial stratification occurs with the flow near to the head exhibiting intake motion memory effects, and that near to the piston performing solid body rotation [6,40].

At the end of intake and the beginning of compression the flow begins to redistribute, with the swirl velocities near the piston slowing and mid-cylinder values increasing [40]. In the absence of radial gas inflows, a trend towards total solid body rotation continues throughout the compression stroke [6,7,40,83]. Despite this imposition of bulk flow velocities, turbulence levels become homogeneous as TDC is approached [7,8,40,83], the principal source being a frictional interaction with the chamber boundaries [6,55]. Little enhancement in intensity over the non-swirl case is reported however [8] and it is possible for high levels of swirl to suppress turbulence generation [88].

With an off-axis inlet valve, as is almost universally the case, the non swirl induction stroke bulk flow becomes non-symmetrical [40]. The intake jet forms a main barrelling type

vortex directly, which occupies the majority of the chamber, and a smaller recirculation develops in its wake. The flow structure is less stable than the idealised case and breaks down sooner. The swirl motion history will depend upon the method of generation, but the scenarios outlined above should broadly hold (see [9]).

Swirl and barrelling represent the longest lived flow structures in an engine. Unlike swirl, barrelling motions work against the geometry of the cylinder. However if explicitly generated by the inlet valve and port design, high bulk velocities can result as the piston approaches TDC because of a conservation of momentum by the vortex, and significantly higher levels of turbulence follow [6]. By the same virtue, bowl-in-piston configurations can be used to counter the frictional dissipation of swirling motions. Although effective in restoring circumferential velocities, only re-entrant type bowls appear to enhance turbulence levels significantly, by exploiting a swirl-squish interaction [8].

1.6 In-Cylinder Turbulence Analysis

Conventionally instantaneous gas velocity measurements are resolved in a mean and a turbulent component such that:

$$U(t) = \overline{U} + u(t) \qquad (1.2)$$

where U = instantaneous velocity (m/s)

$\overline{U}$ = mean velocity (m/s)

u = turbulent velocity (m/s)

and t = denotes the time of measurement.

Within the combustion chamber the classification of a net mean velocity in cartesian co-ordinates is not clear, but it is desirable to resolve between the bulk fluid motions and their subsequent decay by shearing processes nevertheless. In a swirl flow the former may be assigned to the average circumferential velocity at a given off-axis radius, whereas in less well defined situations it might apply to large scale vortical speeds. In transposing the standard definitions to the time dependent motion histories within the cylinder, a convention of "ensemble" or "phase" averaging is usually adopted [40] such that:

$$\bar{U}(\theta) = \frac{1}{Nc} \sum_{i=1}^{Nc} U(\theta,i) \tag{1.3}$$

$$u'(\theta) = \left[\frac{1}{Nc} \sum_{i=1}^{Nc} (U(\theta,i) - \bar{U}(\theta,i))^2 \right]^{1/2} \tag{1.4}$$

where $U(\theta,i)$ = instantaneous velocity (m/s)

$\bar{U}(\theta)$ = mean velocity (m/s)

$u'(\theta)$ = RMS turbulence intensity (m/s)

and θ = crank angle (°)

i = engine cycle number

Nc = total number of cycles considered.

Although on average the overall flow pattern within the cylinder will repeat for a given crank angle, small perturbations are capable of producing significant changes in

the mean velocity perceived at a fixed point. In swirl generation such variations include instabilities in the helical path described during induction [6] and precession of the centre of the solid body rotation relative to the cylinder axis during compression [59,90]. The recirculating flows in non swirl situations are strongly sensitive as the vortices develop in the intake stroke [40]. Although the ensemble mean velocity is still important in summarising the general in-cylinder aerodynamic behaviour, an erroneously high turbulence level is hence evaluated if equation 1.4 is applied directly. To counter this problem the analysis in this study will be extended such that:

$$U(\theta,i) = \bar{U}(\theta) + \hat{U}(\theta,i) + u(\theta,i) \qquad (1.5)$$

where $\hat{U}$ = the cyclic variation in the mean (m/s).

The structure of turbulence can be regarded as an assembly of small vortices which interact and continually change, and possess a proportion of dissipative and conservative energy [80]. Classifications used to characterise different attributes of the eddy spectrum are the integral, Taylor micro - and Kolmogrov length scales [40,50]. Throughout induction and compression it is a function of valve lift, chamber dimensions and ultimately the piston to cylinder head clearance height [41,85,89]. The Taylor microscale relates the fluctuating strain rate of the turbulent flow field to the intensity and can be found from the integral scale providing that $u'/U << 1$, a criterion which is rarely met in engines

[85]. The Kalmagrov scale represents the smallest eddy size at which viscous dissipation to heat takes place.

1.7 Flame Development History and Cyclic Variation

The spark-ignited flame growth history can be categorised into four components [6,51]:

(i) Ignition and kernel growth.

(ii) Flame development.

(ii) Fully developed propagation.

(iv) Termination.

The scenario from a laminar kernel to a fully developed wrinkled propagation can be regarded in terms of the corrugating influence of eddies of increasing size as the flame front expands [51,89] and the turbulent Reynold's number [36]. The action of small scale turbulence, in enhancing local heat and mass transfer rates, is assumed to be less important in comparison [51]. Another approach is to consider the counter effects of velocity gradients and a self smoothing action, resulting from the flame's propagation normal to its surface and geometric stretching [79,80]. The termination phase, where the degree of wrinkling appears to drop, may be associated with large scale quenching or eddy size suppression as the flame approaches the cylinder walls [51] or the time-temperature related turbulence decay [80].

Lancaster directly relates the degree of wrinkling of the flame front in the fully developed phase to the level of turbulence. It is argued that scales and intensity are inter-

related and are a function of the flow characteristics of the intake jet [50], and that intensity alone specifies the magnitude of a range of eddy frequencies [51]. Groff [36] further extends this analysis to account for the compression effects on the flow structure.

Apart from the self smoothing action discussed earlier, other factors which may be important in relating the flame development to the gas flow field are [80]:

(i) An order of magnitude rise in the kinematic viscosity across the flame.

(ii) Local density variations within the front.

(iii) The increase in volume associated with burning.

(iv) The possible destruction of vortex stability.

and also:

(v) The irreversability in the rapidly changing state in the flame.

It is also possible that the reactant turbulence intensity is enhanced ahead of the flame [6,31]. Off-centre ignition combined with swirling bulk fluid motions may result in large scale "smearing" distortions [55,88] or even a centrifugal migration of the lighter burned gases to the cylinder axis [39], reducing the distance to be travelled for complete combustion.

The onset of cycle-by-cycle peak pressure or power variations is generally accredited to the early stages of flame development, and increases as the combustion charge becomes leaner. A possible cause is the relatively quiescent progress across Taylor microscale eddies, followed by a rapid progression along Kalmogrov scale Tennekes vortex tubes [41].

A more tangible source is attributed to intense small to medium scale turbulence or velocity gradients around the spark gap, yielding consequent high levels of heat transfer from the developing kernel [10,16,33,79]. Mixture homogeneity is important [6] and a preferred velocity component towards the cylinder centre indicates that early flame quenching is undesirable [22,23,78]. The variability in the early combustion phase has been quantified in terms of the time to burn the first 5% [12] or 10% [10,33,55] of the charge, and initial flame kernel sizes at which the sensitivity to the velocity field becomes important ranges from 0.5-4 mm [79] or 10 mm [86].

High subsequent burning rates following the early period improve the engine performance stability [48,55] by reducing the overall burn time variability compared to the initial "delay". This permits a better phasing of the peak heat release rate with respect to TDC and an increase in the spark timing retard, giving an improvement in ignition consistency. Very high pressure rise rates are to be avoided however because of the onset of "roughness" [55] or knock by detonation or fast entrainment mechanisms [26].

1.8 Experimental Objectives and Overview

It has been established in the previous sections that the combustion of a lean air to fuel charge is associated with an inconsistency of ignition and a slow overall burning rate. The chosen interest of the present study is therefore the cycle-by-cycle effects of the combustion chamber gas motion intensity on both the early and the fully developed phases of flame

propagation. To this end a Ricardo E6 research engine and test bed, a photograph of which is shown in Figure 1.4, has been adopted as a source in-cylinder measurements under various operating conditions.

The engine is coupled to a D.C. dynanometer (brake), which can be manually switched and controlled as a generator to absorb power or as a motor to drive the engine directly. The fuel system comprises a mechanical pump and rack that is timed to inject into the inlet manifold at 15 degrees after induction TDC. The spark energy is provided by a magneto, with an ignition advance range of 20-60 degrees before TDC compression, which is coupled to the overhead camshaft. The temperature of the cooling water, oil and fuel lines is controlled by counter flow (water) heat exchangers. The circulation system for the former has been modified by fitting a thermostatic control valve to regulate the temperature, when firing, to ± 1°C.

Figure 1.5 illustrates how the compression ratio is continuously variable (within limits) by mechanically sliding the cylinder relative to the engine block. The combustion chamber has a "pancake" geometry, that is to say that the piston crown and cylinder head are essentially flat. The three points of access and the valve locations can be seen by referring to Figures 2.1 and 2.3. The smaller of these ports has been fitted with a flush mild steel blank, which may serve as an anchor for future cylinder head modifications.

The gas motion intensity is regulated by changes in the engine speed and compression ratio or by the use of a shrouded intake valve, as illustrated in Figures 1.6 and 1.7. The assembly has been built to a Ricardo design [71] using castings

supplied by the manufacturer. The degree of shrouding is limited by the geometry of the inlet port and the aim is to cause a tangential impingement of the intake jet on the cylinder wall. Location is provided by a silver steel dowl that slides in a slot machined into the valve guide and is encased by a thin mild steel cap. Careful tolerancing has hopefully prevented the pumping of oil into the cylinder head. A butterfly valve has been added to the inlet system, but all tests presented here are conducted at wide open throttle (WOT).

Hot wire anemometry has been selected to measure turbulence, mean velocity and spatial gradients. The ramifications of this choice and its subsequent application are discussed in Chapter 2, but it is sufficient to say here that the sought advantage is that it yields a continuous analogue signal. This facilitates the phasing of readings taken in a single, or many separate, cycles and thus permits the direct measurement of spatial velocity gradients. The main disadvantage is that the associated probes cannot withstand a combusting environment. Thus a statistically significant number of readings from separate non-firing ("motoring") and firing experiments must be taken to analyse the cause and effect of imposed changes. As a result large scale "figures of merit" rather than perfect correlations are primarily sought in this study.

The overall objective is to firstly map the averaged engine performance for different speeds, compression ratios and inlet geometries. Hence criteria are identified for the subsequent logging of detailed in-cylinder pressure records. Combustion histories are hence calculated to serve as a source

of correlation of motored anemometric data. The latter is to be obtained from the spark plug region and within the combustion chamber. Both an ensembled and a cycle-by-cycle analysis is performed.

The instrumentation bank developed to this end is illustrated in Figures 1.8 to 1.9. It broadly resolves into two sections, reflecting the limitation discussed earlier, which are linked by a central microcomputer. The anemometric equipment is mounted on a mobile trolley to permit the use of the same system to calibrate the hot wire probes in a remote wind tunnel. The static group is principally concerned with the acquisition of engine performance parameters. The details of the equipment, its implementation and the results subsequently obtained are discussed in Chapters 3-7.

1.9 Summary

It has been shown that an improvement in efficiency, coupled with some control in exhaust gas emissions, is attainable by fuelling a spark-ignition four-stroke engine with a lean homogeneous mixture. A consequent decay in cycle-by-cycle performance results however, which is the area of study of this thesis. To this end anemometric and engine performance data are to be compared in an attempt to identify the effects of gas motion intensity changes.

CHAPTER 2

IN-CYLINDER GAS VELOCITY MEASUREMENT

2.1 Introduction

At present there are two competing approaches to the quantitative measurement of gas motion at a given point in space within an engine cylinder, namely hot wire anemometry (HWA) and laser Doppler velocimetry (LDV). The former gives a measure of speed alone whereas the latter can also resolve the flow direction. Both methods have limitations and to discuss their relative merits it may be useful to briefly outline the principles of operation of each.

The hot wire in an HWA system is a fine metal filament, with a diameter of the order of microns, which is spot welded to two supporting prongs and is electrically heated to a temperature above ambient conditions. The power supplied can be calculated and the rate of convective heat transfer, rather than a direct measure of velocity, is obtained. It is for this reason that the sensor is essentially "blind" to the gas flow direction and the output is strongly influenced by gas properties.

Within the broad heading above there are constant current (CCA) and constant temperature (CTA) modes of operation. The constant current mode is rarely used in modern applications for two reasons. Firstly, the greater the temperature difference between the wire and that of the surrounding gas, the higher the system's sensitivity to velocity fluctuations. It is difficult to set the current supply at a fixed level to obtain a good resolution at high velocities without causing sensor

'burn out' in stagnant conditions. Secondly, as the heat transfer rate fluctuates, so does the temperature of the wire. This brings the aspect of thermal inertia into the problem, physically reducing the device's frequency response.

Improvements in the design of d.c. electronic components has resulted in the adoption of the constant temperature mode in preference. In this case the sensor resistance is fixed, and therefore by implication so is its mean temperature, and the thermal inertia effect is greatly reduced (but not entirely eliminated). The risk of 'burn out' at low or zero velocities is avoided while the sensitivity of the system is optimised by the selection of the highest practical filament temperature.

In laser Doppler velocimetry, a beam of laser light is split and focussed on a fixed position within the engine cylinder. Sub-micron particles are seeded into the gas flow and scatter light when passing through the point of focus. By counting interference fringes and analysing the Doppler shift in frequency of this light, it is possible to deduce the particle speed and resolve its direction of motion. A discrete measurement is thus obtained.

Again there are two modes of operation, forward and back-scatter. The former gives the highest signal to noise ratio, a greater intensity in collected scattered light resulting, but it requires the fitting of at least two glass or quartz windows in the clearance volume. Back scatter is more economic with respect to cylinder access, but at a great cost to signal quality. Due to the complexity of engine design it is the more common approach however.

The relative merits of the two systems in application can be listed as follows [25,87]:

HWA - Advantages

1. Purely analogue device giving a continuous signal. This enables the phase averaging of results. Its high frequency response permits time correlation and turbulent scale measurements.
2. Reliable, well established electronics. Output has a high signal to noise ratio.
3. Probes can be easily inserted into several postions in the combustion chamber.
4. Inexpensive, costing one tenth of an LDV system.

HWA - Disadvantages

1. Directional insensivity. Even with three-wire probes the measured velocity can come from any octant.
2. Measurements are gas property dependent.
3. Combustion incompatibility. Probes too delicate to withstand a combusting environment and the provision of a sufficient temperature excess to measure gas velocities is impossible with present wire materials.
4. Flow perturbing. Careful design of supports necessary to avoid the undue distrubance of the gas flow being measured.
5. Probes are physical devices requiring calibration. It is impractical to perform this task throughout the property range anticipated.

LDV - Advantages

1. Absolute measurement of velocities, although there are some problems in matching the statistics of seed

particles to the fluid mechanics of the flow (the number of particles passing through the measurement volume increases with gas velocity).

2. Combustion compatible. Can take measurements in a firing engine.
3. Non perturbing.
4. Calibration free, although much faith must be placed in a series of 'black boxes'.

LDV - Disadvantages

1. Intermittent signal. Relying upon a seed particle passing the focal point at a given time. Problems in synchronising data from separate cycles result.
2. Optical access necessary. Some researchers have opted for a side value design with a perspex cylinder head, (e.g. [25,66]) which is not typical of modern production engines.
3. Necessary to process a very high frequency signal (tens of MHz).
4. Low signal to noise ratio. The fouling of access windows by oil and soot, interference from combustion generated emissions and scatter from multiple particles add to the deterioration in the system's response.
5. Difficulty in maintaining a seeding of monodisperse sub-micron particles of adequate distribution and concentration.
6. Expensive. Costing ten times that of hot wire system.

Apart from the compelling argument of cost, it is consistent with the aim of this study to choose a system

with an analogue output for the measurement of turbulence and spatial velocity gradients at the spark plug location and in the main combustion chamber. The latter requirement especially dictates synchronisity in the acquisition of data and although there are means of phase averaging discrete LDV readings (see Rask [66,67,68], the benefit in obtaining the initial absolute value may easily be lost.

Three critical problems in hot wire anemometry must be reconciled before it is adopted for use in an engine. Namely:

1. The property dependence of the measurements must be tackled by taking pressure and temperature data for subsequent use in a result processing procedure.
2. The uncertainty in gas flow direction must either play little part in any conclusions drawn, or be overcome by making simplifying assumptions relating to the hot wire probe position and orientation.
3. A direct cause and effect type of analysis (see Cole and Swords [23] for example) is not possible because of the combustion incompatibility. Therefore the results from a large number of mutually exclusive fired and motored engine tests must be related statistically.

Point 1. above is also of importance when a probe calibration obtained in ambient conditions is to be adopted in the processing of in-cylinder data. There appears to be little agreement amongst authors on a correct procedure to exploit and the form of data analysis finally chosen is discussed in the next section. The remainder of this chapter is concerned with the design and signal interpretation of the transducers that

are subsequently used for the anemometric and gas property measurements.

2.2 Calculation of a Heat Transfer Rate Between a Filament and a Gas Fluctuating Properties.

Hot wire measurements in ambient conditions are frequently based upon King's Law [47], which can be written in the form;

$$W = A + B\,V^{1/2} \qquad (2.1)$$

where

W = wire heat loss (W)

A,B = convection constants (functions of temperature and diameter)

V = gas velocity (m/s)

The relationship evolves from the assumption of a frictionless, incompressible fluid describing a potential (irrotational) flow. The experimental apparatus consists of a small diameter (in the order of millimetres) heated platinum wires mounted on a rotating arm.

The above equation can be translated into a form that accounts for differences in ambient temperatures and wire diameters such that:

$$Nu = A + B\,Re^{c} \qquad (2.2)$$

where

Nu = Nusselt number (hd/k)

Re = Reynolds number ($\rho vd/\mu$)

A,B,c = empirical constants (c = 0.5)

h = heat transfer coefficient (W/m^2K)

d = wire diameter (m)

k = gas thermal conductivity (W/mK)

ρ = gas density (kg/m^3)

V = gas velocity (m/s)

μ = gas viscosity (kg/ms)

The use of a rotating arm avoids some of the limitations of the wind tunnel designs of the day, but a susceptibility to draughts and the entrainment of ambient air by the whirling mechanism biases the results thus obtained. Compounded to this, several factors are side-stepped by King's analysis. The description of potential flow only applies to small Reynolds numbers. At lower velocities the heat transfer is buoyant rather than forced and beyond the potential case a boundary layer develops around the wire. The temperature at which properties are evaluated requires clarification and in non-ambient conditions other modes of heat transfer may prove important.

To formulate a truly general convective heat transfer relationship the Prandtl number (Pr) should also be included. For air Pr varies by less than 2% in the range of 0-1800°F and therefore it is not explicitly used here. Choices of a temperature at which to evaluate properties include:

T_w - wire surface temperature

T_g - gas temperature

T_f - film temperature (= $(T_w + T_g)/2$)

T_{lm} - logarithmic mean temperature.

Douglas and Churchill [30] state that as there is no theoretical justification for any of the above approaches, the choice should be based on the success and convenience of the correlation. The range of applicability of a calibration will depend upon the nature of the flow over the heated filament.

The above authors noted its development with increasing gas velocity as follows:

1. For Re < 1.0, potential flow is approached.
2. As the Reynolds number increases, the boundary layer separates from the wire surface at about 80° from the forward stagnation point, and standing eddies form at the rear half of the cylinder.
3. At a Reynolds number of approximately 1000, eddies shed periodically and a turbulent wake is formed. With very high velocities the boundary layer itself becomes turbulent and the point of separation shifts towards the rear of the cylinder.

The empirical formula thus arising attempts to combine the laminar and turbulent components of heat transfer:

$$Nu_f = 0.46\ Re_f^{1/2} + 0.00128\ Re_f \qquad (2.3)$$

The dominance of the latter term increases with velocity and the f subscript denotes the use of a film temperature for the evaluation of properties. This relationship has been found to work well for $Re_f \geq 500$.

Richardson [72] follows a similar tack with the relation:

$$Nu = 0.3737 + 0.37\ Re^{1/2} + 0.057\ Re^{1/3} \qquad (2.4)$$

This covers a range of $1.0 < Re < 10^5$, although the temperature at which properties are measured is not given.

Relationships of the form $Nu = A + B\ Re^c$ can be used within a more limited range of Reynolds number however, where a change in the flow regime does not occur. Two approaches here are possible. Either the above form is used directly, as

proposed by McAdams [57] or Davis and Fisher [28], or a loading factor as chosen by Hilpert [42,57] or Collis and Williams [24] is explicitly included to account for the temperature jump between the surrounding fluid and the sensing wire. These four correlations are listed below:

i) McAdams

$$Nu_f = A + B\left[\frac{dG'}{\mu_f}\right]^c \tag{2.5}$$

where

G' = mass velocity of fluid ($\rho_g V$)

and

$dG'/\mu f$	c	A	B
0.1-1000	0.52	0.32	0.43
1000-50,000	0.60	0	0.24

ii) Davis and Fisher (as interpreted by Witze [87])

$$Nu_w = 0.425\ Re_g^{1/3} \tag{2.6}$$

where subscripts w and g denote the use of wire and gas temperature for property evaluation respectively.

iii) Hilpert

$$Nu_f = B\left[Re_f\left[\frac{T_w}{T_g}\right]^{0.25}\right]^c \tag{2.7}$$

where (T_w/T_g) = Hilpert's temperature loading factor

and

Re_f	B	C
1-4	0.891	0.330
4-40	0.821	0.385
40-4000	0.615	0.466

iv) Collis and Williams

$$Nu_f \left[\frac{T_f}{T_g}\right]^{-0.17} = A + BRe_f^c \qquad (2.8)$$

where (T_f/T_g) = Collis and Williams temperature loading factor

and

Re_f	A	B	C
0.02-44	0.24	0.56	0.45
44-140	0	0.48	0.51

The above relationships show a variety in the selection of property evaluation temperature combinations. In considering non-convective heat loss, Davis and Fisher deliberately designed probes with a low aspect (length/diameter) ratio, and investigated a one-dimensional relation to account for the conduction of heat to the wire supports. Collis and Williams avoided the issue by using an aspect ratio in excess of 2000. Generally the heat loss by radiation and the temperature gradients across the diameter of the fine wires used for anemometry are considered to be negligible.

A change in correlation in the Reynold's number range of 40-44 has been noted. This has been attributed by Collis and Williams [24] to the development of a Von Karmen type vortex street in the wake of the wire when Re exceeds this range.

The area of interest here is generally described by $0.02 < Re < 44$. The form of correlation to be chosen and the temperature at which properties are to be evaluated remain unresolved at this stage.

Bradbury and Castro [17] noted a 2:1 difference in the evaluated Nusselt number (calculated on a common basis) from the relationship of Davis and Fisher, when compared to Collis and Williams, with a wire temperature excess of 20°C. The results coincided for an excess of 600°C, but this is unattainable at compression TDC in motored engine tests. By measuring the sensor time response it appears that the Collis and Williams relationship is the most representative, but a property evaluation temperature weighted move towards that of the surrounding fluid would be more suitable.

Probably the best way to conclude the discussion is to compare HWA results to the competing and less disputable data as obtained by laser Doppler velocimetry. To this end Witze [87], using a side valve engine developing a strong swirling flow with little cycle-to-cycle variation and known direction of motion, compared with LDV results with those from hot wires with a temperature of 350, 500 and 650°C

The conclusions reached were:

1. Properties should be evaluated at the fluid temperature.
2. Conduction-to-support losses should be included by using the method proposed by Davis and Fisher, with the

supports being considered to remain invariantly at room temperature. (In practice the temperature of the prongs was found to sluggishly lag that of the bulk fluid, but its inclusion in the analysis proved detrimental).

3. Convection is to be evaluated with a relationship of $Nu = A + B\ Re^{c}$. It was found that "c" varied from 0.24 to 0.47 in calibration, but by fixing it at a value of 0.45, as per Collis and Williams, indistinguishable results are obtained.

Corkhill, Bullock and Wigley [25] in performing similar tests concurred with Witze in all respects, except that the addition of a Collis and Williams type temperature loading factor improved the agreement of HWA with LDV.

As a postscript to the above, in a later paper by Tindal, Brown and Kyriakides [82], probes were calibrated at both ambient conditions and at fluid temperatures up to 450°C and pressures up to 15 bar. The relationship thus obtained gives:

$$Nu_f \left[\frac{T_f}{T_g}\right]^a = A + B\ Re_g^{\ c}$$

where a = 0.5.

The 'correct' calibration procedure is therefore still the subject of some debate, but as the output from LDV is widely respected, the conclusions drawn by Corkhill, Bullock and Wigley [25] have been adopted.

Finally the point of the onset of buoyant rather than forced convective heat transfer requires some consideration. Van der Hegge Zijnen [84] provides an interesting approach in

vectorially combining the two modes to find the dominant component. A more straightforward criterion is provided by Collis and Williams [24], who state that buoyancy effects will be small providing:

$$Re_g > Gr_g^{1/3} \qquad (2.10)$$

where Gr = Grashof number

$$= \frac{g\beta(T_w - T_g)d^3\rho_g}{\mu_g^2}$$

and g = acceleration due to gravity (m/s^2)

β = gas volume coefficient of expansion ($= 1/T_g$).

This criterion is dependent upon the wire orientation with respect to the horizontal, vertical wires being less sensitive to buoyant effects.

2.3 Introduction to Motored Engine Data Processing

The details of the data acquisition system are discussed in Chapter 3, however the application of HWA to a situation with varying gas properties and the processing calculations involved are outlined in this section.

In-cylinder pressure is measured by the use of a piezo-electric transducer and associated charge amplifier, as detailed in Chapter 3. The result thus obtained is relative rather than absolute. To overcome this problem the approach adopted by Lancaster, Krieger and Liensch [49] is used, where the value obtained at the intake stroke bottom dead centre is shifted so as to equal the mean pressure of the inlet manifold. The associated argument is that at this point the piston has stopped moving, the exhaust valve is closed and the partially open intake valve sees little pressure drop or flow. Wave

effects in the manifold may invalidate this assumption but the intake system used here is of large bore and is not tuned to give a ram effect.

Having found the pressure, a measurement of the surrounding gas temperature is necessary to convert the hot wire's power dissipation into a velocity reading. This may seem superfluous in a motored I.C. engine, where a knowledge of the enclosed volume and measured pressure are sufficient to calculate the bulk fluid temperature during the closed part of the cycle. However near to the cylinder boundaries the gas will experience local heating or cooling effects, depending upon the mean fluid temperature relative to the walls, introducing the following problems:

1. An element of 'temperature turbulence' is introduced as gas from different regions mix.
2. During the intake stroke especially, measurements will be location dependent (see Witze [87]).
3. At compression top dead centre, errors in gas temperature will be large relative to the overheat of the hot wire sensing element.

Semenov [77] developed a purely analogue system for motored engine applications where anemometer signals are processed directly with the output from a pressure transducer and a resistance thermometer. A similar approach is adopted here by mounting a 'hot' (anemometer) and a 'cold' (resistance thermometer) sensing filament on parallel supports in close proximity. Due to the sensor's thermal inertia the temperature of the thermometer will lag that of the surrounding fluid during the compression stroke and lead during expansion. To

measure the resistance a Wheatstone bridge is used, and although the deficit in the energy balance will be provided in part by a small degree of electrical heating, the principle source will be convective. When processing 'hot' and 'cold' wire data the solution of simultaneous equations will be necessary because the gas velocity cannot be found without knowing its temperature, and vice versa.

The same probes designs are then used to seek a direct measurement of the spatial velocity gradients within the engine cylinder. In this case both filaments are used as hot wire anemometers and due to the confines of the access into the E6 cylinder head and the delicacy in assembling the probes, the addition of a third wire to be used as a resistance thermometer has been rejected. Instead the ensemble averaged results from a previous hot/cold wire experiment are used to provide the temperature values to calculate the two sets of velocities. To improve the repeatability from test to test, the bulk accumulation of heat within the engine block is discouraged by monitoring the temperature of the continuously circulating cooling water. The sensitivity of the twin hot wire results to the local in-cylinder temperature fluctuations that remain however is discussed in Section 5.3.

2.4 Design of Anemometer Probes

Figure 2.1 shows the geometry of the cylinder head spark plug and pressure transducer access ports. Figure 2.2 illustrate the probe designs employed in the current study and Figures 2.3-2.4 details the resulting wire locations. Both probes consist of an outer body which screws into the spark plug port of the cylinder head, and a removable brass insert.

Previous projects, Al-Sudani [2] for example, have used modified spark plugs as a basis for their probe design. However the aforementioned assemblies were built with three criteria in mind, namely:

1. Machining time is reduced by the manufacture of a single outer body and several relatively simple inserts.
2. In the case of the 'flush' probe, correct orientation is retained by fitting the outer body with the cylinder head removed and by locating the insert by means of a key slot.
3. Removal and refitting of the insert is relatively easy, aiding the necessary frequent replacement of the fine sensing filaments.

In association with point 2. above, flushness was achieved by milling the initially proud probe holder and insert(s) when fitted into the removed cylinder head. A remaining small cavity between the outer body and the head is filled with ' 24-hour Araldite'.

The aim is to take gas flow measurements both in the spark plug cavity and in the main body of the cylinder. Ideally both designs should take the form of a standard spark plug with wire supports incorporated. This is difficult to achieve in practice and the designs in Figure 2.2 represent a compromise between the measurement of realistic results and ease in manufacture. When taking readings from the main combustion chamber it would also be more appropriate to use the plug cavity probe with longer wire supports. However vibration is a problem, the filaments having little strength of their

own, and therefore it is desirable to minimise the length of exposed needle. The flush design in Figure 2.3 thus can be said to be of use in taking measurements of the main in-cylinder flow in the absence of an interference from the plug cavity.

The supports are standard sewing (darning) needles. Such a choice may appear unscientific, but needles have several inherent features other than cheapness and availability that lend them to this application. They are stiff, tapered and have a smooth surface finish. The sensing wires readily spot-weld to their points and the eye at the opposite end provides a good key for the soldering of connecting cables. 1 mm diameter (Nu (80%) - Cr (20%) wire has been tried as an alternative, but difficulties in spot-welding and soldering were encountered.

A drilled nylon core serves to initially space the needles before the remainder of the brass insert cavity is packed with '24 hour Araldite'. A mild interference fit between the inner and outer body and concentricity in the machined surfaces prevents gas leakage. This is important if erroneously high turbulence levels are not to be measured.

Figure 2.5 shows some photographs illustrating the steps involved in the construction of the flush probe inserts. A perspex jig is constructed in two halves. The upper part serves to locate the brass body and drilled holes in the lower section give the desired spacing and length of exposure of the needles.

The choice of wire diameter will necessarily be a compromise between strength and thermal inertia, both of which increase with thickness. The specification of suitable wire

materials available from Dantec (previously known as DISA), one of the principal manufacturers of hot wire equipment, are listed in Tables 2.1 and 2.2 below [27,74]:

Table 2.1: Wire Temperature Coefficients of Resistance and Possible Operating Temperatures

Material	Diameter (μm)	α	ΔT with 100% overheat
Platinum-plated tungsten (W)	2.5	0.0036	278
	5.0	"	"
	9.0	"	"
Platinum (80%)-Iridium (20%) (Pt-Ir)	10.0	0.0007	1429
Platinum (90%)-Rhodium (10%) (Pt-Rh)	10.0	0.0016	625

where

α = quoted temperature coefficient of resistance (K^{-1})

$\Delta T = (T_w - T_o)$, (K)

ΔT is obtained from the relation

$$R_w = R_o \ (1 + \alpha \ (T_w - T_o)) \qquad (2.11)$$

where

R_w = mean wire operating resistance (ohms)

R_o = measured wire resistance at T_o (ohms)

T_w = mean wire operating temperature (K)

T_o = reference temperature at which resistance is measured (K)

Table 2.2: Further Wire Material Properties

Material	Specific Heat Capacity (J/Kg°C)	Resistivity (ohm metres)	Density (Kg/m3)	Thermal Conduct (w/mK)
W	137.94	7×10^{-8}	19,300	178
Pt-Ir	133.76	32.04×10^{-8}	21,610	25.5
Pt-Rh	147.97	18.92×10^{-8}	19.950	50.1

A DISA type 55M anemometer system used at the start of this study, requires the setting of R_w explicitly to obtain the desired mean wire operating temperature. The bulk of the experimental work has been performed with a PSI model 6110 unit however where the percentage overheat ($((R_w/R_o) - 1) \times 100$) is the input parameter.

The desired hot wire temperature here is in the order of 500-600°C. The possible range for R_w with the DISA anemometer is 0-99.99 ohms. Nine micron platinum-plated tungsten wire was chosen for this bridge, principally because of the strength of the wire material. In spite of this attribute it has some limitations relative to the other materials quoted. Tungsten oxidises at a temperature of 450°C, although Benson and Brundrett [14] have reported success in its intermittent use in reducing atmospheres. The platinum plating should provide protection, but a hysteresis in R_o measurements found in practice is attributed to oxidation at the point of spot-welding to the supports. Its high thermal conductivity will increase the non-convective heat transfer component in the analysis of the anemometer signal, and the low resistivity poses problems in the selection of a balancing resistor in the

Wheatstone bridge circuit when used as a thermometer (see Section 2.6).

The PSI anemometer has an overheat setting range of 0-99%, and thus the maximum mean temperature attainable with tungsten wire is inadequate here. The Pt-Ir and Pt-Rh alloys, with their lower temperature coefficient of resistance, can be used with this limitation.

The platinum-iridium wire has a low thermal conductivity, but also a small temperature coefficient of resistance, which will limit the resolution obtained when used as a thermometer. Thus, in common with Horvatin and Hussman [44], platinum-rhodium has been selected as a wire material for the PSI anemometer bridge. In terms of its temperature coefficient of resistance, it represents a 'half-way house' between the other two examples, and its thermal conductivity is reasonably low. To obtain a consistent result however, the sensor must be electrically heated for a few minutes to anneal the material prior to the final calibration.

2.5 Anemometer Signal Interpretation and Processing

Figure 2.6 shows the basic design of a constant temperature anemometer bridge. Resistor R2 represents the sensing filament and the connecting cable (5 metres of co-axial lead plus extension wires). To measure the 'cold' resistance, the magnitude of R4 is adjusted to obtain balance in the bridge. Compensation for the connecting leads is achieved by replacing the sensing wire with a shorting probe, and adjusting a potentiometer in series with R4, again to obtain balance.

R1 is set at 50, and R3 initially at 500 ohms, and the arrangement is such that the right-hand resistors are ten times

in magnitude of those of the left. This reduces the overall current supply, increasing the system response. Overheat in R2 is obtained by shunting resistors across R3. When active, the feedback amplifier responds to an imbalance, E_b, by altering the supply voltage E_o. E_o is also the signal output of the anemometer.

The energy balance of the sensing wire is given by

$$q_e = q_h + q_c + q_r + q_s \tag{2.12}$$

where

q_e = electrical power supplied (all units for q are watts)

q_h = convected heat transfer rate

q_c = rate of conduction loss to supports

q_r = power loss by radiation

q_s = rate of heat storage by the filament.

In CTA mode q_s should be zero. This is not entirely true due to a change in temperature distribution with fluctuating gas velocities, but in considering other experimental uncertainties it can be neglected. Likewise, q_r is estimated to be small in the range of interest. The modified version of (2.12) is thus:

$$q_e = q_h + q_c \tag{2.13}$$

The supply of electrical power by the bridge to the wire is given by:

$$q_e = i_p^2 R_w \tag{2.14}$$

where

i_p = current through probe (amps)

R_w = resistance of the wire as its set operating temperature (ohms)

A negligible current will flow through the feedback amplifier circuit and thus the value of i_p is easily found from the anemometer output signal by:

$$i_p = E_o/(Rl + R_{ca} + R_w) \tag{2.15}$$

where R_{ca} = connecting cable resistance (ohms).

The Value R_w is obtained from the bridge overheat setting:

$$OVH = ((R_w/R_o) - 1) \tag{2.16}$$

where OVH = overheat setting (%).

To obtain the mean wire temperature when operating at R_w, the temperature coefficient terms α and β are used such that

$$R_w = R_o\ (1 + \alpha(T_w - T_o) + \beta\ (T_w - T_o)^2) \tag{2.17}$$

where

T_o = temperature (usually room) at which R_o is found (K)

T_w = mean temperature of operating wire (K).

Hence:

$$T_w = T_o + \frac{(-\alpha + (\alpha^2 - 4\beta(1 - R_w/R_o))^{1/2}}{2\beta} \tag{2.18}$$

On finding T_w, the convective heat transfer component can be found using a modified Collis and Williams equation (see Section 2.2):

$$Nu_g \left[\frac{T_f}{T_g}\right]^{-0.17} = A + B\ Re_g^c \tag{2.19}$$

where

$Nu_g = hd/k_g$

$Re_g = \rho_g Vd/\mu_g$

as defined previously. The properties with a subscript g can be found as empirical function of gas temperature and pressure. Viscosity is a function of temperature alone, and can be found from:

$$\mu_g/\mu^* = (T_g/T^*)^n \qquad (2.20)$$

where the subscript (*) denotes reference conditions. The value of the exponent 'n' is given by Perry [65] as 0.71 and Collis and Williams as 0.76. Using data given by Rogers and Mayhew [73] Table 2.3 serves as a source of comparison. Here $\mu^* = 1.846 \times 10^{-5}$ kg/ms for T* = 300 K;

Table 2.3: A Comparison of Empirical Air Viscosity Values

T_g(K)	$\mu \times 10^5$ (R + M)	$\mu \times 10^5$ n = 0.71	% Diff.	$\mu \times 10^5$ n = 0.76	% Diff.
250	1.599	1.622	1.4	1.607	0.5
350	2.075	2.059	-0.75	2.075	0
450	2.485	2.461	-0.99	2.512	1.10
550	2.849	2.838	-0.36	2.926	2.7
650	3.178	3.196	0.57	3.322	4.5

In the range of interest, namely 300-650K, Perry's exponent appears to give the best results.

In common with viscosity, the gas thermal conductivity is a function of temperature alone. Two types of relationship are

tested here. Firstly a form similar to equation (2.20), namely:

$$k_g/k^* = (T_g/T^*)^n \qquad (2.21)$$

and secondly an equation proposed by Kannuluik and Carman [46] converted to Si units:

$k_g = 5.277 \times 10^{-4} (10.197\ T_g) - 19.58 \times 10^{-5}\ T_g^2) - 1)$ (2.22)

For equation (2.21), Perry gives n = 0.86, and Collis and Williams n = 0.8. A value of 0.815 appears to correlate with Rogers and Mayhew's data more effectively, as shown in Table 2.4:

Table 2.4: A Comparison of Empirical Air Thermal Conductivity Values

Tg(K)	k x 10^2 (R + M)	k x 10^2 n = 0.86	% Diff.	k X 10^2 (K + C)	% Diff.	n = 0.815	% Diff
250	2.227	2.243	0.72	2.229	0.01	2.262	1.6
350	3.003	2.996	-0.2	2.965	-1.3	2.975	-0.92
450	3.710	3.719	-0.23	3.600	-3.0	3.652	-1.57
550	4.357	4.419	1.4	4.133	-5.0	4.300	-1.3
650	4.954	5.102	3.0	4.566	-7.8	4.928	-0.5

Here, $k^* = 2.624 \times 10^{-2}$ W/mK and $T^* = 300$ K.

Gas density can be evaluated also from reference conditions.

At 300 K and one atmosphere pressure, $\rho^* = 1.177$ Kg/m^2. Thus,

$$\rho_g = 1.177\ (P/1.01325 \times 10^5)(300/T_g)$$

$$= 3.485 \times 10^{-3}\ (P/T_g) \qquad (2.23)$$

where P = absolute pressure (N/m^2).

Knowing T_g, the unknowns remaining in (2.19) are the gas velocity, 'V' (to be found) and the heat transfer coefficient 'h'. In the absence of conduction losses to the supports:

$$q_e = hA_s(T_w - T_g) \tag{2.24}$$

where A_s = wire surface area (m^2)

$= \pi d \iota$

ι = length of wire between supports (m).

However if the conduction loss is to be incorporated into the procedure, 'h' is not so directly defined. A proof of one-dimensional analysis proposed by Davis and Fisher is given in Appendix A. The equations resulting are:

$$C_1 = \frac{2T_s \tanh (C_2^{1/2} \iota/2) - T_w \iota C_2^{1/2}}{2\tanh (C_2^{1/2} \iota/2) - \iota\, C_2^{1/2}} \tag{2.25}$$

where T_S = support temperature (K)

$$C_2 = \frac{4}{k_w d}\left[h - \frac{i_p^2 \alpha\, R_o}{\pi d \iota}\right] \tag{2.26}$$

where k_W = wire thermal conductivity (W/mK)

$$C_2 = \frac{4}{C_1 k_w d}\left(\frac{i_p^2 R_o\,(1 - \alpha\, T_o)}{\pi d \iota} + h\, T_g\right) \tag{2.27}$$

$$h = \frac{C_2 k_w d}{4} + \frac{i_p^2 \alpha R_o}{\pi d \iota} \tag{2.28}$$

To solve (2.28), an iterative procedure is necessary. This can be summarised as follows:

i) Estimate h from (2.24)

ii) Find C_2 from (2.26)

iii) Find C_1 from (2.25)

iv) Find C_2 from (2.27)

v) Find h from (2.28)

vi) Seek convergence in h. If this is not attained, go to step (iii). The above equations contain α, but not β. To find an equivalent value, α', for the mean operating temperature in question:

$$\alpha' = \alpha + \beta (T_w - T_o) \tag{2.29}$$

Equation (2.19) can now be solved to give velocity by rewriting it in the form:

$$Nu' = Nu_g \left[\frac{T_f}{T_g}\right]^{-0.17} \tag{2.30}$$

and

$$V = \left[\frac{Nu'-A}{B}\right]^{1/c} \left[\frac{\mu_g}{\rho_g\ d}\right] \tag{2.31}$$

2.6 Resistance Thermometer Signal Interpretation and Processing

Figure 2.7 shows the basic circuit of the 'quarter' bridge used. A constant voltage, E_{bd}, is applied across points B and D. The out-of-balance voltage, E_{ac}, is amplified and shifted to give the desired output signal range. Dummy resistors R_{D2} and R_{D3} are set to 2,000 ohms. R_{D1} is ten ohms, which is comparable to the resistance of most of the platinum-rhodium probes used in this study (for tungsten R_{D1} = 2.66 ohms).

The connecting cable resistance can readily be evaluated by using a digital voltmeter across points A and D, B and A, such that:

$$R_{ca} = (E_{ad}/E_{ba})R_{D3} - R_o \tag{2.32}$$

where,

E_{ad} = voltage from point A to D

E_{ba} = voltage from point B to A

The output signal can be regarded as:

$$E_{op} = GE_{ac} + S \tag{2.33}$$

where

E_{op} = amplifier bridge voltage (volts)

E_{ac} = voltage from A to C (volts)

G = amplifier gain (volts^{-1})

S = amplifier shift (volts)

E_{ac} is given by

$$E_{ac} = E_{bd}\left[\frac{R_p}{R_p + R_{D3}} - \frac{R_{D1}}{R_{D1} + R_{D2}}\right] \tag{2.34}$$

where

$R_p = R_w + R_{ca}$

R_w = resistance of thermometer wire (ohms)

If: $C_3 = (E_{op} - S)/GE_{bd}$

$R_{D121} = R_{D1}/(R_{D1} + R_{D2})$

then,

$$R_w = R_{D3}\left[\frac{C_3 + R_{D121}}{1 - (C_3 + R_{D121})}\right] \tag{2.35}$$

Having found R_w, the mean thermometer wire temperature, T_w can be found from equation (2.18).

To generally define the heat balance of the wire, equation (2.12) can again be used. However to simplify the analysis the approach is slightly different here.

The temperature of the thermometer will always be less than the HWA case, so q_r can be confidently set to zero. The conduction loss term, q_c, is difficult to evaluate in this situation because of the power storage, q_s, is not negligible. To use the analysis in Appendix A, the rate of heat storage as a function of distance along the wire needs to be known. This in turn requires a knowledge of the time variation in gas temperature, which is itself the subject of the investigation. Benson [14] has assumed a sinusoidal dependence for his temperature measurements.

The principal mode of heating is convective rather than electrical and the filament itself will be cooler relative to its supports than that of the anemometer. Thus a shallow temperature gradient at the ends of the wire is anticipated, reducing q_c. (If in a sensitivity analysis the conduction loss is to be investigated, a parabolic distribution of temperature, as assumed by Horavatin and Hussmann [44] can be adopted). The simplfied version of equation [2.12] becomes:

$$q_e = q_h + q_s \tag{2.36}$$

A lumped heat balance approach is taken, considering q_h and q_s in terms of the mean filament temperature. The power storage component hence is given by:

$$q_s = \frac{\pi d^2}{4} \iota \rho_w \, Cp_w \, \frac{dT_w}{dt} \qquad (2.37)$$

where

ρ_w = density of wire material (Kg/m^3)

Cp_w = heat capacity of material (J/Kg K)

t = time (seconds)

The electrical heating term is found in the same manner as that of the anemometer, using equation (2.14). Since there is no current flow between points A and C on Figure 2.7,

$$i_p = E_{bd}/(R_{D3} + R_w + R_{ca}) \qquad (2.38)$$

The rate of convective transfer is again covered by equation (2.19), but in this case the gas temperature rather than velocity is to be found. Here a problem arises in that the properties used are themselves temperature dependent, hence an iterative approach is necessary. To this end updated estimates of the temperature are used until convergence in T_g is achieved.

In the absence of conduction losses, the heat transfer coefficient 'h' is directly defined by:

$$q_h = hA_s \, (T_w - T_g) \qquad (2.39)$$

By modifying equation (2.19):

$$h = (A + B \, Re_g^c) \left[\frac{T_f'}{T_g'}\right]^{0.17} \frac{k_g}{d} \qquad (2.40)$$

where T_f', T_g' and all properties are found from previous estimates of T_g. Combining equations (2.36) and (2.39),

$$T_g = T_w + (q_s - q_e)/(h\ A_s) \qquad (2.41)$$

2.7 Motored Pressure Record Evaluation

Figure 2.8 illustrates the piezo-electric transducer and its carrier prior to mounting in the indicator port of the cylinder head. The cooling achieved by passing tap water through the pipes shown, serves to protect the sensor and to maintain a steady output signal. The associated charge amplifier has a variable gain and a grounding facility to compensate for signal drift. Drifting is also reduced by the adjustment of the amplifier itself and by the periodic cleaning of the connecting cable. A switchable time constant is set for 'short' to monitor transient pressures, and 'long' for calibration.

The form of relationship obtained is,

$$P = A_0 + A_1\ E_p \qquad (2.42)$$

where

E_p = output from charge amplifier (volts)

P = relative pressure (N/m^2)

A_0, A_1 = calibration constants

The mean inlet manifold pressure, chosen as the point of reference, is evaluated by:

$$P_{ref} = (1.01325 \times 10^5 P_b/760) - (P_m \times 2.54 \times 10^{-2} \times 9.81 \times 1000) \qquad (2.43)$$

where

P_{ref} = reference pressure (N/m^2)

P_b = ambient barometric pressure (mm Hg)

P_m = measured mean manifold depression (inches of water).

This is equated to the reading obtained at inlet bottom dead centre to obtain a 'pressure correction factor' such that:

$$P_{cf} = P_{ref} - (A_0 + A_1 E_{bdc}) \quad (2.44)$$

where

P_{cf} = pressure correction factor (N/m^2)

E_{bdc} = output obtained at inlet bottom dead centre (volts)

Hence, subsequent absolute values are obtained from:

$$P_{abs} = P_{cf} + A_0 + A_1 E_p \quad (2.45)$$

2.8 Summary

Hot wire anemometry is the selected method of continuous, analogue gas velocity measurement. To this end probes with parallel sensing elements are designed to measure flows both in the main cylinder clearance volume and in the spark plug cavity.

To account for local variations, a separate measure of temperature is to be taken for some of the tests. A relative value of bulk pressure is referenced to absolute conditions by the use of the mean inlet manifold depression. An analysis proposed by Corkill, Bullock and Wigley [25] is used to find gas velocity, whereas a lumped heat balance is adopted to find the free stream temperature which is then used to calculate the gas properties in an iterative solution procedure.

CHAPTER 3

HIGH SPEED LOGGING EQUIPMENT, SENSOR CALIBRATION AND DATA PROCESSING

3.1 Introduction

The concern of this Chapter is the acquisition of in-cylinder anemometric data and the calibration of the associated transducers. The scale to which the former is related is one of crank angle rather than time. The system developed is built around an 'Apricot P.C'. micro-computer, which is used principally to program peripheral devices and act as a temporary store for the gathered results.

The Apricot has been marketed mainly as a business machine to rival the 'IBM P.C'., however features which lend it to the present application include a 16-bit '8086' micro-processor and twin large capacity $3^1/_2$ inch, 720 Kbyte disk drives. In common with the IBM, a 'Microsoft' disk operating system and Basic programming language are used. For the latter, the 8086 is treated as though it were an 8-bit processor, limiting the computer's potential in some respects. However 16-bit data acquisition is possible.

The size of the system memory is 256 Kbytes, but not much of this is directly accessible. Of the two languages supplied, namely 'MS' and 'GW-Basic', the available programming memory is 60 and 44 Kbytes respectively. At a small cost in sophistication, the former is used generally. Where necessary, programs are compiled to give a three to ten times increase in processing speed. A 'GSX' graphics package is used to give a graphical output on either the computer screen or a dot matrix printer.

The computer mother-board has three expansion slots, all of which are used. The first is taken by a 512 Kbyte memory extension card. Again this cannot be accessed directly by a Basic program, and is used instead as a 'RAM' disk'. The second and third slots are taken by data logger interface circuits, one of which is of concern in this Chapter.

A separate logging unit is used to collect data from the cylinder transducers. Although the Apricot potentially has three disk drives and a reasonable amount of programmable memory, the total storage space and processing speed are inadequate to handle the large quantities of data thus obtained. The solution is provided by connecting the P.C. to the University 'IBM 3083' mainframe computer, via a 'Gandalf' serial link. The facilities offered by the 3083 of interest here include the use of a large (expandable) disk storage area, faster processing times and the ability to dump data to tape or to 'archive' files that are not of immediate use. The availability of many system routines also reduces the depth of application - specific programming in some cases.

The remainder of this Chapter is devoted to the description of the logging equipment used and its application with respect to the theory in Chapter Two. The handling and storage of results thus obtained is also discussed.

3.2 The High Speed Logging Equipment

i) Data Acquisition

Figure 3.1 illustrates a block diagram of the 'Microlink' data acquisition system assembled to monitor the output from the cylinder head transducers. A controller, time base '(TB)'

and three transient capture '(CH12)' modules are slotted into a Microlink 'MF18' mainframe. Connection to the Apricot microcomputer is achieved via an 'IEEE-488' parallel interface card and cable. The programming and polling procedure is summarized in Appendix D. The specification of the latter units is summarised below:

Module	No. of post-trigger samples	Memory Size (16-bit words)	Max.Clocking rate (KHz)	Max. Input signal (Volts)
TB	960K	-	1,000	(TTL)
CH12/16	_	16K	50	0-10, ± 5
CH12BEM	_	128K	125	0-10, ± 5

The CH12 units consist of an on-board memory and a programmable gain amplifier, coupled to a 12-bit A-D converter. A sample is taken each time a clocking pulse is sent by the timebase. The structure of the memory is such that it acts like a 'merry-go-round'. It will start storing data at any position, and will continue until the timebase pulses cease. This makes it possible to use a CH12/16 in conjunction with CH12BEM modules, provided that the CH12/16 clocking rate is not exceeded (no damage is caused to the former if it is though).

The timebase is configured universally to operate with an external clocking signal, to avoid the repeated use of an internal switch, and a software or hardware trigger. For the former and latter, the input must be TTL compatible with a pulse duration of at least two microseconds.

Sample pulses are sent from the timebase in blocks, the size and number of which range from 512 to 64K and 0-15 respectively. If the full 128K of CH12BEM memory is not filled by this specification, pre-trigger data will be taken. The configuration used here is as follows:

Size of blocks (hardware setting)	=	16,384
No. to be taken (software programmable)	=	8
Total no. of post-trigger samples	=	128K

This means that the memory pointer cycles once in the CH12BEM units, and eight times in the CH12/16.

The 12-bit A-D resolutions corresponds to an integer data range of 0-4095. The bipolar setting is used for the in-cylinder pressure measurements, and the unipolar mode for the anemometer and resistance thermometer. The potential dividers added serve to rescale the input, should it exceed the ten volt limit. To convert the resulting data into a voltage reading

$$E_o = \frac{\text{Pset} \times Y\%}{409.5} \qquad (3.1)$$

where E_o = transducer output signal (volts)

Pset = potential divider setting

= E_o/E_i

E_i = signal measured by logger (volts)

= Y%/409.5

Y% = a logged 16-bit data word

ii) Clock and Trigger Source

To calibrate transducers, a signal generator connected to the time base clock input gives 10 kHz TTL pulses of 10

microsecond width. For in-cylinder measurements however, the output from a crank shaft mounted Ferranti '23L47/M116' optical encoder gives an angle of rotation related time base. Figure 3.2 illustrates an encoder interface (MEE13007), that has been built by the Department to process the Ferranti output. It has been specifically designed to permit the repeated logging of data from a crank angle 'window' in the complete engine cycle.

Four inputs, A, $\overline{A}$, B and $\overline{B}$ are taken from the shaft encoder. Each line carries 900 pulses per revolution, but the signal on B is ninety degrees out of phase with that on A. Thus by using each rising edge, 3600 pulses per revolution can be derived, giving an angular resolution of 0.1 degrees. Divide-by-two and divide-by-five circuits can be used to reduce this to 0.2 or 0.5 degrees.

A further input is a top dead centre reference. It is possible to log one window per revolution, or one per cycle, depending upon the TDC pulse rate and phase (to select the first or second cycle revolution). The decade units count down from the reference and clocking pulses can be obtained from inside or outside the 'start' and 'stop' settings (the two being inclusive or exclusive respectfully). The TDC reference must lie outside the window selected.

As the Microlink logger begins to take data on the first post-trigger clocking pulse, the signal from the 'stop' counter is used to initiate the acquisition process. All subsequent triggers are ignored.

iii) Hot Wire Bridges

The majority of the in-cylinder velocity measurements have been taken with a Prosser '6110' anemometer system, a block diagram of which is shown in Figure 3.3. Two '6110' hot wire bridges share a common '6170' power supply. A '6152' twin meter display unit gives a visual check of the bridge output voltages for steady state tests, and an immediate indication of wire breakage. As the measurements are taken principally in non-ambient conditions, voltage linearisers and signal conditioners have not been purchased.

Having compensated for the five metres or so of connecting co-axial cable, the resistance of the sensing wires can be measured within a range of 0-99.99 ohms. The sensor overheat is then set, according to equation (2.16), between 0 and 99%. A non-resistive impedance of the hot wire and associated cables will affect the response of the feedback amplifier shown in Figure 2.6. Compensation is achieved by placing an operating probe in a steady air flow and superimposing an electrical pulsed disturbance on the input signal, representing a step change in velocity. The bridge is adjusted until a sharp input signal, with a minimum of spurious oscillations, is observed on an oscilloscope. The maximum pulse frequency is 30 kHz, and the anemometer response limit is 200 kHz.

iv) Resistance Thermometer Bridge

A Fylde 'FE-492-BBS' bridge conditioner and 'FE-254-GA' differential pre-amplifier are used for resistance thermometer measurements. Figure 3.4 illustrates the bridge circuit board, which has been modified by the removal of 'R_{zero}' and 'R_{offset}'

to give the layout in Figure 2.7.

The '1/4 bridge' is configured in constant voltage mode 'E_{bd}' being set to ten volts generally. The dummy resistors, 'R_{D1}', 'R_{D2}' and 'R_{D3}' were obtained from the 'Holdsworthy' company, and have the following specifications:

R_{D1} = 10 ohms, tolerance = 0.1%
temp. coeff. = 50 ppm
type = H8

R_{D2},R_{D3} = 2 KO, tolerance = 0.16%
temp. coeff. = 15 ppm
type = H8

The amplifier has coarse and fine gain and signal shift adjustments, which are set to give a reasonable resolution in the 0-10 volt range. The upper frequency limit is 40 kHz. A Solartron 'LM1420.2' digital volt meter is connected to help with range setting, calibration and sensor breakage detection.

v) Pressure Transducer and Amplifier

In-cylinder pressure measurements are taken with a Kistler model '601A' piezo-electric transducer fitted to a '628B' water-cooled carrier. The output signal is taken from a model '566' charge amplifier with a switchable gain in the range of 0.05 to 100 mV/Cb. 10 to 20 mV/Cb is generally selected to give a satisfactory ± 5 volt bipolar output. The frequency range is d.c. to 150 kHz, and a long or short time constant is switchable for calibration and transient measurements respectively.

It is necessary to measure a reference pressure, as discussed in Section 2.7, to scale the data obtained. To this

end, a pressure tapping in the intake manifold, close to the inlet valve, is connected by small diameter tubing to a remote water filled manometer. By reading the manometer depression and the ambient barometric pressure, an absolute value corresponding to the bottom dead centre indicator reading can be found.

3.3 Wire Calibration to Evaluate a Heat Transfer Relationship (Hot Wire Calibration)

The two areas of concern in this section are the properties of the sensing wire itself, and the heat transfer relationship necessary to interpret anemometric or resistance thermometer data. For the former, the material temperature coefficients of resistance and the resistivity have been found experimentally. Other parameters have been taken from literature sources [27,74]. To find the heat transfer relationship, a steady-state rig has been built to calibrate in ambient conditions.

i) Wire Properties

The suppliers quote a single value, α for the wire temperature coefficient of resistance. When the sensing filament temperature is high and its accurate determination is necessary, both α and β in equation (2.17) must be found. To this end a bracket in Figure 3.5 has been made to replace the door on a Towers high temperature electrical oven.

The approach taken is similar to that of Ghirlando [34]. A length of sample wire is clamped by copper blocks, whose surfaces have been ground to give a good area of contact. Heavy gauge tin-plated copper wire connects the clamps to a

DISA '55 M' anemometer bridge and associated co-axial cable. Temperature in the region close to the wire is measured by a Ni-Cr, Ni-Al spot-welded thermo-couple connected to a Farnell 'DTT2 type K' digital thermometer.

Measurements are taken in a step-wise fashion. Power is supplied to the oven until a given temperature is approached. When the sample resistance, as measured by the anemometer bridge, has stabilised and is just about to fall, the components in the oven confines have reached a thermal equilibrium and a reading is taken.

Figure 3.6 illustrates the temperature-resistance plot obtained for 9 μM platinum-plated tungsten wire. On cooling after this first test, the copper blocks were distorted. To overcome this problem short lengths of sewing needles were brazed, as shown in Figure 3.5, the sample being spot-welded to their points. Figure 3.7 shows the temperature-resistance plot for 10 μM platinum-rhodium wire subsequently obtained.

To find α and β, a modified form of equation (2.17) is used such that:

$$\left[\frac{R_w}{R_o} - 1\right]\frac{1}{\Delta T} = \alpha + \beta\Delta T \qquad (3.2)$$

where ΔT = temperature rise (K)

$= T_w - T_o$

T_w = temperature corresponding to resistance R_w (K)

T_o = temperature corresponding to resistance R_o (K)

A first-order least squares fit is hence used to calculate the coefficients (see Appendix C).

The resistivity of the material is in part a function of the drawing process used in manufacture. With this in mind, the length of wire between the spot-welds of a probe, whose R_o value has been found, is measured with a travelling microscope. The resistivity averaged from several probes is found by:

$$RTY = \frac{R_o A_x}{\iota} \qquad (3.3)$$

where RTY = resistivity (ohm metres)

A_x = wire cross-sectional area (m^2)

ι = measured length (m).

A summary of the experimental values is given in Table 3.1 below:

Table 3.1: Experimentally Determined Wire Properties

Wire Material	α (K^{-1})	β (K^{-2})	Resistivity (ohm metres)	Quoted Values α	Quoted Values Resistivity (ohm metres)
Platinum-plated Tungsten	3.333×10^{-3}	1.253×10^{-6}	6.32×10^{-8}	3.6×10^{-3}	7×10^{-8}
Platinum (90%) - Rhodium (10%)	1.586×10^{-3}	-9.743×10^{-8}	20.37×10^{-8}	1.6×10^{-3}	18.92×10^{-8}

For both materials the calculated and quoted temperture coefficients of resistance give very close answers with a wire overheat of 200°C (Figures 3.6 and 3.7), this being the usual temperature for wind tunnel anemometric measurements. The connecting components appear to make a negligible contribution to resistance with increasing temperature. The discrepency in resistivity may be related to the material manufacturing process or the wire diameter.

Other properties, which cannot be readily determined by experiment, are taken from Table 2.2.

ii) Heat Transfer Calibration-Logging

Figures 3.8 and 3.9 illustrate the steady-state rig that has been assembled for ambient condition wire calibration. The speed of the centrifugal fan, which extracts air from the wooden buffer box, is controlled by regulating a 'Variac'. A feedback loop is fitted to obtain a steady flow at low velocities, the butterfly valve determining the proportion of air returned.

A ± 0.15 p.s.i. differential pressure transducer is fitted in parallel with a methylated spirit-filled micro-manometer. This manometer has a range of 0-25 mm head of meths. and is used to calibrate the transducer, which gives readings of better accuracy at low velocities and extends the upper limit of measurements taken (usually 65 mm). A Fylde 'FE-492-BBS' bridge conditioner (configured in full bridge mode) and a 'FE-254-GA' differential pre-amp, amplify the signal thus obtained.

The flow chart of a compiled Basic program used to log data from the steady-flow rig is illustrated in Figure 3.10. Two wires can be calibrated in parallel, although another version for single wires has also been written. The output from both channels of the Prosser anemometer unit is fed to the potential dividers and hence to the CH12BEM channels of the Microlink logger. The signal from the bridge conditioner is connected to the CH12/16 channel. An external pulse generator provides the clocking pulses.

The level of turbulence in the test section is very low, but to compensate for any shielding effect the wire orientation is reversed to give a second set of data. Ideally the probe is also recalibrated after taking in-cylinder measurements and four sets of coefficients are averaged to give the final heat transfer relationship.

Two data files result combining user input, logged and 'hard-wired' data. The records are as follows:

Parameter	Symbol	Record No.
Potential divider (E_i/E_o)	Pset	1
Connecting cable resistance (ohms)	R_{ca}	2
Temperature coeff. of resistance (K^{-1})	α	3
Temperature coeff. of resistance (K^{-2})	β	4
Resistivity (ohms metres)	RTY	5
Wire conductivity (W/mK)	k_w	6
Reference sensor resistance (ohms)	R_o	7
Reference (ambient) temperature (°C)	T_o	8
Wire diameter (m)	D	9
Operating resistance (ohms)	R_w	10
Air (ambient) temperature (°C)	T_g	11
Barometric pressure (mm Hg)	P_b	12
No. of logged results	NPTS	13
Manometer reading (mm)	Ht(1-NPTS)	14 etc.
Bridge signal (volts)	Vo(1-NPTS)	15 etc.

The bridge signal is calculated from the potential divider setting by using equation (3.1). The manometer reading

is found by a first-order least squares calibration of the differential pressure transducer, thus:

$$Ht_j = A_0 + A_1 \; Y\%_j \qquad (3.4)$$

where Ht_j = manometer reading No. J, (mm)

$Y\%_j$ = averaged logged word No. J

A_0, A_1 = calibration constants (see Appendix C)

The computer displays the heights and voltages in a continually updated table. It is possible to reject the last set of readings taken, as shown in the flow chart. This is occasionally necessary if there is a poor data transfer from the Microlink to the Apricot.

iii) **Heat Transfer Calibration-Processing**

The flow chart of a Basic program, written to process the data files created in the previous section, is illustrated in Figure 3.11. The aim of the routine is to fit the data obtained from the steady-flow rig to equation (2.19). To this end it is possible to allow all three coefficients ('A','B' and 'c') to float in seeking a calibration of minimum error, or to fix 'c' and hence optimise 'A' and 'B'.

The first step is to calculate the air velocity, Reynolds and Nusselt numbers from the manometer readings and bridge voltages. The air velocity can be found by relating Bernouilli's equation to the pitot-static tube;

$$V = \left[\frac{2\Delta P}{\rho_g}\right]^{1/2} \tag{3.5}$$

where V = air velocity (m/s)

ΔP = (velocity-static) pressure (N/m^2)

The pressure difference is related to the micro-manometer reading by:

$$\Delta P = \rho_m \text{ GHt x } 10^{-3} \tag{3.6}$$

where ρ_m = density of meths. (823 Kg/m^3)

G = acceleration due to gravity (9.81 m/s^2)

Ht = manometer reading (mm)

Air density is related to ambient pressure and temperature by

$$\rho_g = \left[\frac{P_b \text{ x } 300}{760 \text{ x } T_g}\right] \text{x } 1.177 \tag{3.7}$$

where P_b = barometric pressure (mm Hg).

Hence,

$$V = 5.895 \left[\frac{T_g \text{ Ht}}{P_b}\right]^{1/2} \tag{3.8}$$

By using equation (2.20) to find the air viscosity,

$$Re_g = 8513600\left[\frac{P_b D}{T_g^{1.21}}\right] \qquad (3.9)$$

The procedure outlined in Section 2.5 is used to find Nusselt numbers and then a best straight line fit for Nu' versus Re_g^c is sought. If 'c' is allowed to float a parabolic error minimising technique, as detailed in Appendix B, is used. However in accepting that the Reynolds number range of the steady-flow rig is somewhat limited (approximately 0-20), the exponent is usually set as 0.45, as discussed in Section 2.2.

In plotting Nu' against Re_g^c, the resulting calibration can be compared with the processed data. The log (Nu' - A) versus log (Re_g) graph gives a confirmation of linearity with a greater emphasis on low velocity readings. Typical examples of the plots thus obtained are illustrated in Figures 3.12 and 3.13 (c = 0.45).

3.4 Resistance Thermometer Calibration

The heat transfer constants A, B and c are found by the procedure outlined in Section 3.3, by operating the sensing element as an anemometer. As the thermometer is simply 'hot wire' connected to a Wheatstone bridge, the property values previously listed also apply.

The cable resistance measurement is described in Section 2.6. The amplifier gain and shift are the remaining factors to be found in using equation (2.33). Oven type calibrations are impractical because of the delicacy of the sensing element and the unnecessary heating of the supports. Instead a decade

resistance box is used to simulate temperature changes. Hence the method of least squares (Appendix C) is used to solve the linear equation:

$$E_{op} = G'E_{bd}\left[\frac{R_d + R_{ca}}{R_d + R_{ca}\ R_{D3}} - \frac{R_{D1}}{R_{D1} + R_{D2}}\right] + S \qquad (3.10)$$

where R_d = decade resistance box setting (ohms).

R_{ca} = connecting cable resistance (ohms).

3.5 Pressure Transducer Calibration

Figure 3.14 illustrates the flow chart of a program written to calibrate the piezo-electric transducer and associated charge amplifier. Pressure is supplied by a 'Budenburg' deadweight tester, and the output signal is measured by the Microlink logger. Equation (2.42) is modified slightly such that coefficients 'A_0' and 'A_1' are directly related to the average logged word by:

$$P_a = A_0 + A_1\ Y\%_j \qquad (3.11)$$

where P_a = absolute pressure (N/m^2)

$Y\%_j$ = average logged word (J)

Charge leakage and amplifier drift can be a problem here, hence a graph, of which 3.15 is an example, is plotted by the program as a confirmation of linearity.

3.6 In-Cylinder Data Acquisition and Signal Processing

i) Data Logging

Figure 3.16 illustrates the flow chart of a compiled Basic program written for the interactive acquisition of in-cylinder data. The user input parameters are the 'START',

'STOP' and angular resolution settings of the MEE13007 encoder interface, the number of Microlink transient capture channels to be used and the amplifier gain programming bytes. The aim of the routine is to configure the logger, display and data obtained graphically and to write the results obtained to disk (if passed by the user). The speed of the program is such that it can mimic the actions of a storage oscilloscope.

The angular resolution setting of ME13007 is restricted by the operational limits of the CH12 modules discussed in Section 3.2. This can be interpreted in terms of engine speed, as summarised below;

Angular Resolution (Degrees)	Speed Limit (rpm)	
	CH12/16	CH12BEM
0.1	883	2083
0.2	1667	4166
0.5	4166	10416

The clocking pulse rate, used to determine the above values, is found by:

$$L_f = 6 \times RPM/RES \qquad (3.12)$$

where L_f = logging frequency (Hz)

RES = angular resolution (degrees)

RPM = engine speed (rpm).

The maximum motoring speed of the 'E6' engine is 3000 rpm, but hot wire breakage increases rapidly on passing 2000 rpm. To optimise the acquisition rate, using all three transient capture channels where possible, an angular resolution of 0.2 degrees is chosen. Given the above

limitations, the motoring measurements are obtained from a single or two separate experiments as follows:

a) At or Below 1500 rpm

Microlink Module	Analogue Input
CH12BEM (1)	Hot wire (1)
CH12BEM (2)	Hot wire (2) or resistance thermometer
CH12/16	Pressure transducer

b) Speeds in Excess of 1500 rpm

Microlink Module	Analogue Input
Test (1): CH12BEM (1)	Hot wire (1)
CH12BEM (2)	Hot wire (2) or resistance thermometer
Test (2): CH12BEM (1)	Pressure transducer

The above procedures rely upon the fact that the motored pressure signal is very repeatable from cycle to cycle.

The size of the window, or the number of windows logged, depend upon the capacity of the larger of the two transient capture memories available, such that:

$$NPTS = INT (D128K/NWIND) \qquad (3.12)$$

where NPTS = number of data points per window

D128K = storage capacity of CH12BEM units

NWIND = number of windows logged

INT() = integerise (value)

It is unlikely that NPTS will divide exactly into 16,384 (16Kb). Hence there are two problems to be solved. Firstly, the phase of the CH12/16 data must be matched to that of the CH12BEM units. Secondly, the number of values in the fractional window at the end of the channel memories must be determined to permit the repositioning of the memory pointers prior to disk dumping. If two blocks are labelled 'shift' and 'final' data, as per Figure 3.13, then:

$$NSHIFT = NPTS - INT((C112K - INT(C112K)) \times NPTS) \quad (3.13)$$

where NSHIFT = number of 'shift' data points

C112K = number of windows in 112K of data

$$NL16K = INT((C16K - INT(C16K)) \times NPTS) \quad (3.14)$$

where NL16K = number of 'final' points at end of CH12/16 memory

C16K = number of windows in 16K of data

$$NL128K = INT((C128K - INT(C128K)) \times NPTS) \quad (3.15)$$

where NL128K = number of 'final' points at end of CH12BEM memory

C128K = number of windows in 128K of data.

In seeking a statistically acceptable data set, ME13007 has been configured to give one hundred windows per test, at a rate of one window per motored cycle. This is summarised by below:

Hardware Setting	Value
Angular resolution	0.2 degrees
'START' decade counter	900 pulses (180°) from reference TDC
'STOP' decade counter	2205 pulses (441°) from reference "
Reference pulse rate	TDC/2
Reference TDC phase	Exhaust/inlet revolution

Thus data acquisition in each cycle begins at the compression stroke bottom dead centre and ends 1306 values later at 82° after top dead centre.

The logged integers are written to disk character by character in ASKII format. Each record is appended by a 'line feed' and a 'carriage' return'. To save space the values are converted to hexadecimal notation. The IBM 3083 mainframe computer will accept data in this form provided that the field width is filled. Thus the integer range of 0-4095 becomes 000 to FFF. Each character occupies one byte and the total data set of 100 windows, containing 1306 values, occupies 653K out of a possible 720K of disk space. Three disks are used for each test.

ii) Data Transfer

Having logged the necessary data, the files are sent to the IBM 3083 mainframe via a Gandalf serial link, as discussed in Section 3.1. The recent purchase of an IBM (but non-Apricot) compatible 'Opus PCV' has made two possible transfer routes available. These are listed below:

Route No.	From	To	Baud Rate	Net Baud Rate
1	Apricot	IBM 3083	2400	2400
2	Apricot	Opus	9600	
	Opus	IBM 3083	9600	4800

The first option is slow and requires the breaking down of larger files into smaller units to be successful. The second route is faster and releases the Apricot for further data logging when the transfer to the Opus is complete. A

further time saving is achieved by reducing the contents of the motored cylinder pressure file to one cycle, since its measurement is very repeatable.

iii) Hot and Cold Wire Signal Processing

Figure 3.17 illustrates the flow chart of a Fortran 77 program written to process pressure, and simultaneous resistance thermometer and anemometric data. The type and format of the associated input and output files are listed below:

Channel	Medium	Contents	Format
9	Disk	Calibration Data	Free
10	Disk	Anemometric Data	Z3
11	Disk	Thermometer Data	Z3
12	Disk	Pressure Data	Z3
13	Tape	Reference, velocities, temperatures	16, F6.3, F6.2
14	Disk	Pressure, averaged velocities, temperatures	Free
31	Disk	Resumé of errors	Free

The anemometric, thermometer and pressure data is fixed, three character length, hexadecimal (Z3) form. Computed velocities and temperatures are written to tape and as it is not explicitly possible to use a name, a reference number, written as the first record in each file, serves as some form of identification. The ensembled averaged values sent to channel 14 provide the useful check on the magnitude of the calculated values. The error file is only opened if the number of iterations within a given data window proves to be excessive. Here the point of failure and the last computed values are recorded before the computer jumps to the next engine cycle.

The outline of the analysis performed is discussed in Sections 2.5 to 2.7. The only major problem in its interpretation arises in the calculation of the dT_w/dt term in equation (2.37). here the 'bit-stepping' of the digital resistance thermometer data makes it impossible to use a simple central difference method to find the gradient. Instead calculated wire temperatures are fitted by a second-order, 25-point least squares curve (Appendix C) of the form:

$$T_w = A + Bx + Cx^2 \tag{3.16}$$

where x represents an ordinate axis of unit steps

A,B,C = quadratic coefficients

T_w = cold wire temperature (K)

A considerable time saving is achieved for mid-window values by setting the x-axis range to ± 12, and hence finding T_w and dT_w/dx at x = 0. In this case,

$$T_w = A \tag{3.17}$$

$$\frac{dT_w}{dx} = B$$

Hence,

$$\frac{dT_w}{dt} = \frac{dT_w}{dx} \times \frac{6 \times RPM}{RES} \tag{3.18}$$

Pressure data is processed in a similar way, although it is anticipated that any improvement achieved here will be much less significant.

iv) Twin Hot Wire Processing

Figure 3.18 illustrates the flow chart of a Fortran 77 program written to process pressure and simultaneous data from parallel hot wire aneomometers. Again the type and format of the associated input and output files are listed below:

Channel	Medium	Contents	Format
9	Disk	Calibration Data	Free
10	Disk	Anemometer (1) Data	Z3
11	Disk	Anemometer (2) Data	Z3
12	Disk	Pressure Data	Z3
13	Disk	Temperature Data	Free
14	Tape	Reference No., velocities 1,2	I6,F6.2, F6.2
15	Disk	Averaged velocities	Free

The procedure adopted here is similar to that of the last section, but as no temperature measurements are taken, ensembled values from a previous test are used. The format of the tape files is slightly different, but the record length remains the same. As the program is relatively free from iterative loops, the processing times are correspondingly faster.

3.7 Summary

The hardware and computer programs used to log in-cylinder data from a motored engine to calibrate the associated transducers and process the results obtained have been discussed. The path from the acquisition to the subsequent processing of the former is summarized by the block diagram in Figure 3.19.

CHAPTER 4

ENGINE PERFORMANCE ANALYSIS, FIRING PRESSURE DATA ACQUISITION AND PROCESSING

4.1 Introduction

In this Chapter the acquisition of parameters produced by the firing engine is discussed. The aim here is twofold. Firstly the general trend of engine behaviour is established under varying operating conditions. The compression ratio, crank shaft speed, air to fuel mass ratio and ignition advance are possible inputs. Secondly, having isolated key areas of interest, the tests are repeated to obtain data of greater detail. In all experiments the inlet manifold throttle is fully open.

The first objective is approached by the development of constant brake and mean effective pressure (BMEP) and IMEP respectively) contour maps, on a grid of ignition advance versus air to fuel mass ratio (AFR). The bounds of this potentially cumbersome analysis are set by 'drivability' and 'knock' limit curves. The former is a description of the onset of erratic engine behaviour, resulting from the variable burning rate of weak mixtures, and the latter of the explosive and destructive auto-ignition of reactants in the end gas region (see Cuttler [26] for a more detailed discussion). Neither necessarily requires arbitrary definition.

In repeating the tests, high resolution cylinder pressure data is logged and stored with the engine operating according to specific performance map co-ordinates. Although the variability of the readings thus obtained may stand alone as a

source of discussion, the pressures are also post-processed by a simple two zone reaction rate computer model to give a first order analysis of the combustion histories.

The category of measurements can be described as non-transient in the case of brake load and air mass flow rate readings for example, and transient in the acquisition of pressure data. For the former a direct interface to the Apricot computer has been built by the Department. The Microlink capture system, described in Section 3.2, is used for the latter.

The details of the interface programming and polling are documented in Appendix D. The primary concern of the remainder of this Chapter is the instrumentation and procedures used to develop the performance maps and to obtain and process the cylinder pressure data.

4.2 Non Transient Data Acquisition

Figure 4.1 illustrates a block diagram schematic of the 'MEE12030' interface unit built for the Apricot microcomputer. It has been over designed to some extent to permit an expansion in measurement possibilities in future years.

The key components are three ten-bit analogue to digital converters (ADC 1-3), two ten-channel thermocouple reading devices (thermo. 1 and 2), a digital tachometer (tacho) and a TTL input/output board. Connection to the controlling computer is by means of a ribbon cable, terminating in a printed circuit card that slots into the Apricot mother board. The signal transfer consists of eight address, 16 data, read, write and

ground lines running at 5 MHz clock speed. The operating ranges are summarized in Table 4.1 below:

Table 4.1: The Resolution of the MEE12030 Interface Modules

Element	Maximum Range	Resolution
Analogue-digital converter	± 5 v	0.0196 V
Thermo. 1	-15 to 199.99°C	0.1°C
Thermo.2	-40 to 1350°C	1.0°C
Tachometer	60 to 9999 rpm	1 rpm

The elements used in the present application, and their interfacing with test bed mounted transducers, will be discussed in the following sections.

4.3 Brake Load Measurement and BMEP Calculations

A directly coupled D.C. electrical dynanometer (brake) absorbs the engine output shaft power, which in turn is dissipated in the form of heat by a bank of resistors connected in series with its armature. The current generated, and hence the power absorbed, is regulated by adjusting a manual shunt rheostat connected to the separately exited field windings. The result is a torque exerted on the brake outer casing, which is free to pivot about the drive shaft axis (although the angle of rotation is restricted by adjustable stops).

In the original system the torque acting upon the casing is measured by applying a load to a radius arm using a weight carrier and opposing spring balance arrangement. In lean-burn operation the cyclic variation in power is high, and the engine stability low. Hence this manual measurement technique would

be difficult to perform in practice. Thus the system has been modified, as illustrated in Figure 4.2.

A 'Novatech' type 'F241' load cell locates the brake casing, via the radius arm, in its balancing position. The load range possible is ± 30 Kg, and ball joints ensure that the force applied to the cell is axial. The spring balance and weight platform are used for calibration only.

A 'Fylde FE492BBS' strain gauge bridge (connected in four arm mode) and associated 'FE254GA' amplifier convert the force to a voltage. The resulting signal is fed, via a low-pass filter, to the ADC1 unit of the MEE12030 computer interface. The circuit is summarised in Figure 4.3.

The bridge and amplifier are adjusted to give a response in the ± 5 volt range, with the negative and near zero readings corresponding to motoring and no load conditions respectively. Figure 4.4 gives a typical graph of the resulting linear calibration, found by the method of least squares (Appendix C), which takes the form:

$$WT = A0 + (A1 \times ADC1) \qquad (4.1)$$

where WT = brake load (lbs)

A0,A1 = calibration constants

ADC1 = analogue-digital conversion from ADC1

Using the manufacturer's data (70), and Imperial-to-SI conversion constants, the values that hence follow are:

$$BMEP = 0.504 \times WT \qquad (4.2)$$

where BMEP = brake mean effective pressure (N/m^2)

$$BP = WT \times RPM/4693.58 \quad (4.3)$$

where BP = brake power (kw)

RPM = shaft speed (rpm)

$$SFC = \dot{m}_f/BP \quad (4.4)$$

where SFC = specific fuel consumption (kg/kws)

$\dot{m}_f$ = fuel mass flow rate (kg/s)

4.4 Air Mass Flow Rate Measurements

An 'Alcock' type '323' viscous flow meter is mounted between an upstream filter and a downstream pre-heater, on a two inch bore pipe that supplies air to the engine. The deflection of an associated methylated spirit manometer is converted to give the volumetric flow rate. Again with an anticipated fluctuation in performance for a given test condition, it is desirable to digitise the readings thus obtained to permit continuous computer logging. This is achieved by using the system illustrated in Figure 4.5.

A 'Schloevitz' type 'P2002-001 mV', 0-1.5 psi differential transducer is isolated from pressure pulsations by two buffer volumes and connecting narrow bore tubing. The size of the buffers has been determined by a crude application of Bernouilli's equation, seeking a 0.1% signal variation from measured intake pipe pressure waves, at 1500 rpm shaft speed [35]. A bridge conditioner, amplifier and low-pass filter, of similar configuration to the system used in the previous section (Figure 4.3), yield a signal in the ± 5 V range, which is in turn fed to ADC2 of the MEE12030 interface.

A typical manometer deflection versus ADC reading linear calibration graph (found by the method of least squares -

Appendix C) is illustrated in Figure 4.6. The relation which hence follows is:

$$MN = BO + B1 \times ADC2 \qquad (4.5)$$

where MN = manometer deflection (cm of meths.)

BO,B1 = calibration constants

ADC2 = analogue-digital conversion from ADC2

The manometer deflection is converted to an air mass flow rate by considering a temperature correction factor and the gas density. The former is usually determined graphically, however in the range of interest the following linear relationship has been found to hold:

$$CF = 1.055 - (0.00275\ T_{fm}) \qquad (4.6)$$

where CF = temperature correction factor

T_{fm} = gas temperature at flow meter inlet (°C)

Adapting the manufacturer's imperial volumetric relationship [3] to find the mass flow rate in SI units;

$$\dot{m}_a = 0.001189 \times MN \times CF \times \rho_a \qquad (4.7)$$

where $\dot{m}_a$ = air mass flow rate (kg/s)

ρ_a = air density (kg/m^3)

$=(P_b \times 0.4646)/(T_{fm} + 273)$

P_b = barometric pressure (mm Hg) (or equivalent if super charged).

4.5 Fuel Flow Measurement and Air-Fuel Ratio Evaluation

Petrol is delivered to the engine by a 'CAV' mechanical injection system. A positive displacement pump draws fuel from the supply and from this a fraction is removed by an adjustable rack mechanism to be injected into the engine inlet manifold. The remainder is sent back to source via a non-return valve. Simple counterflow water cooled heat exchangers fitted to the supply and return lines serve to standardise the fuel temperature.

In the original design a four way junction connects the pump supply and return lines, the fuel tank and a glass pipette. When a manual valve isolates the petrol tank this pipette is used to measure the volumetric consumption by timing the level drop between marks above and below 50 or 150 cc bowls. It also permits vapour, which is apparently generated by the pulsating nature of the flow, to vent to the atmosphere. The result of this gas release is a tall bubble column. To give the operator freedom to control the engine speed, and to improve the experimental repeatability, it is desirable to automate the fuel flow measurement.

Commercial gravimetric systems are available, but this option has been rejected on the grounds of cost and fears that the flow pulsations will detrimentally influence the results. Somewhat cheaper mechanical rotameters ('RS' type '304-431)' have been tried. The total demand is too low for a single unit to respond, and mounting a separate meter in the supply and return lines gives a net negative result because of the fuel

vapourisation. The approach finally adopted uses an optical system, built around the original glass pipette, to obtain a volumetric measurement.

Photo detectors, as detailed in Figure 4.7, are mounted above and below the selected 50 cc measuring volume. An associated two channel driving unit, 'ME10406', gives outputs that switch from TTL high to low when the passage of a focussed infra red beam is blocked by fuel. These are connected to the input/output board of the MEE12030 logger.

The generated bubble column will falsely trigger the detectors. Figure 4.8 illustrates an early attempt to solve the problem by fitting a part filled buffer volume to damp the pulsations and reabsorb the vapour. However the fuel volume so contained does not reach an anticipated steady state, being influenced by the changing pressure head as the pipette fills or empties. The result is an erroneously low measurement of the volumetric consumption rate.

Figure 4.9 illustrates the approach finally adopted. Two 'Amal' vintage motorcycle float chambers receive fuel directly from the measuring pipette, providing the net demand from the supply and return lines. Vapour is either reabsorbed by the petrol within the body of the chambers, or escapes via vents at the top, while the level contained is held constant by the floats themselves.

A normally closed solenoid valve isolates the system from the fuel tank. An associated driving unit, 'ME12400', opens the valve when triggered by a TTL high signal from the input/output board of the ME12030 logger. The quantity of fuel contained by the glass pipette is kept to a minimum by

operating the solenoid intermittently, because an excessive pressure head will force open the float chamber needle valves.

Having refilled the pipette, the Apricot computer is programmed to time the interval between the triggering of the upper and lower detectors, to obtain a volumetric consumption measure. The mass flow rate is hence found by:

$$\dot{m}_f = 0.05 \times F_{sg}/t_c \qquad (4.8)$$

where $\dot{m}_f$ = fuel flow rate (Kg/s)

F_{sg} = fuel specific gravity

t_c = time interval (seconds) to consume 50 cc of petrol.

Hence,

$$AFR = \dot{m}_f/\dot{m}_a \qquad (4.9)$$

where AFR = air fuel mass ratio.

4.6 Temperature and Crank Shaft Speed Measurement

Two 'Farnell DTT22' digital pyrometers, a 'type T' and a 'type K' are fitted to the MEE12030 logger. Each is connected to a 10-channel scanning relay board, designed to accept inputs from copper-constantan and chromel-alumel thermocouples respectively. The former (Thermo. 1) is intended for the measurement of air, water and oil temperatures. The latter (Thermo. 2) is designed for exhaust temperature reading and is not used in the current study. The resolution of each is listed in Table 4.1 (Section 4.2).

Although both units possess ambient temperature variation compensation circuitry, the readings thus obtained upwardly drift by as much as 5°C as the logger itself warms up. This is probably due to thermo-electric E.M.F. generation in

non-balanced dissimilar metal junctions within the scanning relay board, or between the thermocouple leads and their connecting plugs. To cure this problem one of the channels measures the temperature of crushed ice, providing a simple error value that is subtracted from the other readings taken. The relay board channel allocation is listed in Table 4.2 below:

Table 4.2: The Channel Allocation for the Type T Thermocouples

Channel	Temperature Measured
0	Crushed ice
1	Air Flow meter inlet
2	Inlet manifold
3	Cooling water to the engine
4	Cooling water from the engine
5	Oil supply
6	Sump oil

Thermocouple channels 3 to 6 share existing test bed housings with mercury thermometers, which provide a useful check on the readings obtained. Channel 2 is mounted upstream of the air flow meter and the value thus found is used in equations 4.6 to 4.7.

A 'Farnell' type 'DMT2' digital tachometer gives a direct measure of engine crank shaft speed when supplied with a TTL signal, with a frequency of 60 pulses per revolution. The source of this signal is discussed in Section 4.7. The result thus obtained is used in equation (4.3).

4.7 Engine Performance Monitoring and Data Acquisition Program

i) Objectives

The aim of the routine developed is to satisfy the first criterion outlined in Section 4.1, namely the acquisition of data suitable for the development of constant BMEP and IMEP contour maps. To this end the Apricot computer is used to drive the MEE12030 interface to obtain engine performance data, and a Microlink transient capture system (see Section 3.2) to store in-cylinder pressure records.

The first step is to develop BMEP and IMEP versus AFR curves, and to this end the nature of measurements sought resolve into three categories:

a) Test state parameters. This includes the average crank shaft speed and the seven temperatures listed in Section 4.6.

b) Calculated experimental data, such as the air/fuel mass ratio (AFR), BMEP and IMEP.

c) Boundary conditions. Some measure of the level of drivability and knock are required to define the ignition advance and AFR testing limits.

To maintain the engine fuel supply (see Section 4.5), the following attributes are desirable:

a) Computation and data transfer functions are matched to the 50 cc of fuel consumption rate.

b) A program default to an active scanning state when not testing.

c) Data protection and a quick recovery in the event of a hardware failure.

ii) General Description

A block diagram summary of the system developed is illustrated in Figure 4.10. Connections to the MEE12030 interface have been described in previous sections in this Chapter. The Microlink transient capture system is driven by an 'MEE13003' encoder interface. This differs from the MEE13007 unit described in Section 3.2 by having an increased angular resolution range (0.1-4°), a continuous clocking pulse output (for complete cycles) and a separate trigger pulse position setting.

Flow charts for the controlling computer program are illustrated in Figures 4.11 to 4.13. It is written in BASIC, and has been compiled to improve processing speed and to make the use of computer graphics feasible. The four main parts are a main program, a function menu, monitoring and testing routines.

The purpose of the main program is to initialise the system. One of its roles is to read a calibration file generated by a separate routine. This contains the result data file name, the ambient barometric pressure, the fuel specific gravity, load cell and air flow meter constants (see Sections 4.3 and 4.4). Hence, if reset in the event of a hardware failure, the system becomes active immediately.

The function menu is designed to default to the monitoring routine if no response is typed by the user. The emphasis is to log data for changing AFR values with constant ignition advances. Hence the latter is only updated when necessary.

The monitoring routine serves both to maintain the fuel supply, by filling the pipette if required, and to provide a visual display of the current status of the engine test rig. To this end the measured temperatures, the calculated brake load and flow meter manometer deflection are displayed. These readings can be checked by referring to the rig's original instrumentation.

The testing routine can be split into 'before', 'during' and 'after' phases. In the former and latter the fuel level is replenished, the seven temperature channels are scanned and the Microlink logger is programmed and polled. The pressure traces hence obtained are displayed graphically in unprocessed form, giving a visual assessment in the success of the transfer and the degree of cyclic dispersion.

Having refilled the pipette, the middle phase begins when the top photo-detector is triggered (see Section 4.5). The brake load, flow meter manometer deflection and crank shaft speed are measured and displayed at roughly one second intervals. Priority however is given to the polling of the bottom photo-detector which, when triggered ends this section of the routine. Following the second plot of pressure data, a graph of the calculated BMEP versus AFR points for the current advance value is displayed. The IMEP versus AFR relationship is assumed to follow suit.

iii) Boundary Conditions

The two boundary conditions sought on the AFR-ignition advance grid are in the form of curves representing the onset of knock and poor drivability. In qualitative terms knocking

can be detected by the operator both audibly and by using an oscilloscope, to observe the high frequency noise on the peak of the in-cylinder pressure traces. Poor drivability is similarly observed in the form of large peak pressure variations and a difficulty in maintaining a constant crank shaft speed. If possible it is desirable to measure these phenomena in quantitative terms.

Previous attempts in measuring knock have included the use of force detectors mounted under cylinder head bolts, tuned accelerometers and the spectral analysis of in-cylinder pressure signals [20]. The results thus obtained are characteristic of the engine under test, and in the latter case a high data acquisition rate (Leppard [52] uses 21 points/crank angle) is necessary to detect the frequencies of interest.

Checkel and Dale, [20,21] present a knock detection algorithm which is capable of working with an acquisition rate as low as one point per degree. It exploits the rapid rise and narrow peak of an associated indicator diagram, which will give a large negative third derivative of the pressure-crank angle curve.

The process is in four stages. The slope of a best-fit spline function is found by:

$$dP_\theta = (86\,(P_{\theta-4} - P_{\theta+4}) + 142\,(P_{\theta+3} - P_{\theta-3}) + 193\,(P_{\theta+2} - P_{\theta-2}) + 126\,(P_{\theta+1} - P_{\theta-1}))/1188d\theta \quad (4.10)$$

where dP_θ = derivative at point θ

$d\theta$ = angular resolution (degrees)

P = pressure (N/m^2)

A repeated use of the formula gives successive differentials. A filter is incorporated between the second and third application of the above to reduce noise amplification, and gas the form,

$$F_\theta = (2\ (S_{\theta-4} + S_{\theta+4}) + 3(S_{\theta-3} + S_{\theta+3}) + 4\ (S_{\theta-2} + S_{\theta+2}) + 5(S_{\theta-1} + S_{\theta+1}))/13 \qquad (4.11)$$

where F_θ = the filtered value at point θ

S_θ = the second derivative at point θ

The onset of significant knock is attributed to a third derivative value of - 7 KN/m^2, and the algorithm appears to be reasonably immune to transducer related pressure distortions [21].

The Microlink data acquisition channels available are CH12/16 and CH12BEM units with 16 and 128 Kbytes of on board memory respectively (see Section 3.2). The latter must be selected to log an adequate number of cycles at a one degree crank angle resolution. Two major problems have hence prevented the adoption of Checkel and Dale's method as an on-line technique:

a) The memory capacity of the CH12BEM unit exceeds that which is available within a Basic program, and the piecewise method of data transfer and calculation hence necessary proved to be a very slow process.

b) At each successive step in the algorithm eight data points are lost. This increases the crank angle range which must be scanned to find an already uncertain peak pressure value location.

Given the above limitations, knock has been detected here by listening to the engine and by observing the cylinder pressure records on an oscilloscope.

The approach in determining the degree of drivability is taken from Kuroda et al. [48]. Here the use of peak pressure, or $(dP/d\theta)_{max}$ has been rejected on the grounds that it varies with spark timing and does not always correspond with engine power surges. IMEP variations are however anticipated to bear a direct relationship and a coefficient Cpi is successfully compared to measurements of the test bed mounted engine's transverse movement, where:

$$Cpi = \left[\frac{\sigma_{IMEP}}{\overline{IMEP}} 100 \right] \% \qquad (4.12)$$

where σ_{IMEP} = the IMEP standard deviation (N/m^2)

$\overline{IMEP}$ = the mean IMEP (N/m^2)

A Cpi value of 10% has been taken as a reasonable measure of the onset of poor drivability.

Given the problems of data transfer and storage cited previously, the number of cycles logged and the crank angle resolution must be considered again here. Kuroda et al. [48] use 400 cycles whereas Lancaster et al. [49] recommend between 40 and 300 as a representative sample, depending upon the level of variability. As a compromise a Microlink CH12/16 acquisition channel is used to log two sets of 91 cycles at a coarse resolution of 4 degrees per point.

The IMEP for each cycle is found by the trapezium rule of integration, where

$$IMEP = \frac{\sum_{\theta=0}^{179} \left[\frac{P_{\theta+1} + P_{\theta}}{2}\right] (V_{\theta+1} - V_{\theta})}{V_s} \qquad (4.13)$$

where V_θ = cylinder volume at point θ (m^3)

V_s = swept volume (m^3)

$(\theta+1) - \theta = 4°$

As the above equation uses a closed loop summation, no referencing of the relative values obtained from the piezo-electric cylinder pressure measurements is necessary (see Section 2.7).

iv) Result Calculation and Output

The analogue to digital converter and tachometer readings obtained during the fuel flow measurement cycle are averaged. hence the BMEP's are calculated from equation (4.2), and the air to fuel ratio from (4.9). The mean IMEP and the drivability coefficient are found from the top two sets of 91 cycles discussed previously. Figure 4.1 shows a typical test printout which then follows.

If accepted, the calculated results are dumped to disk. The data file is in "append" mode so that in the event of a computer failure the contents are protected. The pressure records are not saved at this stage however because of the sheer quantity of data involved.

4.8 Fitting Discrete Performance Data

As a first step in developing the mean effective pressure maps, plots against the calculated air to fuel ratio for each ignition advance are required to find the contour co-ordinates.

The shape of the relationships lends itself to a polynomial fit, and the flow chart in Figure 4.15 illustrates an interactive application of the method of least squares (Appendix C) to this end.

An example plot is shown in Figure 4.16. The final result is a list of advance and AFR co-ordinates for decreasing mean effective pressure increments. These are obtained by applying the method of bisection to the left and right of each polynomial curve.

The shape of the drivability coefficient relationship for each advance is less predictable. It is very much a 'snap shot' measurement, giving a high point scatter at weak air to fuel ratios. Few exact values are sought (5, 10 and 20% for example), thus it is profitable to plot this data by hand. A similar argument applies to the knock boundary condition. The contour maps that finally result are illustrated in Chapter 5.

4.9 Detailed Pressure Record Acquisition

The four degree crank angle resolution chosen in Section 4.7 is too coarse for a serious analysis of the indicator diagrams. Having assessed the general trend in engine behaviour, it is now possible to log in-cylinder pressure histories of greater detail, accepting the increase in data transfer time that results.

The aim is to apply the procedure illustrated in Figures 4.11 to 4.13, to repeat the format of the performance data associated with the pressure records obtained. A block diagram summary of the hardware used is shown in Figure 4.17 and the modifications to the original analysis are discussed below.

Two separately driven Microlink transient capture systems are used. The first is associated with the MEE13003 encoder interface, and is used to obtain two sets of 91 complete cycles at a four degree resolution as before. The second is driven by the MEE13007 clock pulse generator described in Section 3.2. A CH12BEM channel stores 182 windows of 0.5 degree resolution data, the range of each spanning from the compression to the expansion bottom dead centres of each cycle.

The second Microlink logger is programmed prior to the test result calculation section in Figure 4.13. Should the engine performance parameters prove acceptable, the data hence obtained is transferred to the computer cycle by cycle, to be dumped to disk in hexadecimal form (see Section 3.3). While performing the latter function the pipette photo detectors are continually polled to maintain the injector fuel supply. A reference pressure value is also required, and is measured as described in Section 2.2.

4.10 Fuel Mass and Volume Fraction Burnt Analysis

i) Introduction

The analysis presented here is a summary of a departmental computer model to interpret the indicator diagrams obtained in Section 4.9, in terms of a calculated rate of fuel combustion. The core of the procedure stems from equations and data given in Benson [15]. The charge volume is split into a reactant and a product zone, with independent temperatures for each. Heat transfer to the cylinder walls and product dissociation are considered, but the routine does not extend to

the calculation of the flame front geometry or the radiation and conduction exchange across it.

The properties of the reactants and the products are determined by balancing the first law of thermodynamics for each zone. The chemical equations involved have been written in terms of the total number of Kg-mols in this Section. When calculating gas species dependent parameters such as enthalpy or specific heat capacity these values are suitably adjusted by the estimated mass fraction of the fuel burned.

ii) Initial Conditions

The fuel is assigned the formula C_nH_m and in this case is assumed to be octane, hence n = 8 and m = 18. An air composition of 21% oxygen and 79% nitrogen (by volume) is used. The effect of the residual gas from the previous cycle is not considered, and is estimated to be small. The analysis begins at the crank angle value when the spark is passed. The following conditions are set out at this point;

$$F_\theta = 0$$

$$V_r = V_\theta$$

$$T_r = \frac{P_\theta V_r}{RM_r} \qquad (4.14)$$

$$V_c = 0$$

$$T_c = T_r$$

where F_θ = mass fraction of fuel burnt

R = universal gas constant (J/kg-mol.)

M = no. kg-mols.

V = volume (m^3)

subscript r = reactants

c = products

θ = data point no. ($(\theta + 1) - \theta = 0.5°$)

iii) Reactants, First Law

For each crank angle increment, an initial guess of the new fuel mass fraction burnt is made by:

$$F_\theta = F_{\theta-1} + 0.005 \tag{4.15}$$

The first law is hence used in the following form:

$$E = Q_r + V_r\Delta P - \Delta H \tag{4.16}$$

where

$$V_r\Delta P = (V_{r\theta} + V_{r\theta-1})(P_\theta - P_{\theta-1})/2 \tag{4.17}$$

$$\Delta H = (1 - (F_\theta + F_{\theta-1})/2)(H(T_{r\theta}) - H(T_{r\theta-1})) \tag{4.18}$$

Table 4.3 Polynomial Coefficients $G_{j,k}$

GAS	J	0	1	2	3	4	5
H_2	0	-1.44392E-11	9.6699E-8	-818E-6	3.43328	-3.8447	0
CO	1	-2.1945E-12	-3.2208E-8	3.7697E-4	3.317	4.63284	-1.39977E4
N_2	2	-6.5747E-12	1.953E-9	2.9426E-4	3.34435	3.75863	0
CO_2	3	8.66002E-11	-7.88542E-7	2.73114E-3	3.0959	6.58393	-4.73184E4
O_2	4	1.53897E-11	-1.49524E-7	6.5235E-4	3.25304	5.71243	0
H_2O	5	-1.81802E-11	4.9524E-8	5.6559E-4	3.74292	9.6514E-1	-2.87565E4
C_8H_{18}	6	2.67009E-9	-1.68385E-5	4.6426E-2	-.71993	0	-0.24E5

and E = error in the first law (J)

Q_r = reactant loss by heat transfer (J)

H = enthalpy (J)

ΔH = a lumped enthalpy parameter (J)

The enthalpy is found both as a function of temperature and the original concentration of reactants:

$$h_j(T_r) = R \sum_{k=0}^{3} G_{j,k}\ T_r^{(4-k)} \qquad (4.19)$$

where $G_{j,k}$ = constants from Table 4.3

h(T) = specific enthalpy (J/Kg-mol)

k = Table 4.3 column no.

j = Table 4.3 row no. (species type)

Hence,

$$H(T_r) = M_6 h_6\ (T_r) + M_a\left(h_4\ (T_r) + \frac{79}{21} h_2\ (T_r)\right) \qquad (4.20)$$

where M_a = No. Kg-mols. of air.

The reactant zone heat transfer is small compared to that of the products, so Q_r is set to zero here. The solution procedure used to find the unknown gas temperature is to adjust T_r and use the method of false position to find the root E = 0. Two conditions are imposed, namely,

$$V_{r\theta} \lessgtr 0 \text{ and } V_{r\theta} \gtrless V_\theta \qquad (4.21)$$

iv) Chemical Reactions

The dissociation of the products has been found to be significant at temperatures in excess of 1900 K. Hence depending upon the value of T_c, two possible reaction paths are considered.

a) No Dissociation ($T_c \geq 1900$ K)

Equating the total number of Kg-mols. present,

$$M_6\ (C_nH_m) + M_a\ (O_2 + \frac{79}{21} N_2) \rightarrow$$

$$M_2N_2 + M_3CO_2 + M_4O_2 + M_5H_2O \qquad (4.22)$$

where,

$$M_6 = \frac{120\ \dot{m}_f}{RPM \times (12n + m)} \qquad (4.23)$$

$$M_a = \frac{120\ \dot{m}_f \times AFR}{RPM \times (32 + \frac{79}{21} \times 28)} \qquad (4.24)$$

and

$\dot{m}_f$ = fuel flow rate (Kg/s)

M_a = No. Kg-mols. of air

$M_2 = \frac{79}{21} M_a$

$M_3 = n\ M_6$

$M_4 = M_a - M_6\ (n + m/4)$

$M_5 = \frac{m}{2} M_6$

b) With Dissociation ($T_c > 1900$ K)

The following reversible dissociation reactions are considered to be significant;

1. $CO_2 + H_2 \leftrightarrow CO + H_2O$ (4.25)

2. $CO + \frac{1}{2} O_2 \leftrightarrow CO_2$ (4.26)

Equating the total number of Kg-mols. present,

$$M_6(C_nH_m) + M_a\ (O_2 + \frac{79}{21}\ N_2) \rightarrow \tag{4.27}$$

$$M_0H_2 + M_1CO + M_2N_2 + M_3CO_2 + M_4O_2 + M_5H_2O$$

The unknown product quantities are evaluated by calculating the equilibrium constants for the reactants in 4.25 and 4.26;

$$K_p\ (1) = \frac{M_3 M_0}{M_1 M_5} \tag{4.28}$$

$$K_p\ (2) = \frac{M_3}{M_1}\left[\frac{M_c P_{ref}}{M_4\ P_\theta}\right]^{1/2} \tag{4.29}$$

where K_p = equilibrium constant

M_c = number of product Kg-mols.

P_{ref} = 1.01325×10^5 N/m^2

The value of K_p is dependent upon the reversible reaction stoichiometry and the product temperature such that,

$$\ln (Kp) = \sum_j^{lhs} \frac{\nu_j g_j(T_c)}{R\ T_c} - \sum_j^{rhs} \frac{\nu_j g_j(T_c)}{R\ T_c} - \frac{\Delta h_o}{R\ T_c} \tag{4.30}$$

where

$g(T)$ = specific Gibbs free energy (J/Kg-mol.)

h_o = specific enthalpy of formation (J/Kg-mol.)

ν = stoichiometry constant

lhs, rhs = left and right hand side of reaction equation respectively.

$$\text{and } \frac{g_j(T)}{RT} = G_{j,3}\,(1 - \ln(T)) - G_{j,2}T - \frac{G_{j,1}T^2}{2} - \frac{G_{j,0}T^3}{3} \quad (4.31)$$

$$\frac{\Delta h_o}{RT} = \sum_{j}^{lhs} \frac{\nu_j G_{j,5}}{T} - \sum_{j}^{rhs} \frac{\nu_j G_{j,5}}{T} \quad (4.32)$$

Considering the molar balance of carbon, hydrogen and oxygen in 4.27,

$$n\,M_6 = M_1 + M_3 \quad (4.33)$$

$$\frac{m}{2} M_6 = M_0 + M_5 \quad (4.34)$$

$$2M_a = M_1 + 2M_3 + 2M_4 + M_5 \quad (4.35)$$

From 4.29, 4.33, 4.28 and 4.34,

$$\frac{M_3}{M_1} = K_p\,(2) \left[\frac{M_4 P_\theta}{M_c P_{ref}}\right]^{1/2} \quad (4.36)$$

$$M_3 = \frac{nM_6}{\left[\frac{M_1}{M_3} + 1\right]} \quad (4.37)$$

$$M_5 = \frac{m\,M_6}{2\left[1 + \frac{K_p(1)M_1}{M_3}\right]} \quad (4.38)$$

and from 4.33 and 4.35,

$$M_3 = 2(M_a - M_4) - n\,M_6 - M_5 \quad (4.39)$$

The solution procedure is as follows:

1. Estimate M_4
2. Find M_3 from 4.36 and 4.37
3. Find M_5 from 4.38
4. Find M_3 from 4.39
5. Find the error M_3 (step 2) - M_3 (step 4)

Having made two passes at steps 2 to 5, the method of false position is used to find the root of zero error in M_3 estimation as a function of the number of Kg-mols. of oxygen. If this error exceeds $M_4/100$ then steps 2-5 are repeated.

v) Heat Transfer

The heat transfer from the reactants to the chamber walls has been found to be negligible. The component from the products is however calculated by applying an equation proposed by Annand [4], which can be written as,

$$\frac{Q_c}{A\Delta t} = \frac{ak}{D}(Re)^b + c(T_c^4 - T_w^4) \qquad (4.40)$$

where Q_c = heat loss (J)

A = chamber surface area (m^2)

k = gas thermal conductivity (W/mK)

D = cylinder diameter (m)

T_w = mean chamber wall temperature (taken as 575 K)

a,b,c = heat transfer constants

Δt = time per crank angle increment (s)

and Re = Reynolds number

$= \rho SD/\mu$

ρ = gas density (Kg/m^3)

μ = gas viscosity (K_g/ms)

S = mean piston velocity (m/s)

= L x RPM/30

L = engine stroke (m)

Typical values of a, b and c for a four stroke spark ignition engine are quoted as [4]:

a = 0.35 - 0.8 (depending upon gas motion intensity)

b = 0.7

c = 4.3×10^{-9} W/m^2K^4

The gas density is found from the product mass to volume ratio and the viscosity by applying equation 2.20, with an exponent of 0.67. The thermal conductivity is hence calculated from Prandtl's number (taken as 0.7) and a differential form of equation 4.20 (applied to the products) to yield the specific heat capacity.

Finally the chamber surface area exposed to the product temperature depends upon the travelling flame geometry. Such an analysis is beyond the level of computation performed, hence the following assumption is made:

$$A = \left[\frac{F_\theta + F_{\theta-1}}{2}\right]\left[\frac{A_{s\theta} + A_{s\theta-1}}{2}\right] \qquad (4.41)$$

where A_s = total exposed chamber area (m^2).

vi) Closing Argument

The estimate of the fuel mass fraction burned, found in equation 4.15, can now be updated by applying the calculated values to a first law analysis of the product volume. Hence,

$$\Delta H_{rc} = - Q_c + F_\theta H_{c\theta} - F_{\theta-1} H_{c\theta-1} - V_c \Delta P \qquad (4.42)$$

where

ΔH_{rc} =enthalpy exchange from the reactant to the product zone (J) and

$$\Delta H_{rc} = (F_\theta' - F_{\theta-1}) \left[\frac{(H_{r\theta} + H_{r\theta-1})}{2} + (H_{or} - H_{oc}) \right] \qquad (4.43)$$

H_{or} = enthalpy of formation of reactants (J)

$= M_6 G_{6,5}$

H_{oc} = enthalpy of formation of products (J)

$= M_1 G_{1,5} + M_3 G_{3,5} + M_5 G_{5,5}$

F' = new mass fraction estimate

$$H_c = \sum_{j=0}^{5} M_j h_j \ (T_c) \qquad (4.44)$$

$$V_c \Delta P = \left[\frac{V_{c\theta} + V_{c\theta-1}}{2} \right] \left[\frac{P_\theta - P_{\theta-1}}{2} \right] \qquad (4.45)$$

Convergence in the values of F_θ and F_θ' is sought. If this is not achieved, the mass fraction estimate is updated, and the analysis repeated from equation 4.16 onwards.

At the end of combustion, a mass fraction value of 1 is sought, which should be sustained throughout the remainder of the expansion stroke until the exhaust valve opens. Given a correct estimate of the fuel's enthalpy of formation, the

remaining governing factor at the end of combustion is the rate of heat transfer to the chamber walls. In the present analysis this can be adjusted by changing the surface temperature (T_w) or the Annand constant "a" value. The latter approach is taken here.

Figures 4.18 to 4.20 illustrate three examples of the mass fraction burned calculation with "low", "high" and "correct" levels of heat transfer. In each case the data is calculated from the first logged pressure cycle where the engine is running at 1500 rpm, an 8:1 compression ratio and a 5% coefficient of IMEP variation (air to fuel ratio = 18.06:1).

4.11 Summary

Transducers and metering systems have been added to the engine test bed to assist in the acquisition of data in unstable operating conditions. The engine performance is then mapped between the bounds of knock and drivability for lean air-fuel ratios and varied ignition advances. The onset of knock is determined by ear and by observing the oscilloscope trace of the in-cylinder pressure signal. The degree of drivability is calculated from the proportional variation of IMEP values. Detailed pressure records are then logged from chosen performance map coordinates and a two-zone model is used to calculate the mass fraction burnt combustion histories.

CHAPTER 5

An Overview of the Motored Engine Anemometric Measurements and the Firing Engine Performance

5.1 Introduction

The aim of this section is to quantify in global terms the influence of the engine speed, compression ratio and inlet valve geometry on the measured in-cylinder gas flow and the subsequent changes in performance. The former is represented by plots of the ensemble mean velocity and RMS turbulence, to quantify the motion intensity within the combustion chamber. The latter takes the form of BMEP and IMEP (brake and indicated mean effective pressure respectively) contour maps, to describe the operating stability if the engine for given ignition advance and air to fuel ratio co-ordinates. The data acquisition hardware and the associated computer processing routines are discussed in Chapters 3 and 4.

A direct measure of the magnitude of gas motion velocity gradients is sought by using parallel hot wires. Before this is possible however, a high degree of consistency in the two sets of velocities calculated for each test condition is required. Therefore results from twin anenometric measurements are presented to assess the viability of this technique. The performance maps are used to identify suitable operating conditions for the subsequent acquisition of pressure data (to calculate the combustion histories of the firing engine). Examples of the indicator diagrams hence obtained are also included. A summary of the test results can be found in Appendix H.

5.2 Experimental Design

Hot wire measurements are strongly property dependent, requiring a simultaneous measurement of temperature and pressure before a velocity can be calculated. The underlying theory and the data logging strategy hence adopted is outlined in Chapters 2 and 3. The anemometer and resistance thermometer filaments cannot withstand a burning environment, as discussed in Sections 1.8 and 2.1. Therefore separate experiments are performed with the engine in motoring and firing modes, to evaluate the gas motion intensity and the combustion behaviour respectively.

a) Motoring Experiments

Anenometric measurements from a large number of cycles and at a high angular resolution, which span the compression and part of the expansion stroke, are sought. The latter criterion permits some evaluation of the gas motion development prior to the time of sparking and should give a reasonable overlap with the separately calculated combustion histories. To this end the approach outlined in Section 3.6 is adopted. The reference crank angle (θ = 0°) corresponds to the top dead centre (TDC) of the exhaust stroke, and the associated logging window details can be summarised as follows:

Start of data logging	= 180°
End of data logging	= 441°
Angular resolution	= 0.2°
Number of points per window	= 1306
Number of windows logged	= 100

The aim is to investigate the flow intensity of the two inlet valve geometries at different engine speeds and compression ratios. The range of the former is limited by the onset of an unacceptable degree of anemometer and resistance thermometer filament breakage. The upper value of the latter is determined by the convergence of the knock and drivability curves on the performance maps.

The gas motion intensity measurements are taken using the probes illustrated in Figure 2.2, representing the spark plug region and the combustion chamber clearance volume. Temperatures obtained by the simultaneous processing of anemometer, resistance thermometer and pressure transducer data are ensembled for the subsequent processing of twin hot wire results in similar operating conditions. The temperature measurements are taken using the plug cavity and flush radial wire probes, to evaluate the average conditions in their respective areas.

The slowest Microlink transient capture channel will not operate, for the chosen angular resolution, when the crank shaft speed exeeds 1666.7 rpm. This complicates the logging procedure slightly (see Section 3.6) and therefore the study has been designed so that the majority of the tests are performed at, or below, 1500 rpm. To this end, the experiments proceed as follows:

i) **<u>The effect of compression ratio</u>**

Crank shaft speed = 1500 rpm

Minimum compression ratio = 7:1

Maximum compression ratio = 9:1

Compression ratio increment = 0.5:1

ii) **The Effect of Engine Speed**

Compression ratio = 8:1

Minimum crank shaft speed = 1000 rpm

Maximum crank shaft speed = 2000 rpm

Crank shaft speed increment = 250 rpm

The case where the compression ratio is 8:1 and the engine speed is 1500 rpm is common to both (i) and (ii). Therefore nine tests are performed for each probe configuration and five points are avaible for the changes in the two parameters listed.

b) **Firing Experiments**

The performance maps are developed according to the procedures outlined in Sections 4.7 and 4.8. The experiments follow the same route as the motoring tests, excepting that the ignition advance and the air to fuel ratio become additional parameters to be considered. The full range of the former is covered, namely 20-60°, whereas the latter is generally restricted to mixtures leaner than 17-18:1. Pressure records for the subsequent study of the combustion process are logged in the manner described in Section 4.9.

5.3 Motored Engine Results

An example of 1 window of anemometer, resistance thermometer and pressure transducer data logged from the engine is illustrated in Figure 5.1. Referring to Figure 2.3, the channels are assigned as follows:

Channel 1 = wire 1 (anemometer)

Channel 2 = wire 2 (resistance thermometer or anemometer no.2)

Channel 3 = pressure transducer

At crank shaft speeds in excess of 1500 rpm, channel 1 is used again to log the in-cylinder pressure (see Section 5.2) in a separate test.

The configuration of the Microlink logger and the associated instrumentation is detailed in Section 3.2. The window range used includes IVC (inlet valve closure, θ = 216°) and the compression stroke TDC (θ = 360°). The pressure transducer signal is very repeatable and its processing is reasonably straightforward. The resistance thermometer and anemometer signals are less so and the results hence obtained are discussed below.

a) **Gas Temperature Measurements**

The response lag caused by the thermal inertia of the resistance thermometer wire is clearly visible in the channel 2 signal plot in Figure 5.1. On processing the data however, as illustrated in Figure 5.2 and 5.3, the phase of the calculated gas temperature with respect to the compression stroke TDC is restored. The results obtained have been found to be largely insensitive to gas velocity fluctuations and the heat transfer constants of the sensor, and respond more readily to the rate of change of the associated bridge output signal. A judicious amount of smoothing (see Section 3.6) has suppressed the generation of noise associated with the "bit-stepping" of the logged digital data. The remaining oscillations are attributed

to the convective activity between the enclosing boundaries and the inner core of the gas in the combustion chamber.

A comparison with the ideal gas law for a plug cavity measurement is illustrated in Figure 5.4. The analysis begins at IVC, using the measured pressure and calculated cylinder volume to find the mass of gas enclosed. The experimental temperature plot lies within the theoretical curve for the majority of the crank angle range covered. The deviation in the graphs are attributed to the difference in temperature between the cylinder head boundary layer and that of the bulk within the combustion chamber and the leakage of gas past the piston rings. However the Figure serves as a reasonable validation of the results obtained.

On ensembling the temperature plots are smoothed, as illustrated in Figures 5.5 and 5.6. The change in peak amplitude for different compression ratios is readily explained in terms of the in-cylinder pressure values. The effect of crank shaft speed is less expected and may result from a reduced time for losses to the chamber walls, a fall in gas leakage past the piston and the storage of heat by the engine as successive tests are performed. Graphs of the temperature measurement standard deviation (determined in the same manner as RMS turbulence, see equation 1.3) are shown in Figure 5.7. The apparently cumulative fluctuation in terms of crank angle is attributed to the increase in gas temperature as TDC is approached and convection between the boundaries and the bulk fluid at reduced gas velocities as the piston descends.

b) **Gas Velocity Measurement**

An overheat setting of 74% is used for the hot wire measurements presented in this study (see Section 2.5). This gives an operating temperature of 500°C and an excess over the surrounding gas at TDC of more than 130°C. The probe wire orientations are detailed in Figures 2.3 and 2.4. The ensemble mean velocities and RMS turbulance are found using equations 1.3 and 1.4 respectively, where N_c = 100.

A sensitivity analysis of the single cycle represented in Figure 5.2 is illustrated in Figure 5.8. An uncertainty in the gas temperature (T_g) at TDC appears to have the most dramatic effect on the calculated velocity. However the standard deviations reported previously (Figure 5.7) represent only 1.5% of the averaged peak value. Errors in the gas pressure (P) appear to have little influence.

The result of 330 hot wire calibrations (see Section 3.3) are listed below:

Symbol	Average	Standard Deviation
A	0.542	0.068
B	0.573	0.027
c	0.45	-

The magnitude of "c" has been fixed at 0.45 and the constant "B", which in ambient conditions is purely a function of velocity, is in good accord with that of Collis and Williams [24]. However a value for "A" is not quoted for the form of heat transfer analysis used [25], but an uncertainty in its value appears to be relatively unimportant. Further calibration inconsistencies will stem from an assumption that

each wire is straight and has a smooth surface, and the variable spot weld qualities at the supports.

The influence of the wire orientation for flush probes used in the engine with the standard inlet valve is shown in Figure 5.9. The plots are labelled according to the notation used in Figures 2.3 and 2.4, rather than an interpreted gas motion direction. A lack of orthogonality will give an error of 5% (sin (90 - 18.8) = 0.9466) in the interpretation of velocities in polar co-ordinates. However the statements listed below should broadly hold:

(i) The radial wires are sensitive to circumferential and axial velocities.

(ii) The circumferential wires are sensitive to radial and axial velocities.

(iii) The vertical wires are sensitive to circumferential and radial velocities.

The measurements plane of the inclined flush probe is parallel to that of the plug cavity and represents an intermediate condition between the radial and vertical wire cases.

The broad features in Figure 5.9 indicate a slight decay as IVC is approached. A small peak at TDC for the radial and inclined wires may either indicate the amplification of a barrelling type vortex or a change in the measurement position relative to the combustion chamber geometry. The high circumferential wire measurement is unexpected and is a reflection on the disorder of the in-cylinder flow pattern. The contribution of axial velocities to the mean is uncertain, but is assumed to be small

when the chamber has a large aspect ratio, because the wires are mounted close to the cylinder head surface.

The ensembled RMS turbulence plots in Figure 5.10 broadly follow the amplitude of the mean velocities. On the whole no decay with time is observed, but a tendency towards isotropy at TDC is indicated. The onset of a flow direction reversal, which will bias the results discussed above, has not been noted when studying measurements taken from single cycles. The presence of small eddies around the anemometer may however mask the observation of near zero instantaneous velocities. A single cycle logged from $\theta = 0$ (exhaust stroke TDC) is shown in Figure 5.11 which puts the relatively low amplitudes reported above into perspective, in terms of the high intake motion intensity. The rapid decay prior to BDC (bottom dead centre of the intake stroke) is a much a reflection of the measuring probe location as the behaviour of the bulk of the fluid.

Measurements of the ensemble mean velocity and RMS turbulence levels obtained from parallel anemometer probes are shown in Figures 5.12 to 5.25. The wire spacing is relatively small and lies between 3.5 and 5.5 mm, the latter value applying to the circumferential probe only. A good agreement between the results obtained from each is therefore expected. The significant differences which result in practice are in part attributed to errors in the calibration of the hot wires. In Figure 5.20 for example, because the filaments are highly stressed by the intake flow generated by the shrouded valve, a high breakage rate is encountered. Illustrated is the difficulty in matching the results from the three lower speed

plots with those of the remainder, which have been logged after the probe has been repaired.

The probe supports also appear to be interfering with the flow that is being measured. This is apparent along the crank-angle axis of the ensembled mean velocity graphs, where the highest value tends to switch from one wire to the other. The RMS turbulence intensity that is measured in the wake of this disturbance may then increase disproportionately, as is suggested by the wire 2 results in Figure 5.15 for example. For both valve geometries the circumferential probes give the best agreement, the relative proximity of wire 2 to the inlet valve being readily attributed to the observed difference prior to IVC.

For the standard inlet valve, the mean velocities and RMS turbulence intensity are broadly similar for the three probe designs considered, but the results from the circumferential wires show a slight dominance. The levels are observed to increase with speed (Figures 5.12 to 5.17), but the effect of compression ratio (Figures 5.18 and 5.19) appears to be less than the experimental accuracy of the readings taken. This agrees with Lancaster's observations [50] and for this reason these experiments are not repeated for the shrouded valve analysis.

The results from the shrouded valve (Figures 5.20-5.25) show a clearly higher radial measurement compared to that of the circumferential wires. The latter is not insignificant however and the subsequent decay of both may reflect the axial intake flow stratification and the onset of solid body rotation arguments discussed in Section 1.5. A realignment of the swirl

centre may also contribute to the changes in velocity as TDC is approached. The plug cavity ensemble mean and RMS turbulence levels exceed those found in the standard valve case, but the latter appears to be little enhanced in the main body of the combustion chamber.

The plots of the mean velocity and RMS turbulence intensity are too noisy to be meaningfully superimposed on the same axes for each probe and inlet valve design. This is in part a consequence of the small size of the speed increment chosen (250 rpm) and the low number of cycles logged for each test. An increase in the latter however is considered to be imprudent because of the failure rate of the anemometer and resistance thermometer filaments. Therefore this problem has been tackled by smoothing representative data sets for each test condition as discussed in Chapter 6.

5.4 Firing Engine Results

The engine speed and compression ratio used in the motoring tests are repeated in studying the firing engine characteristics. The analysis is restricted on the whole to lean air to fuel ratios and does not extend beyond the knocking boundary. In mapping the engine performance the coordinates for the constant levels of BMEP and IMEP are found by fitting experimental data using the method of least squares (see Section 4.8). Curves representing the degree of drivability and the onset of knock are plotted by hand. Pressure data for the subsequent analysis of combustion histories is then obtained at air to fuel ratios and ignition advances between

these latter two limits. The tests performed and the results obtained are discussed below.

a) **Performance Mapping**

A summary of the plots from the engine, fitted with the standard inlet valve and operating at a compression ratio of 8.1, is illustrated in Figure 5.26 to 5.28. The maps represent averaged values and the spacing of the MEP contours indicates the consequences in performance of cycle-by-cycle charge mixture and flame development variations (the outcome of the latter being similar to a change in the ignition advance). A maximum stability is indicated in the region close to the knock boundary and a good accord with the drivability coefficient curves is observed. A comparison between IMEP and BMEP maps in Figure 5.28 shows an agreement in the trend of independent in-cylinder pressure and dynamometer readings, the difference in amplitudes being the frictional losses in the engine.

At 1000 rpm an advance in the spark timing from 20° yields an increase in the leanness for an acceptable degree of drivability (taken as a Cpi of 10%) initially. However a point is reached where no further benefit is gained and the performance subsequently deteriorates. The meeting of the drivability and the knock boundary curves at high ignition advances indicates the occurance of both slow and fast burning cycles at the same operating coordinates.

The performance stability at weak mixtures and low ignition advances at 1250 rpm deteriorate in comparison. However as the engine speed is raised further a recovery in the drivability is observed. The advance for the maximum

acceptable air to fuel ratio increases on the whole, but inconsistencies in the day-to-day behaviour of the engine (attributed to changes in the atmospheric pressure and humidity) have partly masked this trend. A rise in the compression ratio, illustrated in Figures 5.27 and 5.29, serves to increase and reduce the lean limit for stable performance at high and low ignition advances respectively. As the onset of auto ignition becomes dominant the operating range is restricted to a narrow band that lies between the knock and drivability curves.

The performance stability of the engine is observed to gradually fall as the mixture becomes leaner. This is further illustrated by example plots of the proportional IMEP variation data represented in Figure 5.30. An increase in the ignition advance can counter this effect by yielding an improvement in the phasing of the peak heat release rate with TDC (see Section 1.7). However at high values a greater negative contribution to the net cyclic power output and the initiation of the combustion process at low temperatures and pressures will serve to oppose this trend.

An increase in the engine speed both reduces the pre-TDC time available and amplifies the intensity of the in-cylinder gas motion, the latter being assumed to increase the rate of combustion. The combination of these effects is illustrated in the change of the ignition advanced required to operate with the leanest acceptable mixture and the overall changes in the drivability and knock boundary curves.

An increase in the compression ratio serves to improve the MEP levels and the performance of high air to fuel ratios.

However the associated rise in combustion rates is not able to compete with a greater tendency for the end gas to autoignite, as a consequence of the reactant temperatures and pressures. The fall in the drivability at low ignition advances is unexpected and may be the result of an increased degree of flame quenching as the cylinder clearance height is reduced. With increasing compression ratio the engine's scavenging will improve and therefore it is also possible that the effect of the residual exhaust gas left behind by a preceeding misfire cycle will become more prominent.

The maps obtained in using the shrouded inlet valve, illustrated in Figure 5.31 to 5.33, are very different to those reported previously. The knock boundary has disappeared from the ignition advance range considered and the 5 and 10 percent drivability curves are close together. Data for a Cpi value of 20% has not been obtained with a sufficient consistency to be plotted, because of the steep deterioration in performance associated with the latter effect. A difficulty in fitting a polynomial to the MEP results and their general insensitivity to changes in the air to fuel ratio for each ignition advance is reflected in the sparsity of the plotted curve fit coordinates associated with each contour. The maps have therefore been largely developed by a direct reference to the original experimental results.

The cylinder head pressure transducer signal, observed on the computer screen when using the acquisition routine outlined in Section 4.7, differs markedly from the standard valve case. The rate of increase appears to be greater and there is little oscillation in the peak amplitude until the lean limit reached.

The resulting MEP levels for the majority of the range covered in the performance maps are relatively unaffected by a change in the air to fuel ratio, but steadily fall as the advance is increased. The wide spacing of the contours is reflected in the proportional IMEP variation curves, examples of which are presented in Figure 5.34 where the Cpi values remain at 2% until the drivability begins to deteriorate.

A poor engine performance at low ignition advances, coupled with the convergence of the drivability curves, indicates the occurrence of both fast and slow burning cycles has been suppressed in reducing the variation of the in-cylinder pressure histories. The timing and magnitude of the heat release rates that result prove to be complimentary in maintaining the MEP levels as the air to fuel ratio is changed. However a disproportionately negative contribution to the net cycle power output is achieved by increasing the ignition advance or the mixture richness at low engine speeds.

The effect of an engine speed increase is broadly similar to that reported for the standard inlet valve tests, in that a recovery in performance overcomes the reduction in the pre-TDC time available. However the maximum attainable air to fuel ratio for a drivability co-efficient of 10% is yielded at the highest ignition advance plotted in all cases. The disappearance of the knock boundary (from the range of experimental conditions considered) may be attributed to a reduction in the in-cylinder pressures, resulting from increased pumping losses associated with the use of the shrouded intake valve. An attempt was made to mildly supercharge the engine, but time did not allow the development

of a suitably sensitive control method and the idea was abandoned. A comparison of the volumetric efficiencies illustrated in Figure 5.35, however shows a difference of less than 5% and the trend of the MEP plots bear no resemblance to the low compression ratio case reported previously. Therefore it is assumed that either an enhancement of the combustion rate (by flame wrinkling or improved air/fuel mixing) has decreased the time available for autoignition reactions to take place or a high gas motion intensity has increased the heat transfer in the end gas region.

b) <u>In-Cylinder Pressure Data Acquistion</u>

When operating the engine with the standard inlet valve it has been noted that the ignition advance to attain the maximum leanness for an acceptable degree of drivability increases with crank shaft speed. In seeking a wide range of air to fuel ratios to study, this trend has been followed by choosing to pass the spark at a constant time before TDC. To this end an ignition advance of 30 and 60 degrees has been chosen for crank shaft speeds of 1000 and 2000 rpm respectively, which is broadly in accord with the shape of the performance maps presented.

The original aim was to observe the similarities in the results obtained with the two inlet valve designs. Therefore the drivability coefficient was chosen as a further criterion and results for Cpi value of 5, 10 and 20% have been sought. On subsequently rebuilding the engine with the shrouded intake valve, the large changes in performance behaviour and the small spacing of the resulting drivability curves were unexpected.

Therefore the air to fuel ratio ranges in this case have been extended to overlap the data obtained with the original configuration. Additional ignition advances have also been covered, to try to isolate the effect of reactant property changes on the early stages of flame growth.

The data has been logged in the manner described in Section 4.9. A relaxation in the angular resolution used, compared to that of the motoring experiments, has permitted an extension in the window range and the number of cycles logged. The associated details can be summarised as follows:

Start of data logging	= 180°
End of data logging	= 540°
Angular resolution	= 0.5°
Number of points per window	= 721
Number of windows logged	= 182

The window range spans IVC, TDC and EVO (exhaust valve opening, θ = 498°) and two examples of the pressure transducer data logged are illustrated in Figures 5.36 and 5.37. Each plot represents 10 cycles acquired at an engine speed of 1500 rpm, a compression ratio of 8:1 and an air to fuel ratio of approximately 18:1. Illustrated are the different rates of pressure rise and the spectrum of amplitudes for the two valve designs. An analysis of the results thus obtained is discussed further in Chapter 7.

5.5 Summary

The ensemble averaged mean velocity and RMS turbulence levels, measured in the spark plug cavity and the clearance volume of the motored engine broadly increase with crank shaft

speed. The effect of the compression ratio appears to be less than the experimental accuracy of the measurements taken. Significant differences in the magnitude of the gas flow pattern resulting from the use of standard and shrouded inlet valve geometries have been observed, although in comparison the RMS turbulence levels appear to be enhanced in the spark plug cavity region only. The performance behaviour of the engine for the two cases differs greatly, with the suppression of knock and a large improvement in the degree of drivability when the shrouded valve is used. A strategy for the acquisition of in-cylinder pressure data has been formulated and subsequently modified on the basis of the performance maps obtained.

CHAPTER 6

MOTORED ENGINE DATA SMOOTHING AND CYCLE-BY-CYCLE ANALYSIS

6.1 Introduction

The concern of this section is the reappraisal and further processing of the anemometric results presented in Chapter 5. In addressing the former objective, a consistent set of ensemble (phase) averaged gas velocity and RMS turbulence levels are sought for each measurement probe and inlet valve design to represent the general in-cylinder flow patterns. For the latter the study is extended to a cycle-by-cycle analysis of turbulence and spatial velocity gradients.

Within the limited range considered, a change in the engine compression ratio appears to have little effect on the ensembled values presented in Section 5.3. The subsequent influence on the firing engine performance is therefore assumed to be largely a consequence of the prevailing reactant temperature and pressure and this particular analysis is not pursued further. The engine speed however has been found to be a significant parameter and is adopted as a source of comparison for each test configuration.

In seeking consistency the limitations of the probe design and calibration repeatability are considered. Measurements from a single, and hopefully upstream, hot wire are required for the calculation of mean velocities and turbulence levels. It will be shown later that these criteria can be extended to the estimation of spatial velocity gradients. With the above factors in mind, the following data

sets have been selected as a basis for further processing (the wires have been numbered according to Figure 2.3).

Inlet Valve Design	Probe Configuration	Wire Number	Type of Experiment Performed
Standard	Flush, radial	1	Anemometer, resistance thermometer
Standard	Flush, circumferential	1	Twin anemometer
Standard	Plug cavity	2	Twin anemometer
Shrouded	Flush radial	1	Twin anemometer
Shrouded	Flush, circumferential	1	Twin anemometer
Shrouded	Plug cavity	2	Twin anemometer

A summary of the calibration details associated with each test condition can be found in Appendix H. The remainder of this Chapter is devoted to the analysis of the results associated with the above experiments.

6.2 Ensemble Mean Velocity and RMS Turbulence Data Smoothing

Example plots of ensemble mean velocities and RMS turbulence intensities, calculated from twin aneomometer measurements (using equations 1.3 and 1.4) with different wire orientations, inlet valve designs and engine speeds, have been presented in Figures 5.12 to 5.25. Having selected a single data set for each experimental condition (see Section 6.1), the noise on the successive graphs still remain as a hindrance in the interpretation and possible correlation of the results obtained. This is especially true in the case of RMS turbulence intensities and has been attributed (see Section

5.3) to the relatively small number of cycles data logged for each experiment.

The simplest solution to the above problem is to adopt a time average, or window, analysis to increase the number of data values for each crank-angle increment. To this end equations 1.3 and 1.4 are modified such that:

$$\bar{U}\left(\theta \pm \frac{\theta}{2}\right) = \frac{1}{Nc \times M} \sum_{i=1}^{Nc} \sum_{j=1}^{M} U(\phi_j, i) \qquad (6.1)$$

$$u'\left(\theta \pm \frac{\theta}{2}\right) = \left[\frac{1}{Nc \times M} \sum_{i=1}^{Nc} \sum_{j=1}^{M} \left(U(\phi_j, i) - \bar{U}\left[\theta \pm \frac{\Delta\theta}{2}\right]\right)^2\right]^{1/2} \qquad (6.2)$$

where $U(\phi_j, i)$ = instantaneous velocity (m/s)

$\bar{U}\left(\theta \pm \frac{\theta}{2}\right)$ = windowed ensemble mean velocity

$u'\left(\theta \pm \frac{\Delta\theta}{2}\right)$ = windowed RMS turbulence intensity (m/s)

Nc = total number of cycles considered

θ = crank-angle (degrees)

i = cycle number

and $\Delta\theta$ = window size (degrees)

ϕ_j = a crank angle within the window range (degrees) corresponding to the ordinate j

M = number of ordinates within window = $\Delta\theta$/RES

RES = data logging angular resolution (degrees)

j = window ordinate number.

It must be noted at this stage that the term 'window' has been used both in the context of data logging (see Section 3.2) and time averaging, to describe a limited crank-angle segment within the 720 degrees of the complete cycle. In this section the latter definition will apply throughout.

The above approach is frequently adopted when ensembling laser Doppler velocimetry measurements, where the phasing of the discrete data from cycle to cycle is not possible. To this end Ball et al. [11] adopt a 10° averaging scheme whereas Rask [67] identifies 5° as "a good compromise between accuracy and expediency of measurement". The translation of the scale of crank-angle to time may be reflected in the differing increments chosen (960-2400 rpm and 300 rpm in the former and latter cases, respectively), although in the end the selection of a suitable window size appears to be arbitrary.

Compounded to the problem noted above is the concept of 'crank-angle broadening' [67,68], where a step averaging scheme is used to calculate the time varying ensemble mean velocity. The result is an erroneously high estimation of the RMS turbulence intensity, an example of which would be the application of equation 6.2 to the shrouded valve measurements reported in Section 5.3. A possible solution is to curve fit the data contained within each window by using the method of least squares (Appendix C). However the result obtained may oscillate excessively [37] and the selection of a suitable polynomial order adds to the 'open-endedness' of the analysis.

Rask [66,67,68] employs a spline smoothing routine, originally developed by Reinsch [69], to curve fit both

ensemble mean velocities and RMS turbulence intensities. As proposed above, discrete (cubic) polynomials are applied to the raw data, thus tackling the problem of crank-angle broadening. However splines themselves are non-oscillatory [37] and continuity in the complete curve is attained by matching the zeroth and first derivative at the points where the polynomials meet (knots). Unlike the usual application of interpolation however the smoothness, in the form of the second derivatives, is controlled by the scatter and number of values contained in the raw data available. The latter point is particularly relevant in this case and the subsequent adoption of the smoothing procedure used is outlined in Appendix G.

The aim is to evaluate the coefficients a, b, c and d of the cubic polynomial in equation G.1 (Appendix G) at the mid-point of each window. When fitting the ensemble mean velocity measurements, the input y-ordinate data is given by the estimates obtained from equation 6.1. The remaining information that is required is a corresponding set of weighting functions and a smoothing parameter. The former is defined by the anticipated scatter, expressed as a standard deviation, in the mean velocity estimates. The latter is a function of the number of windows through which the complete curve passes.

The definition of the step averaged RMS turbulence intensity given by equation 6.2 is virtually identical to that of the standard deviation of the velocity values contained within each window. The standard deviation of the mean estimates can hence be found according to Moroney [61] by:

$$\delta y\left[\theta \pm \frac{\Delta\theta}{2}\right] = \frac{u'(\theta \pm \frac{\Delta\theta}{2})}{\sqrt{(Nc \times M)}} \qquad (6.3)$$

where $\delta y(\theta \pm \frac{\Delta\theta}{2})$ = weighting function for the window centered at θ. The analysis can be further extended to fit RMS turbulence intensities by treating the estimates in equation 6.2 in a similar manner to the mean velocities. In this case however the weighting functions are found by [61]:

$$\delta y\left[\theta \pm \frac{\Delta\theta}{2}\right] = \frac{u'(\theta \pm \frac{\Delta\theta}{2})}{\sqrt{(2xNcxM)}} \qquad (6.4)$$

Finally, according to Reinsch [69] the statistically expected degree of acceptable smoothing, expressed as a parameter S, should lie within the range:

$$S = N \pm \sqrt{(2N)} \qquad (6.5)$$

where N = the number of points (windows) fitted + 2.

In this application it is possible to drop the use of windows altogether, because the cycle-to-cycle velocity measurements are in phase on a crank-angle basis. However to limit the size of the matrices generated (see Appendix G), a 1.4 degree averaging scheme has been adopted. This differs slightly from the 1 degree interval chosen by Rask [66,67,68] but the apparent arbitrariness in its selection is countered by the corresponding weighting function magnitudes which result. Examples of the smoothed ensemble mean velocity and RMS

turbulence intensities, compared to those calculated directly by equations 1.3 and 1.4, are illustrated in Figures 6.1 and 6.2.

The difference in the fitted and directly phase averaged results is most significant in the RMS turbulence intensity example. Within the statistical limits [60,69] a change in the parameter S appears to have little effect and Rask's value (S = No. of windows + 1) has been retained. It is believed at this stage that the general objective of smoothing has been achieved and further refinements, such as an increase in the window size or a repeated screening of the initial data to remove the most scattered values [66,67], have not been adopted. Generally four iterations are required for convergence and the solution procedure, although involved, is more efficient than the least squares approach previously suggested.

The smoothed ensemble mean velocities and RMS turbulence intensities, calculated from the test cases isolated in Section 6.1, are illustrated in Figures 6.3 to 6.8. The 'noise' component has been filtered out of the successive graphs, but lower frequency oscillations still remain in the turbulence intensity plots. These may be a reflection of recurring patterns in the gas flow structure and therefore the original data has not been processed beyond the statistical bounds (e.g. of window size or smoothing parameter magnitude) discussed previously.

The initial observations reported in Section 5.3 can now be built upon for the two inlet valve geometries considered:

i) Standard Valve

The flush probe ensemble mean velocity plots illustrate a lack of flow directional preference in the main combustion chamber. The exception to this observation is a peak in the radial wire graphs at TDC. Considering the motion histories in the two orthogonal directions, an attributable cause to this effect is an amplification of barrelling vortices in the plane normal to the inlet port as the piston rises. The plug cavity results represent the lowest magnitudes of the three cases, reflecting the sheltered position of the associated anemometer probe. The RMS turbulence intensity plots are of a similar shape to those of the ensemble mean velocities and in general both parameters increase with engine speed.

ii) Shrouded Valve

The decay in the flush probe ensemble mean velocity magnitudes prior to TDC is not reflected in a corresponding increase in RMS turbulence intensity. Therefore the scenario outlined in Section 1.5, namely an unsteady helical motion redistributing to a solid body rotation, is suggested rather than a universal swirl decay (to turbulence) as the piston rises. The high plug cavity results indicate an entrainment of the bulk motion in the main chamber and may be biassed by the non-resolution of large-scale velocity direction changes that would be present in the resulting recirculatory flow. The shape of the RMS turbulence graphs differ from those of the associated ensemble mean velocities and in general both parameters increase with engine speed. However the apparent convergence of the flush probe radial wire plots at TDC may

reflect a geometrical or viscous constraint on the maximum motion intensities attainable, although it must be noted that at this point the associated hot wire measurements will be at their least accurate (see Section 5.5)

In accord with the observations of Dent [29], the turbulence intensities are isotropic during most of the compression stroke, tending to anisotropy as TDC is approached. In comparison with the standard valve graphs, the shrouded valve main chamber RMS turbulence intensities do not reflect the magnitude of the ensemble mean velocity results. It is argued that the cyclic fluctuation component introduced in equation 1.5 is less significant in the more organised flow structure of this latter case. This assertion is investigated further in Section 6.3, where the mean turbulence is to be re-evaluated on a cycle-by-cycle basis.

6.3 A Cycle-by-Cycle Resolution of Mean Velocity and Turbulence

The use of the phase averaging (or ensembling) technique is a compromise that permits an application of conventional mean velocity and turbulence calculation procedures to non-stationary in-cylinder anemometric measurements. The assumption implicit in the adoption of this approach is that there is a general flow pattern which repeats from cycle-to-cycle and superimposed upon this is the random turbulent component. Situations where this might not apply to measurements taken from a fixed position in the cylinder clearance volume, discussed in Section 1.6, either stem from a complete independence in the bulk motion structure from one cycle to the next or a positional instability in the rotational

centres of large scale vortices and solid body swirling motions. The net result may be an over-estimation of the turbulence level attributable to flame surface wrinkling, discussed in Section 1.7, and the subsequent masking of the aerodynamic effects responsible for the problematic dispersion of peak cylinder pressures encountered in lean burn engines.

Figure 6.9 illustrates a comparison between ensemble mean and single cycle velocities calculated from measurements in the main combustion chamber. Of the two examples the shrouded valve ensemble mean follows its associated single cycle velocity plot the more faithfully, reflecting the relatively low RMS turbulence intensities reported in Section 6.2. Following the arguments presented above, the aim of this section is to calculate a unique 'mean' for each cycle to compensate for changes in the phase and magnitude of the underlying trend in the velocity measurements. A cycle-by-cycle (CBC) variation and an adjusted turbulence intensity component, as suggested by equation 1.5, will hence follow.

A possible solution is to use equation 6.1, with $N_c = 1$, in adopting a simple time averaging technique. To this end Ball et al. [11], Groff et al. [36], Wakisaka et al. [85] and Lancaster [50] use 10,20,43 and 45 degree windows respectively. Lancaster subsequently tackles the problem of crank-angle broadening, introduced in Section 6.2, by subtracting the ensemble mean from the instantaneous velocities before calculating turbulent parameters, whereas Witze [91] curve fits by using third order polynomials. Another approach is taken by Dent [18,29] who uses an analogue low-pass filter on the anemometer bridge signals during the data acquisition process,

but in all cases the selection of a suitable window size, polynomial order or cut-off frequency appears to be arbitrary.

The anemometric results obtained as bulk motions carry turbulent eddies past a fixed measuring point can be interpreted in terms of superimposed sinusoidal functions of differing period and amplitude. To this end Liou and Santavicia [53] use a Fourier analysis, truncating the series of the inverse transform to obtain a mean velocity for each cycle. Three forms of discrete Fourier transform (DFT), outlined in Appendix F, have been investigated in this study to assess whether sine, cosine or combined sine and cosine harmonics are the more suited to the data available.

Ideally a DFT analysis of single cycle velocity histories would reveal two clusters of significant amplitudes in the calculated spectrum of coefficients, permitting a resolution between the mean velocity and turbulent components. This is not observed in practice however [53] and the associated ensemble mean graphs, which reflect flow patterns which repeat from cycle-to-cycle, are used as an alternative route to evaluate a suitable cut-off frequency (or coefficient number). Figures 6.10 and 6.11 illustrate the coefficient magnitudes hence obtained from main chamber ensemble mean velocity plots for the standard and shrouded inlet valve geometries.

The results indicate a decay, but no distinct cut-off in amplitudes as the associated frequency increases. The possible values which can be selected for the two inlet valve geometry examples appear to be similar and for the purpose of comparison 12 and 25 coefficient inverse transforms have been applied to

single cycle velocity records in Figures 6.12 and 6.15. The cut-off frequencies associated with these limits are found by:

$$F_{max} = \frac{6 \times (CPM \times NPI \times CF_{max})}{RES \times NPTS} \qquad (6.7)$$

where F_{max} = the cut-off frequency

CPM = the number of engine cycles/minute (= RPM/2)

CF_{max} = the cut-off coefficient number

NPTS = the number of points logged/cycle (= 1306)

NPI = 1 for half-range transforms

2 for full-range transforms

The following values follow at 2000 rpm:

CF_{max}	Half Range (Hz)	Full Range (Hz)
12	276	551
25	574	1,148

Qualitatively the 12-coefficient full-range and the 25 coefficient half-range inverse transforms follow the low frequency oscillations in the single cycle velocity histories the more closely. Of these the half-range even (cosine based) plots are the more successful throughout the crank-angle range considered and the associated cut-off frequency is similar to the 650 Hz quoted by Liou and Santavicia [53]. However the curve fit appears to be poorly phased with the original data during the early part of the compression stroke in Figure 6.15, which may in part reflect the limitations of the Fourier analysis itself or changes in the turbulent energy spectrum throughout the engine cycle reported by Dent [29]. The

cyclically resolved turbulence intensity which would hence be calculated is strongly dependent upon the number of inverse transforms chosen and it is suggested that the use of a single function and cut-off frequency to calculate the mean velocity curves is too inflexible for the present application.

Rask [67,68] expresses an extension to the smoothed ensemble technique, described in Section 6.2, that is suitable for CBC analysis. The procedure interpreted for the equally spaced hot wire data in the present application is outlined below:

i) Equation 6.1, with Nc = 1, is used to calculate the required mean estimates in each cycle's velocity history.

ii) The associated weighting functions are found by [61]:

$$\delta y\ (\theta \pm \frac{\Delta\theta}{2}) = \frac{u'_c\left[\theta \pm \frac{\Delta\theta}{2}\right]}{\sqrt{M}} \qquad (6.8)$$

where $u'_c\ (\theta \pm \frac{\Delta\theta}{2})$ = the cyclically resolved ensembled RMS turbulence intensity (m/s), which is initially estimated by mid-window values from the smoothed esemble analysis.

iii) The spline smoothing routine, outlined in Appendix G, is applied to the mean velocity estimates, using the weighting functions found by equation 6.8. The portion of the curve spanning each window is designated F (ϕ,i).

iv) the turbulence values are esembled using equation 6.2,

replacing $\bar{U}(\theta \pm \Delta\theta/2)$ by the appropriate $F(\phi,i)$ values. The resulting windowed RMS intensities are hence curve fitted by the smoothing routine. The weighting functions appropriate to this case are found by [61]:

$$\delta y\ (\theta \pm \frac{\Delta\theta}{2}) = \frac{u'_c\left[\theta \pm \frac{\Delta\theta}{2}\right]}{\sqrt{(2 \times Nc \times M)}} \qquad (6.9)$$

The portion of the fit spanning each window is designated $f(\phi)$.

v) The analysis is repeated from step (ii) onwards, replacing the turbulence estimates by the mid-window of $f(\phi)$ values, until convergence in the mean velocities and turbulence intensity is achieved.

The route outlined above, using 1-3 degree windows and a smoothing parameter that lies within the bounds indicated by equation 6.5, converges in 4-5 iterations. In the crank-angle range considered however, which does not include the highly turbulent intake and exhaust strokes (see Figure 5.11 for example), the difference between the spline curve and the original data is small. This observation is in accord with the applicable portion of the single cycle results presented in [67] and appears to stem from the importance placed upon the averages found in step (i) above as estimates of the mean velocity. These values are fitted with increasing precision as the weighting functions, found by equation 6.8, rapidly decay in each iterative loop. The difference which remains simply reflects the scatter between the discrete cubic polynomials,

which constitute the complete spline curve, and the original data obtained within the small windows chosen.

Without an 'a priori' knowledge of the anticipated turbulence intensity in each cycle, the use of windows is an "Achilles' heel" necessary to prevent the occurrence of pure interpolation and the subsequent collapse of the procedure at equation G.7 in Appendix G. The aim therefore is to retain the use of small crank-angle windows and to increase the size of the associated weighting functions, which reflect the degree of confidence in fitting each point, while still maintaining a statistical justification in performing the analysis. To this end the averages, calculated in step (i) above, are downgraded from the status of a 'mean' to that of a 'velocity' estimate. The spline fits are hence taken as the 'true mean' and the scatter of the original data as the 'true standard deviation'. The intention is that at the end of the iteration process the standard deviation values will produce the statistically correct mean and vice versa.

In contrast to Rask's approach, it would be desirable to have a routine which performs on each cycle without reference to the ensemble of data available. However the small number of points which fall within each window are not sufficient to attain a continuity in the trend of the standard deviation weighting function values along the crank-angle axis. Therefore averaged values are used to retain the order of magnitude which would occur on a CBC basis such that:

$$\delta y\ (\theta \pm \frac{\Delta\theta}{2}) = \frac{1}{Nc} \sum_{i=1}^{Nc} \left[\frac{1}{M} \sum_{j=1}^{M} (U(\phi_j, i) - F(\phi_j, i))2 \right]^{1/2} \qquad (6.10)$$

The approach subsequently adopted proceeds as far as step (iii) in the method previously outlined, replacing equation 6.8 with 6.10. To achieve the first fit the window averages are substituted into equation 6.10 and the weighting functions are updated at the end of each iterative loop by the latest $F(\phi,i)$ values. The sum of these weighting functions for the windows considered is taken as a criterion for convergence and since the initial scatter is small, 10-20 iterations are required. The resulting procedure filters on the basis of the randomness of the original data and the second derivative between the velocity estimates, rather than the explicit cut-off frequency used in the Fourier technique outlined earlier.

The procedure is sensitive to both window size (M points) and the smoothing parameter (S), which should lie within the bounds expressed by equation 6.5. If the cyclically resolved mean velocities are reasonably defined and the resolved turbulence is purely random, the following arguments should hold:

a) $$\bar{U}(\theta) = \frac{1}{Nc} \sum_{i-1}^{Nc} (\bar{U}_c(\theta,i) + u_c\ (\theta,i)) \qquad (6.11)$$

b) $$\frac{1}{Nc} \sum_{i=1}^{Nc} u_c(\theta,i) = 0 \qquad (6.12)$$

c) $$\bar{U}(\theta) = \frac{1}{Nc} \sum_{i=1}^{Nc} \bar{U}_c\ (\theta, i) \qquad (6.13)$$

where $\bar{U}_c\ (\theta, i) \equiv F(\phi, i)$

= the cyclically resolved mean velocity (m/s)

$u_c\ (\theta, i)$ = the cyclically resolved turbulence (m/s)

Therefore the sum of cyclically resolved means should reproduce the associated ensemble mean velocity.

In practice it is found that over-smoothing biases the computed turbulence and hence yields a significant difference between the average of the CBC means and the ensemble mean velocity curves, whereas the degree of under-smoothing remains undefined. A nine-point, 1.4 degree, window size has been chosen and the effect of three values of the parameter S are illustrated in Figures 6.16 to 6.18.

Using the above criterion, the shrouded valve results represent an extreme that requires the lowest degree of smoothing specified by equation 6.5 and to maintain consistence the same value of S has hence been used throughout. Comparisons of 'over-smoothed' and 'reasonably-smoothed' means and their associated single cycle velocities are given in Figures 6.19 and 6.20 to 6.25 respectively. The resulting curve fits are non-oscillatory, responsive to low frequency trends and do not possess the phasing problems reported in the DFT analysis. The tape stored data files hence created are listed in Appendix H.

The cyclically resolved turbulence intensity and the variation in the mean velocity can be ensembled in a similar

manner to the RMS turbulence intensity in equation 1.4. To this end the following definitions may be adopted:

$$u'_c(\theta) = \left[\frac{1}{Nc}\sum_{i=1}^{Nc}(U(\theta,i) - \bar{U}_c(\theta,i))^2\right]^{1/2} \qquad (6.14)$$

$$U'(\theta) = \left[\frac{1}{Nc}\sum_{i=1}^{Nc}(\bar{U}(\theta) - \bar{U}_c(\theta,i))^2\right]^{1/2} \qquad (6.15)$$

where $u'_c(\theta)$ = the ensembled CBC intensity (m/s)

$U'(\theta)$ = the ensembled mean variation intensity (m/s).

Example plots for the results obtained by this method for main chamber measurements are illustrated in Figures 6.26 and 6.29. The difference between the results obtained from parallel anemometer wires reported in Section 5.3, persist in both the CBC ensembled turbulence and mean variation intensities. In the standard valve case the mean velocity variation is the dominant factor and for both intake geometries the remaining turbulence level is in the order of 50% of the RMS values reported in Section 6.2.

The ensembling technique discussed above does not permit an analysis of the turbulence intensity on a cycle-by-cycle basis, as might be required in seeking a correlation with in-cylinder pressure dispersions in the firing engine for example. Therefore it is proposed to revert to a marching time averaging procedure, as used by Ball et al. [11], while exploiting the

spline derived means to avoid the effect of crank-angle broadening. The intensity is hence found by:

$$u'_c\ (\theta,i) = \left[\frac{1}{M}\sum_{j=1}^{M}\left(U(\phi_j,i) - \bar{U}_c\ (\phi_j,i)\right)^2\right]^{1/2} \qquad (6.15)$$

where $u'_c\ (\theta,i)$ = the cyclically resolved, time averaged turbulence intensity for cycle i (m/s).

In the spline curve fitting procedure the size of the windows used is constrained by the amount of raw data that is to be fed to the smoothing routine and the flexibility of the third order polynomials. In this case it is desirable to maximise the range covered to obtain a suitable sample of values to process in equation 6.15, while minimising the range so as to avoid masking the crank-angle dependence of the intensity values.

In attempting to satisfy these conflicting requirements, Figure 5.30 illustrates an investigation of the effect of the window crank-angle range on the averaged CBC turbulence intensity values which follow from a window centred 90° before TDC, where:

$$\bar{u}'_c\ (\theta) = \frac{1}{Nc}\sum_{i=1}^{Nc} u'_c\ (\theta,i) \qquad (6.16)$$

and $\bar{u}'_c$ = the averaged CBC intensity (m/s).

An alternative approach is illustrated in Figure 6.31, which shows the averaged coefficients of a (half-range even) DFT analysis performed on the raw turbulence values $(U(\theta,i)-\bar{U}_c(\theta,i))$, to assess the window size necessary to

capture the lowest frequencies reasonably anticipated. The common conclusion is that a 30 degree (150 point) range yields a compromise for the criteria outlined above. A comparison between ensembled and averaged intensities hence found by equations 6.14 and 6.16 respectively, is illustrated in Figure 6.32. The peaks in the ensembled intensity do not repeat from test to test and are not considered to be significant. Both plots possess similar magnitudes, but the averaged CBC example yields a smoother and more manageable relationship.

Averaged marching window CBC turbulence intensity graphs for the data sets isolated in Section 6.1 are illustrated in Figures 6.33 and 6.35. The beginning and end of each plot represents the first and last mid-window values obtainable within the data logging range employed. The general trends may be summarised as follows:

i) Standard Valve

The averaged main chamber turbulence intensity is isotropic for the majority of the crank-angle range considered, tending to a slight anisotropy at TDC. The plug cavity values are relatively low after IVC, suggesting that the anemometer is shielded from the main chamber gas flow, and decay rapidly. In all cases the averaged intensity increases with engine speed.

ii) Shrouded Valve

The averaged main chamber intensity is isotropic during the early part of the compression stroke, tending to a strong anisotropy before TDC. The peak in the radial

wire measurements suggests a decay of bulk swirling motions into turbulence, but the rise, convergence and subsequent fall in these values with increasing engine speed may reflect the associated reduction in the time available for this process to occur. The plug cavity measurements illustrate the greatest magnitude of the three cases, suggesting an entrainment of the bulk flow from the main chamber.

In contrast to the ensembled RMS values reported in Section 6.2, the averaged CBC turbulence intensities are higher for the shrouded inlet value geometry in all three measuring positions. The observation is in accord with the magnitude of the associated ensemble mean velocities and illustrates the significance of low frequency CBC variations in the standard valve case, where the intake flow structure is less directed.

6.4 A Cycle-by-Cycle Estimation of Spatial Velocity Gradient Intensity

Thomas [79,80] investigates the spatial velocity gradients intensity as an alternative mechanism for the wrinkling and stretching of a flame surface in a turbulent flow field. As discussed in Section 2.1 the measurement of this quantity using laser Doppler velocimetry is difficult to achieve in practice because of the discrete nature of the data obtained. The original aim was to exploit the analogue signal output by a hot wire anemometry system to evaluate the simultaneous velocity difference found by parallel wires of a known distance apart. The effect of turbulent scale on the magnitude of the calculated values in a motored engine could

hence be investigated by varying the spacing of the sensing elements.

In the absence of a knowledge of the flow direction, it is necessary to have a well ordered mean velocity to carry the turbulence eddies past the hot wires to obtain sensible readings from the technique outlined above. Each anemometer is still sensitive to the component of fluctuations that is perpendicular to their common plane, thus a one-dimensional difference in two-dimensional measurements would be sought, and therefore a 'figure of merit' would primarily result. Putting aside these theoretical reservations, the inconsistencies in the ensembled results discussed in Section 5.3 has precluded the further pursuit of this approach.

Using the measurements from a single hot wire it is however possible to estimate the time rate of change of velocity, dU/dt. If this is taken a step further, by assuming that the smoothing spline curves developed in Section 6.3 represent the mean velocities which carry the turbulent fluctuations past the anemometer, a number which has the dimensions of (and is equal to in the absence of friction and pressure gradients) a spatial velocity gradient can hence be found such that:

$$\frac{dU}{dx}(\theta,i) = \frac{1}{\overline{U}_c\ (\theta,i)} \times \frac{dU}{dt}(\theta,i) \qquad (6.17)$$

where $\frac{dU}{dx}(\theta,i)$ = the estimated spatial velocity gradient (1/s) (velocity gradient parameter).

This approach avoids the uncertainty relating to turbulent scales discussed above in that the calculated result

stems from point measurements. Some ambiguity with respect to direction still remains and thus the estimated spatial gradient must still be considered as a figure of merit. The cyclically resolved mean used here is simply a smooth function which is used for scaling, therefore its rigourous definition is not as important as in the evaluation of CBC turbulence intensity in Section 6.3. Equation 6.17 is non-dimensional in terms of velocity and thus partially tackles the uncertainty relating to the anemometer calibration accuracy.

The aim is to calculate an RMS intensity in a similar manner to the CBC turbulence values in Section 6.3. To this end the time gradient, dU/dt, is estimated by a simple central difference technique for each crank-angle increment. The same 30° (150 point) windowing scheme subsequently adopted in equation 6.15 is hence employed such that:

$$\left[\frac{dU}{dx}\right]_c'(\theta,i) = \left[\frac{1}{M}\sum_{j=1}^{M}\left[\frac{1}{\overline{U}_c(\phi_j,i)}\frac{dU}{dt}(\phi_j,i)\right]^2\right]^{1/2} \qquad (6.18)$$

where $\left[\frac{dU}{dx}\right]_c'(\theta,i)$ = the cyclically resolved RMS spatial velocity gradient intensity (1/s).

In this section the values thus obtained are hence averaged in a similar manner to equation 6.16. An alternative approach would be to use constant crank-angle phase averaging, or ensembling, and a comparison of example plots calculated by the two methods in Figure 6.36 shows both results to have the same overall magnitude.

Averaged marching window CBC spatial gradient intensities for data sets isolated in Section 6.1 are illustrated in Figures 6.37 to 6.39. The x and y notation adopted denotes measurements resolved in the circumferential and radial directions respectively (perpendicular to the hot wire notation), although each graph will contain significant contributions from the axial component of the velocity gradient also. The results can be summarised as follows:

i) Standard Valve

The plots are broadly similar in shape and magnitude for all three measuring positions. In the main chamber the isotropy in the spatial velocity gradient intensity is consistent with the lack of flow direction preference noted in Section 6.2. The calculated values are similar for the plug cavity region for the early part of the compression stroke, but they subsequently decay significantly as TDC is approached.

ii) Shrouded Valve

Again the plots are broadly similar in shape and illustrate a peak in amplitudes at or near TDC, which is greatest for the plug cavity measurements. As the piston approaches TDC, a tendency towards solid body rotation is anticipated in the bulk gas motion structure (see Sections 1.5 and 6.2). Although a change in the mean velocity across the swirling flow will therefore exist in the radial direction, a single hot wire will not be sensitive to this effect. An accompanying spatial variation in turbulence intensity (carried by the radial

mean velocity), assuming the eddies are three-dimensional, may explain the dominance of the circumferential wire measurements in the main chamber. The high peak values obtained in the plug cavity region may reflect the high level of shear generated by an entrainment of the bulk swirling flow.

As a source of comparison, Figure 6.40 illustrates the ensembled spatial velocity gradient intensity evaluated directly from twin circumferential anemometer measurements. In noting the probe design and calibration limitations discussed in Section 5.3, the instantaneous velocities are weighted to compensate for the difference in the ensemble means before a gradient is subsequently calculated. The graph which results differs both in shape and amplitude from the associated averaged CBC plot illustrated in Figure 6.38.

The two-wire results may be biassed by the theoretical considerations outlined previously. However one concern in applying equation 6.17 is the dominance and significance of the spline resolved mean velocities used to convert the time rate of change to a spatial gradient. The simple reciprocal relationship which might result would be reflected in the trend of the averages of both factors in Figures 6.3-6.5 and 6.37-6.39. This does not appear to occur consistently throughout the crank-angle range considered in practice and consequently it is believed that the results presented are of physical significance.

6.5 Summary

From the anemometric measurements broadly surveyed in Chapter 5, representative single-wire examples have been isolated to investigate the effect of engine speed, inlet valve geometry and measurement location in greater detail. A smoothing spline routine has been adopted to statistically compensate for the limited quantity of data available, to calculate ensemble mean velocity and RMS turbulence intensity histories. Following a review of the associated weighting functions, the routine is subsequently used to calculate unique mean velocity histories for each cycle on a similar basis. From these a mean variation, cyclically resolved turbulence and a spatial velocity gradient intensity parameter hence follow.

Marked differences in the ensembled mean velocities are noted for the different inlet geometries and anemometer measurement positions. The mean velocity variation, attributed to stem from oscillatory instabilities in the bulk gas flow field, has been shown to bias the ensembled RMS turbulence intensities hence calculated. Although an attempt has been made to provide some level of feedback, the magnitude of the cyclically resolved turbulence intensity is dependent upon the type of curve fitting routine used on the raw velocity data and the magnitude of the external input parameters required. The single-wire estimated velocity gradient intensity parameter that has been introduced is less sensitive to these uncertainties and appears to be the only function which clearly and consistently increases with engine speed in all cases.

CHAPTER 7

POSSIBLE ANEMOMETRIC INFLUENCES ON THE FIRING ENGINE PERFORMANCE IN THE CONTEXT OF THE IN-CYLINDER FLAME DEVELOPMENT

7.1 Introduction

The proportional IMEP variation plots presented in section 5.4 illustrate that the cycle-by-cycle power fluctuations of the engine in its standard configuration and operating at a given ignition advance become increasingly apparent as the air/fuel mixture becomes leaner. This effect is assumed to stem from the associated fall in the rate of heat release during the combustion process and as the drivability limit is approached, the late timing of the peak pressure generation with respect to TDC. The magnitude of this pressure will be very sensitive to the crank-angle at which it occurs, because the cylinder volume is rapidly changing, and therefore to fluctuations in the rate of burning from the instant of sparking. As discussed in Section 1.4, an increase in the ignition advance does not necessarily solve the problem, because of the unfavourable reactant properties at the time of the early flame development, and occasional knocking may occur if some fast-burn cycles remain [64]. Therefore to minimise cycle-by-cycle performance variations, a fast overall burn time is desirable [48,55,88,93].

A significant improvement in the operational stability of the firing engine has been observed for the shrouded valve intake geometry in the performance and drivability curves reported in Chapter 5. Similarly marked differences in the motored engine mean velocity, turbulence and velocity gradient

intensities at fixed measuring locations has been noted in Chapter 6. The aim of this Chapter is to compare the firing engine pressure data, acquired according to the scheme outlined in Section 5.4 and documented in Appendix H, with the available anemometric parameters.

Performance descriptors such as the peak in-cylinder pressure or the maximum rate of pressure rise are strongly crank-angle dependent [48]. Therefore the results of the mass fraction burnt analysis outlined in Section 4.10, which are more descriptive of the overall combustion process, are primarily used as a source of comparison. The origin of cycle-by-cycle combustion variations, discussed in Section 1.7, is generally attributed to the early stages of the flame development. The initial aim is to investigate this assumption and to quantify this effect. The relative duration and variability of the early and remaining burn times are then assessed and an attempt is made to evaluate the degree of flame area enhancement by turbulent or velocity gradient mechanisms.

7.2 The Correlation Between Early and Total Burn Times

Figures 7.1 and 7.2 represent the results of mass fraction burnt calculations applied to 182 consecutive pressure records from the firing engine at 2000 rpm, with the standard inlet valve fitted. The 5 and 10% Cpi (proportional IMEP variation - see Section 4.7) values represent acceptable and drivability limit performance regimes respectively. The plots indicate that although the histories initially follow a similar path, a region of separation is reached beyond which it is possible to resolve the fast slow-burn cycles. Previous work

has observed that the flames which start quickly appear to maintain that advantage [78]. It is argued therefore that the early combustion stage is critical in relation to the magnitude and phase of the peak in-cylinder pressure subsequently developed.

An attempt to identify the onset of rapid combustion by considering the derivatives of the original pressure records has proved to be unreliable. The results of the combustion calculations are therefore used to seek a possible relationship between the early and total burn times and thus to identify the critical period in the process history which reflects the final outcome. To this end different mass and volume fractions burnt and product volumes (assuming the 2-zone model discussed in Section 4.10) are used as criteria for the above analysis. It should be noted at this stage that if the process is continuous, there will be no apparent value to indicate the onset of a relationship, and if initially slow flames are capable of recovery at some random time, no correlation will be observed.

The crank-angle period required to attain a given value of one of the above parameters, referred to as a "delay" (before correlation is achieved), is compared to the time taken to burn in excess of a 90% mass fraction of the reactants (the 90% burn time - the mass fraction computation is truncated at 98%). Two measures of the onset of a relationship are used, namely,

i) A correlation coefficient, defined by [19];

$$r = \frac{\sum_{i=1}^{Nc} (x_i - \bar{x})\,(y_i - \bar{y})}{\sqrt{\left(\sum_{i=1}^{Nc} (x_i - \bar{x})^2\right)\left(\sum_{i=1}^{Nc} (y_i - \bar{y})^2\right)}} \qquad (7.1)$$

where r = the correlation coefficient
x = the "delay" crank-angle from the time of sparking (°)
y = the 90% burn time (°)
Nc = the number of cycles which reach 90% mass fraction burnt.

ii) The sum of squared errors from a first order least squares fit (see Appendix C).

Although a linear relationship is sought by the latter approach, there is no pretext that one should actually exist. It is noted however that in the extremes of a delay defined as the time taken to burn a 0 or 90% mass or volume fraction of the reactants, a perfect straight line fit would result.

Comparisons between the delay, defined on a mass fraction basis, and the 90% burn time for the data set illustrated in Figure 7.1 are presented in Figures 7.3 to 7.5. At 2% mass fraction burnt no real relationship appears to exist, but when the delay criterion is relaxed to 10% a significant improvement in the correlation is observed. Similar results are obtained when considering the volume fraction burnt and the product volume parameters. The sum of squared errors and the correlation coefficient values which follow are summarized in Figures 7.6-7.9.

Attempts to quantify the onset of a significant relationship by calculating the deviation from a straight line

fit of the right hand portion of the correlation coefficient and sum of errors curves have been found unreliable. Within the limited range considered, a variation in the air/fuel ratio appears to have little effect on the conclusions drawn. Viewing the graphs representing 20% Cpi performance regimes (where the correlation is usually strongest) by eye, the delay criteria listed in Table 7.1 have been estimated for the engine fitted with the standard inlet valve;

Table 7.1 ; Possible "Delay" Criteria

Engine Speed (rpm)	Compression Ratio	Mass Fraction Burnt (%)	Volume Fraction Burnt (%)	Product Volume (cc)
1000	8:1	4	4	3
1250	"	4	4	3
1500	"	5	6	5
1750	"	6	8	6
2000	"	7	10	9
1500	7:1	5	6	5
"	9:1	5	6	4

It is possible that the product volume values in the 1000-2000 rpm engine speed range reflect the size of flame kernel required to interact with the prevalent turbulent integral scales before rapid combustion ensues [63]. Similarly the mass fraction burnt results may indicate the heat release required to establish a stable flame kernel against adverse turbulent cooling effects [10,33]. However it is equally likely in this case that the increasing values with engine speed reflect the different gas

properties and combustion chamber geometry associated with the chosen ignition advance values (namely 30-60°) at 1000-2000 rpm, see Appendix H). The latter proposal is weakly reflected in the increasing product volume values for reducing compression ratios.

It is desirable to have a single value for the delay criterion to compare the early burn times with the anemometric data developed in Chapter 6. From this point of view the mass fraction burnt results appear to vary least throughout the test condition range for the standard inlet valve geometry. In previous studies 1% [93], 5% [12] and 10% [10,33,55] mass fractions have been identified to this end. In this case 6% appears to be reasonable for the data presented.

Examples of a similar analysis performed on shrouded valve data (2000 rpm) are illustrated in Figures 7.10 to 7.12. At near stoichiometric air/fuel ratios the correlation between the early and 90% burn times is very weak, largely because the coordinates of the associated graph are very tightly packed. As the lean limit is approached a relationship begins to emerge and the 6% mass fraction delay criterion still appears to be acceptable.

The bar charts presented in Figures 7.13 to 7.17 seek to establish a cause-and-effect relationship between the motored engine spark-plug cavity anemometric results, at the ignition timing crank-angle, and the 0-6% mass fraction burn times, at a common 18:1 air/fuel ratio. Although the ignition advance is varied between the 1000-2000 rpm speed range, it is the same for each standard-shrouded valve data pair. The turbulence and velocity gradient intensities are evaluated on an RMS windowed

cycle-by-cycle basis according to equations 6.15 and 6.18 respectively, whereas the velocity distributions represent single crank-angle measurements. The spline fit distribution is also calculated on a windowed CBC basis to represent the RMS difference between the spline fit curves developed in Section 6.3 and the ensemble mean velocity, and may be viewed as a form of low-frequency turbulence or a cycle-by-cycle bulk flow variation.

The shrouded valve 0-6% mass fraction burnt times illustrate a narrower distribution, the median of which is slightly faster, than those calculated from the standard configuration experiments. In seeking a comparison with the anemometric results, overlapping distributions with slightly higher valves of the perceived beneficial factor for the shrouded valve case are sought. Both the spline fit and the velocity distribution measurements fall into this category.

At first sight the spline fit distribution results would appear to concur with the findings of Cole and Swords [22,23] and Swords, Kalghatigi and Watts [78] where the peak in-cylinder pressure and the rate of the first 10 mm of flame travel have been found to correlate with a horizontal velocity component towards the cylinder centre. However given the marked difference in the velocity field itself for the two intake geometries, it is difficult to accept that this bulk variation alone is responsible for the enhancement or otherwise of the early stages of combustion. Therefore on the basis of the present analysis, the velocity gradient intensity parameter would appear to be a better candidate.

Figure 7.18 illustrates a standard/shrouded valve geometry average burn time ratio up to a range of mass fraction burnt values, with the engine operating at an 18:1 air/fuel ratio and different speeds. The indications are that although the 0-6% combustion rate is faster in the shrouded valve case, the time to attain smaller values (0-0.5% to 0-3%) is actually increased. In considering the velocity and turbulence intensity bar charts in Figures 7.14 and 7.15, the suppression of the very early flame kernel development by gas cooling effects [10,33] is suggested. For the shrouded valve configuration this argument is supported by an increase in the average CBC plug cavity turbulence and velocity gradient intensity as TDC is approached illustrated in Figures 6.35 and 6.39, and the performance maps, in Figures 5.31 to 5.35, where the engine fails to operate (suggesting that the kernel is actually extinguished) with lean mixtures and low ignition advances.

Previous work has indicated that early quenching on the cylinder boundaries [63] and very flexuous, irregular initial flame geometries [48] are detrimental to the peak pressure and IMEP values subsequently developed. In an (square piston) engine of similar dimensions to the Ricardo E6 used in this study, the flame is said to be fully developed (in terms of its ability to interact with the turbulent flow field) after travelling 2 cm [63]. The stage at which these factors are important is believed to broadly concur with the 6% mass fraction criterion discussed previously. However it is likely that the overall early (delay) burn time cumulatively represents the initial gas mixing mechanisms at the time of

sparking, flame positioning effects by the bulk velocity field or low frequency turbulence and the subsequent onset of rapid propagation when the kernel is of sufficient size to stably interact with high frequency turbulence or velocity gradients.

7.3 The Relative Duration and Variability of the Early, Remaining and Total Burn Times

In Section 7.2 the 0-6% mass fraction burn time has been identified as a critical period in determining the outcome of a combustion history for a given firing engine cycle. The aim of this section is to take a cursory look at its duration and variability in relation to the "remaining" (6-90%) and 90% mass fraction burnt times. As a result it may be possible to comment upon the independence of the "developed" (see Section 7.2) flame's interaction with the flow field in the main combustion chamber, in comparison to the behaviour of the growing flame kernel as it emerges from the spark plug cavity in the cylinder head. However no further attempt to compare the results with the relevant anemometric data is made at this stage.

Figure 7.19 illustrates the average time taken to attain given mass fraction burnt values for the two inlet valve geometries at a range of air to fuel ratios. The duration of the 0-6% period is comparable for both examples and accounts for approximately half of the 90% burn time. A significant improvement in the combustion rate and tolerance to lean mixtures is apparent in the shrouded valve case in the 6-70% range, which relaxes subsequently between 70 and 90%. These observations are confirmed by Figures 7.20 to 7.22, which

compare average early, remaining and 90% burn times, all of which also reduce with increasing engine speed.

Bar charts for the remaining 90% burn times for an 18:1 air/fuel ratio are illustrated in Figures 7.23 to 7.24. The mean crank-angles associated with these events (derived from Figures 7.20 and 7.22) can be obtained from Tables 7.2 and 7.3.

Table 7.2: 0-6% Mass Fraction Burnt (Start of 6-90% Period).

		Standard Valve		Shrouded Valve	
Engine Speed (rpm)	Ignition Advance (°)	Time Taken (ms)	Angle From TDC (°)	Time Taken (ms)	Angle From TDC (°)
1000	30	4.54	-3	4.29	-4
1250	37.5	4.14	-6.5	3.75	-9.5
1500	45	3.82	-11	3.5	-13
1750	52.5	3.61	-14.5	3.25	-18.5
2000	60	3.5	-18	3.07	-23

Table 7.3; 0-90% Mass Fraction Burnt (End of 6-90% Period)

		Standard Valve		Shrouded Valve	
Engine Speed (rpm)	Ignition Advance (°)	Time Taken (ms)	Angle From TDC (°)	Time Taken (ms)	Angle From TDC (°)
1000	30	9.93	30	7.57	15
1250	37.5	8.79	28.5	6.64	12.5
1500	45	7.79	25	6.00	9
1750	52.5	7.09	21.5	5.50	5.5
2000	60	6.64	20	5.14	2

The 6-90% remaining burn times begin at similar crank-angles for the two inlet valve geometries at each engine speed test condition, but it is not reasonable to repeat the one-to-one comparisons performed in Section 7.2. The duration and variability of the delay period is such that the prevailing anemometric and gas property conditions will correspondingly differ at the outset for each cycle.

The shape of the 0-6% distributions in Figure 7.13 generally persist in the 6-90% results for the standard configuration, whereas those for the shrouded valve show an increasing independence at high engine speeds. In the latter case the majority of the 6-90% period occurs before TDC and a proportional preference for fast-burn cycles is apparent. The overall enhancement of the main combustion process serves to reduce the relative variability of the 90% burn times which result and hence weaken the cause-and-effect relationship with the delay period. These observations are reflected in the associated correlation graphs reported in Section 7.2 and the proportional IMEP variations plotted in Section 5.4.

7.4 Combustion Rate Enhancement and Flame Propagation Modelling

As discussed in Sections 1.4 and 7.1, a fast overall burn time is desirable to optimise the phasing of the peak in-cylinder pressure with respect to TDC. It is correspondingly observed in Sections 7.2 and 7.3 that a reduction in the "remaining" 6-90% mass fraction burnt time serves to weaken the significance in the "delay" period in the combustion history duration, improving the engine performance stability and tolerance to lean mixtures. The aim of this section is to

examine the associated enhancement of the "developed" flame, as defined in Section 1.7, in terms of the main chamber anemometric results reported in Chapter 6.

Performance descriptors such as the peak in-cylinder pressure, the maximum rate of pressure rise and the mass fraction burnt times are reactant property and composition dependant. An attempt to quantify the degree of flame surface "wrinkling", as discussed by Thomas [79,80], is therefore adopted as a dimensionless route to seek possible correlations with the main chamber anemometric measurements. This approach has also been taken by Groff [36], Lancaster [51] and Mattavi [56] to calculate a burning velocity ratio (misnamed a flame speed ratio), which will be shown to be an equivalent parameter, from in-cylinder combustion data.

The results from the mass fraction burnt analysis, outlined in Section 4.10, are again used as a basis for the calculations. It is consequently assumed that the flame front is a thin interface between the product and reactant zones and that no pre-reactions occur in the latter region. The associated burning velocity is taken to retain its laminar value throughout and the combustion rate is enhanced purely by virtue of an increase in flame surface area, which is wrinkled by turbulent or velocity gradient mechanisms [79,80]. The concept of a unique turbulent burning velocity, which is itself an independent function of the reactant properties and composition, is hence dropped and the local heat and mass transfer effect of eddies of a smaller scale than the laminar flame front is assumed to be small [51].

The surface area of a "smoothed flame", used as a reference to evaluate the degree of wrinkling, is found from the calculated product volume in the two-zone combustion analysis. Two idealised geometries used to this end, where this flame is assumed to progress spherically across the combustion chamber until quenched by the enclosing boundaries, are detailed in Appendix I. The first (Model 1) is based on the cylinder centre line and is a simple approach which can be solved analytically in most situations. The second (Model 2) used the location of the spark plug electrodes as the origin of the growing sphere and requires a numerical solution procedure. The latter is perceived to be the most appropriate interpretation of the progress of the smoothed flame in a quiescent combustion chamber. Model 1 may however prove to be applicable in high swirl cases, should the lighter gasses of the developing flame kernel migrate towards the cylinder centre line, as has been observed in the bomb studies of Hanson and Thomas [39] and the engine "flame blow-off" cycles reported by Namazian et al. [63].

The wrinkled surface area of the flame front is found by considering the diffusion of the reactants into the product volume zone by means of the laminar burning velocity such that;

$$\frac{dM_r}{dt} = A_t \; S_l \rho_r \qquad (7.2)$$

where dM_r/dt = the rate of reactant combustion (Kg/s)

A_t = the wrinkled flame surface area (m^2)

S_l = the laminar burning velocity relative to the reactants (m/s)

ρ_r = the density of the reactants (Kg/m^3)

The rate of reactant combustion is found by a simple central difference method. The equation can be rewritten to express the degree of wrinkling or an equivalent turbulent velocity as follows;

$$\frac{dM_r}{dt} = WA_s\ S_l \rho_r \tag{7.3}$$

$$= A_s\ S_t\ \rho_r \tag{7.4}$$

where W = the degree of wrinkling

A_s = the smoothed (or projected) flame surface area (m^2)

S_t = the equivalent turbulent burning velocity (m/s)

Hence;

$$W = \frac{A_t}{A_s} = \frac{S_t}{S_l} = BSR \tag{7.5}$$

where BSR = the burning velocity (speed) ratio.

The laminar burning velocity is calculated using empirical (bomb study) relationships evaluated by Metghalchi and Keck [58] for a wide boiling point range blended Indolene fuel/air mixture at high temperatures and pressures, where;

$$S_l = S_l^* \left[\frac{T_r^\bullet}{T^*}\right]^\alpha \left[\frac{P}{P^*}\right]^\beta (1-2.1F) \tag{7.6}$$

and S_l^* = the reference laminar burning velocity (m/s)

$T_r^\bullet$ = the reactant temperature in adiabatic conditions (K)

P = the in-cylinder pressure (N/m^2)

F = the exhaust residual mass fraction

T^* = 298 K

P^* = 1.01325×10^5 N/m^2

α, β = empirical constants

The reference laminar burning velocity depends upon the fuel type and equivalence ratio, whereas the empirical constants are functions of the equivalence ratio only, as follows;

$$S_l^* = B1 + B2\ (\phi-\phi^*)^2 \tag{7.7}$$

$$\alpha = 2.18 - 0.8\ (\phi-1) \tag{7.8}$$

$$\beta = -0.16 + 0.22\ (\phi-1) \tag{7.9}$$

where ϕ = the equivalence ratio
(taken as 15/AFR)

AFR = the air/fuel mass ratio of the reactants

and B1 = 0.2758 m/s

B2 = 0.7834 m/s

ϕ^* = 1.13

In the combustion analysis the heat transfer is considered to be negligible in the reactant zone, which is in accord with the adiabatic criteria required above. The firing tests have been performed at wide open throttle conditions and at relatively low engine speeds. Consequently the exhaust residual mass fraction, which has neither been measured nor estimated, is assumed to be negligible. The reference burning velocity has been found to be insensitive to the fuel type for the liquid hydrocarbons studied by Metghalchi and Keck [58] and

therefore the empirical constants quoted above should be readily applicable to the gasoline used in this study.

Local bulk flow, turbulence and velocity gradient perturbations are considered to play an important part in the cycle-by-cycle intensity variations discussed in Sections 6.3 and 6.4. The burning velocity ratio is a global parameter, representing the overall enhancement of the flame surface area as it traverses the combustion chamber. Consequently it is inappropriate to use the distributions of the fixed point anemometric measurements at given crank-angles as a source of comparison, as in Section 7.2. Bulk differences in the gas property values between the motored and firing engine experiments and local variations across the flame front itself, as discussed in Section 1.7, also preclude the establishment of an exact cause-and-effect relationship. Therefore averaged values are used to seek a qualitative link between descriptors of the gas motion intensity and the associated wrinkling of the idealised smoothed flame geometries.

Example plots of the averaged burning velocity ratio, as a function of crank-angle and smoothed flame radius for the two models in Appendix I, are presented in Figures 7.25 to 7.29. Associated estimates of the averaged flame speeds, calculated from the rate of change of these radii, are illustrated in Figure 7.30. The latter can be split into two components to encompass the burning and an expansion velocity [56] such that;

$$\frac{dR}{dt} = S_t + S_e \qquad (7.10)$$

where dR/dt = the estimated flame speed (m/s)

S_e = the expansion velocity of the products relative to the reactants (m/s)

The incongruities of the cylinder head surface (see Figures 2.1 and 2.4) necessitate that the analysis does not begin until the flame has cleared the spark plug port cavity. The volume of the latter is estimated to be 0.9 cc and consequently the initial kernel development from the instant of sparking, where the mass fraction burnt calculation will also be at its least accurate, is not considered. The instantaneous magnitude of the burning velocity ratio has been found to be related to the radius of the smoothed flame models. Therefore the results are averaged at fixed radial increments, by interpolating the crank-angle phased data from each cycle, to yield the graphs in Figures 7.27, 7.29 and 7.30 directly. It is also dependent upon the idealised geometry chosen from Appendix I, Model 1 giving the greater projected area of the two cases and consequently the lower BSR values.

The rise, peak and subsequent decay in the burning velocity ratio plots is taken by Lancaster [51] to reflect the flame's ability to interact with the spectrum of turbulent scales present in the combustion chamber. As the flame grows it will be influenced by eddies of increasing size, but as the cylinder walls are approached the turbulent scales themselves must decrease, because of the physical boundaries which restrict the recirculatory gas motions. Groff, Lancaster and

Mattavi [36,51,56] also note that the idealised models fail to account for the actual thickness of the wrinkled flame front, taken to be 8-12 mm in engine like conditions [51]. Therefore the estimated burning velocity ratio will be undervalued when the degree of interaction with the combustion chamber walls is high, because the peaks in the flame topography will be truncated by the enclosing boundaries. This effect will also account for the initial step in the BSR graphs, when it is assumed that the flame front rapidly changes shape as it is quenched by the cylinder walls and the piston crown.

The peak burning velocity ratio is therefore taken to represent conditions where the surface of the progressing flame experiences a minimum of interference with the combustion chamber boundaries. In the example graphs presented in Figures 7.25 to 7.27, its averaged value increases with engine speed and is found to be significantly greater for the shrouded inlet valve results. The estimated flame speed plots in Figure 7.30 illustrate a corresponding trend, reflecting the degree of enhancement in the combustion rate that results. However the maximum values occur at smaller radius and crank-angle values, probably because the compression of the reactants in the end-gas region progressively retards the expansion of the product zone (see equation 7.10).

Figures 7.28 and 7.29 suggest that the peak burning velocity ratio increases with mixture leanness. This may simply reflect the crank-angle at which it occurs and therefore the gas motion conditions which prevail. However it is also anticipated that the self-smoothing action of the flame's propagation normal to its wrinkled surface [79,80] and the

viscous damping of the anemometric mechanisms, discussed in Section 1.7, will also reduce by virtue of the lower associated laminar burning velocities and flame temperatures to yield this effect.

Of the main chamber anemometric parameters reported in Chapter 6, the averaged cycle-by-cycle turbulence and velocity gradient intensities are taken to be possible causes of flame surface wrinkling. Assuming that the gas property and composition factors discussed above are of secondary importance within the limited range of air/fuel ratios considered, the average peak burning velocity ratios are compared with these measurements on a simple one-to-one basis. Treating each as a figure of merit, the values calculated at coincident crank-angles are plotted in Figures 7.31 to 7.42 for the different hot wire orientations and smoothed flame geometry models. A simple second-order least squares fit is calculated to give a qualitative indication of the level of correlation achieved. The associated data along with further results from the combustion and flame wrinkling analysis are listed in Appendix J.

In Figures 7.31 to 7.38 the circumferential wire results illustrate a reasonable degree of correlation for the two inlet valve designs. Among these the velocity gradient graphs exhibit the greatest linearity, but the turbulence intensity relationship is unconvincingly exponential. The latter observation may illustrate the cumulative distortions caused by the anemometer calibration uncertainty and design limitations discussed in Section 6.3. Groff [36] and Mattavi [56] use a dimensionless turbulence intensity/laminar burning velocity

ratio (u'/S_l) as a basis for correlation, which is attractive in that it appears to tackle the flame self-smoothing effect discussed previously. However the variation in the averaged laminar burning velocity values tabulated in Appendix J appears to be too small to significantly influence the general outcome of the graphs presented.

Figures 7.39 to 7.42 illustrate an attempt to marry the results obtained from the two idealised flame geometries to reflect the anticipated bulk in-cylinder gas flow conditions. To this end Models 1 and 2 are applied to the shrouded and standard valve results to represent the flame propagation in swirl and quiescent chambers respectively, as discussed at the beginning of this section. The result is a collapse in all but the radial wire velocity gradient correlation, which improves considerably. However the standard and shrouded valve coordinates are now superimposed, which does not agree with the reduced 6-90% mass fraction burnt times illustrated in Figures 7.21 and 7.23 for the latter case. Consequently the Model 2 flame geometry is assumed to be the more representative for both in-cylinder flow regimes.

The circumferential wire velocity gradient intensity yields the most convincing correlation with the peak burning velocity ratios presented in this section. This velocity gradient is less sensitive than the turbulence intensity to the inaccuracies in the hot wire calibration and the form of cycle-by-cycle variation analysis performed, when estimated in the manner outlined in Section 6.4. It is also independent of scale [81] and therefore conceptually an easier parameter to associate with the overall spectrum of flame area enhancement

mechanisms. Therefore apart from the small scale surface wrinkling discussed previously, the analysis may also successfully encompass the bulk smearing of the flame that is reported by Witze [88] and Patterson [64], in high swirl combustion chambers, and observed in the bomb studies of Hanson and Thomas [39], in conditions of high shear and low turbulence intensity.

7.5 Summary

On the basis of a least-squares error and correlation coefficient analysis, the 0-6% mass fraction burnt time is identified as a consistent indicator of the overall combustion period duration for the standard configuration engine and lean reactant mixtures. The variability in this correlation "delay" persists in the "remaining" (6-90%) burn time distributions and is therefore taken as the origin of cycle-by-cycle peak pressure and power fluctuations. A simple cause-and-effect comparison between standard and shrouded valve motored engine anemometric data suggests a dependence upon the prevailing velocity gradient intensity. However the ratio of the average time taken to reach given mass fraction burnt values for the two test conditions indicates that a high gas velocity of turbulence intensity retards the development of the flame kernel.

The delay period correlations are weak for the shrouded valve combustion data until the drivability limit air/fuel ratio conditions are approached. Although the cycle-by-cycle variation in this delay is less than that of the standard valve experiments, the reduction in the remaining 6-90% mass fraction

burnt time is primarily attributed to the improvement in the engine performance stability that results. An assessment of the degree of flame surface wrinkling suggests a relationship with the averaged turbulence and velocity gradient intensity, calculated from the circumferential probe anemometer measurements in the main combustion chamber of the motored engine. Of these the velocity gradient intensity gives the strongest correlation and is preferred as an explanation of the flame area enhancement because of its independence of scale and its relative insensitivity to the uncertainty in the calibration of the hot wires and to the form of cycle-by-cycle bulk flow variation analysis adopted.

CHAPTER 8

OVERALL SUMMARY AND SUGGESTIONS FOR FUTURE WORK

8.1 Introduction and Experiment Overview

An improvement in the cycle efficiency and a reduction in CO, NO_x and HC exhaust gas emissions are possible by fuelling a four stroke, spark-ignition engine with a lean homogeneous mixture. The attainment of these goals and an acceptable level of drivability with quiescent combustion chambers are hindered by an inconsistency in the early stages of the flame development and an overall reduction in the burning velocity. Simple corrective measures such as an increase in the ignition advance or the cylinder compression ratio must be used judiciously to avoid the onset of knock. The former is also limited by corresponding adverse property conditions at the time of sparking. An increase in the overall combustion rate by enhancing the degree of surface wrinkling in the progressing flame front is however identified as a possible route to reduce the cycle-by-cycle performance variations.

The aim of this study has been to compare the gas motion and lean-burn combustion histories of a Ricardo E6 research engine. The surface wrinkling sought in the compression and expansion strokes has been reported to stem from turbulence or velocity gradient intensities which act to distort the progressing flame front. These in turn are generated by the decay of large scale vortices or swirling motions which can be established during the induction stroke. The inlet valve geometry, the engine speed and the compression ratio have been used as modulating variables to study these effects at wide open throttle conditions. The gas velocities are measured by

hot wire anemometry, which has been chosen primarily because its analogue signal assists in the ensembling of data and may permit a direct measurement of spatial velocity gradients. However the probes cannot withstand a combusting environment, which dictates that separate motored and firing engine experiments are performed. Micro-computer based data acquisition systems have been developed to take a large number of measurements from the two cases and simple statistical comparisons are used to correlate the results obtained.

The voltage from the hot wire bridge represents a measure of heat transfer and is therefore a function of the properties as well as the velocity of the gas in which the flow is to be measured. The probes are calibrated at ambient conditions in a steady air stream by using a small wind tunnel and then simultaneous hot wire, resistance thermometer and pressure transducer signals are combined to calculate the velocities in the motored engine experiments. The latter is achieved by an interactive procedure that is based upon the observations of Corkhill, Bullock and Wigley [25], which has been adopted because it is reported to give a reasonable correlation with absolute in-cylinder measurements obtained by laser Doppler velocimetry (LDV).

The hot wire properties, which are also required to interpret the anemometer bridge signal, have been obtained from the manufacturer, or are determined by experiment where the information is lacking. Parallel wire probes have been designed to take measurements in the spark plug region and in the main combustion chamber. Ten micro-meter platinum-rhodium is used for the majority of the experiments, with one wire

acting as the resistance thermometer when the in-cylinder temperature is to be measured. Twin hot wire tests are also performed in seeking a direct estimate of the spatial velocity gradient intensities. A windowed technique that spans the intake, compression and part of the exhaust strokes is used to log the transducer signals from 100 cycles at a resolution of 0.2 degrees crank-angle. The data is transferred to a Mainframe computer and the processed velocities and temperatures are stored on magnetic tape.

For an overview of the engine performance, BMEP and IMEP (brake and indicated mean effective pressure respectively) contour maps are plotted on air/fuel ratio versus ignition advance coordinates. Transducers and metering systems have been fitted to the engine test bed to permit the acquisition of averaged parameters in unstable operating conditions. A computer program and interface is then used to log the data, to process and display the results and to maintain the fuel supply to the engine. The analysis is restricted to lean air/fuel ratios and lies within the bounds of knock and poor drivability. Knock is determined by ear and by viewing the in-cylinder pressure trace on an oscilloscope. The degree of drivability is quantified by a proportional IMEP variation coefficient, Cpi, as proposed by Kuroda et al. [48]. To this end 182 cycles of in-cylinder pressure data are logged at a course 4 degree crank-angle resolution to calculate the IMEP values.

The shape of the performance maps is used to determine a strategy for the acquisition of more detailed in-cylinder pressure records. Data from 182 consecutive cycles is logged

at a resolution of 0.5 crank-angle degrees and a window range which spans the compression and expansion strokes. A simple two-zone model, based upon a procedure outlined by Benson [15], is used to calculate the combustion histories for each test condition. The principle of the routine is to balance the first law of thermodynamics for the reactant and product zones, which are separated by a thin flame front interface. Dissociation reactions are included in the analysis and Annand's heat transfer relationship [4] is used to estimate the losses to the cylinder walls. The constant 'A' in Annand's equation is adjusted to give 100% total mass fraction burnt at the end of combustion for the first cycle in each data set.

8.2 Motored Engine Anemometric Measurements

The test conditions chosen for the standard inlet valve experiments span an engine speed and compression ratio range of 1000-2000 rpm and 7-9:1 respectively. Radial wire measurements are taken in the spark plug region and both radial and circumferential wire probes are used in the main combustion chamber. The in-cylinder temperatures calculated from parallel anemometer and resistance thermometer data are ensemble averaged and the result is used to determine the gas properties in the twin hot wire experiments. Within the limited range considered the changes in the compression ratio appear to have no systematic effect on the ensembled mean velocity or RMS turbulence intensity values. Therefore the influence of engine speed alone is subsequently investigated when the analysis is repeated for the shrouded inlet valve geometry.

The twin hot wires are mounted in close proximity and a good agreement between the parallel ensembled mean velocity or RMS turbulence intensity plots is therefore expected. However for the majority of the experiments performed a poor correlation is achieved in practice. A sensitivity analysis indicates that an uncertainty in the gas temperature at compression TDC exerts the greatest influence on the magnitude of the calculated velocities. This would suggest a poor repeatability in the wire calibration, data acquisition and processing procedures adopted. However the results also indicate that the probe supports are interfering with the flow, giving an increase in the turbulence intensity that is measured by the wire which is assumed to be in the wake. This observation has discouraged the calculation of spatial velocity gradients from twin anemometer measurements. Instead 'representative', hopefully upstream, single wire data sets have been isolated for each test condition.

High frequency 'noise' on the single wire ensembled mean velocity and RMS turbulence intensity plots makes it difficult to present the trends with increasing engine speed for the different probe and inlet valve designs. This problem is attributed to the low number of measurements used to calculate the crank-angle phased averages. The solution adopted is to employ a cubic spline fitting procedure, originally proposed by Reinsch [69] and applied to LDV velocity data by Rask [66, 67, 68], to smooth the graphs. The aim has been to avoid the 'crank-angle broadening' effects that can arise from simple step averaging schemes, while using the number and scatter of the original data points to obtain a 'statistically correct'

result. The plots that are generated are then superimposed to compare the measurements from the two inlet valve geometries with increasing engine speed.

The ensembled mean velocity and RMS turbulence intensity values generally increase with engine speed for both inlet valve geometries. The standard valve results indicate that there is no preferred flow direction in the main combustion chamber, except for the possible amplification of barrelling type vortices as TDC is approached. The shape of the corresponding shrouded valve plots is consistent with the scenario of an unstable flow pattern that redistributes to a swirling solid body rotation. In this case the RMS turbulence intensity values are lower than would be expected from the high ensembled mean velocities observed. The plug cavity anemometer probe appears to be sheltered from the main flow for the standard valve and subjected to an entrainment of the swirling motions when the shrouded valve is used.

The RMS turbulence intensity that is calculated from the ensembled mean velocity includes a 'cycle-by-cycle variation' component. This may be the result of an independence in the flow structure from one cycle to the next, or the positional instability of the centres of large scale vortices or swirling motions. A comparison of single cycle and ensembled mean velocity plots indicates that the underlying trend of the fixed point measurements is more repeatable in the shrouded valve case, giving correspondingly low RMS turbulence intensity values. To tackle this problem a unique mean is calculated for each cycle, from which a more representative (in terms of a

flame wrinkling mechanism) measure of the turbulence intensity is sought.

Rask [67,68] has extended the spline fitting technique to perform a cycle-by-cycle (CBC) analysis on discrete LDV data and this approach has been chosen in preference to step averaging, polynomial fitting, digital filtering or truncated Fourier series methods to calculate the mean velocity curves. However the procedure appears to be unable to resolve the relatively low turbulence intensities encountered in the compression and expansion strokes, when applied to the hot wire results presented in this study. Therefore the associated weighting functions have been recalculated on the basis that is more sensitive to the original velocity values. Rask's technique calculates the CBC mean velocity curves from the scatter of mean velocity estimates whereas the proposed analysis uses the scatter, or turbulence, in the velocity data itself.

A check for over-smoothing is made by comparing the average of the CBC means with the ensembled mean velocity graphs, but for consistency the curve fitting parameters found for the most turbulent case are applied throughout. The turbulence intensity is calculated for marching 30 degree windows to permit a cycle-by-cycle analysis at specific crank-angle values. These results are then averaged to compare the general trends with the RMS turbulence intensity graphs discussed previously.

The cyclic variation in the fitted mean velocities appears to account for approximately 50% of the RMS turbulence intensity. Also in contrast to the latter, the averaged CBC

turbulence intensity is higher and less isentropic in the main combustion chamber for the shrouded valve results than the standard configuration. The greatest difference is still with the plug cavity measurements, which show very high levels of turbulence in the shrouded valve case. This observation is again attributed to the entrainment of the bulk flow from the main combustion chamber.

Using the single wire measurements it is possible to combine the time rate of change of the velocities with the spline fitted means to give an alternative measure of a spatial velocity gradient parameter. This technique has the advantages of being relatively insensitive to the hot wire calibration accuracy and the aesthetics of the adopted curve fitting procedure. Also as a possible flame wrinkling mechanism it is independent of scale. The intensities are again calculated for marching 30 degree windows and then phase averaged as before.

The averaged CBC spatial velocity gradient intensity clearly increases with engine speed for all of the test conditions. The main chamber and plug cavity plots illustrate broadly similar trends and magnitudes for the standard valve case. The shrouded valve intensities peak towards the end of the compression stroke, when the ensembled mean velocities reported previously are observed to decay. In the main combustion chamber the circumferential probe gives the highest measurements, which is taken to reflect the gradients in the turbulent velocities across the bulk swirling flow. The plug cavity measurements are similar for both inlet valve geometries during the early part of the compression stroke, indicating that high mean velocity and turbulence values do not

necessarily give a corresponding increase in the spatial velocity gradient intensity. As TDC is approached however the shrouded valve results are much higher, which may be a measure of the shear generated as the gas in the spark plug cavity interacts with the bulk swirl in the main combustion chamber.

8.3 The Firing Engine Performance Maps, Combustion Histories and Correlations with the Motored Engine Experiments

The performance maps have been developed for the same speed and compression ratio conditions that are used in the motoring engine experiments. For the standard valve configuration the mean effective pressure and the level of drivability are observed to steadily decay as the mixture becomes leaner. The resulting plots of 5, 10 and 20% IMEP proportional variation values (Cpi) are found to be in good accord with the progressively close spacing of the averaged BMEP and IMEP contours and the most stable operating coordinates follow the knock boundary. Following the work of Kuroda et al [48] the 10% curve is taken to represent the limit of acceptable drivability. The shrouded valve performance maps are very different in appearance in that the mean effective pressure tends to be insensitive to an increase in the air/fuel ratio until the drivability limit is approached. The knock boundary has disappeared from the range of experimental conditions covered and the MEP contours are widely spaced until a point is reached where the drivability suddenly decays. As a result the 5 and 10% proportional IMEP variation curves are very close together and the performance becomes too erratic to obtain the 20% coordinates. The engine also fails to operate

with lean mixtures at low ignition advances. For both valve geometries the air/fuel mixing of the low speed, fuel injected engine is assumed to be good.

The standard valve performance maps indicate that the ignition advance required to attain an acceptable level of drivability for the most lean air/fuel ratio generally increases with engine speed. In following this trend to calculate the combustion histories, the detailed pressure records are logged for ignition advance values which give a constant time interval from the instant of sparking to compression TDC (namely from 30 to 60 degrees advance for engine speeds from 1000 to 2000 rpm respectively). The initial aim was to investigate the similarities in the cycle-by-cycle performance for the two inlet valve geometries and air/fuel ratios which correspond to Cpi values for 5, 10 and 20% have been chosen. Having rebuilt the engine with the shrouded inlet valve, the complete change in the shape of the performance maps and the close spacing of the proportional IMEP variation curves was unexpected. As a result the air/fuel range has been extended to overlap with the standard valve experiments and the study now concentrates on the differences between the two sets of combustion histories.

From the instant of sparking the calculated mass fraction burnt curves follow a similar path until a region of separation is reached, beyond which it is possible to resolve the fast and slow burning cycles. Previous studies have indicated that flames which start quickly appear to maintain that advantage [78] and it is argued that the early stages of combustion are critical in relation to the phase and magnitude of the peak in-

cylinder pressure that is subsequently developed. This assertion is investigated by plotting the correlation coefficient and the least squares errors that arise from a relationship sought between the 'delay' (for correlation) period required to burn given mass fraction, volume fraction or product volume values and the 'total' burn time. The shrouded valve results indicate that there is a range of values through which no relationship appears to exist and that a 6% mass fraction burnt time is the most consistent measure of the onset of a reasonable correlation. The delay-total burn time points from the shrouded valve experiments are very closely packed and consequently illustrate a much weaker relationship. However as the drivability limit is approached a correlation begins to emerge and the 6% mass fraction value appears to hold.

Bar charts are presented to seek to establish a link between the cycle-by-cycle variation in the spark plug cavity motored engine measurements and the 0-6% mass fraction burnt time for an air/fuel ratio of 18:1. The 0-6% delay period results illustrate a narrower distribution, the median of which is slightly shorter, than those calculated for the standard valve. In comparing the anemometric data the cycle-by-cycle velocity gradient measurements appear to be the most likely candidate for a simple cause-and-effect relationship.

A plot of the ratio of the averaged standard/shrouded valve time to burn given mass fractions indicates that although the 0-6% combustion rate is slightly faster for the shrouded valve results, the time to attain smaller values (0-0.5% to 0-3%) is increased. The averaged motored engine measurements and the mapped performance at low ignition advances suggests that

the developing kernel may be cooled, or even extinguished, by the high turbulence or velocity gradient intensities which prevail at the time of sparking. Photographic [63] and autocorrelation studies [22, 23, 78] have also indicated that bulk motion effects are important, the highest peak pressures resulting when the flame migrates away from the cylinder walls. Therefore it is suggested that the 0-6% delay period cumulatively represents the result of gas cooling and mixing effects at the time of sparking, the positioning of the flame kernel by the bulk flow field and the subsequent onset of rapid propagation when the kernel is of sufficient size to stably interact with the prevailing turbulence and velocity gradient intensities.

The average duration and distribution of the mass fraction burnt times are compared to investigate further the strength of the relationship between the early stages and the final outcome of the combustion histories. For a range of air/fuel ratios the 0-6% delay period is comparable for both valve geometries, but the shrouded valve gives a much shorter 'remaining' (6-90%) burn time which is more tolerant of lean mixtures. The shape of the bar charts for an 18:1 air/fuel ratio persists throughout the 0-6%, 6-90% and 0-90% burn times plotted from the standard valve results. As the engine speed increases the shrouded valve remaining burn time becomes more independent of the delay period and a proportional preference for fast burning cycles is apparent. From this it is argued that the associated enhancement in the propagation speed of the developed flame serves to improve the phase of the peak in-

cylinder pressure with respect to TDC and hence give the weakened delay-total burn time correlations discussed above.

Following studies by Thomas [79, 80], Groff [36], Lancaster [51] and Mattavi [56] the degree of wrinkling, or the turbulent/laminar burning velocity ratio, is adopted as a dimensionless measure of the enhancement of the developed flame front. To this end the results of the combustion analysis are used to compare the smoothed surface of an idealised flame with the calculated area required for the diffusion of the reactants into the product zone by means of the laminar burning velocity. Cylinder centre line and spark plug centred propagation models are considered and of the these the latter is taken to be the more representative for both the standard and shrouded valve results. The laminar burning velocity ratio is calculated by an empirical relationship developed by Metghalchi and Keck [58], using the constants for a gasoline/air mixture and assuming that the exhaust residual mass fraction is negligible.

The shape of the burning velocity ratio graphs is found to be a function of the radius of the idealised models, which may reflect the progressive interaction of eddies of increasing scale [51] or the fact that the analysis fails to consider the finite thickness of the wrinkled flame [36, 51, 56]. Following the latter explanation the peak value is taken to represent the conditions where the wrinkled surface is truncated least by the enclosing boundaries. Its averaged value is found to increase with the mixture leanness and the engine speed, and is higher for the shrouded than the standard valve results.

The influence of air/fuel ratio may illustrate the counter 'self-smoothing' action as the flame propagates normal

to its wrinkled surface [79, 80]. Assuming that the prevailing turbulence or velocity gradient intensities exert the greatest influence on the burning velocity ratio however, simple 'figure of merit' comparisons are made with the main chamber anemometric measurements. Of these a possible relationship with the circumferential wire turbulence and velocity gradient intensities is suggested, the latter giving the strongest correlation. As discussed above the calculated velocity gradient intensity parameter is relatively insensitive to the hot wire calibration accuracy and the aesthetics of the cycle-by-cycle curve fitting procedure adopted. It is also independent of scale and may successfully encompass both the effect of local surface wrinkling mechanisms and the bulk flame smearing distortions that would be expected from the shear generated by the swirling flow in the shrouded valve experiments [39, 64, 88].

8.4 Conclusions

The greater efficiency and reduced exhaust emissions theoretically attainable from the combustion of a homogeneous lean mixture can only be practically realised if the engine drivability is acceptable and misfiring or knocking cycles are avoided. This study has concentrated on the cycle-by-cycle stability of a spark-ignition engine fitted with a standard and shrouded inlet valve, for a range of speeds at wide open throttle conditions. To this end the mapped performance and calculated combustion histories for lean air/fuel ratios are compared with the gas motion intensity measured in the spark plug region and the main combustion chamber. Simple

statistical comparisons and idealised geometry models have then been used to investigate the early and developed stages of the flame propagation across the engine cylinder.

The standard valve results suggest that the duration of a 'delay' (for correlation) period to burn a 6% mass fraction of the reactants is a consistent indicator of the final outcome of the combustion histories. The variation of this delay is found to persist by virtue of a slow overall flame speed in the distribution of the remaining and total burn times. The steady decay in the engine drivability as the air/fuel ratio is attributed to the progressively late generation of the peak in-cylinder pressure with respect to TDC, the rapidly changing cylinder volume causing its timing to be correspondingly more critical. An increase in the ignition advance can improve the performance stability, but at low engine speeds both knock and high proportional IMEP variation conditions can occur simultaneously. The shrouded valve gives a narrower distribution in the early burn times and enhanced combustion rates which are more tolerant of lean mixtures during the developed phase of the flame propagation. The faster overall burn time discourages knock and the greater performance stability which results is taken to reflect the improved phasing of the peak in-cylinder pressure with respect to TDC. As a result there is a weak relationship between the delay period and the total burn time until the drivability limit is approached, when the 6% criterion again begins to hold.

The ensembled hot wire measurements in the motored engine suggest a disorganised flow structure for the standard configuration and are consistent with an unstable motion that

redistributes to a solid body rotation in the shrouded valve case. A cycle-by-cycle analysis, which is then used to compensate for the positional instability of the centres of large scale vortices or swirling motions, has proved to be moderately successful in resolving a 'true' turbulence intensity from bulk flow variations. However a single wire measure of a spatial velocity gradient parameter, found by combining the unique mean curves and the time rate of change of the instantaneous velocities, illustrates a more consistent change with engine speed and a greater difference between the standard and shrouded valve results.

The cycle-by-cycle distribution in the delay period and the hot wire measurements in the spark plug cavity suggests a beneficial relationship between the velocity gradient intensity and the variations in the early stages of combustion. However a comparison of the performance maps at low ignition advances, the ratio of the averaged time to attain given mass fraction burnt values and plots of the averaged anemometric measurements indicate that high turbulence or velocity gradients intensities can retard, or even extinguish, the flame kernel as it initially develops from the instant of sparking. Nevertheless the ratio of the calculated flame surface area to that of the idealised spherical propagation models does point to the velocity gradient intensity as a mechanism for an enhancement in the rates of the later stages of combustion. As it is independent of scale this correlation may encompass both local wrinkling and bulk smearing effects which act to distort the flame front and consequently increase its surface area.

8.5 Suggestions for Future Work

Parallel wire probes have been used in the motored engine experiments to calculate the in-cylinder temperature histories and to seek a direct estimate of the spatial velocity gradient intensities. In the latter application plots of the ensembled mean velocity and RMS turbulence intensity have been used to determine the consistency of the close proximity measurements obtained. The poor correlation that has been achieved is attributed to the uncertain repeatability of the hot wire results and the interference to the measured flow by the probe supports. Although there is scope for the further development of a suitable procedure for the use of hot wire anemometers in non-ambient conditions, the quality of the wire and its spot welds to the supports will remain as possible sources of error. Surface contamination (by oil for example) and highly turbulent flow fields can also bias the measurements obtained, by changing the mode of heat transfer from the wire (see Section 2.2). The interference with the measured flow can be tackled by the use of less intrusive single wire probes to measure the turbulence and spatial velocity gradients, the latter being based upon the approach developed in Section 6.4. Should laser Doppler velocimetry be chosen in preference however, the smoothed ensembled and cycle-by-cycle techniques outlined in Chapter 6 will readily apply to the discrete nature of the data obtained.

The cycle-by-cycle analysis has used cubic splines that are weighted by the scatter of the original data to fit continuous, non-oscillatory curves to represent the instantaneous mean velocities. Within the statistical bounds

of the procedure a check for over-smoothing has been made by comparing the average of the cycle-by-cycle and ensembled mean velocity plots, which should concur if the sum of the resolved turbulent fluctuations is zero. Apart from the reservations concerning the repeatability of the hot wire results, the limited success of the cycle-by-cycle turbulence intensity analysis may be attributed to the lack of feedback in the curve fitting procedure. The definition of a 'true' turbulence intensity currently appears to be very much 'in the eye of the beholder'. The truncated Fourier series approach discussed in Section 6.4 for example uses a cut-off frequency to calculate the mean velocity curves, whereas the smoothed spline procedure that has been adopted in preference centres upon the random property of the turbulent fluctuations. The turbulence scale however, in comparison to the cylinder dimensions or the radius of the flame front at a given instant in time, may prove to be a more tangible point of reference for a future cycle-by-cycle analysis.

The velocity gradient intensity parameter has been subsequently calculated from the mean curves and the time rate of change of the instantaneous velocities. The result is relatively insensitive to the accuracy of the calibration of the hot wire probes and the form of the cycle-by-cycle analysis performed. However the implicit assumption is that the mean velocity carries the shearing flow past the point of measurement and there is scope for a study of the gas dynamic equations to check the validity of this simple approach. Work is currently being undertaken at the University of Liverpool to investigate the effect of velocity gradient intensities on the

flame of a steady state combustion rig. This presents an opportunity to experimentally compare the magnitude of the (constant) mean velocity based intensities with direct measurements that are determined by using parallel hot wire probes.

The performance of the firing engine has been summarised by plotting constant BMEP or IMEP contours between the bounds of knock and poor drivability. The greater speed and memory capacity of the micro-computers currently available should make it possible to adopt the on-line knock detection algorithm discussed in Section 4.7 and improve the resolution of the proportional IMEP variations that are used to measure the degree of drivability. Hopefully a faster and more reproducible procedure will result that can be used as a routine assessment of the overall engine behaviour before more detailed studies are undertaken. A faster computer speed can also be used to improve the accuracy of the two-zone model that is subsequently used to calculate the in-cylinder combustion histories. Curve fitting can be used to eliminate the bit stepping in the digital pressure data, which may bias the calculations for the early stages of the flame development, and the heat transfer can be determined on a cycle-by-cycle basis, by balancing the first low equations when no heat release is taking place.

The enhanced combustion rate in the developed phase of the flame history is estimated by comparing its surface area to that of idealised flame propagation models to give a dimensionless degree of 'wrinkling' or burning velocity ratio. The analysis does not however consider the actual thickness of

the wrinkled flame front or the possible migration or bulk smearing effects that may occur in the shrouded valve experiments. A Ricardo Hydra research engine will hopefully be loaned to the University in the near future, which in its photographic build will give additional information on the nature of the in-cylinder flame development in the different flow regimes. This can then be used to interpret or modify the wrinkled flame propagation analysis to seek a more direct correlation with future gas motion intensity measurements.

The remaining objective in the current study with the Ricardo E6 engine is to measure the effect of a small spoiler mounted on the cylinder head in conjunction with the shrouded inlet valve. The anticipated outcome is an increase in the turbulence intensity when the spoiler interacts with the bulk swirl motion as TDC is approached, which may only affect the later stages of combustion. If this proves to be the case the shrouded valve results reported previously can then be used to make a more direct comparison of the effect of turbulence and velocity gradient intensities on the propagation rate of the developed flame front.

REFERENCES

1. AHMADI-BEFRUI, B., GOSMAN, A.D. and WATKINS, A.P.
"Predictions of In-Cylinder Flow and Turbulence with Three Versions of the K-ε Turbulence Model and Comparison with Data".
Proc. ASME Winter Meeting, 1984.

2. AL-SUDANI, A.
"Heat Transfer in a Motored Reciprocating Engine".
PhD Thesis, The University of Liverpool, 1985.

3. ALCOCK
Model 323 Viscous Flow Meter Manual (Supplied by Ricardo & Co., Engineers Ltd.).

4. ANNAND, W.J.D.
"Heat Transfer in the Cylinder of a Reciprocating Internal Combustion Engines".
Proc. I.Mech.E., Vol. 177, pp. 973-990, 1963.

5. ARCOUMANIS, C. (Ed.) and THOMAS, A.
"Internal Combustion Engines".
Academic Press Ltd., Chapter 5, pp. 214-215, 1988.

6. ARCOUMANIS, C. and WHITELAW, J.H.
"Fluid Mechanics of Internal Combustion Engines - A Review".
Proc. I.Mech.E., Vol 201, No. C1, pp. 57-72, 1987.

7. ARCOUMANIS, C., BICEN, A.F. and WHITELAW, J.H.
"Effect of Inlet Parameters on the flow Characteristics in a Four-Stroke Model Engine".
SAE paper 820750, Passenger Car Meeting, Troy, Michigan, June 7-10, 1982.

8. ARCOUMANIS, C., BICEN, A.F, and WHITELAW, J.H.
"Squish and Swirl-Squish Interaction in Motored Model Engines".
Journal of Fluids Engineering, Vol. 105, pp. 105-112, March 1983.

9. ARCOUMANIS, C., VAFIDIS, C. and WHITELAW, J.H.
"Valve and In-Cylinder Flow Generated by a Helical Port in a Production Diesel Engine".
Symposium on Flows in Reciprocating Engines. ASME Winter Meeting, Miami Beach, Florida, 1985.

10. 'AUTOMOTIVE ENGINEERING'
"Lean Combustion: A Review".
Published by SAE, February 1984.

11. BALL, W.F., PETTIFER, H.F., and WATERHOUSE, C.N.F.
"Laser Doppler Velocimeter Measurements of Turbulence in a Direct Injection Diesel Combustion Chamber".
I.Mech.E. paper C52/83. International Conference on Combustion Engineering, Vol. 1, I.Mech.E. Conference Publications, pp. 163-174, 1983.

12. BARTON, R.K., LESTZ, S.S. and MEYER, W.E.
"An Empirical Model for Calculating Cycle-by-Cycle Cylinder Gas Motion and Combustion Variations of a Spark Ignition Engine".
SAE paper 710163, 1971.

13. BENSON, J.D.
"Reductions of Nitrogen Oxides in Automobile Exhaust".
SAE paper 690019, 1969.

14. BENSON, R.S. and BRUNDRETT, G.W.
"Development of a Resistance Wire Thermometer for Measuring Transient Temperatures in Exhaust Systems of Internal Combustion Engines".
Temperature, its Measurement and Control in Science and Industry. Reinhold Publishing Corp., N.Y., Vol. 3, Part 2, pp. 631-653, 1962.

15. BENSON, R.S. and WHITEHOUSE, N.D.
"Internal Combustion Engines".
Pergamon Press, 1979.

16. BLACKMORE, D.R. and THOMAS, A.
"The Scope for Improving the Fuel Economy of the Gasoline Engine".
I.Mech.E. paper C206/79, Conference of the Institution of Mechanical Engineers, London, October 1979.

17. BRADBURY, L.J,S. and CASTRO, I.P.
"Some Comments on Heat Transfer Laws for Fine Wires".
Journal of Fluid Mechanics, Vol. 51, Part 3, pp. 487-495, 1972.

18. BRANDLE, F., REVERENCIC, I., CARTILLIERI, W. and DENT, J.C.
"Turbulent Air Flow in the Combustion Bowl of a D.I. Diesel Engine and its Effect on Engine Performance".
SAE paper 790040, Congress and Exposition, Cobo Hall, Detroit. February 26-March 2, 1979.

19. CHATFIELD, C.
"Statistics for Technology".
pp. 185-190, 2nd Edition, Chapman and Hall, 1981.

20. CHECKEL, M.D. and DALE, J.D.
"Computerised Knock Detection from Engine Pressure Records".
SAE paper 860028, 1987.

21. CHECKEL, M.D., and DALE, J.D.
"Testing a Third Derivative Knock Indicator on a Production Engine".
SAE paper 861216, 1987.

22. COLE, J.B. and SWORDS, M.D.
"An Investigation of the Ignition Process in a Lean Burning Engine Using Conditionally Sampled Laser-Doppler Anenometry".
SAE paper 800043, 1980.

23. COLE, J.B. and SWORDS, M.D.
"On the Correlation between Gas Velocity and Combustion Pressure Fluctuations in a Spark-Ignition Engine".
Proceedings of the Eighteenth Symposium of the Combustion Institute, Waterloo, Canada, pp. 1837-1846, 1981.

24. COLLIS, D.C. and WILLIAMS, M.J.
"Two Dimensional Convection from Heated Wires at Low Reynolds Numbers".
Journal of Fluid Mechanics, Vol. 6, pp. 357-384, 1959.

25. CORKILL, W.J., BULLOCK, K.J. and WIGLEY, G.I.
"Flow and Combustion Measurements Within a Dual Chamber Stratified Charge Engine".
I.Mech.E. paper C402/80, 1980.

26. CUTTLER, D.H. and GIRGIS, N.S.
"Photography of Combustion During Knocking Cycles in Disc and Compact Chambers".
SAE paper 880195, International Congress and Exposition, Detroit, Michigan, February 29-March 4, 1988.

27. DANTEC LTD.
Private Communication.

28. DAVIS, P.O.A.L. and FISHER, M.J.
"Heat Transfer from Electrically Heated Cylinders".
Proceedings of the Royal Society, Ser. A., pp. 486-526, 1964.

29. DENT, J.C. and SALAMA, N.S.
"The Measurement of Turbulence Characteristics in an Internal Combustion Engine Cylinder".
SAE paper 750886, Automobile Engineering Meeting, Detroit, Michigan, October 13-17, 1975.

30. DOUGLAS, W.J.M. and CHURCHILL, S.W.
"Recorrelation of Data for Convective Heat Transfer Between Gasses and Single Cylinders with Large Temperature Differences".
Chem. Eng. Prog. Symp. Ser., Vol. 18, pp. 23-28, 1956.

31. DRISCOLL, J.F. and GULATI, A.
"Measurement of Various Terms in the Turbulent Kinetic Energy Balance within a Flame and Comparison with Theory".
Combustion and Flame, Vol. 72, pp. 131-152, 1988.

32. ETHYL CORPORATION
"Meeting Future Automobile Standards".
Report AM-70-5.

33. GERMANE, G.J., WOOD, C.G. and HESS, C.C.
"Lean Combustion in Spark Ignited Internal Combustion Engines-A Review".
SAE paper 831217, 1983.

34. GHIRLANDO, R.
"Radial Flow in an Engine Cylinder Near the End of Compression".
Ph.D. Thesis, University of Liverpool, 1973.

35. GIDNEY, J.T.
"Progress Report, March 1986".
Internal Publication.

36. GROFF,G. and MATEKUNAS, F.A.
"The Nature of Turbulent Flame Propagation in a Homogeneous Spark-Ignited Engine".
SAE paper 800133, Congress and Exposition, Cobo Hall, Detroit, February 25-29, 1980.

37. HAMMING, R.W.
"Numerical Methods for Scientists and Engineers".
McGraw Hill, 2nd Ed., pp. 352-355, 1973.

38. HAMMING, R.W.
"Numerical Methods for Scientists and Engineers".
McGraw Hill, 2nd Ed., pp. 662-664, 1973.

39. HANSON, R.J. and THOMAS, A.
"Flame Development in Swirling Flows in Closed Vessels".
Combustion and Flame, Vol. 55, pp. 255-277, 1984.

40. HEYWOOD, J.B.
"Fluid Motion Within the Cylinder of Internal Combustion Engines - the 1986 Freeman Scholar Lecture".
Journal of Fluids Engineering, Vol. 109, pp. 3-31, March 1987.

41. HILL, P.G.
"Cyclic Variations and Turbulence Structure in Spark-Ignition Engines".
Combustion and Flame, Vol. 72, pp. 73-89, 1988.

42. HILPERT, R.
"Warmeabgage von geheizten Drahten und Rohren im Luftstrom".
ForschArb. IngWes., 4, pp. 215-224, 1933.

43. HORNBY, R.P.
"Full and Half Range Fourier Series (Discrete Data)".
Internal Publication.

44. HORVATIN, M. and HUSSMAN, A.W.
"Measurement of Air Movements in Internal Combustion Engine Cylinders".
Disa Information, pp. 13-22, July 1969.

45. JEFFREY, A.
"Mathematics for Scientists and Engineers".
Nelson, pp. 701-3, 1971.

46. KANNULUIK, W.G. and CARMAN, E.H.
"The Temperature Dependance of the Thermal Conductivity of Air".
Australian J. Sci., Res. 4, pp 305-314, 1951.

47. KING, L.V.
"On the Convection of Heat from Small Cylinders in a Stream of Fluid: Determination of Convection Constants of Small Platinum Wires with Applications to Hot Wire Anenometry".
Royal Society Philosophical Transactions A, Vol. 214, pp. 373-403, 1914.

48. KURODA, H., NAKAJIMA, Y.N., SUGIHARA, K., TAKAGI, Y. and MURANAKA, S.
"The Fast Burn with Heavy EGR, New Approach for Low NOx and Improved Fuel Economy".
SAE Transactions 780006, Vol. 87, pp. 1-15, 1978.

49. LANCASTER, D.R., KRIEGER, R.B. and LIENESCH, J.H.
"Measurement and Analysis of Engine Pressure Data".
SAE Transactions 750022, Vol. 84, pp. 155-172, 1975.

50. LANCASTER, D.R.
"Effects of Engine Variables on Turbulence in a Spark-Ignition Engine".
SAE paper 760159, Automotive Engineering Congress and Exposition, Detroit, Michigan, February 23-27, 1976.

51. LANCASTER, D.R., KRIEGER, R.B., SORENSON, S.C. and HULL, W.L.
"Effects of Turbulence on Spark-Ignition Engine Combustion".
SAE paper 760160, Automotive Engineering Congress and Exposition, Detroit, Michign, February 23-27, 1976.

52. LEPPARD, W.R.
"Individual Cylinder Knock Occurrance and Intensity in Multi-cylinder Engines".
SAE paper 820074, SAE International Congress, Detroit, 1982.

53. LIOU, J.M. and SANTAVICIA, D.A.
"Cycle Resolved LDV Measurements in a Motored IC Engine".
Engineering Applications of Laser Velocimetry, edited by H.W.Colman and P.A.Pfund, pp. 33-37, 1982.

54. MACKENZIE, D. and WATTS, S.
"Realistic Test Forces New Look at Vehicle Emissions".
New Scientist, 22 April 1989.

55. MATTAVI, J.N.
"The Attributes of Fast Burning Rates in Engines".
SAE paper 800920. The Piston Engine - Meeting the Challenge of the 80's. Engineering Know - How in Engine Design. SP-467, Part 28, pp. 11-29, 1980.

56. MATTAVI, J.N., GROFF, E.G. and MATEKUNAS, F.A.
"Turbulence Flame Motion and Combustion Chamber Geometry - Their Interactions in a Lean - Combustion Engine".
I.Mech.E. paper C100/79, Proc. I.Mech.E. pp. 137-151, June 1979.

57. MCADAMS, W.H.
"Heat Transmission".
McGraw Hill, 3rd Ed., pp. 258-260, 1954.

58. METGHALCI, M. and KECK, J.C.
"Burning Velocities of Mixtures of Air with Methanol, Isooctane and Indolene at High Pressure and Temperature".
Combustion and Flame, pp. 191-209, 1982.

59. MONAGHAN, M.L. and PETTIFER, H.F.
"Air Motion and Its Effect on Diesel Performance and Emissions".
SAE paper 810255, Diesel Combustion and Emissions Part II, SP-484. International Congress and Exposition, Cobo Hall, Detroit, Michigan, February 23-27, 1981.

60. MOOD, A.M. and GRAYBILL, F.A.
"Introduction to the Theory of Statistics".
McGraw Hill, New York, p. 248, 1963.

61. MORONEY, M.J.
"Facts from Figures".
Pelican, Penguin Books Ltd., pp. 135-137, 1986.

62. THE NUMERICAL ALGORITHMS GROUP LTD.
The NAG Fortran Library Manual - Mark 12, 1987.

63. NAMAZIAN, M., HANSEN, S., LYFORD-PIKE, E., SANCHEZ-BARSSE, J., HEYWOOD, J. and RIFE, J.
"Schlieren Visualisation of the Flow and Density Fields in the Cylinder of a Spark-Ignition Engine".
SAE paper 800044, Congress and Exposition, Cobo Hall, Detroit, February 25-29, 1980.

64. PATTERSON, D.J.
"Cylinder Pressure Variations, a Fundamental Combustion Problem".
SAE paper 660129, Automotive Engineering Congress, Detroit Michigan, January 10-14, 1966.

65. PERRY, A.E.
"Hot Wire Anenometry"
Clarendon Press, Oxford, p. 17, 1962.

66. RASK, R.B.
"Laser Doppler Anenometry Measurements in an Internal Combustion Engine".
SAE paper 790094, Congress and Exposition, Cobo Hall, Detroit, Michigan, February 26-March 2, 1979.

67. RASK, R.B.
"Comparison of Window, Smoothed-Ensemble and Cycle-by-Cycle Data Reduction Techniques for Laser Doppler Anenometer Measurements of In-Cylinder Velocity".
Fluid Mechanics of Combustion Systems, published by ASME, edited by T. Morel, R.P.Lohmann and J.M.Rackley, pp. 11-20, 1981.

68. RASK, R.B.
"Laser Doppler Anenometer Measurements of Mean Velocity and Turbulence in Internal Combustion Engines".
L.I.A., Vol. 47, pp. 120-133, 1984.

69. REINSCH, C.H.
"Smoothing by Spline Functions".
Numerisch Mathmatik, Vol. 10, pp. 177-183, 1967.

70. RICARDO & CO. LTD.
Ricardo E6 Engine Manual
Report No. 1472, 28th May 1964.

71. RICARDO & CO. LTD.
Shrouded Valve Design and Assembly Drawings, A-E.6.T./C.164., B-E.6.T./C.161., A-E.6.T./A.26, A-E.6.T./C.163.
3rd and 5th January 1966.

72. RICHARDSON, P.D.
"Convection from Heated Cylinders at Moderate and Low [Bynolds Numbers".
American Institute of Aeronautics and Astronautics, Vol. 3, No. 3, pp. 537-538, September 8th, 1964.

73. ROGERS, G.F.C. and MAYHEW, Y.R.
"Thermodynamics and Transport Properties of Fluids".
Blackwell, 3rd Ed., 1985.

74. SANDBOURNE, V.A.
"Resistance Temperature Transducers".
Metrology Press, Fort Colins, Colorado, 1972.

75. SCHEID, F.
"Schaum's Outline of Theory and Problems of Numerical Analysis".
McGraw Hill, pp. 293-295, 1968.

76. SCHOCK, H.J., SOSOKA, D.J. and RAMOS, J.I.
"Formation and Destruction of Vortices in a Motored Four Stroke Piston-Cylinder Configuration".
AIAA Journal, Vol. 22, No. 7, pp. 948-949, 7 July 1984.

77. SEMENOV, E.S.
"Studies of Turbulent Flow in Piston Engines".
NASA Technical Translation F97, 1963.

78. SWORDS, M.D., KALGHATIGI, G.T. and WATTS, A.J.
"An Experimental Study of Ignition and Flame Development in a Spark Ignited Engine".
SAE paper 821220, 1982.

79. THOMAS, A.
"Flame Development in a Spark-Ignition Engine"
Combustion and Flame, Vol. 50, pp. 305-322, 1983.

80. THOMAS, A.
"Development of Wrinkled Turbulent Premixed Flames".
Combustion and Flame, Vol. 65, pp. 291-312, 1986.

81. THOMAS, A.
"Response to Comment by Iskender Gokalp"
Combustion and Flame, Vol. 68, pp. 87-88, 1987.

82. TINDAL, M.J., BROWN, P.G. and KYRIAKIDES, S.C.
"An Investigation of Swirl and Turbulence in the Cylinders of Direct Injection Diesel Engines".
I.Mech.E. paper C127/82, Diesel Engines for Passenger Cars and Light Duty Vehicles, Proc. I.Mech.E. 5-7th October 1982.

83. VAFIDIS,C.
"Influence of Induction Swirl and Piston Configuration on Air Flow in a Four Stroke Model Engine".
Proc. I.Mech.E. Vol. 198C, No.8, pp. 71-74, 1984.

84. VAN DER HEGGE ZIJNEN, B.G.
"Modified Correlation Formulae for the Heat Transfers by Natural and Forced Convection from Horizontal Cylinders".
Applied Scientific Research, A6, pp. 129-140, 1956-7.

85. WAKISAKA,T., HOMAMOTO, Y., OHIGASHI, S., and HASHIMOTO, M.
"Measurement of Air Swirl and its Turbulence Characteristics in the Cylinder of an Internal Combustion Engine".
J.Mech.E. paper C91/79, Fuel Economy and Emissions of Lean Burn Engines, pp.51-62, 1979.

86. WINDSOR, R.E. and PATTERSON, D.J.
"Mixture Turbulence - A Key to Cyclic Combustion Variation".
SAE paper 730086, 1973.

87. WITZE, P.O.
"A Critical Comparison of Hot Wire Anenometry and Laser Doppler Velocimetry"
SAE paper 800132, 1980.

88. WITZE, P.O.
"Effect of Spark Plug Location on Combustion in a Variable Swirl Engine".
SAE paper 820044, International Congress and Exposition, Detroit, Michigan, February 22-26, 1982.

89. WITZE, P.O., MARTIN, J.K. and BORGNAKKE, K.
"Measurements and Predictions of the Precombustion Fluid Motion and Combustion Rates in a SI Engine".
SAE paper 831697, Fluids and Lubricants Meeting, San Fransisco, California, October 31-November 3, 1983.

90. WITZE, P.O. and MARTIN, J.K.
"Cyclic Variation Bias in Spark Ignition Turbulence Measurements".
Proceedings of Second International Symposium on Applications of Laser Anenometry to Fluid Mechanics, Lisbon, July 1984.

91. WITZE, P.O. and MENDEZ-LOPEZ, J.M.C.
"Direct Measurement of the Turbulent Burning Velocity in a Homogeneous Charge Engine".
Sandia Combustion Research Annual Report, Section 8, pp. 1-3, 1983.

92. WOODFORD, C.H.
"Curve Fitting and Data Smoothing".
Ph.D. Thesis, University of Liverpool, pp. 50-76, December 1968.

93. YOUNG, M.B.
"Cyclic Dispersion-Some Quantitative Cause-and-Effect Relationships".
SAE paper 800459, Congress and Exposition, Cobo Hall, Detroit, Michigan, February 25-29, 1980.

ACKNOWLEDGEMENTS

I would like to thank all the friends, colleagues and members of my family who have fuelled my enthusiasm during this project. I would also like to thank the following specifically;

Mr Paul Walker (supervisor) for his support, encouragement and ready input of fresh ideas, for enabling the purchase and development of new (often novel) pieces of equipment for the project and for patiently helping me to compile this thesis.

Professor Alun Thomas for his sustained interest and enthusiasm, and for a the many discussions and the sometimes fraught (but always useful) brain-storming sessions that have maintained the momentum of this study.

Mr George Swallow, our contract technician, a truely first class machinist who, with much skill and patience, has manufactured some beautiful pieces of equipment. Throughout the project he has been a constant source of enthusiasm and advice that has been much valued by the author.

Mr John Haughie, our engine laboratory technician, for his willing help in dismantling and assembling the research engine and fabricating modifications to the test bed.

Mr Jack Hardcastle, Derek Neary and Mr Frank Hayes for the design and construction of some excellent pieces of electronic equipment and for their welcome help and advice.

Elaine Mooney and Karen Walker for typing this thesis over lunch hours and evenings with such patience.

Mr Jim Henderson and the workshop and woodshop staff for their help during the project.

Figures

Figure 1.1

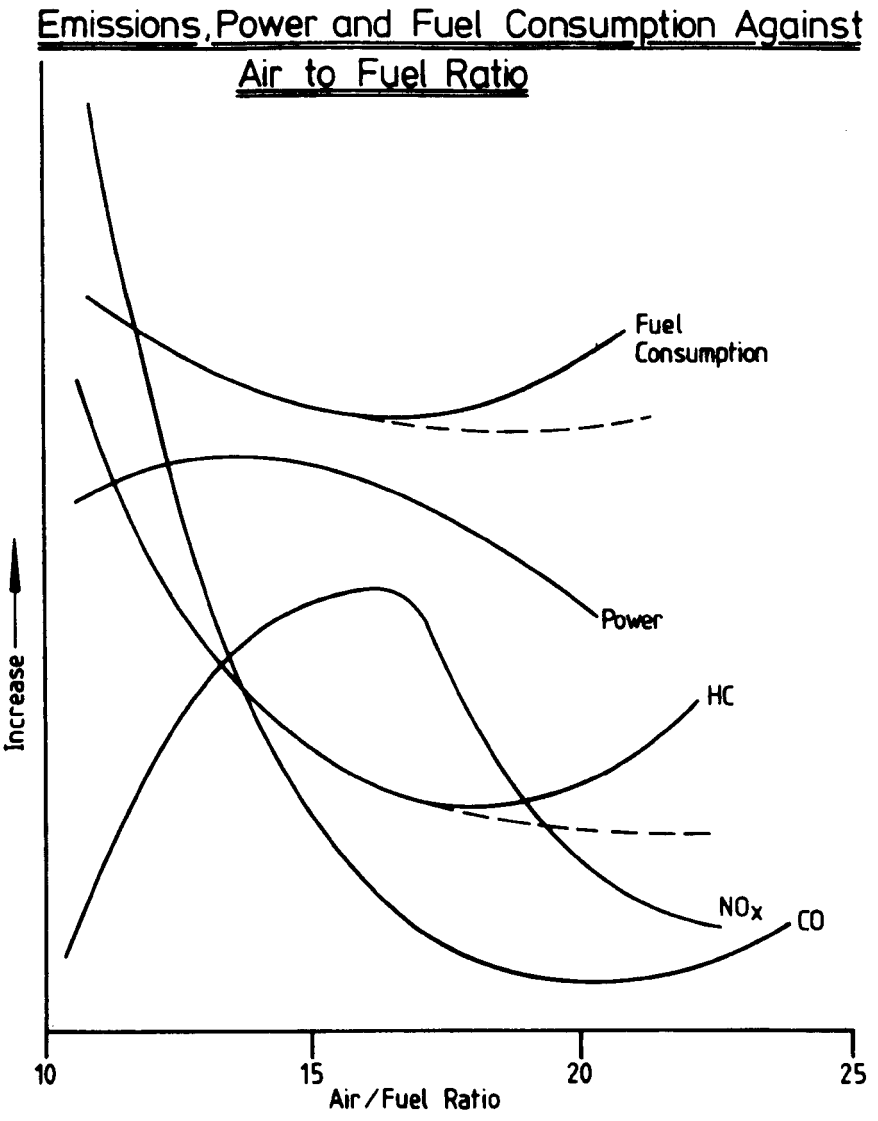
Emissions, Power and Fuel Consumption Against Air to Fuel Ratio
Fuel Consumption
Power
HC
NOx
CO
Increase
10
15
20
25
Air / Fuel Ratio

Figure 1.2

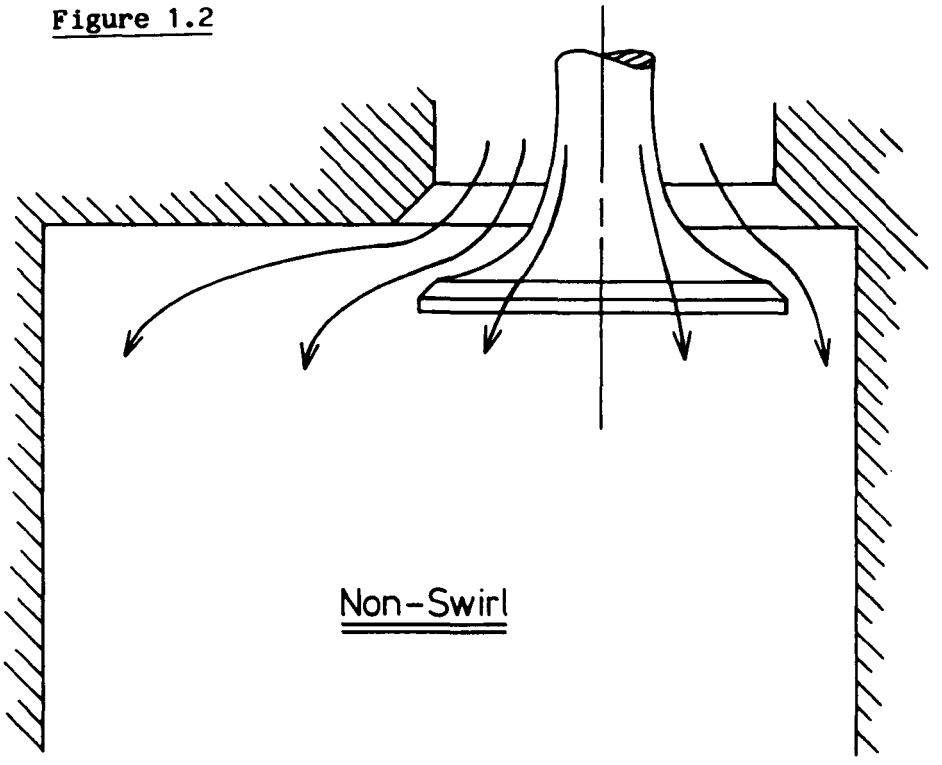

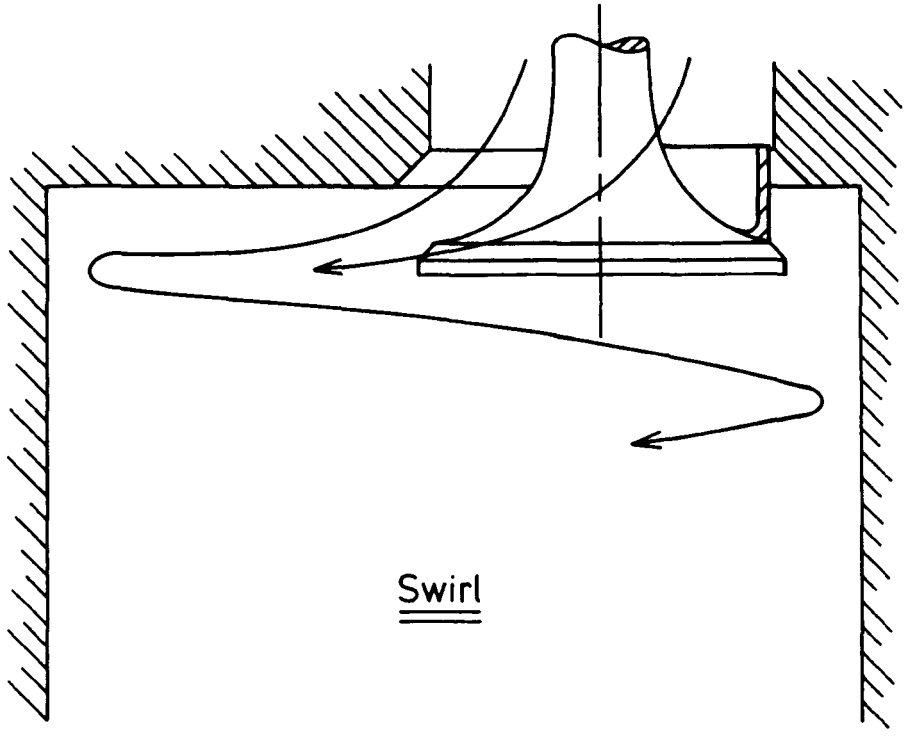

Anticipated Intake Stroke Air Flow Patterns for 2 Valve Designs

Figure 1.3

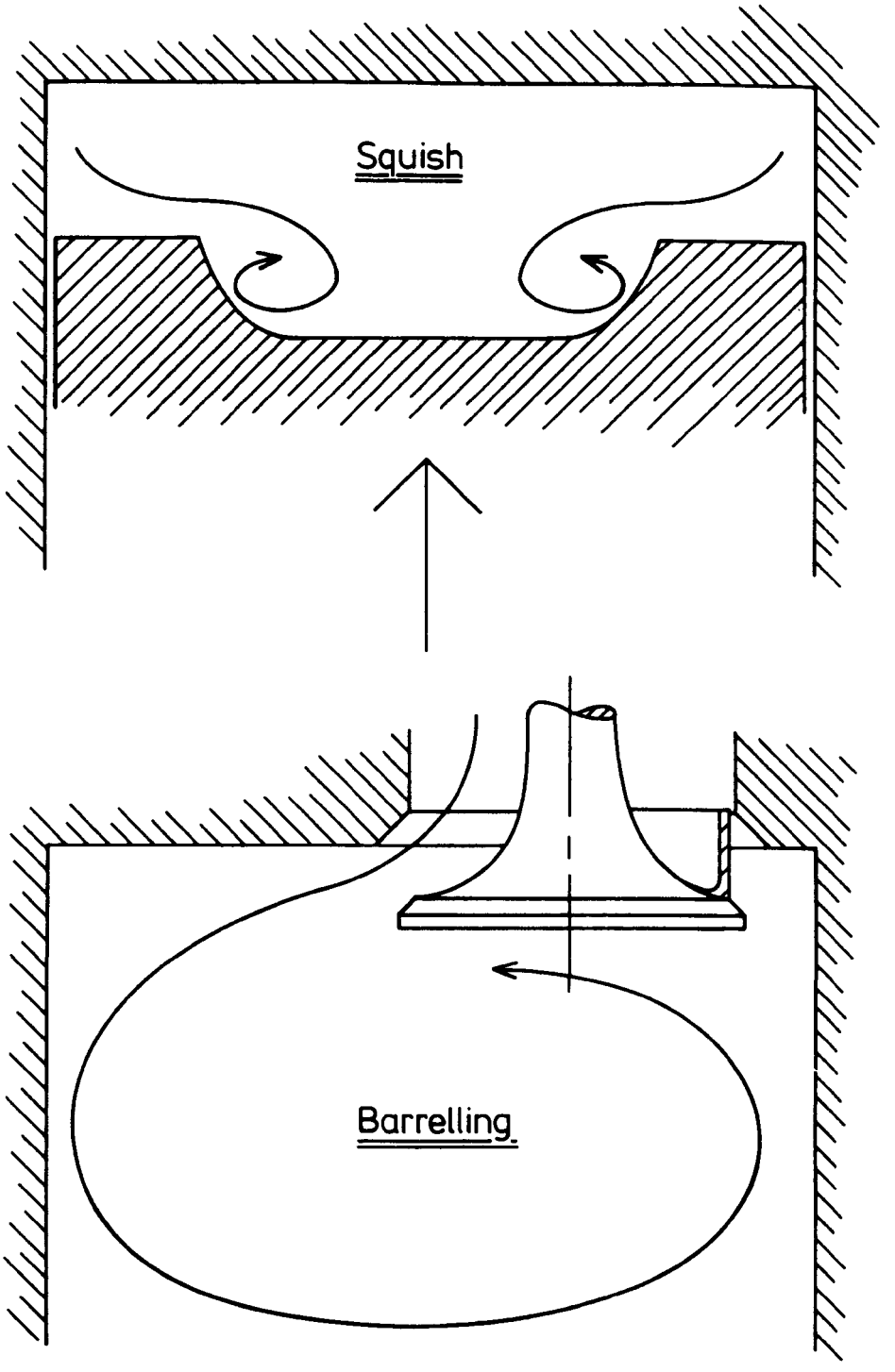

Further Modes of Gas Motion Generation

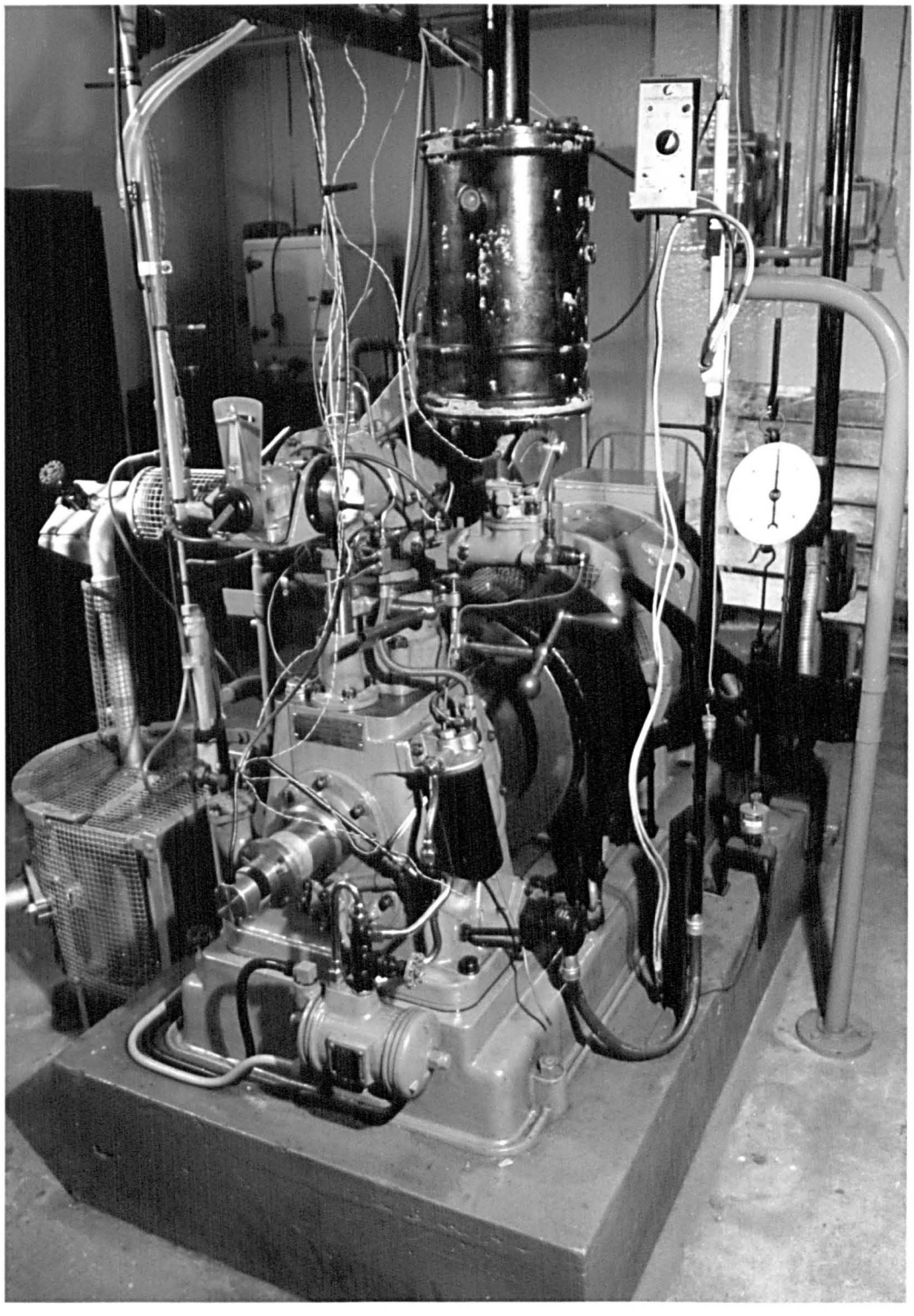

Figure 1.4: Photographic View of Engine Test Bed

Figure 1.5

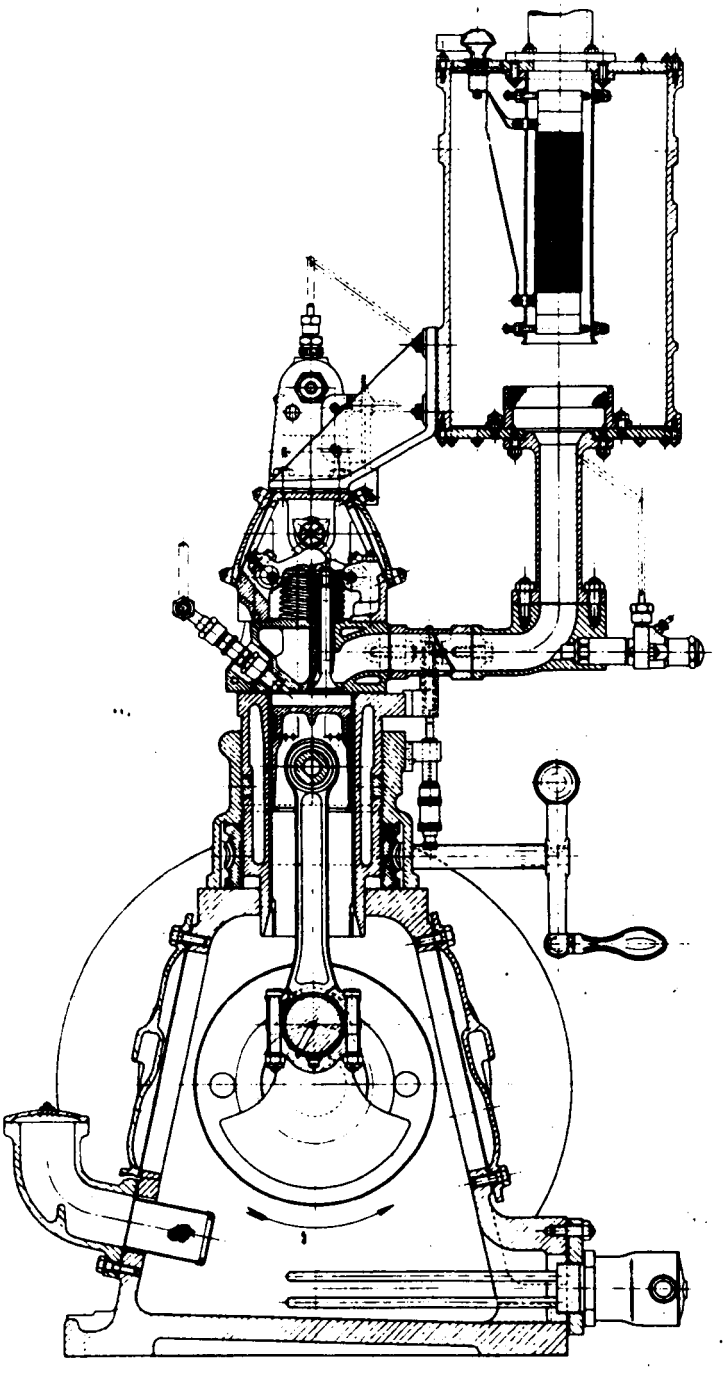

CROSS SECTIONAL ARRANGEMENT OF VARIABLE COMPRESSION RESEARCH ENGINE
3" BORE X 4½" STROKE
SUPERCHARGED VERSION

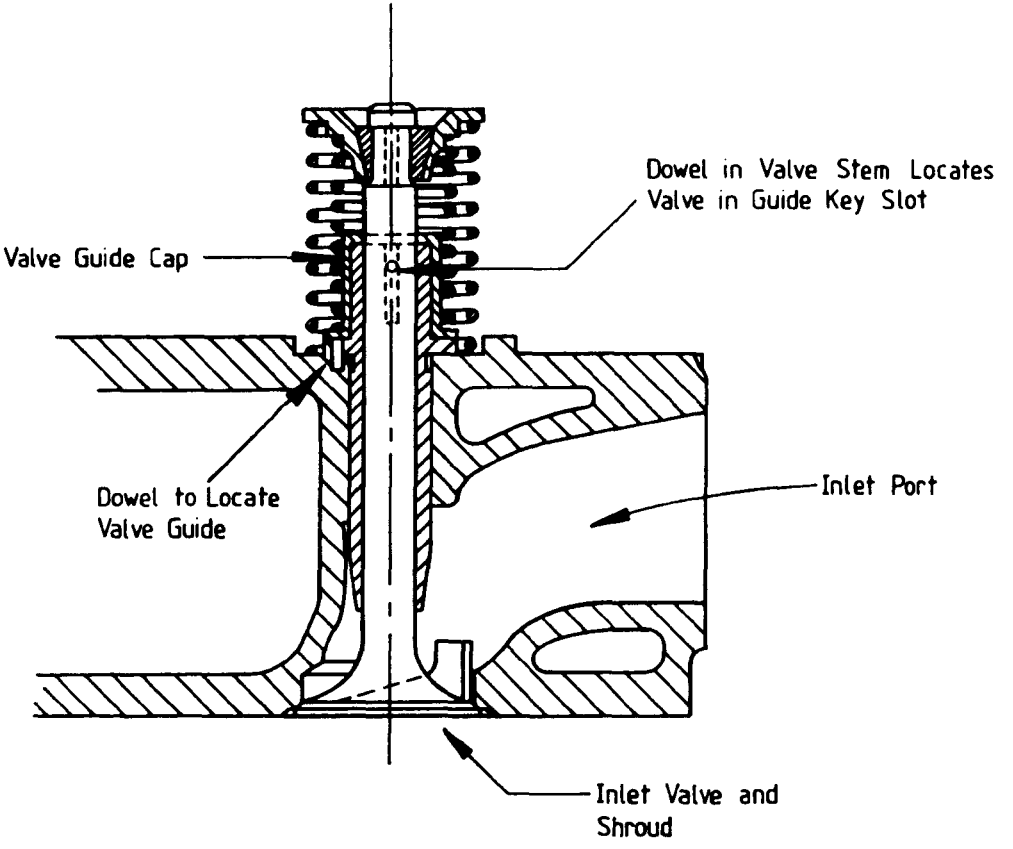

Assembly Drawing Showing Shrouded Valve Location Details

Figure 1.6

Figure 1.7

Sketch to Illustrate Degree of Intake Valve Shrouding.

(As seen from above)

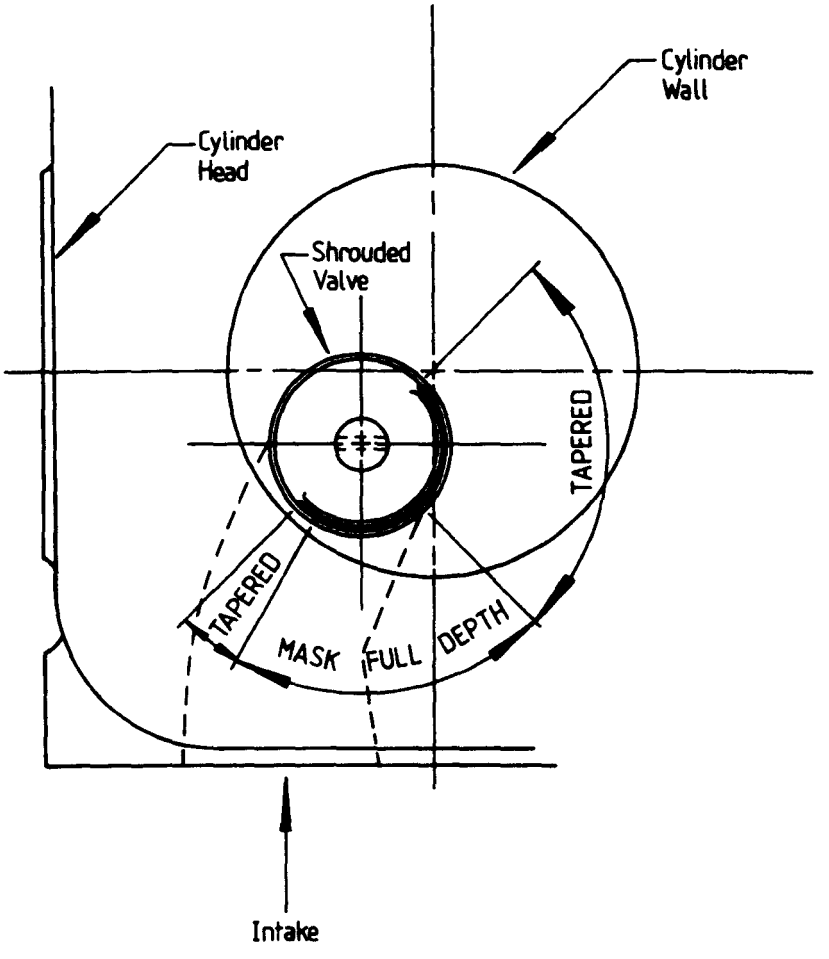

Figure 1.8: Photographic View of Test Bed Instrumentation

Figure 1.9

Instrument Identification Schematic

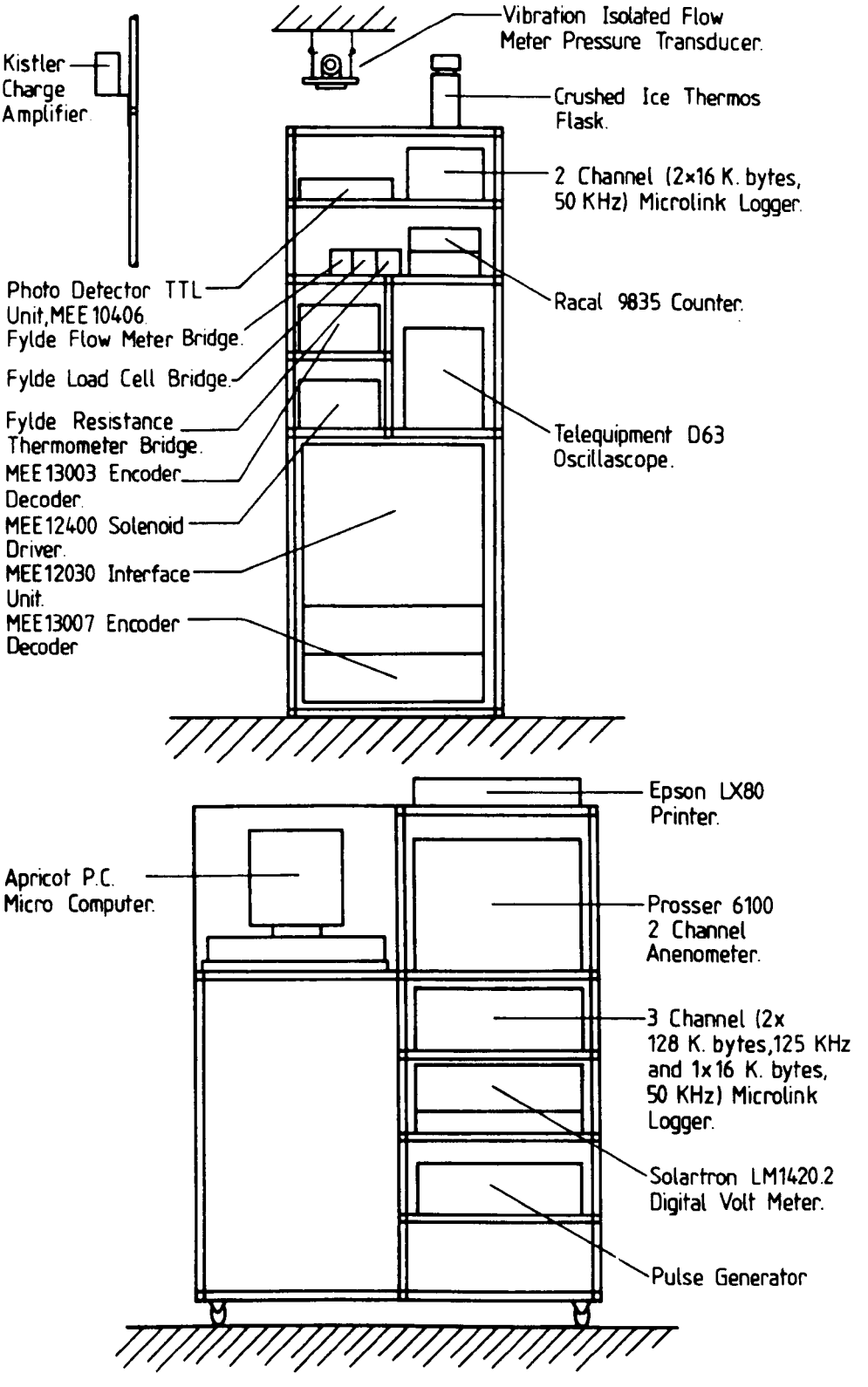

Split-Sectional View of E6 Cylinder Head Illustrating Spark Plug and Indicator Ports

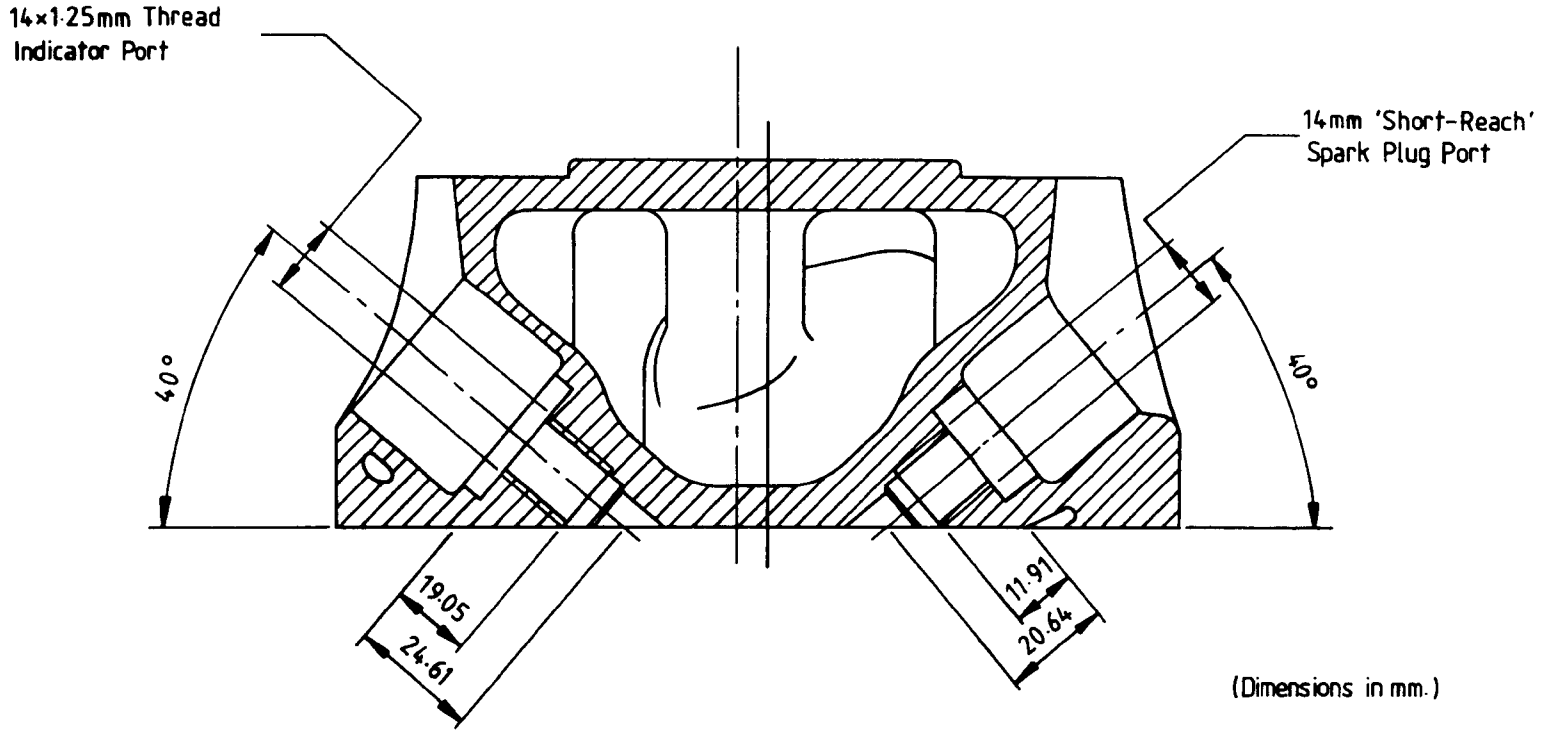

Figure 2.1

Plug Cavity and Flush Probe Details

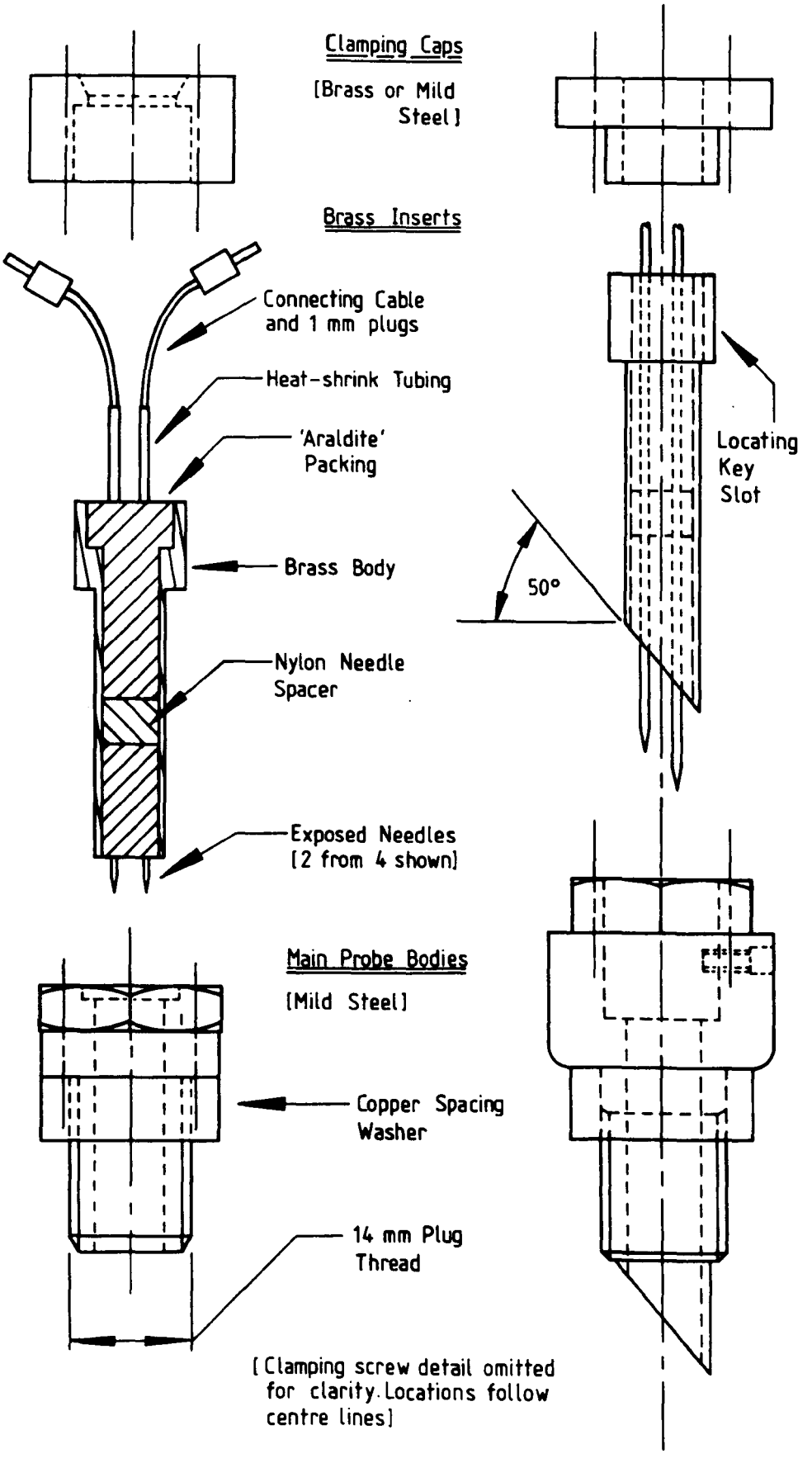

Figure 2.2

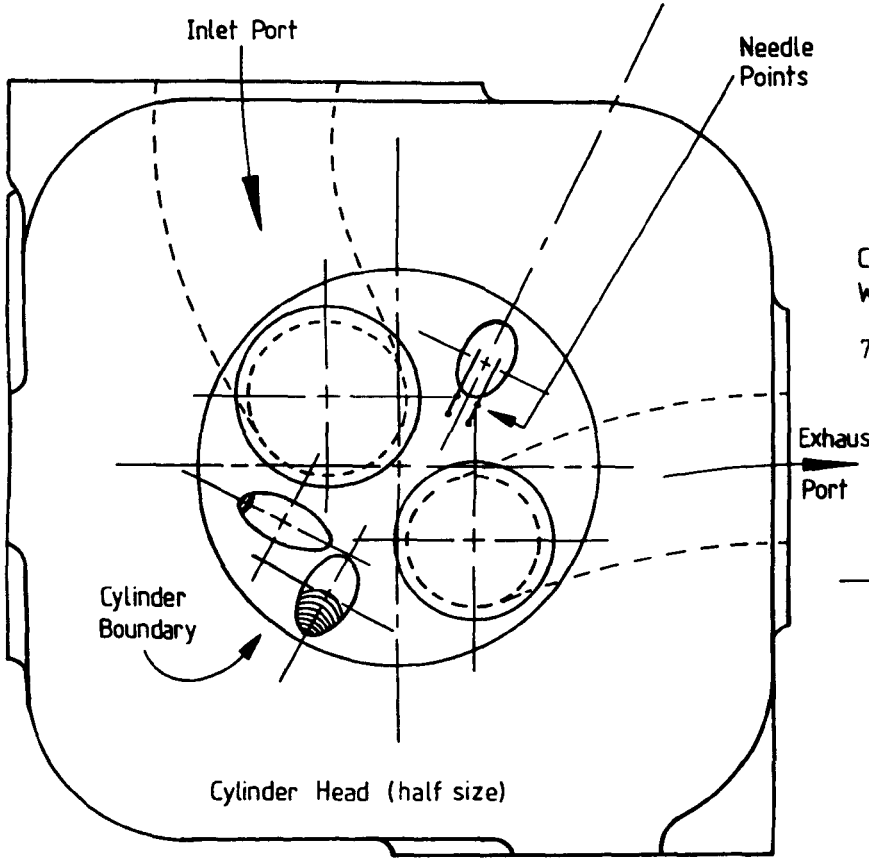

Flush Probe Wire Orientation Sketch

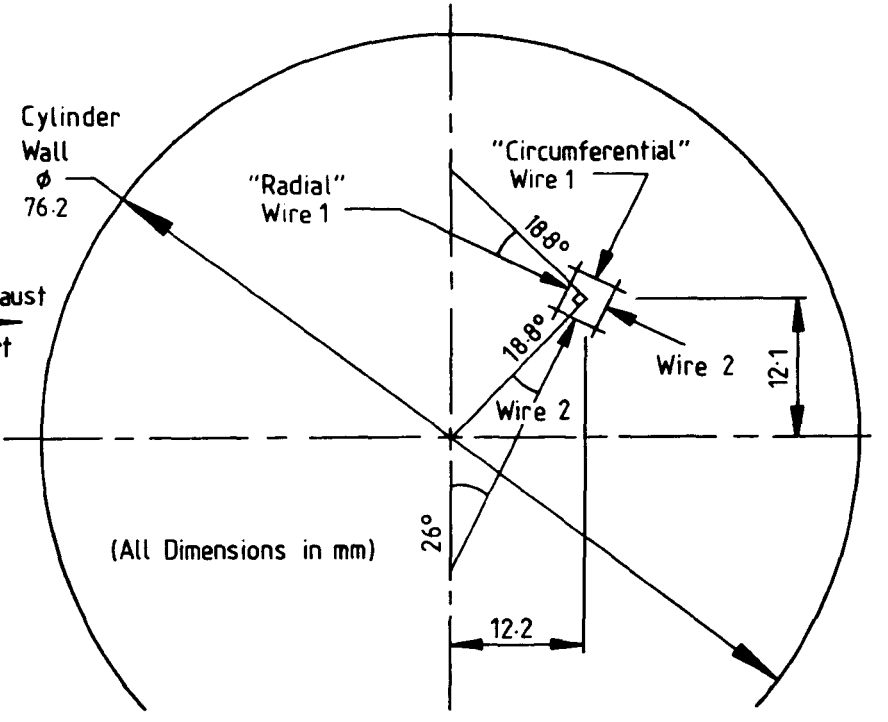

Relative Position of the Flush Probes' Measuring Plane

Figure 2.3

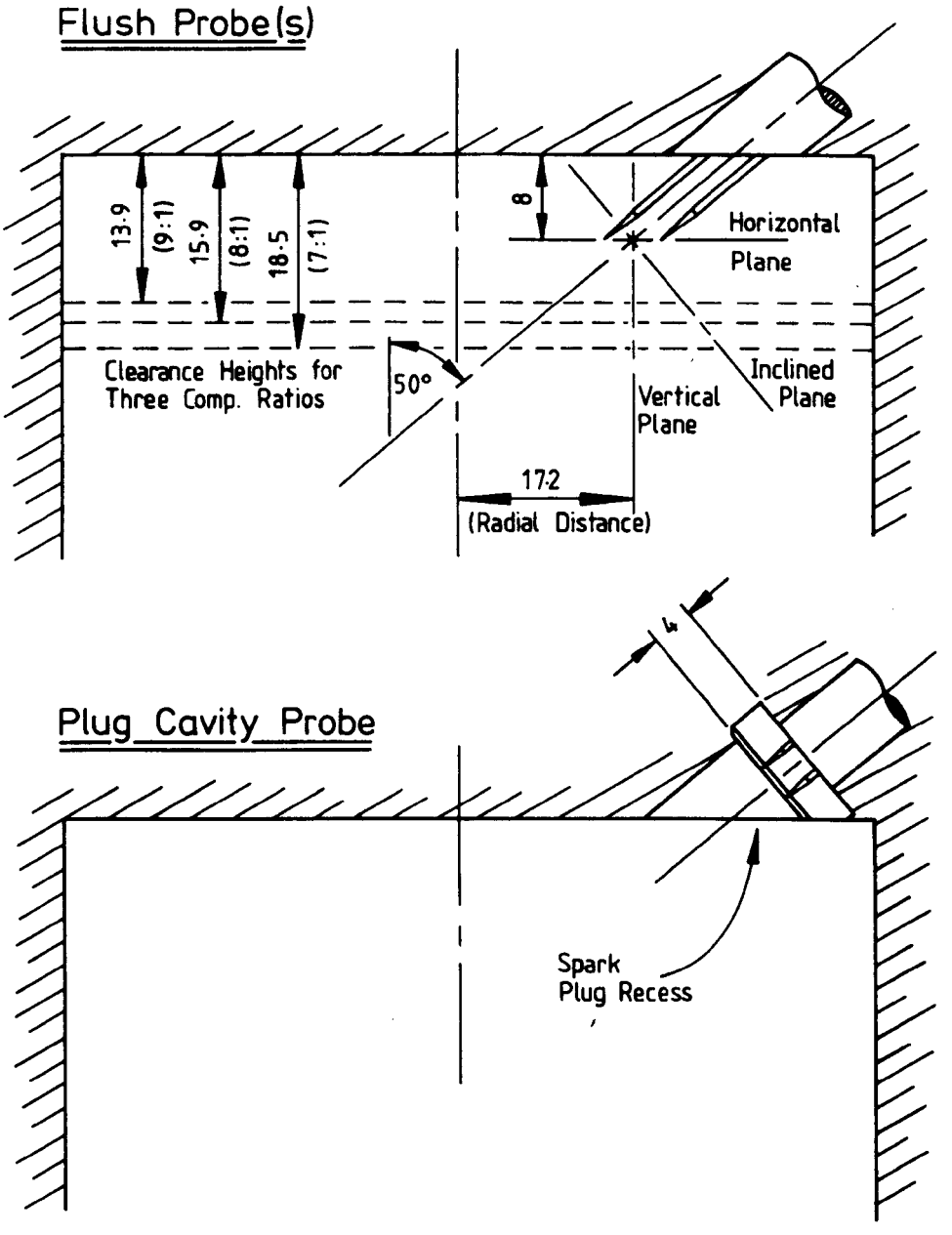

Side View to Illustrate the Relative Location of the Hot Wires

Figure 2.4

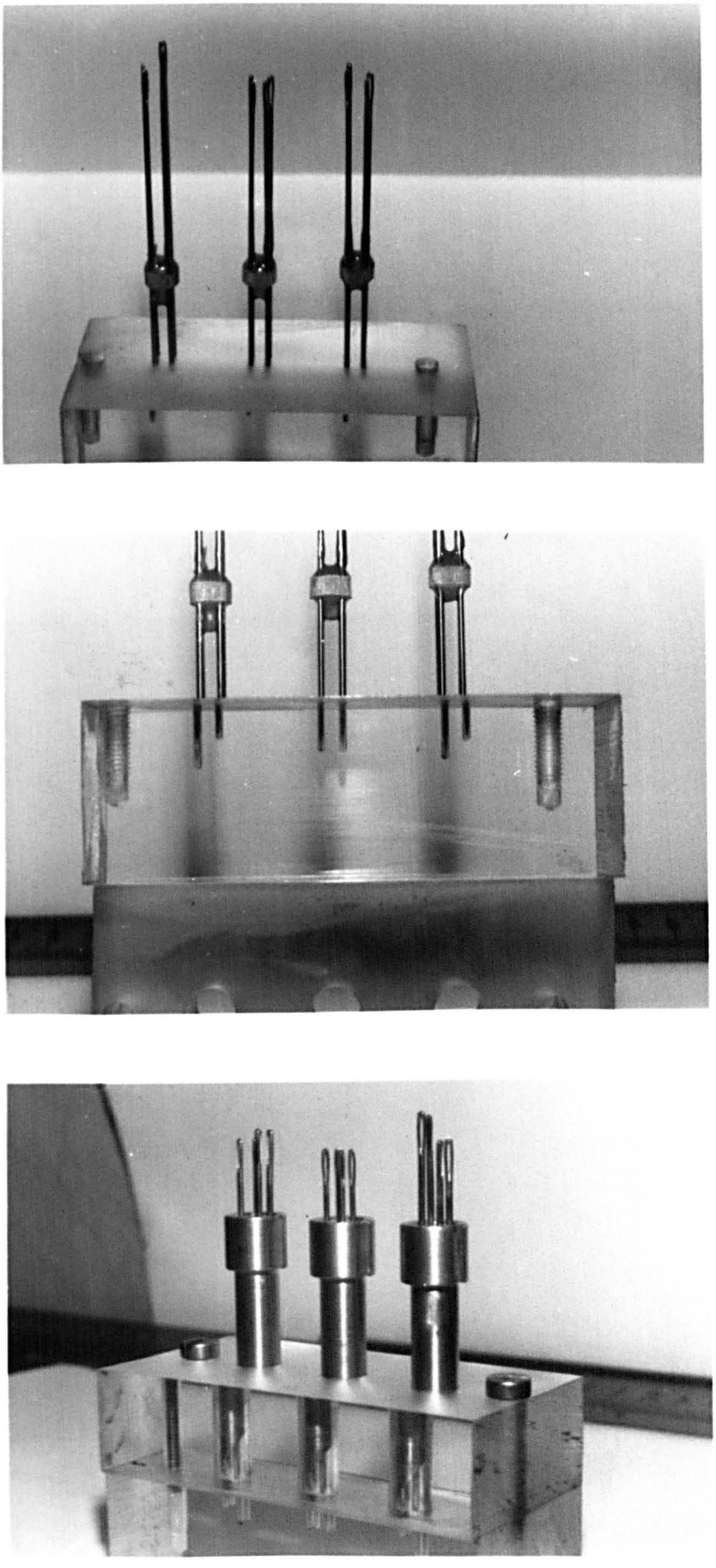

Figure 2.5: Assembly Sequence of Hot Wire Probes

Circuit Diagram Schematic of the Constant Temperature Hot Wire Anenometer Bridge

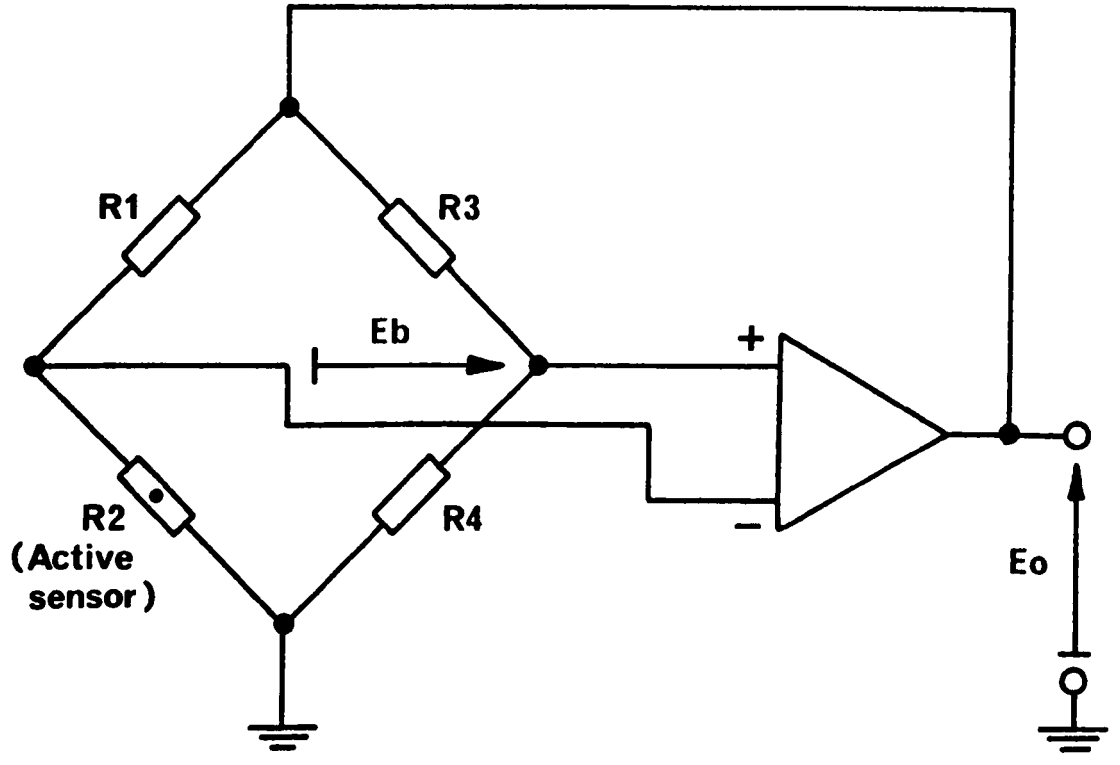

Figure 2.6

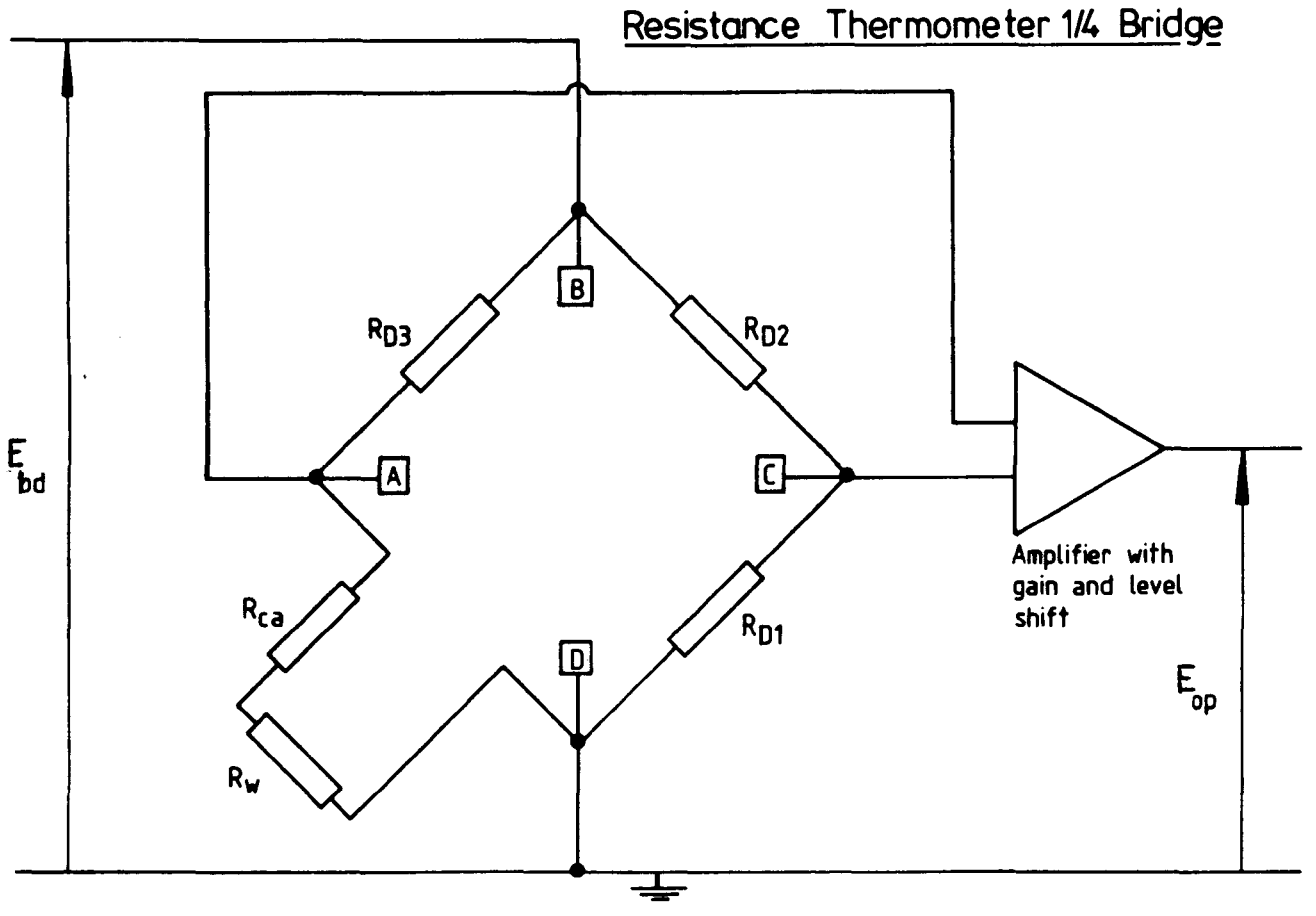
Resistance Thermometer 1/4 Bridge
E_{bd}
B
R_{D3}
R_{D2}
A
C
R_{ca}
R_{D1}
D
R_w
Amplifier with gain and level shift
E_{op}

Figure 2.7

Piezio-Electric Pressure Transducer and Holder

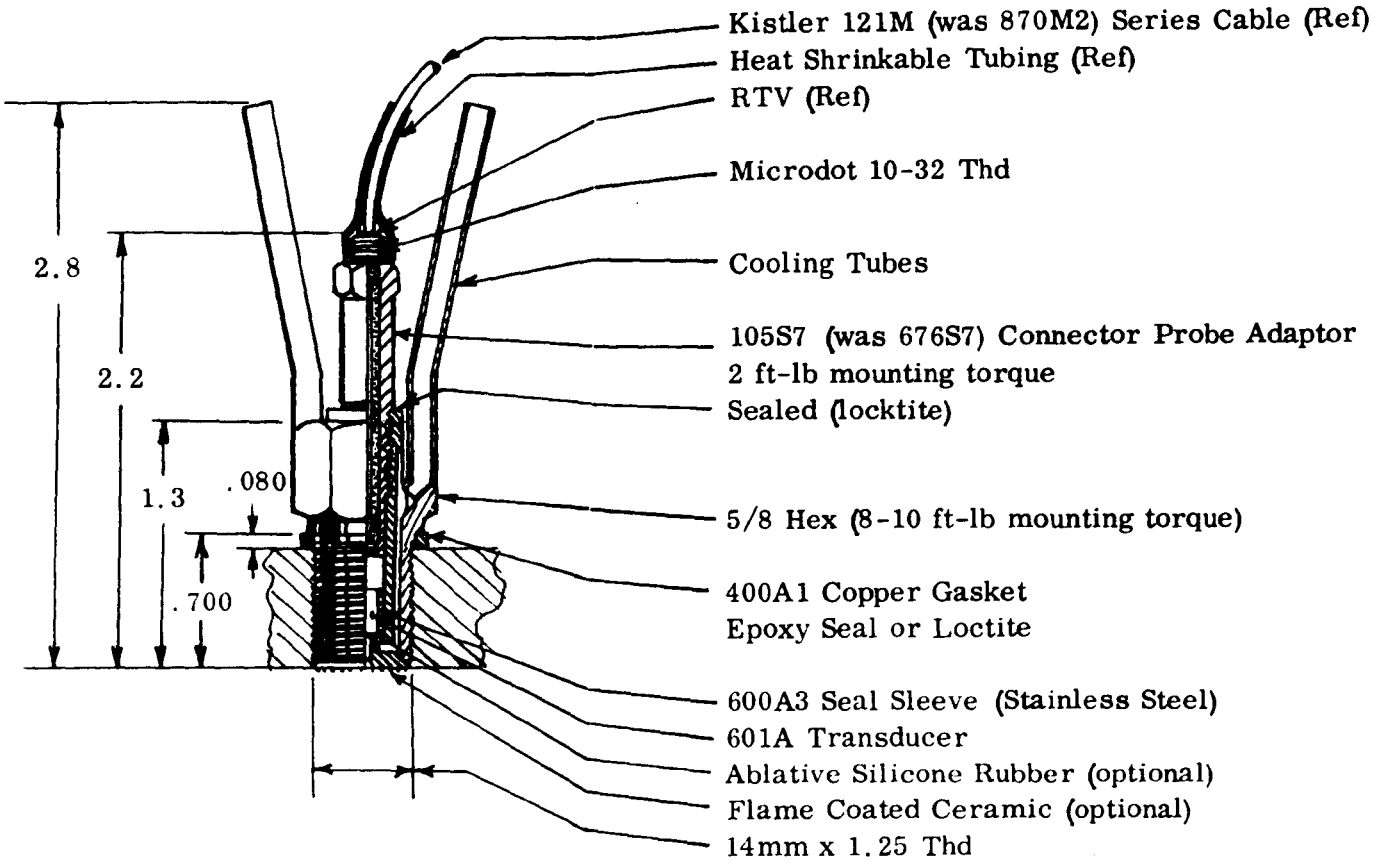

Figure 2.8

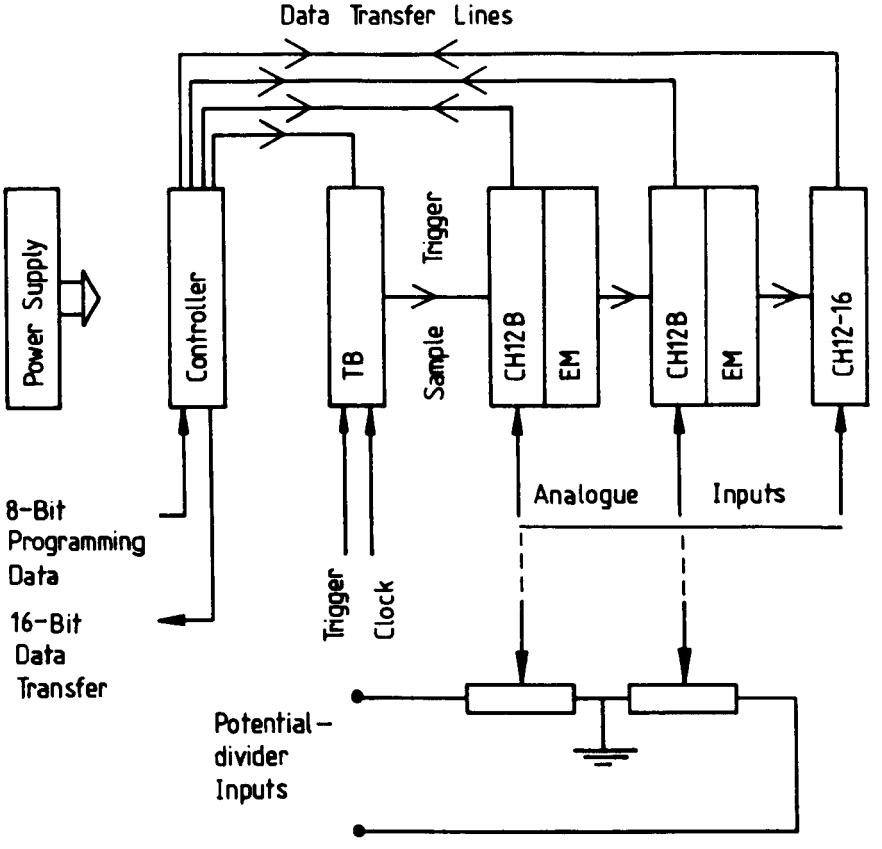

Block Diagram of Microlink Data Logger

Figure 3.1

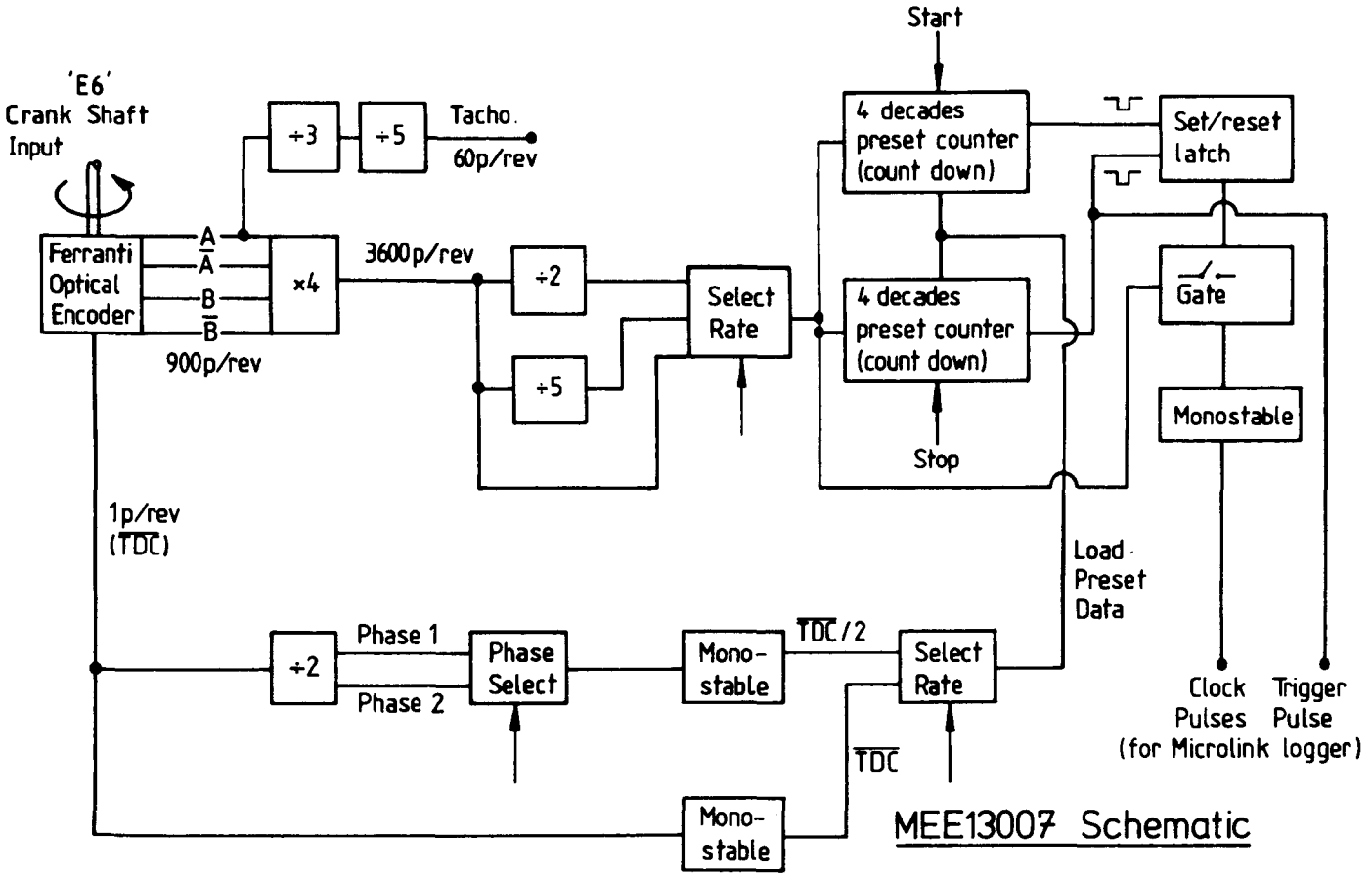
'E6'
Crank Shaft
Input
Ferranti
Optical
Encoder
A
Ā
B
B̄
900p/rev
×4
÷3
÷5
Tacho.
60p/rev
3600p/rev
÷2
÷5
Select
Rate
Start
4 decades
preset counter
(count down)
4 decades
preset counter
(count down)
Stop
Set/reset
latch
Gate
Monostable
1p/rev
(TDC)
Load
Preset
Data
÷2
Phase 1
Phase 2
Phase
Select
Mono-
stable
TDC/2
Select
Rate
TDC
Mono-
stable
Clock
Pulses
Trigger
Pulse
(for Microlink logger)
MEE13007 Schematic

Figure 3.2

Module Layout of Prosser Anenometer

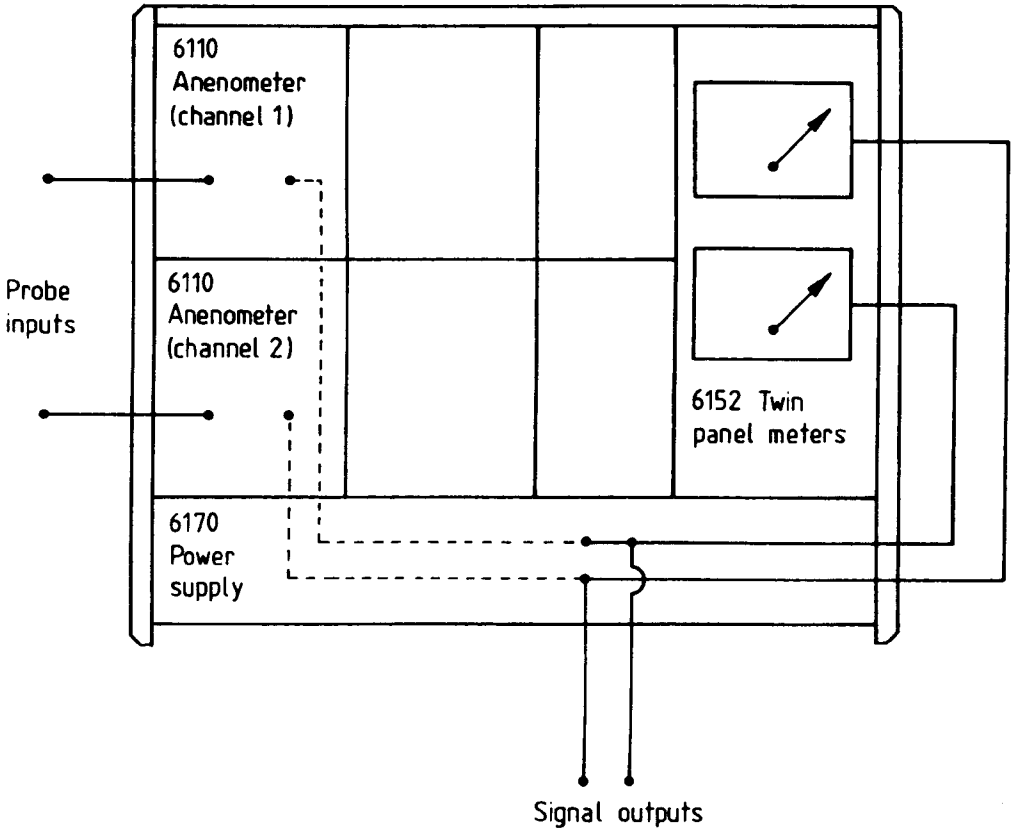

Figure 3.3

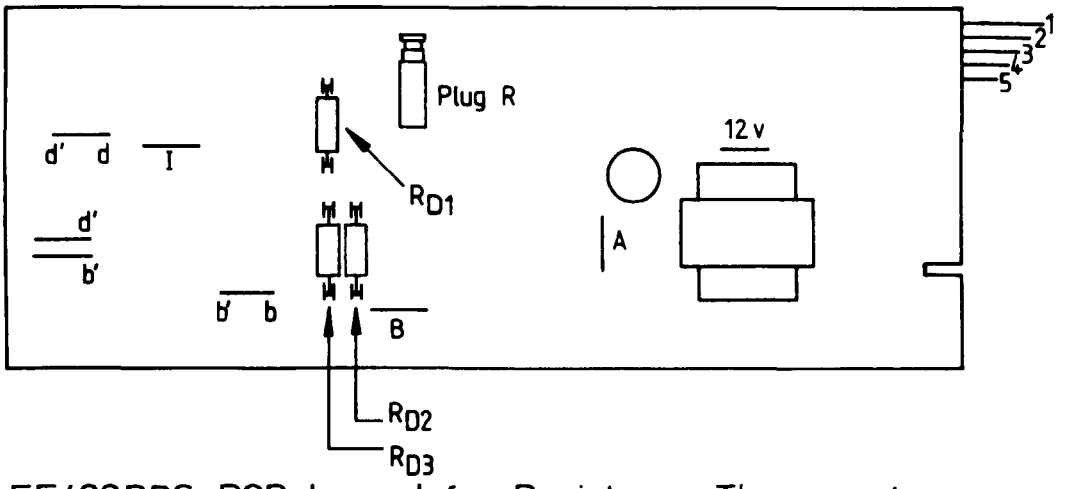

FE492BBS PCB Layout for Resistance Thermometer

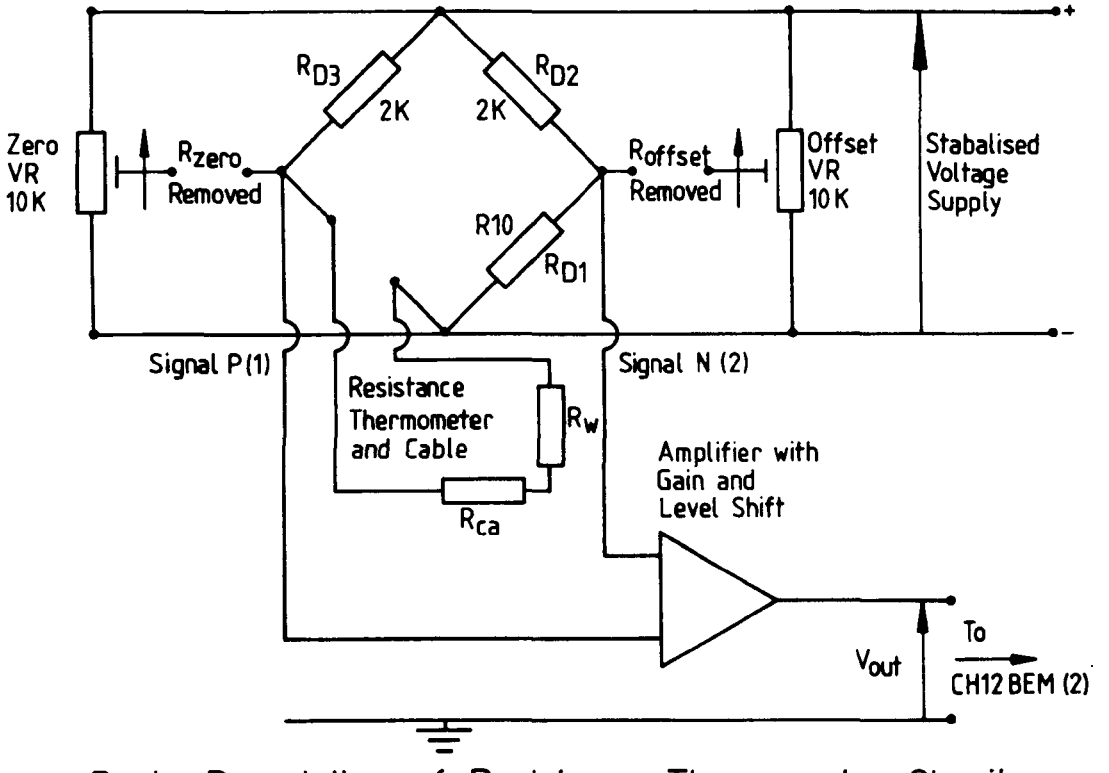

Basic Description of Resistance Thermometer Circuit and Bridge Modifications

Figure 3.4

Oven Door Bracket Used to Find Wire Temperature Coefficient of Resistance

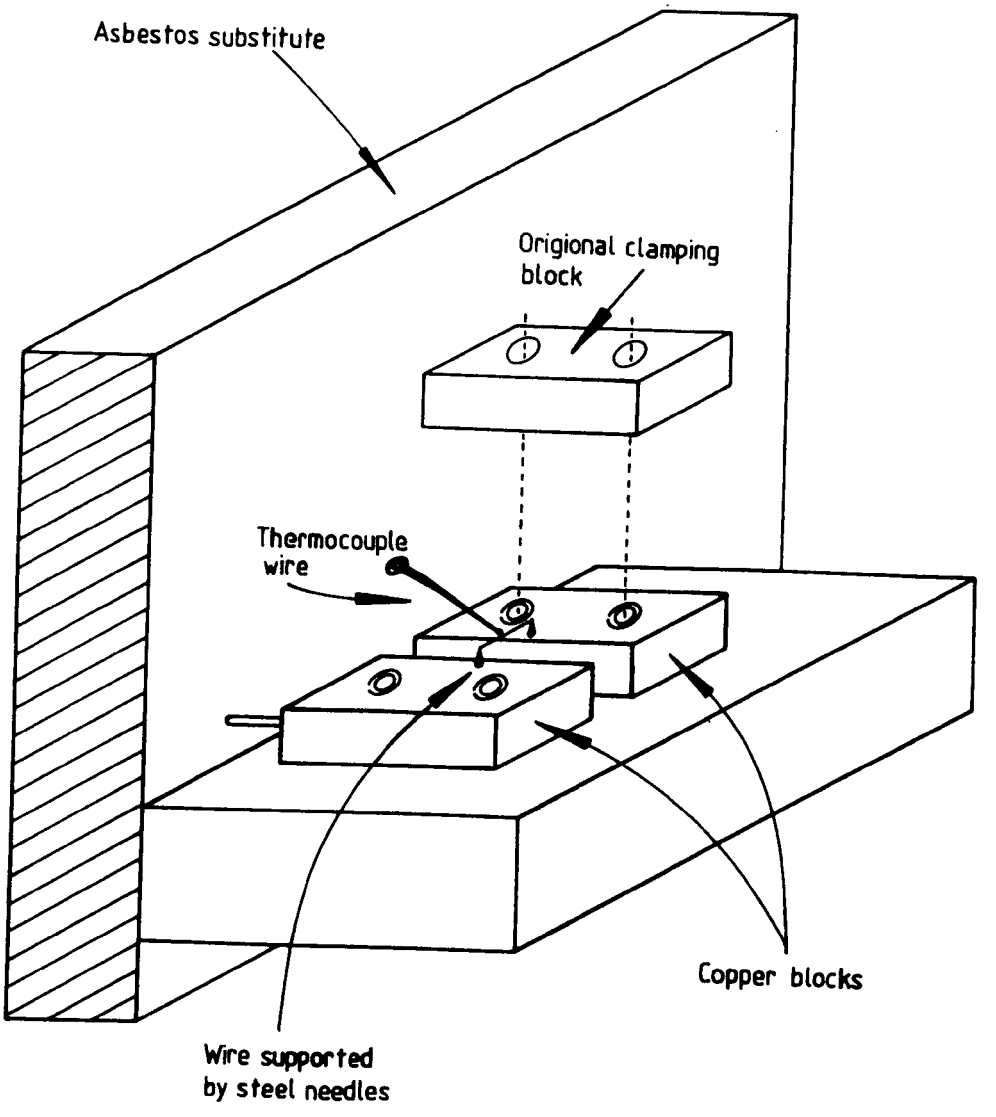

Figure 3.5

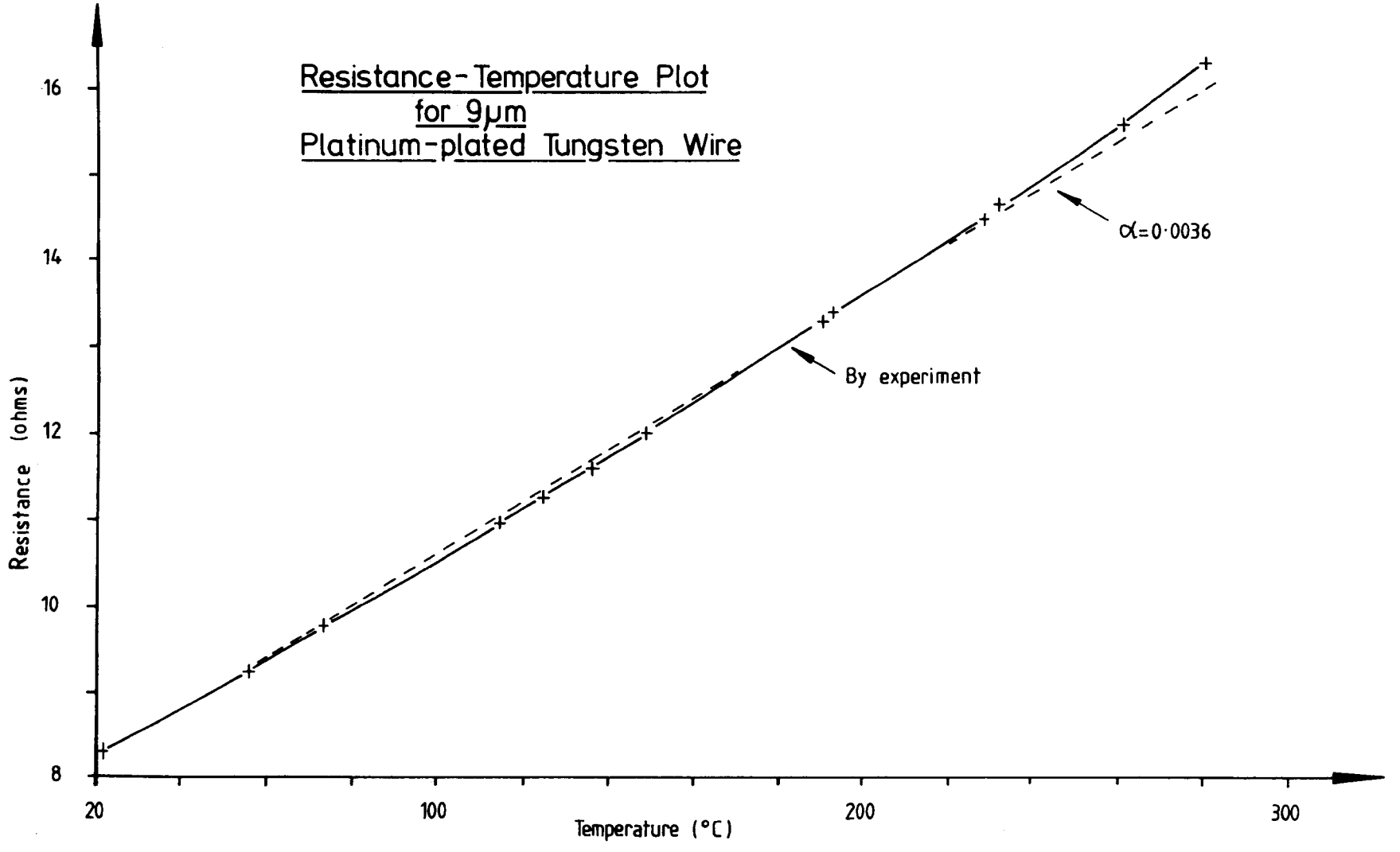
Resistance-Temperature Plot
for 9μm
Platinum-plated Tungsten Wire
α=0·0036
By experiment
Resistance (ohms)
16
14
12
10
8
20
100
200
300
Temperature (°C)

Figure 3.6

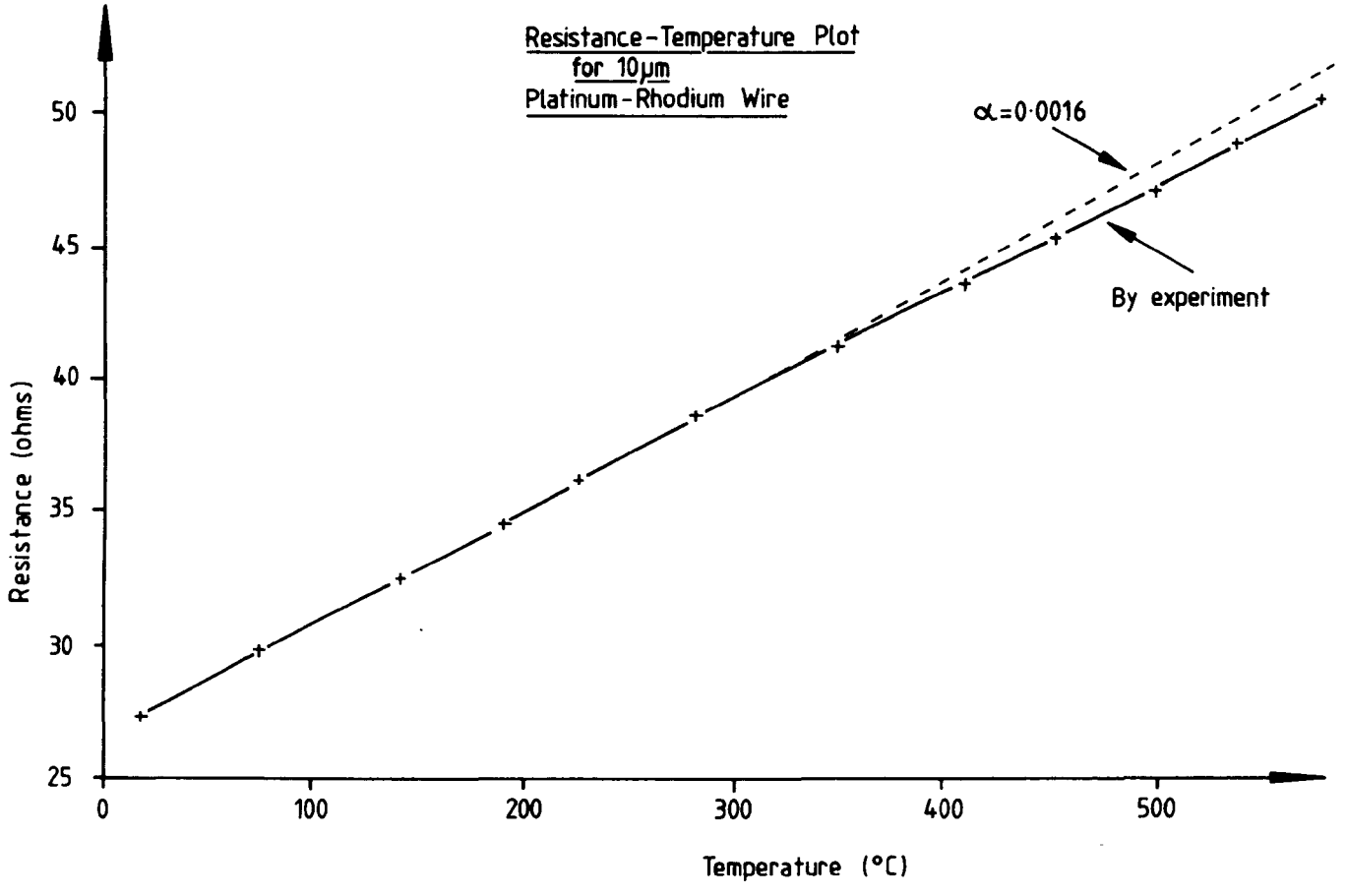
Resistance-Temperature Plot
for 10μm
Platinum-Rhodium Wire
α=0·0016
By experiment
Resistance (ohms)
50
45
40
35
30
25
0
100
200
300
400
500
Temperature (°C)

Figure 3.7

Steady-Flow Hot Wire Calibration Rig

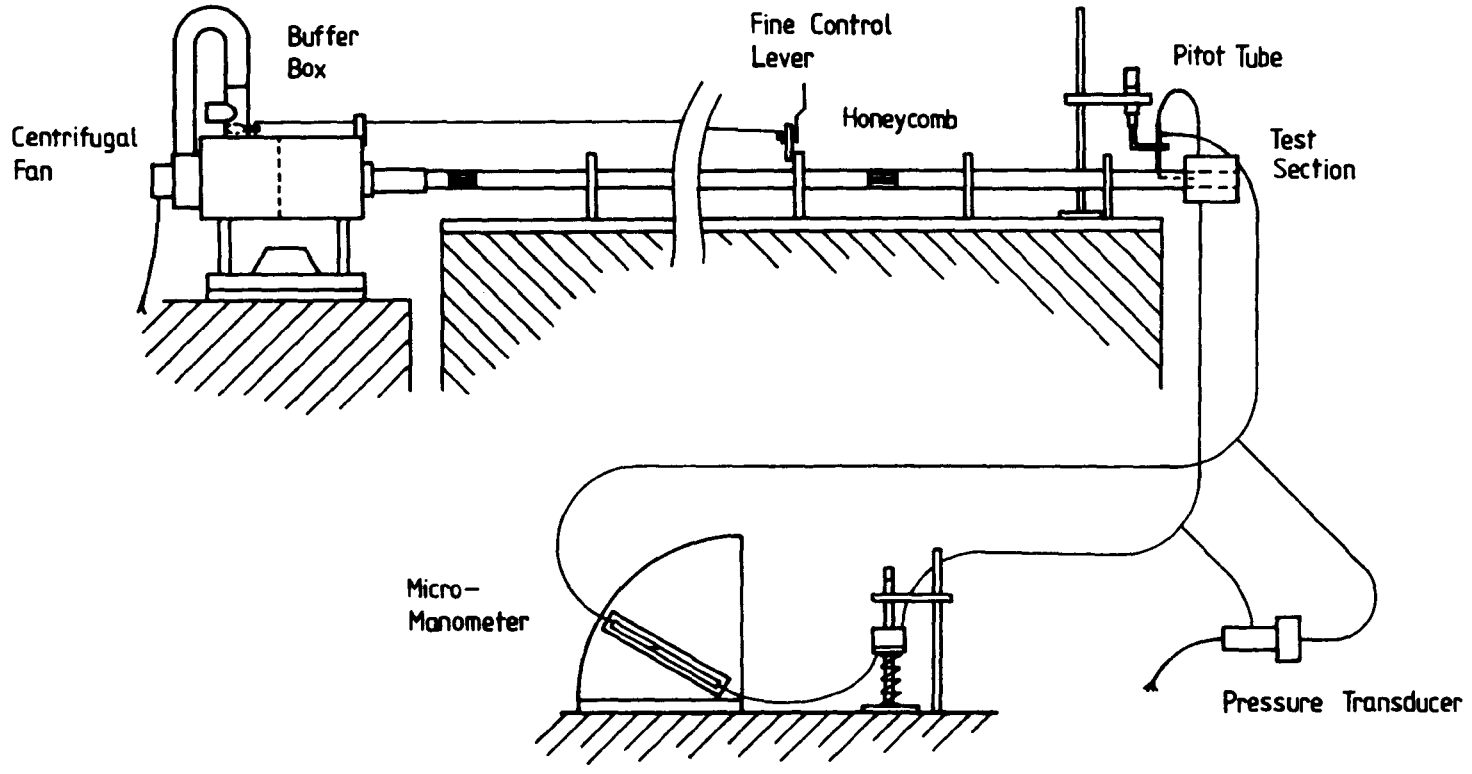

Figure 3.8

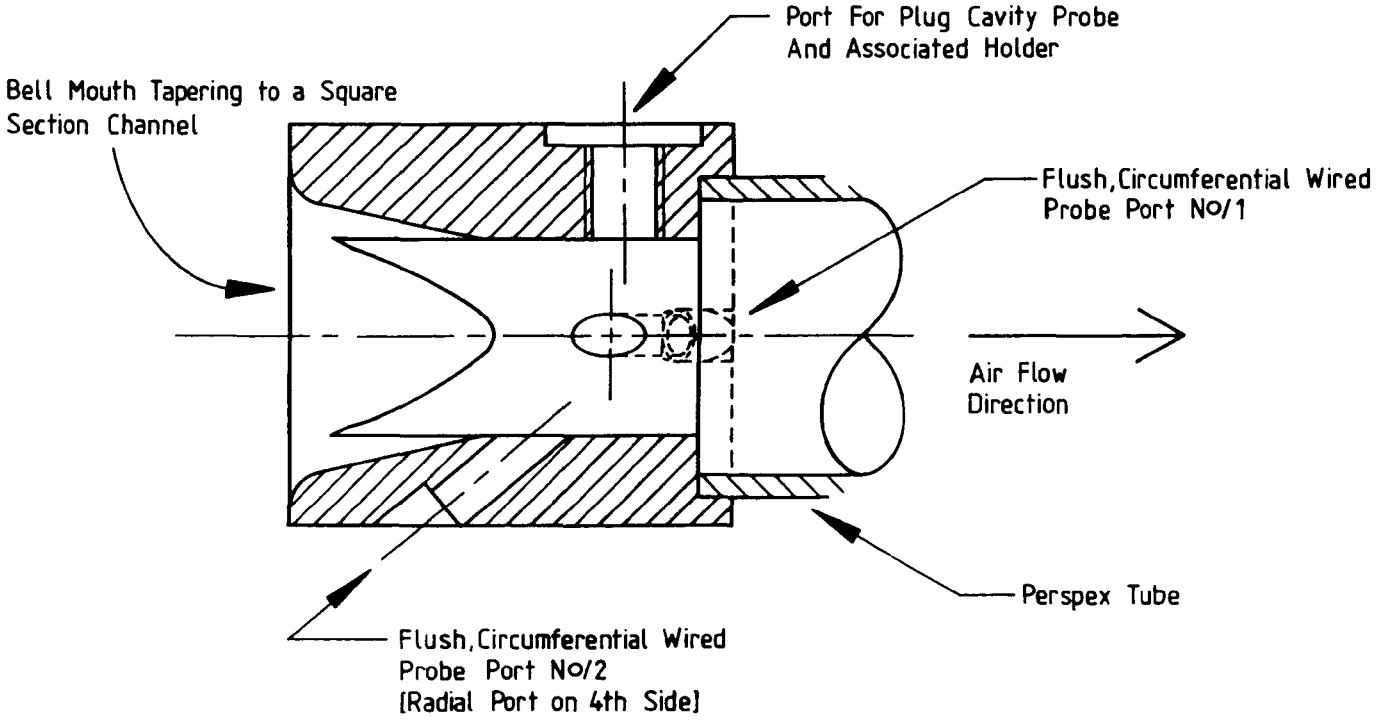

Hot Wire Calibration Rig Test Section

Material ; Perspex
Scale ; Half Size
Machined all over

Figure 3.9

Twin Hot Wire Stead-state Logging

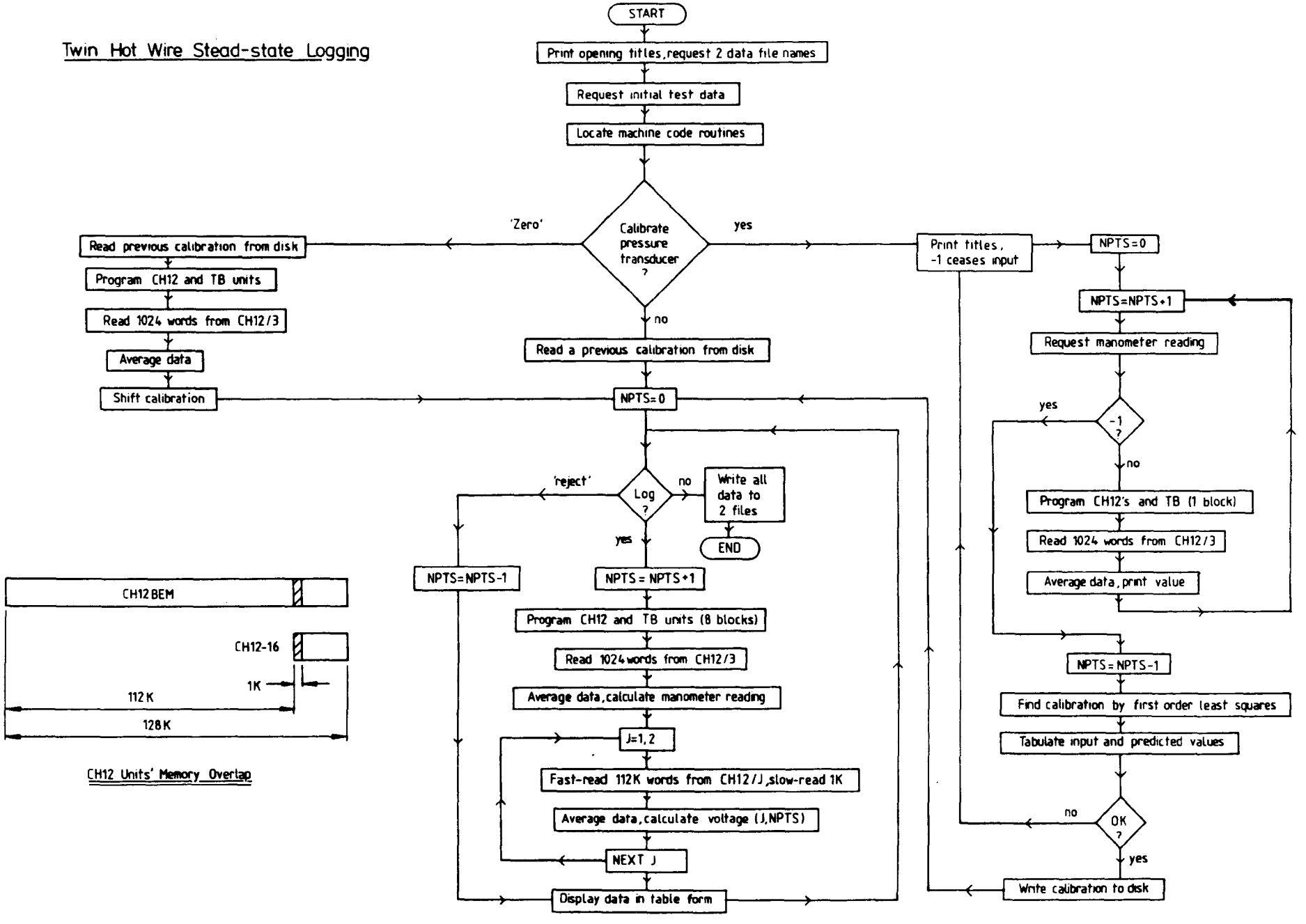

Figure 3.10

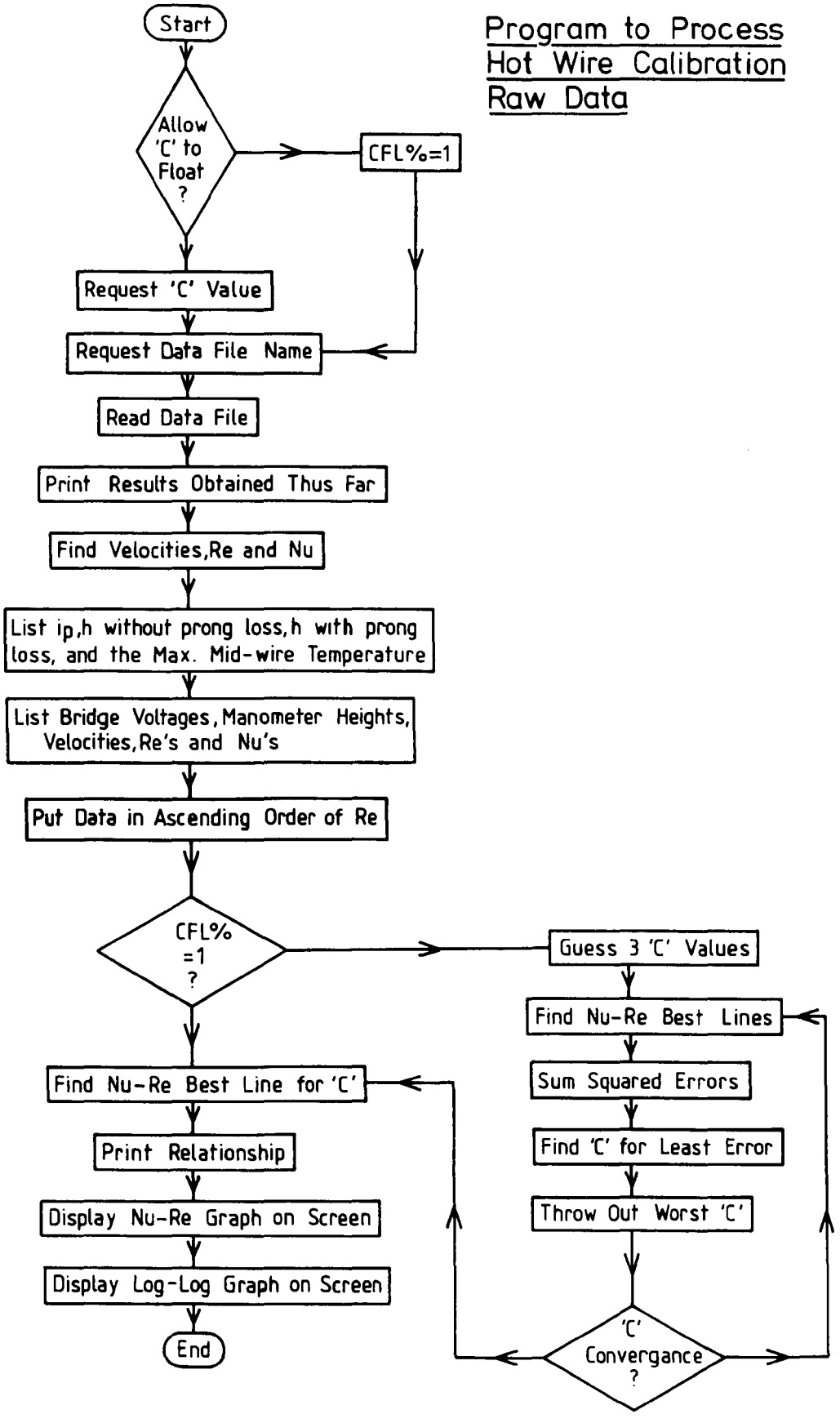
Program to Process Hot Wire Calibration Raw Data
Start
Allow 'C' to Float ?
CFL%=1
Request 'C' Value
Request Data File Name
Read Data File
Print Results Obtained Thus Far
Find Velocities,Re and Nu
List ip,h without prong loss,h with prong loss, and the Max. Mid-wire Temperature
List Bridge Voltages, Manometer Heights, Velocities,Re's and Nu's
Put Data in Ascending Order of Re
CFL% =1 ?
Guess 3 'C' Values
Find Nu-Re Best Lines
Sum Squared Errors
Find 'C' for Least Error
Throw Out Worst 'C'
'C' Convergance ?
Find Nu-Re Best Line for 'C'
Print Relationship
Display Nu-Re Graph on Screen
Display Log-Log Graph on Screen
End

Figure 3.11

Nu-Re Hot Wire Calibration Plot

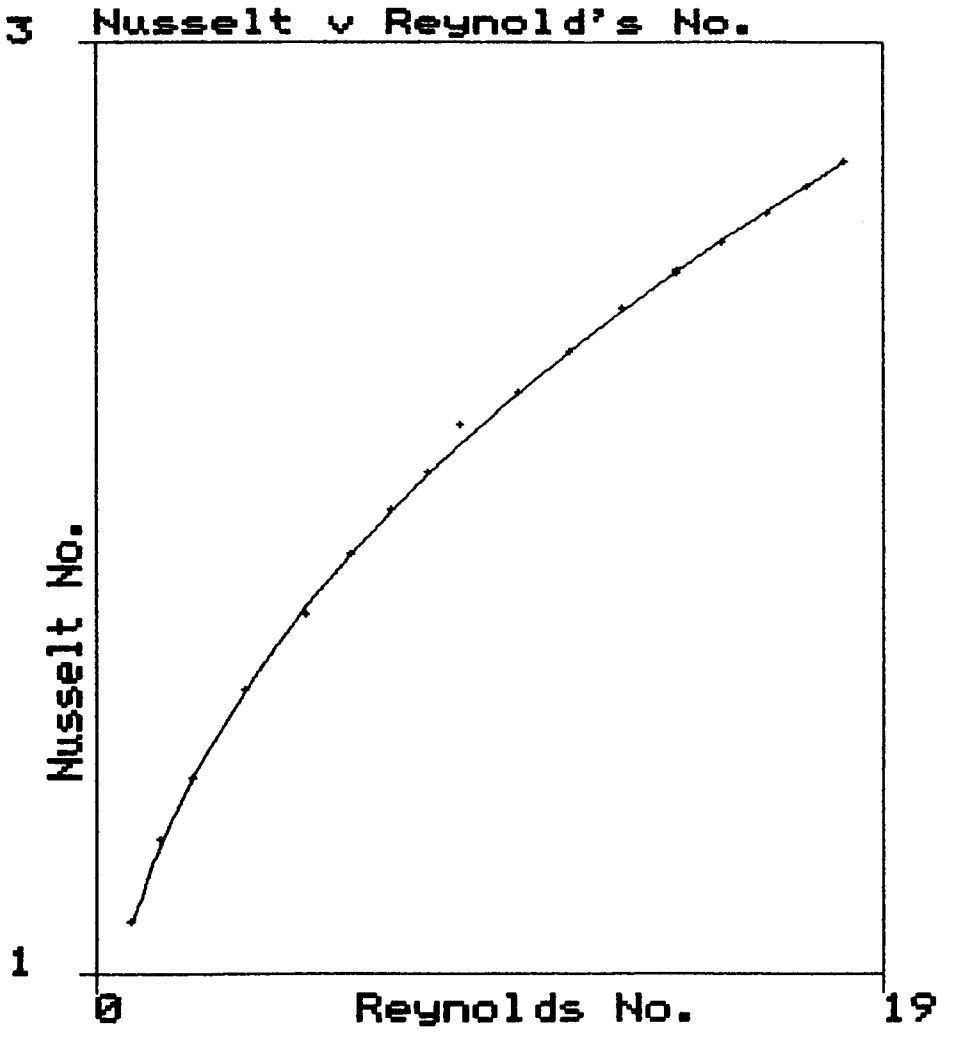

Figure 3.12

Log-Log Hot Wire Calibration Plot

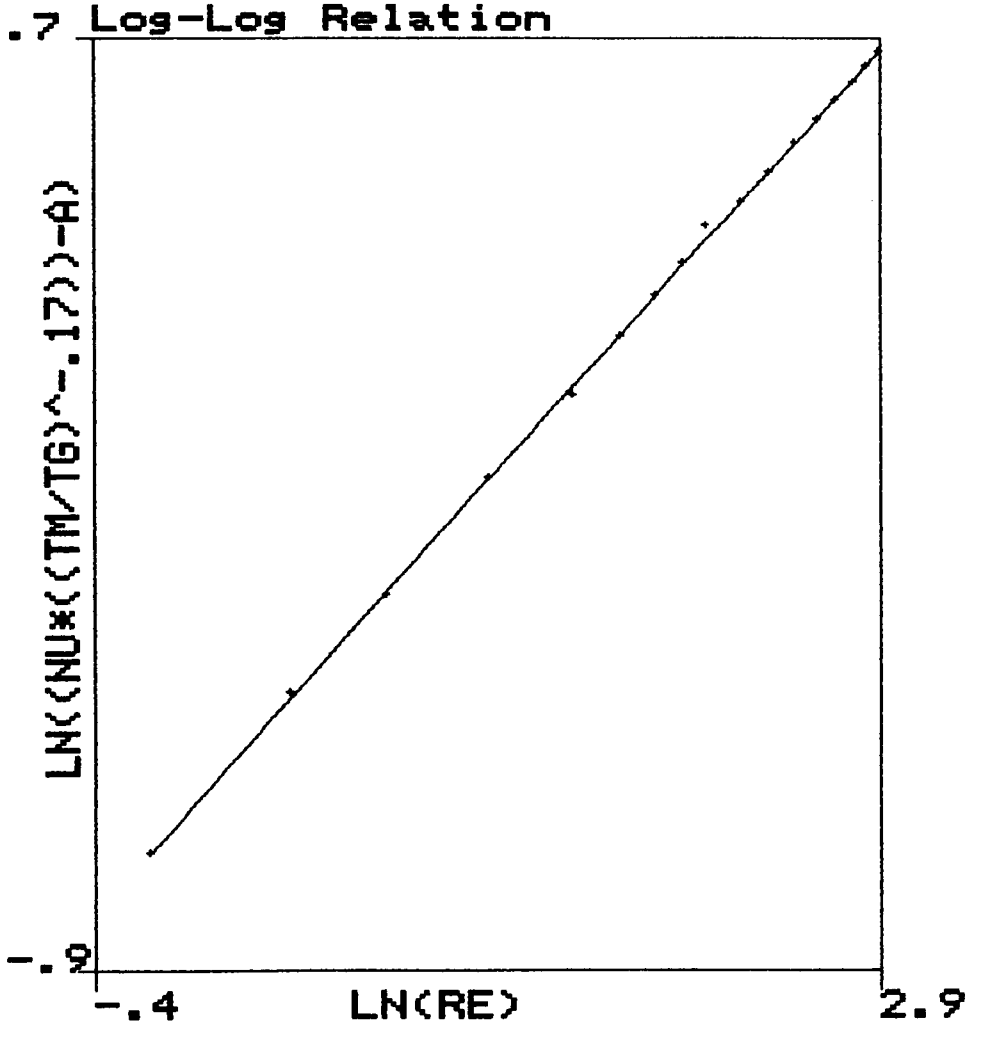

Figure 3.13

Piezio-electric Transducer Calibration Routine

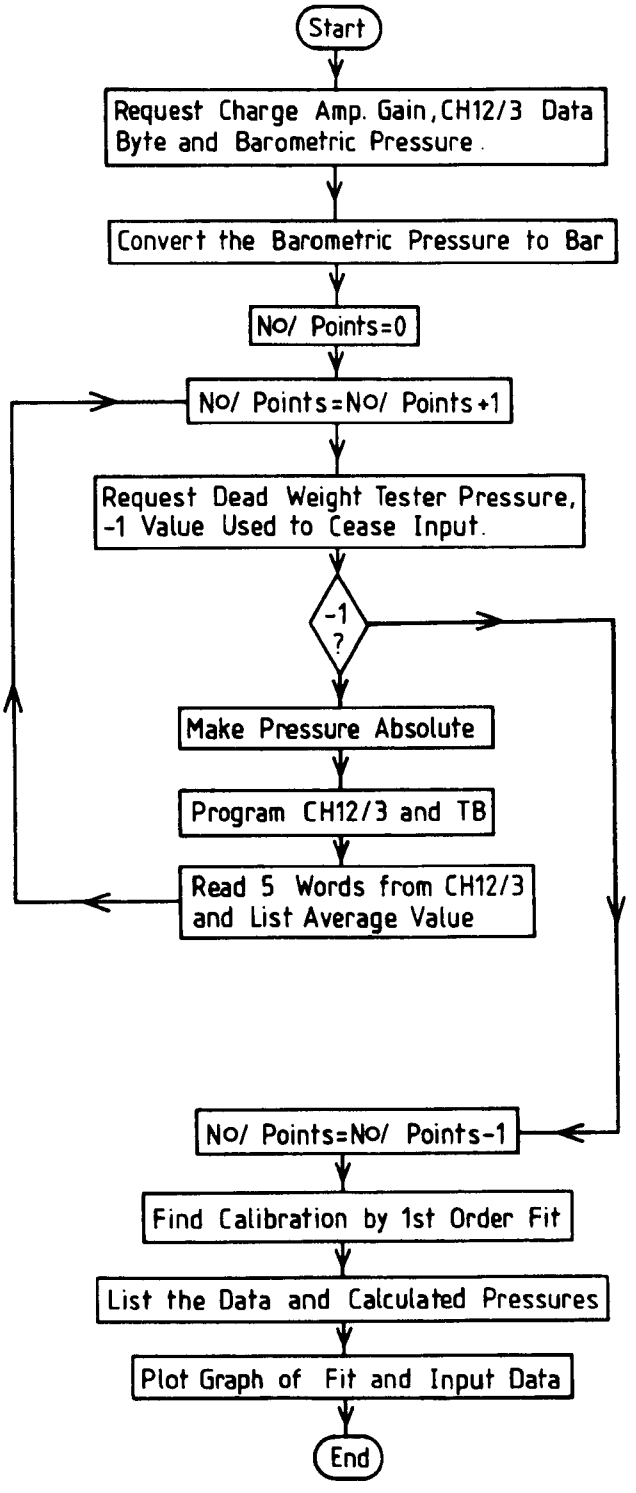

Figure 3.14

Pressure Transducer Calibration Plot

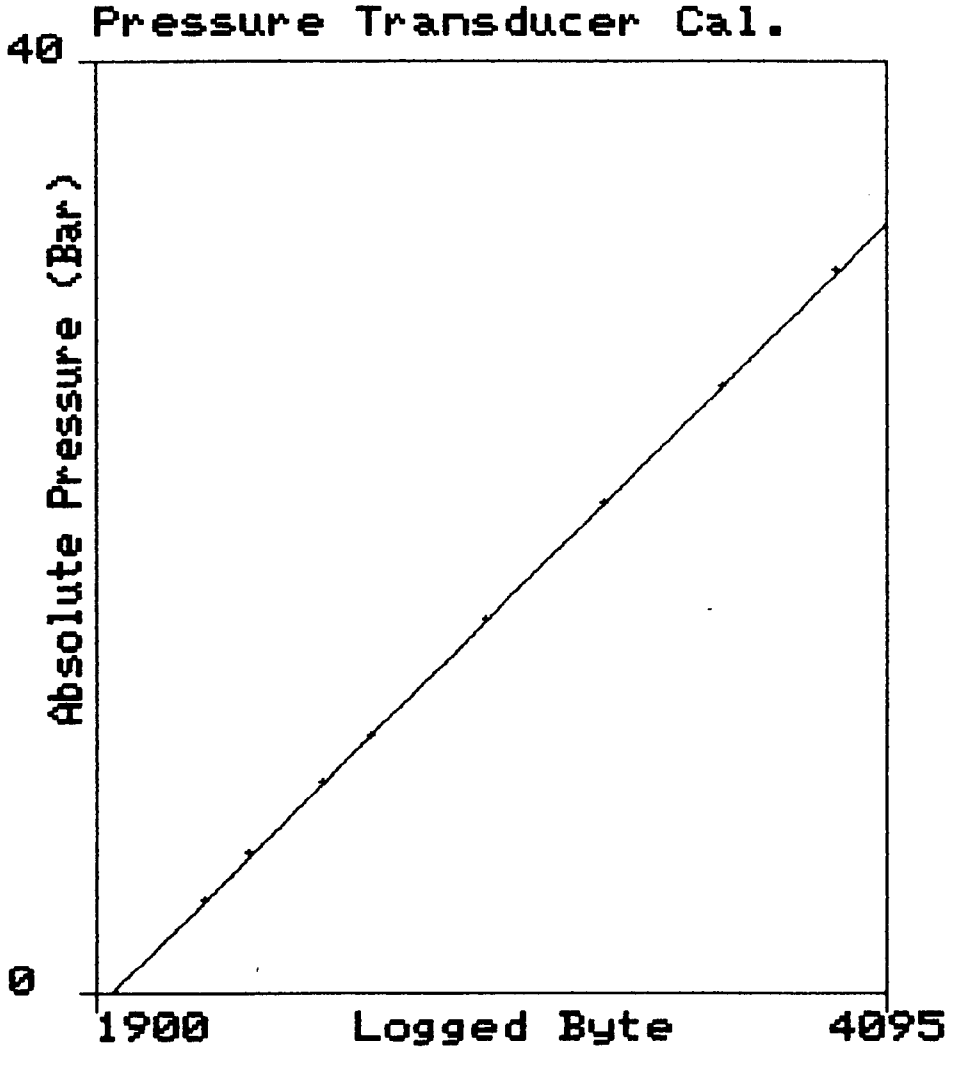

Figure 3.15

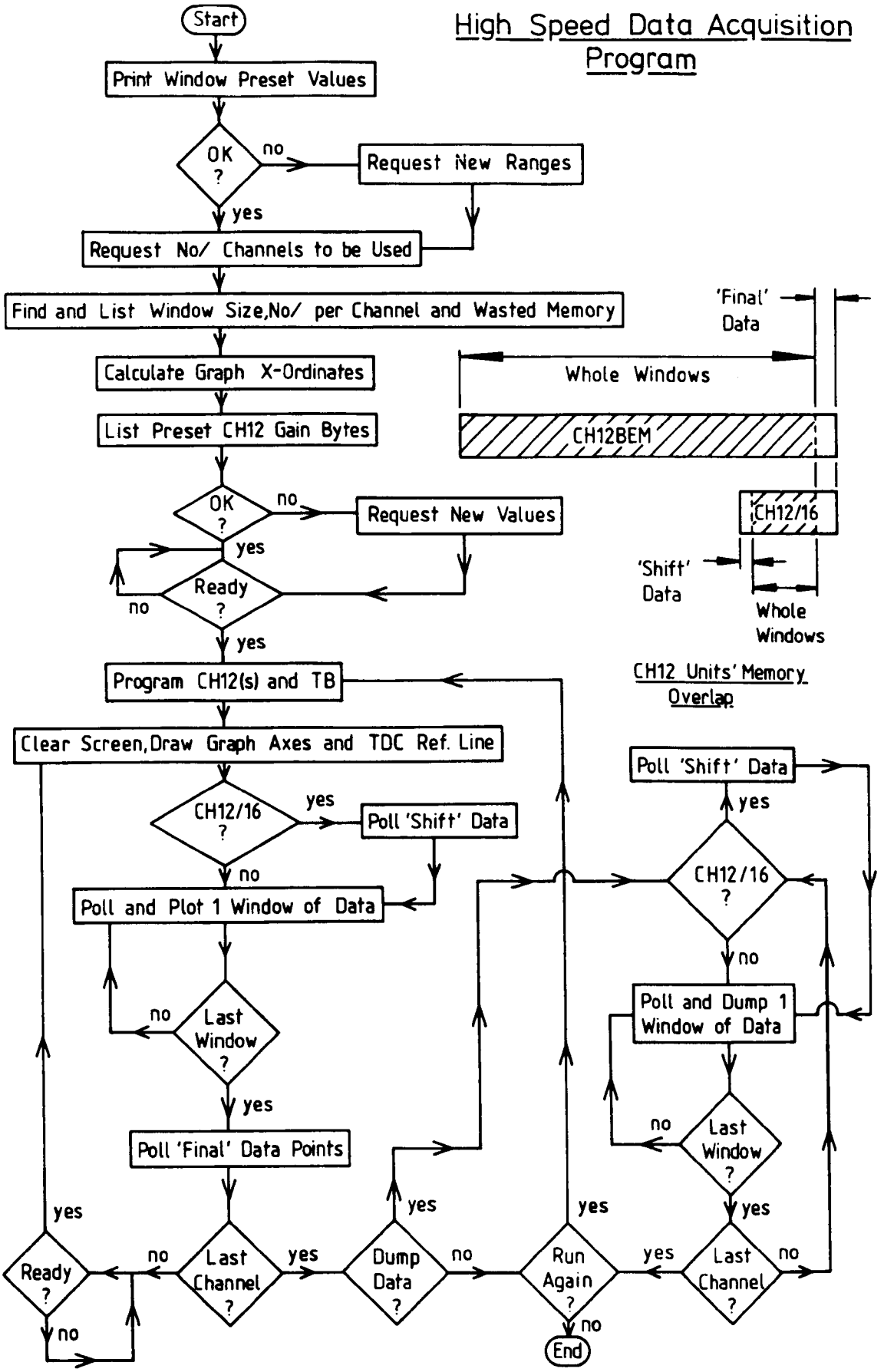
High Speed Data Acquisition Program
Start
Print Window Preset Values
OK ?
no
Request New Ranges
yes
Request No/ Channels to be Used
Find and List Window Size,No/ per Channel and Wasted Memory
Calculate Graph X-Ordinates
List Preset CH12 Gain Bytes
OK ?
no
Request New Values
yes
Ready ?
no
yes
Program CH12(s) and TB
Clear Screen,Draw Graph Axes and TDC Ref. Line
CH12/16 ?
yes
Poll 'Shift' Data
no
Poll and Plot 1 Window of Data
Last Window ?
no
yes
Poll 'Final' Data Points
Ready ?
yes
no
Last Channel ?
no
yes
Dump Data ?
yes
no
Run Again ?
yes
no
End
Last Channel ?
yes
no
Last Window ?
yes
no
Poll and Dump 1 Window of Data
CH12/16 ?
yes
no
Poll 'Shift' Data
'Final' Data
Whole Windows
CH12BEM
CH12/16
'Shift' Data
Whole Windows
CH12 Units' Memory Overlap

Figure 3.16

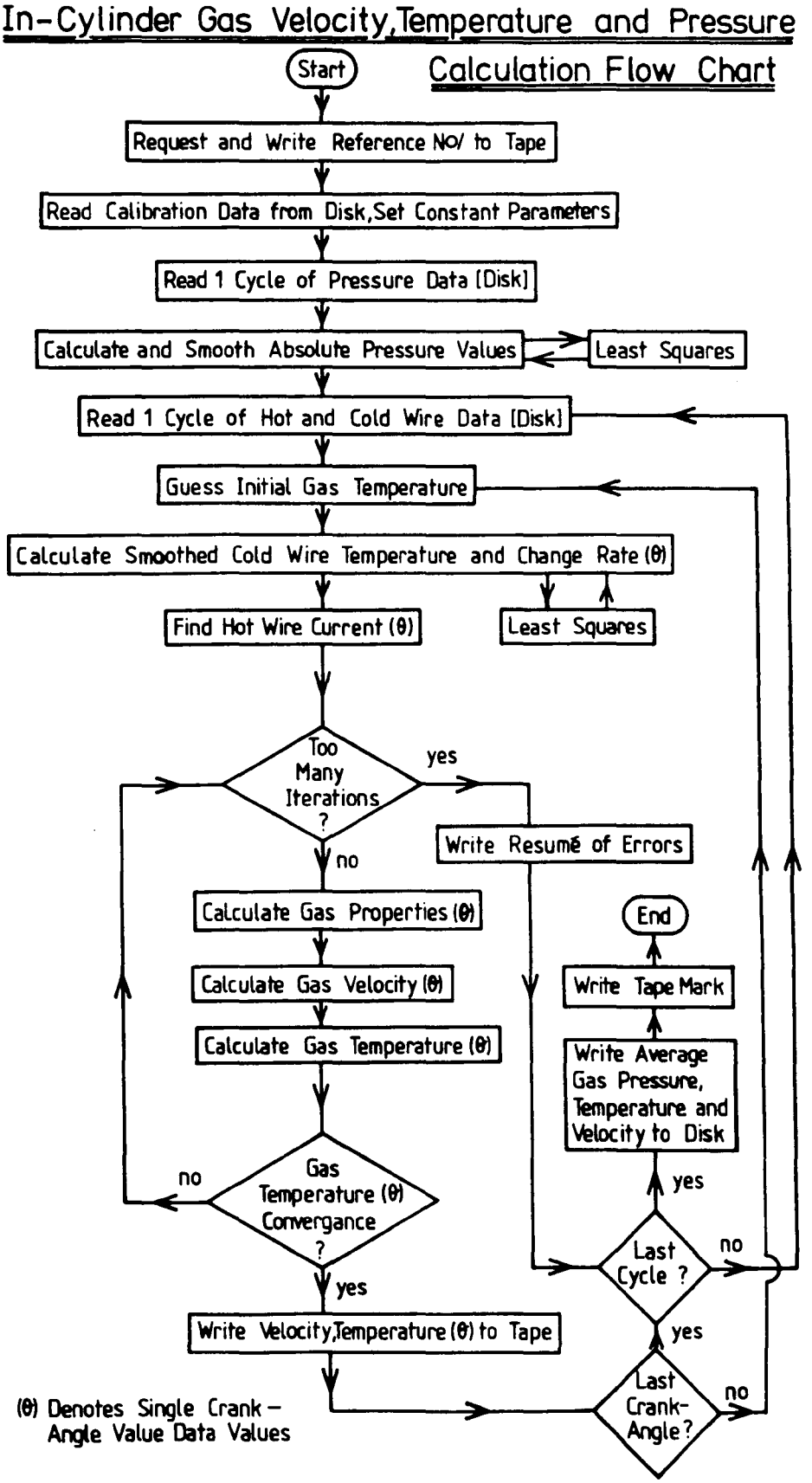
In-Cylinder Gas Velocity,Temperature and Pressure
Calculation Flow Chart
Start
Request and Write Reference NO/ to Tape
Read Calibration Data from Disk,Set Constant Parameters
Read 1 Cycle of Pressure Data [Disk]
Calculate and Smooth Absolute Pressure Values
Least Squares
Read 1 Cycle of Hot and Cold Wire Data [Disk]
Guess Initial Gas Temperature
Calculate Smoothed Cold Wire Temperature and Change Rate (θ)
Find Hot Wire Current (θ)
Least Squares
Too Many Iterations ?
yes
Write Resumé of Errors
no
Calculate Gas Properties (θ)
Calculate Gas Velocity (θ)
Calculate Gas Temperature (θ)
End
Write Tape Mark
Write Average Gas Pressure, Temperature and Velocity to Disk
Gas Temperature (θ) Convergance ?
no
yes
Last Cycle ?
no
yes
Write Velocity,Temperature (θ) to Tape
Last Crank-Angle?
no
yes
(θ) Denotes Single Crank – Angle Value Data Values

Figure 3.17

Twin Anenometer In-Cylinder Velocity Evaluation Program Flow Chart

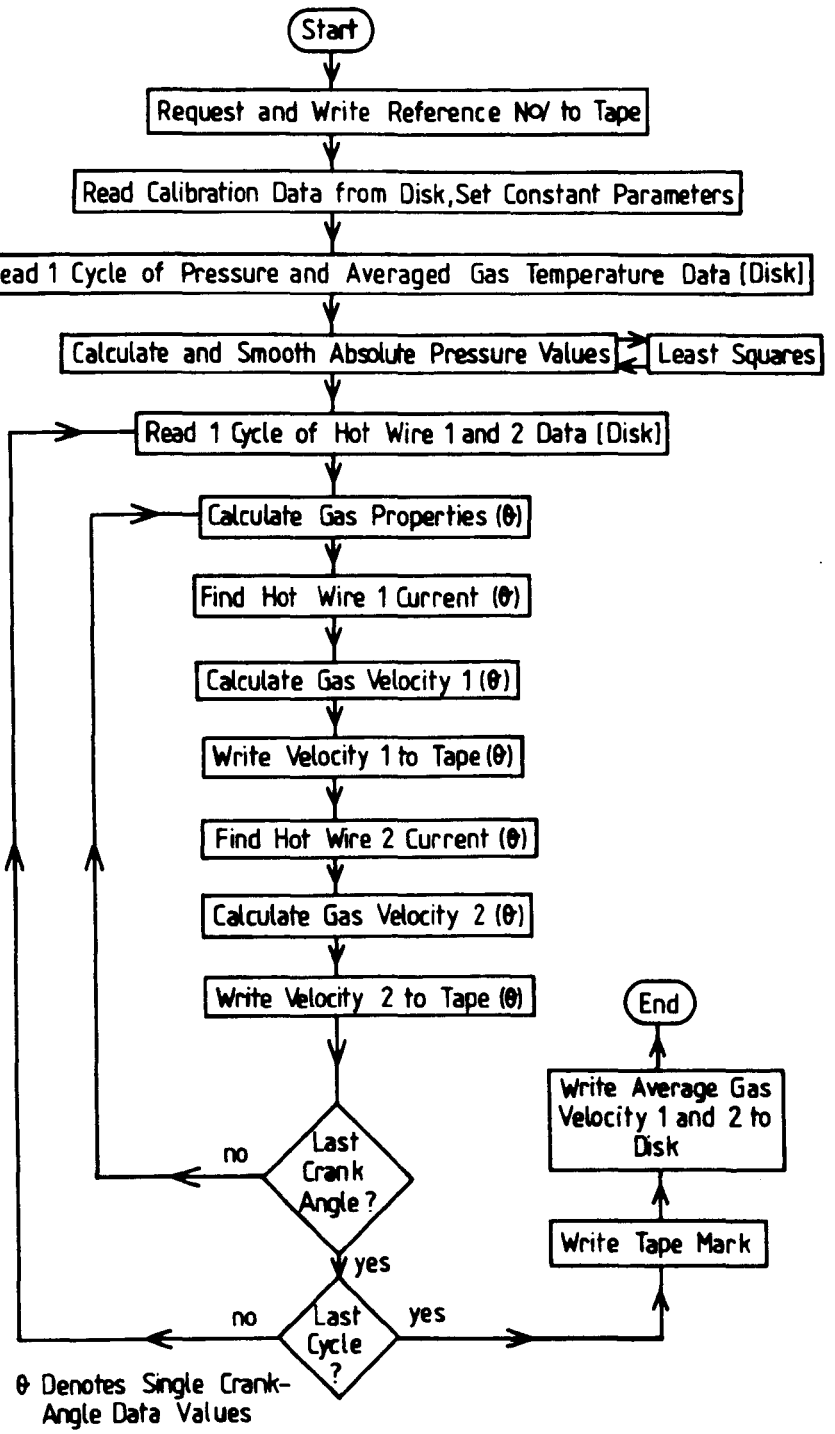

Figure 3.18

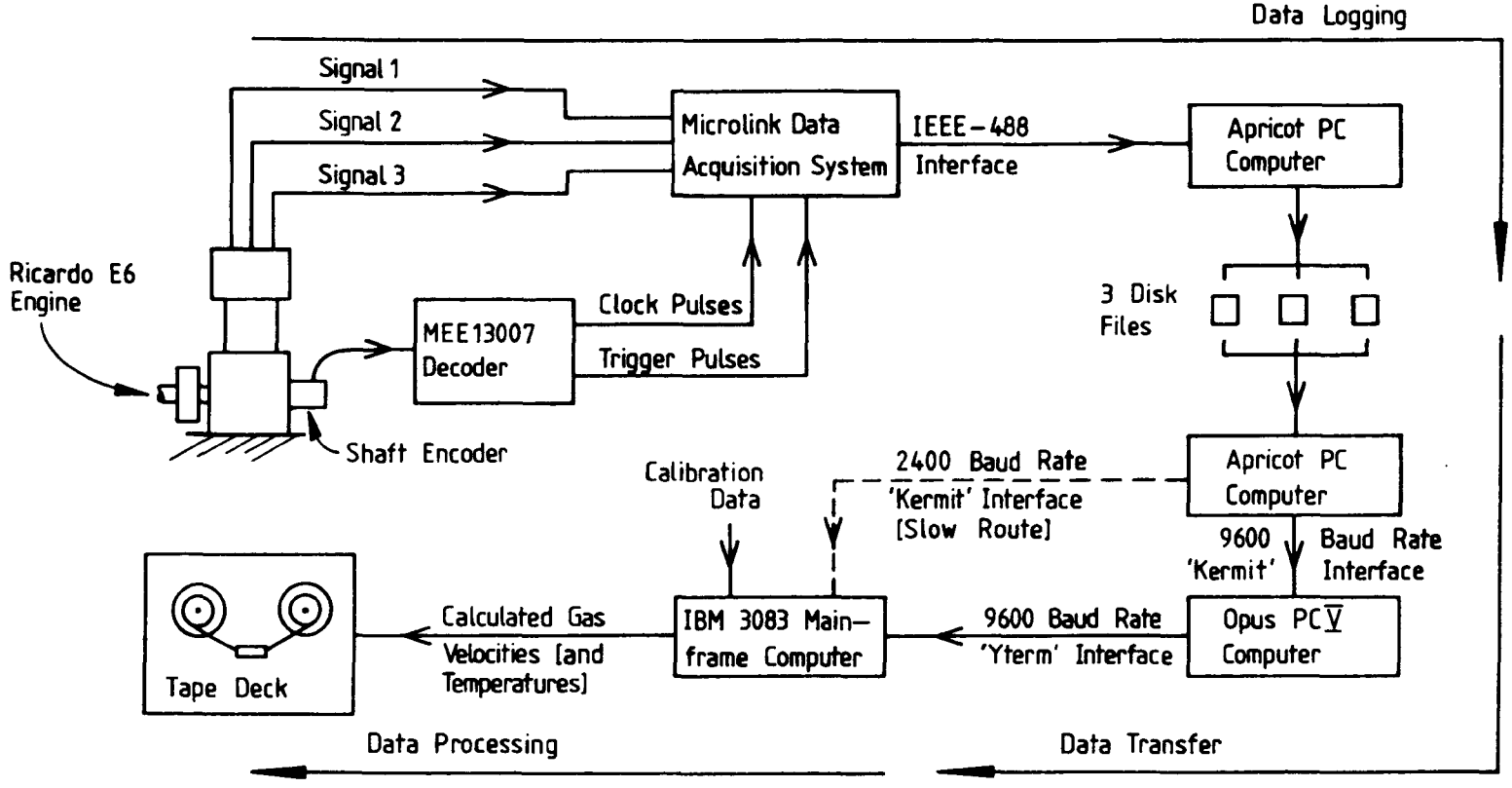

In-Cylinder Data Logging, Transfer and Processing Summary

Figure 3.19

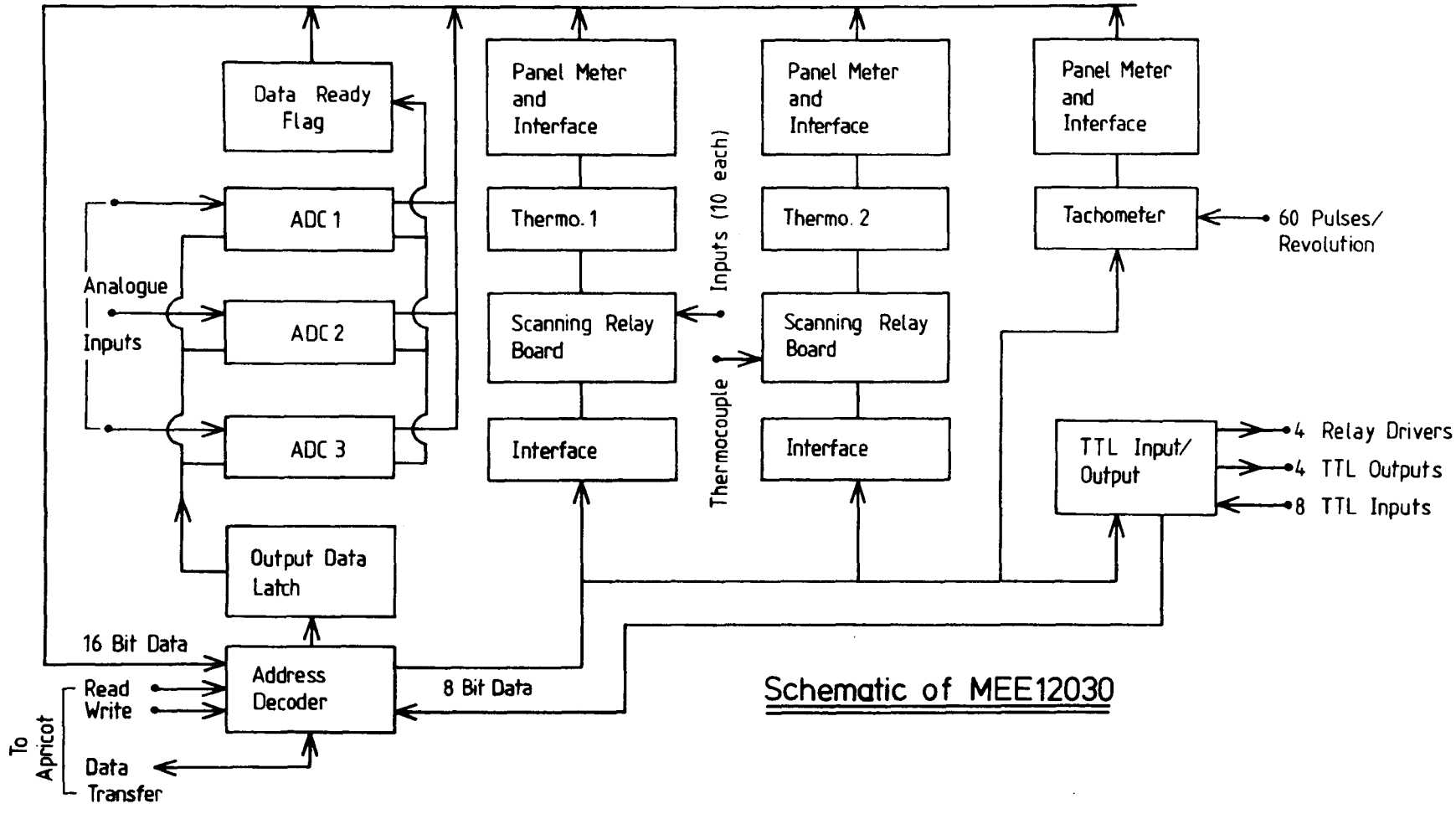
Data Ready Flag
ADC 1
ADC 2
ADC 3
Analogue Inputs
Output Data Latch
16 Bit Data
Address Decoder
Read
Write
Data Transfer
To Apricot
8 Bit Data
Panel Meter and Interface
Thermo. 1
Scanning Relay Board
Interface
Inputs (10 each)
Thermocouple
Panel Meter and Interface
Thermo. 2
Scanning Relay Board
Interface
Panel Meter and Interface
Tachometer
60 Pulses/ Revolution
TTL Input/ Output
4 Relay Drivers
4 TTL Outputs
8 TTL Inputs
Schematic of MEE12030

Figure 4.1

Schematic of Engine Dynometer Load Cell Arrangement

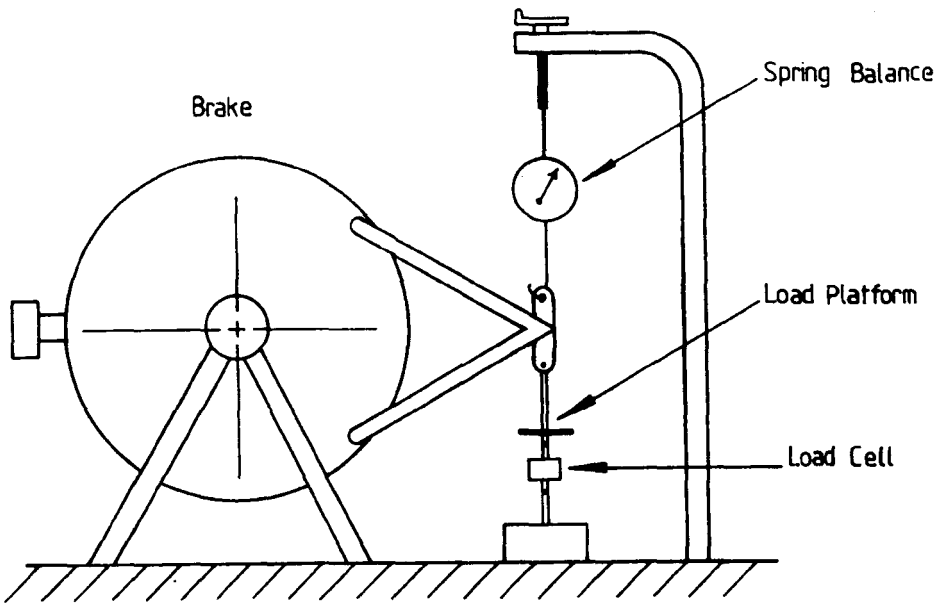

Figure 4.2

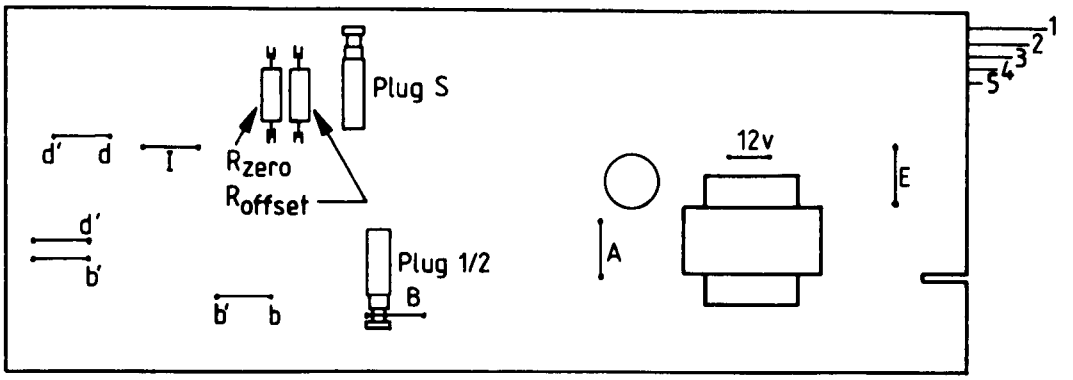

FE492BBS PCB. Layout for Flow Meter and Load Cell

Values for the Above

	Flow Meter	Load Cell
R_{zero}	36K	20 K
R_{offset}	20K	20 K

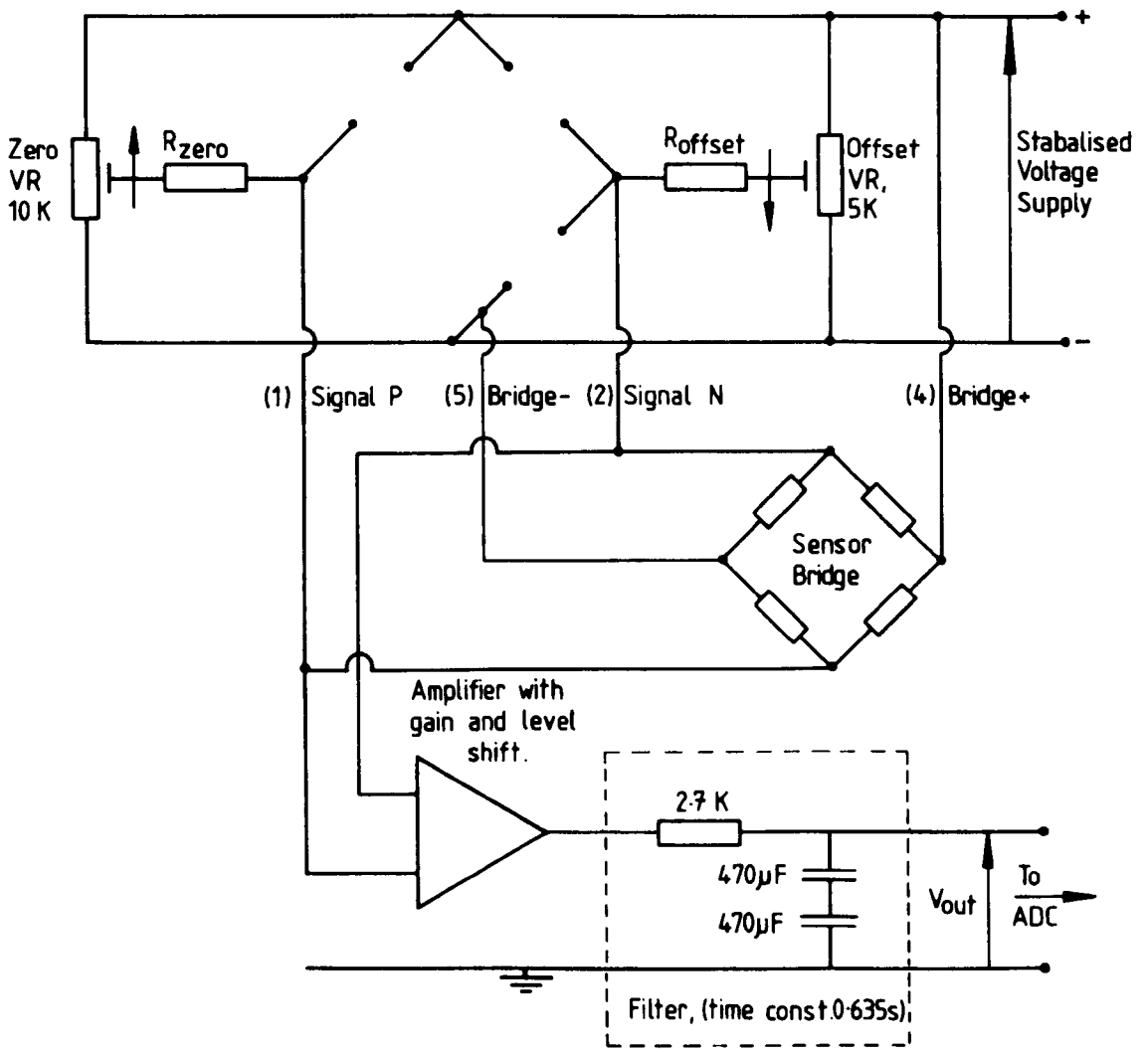

Basic Description of Complete Bridge Circuit for Load Cell and Flow Meter Transducer.

Figure 4.3

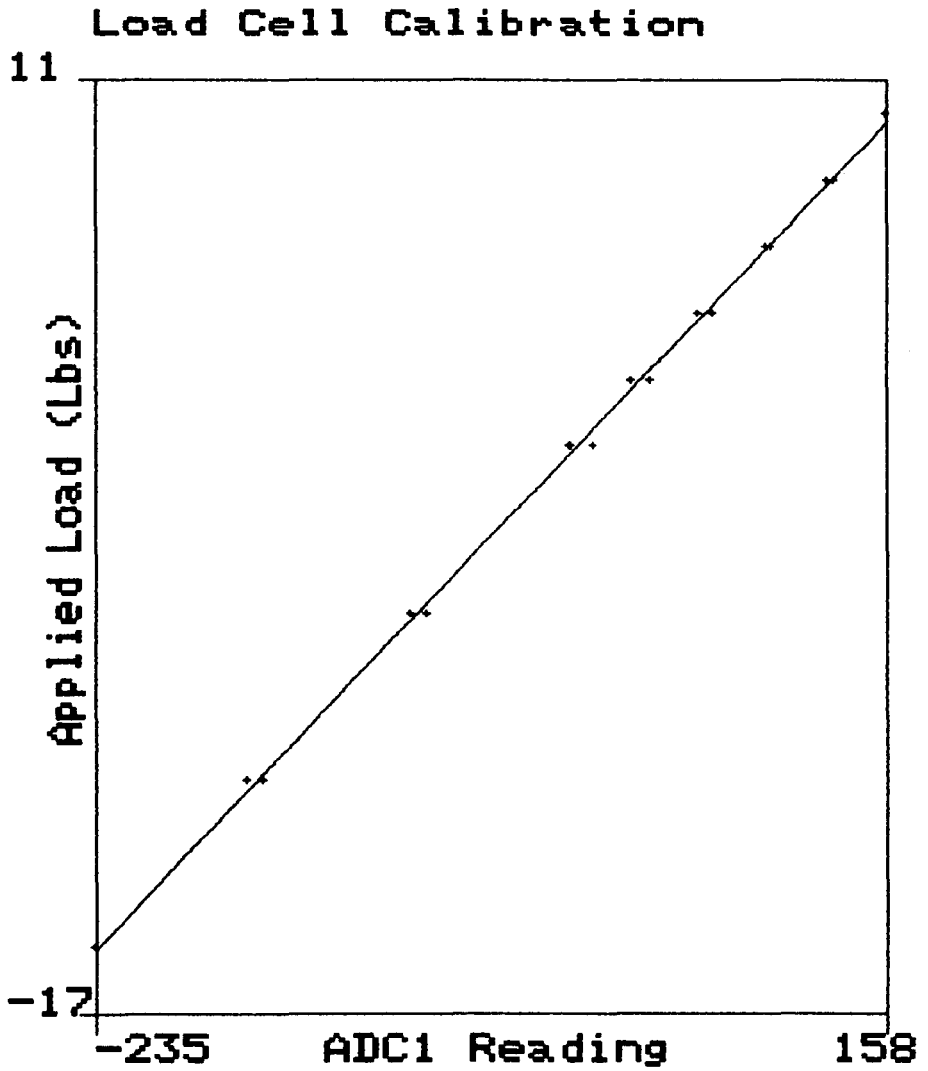
Load Cell Calibration
11
-17
Applied Load (Lbs)
-235
ADC1 Reading
158

Figure 4.4

Schematic of the Air Flow Meter and Pressure Transducer Arrangement

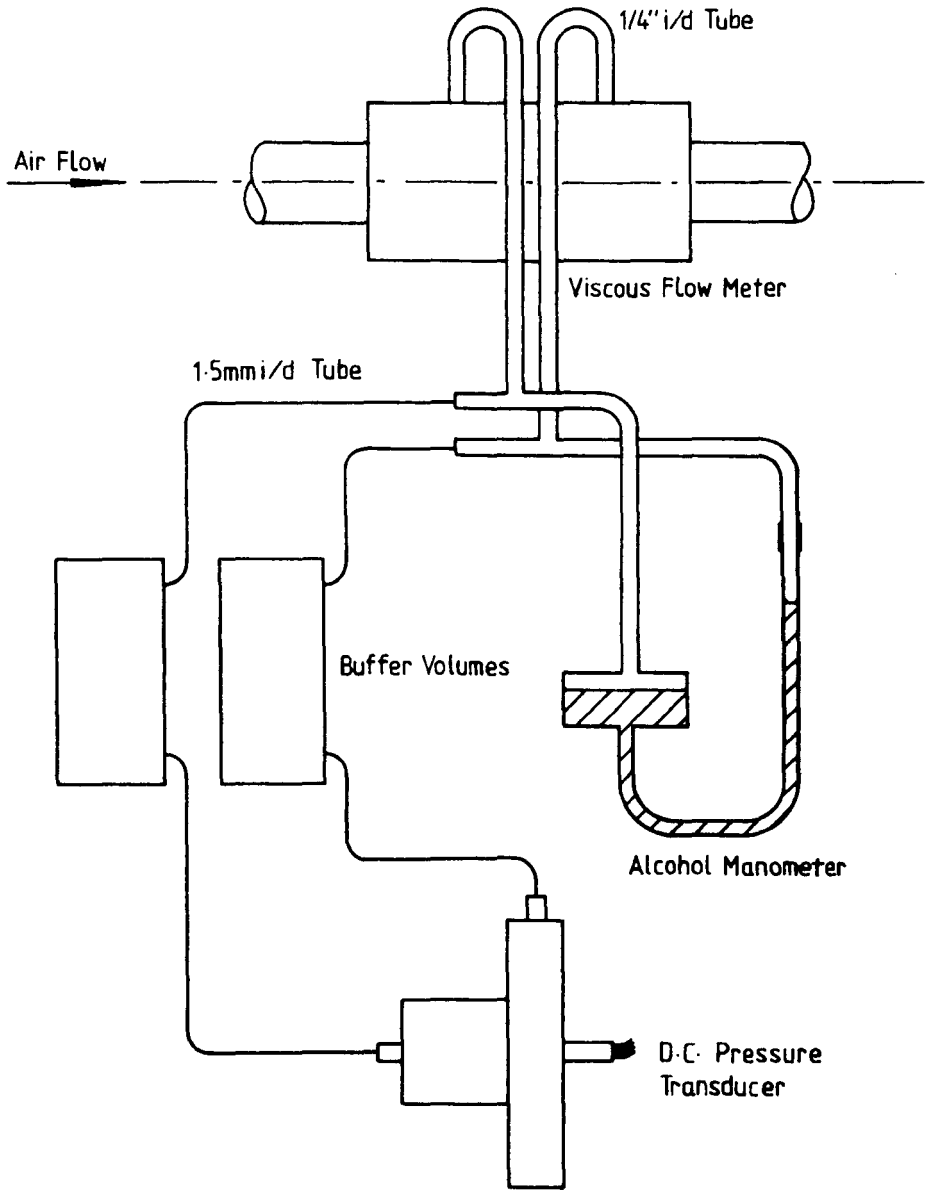

Figure 4.5

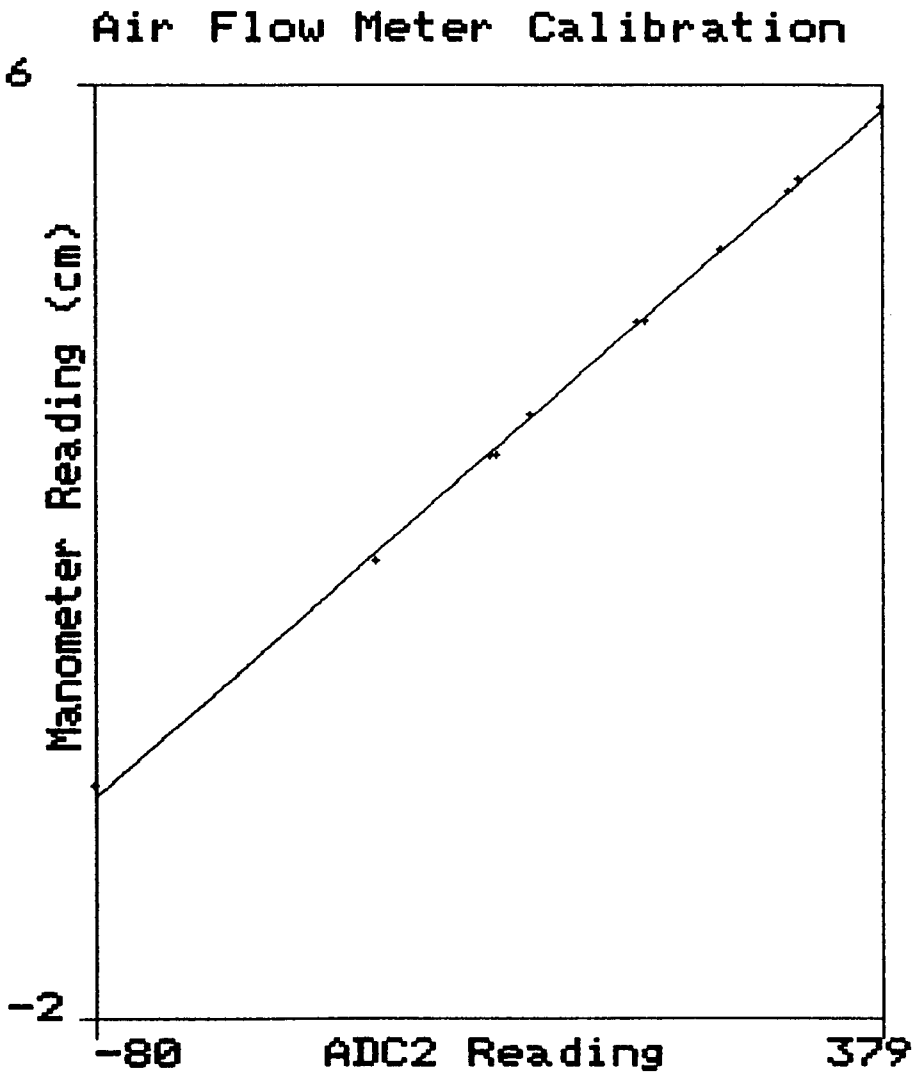
Air Flow Meter Calibration
6
-2
Manometer Reading (cm)
-80
ADC2 Reading
379

Figure 4.6

Fuel Pipette Photo-Detector Mounting Block Details

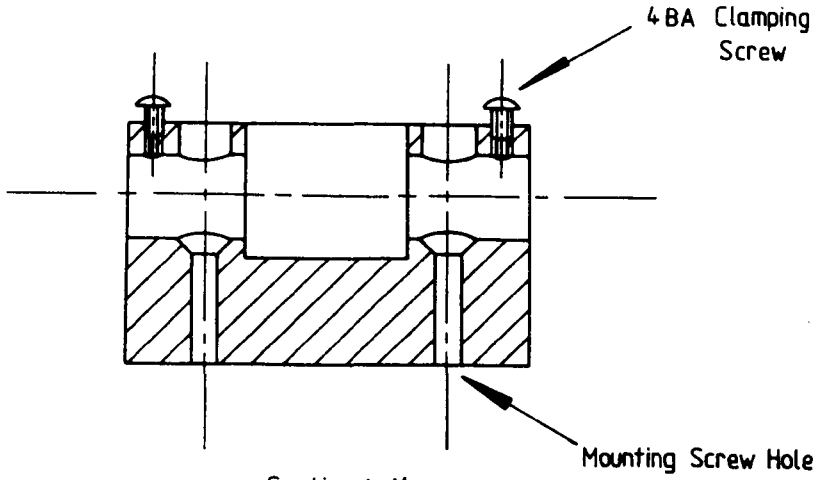

Section A-A'

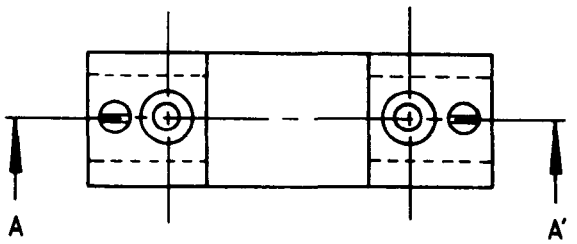

Aluminium Mounting Block

Photo Detector/Diode Lens Tube Sketch

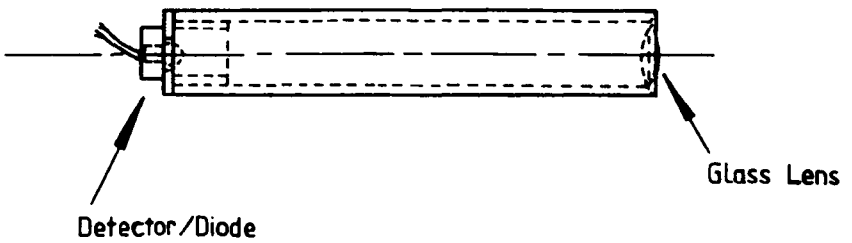

Mild Steel Lens Tube

Figure 4.7

Schematic of Buffer Volume Volumetric Fuel Flow Measurement System

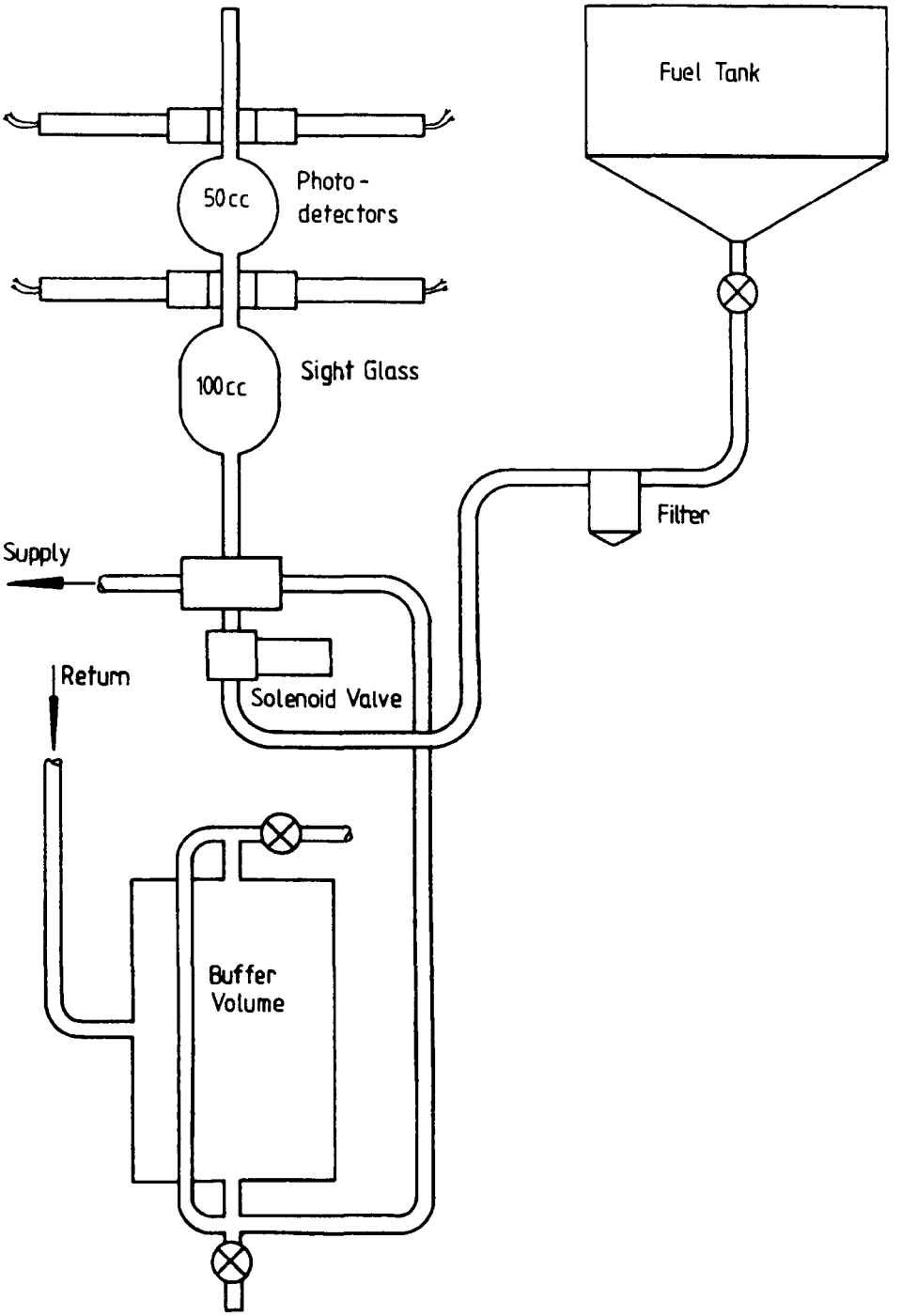

Figure 4.8

Schematic of Float Chamber Volumetric Fuel Flow Measurement System

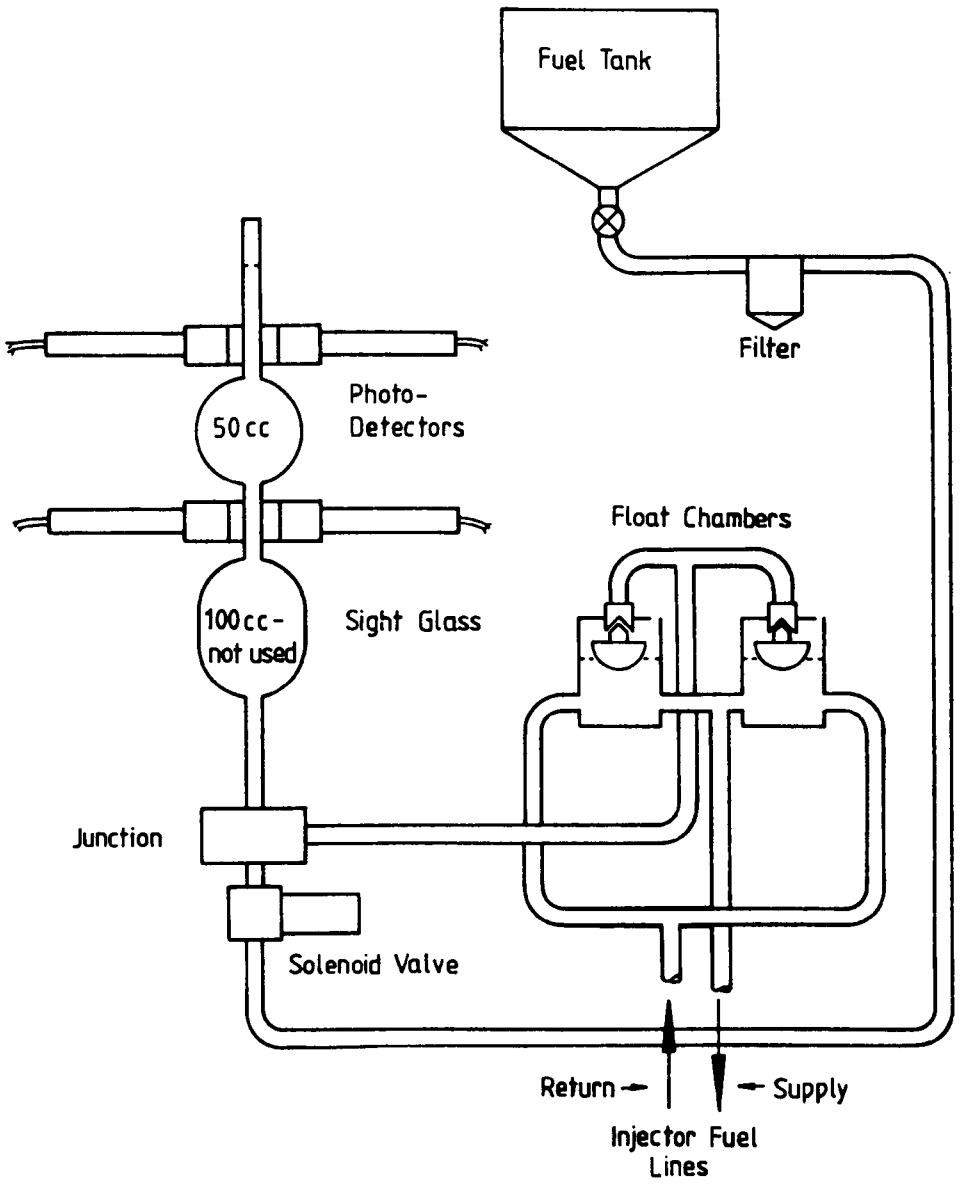

Figure 4.9

Block Diagram of Performance Mapping Data Acquisition Procedure

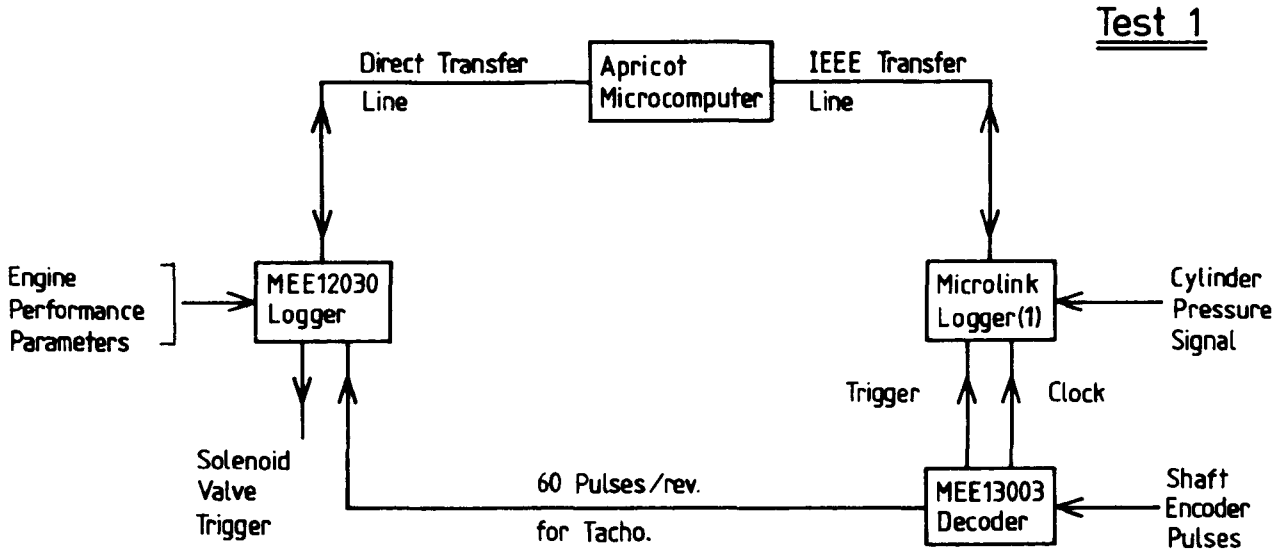

Figure 4.10

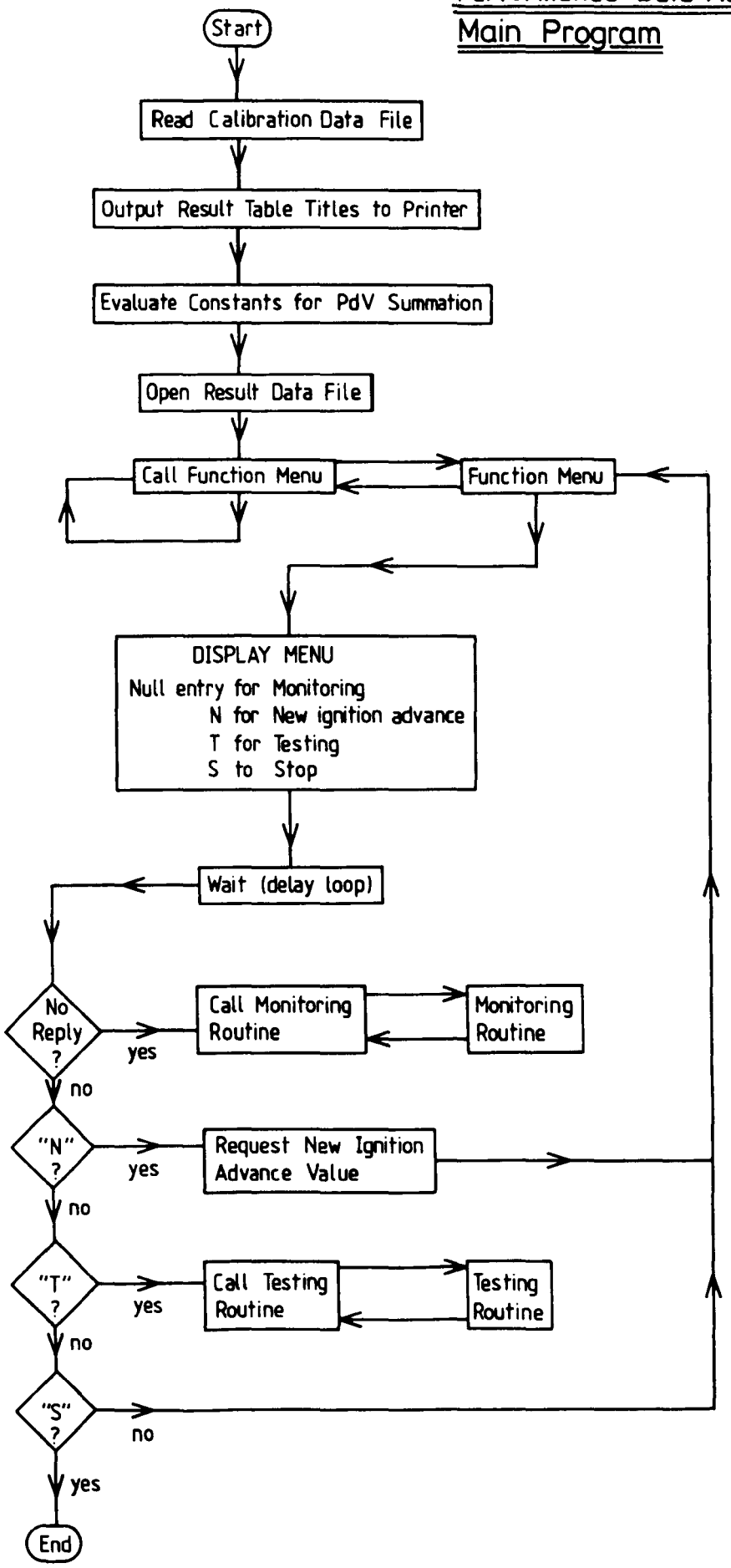
Start
Read Calibration Data File
Output Result Table Titles to Printer
Evaluate Constants for PdV Summation
Open Result Data File
Call Function Menu
Function Menu
DISPLAY MENU
Null entry for Monitoring
N for New ignition advance
T for Testing
S to Stop
Wait (delay loop)
No Reply ?
yes
Call Monitoring Routine
Monitoring Routine
no
"N" ?
yes
Request New Ignition Advance Value
no
"T" ?
yes
Call Testing Routine
Testing Routine
no
"S" ?
no
yes
End

Figure 4.11

Performance Data Acquisition Monitoring Routine

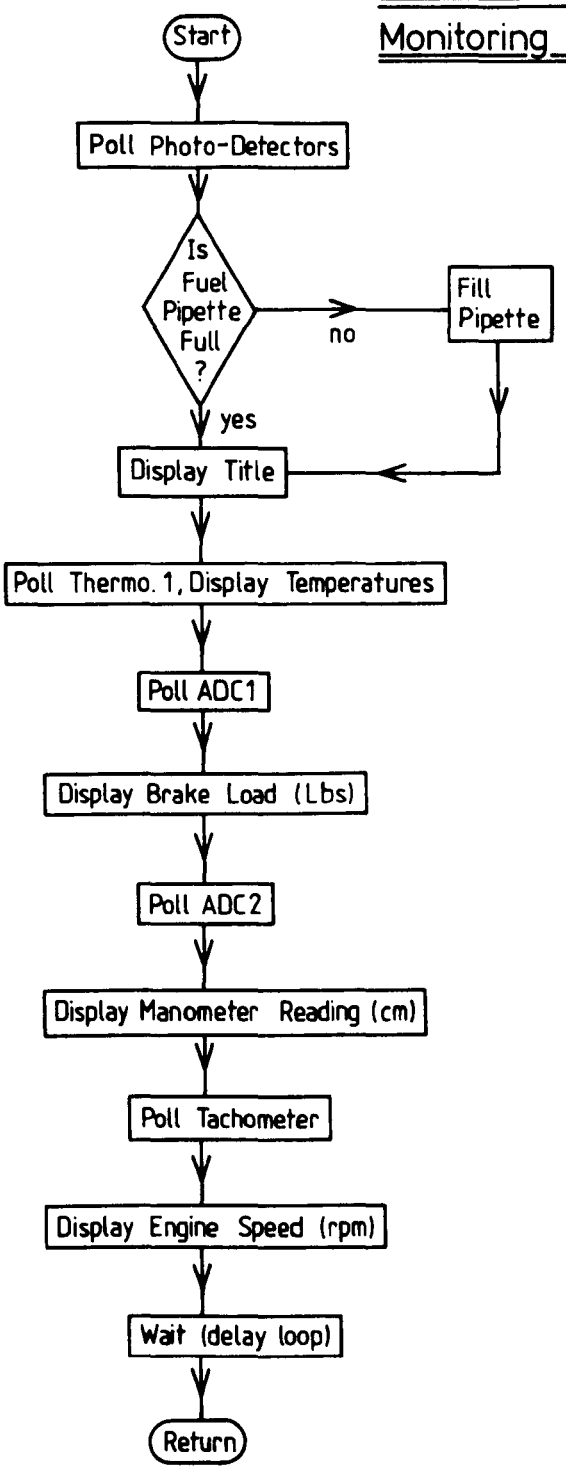

Figure 4.12

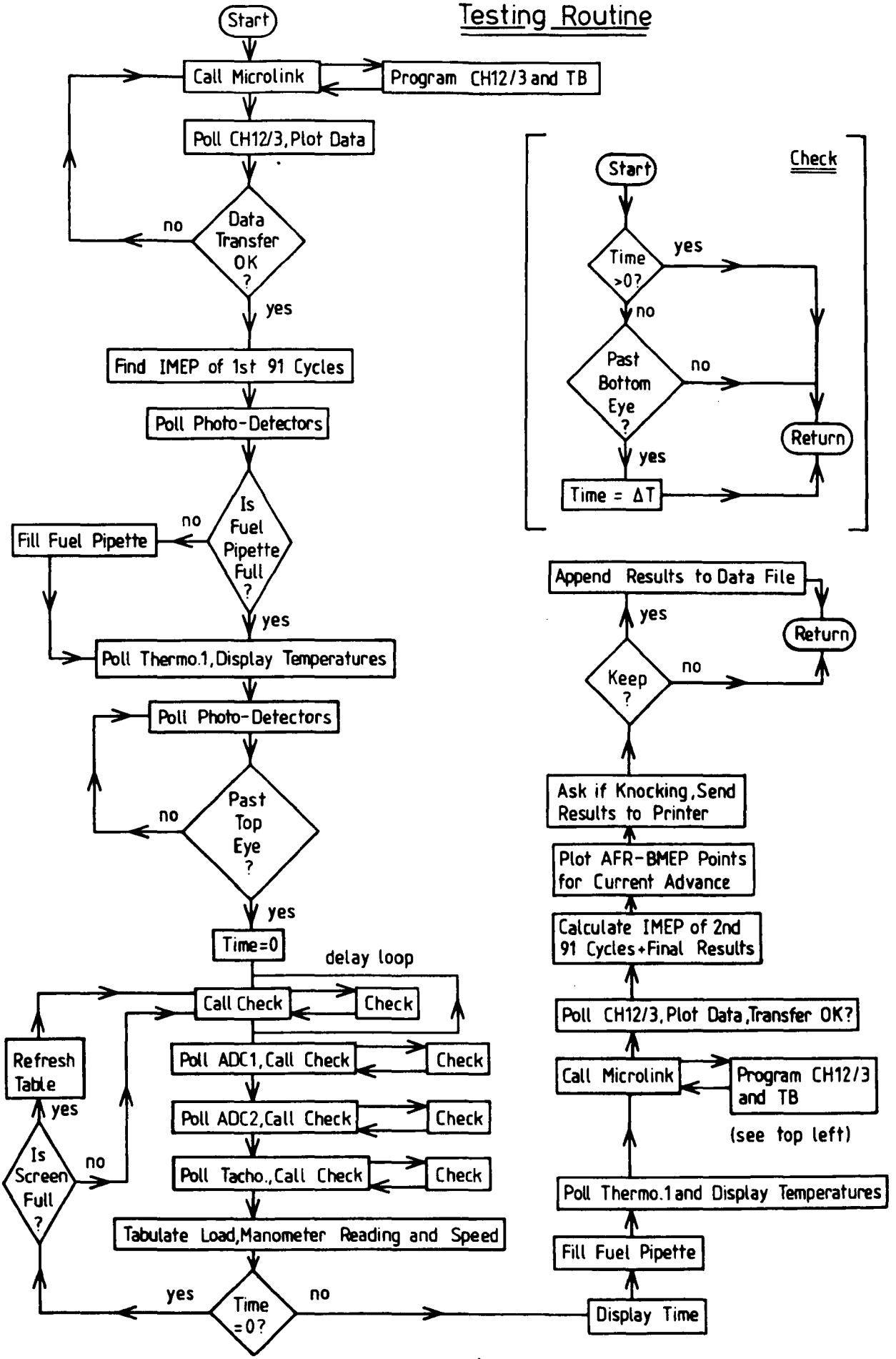
Performance Data Acquisition
Testing Routine
Start
Call Microlink
Program CH12/3 and TB
Poll CH12/3, Plot Data
Data Transfer OK ?
no
yes
Find IMEP of 1st 91 Cycles
Poll Photo-Detectors
Is Fuel Pipette Full ?
no
Fill Fuel Pipette
yes
Poll Thermo.1, Display Temperatures
Poll Photo-Detectors
Past Top Eye ?
no
yes
Time=0
delay loop
Call Check
Check
Poll ADC1, Call Check
Check
Poll ADC2, Call Check
Check
Poll Tacho., Call Check
Check
Tabulate Load, Manometer Reading and Speed
Time =0?
yes
no
Refresh Table
yes
Is Screen Full ?
no
Display Time
Fill Fuel Pipette
Poll Thermo.1 and Display Temperatures
Call Microlink
Program CH12/3 and TB
(see top left)
Poll CH12/3, Plot Data, Transfer OK?
Calculate IMEP of 2nd 91 Cycles + Final Results
Plot AFR-BMEP Points for Current Advance
Ask if Knocking, Send Results to Printer
Keep ?
no
yes
Return
Append Results to Data File
Check
Start
Time >0?
yes
no
Past Bottom Eye ?
no
yes
Return
Time = ΔT

Figure 4.13

Ricardo E6 Performance Test

Date of test	06-13-1988
Compression ratio	8
Barometric pressure (mm Hg)	762.1
Fuel specific gravity	.727
Results data file name	B:TST3

T1	T2	T3	T4	T5	T6	ADV	AFR	BMEP	IMEP	(Cpi) ISD%	RPM	Knock?	Keep?
24	25	68	69	43	52	35	19.25	6.61	7.97	10	1499	N	Y
24	26	68	69	44	53	35	20.1	5.59	6.98	18	1504	N	Y
24	26	68	69	44	53	35	20.64	4.74	6.2	27	1502	N	Y
24	26	68	69	45	54	35	19.88	6.06	7.28	15	1502	N	Y
25	26	68	69	45	54	35	19.25	6.73	8.07	9	1501	N	Y
25	26	68	69	45	54	35	18.34	7.37	8.76	5	1499	N	Y
25	26	68	69	46	55	35	19.82	7.56	8.88	4	1499	N	N
25	26	67	69	46	55	35	18.35	7.44	8.87	4	1508	N	Y
25	26	67	69	46	55	40	18.08	7.59	8.86	3	1498	Y	Y
25	26	67	69	47	55	40	18.62	7.38	8.71	4	1501	N	Y
25	27	68	69	46	56	40	19.07	7.16	8.45	7	1490	N	Y
25	27	68	69	46	56	40	19.94	6.31	7.74	12	1502	N	Y
25	27	68	69	46	56	40	20.7	5.15	6.58	25	1509	N	Y
25	27	68	69	46	56	40	19.65	6.55	7.66	15	1504	N	Y
26	27	67	69	46	56	45	19.78	6.82	8.25	10	1499	N	Y
26	27	68	69	46	56	45	20.29	6.09	7.57	14	1504	N	Y
26	27	68	69	46	56	45	20.95	4.8	6.4	33	1513	N	Y
26	27	68	69	47	56	45	20.59	5.34	6.89	24	1500	N	Y
26	27	68	69	46	56	45	19.92	6.25	7.63	15	1503	N	Y
26	27	67	69	44	56	45	19.35	7.12	8.46	4	1500	N	Y
26	27	67	69	37	55	45	18.75	7.29	8.61	3	1501	Y	Y
26	27	68	69	36	54	45	20.4	6.35	7.86	9	1510	N	Y
26	27	68	69	35	54	50	20.4	6.26	7.64	17	1503	N	Y
26	27	68	69	37	53	50	20.86	5.75	6.98	27	1505	N	Y
26	27	68	69	42	53	50	20.41	6.16	7.74	14	1507	N	Y
26	27	68	69	43	53	50	22.85	5.58	6.82	30	1497	N	N
26	27	68	69	43	53	50	20.95	5.5	7.08	22	1502	N	Y

Figure 4.14

Example of Data Output from an Engine Performance Test

T1=Air Flow Meter In (°C)
T2=Inlet Manifold (°C)
T3=Water In (°C)
T4=Water Out (°C)
T5=Oil Supply (°C)
T6=Sump Oil (°C)

} Temperature Key

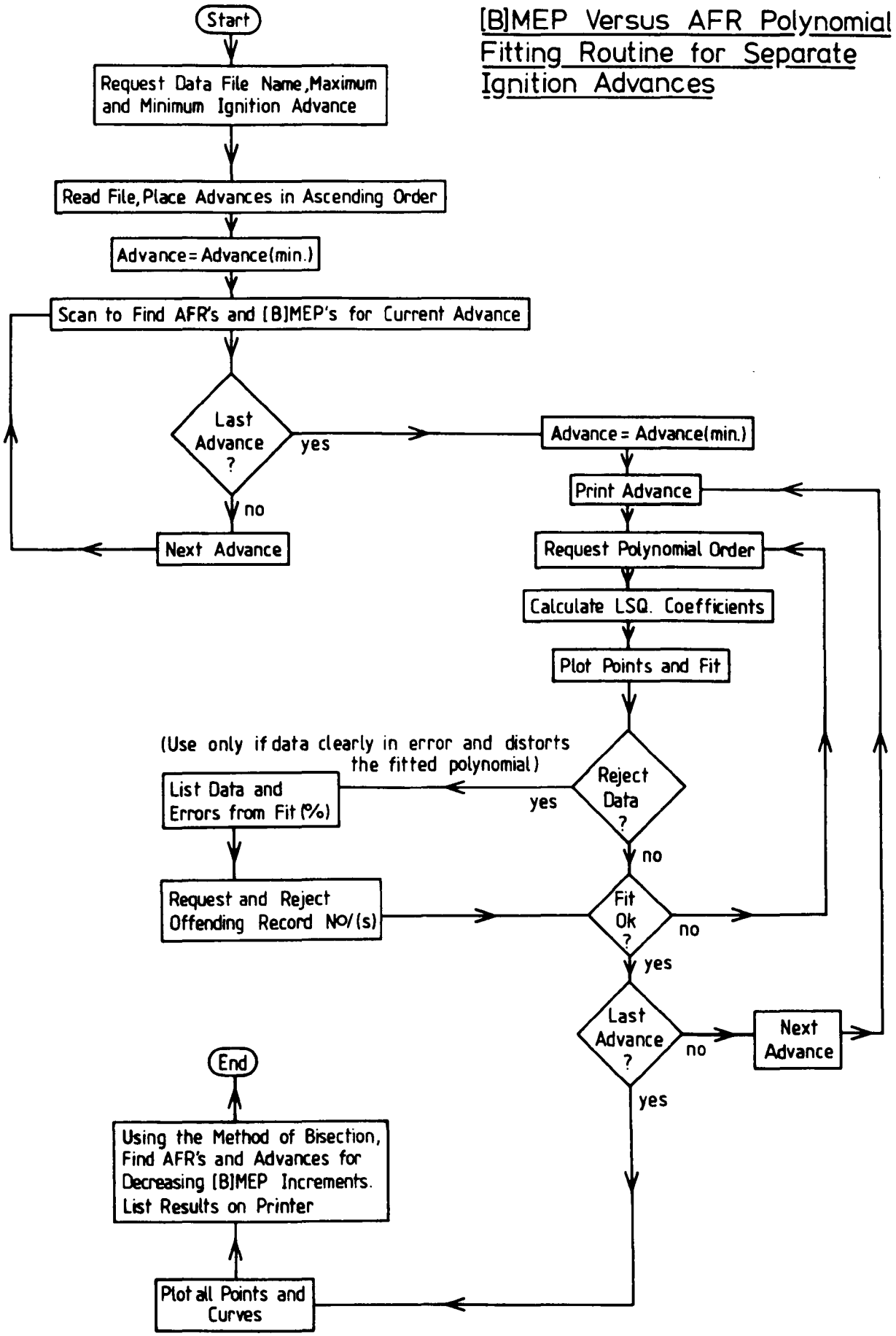
[B]MEP Versus AFR Polynomial Fitting Routine for Separate Ignition Advances
Start
Request Data File Name, Maximum and Minimum Ignition Advance
Read File, Place Advances in Ascending Order
Advance = Advance(min.)
Scan to Find AFR's and [B]MEP's for Current Advance
Last Advance ?
yes
no
Next Advance
Advance = Advance(min.)
Print Advance
Request Polynomial Order
Calculate LSQ. Coefficients
Plot Points and Fit
(Use only if data clearly in error and distorts the fitted polynomial)
Reject Data ?
yes
List Data and Errors from Fit (%)
Request and Reject Offending Record NO/(s)
no
Fit Ok ?
no
yes
Last Advance ?
no
Next Advance
yes
End
Using the Method of Bisection, Find AFR's and Advances for Decreasing [B]MEP Increments. List Results on Printer
Plot all Points and Curves

Figure 4.15

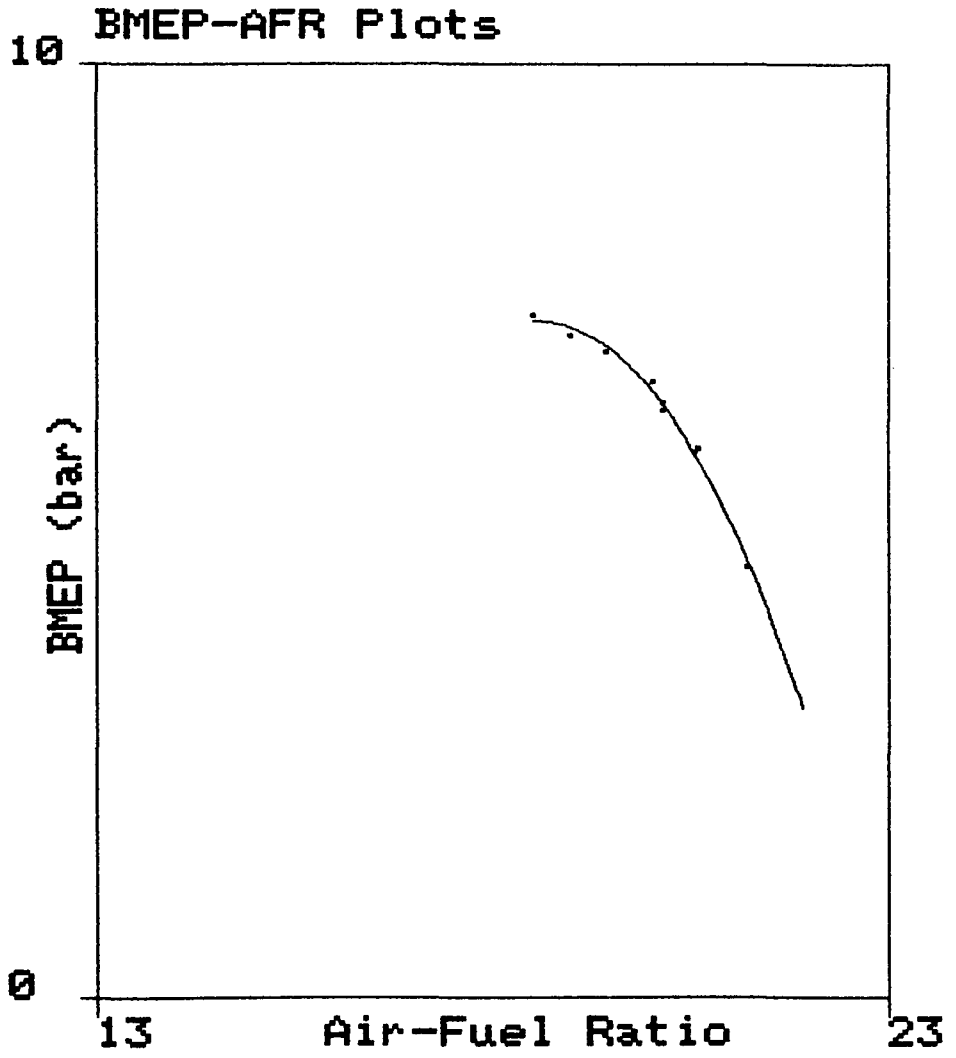

Figure 4.16

Third Order Least Squares Curve Fit of Air/Fuel Ratio-Brake Mean Effecive Pressure Coordinates.[Standard Valve]

Block Diagram of Firing Engine Pressure Data Acquisition Procedure

Test 2

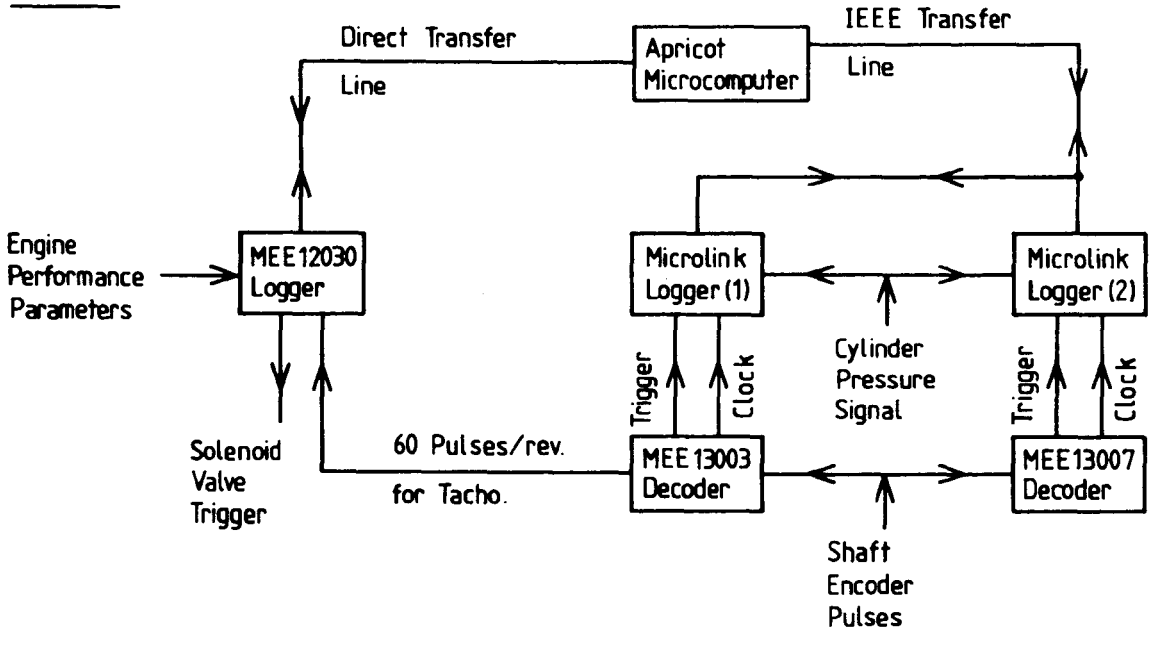

Figure 4.17

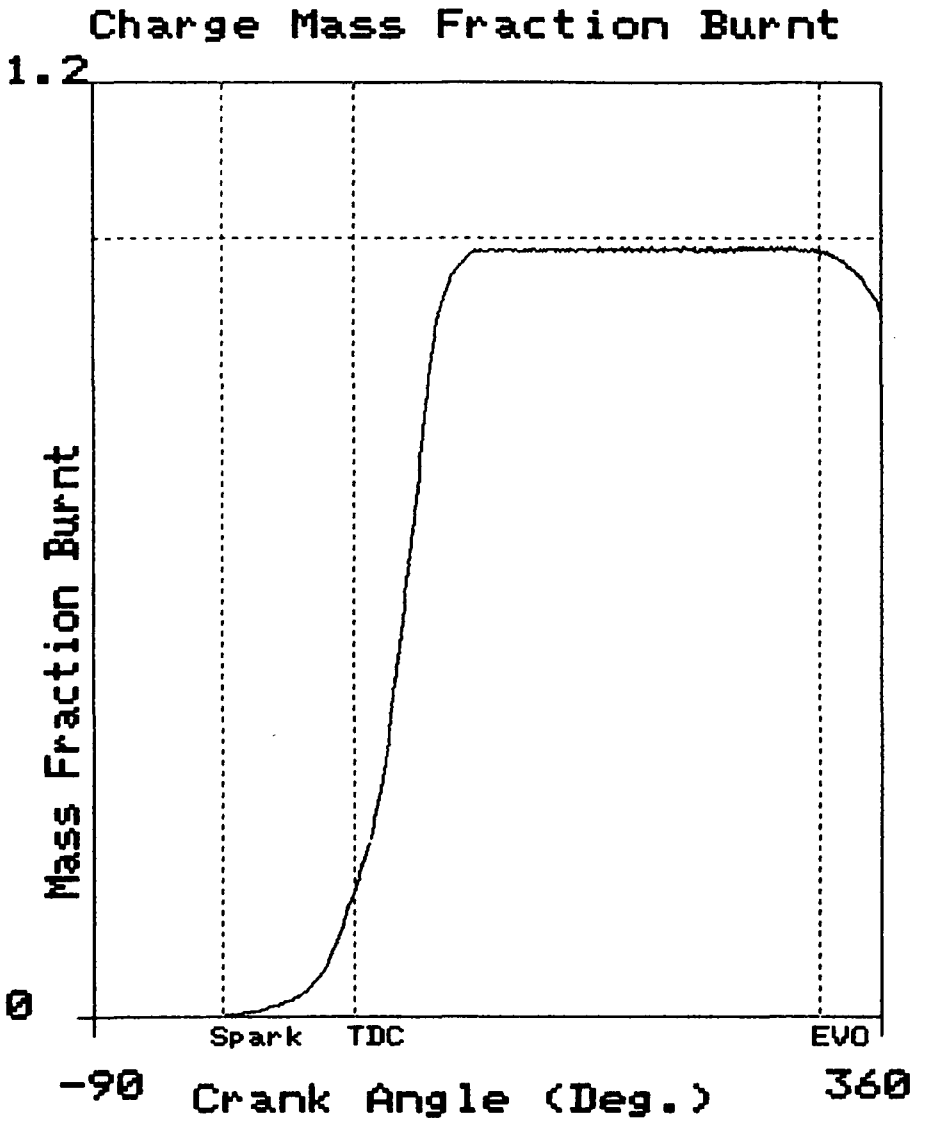

Figure 4.18

Mass Fraction Burnt Calculation for One Cycle
(Heat Transfer Too Low)

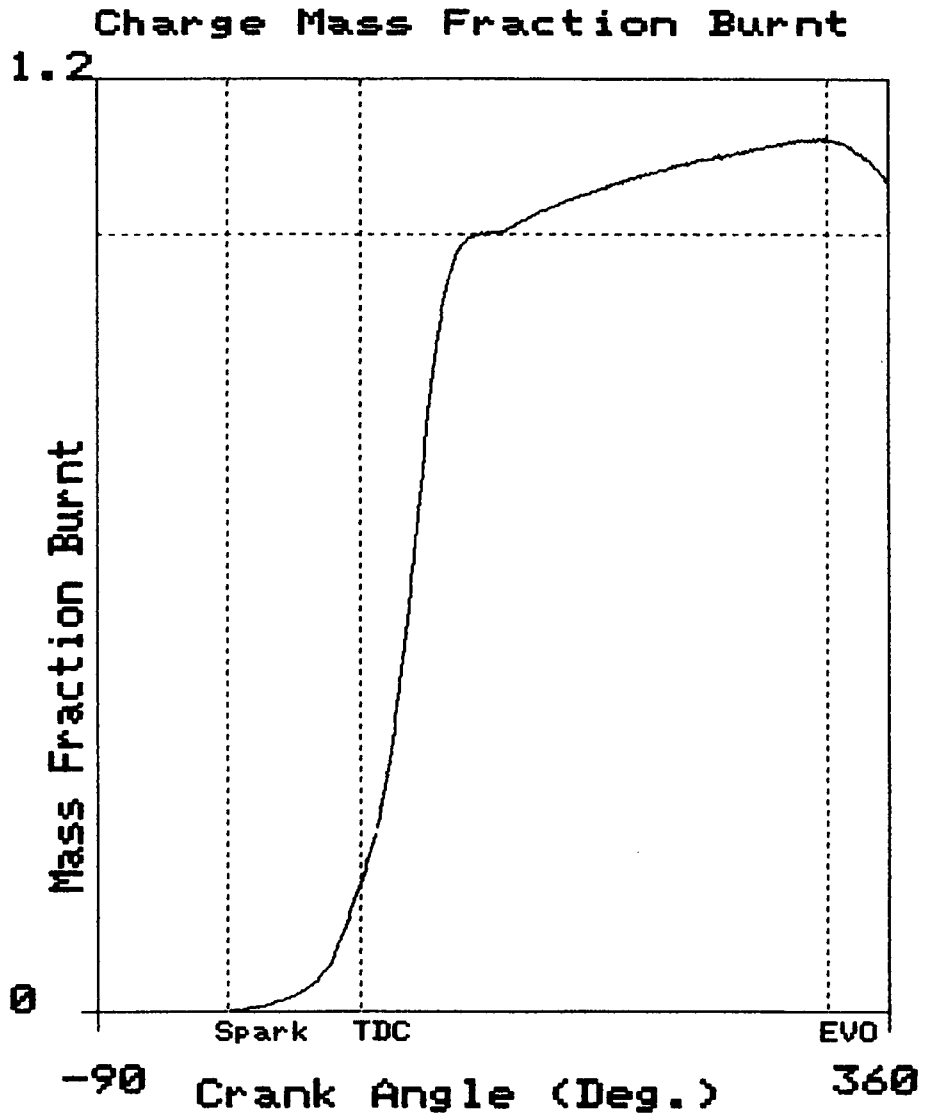

Figure 4.19

Mass Fraction Burnt Calculation for One Cycle
[Heat Transfer Too High]

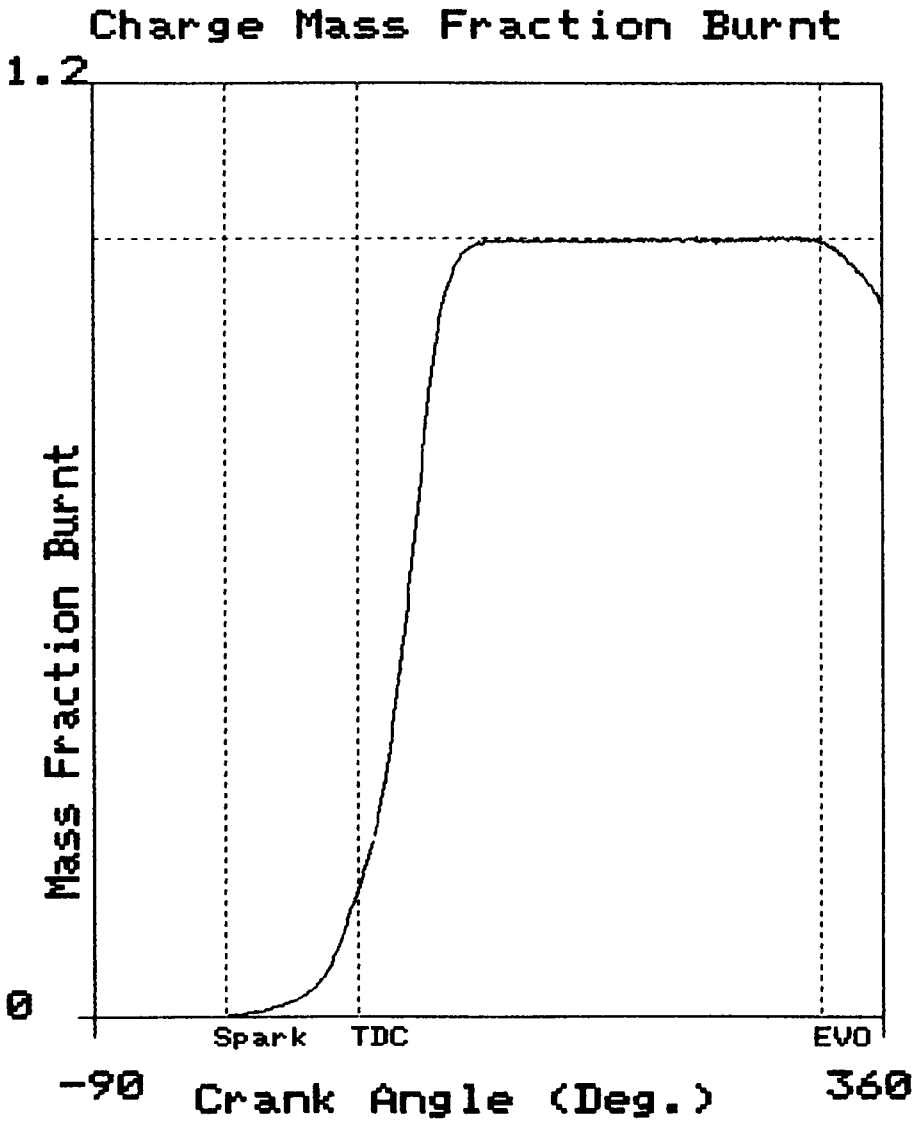

Figure 4.20

Mass Fraction Burnt Calculation for One Cycle
[Heat Transfer "Correct"]

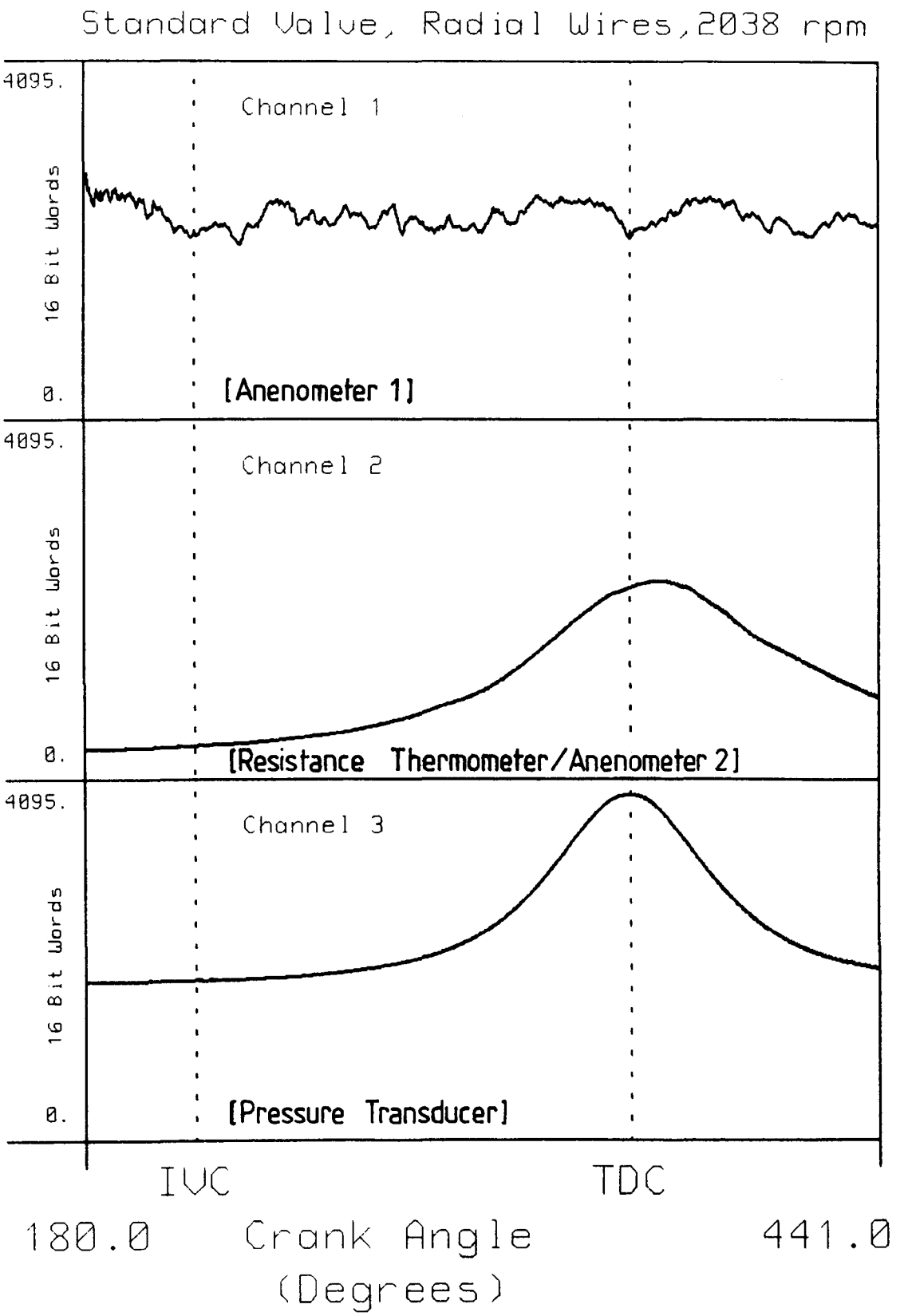

Figure 5.1 Raw Data Logged from 1 Cycle (Standard Valve).

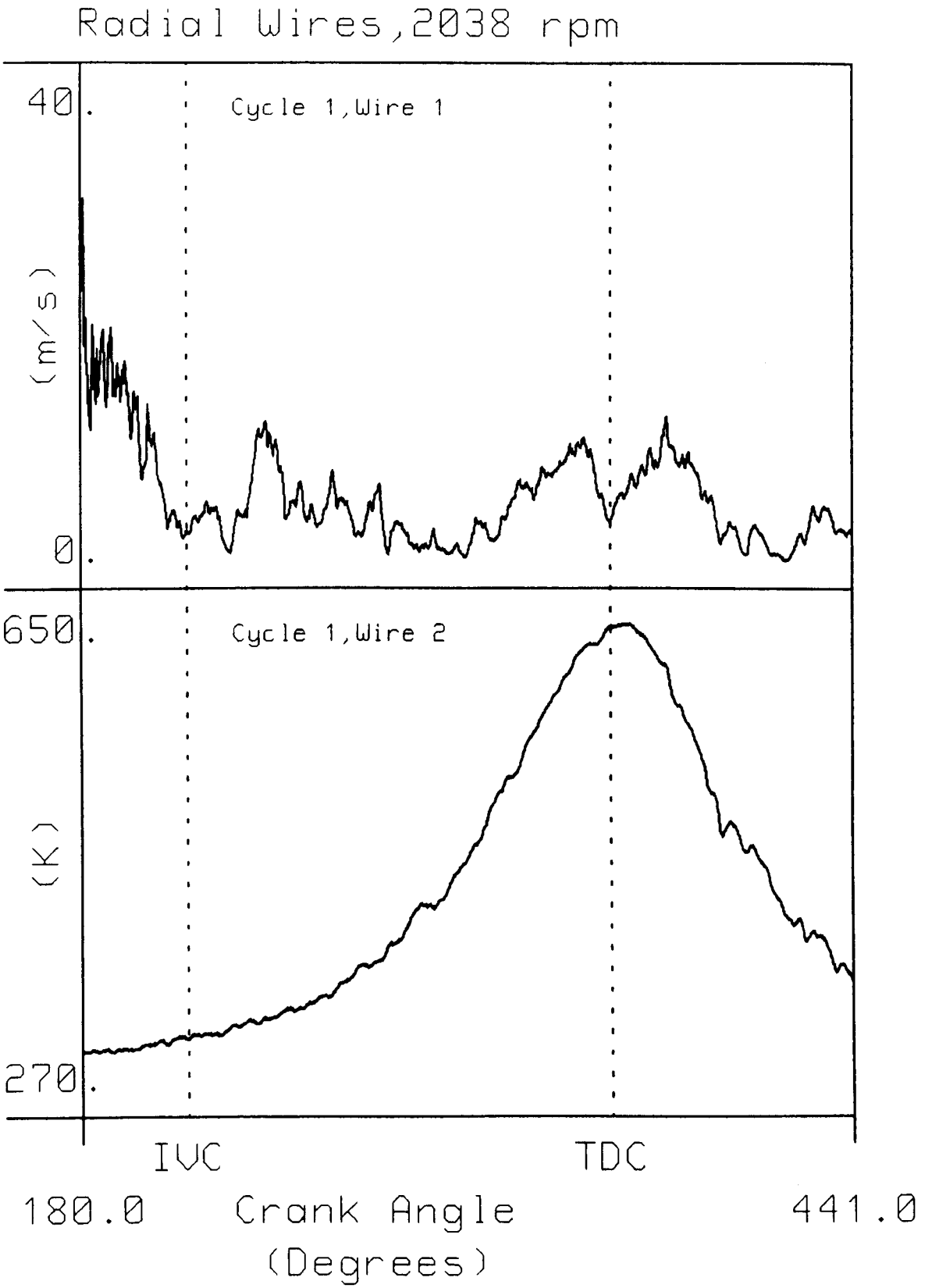

Figure 5.2 Processed Gas Velocity and Temperature from 1 Cycle (Standard Valve)

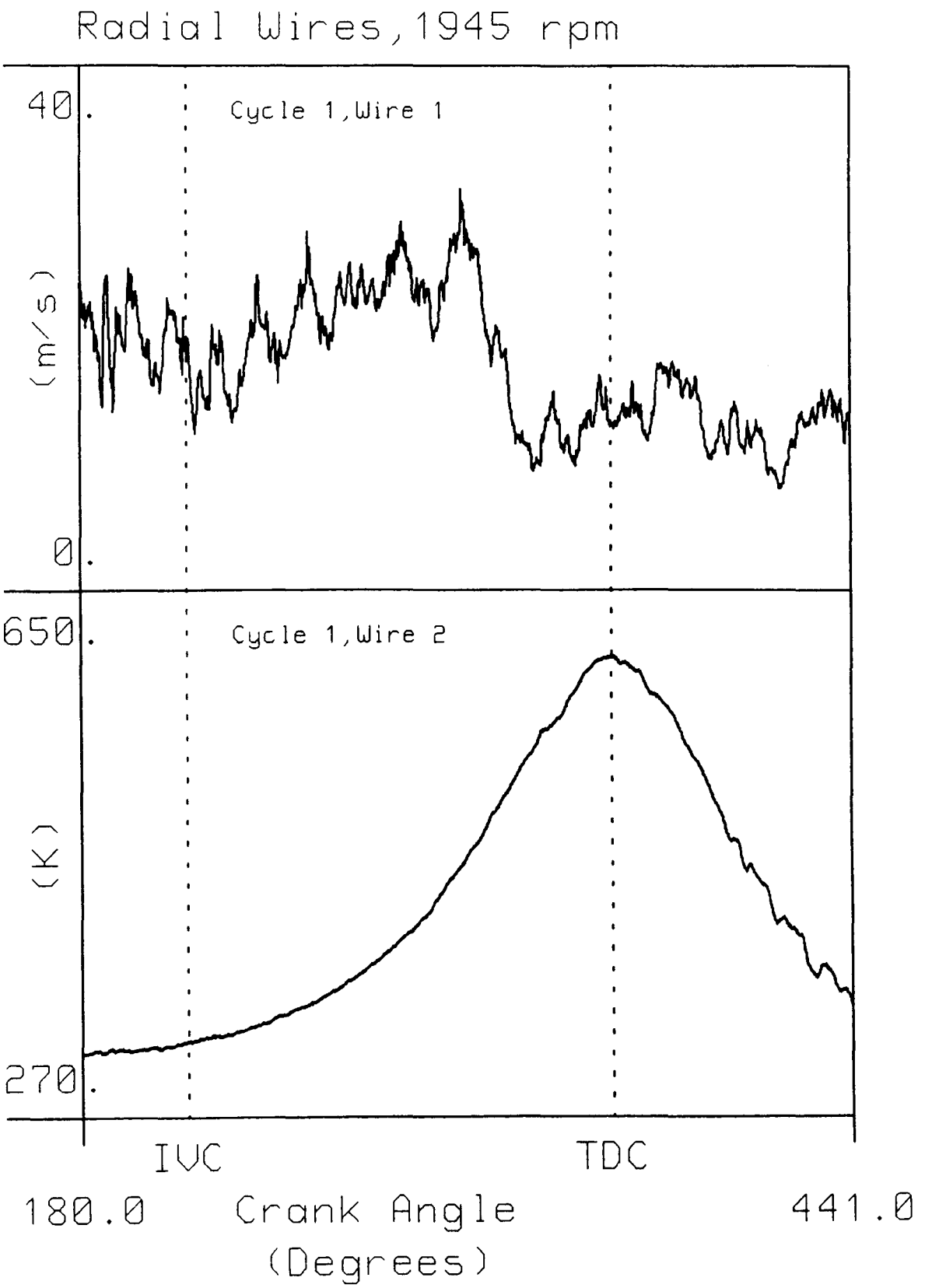

Figure 5.3 Processed Gas Velocity and Temperature from 1 Cycle (Shrouded Valve).

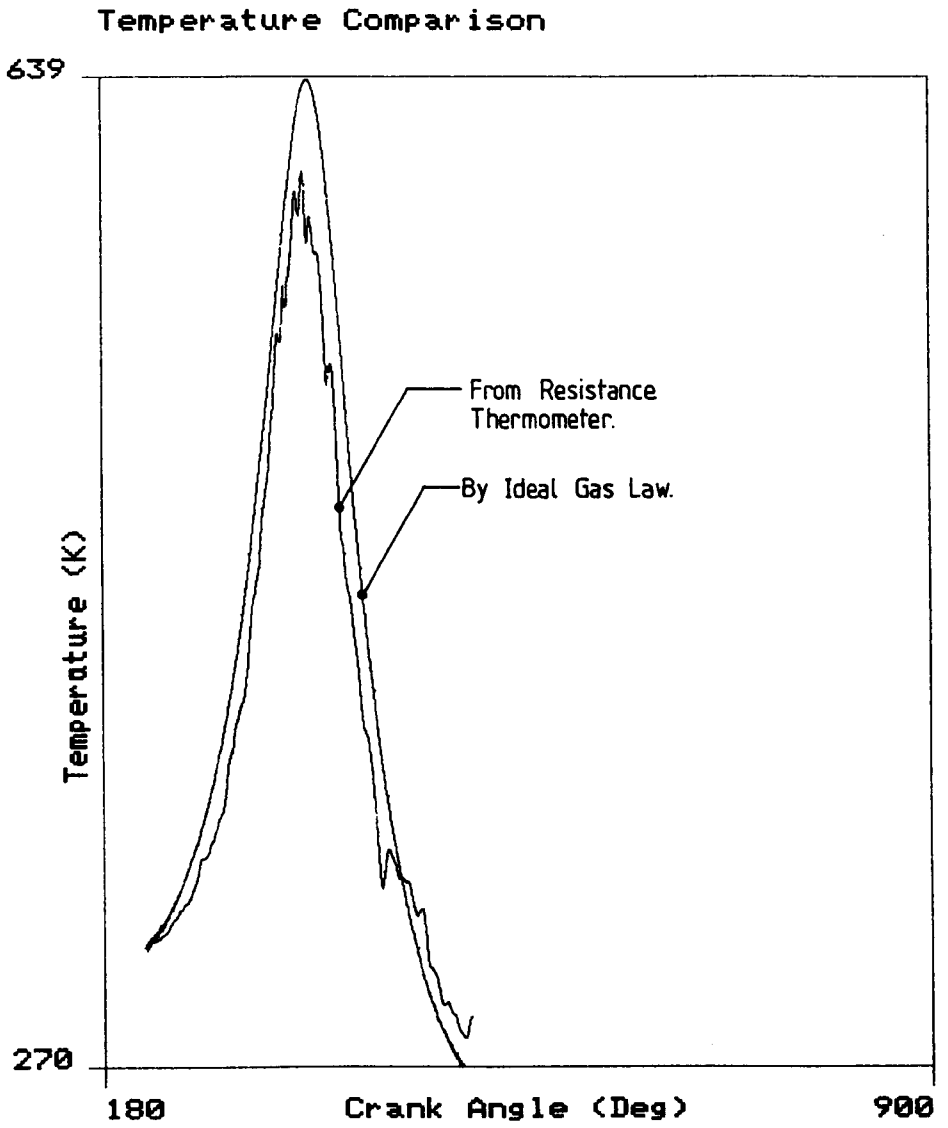
Temperature Comparison
639
270
Temperature (K)
From Resistance Thermometer.
By Ideal Gas Law.
180
Crank Angle (Deg)
900

Figure 5.4

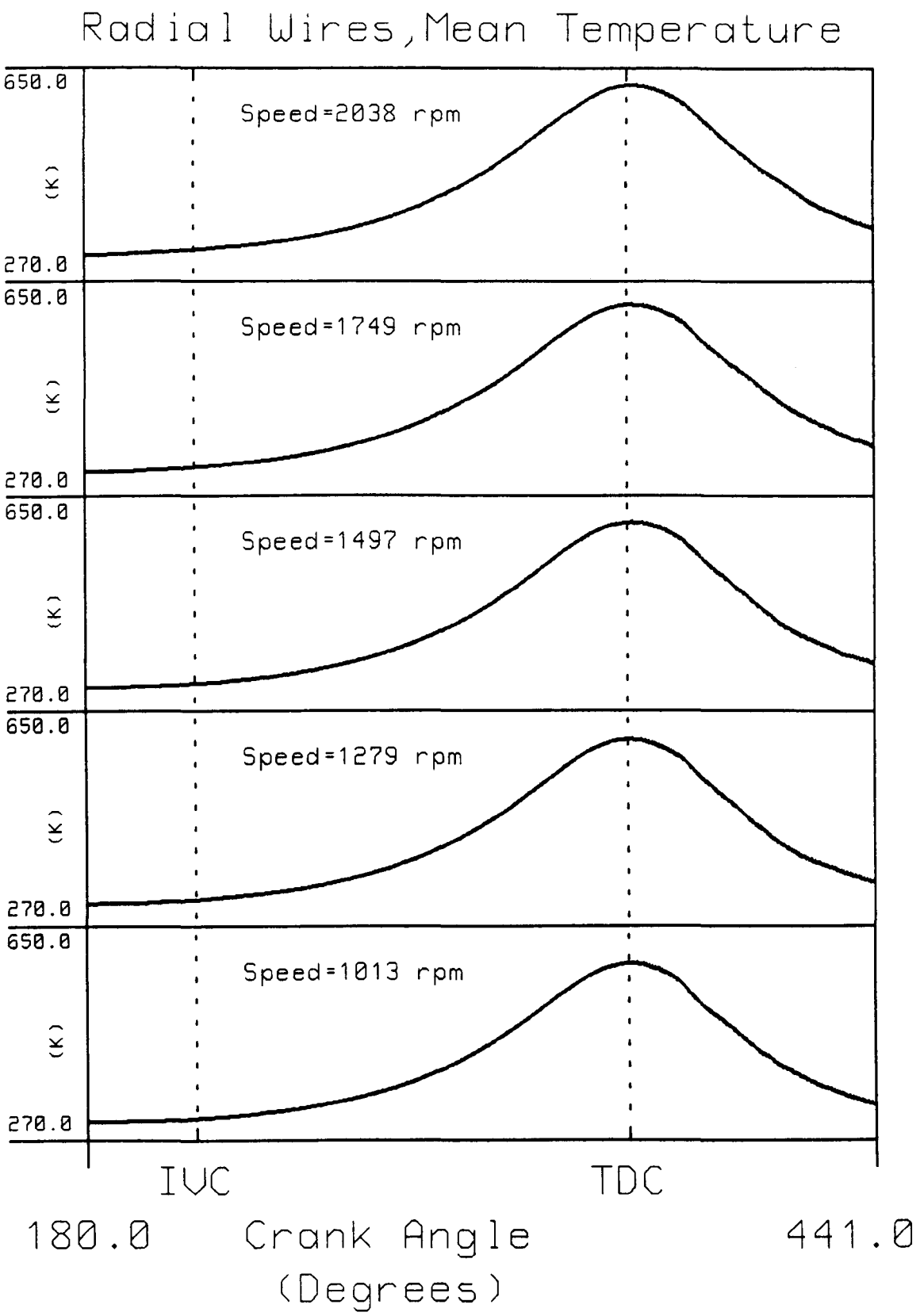

Figure 5.5 Ensembled Gas Temperatures (Standard Valve)

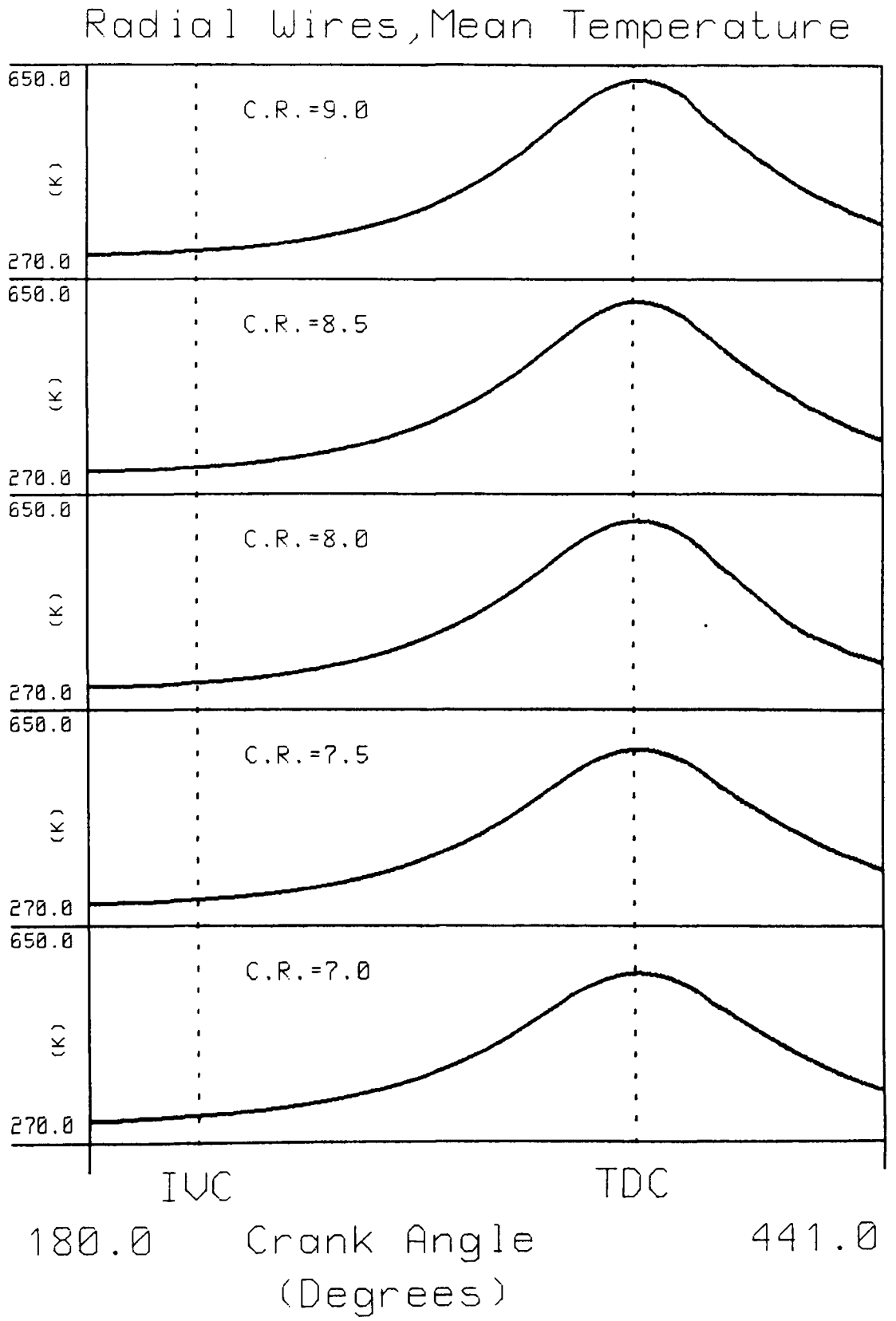

Figure 5.6 Ensembled Gas Temperatures (Standard Valve).

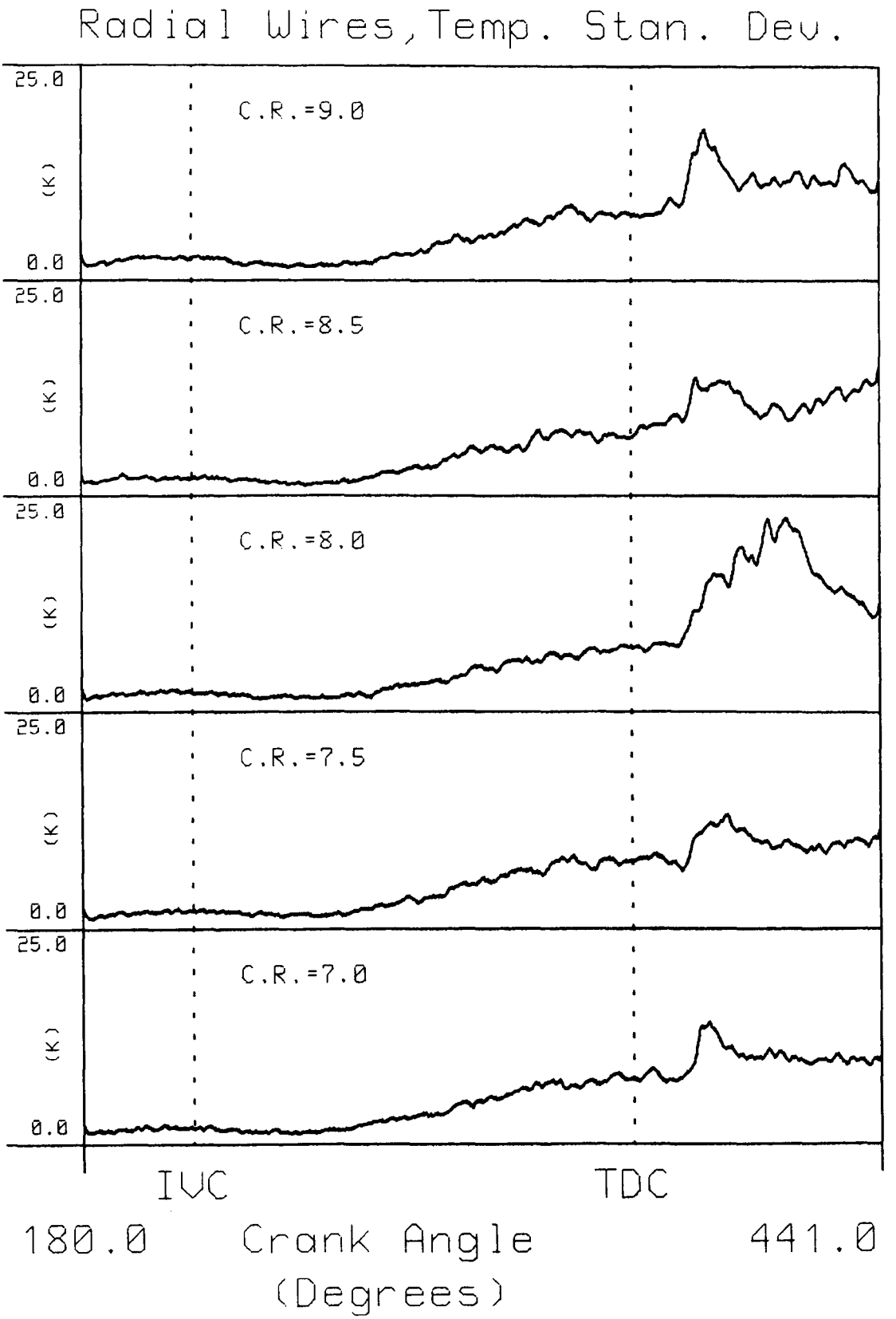

Figure 5.7 Temperature Variations (Standard Valve).

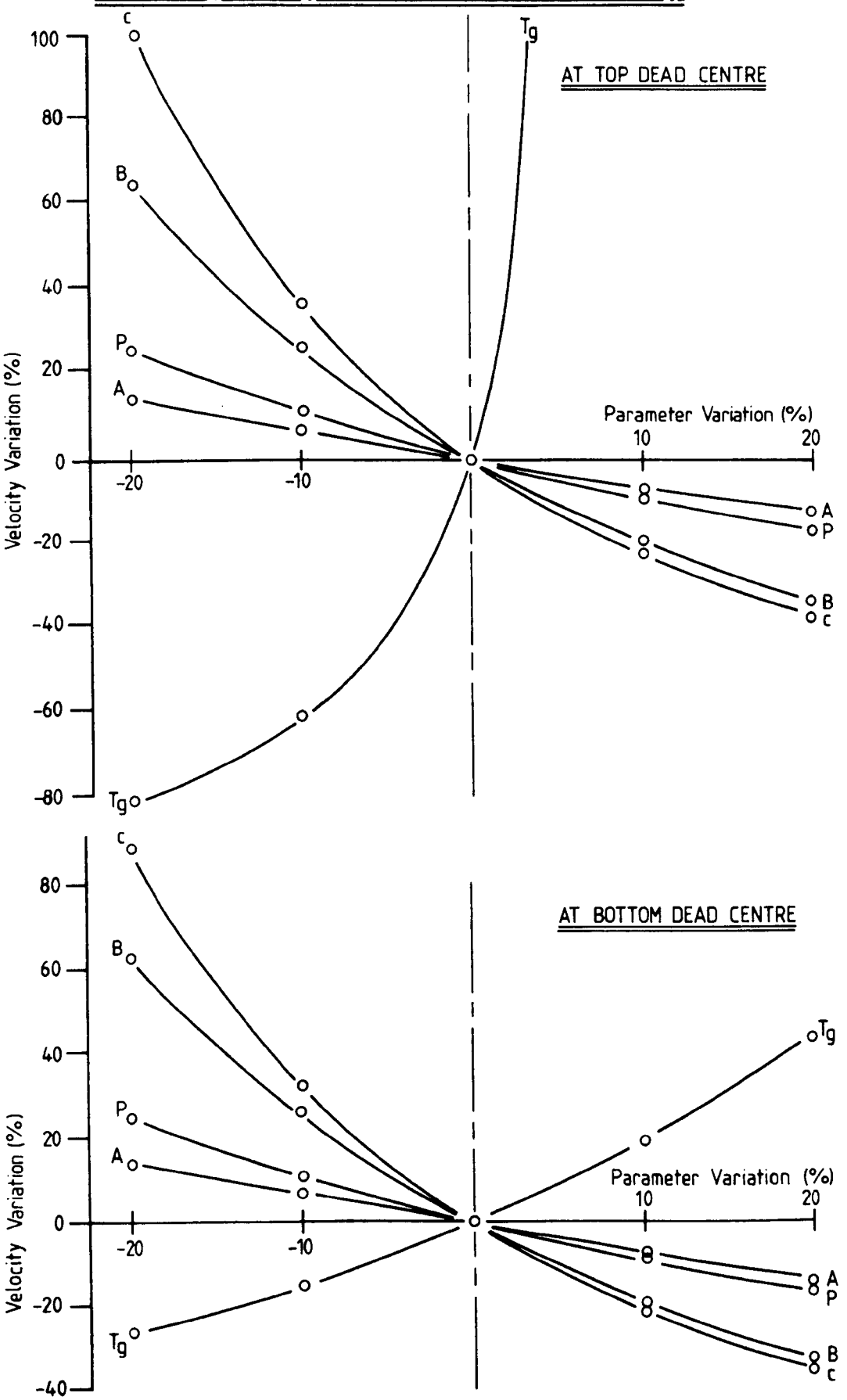
Sensitivity Analysis on Calculated Velocity
AT TOP DEAD CENTRE
AT BOTTOM DEAD CENTRE
Velocity Variation (%)
Parameter Variation (%)
100
80
60
40
20
0
-20
-40
-60
-80
10
20
-10
C
B
P
A
Tg

Figure 5.8

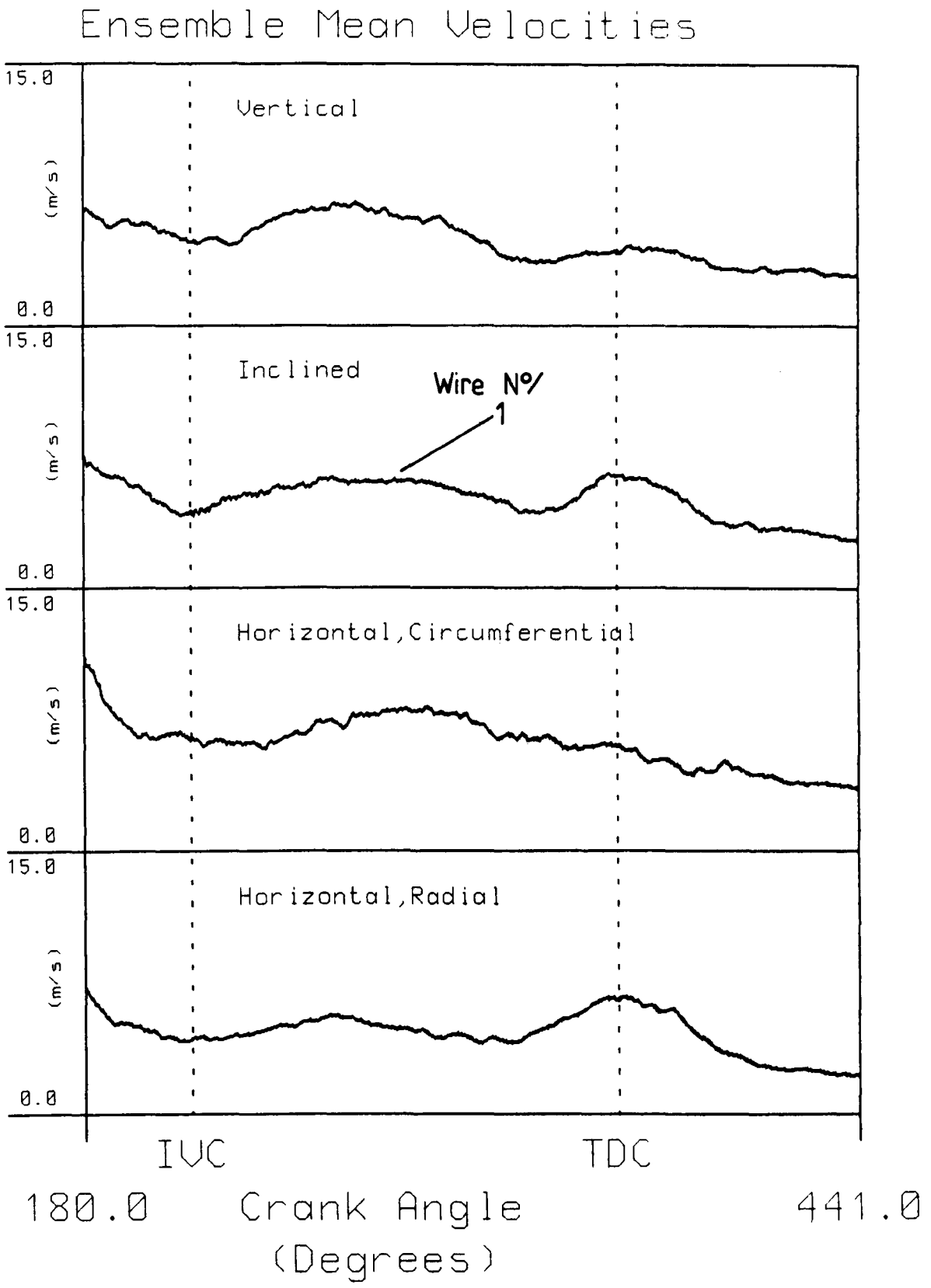

Figure 5.9 The Effect of Wire Orientation (standard Valve).

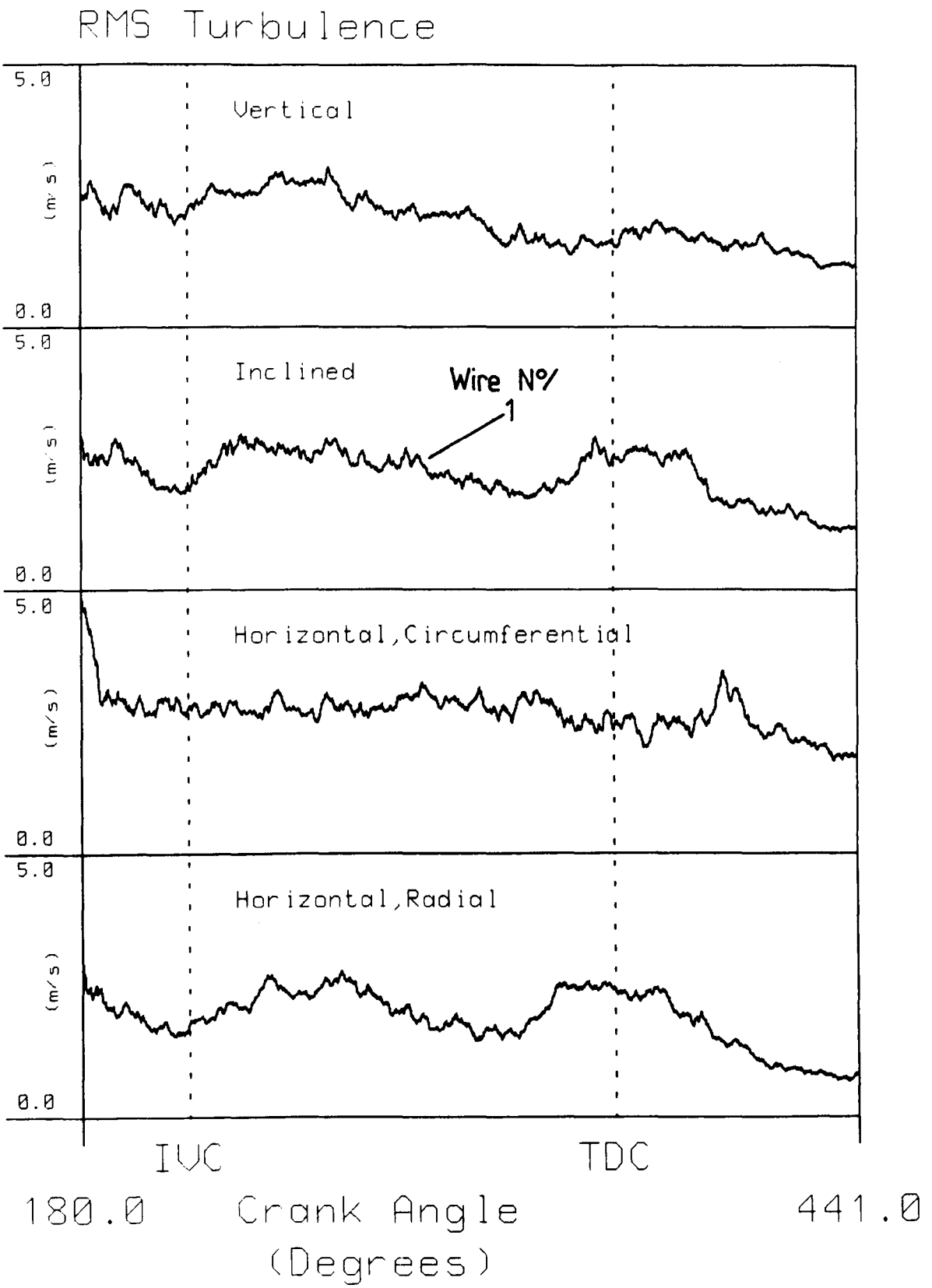

Figure 5.10 The Effect of Wire Orientation (Standard Valve).

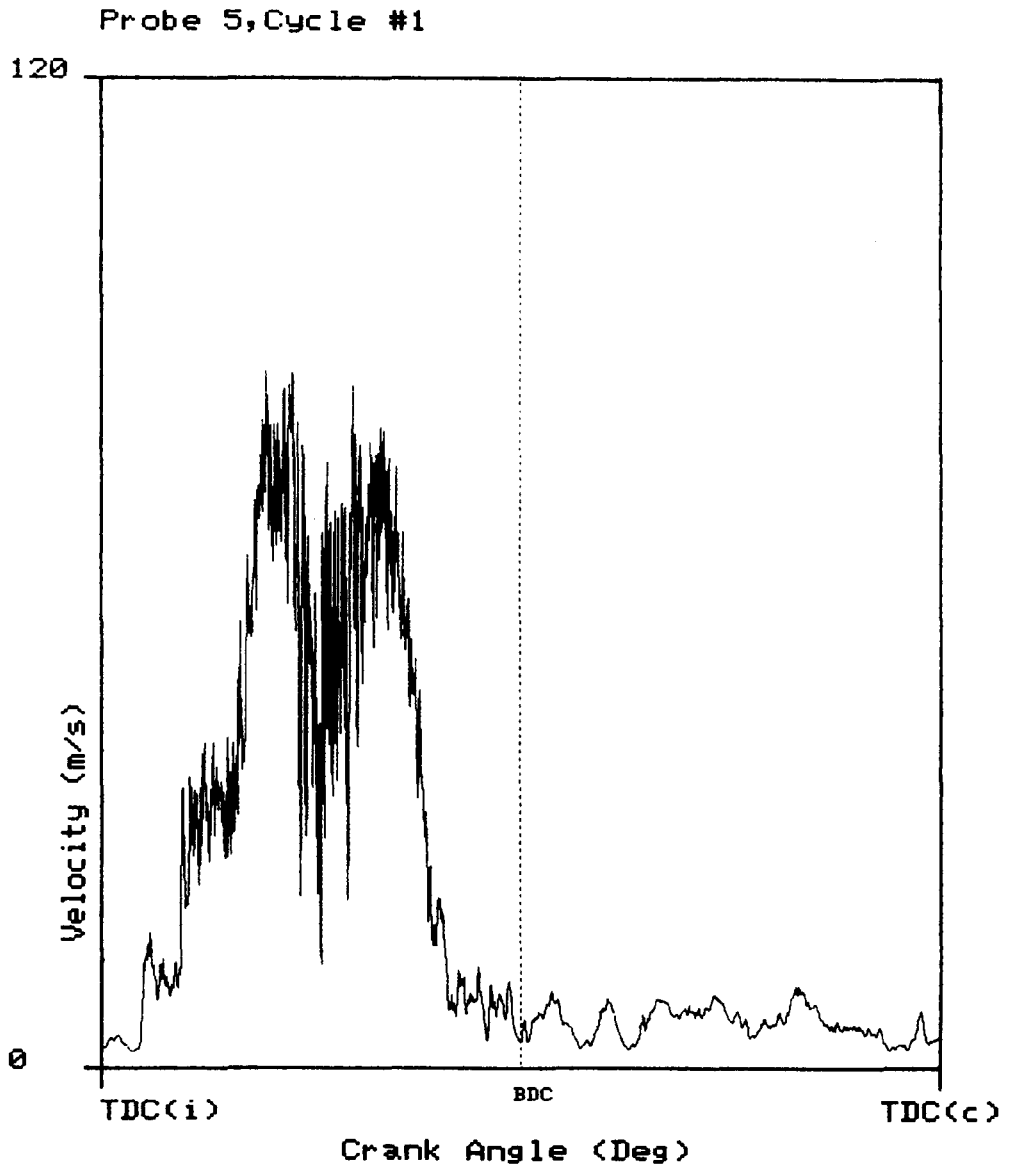

Figure 5.11 1 Cycle of Shifted Window Velocities (Vertical Wire, Standard Valve).

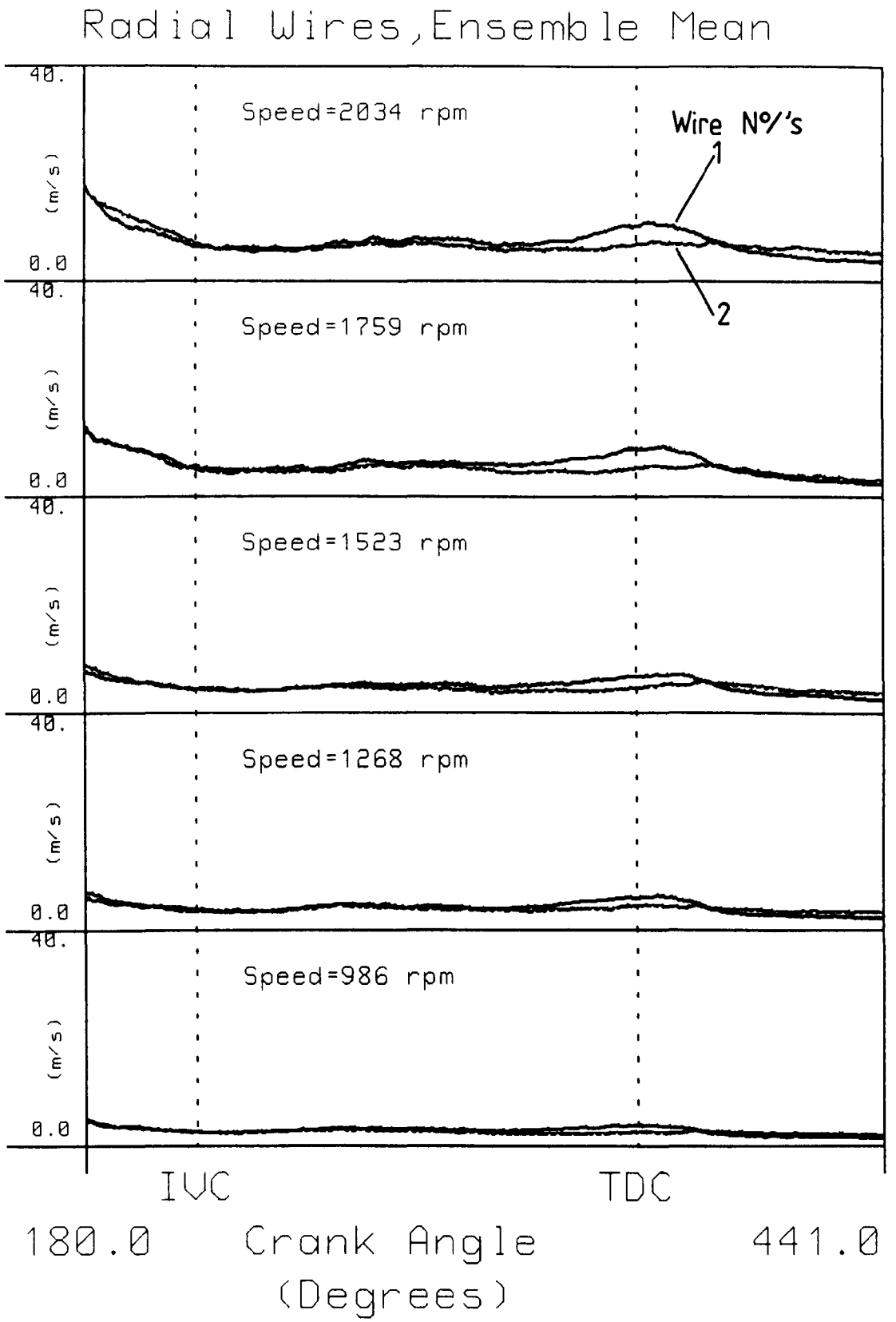

Figure 5.12 Standard Valve.

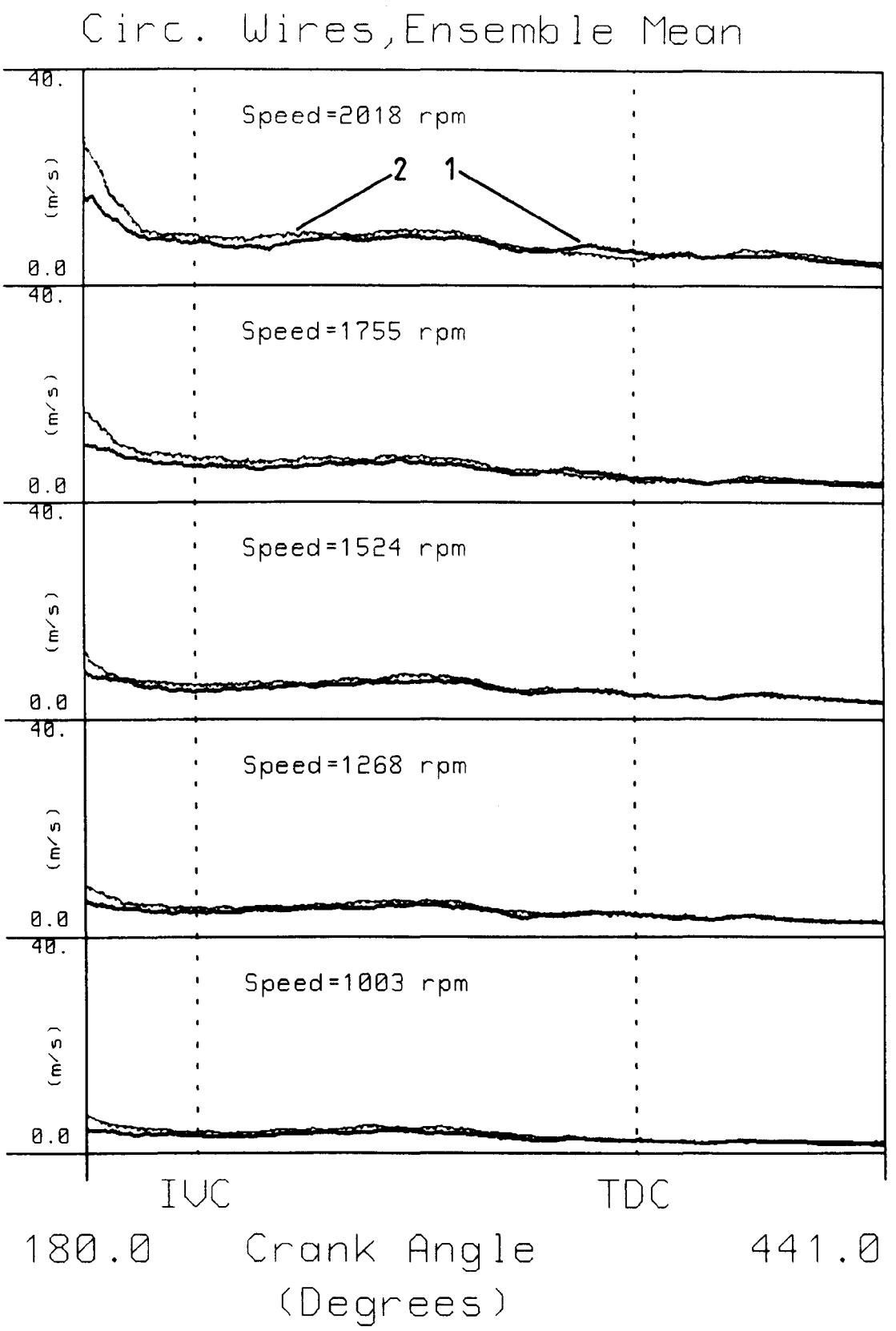

Figure 5.13 Standard Valve.

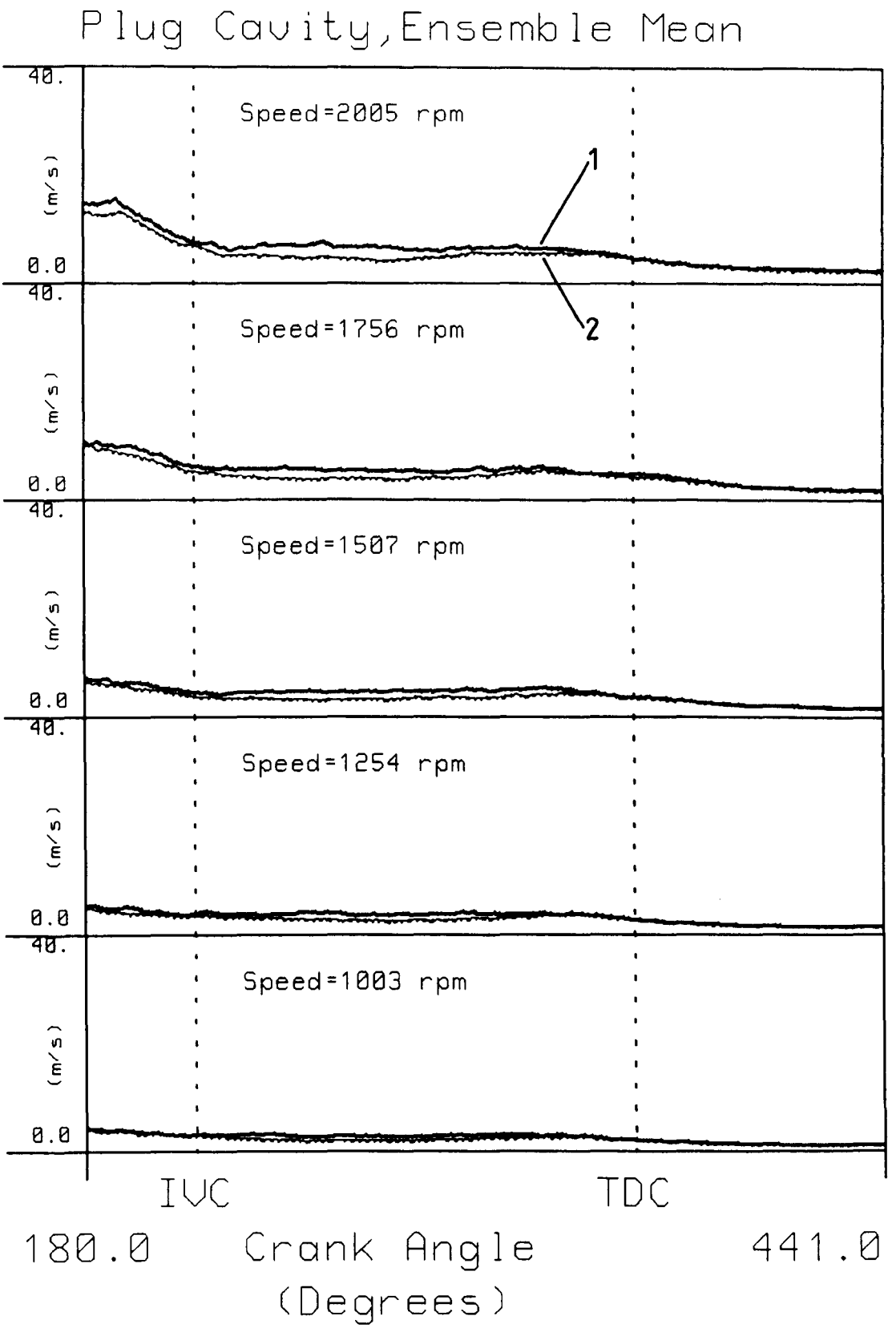

Figure 5.14 Standard Valve.

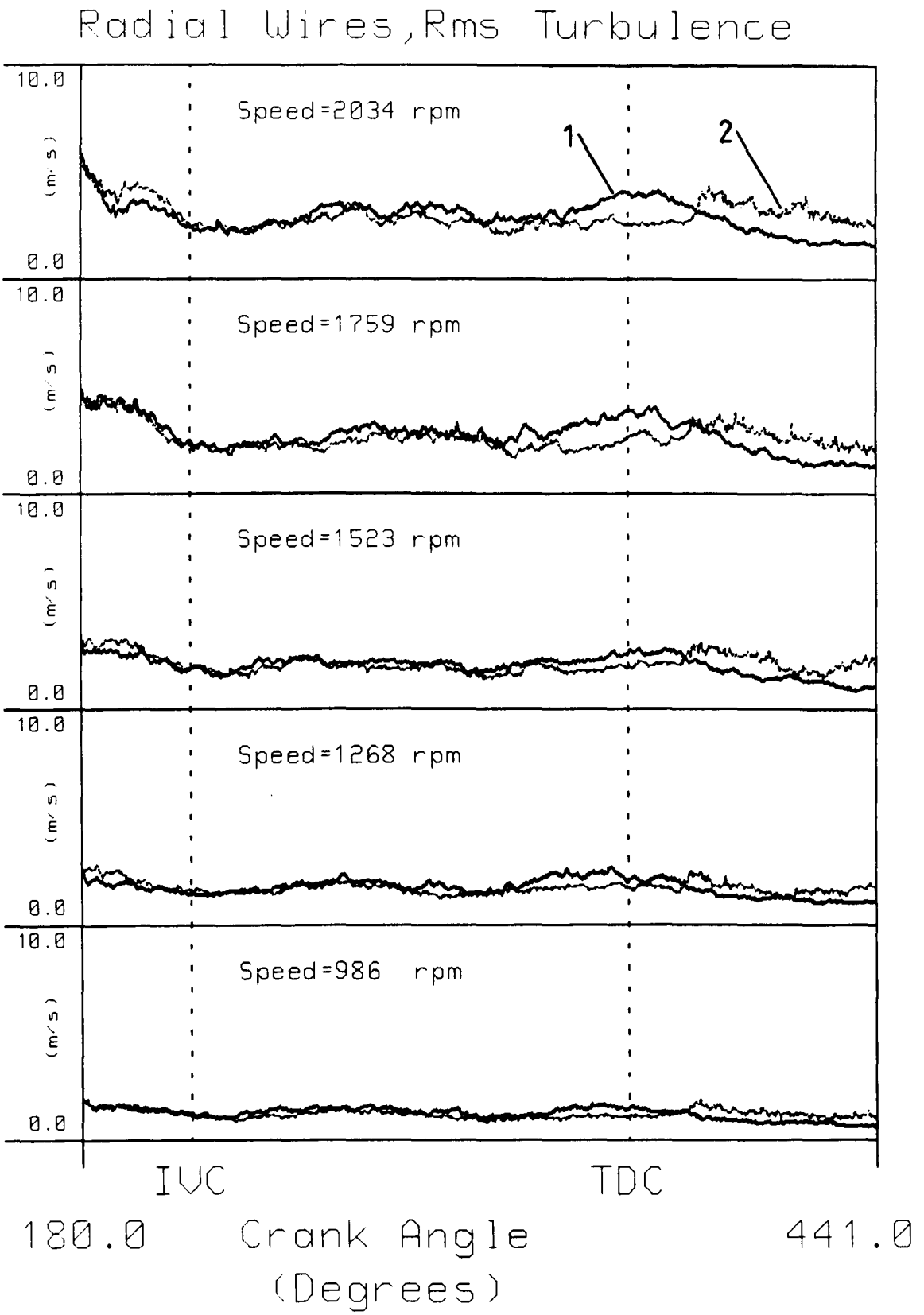

Figure 5.15 Standard Valve.

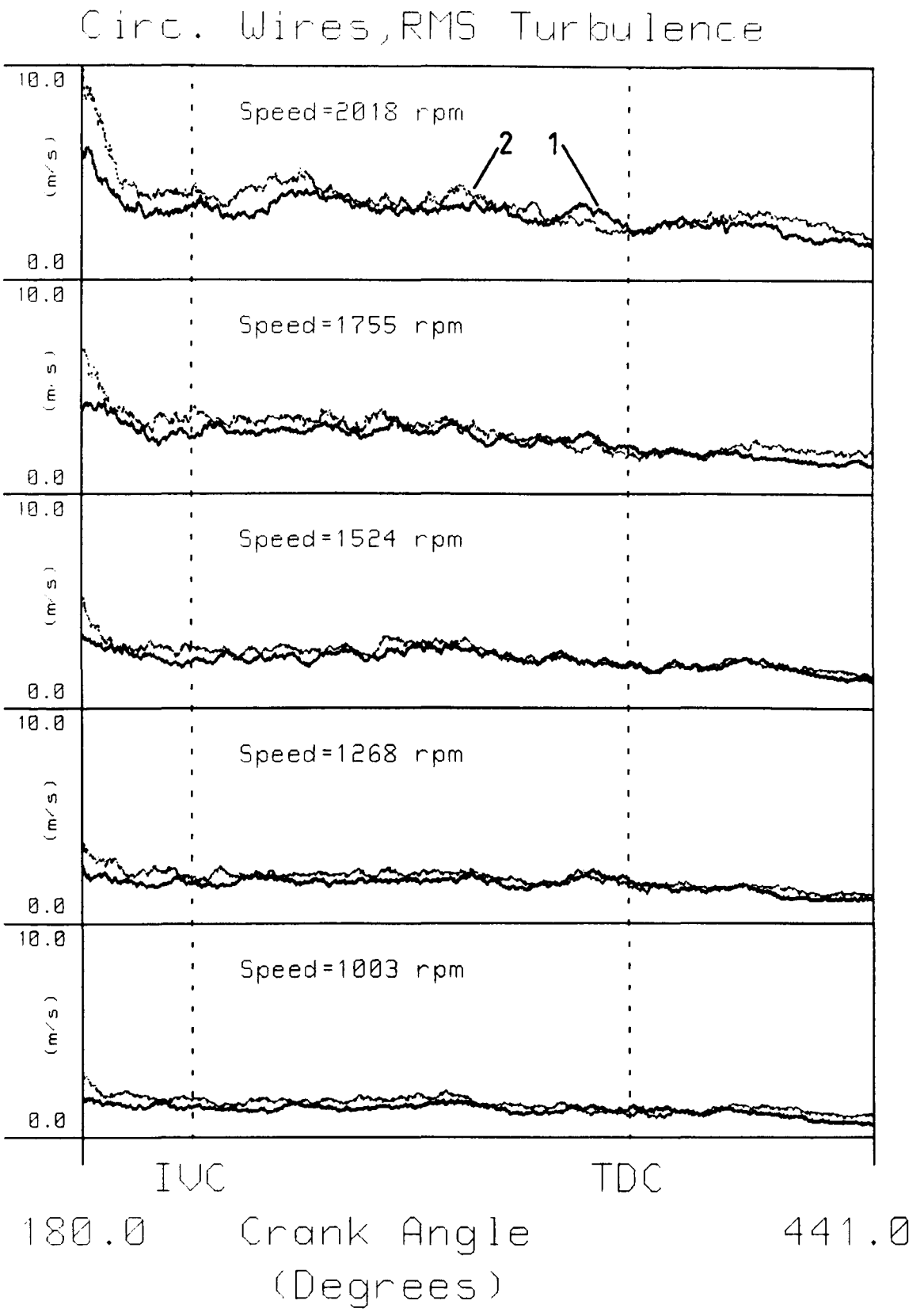

Figure 5.16 Standard Valve.

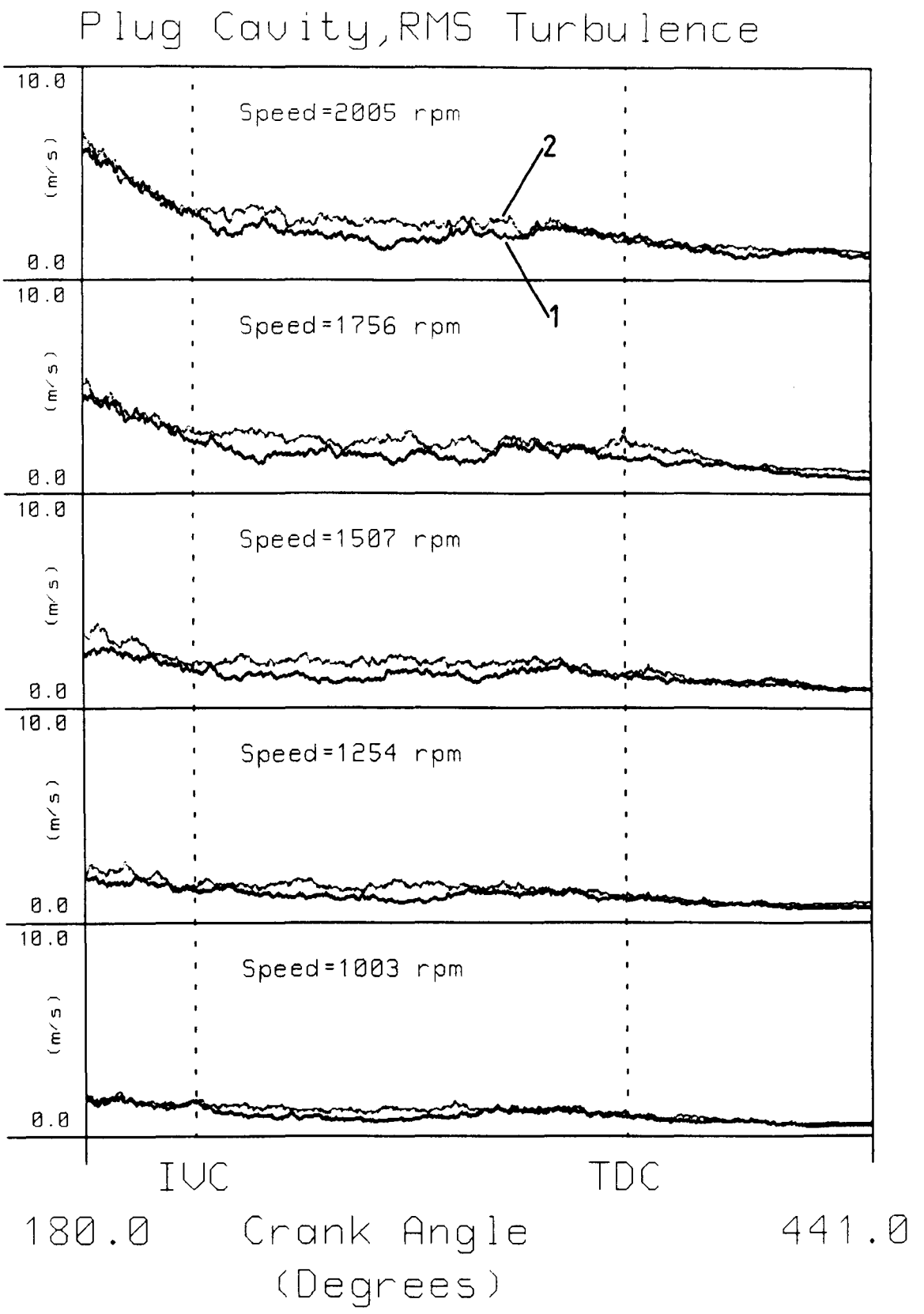

Figure 5.17 Standard Valve.

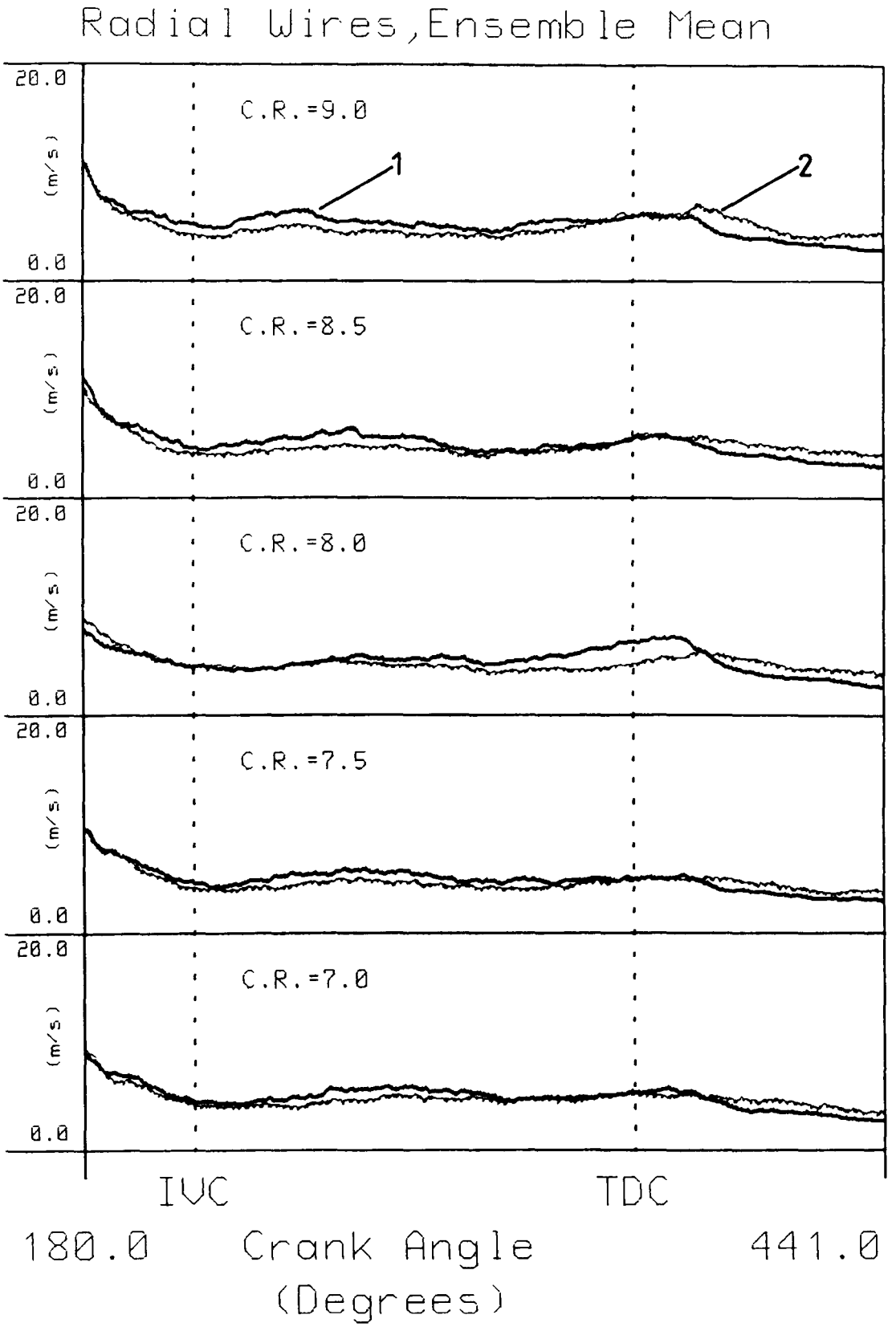

Figure 5.18 Standard Valve.

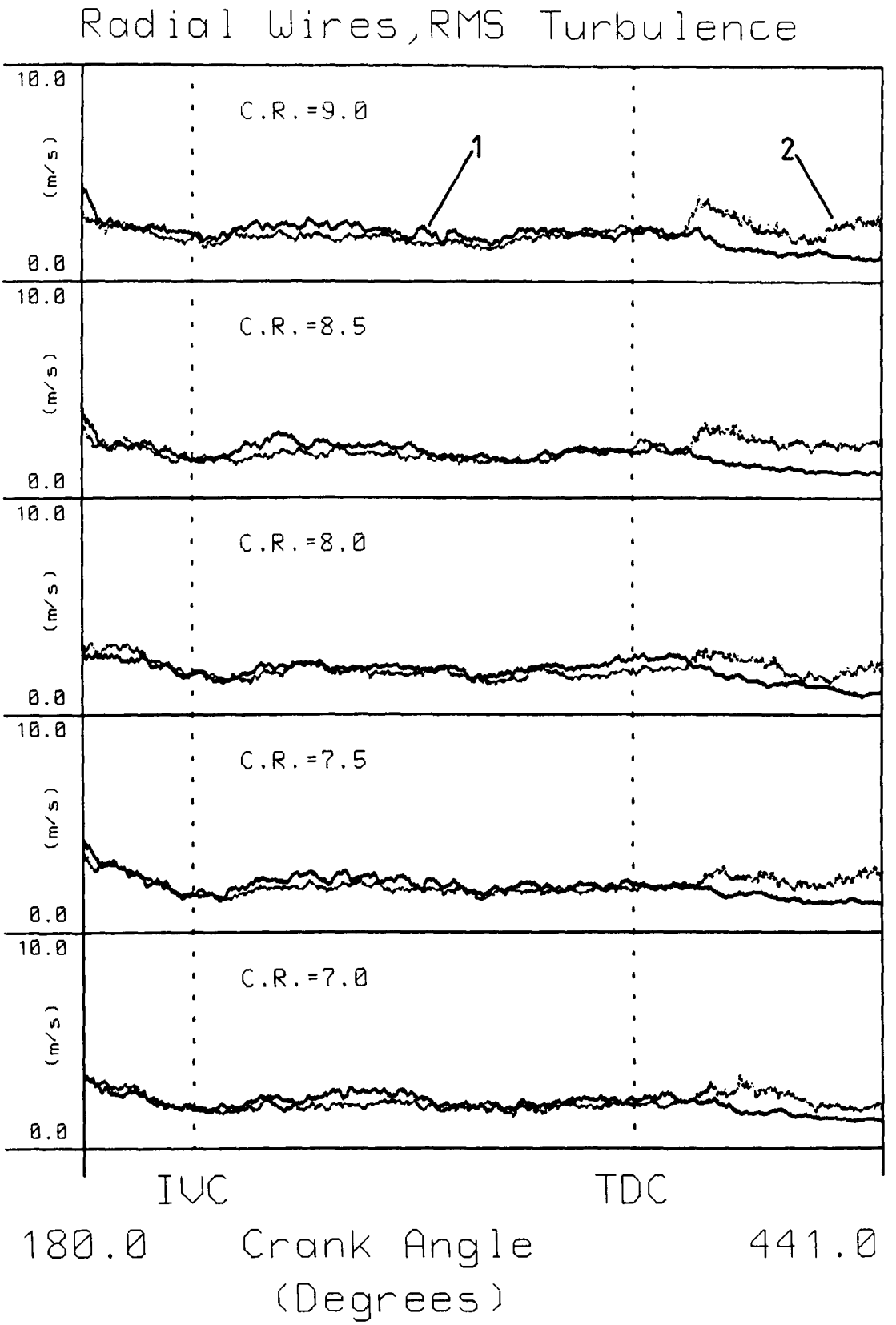

Figure 5.19 Standard Valve

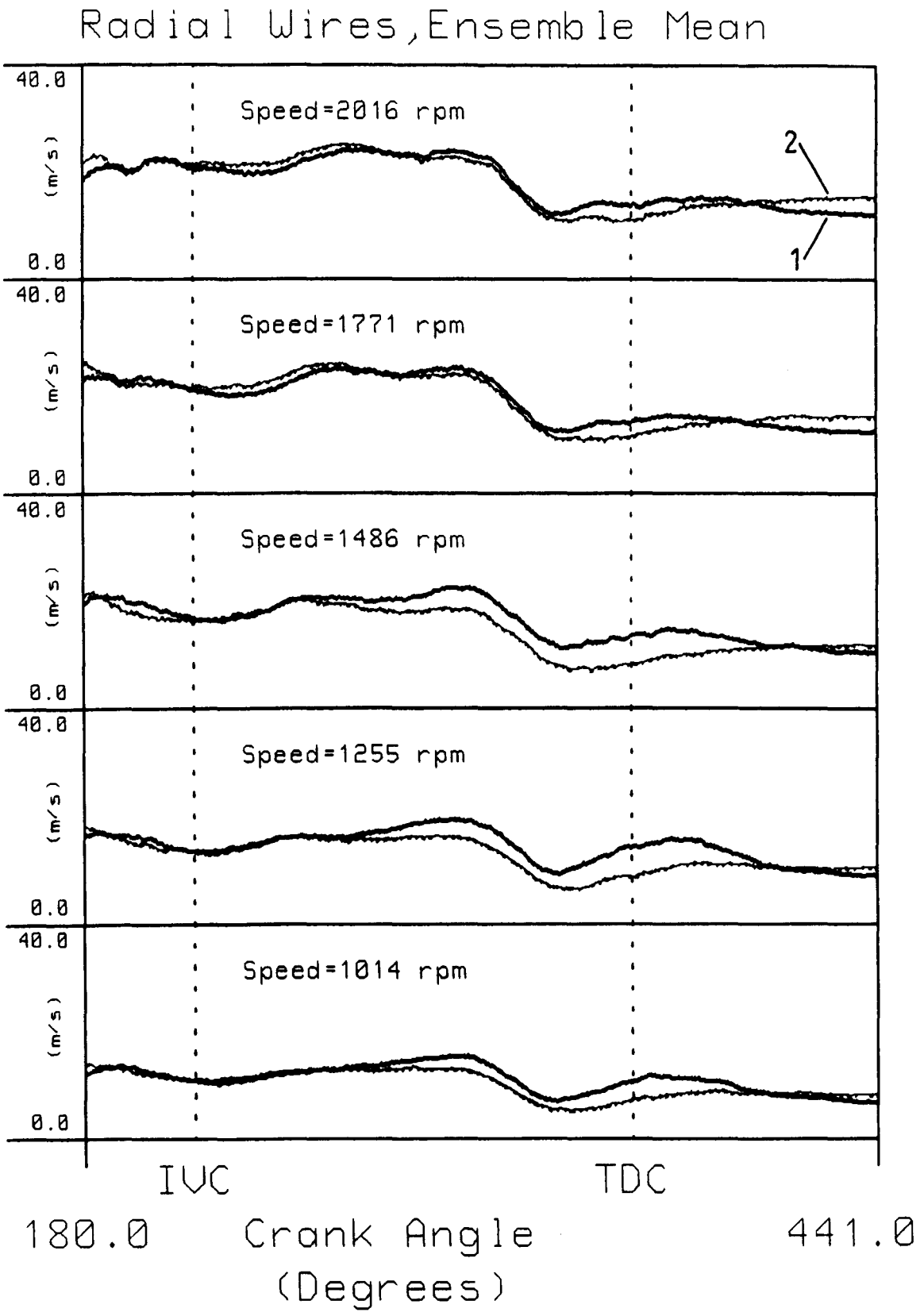

Figure 5.20 Shrouded Valve.

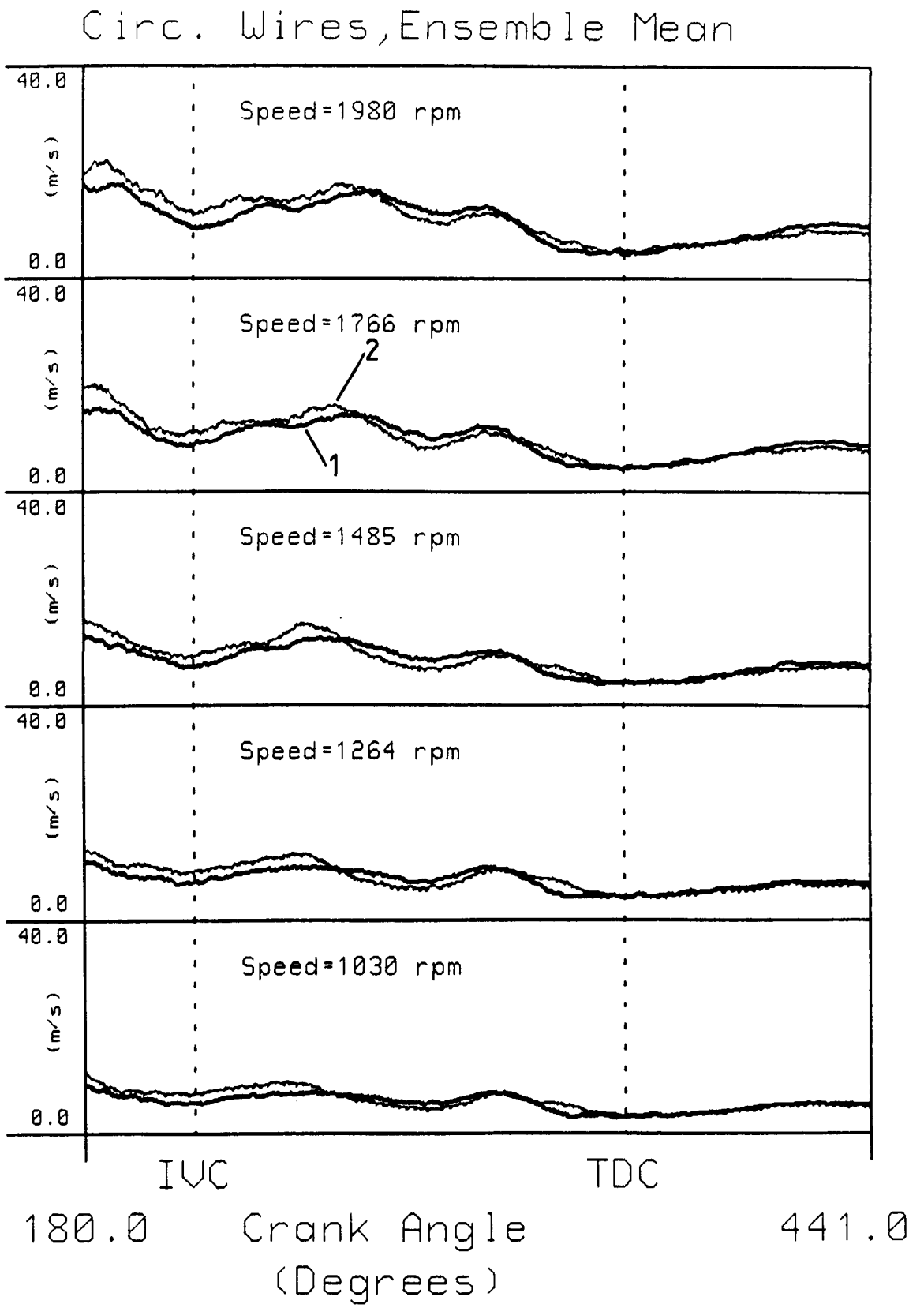

Figure 5.21 Shrouded Valve.

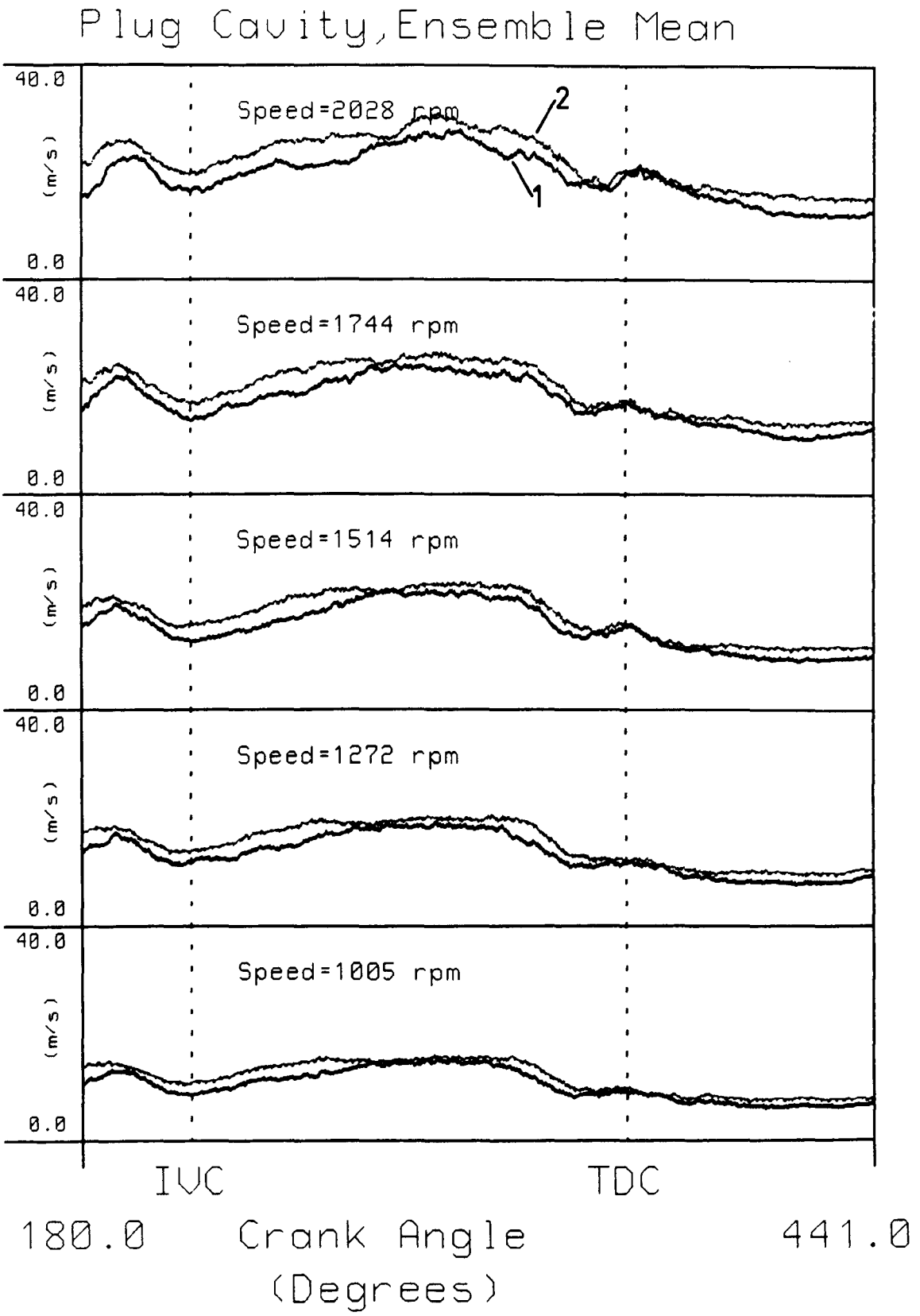

Figure 5.22 Shrouded Valve.

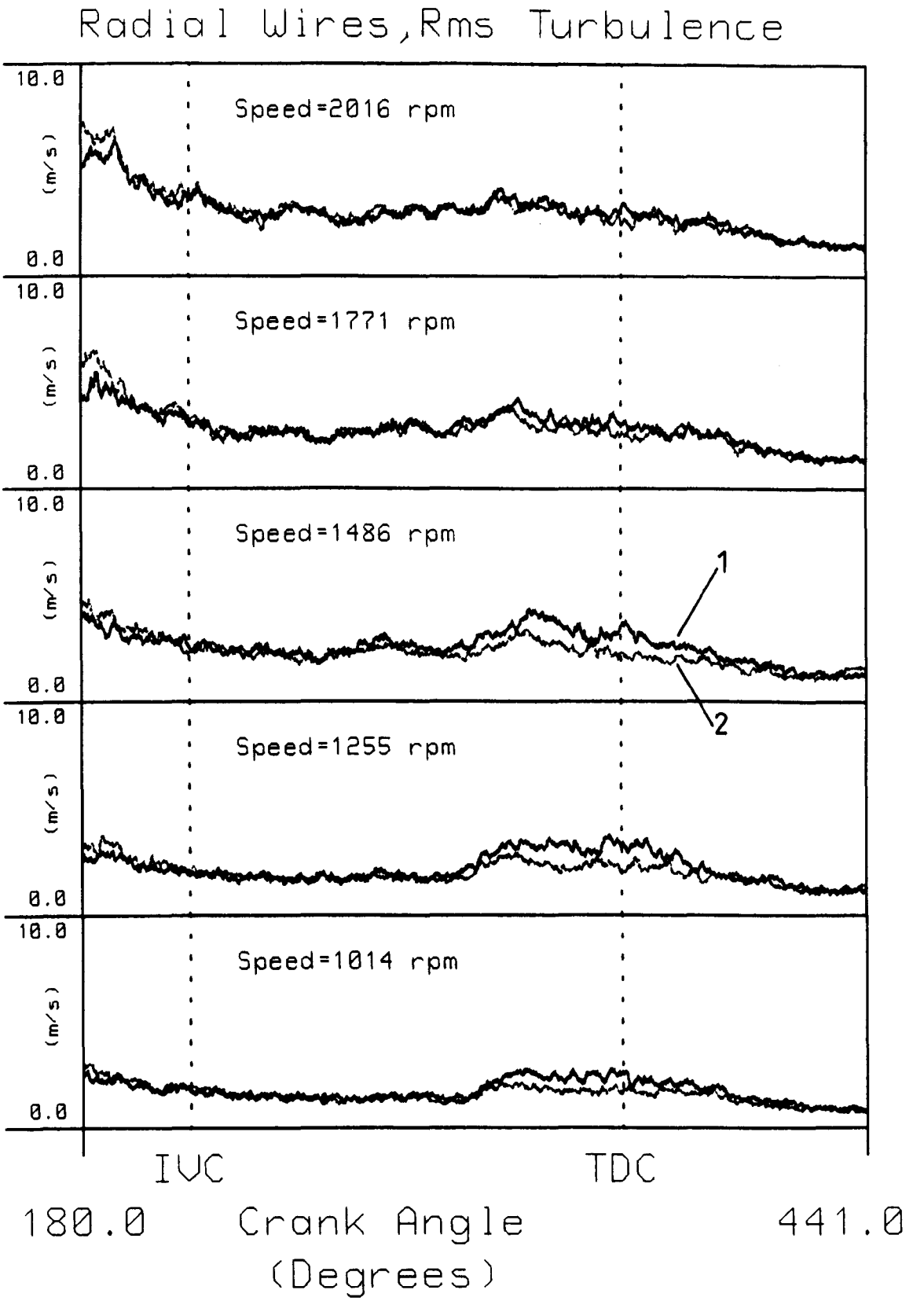

Figure 5.23 Shrouded Valve.

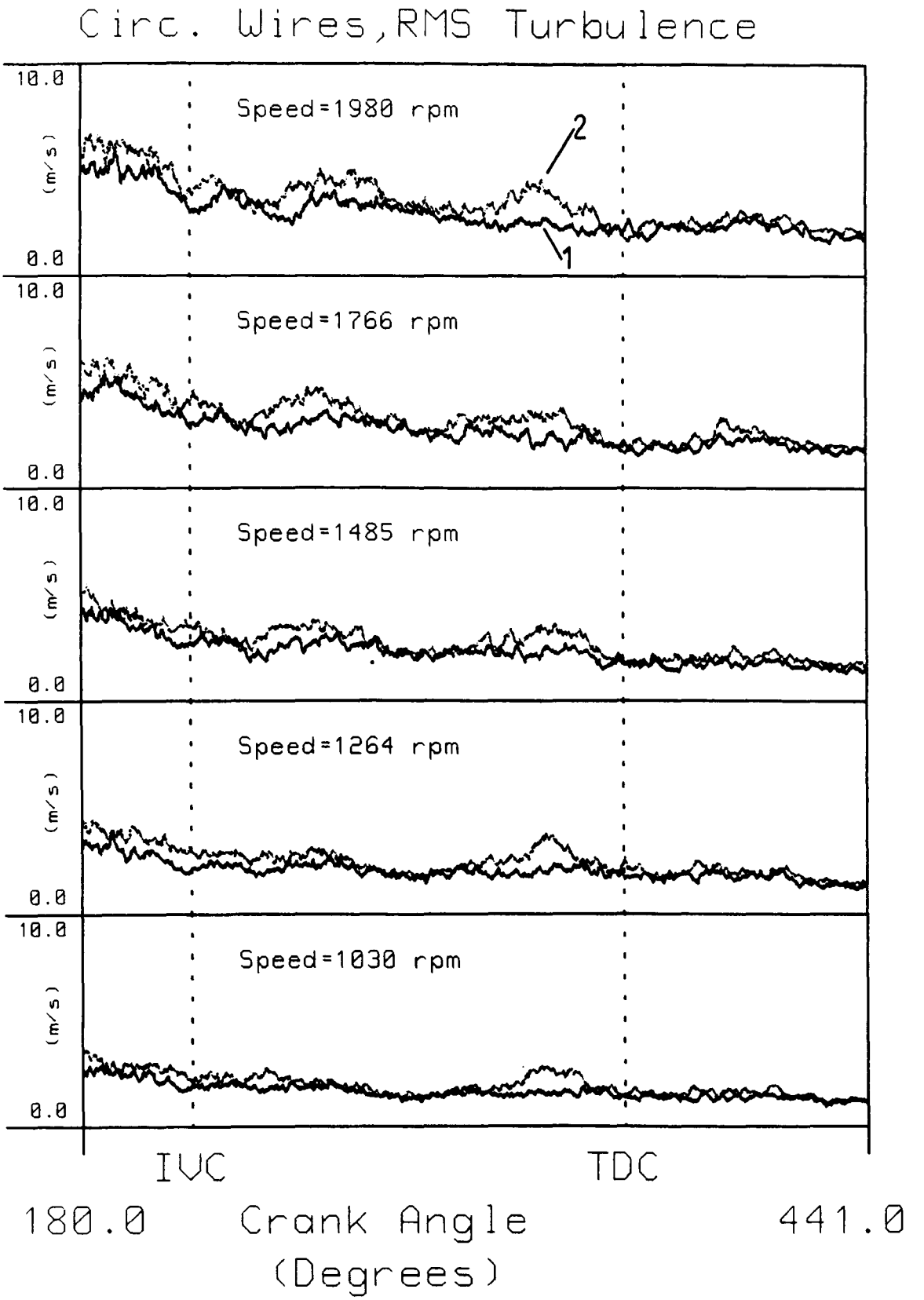

Figure 5.24 Shrouded Valve.

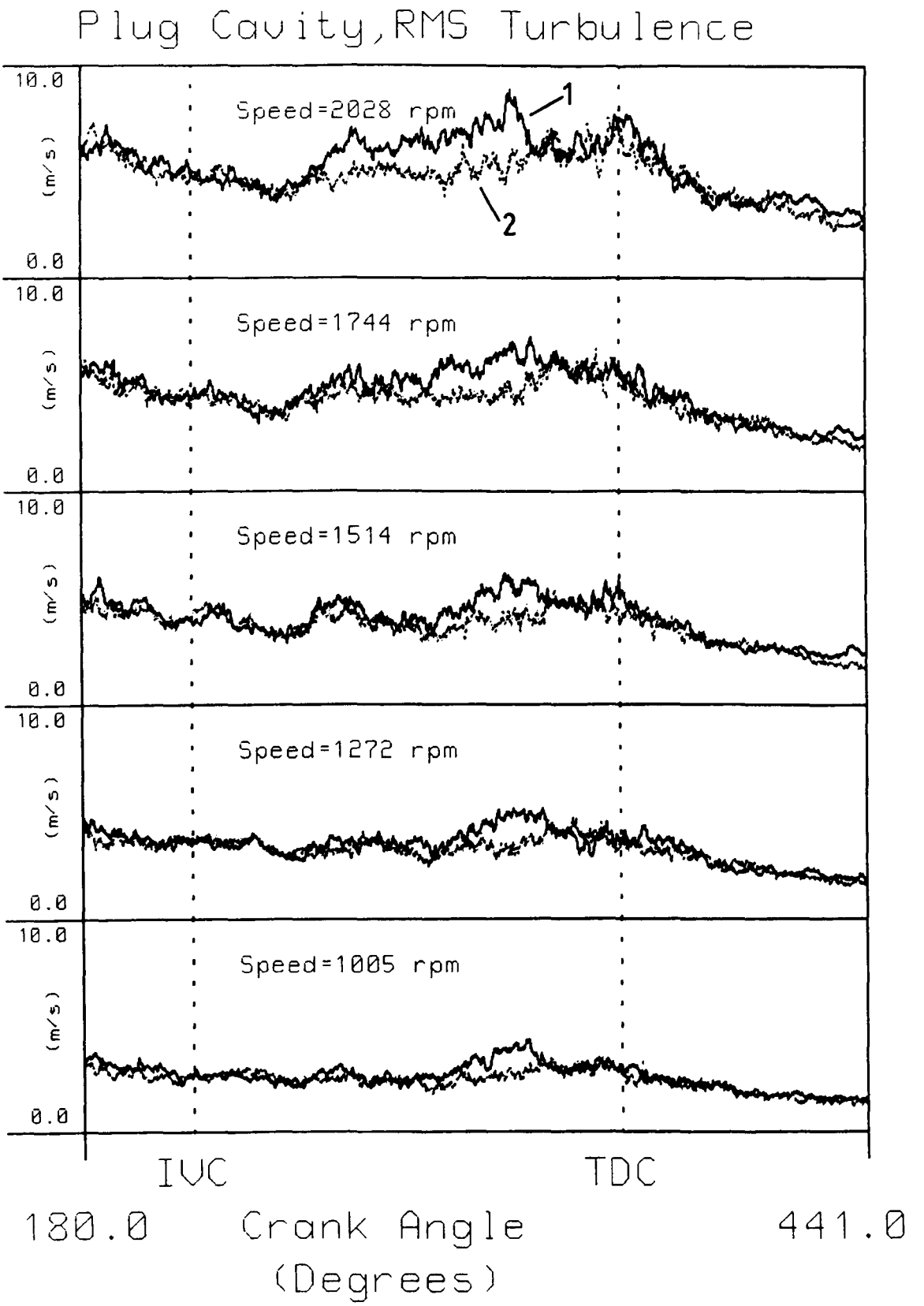

Figure 5.25 Shrouded Valve.

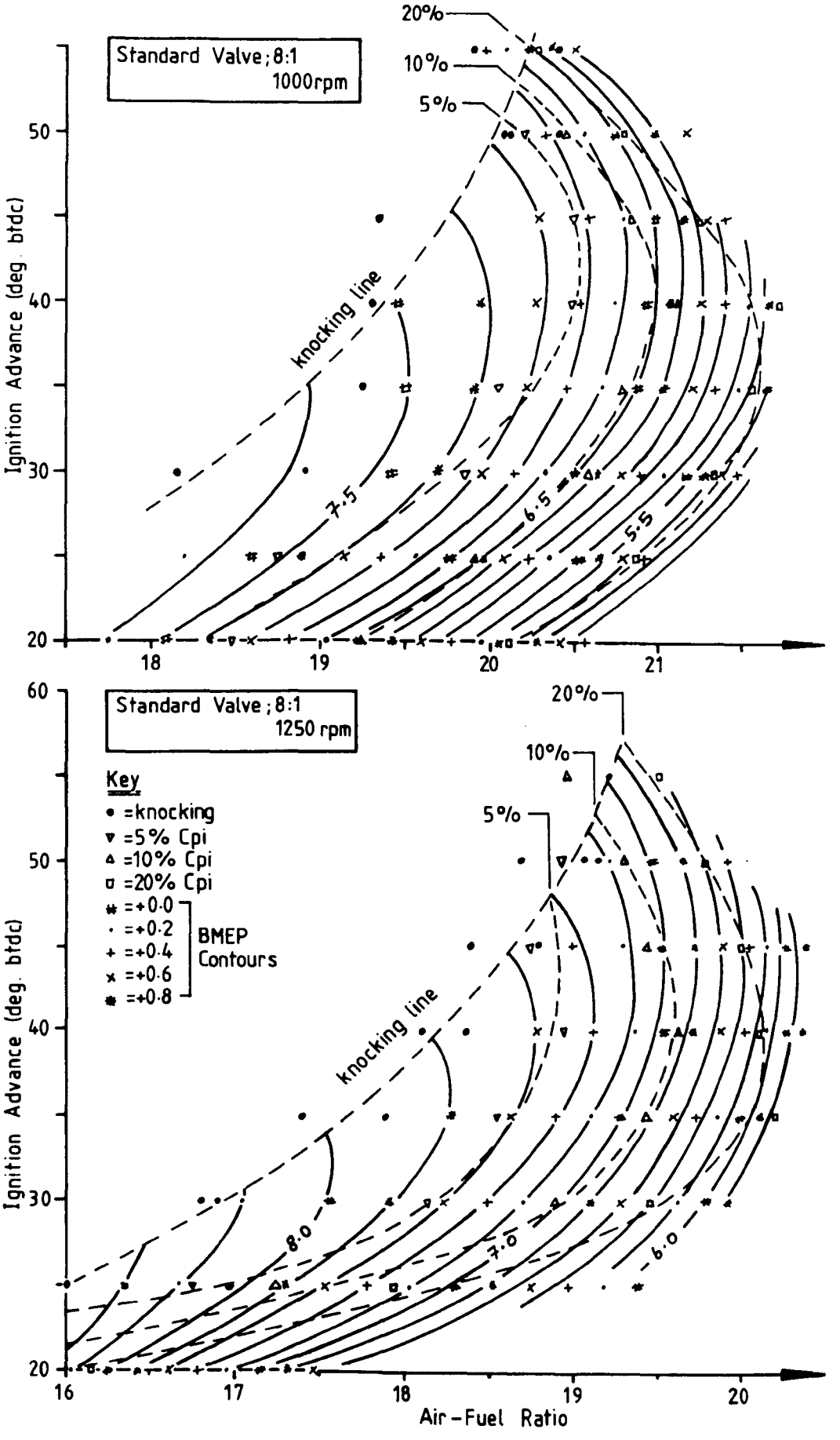
Standard Valve; 8:1
1000rpm
20%
10%
5%
knocking line
7·5
6·5
5·5
Ignition Advance (deg. btdc)
50
40
30
20
18
19
20
21
Standard Valve; 8:1
1250 rpm
Key
• =knocking
▽ =5% Cpi
△ =10% Cpi
□ =20% Cpi
✱ =+0·0
· =+0·2
+ =+0·4
× =+0·6
✱ =+0·8
BMEP Contours
20%
10%
5%
knocking line
8·0
7·0
6·0
60
50
40
30
20
16
17
18
19
20
Air-Fuel Ratio

Figure 5.26

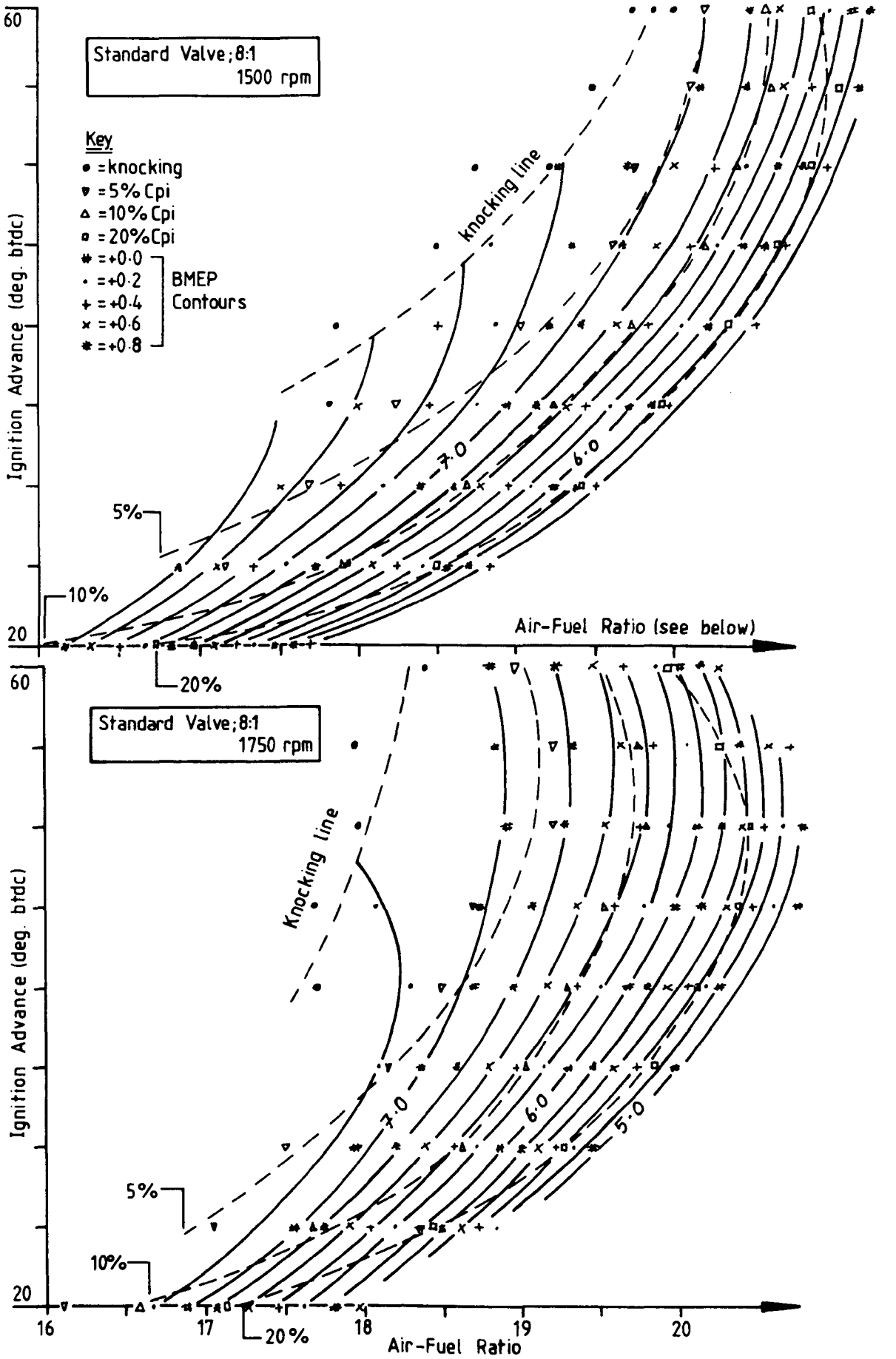
Standard Valve; 8:1
1500 rpm
Key
• = knocking
▼ = 5% Cpi
△ = 10% Cpi
▫ = 20% Cpi
* = +0·0
· = +0·2
+ = +0·4
× = +0·6
* = +0·8
BMEP Contours
knocking line
7·0
6·0
5%
10%
20%
Ignition Advance (deg. btdc)
Air-Fuel Ratio (see below)
60
20
Standard Valve; 8:1
1750 rpm
Knocking line
7·0
6·0
5·0
5%
10%
20%
Ignition Advance (deg. btdc)
16
17
18
19
20
Air-Fuel Ratio

Figure 5.27

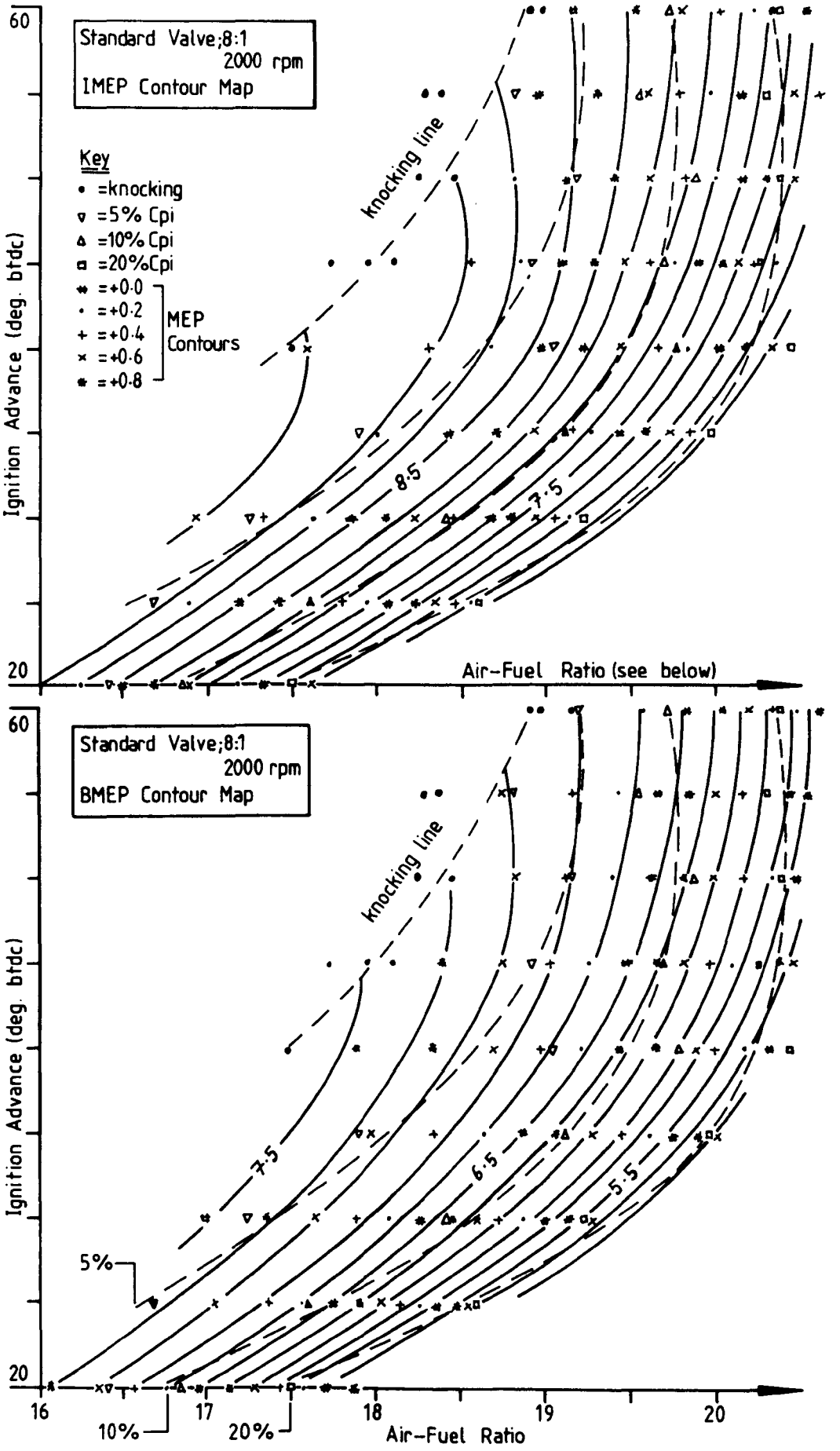
Standard Valve;8:1
2000 rpm
IMEP Contour Map
Key
• =knocking
▽ =5% Cpi
△ =10% Cpi
□ =20%Cpi
=+0·0
· =+0·2
+ =+0·4
× =+0·6
* =+0·8
MEP Contours
knocking line
8·5
7·5
Ignition Advance (deg. btdc)
60
20
Air-Fuel Ratio (see below)
Standard Valve;8:1
2000 rpm
BMEP Contour Map
knocking line
7·5
6·5
5·5
5%
10%
20%
Ignition Advance (deg. btdc)
60
20
16
17
18
19
20
Air-Fuel Ratio

Figure 5.28

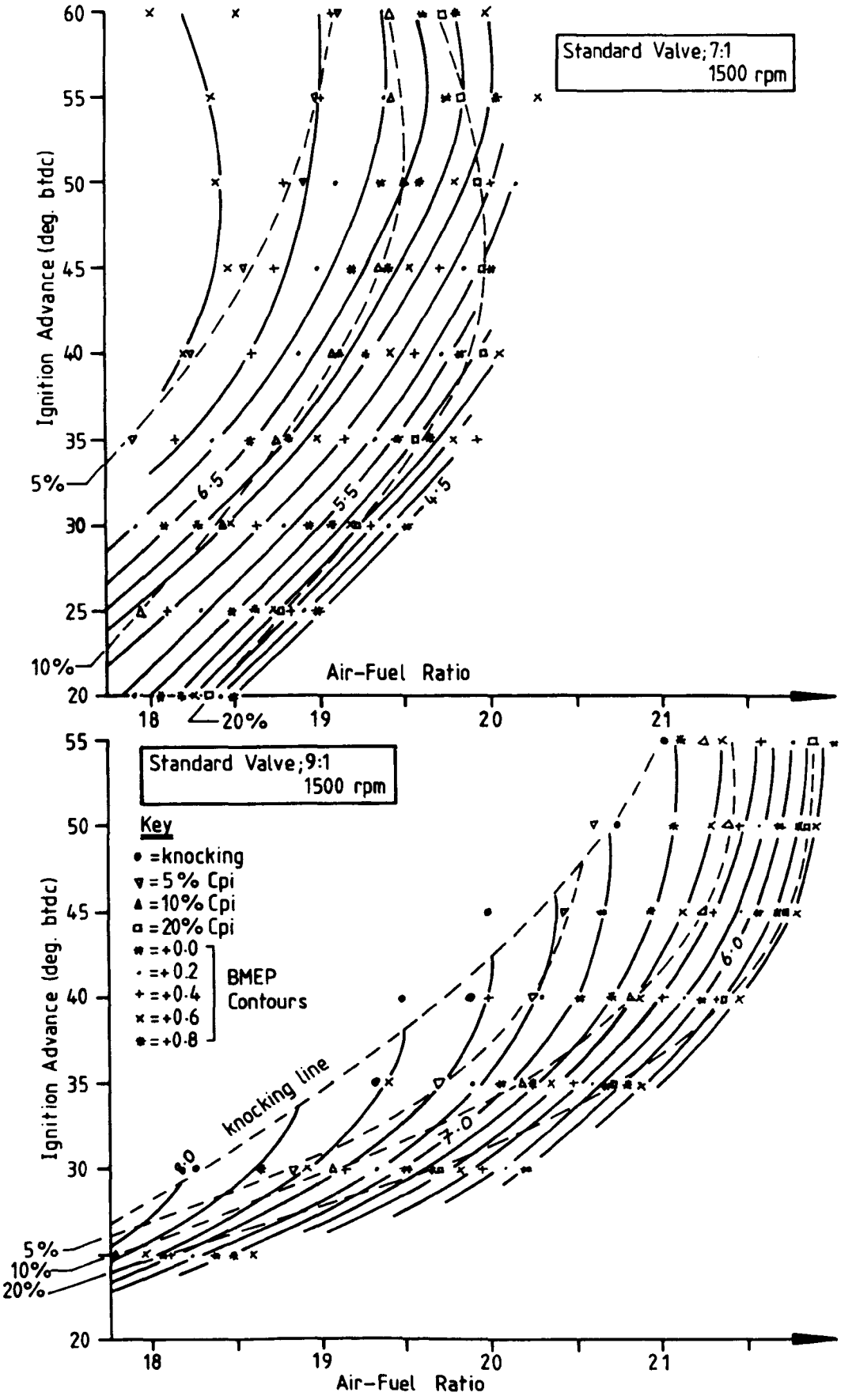
Standard Valve; 7:1
1500 rpm
Ignition Advance (deg. btdc)
Air-Fuel Ratio
5%
10%
20%
6·5
5·5
4·5
Standard Valve; 9:1
1500 rpm
Key
• =knocking
▽ = 5% Cpi
△ = 10% Cpi
□ = 20% Cpi
* = +0·0
· = +0·2
+ = +0·4
× = +0·6
* = +0·8
BMEP Contours
knocking line
6·0
7·0
8·0

Figure 5.29

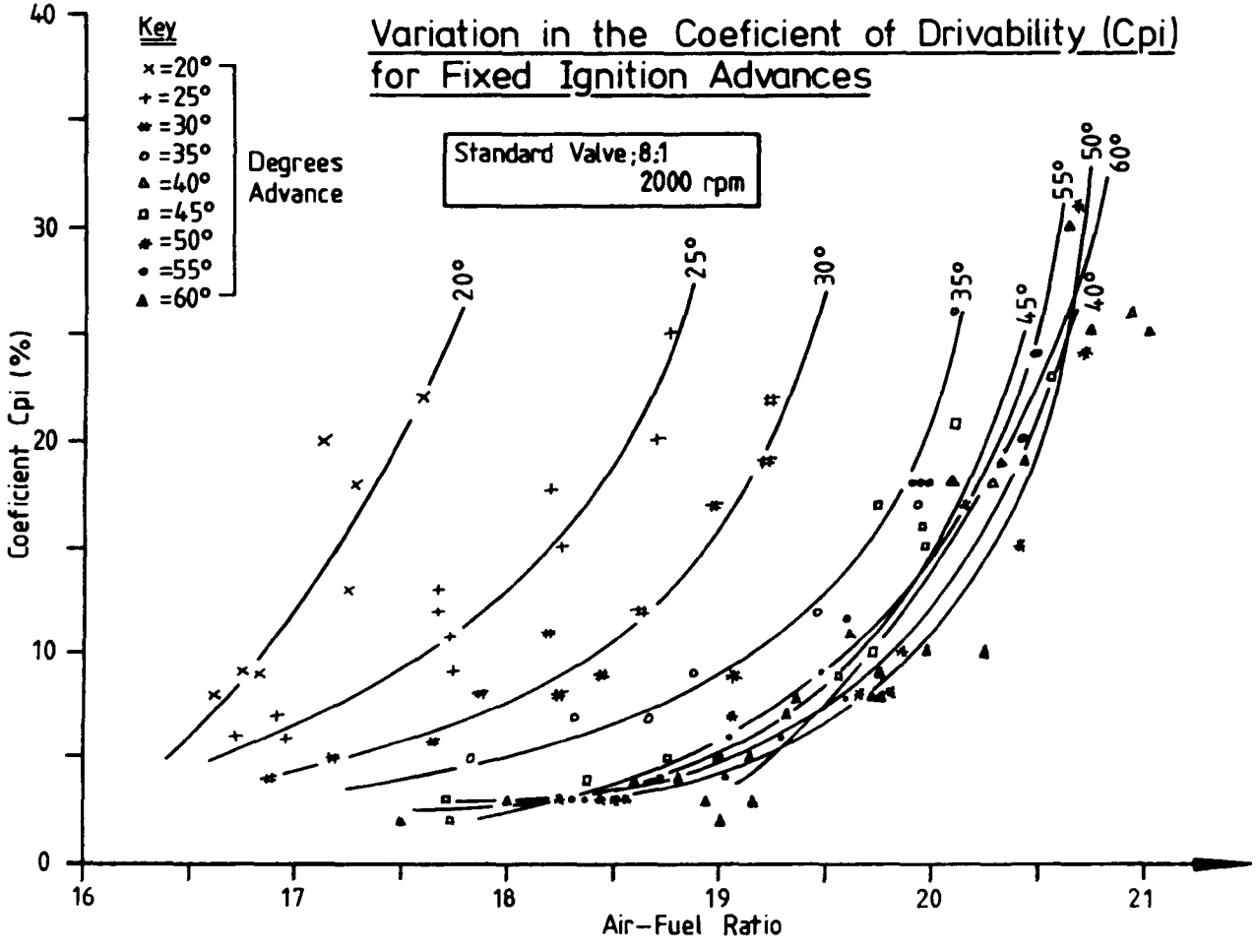
Variation in the Coeficient of Drivability (Cpi)
for Fixed Ignition Advances
Key
x =20°
+ =25°
* =30°
o =35°
▲ =40°
□ =45°
* =50°
• =55°
▲ =60°
Degrees Advance
Standard Valve;8:1
2000 rpm
20°
25°
30°
35°
45°
40°
55°
50°
60°
Coeficient Cpi (%)
0
10
20
30
40
16
17
18
19
20
21
Air-Fuel Ratio

Figure 5.30

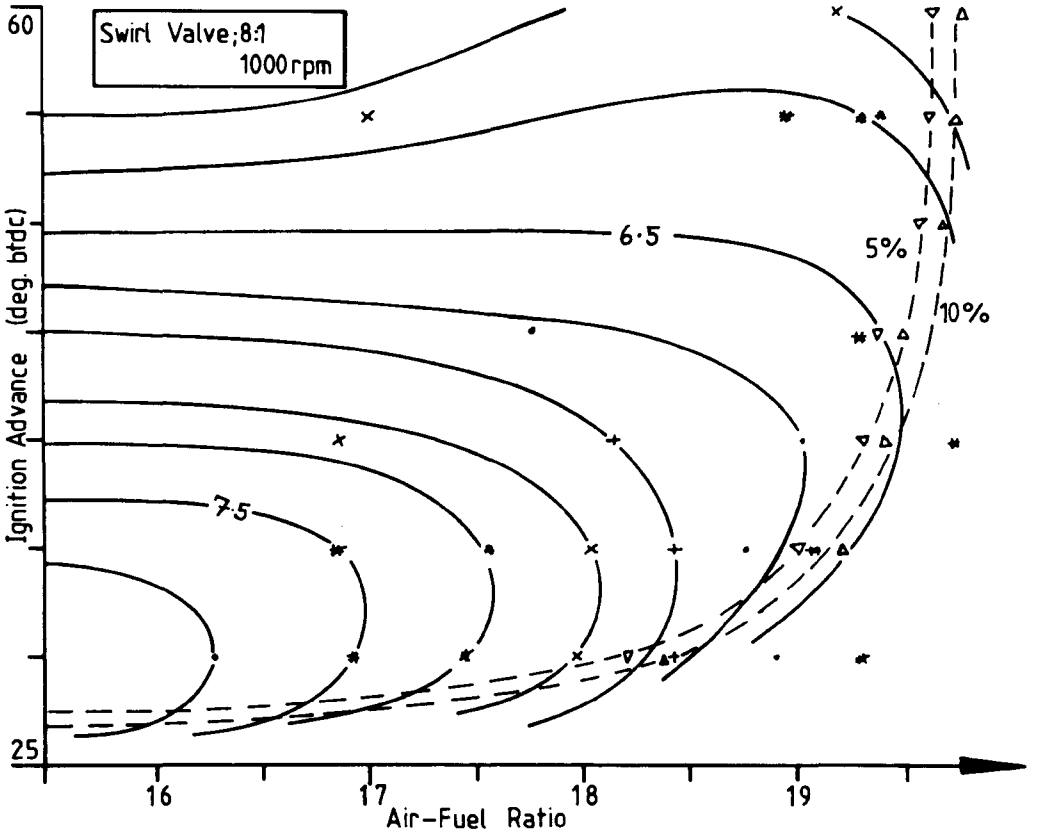
Swirl Valve;8:1
1000 rpm
60
25
Ignition Advance (deg. btdc)
6·5
7·5
5%
10%
16
17
18
19
Air-Fuel Ratio

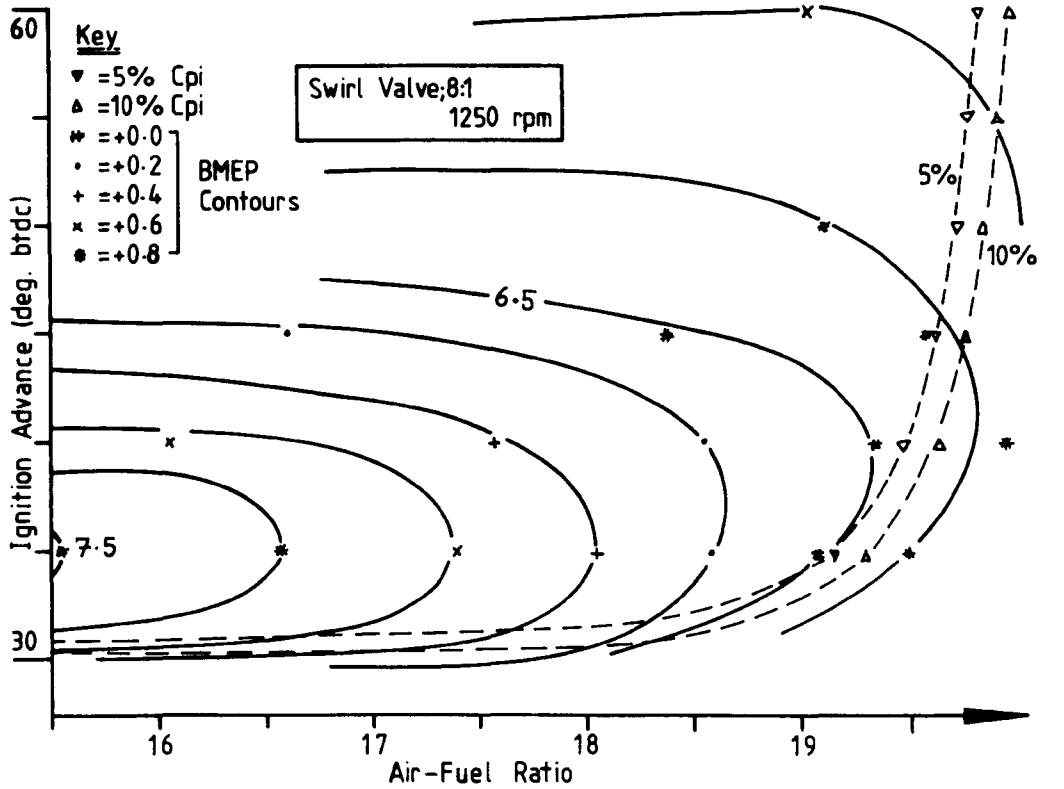
Key
▼ =5% Cpi
▲ =10% Cpi
✱ =+0·0
• =+0·2
+ =+0·4
× =+0·6
✱ =+0·8
BMEP Contours
Swirl Valve;8:1
1250 rpm
60
30
Ignition Advance (deg. btdc)
6·5
7·5
5%
10%
16
17
18
19
Air-Fuel Ratio

Figure 5.31

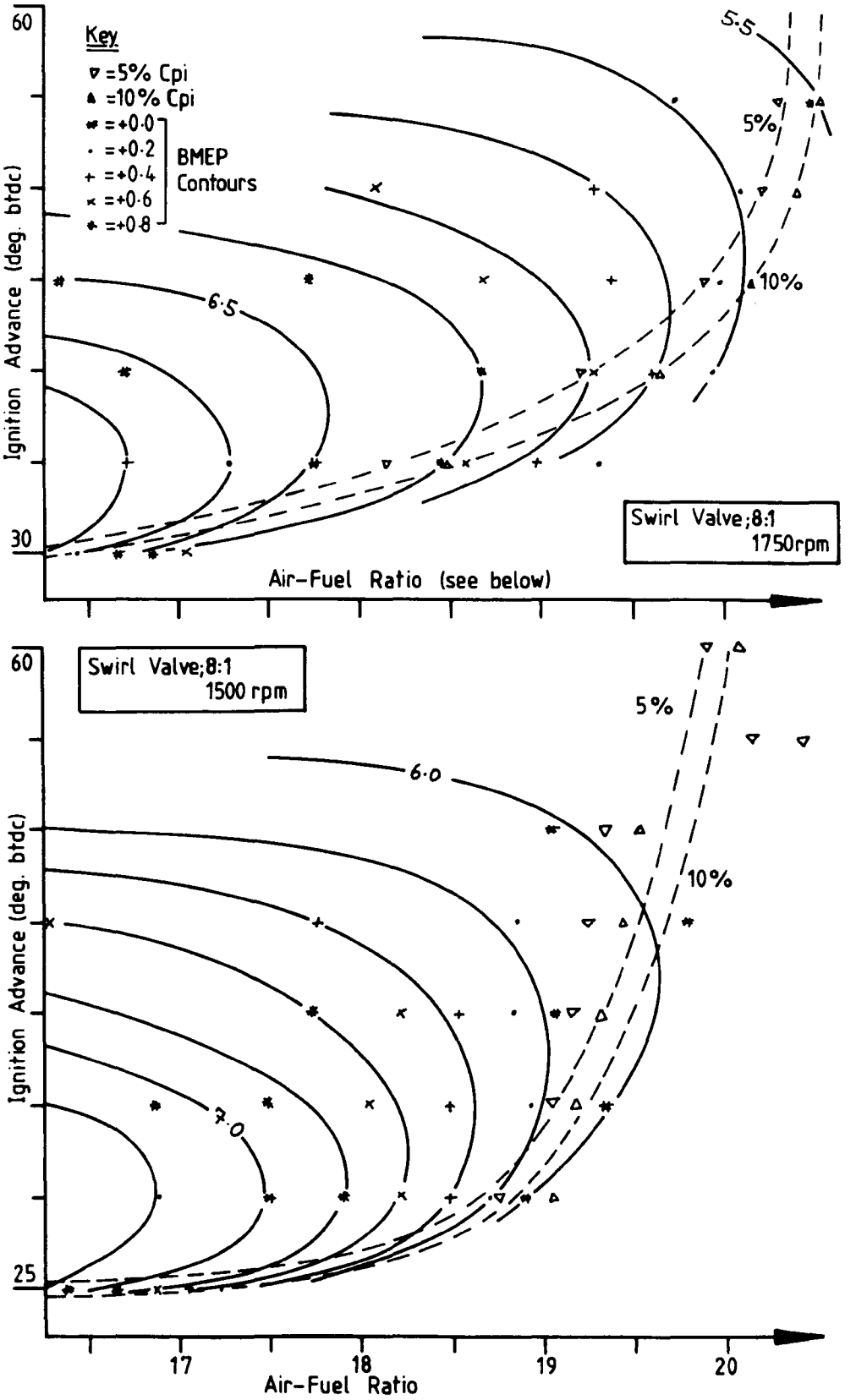
Key
▽ =5% Cpi
▲ =10% Cpi
BMEP Contours
=+0·0
=+0·2
=+0·4
=+0·6
=+0·8
5·5
6·5
5%
10%
60
30
Ignition Advance (deg. btdc)
Swirl Valve;8:1
1750rpm
Air-Fuel Ratio (see below)
Swirl Valve;8:1
1500 rpm
6·0
7·0
5%
10%
60
25
Ignition Advance (deg. btdc)
17
18
19
20
Air-Fuel Ratio

Figure 5.32

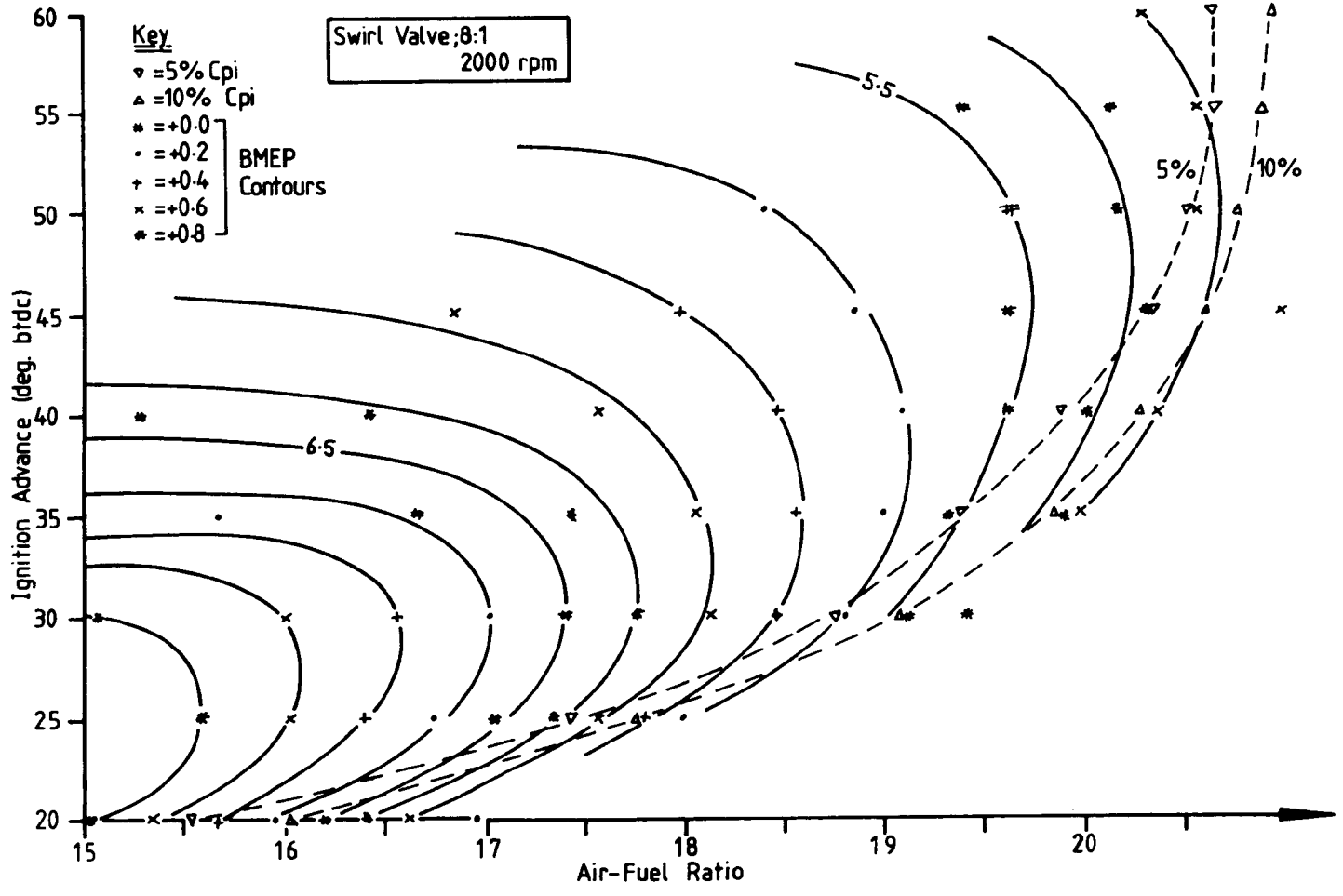
Key
▽ =5% Cpi
△ =10% Cpi
* =+0·0
· =+0·2
+ =+0·4
× =+0·6
* =+0·8
BMEP Contours
Swirl Valve;8:1
2000 rpm
5·5
6·5
5%
10%
Ignition Advance (deg. btdc)
60
55
50
45
40
35
30
25
20
15
16
17
18
19
20
Air-Fuel Ratio

Figure 5.33

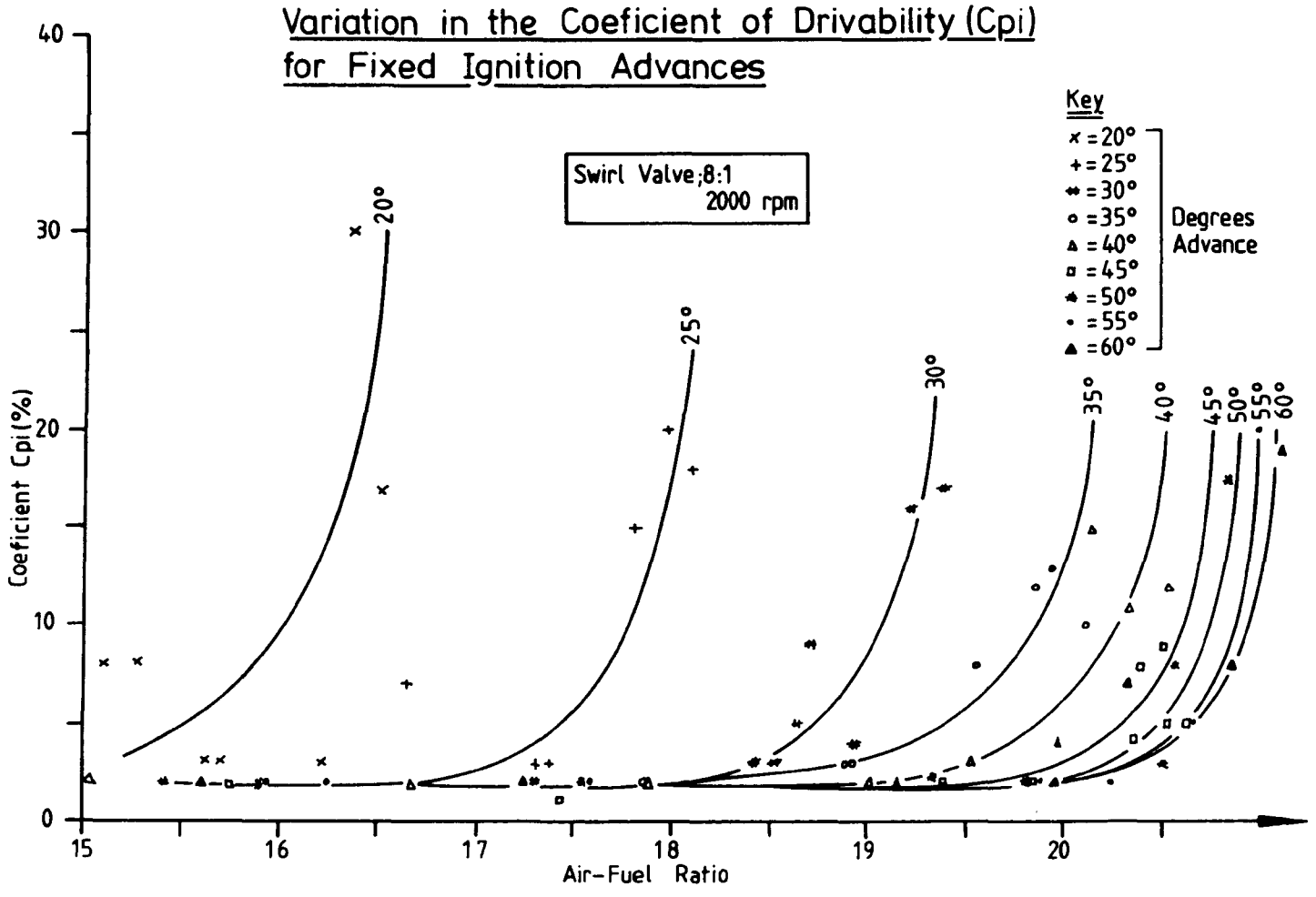
Variation in the Coeficient of Drivability (Cpi)
for Fixed Ignition Advances
Swirl Valve;8:1
2000 rpm
Key
x = 20°
+ = 25°
* = 30°
o = 35°
Δ = 40°
□ = 45°
♣ = 50°
• = 55°
▲ = 60°
Degrees Advance
20°
25°
30°
35°
40°
45°
50°
55°
60°
Coeficient Cpi(%)
0
10
20
30
40
15
16
17
18
19
20
Air-Fuel Ratio

Figure 5.34

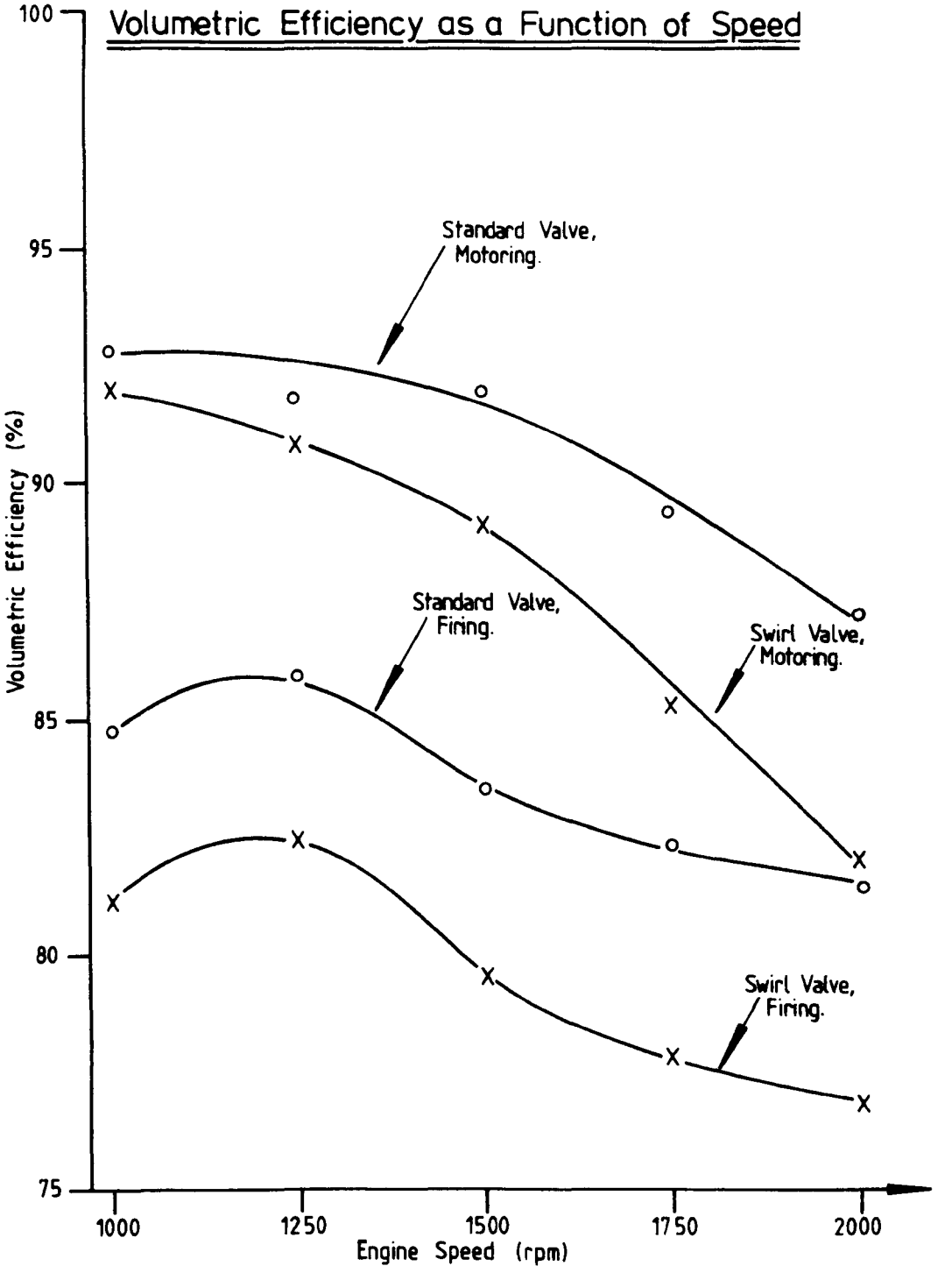
Volumetric Efficiency as a Function of Speed
100
95
90
85
80
75
Volumetric Efficiency (%)
Standard Valve, Motoring.
Standard Valve, Firing.
Swirl Valve, Motoring.
Swirl Valve, Firing.
1000
1250
1500
1750
2000
Engine Speed (rpm)

Figure 5.35

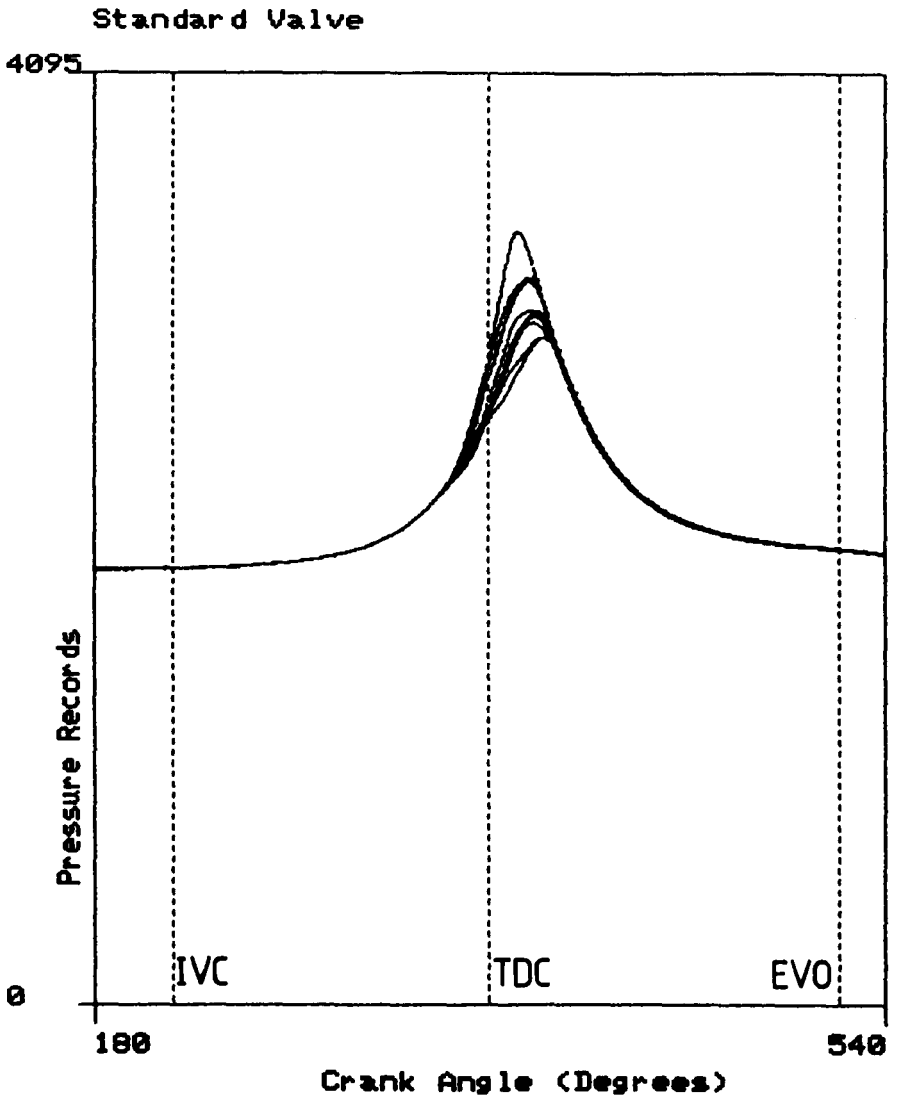

Figure 5.36 Pressure Records from 10 Firing Cycles.

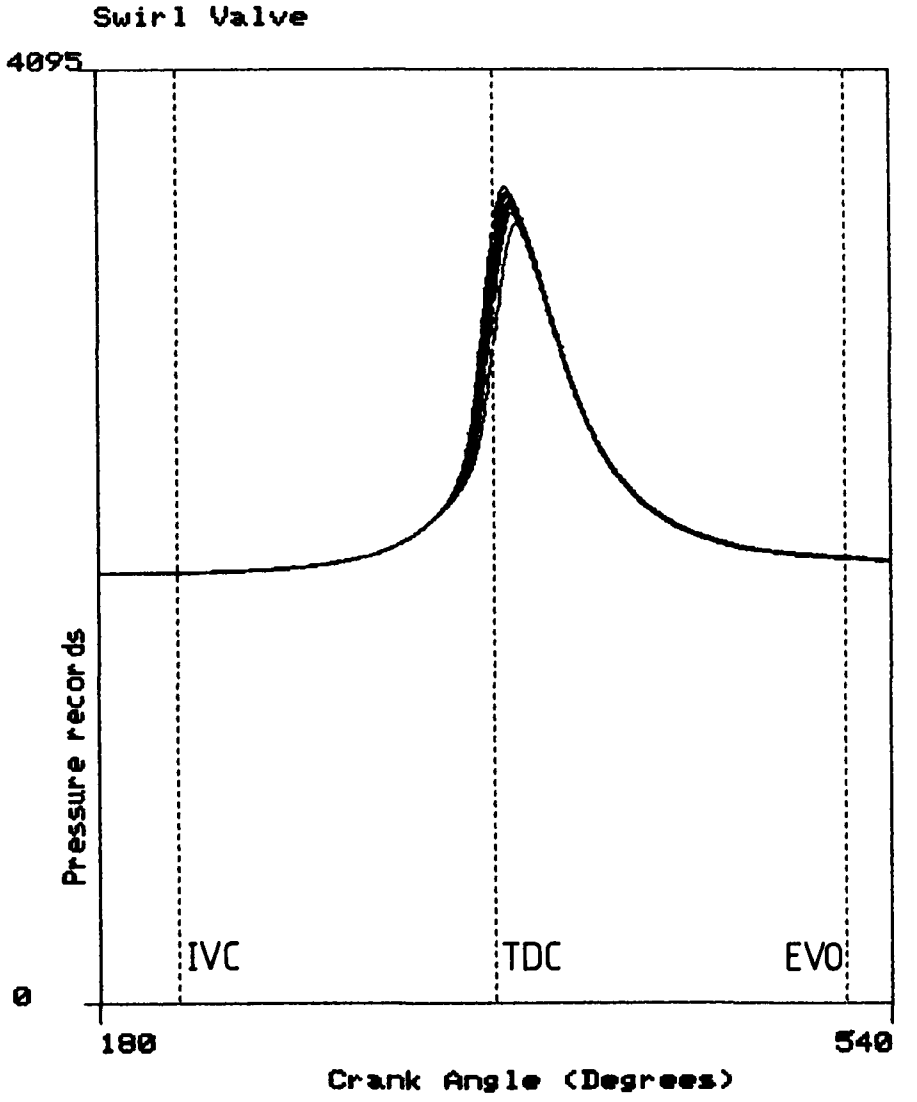

Figure 5.37 Pressure Records from 10 Firing Cycles.

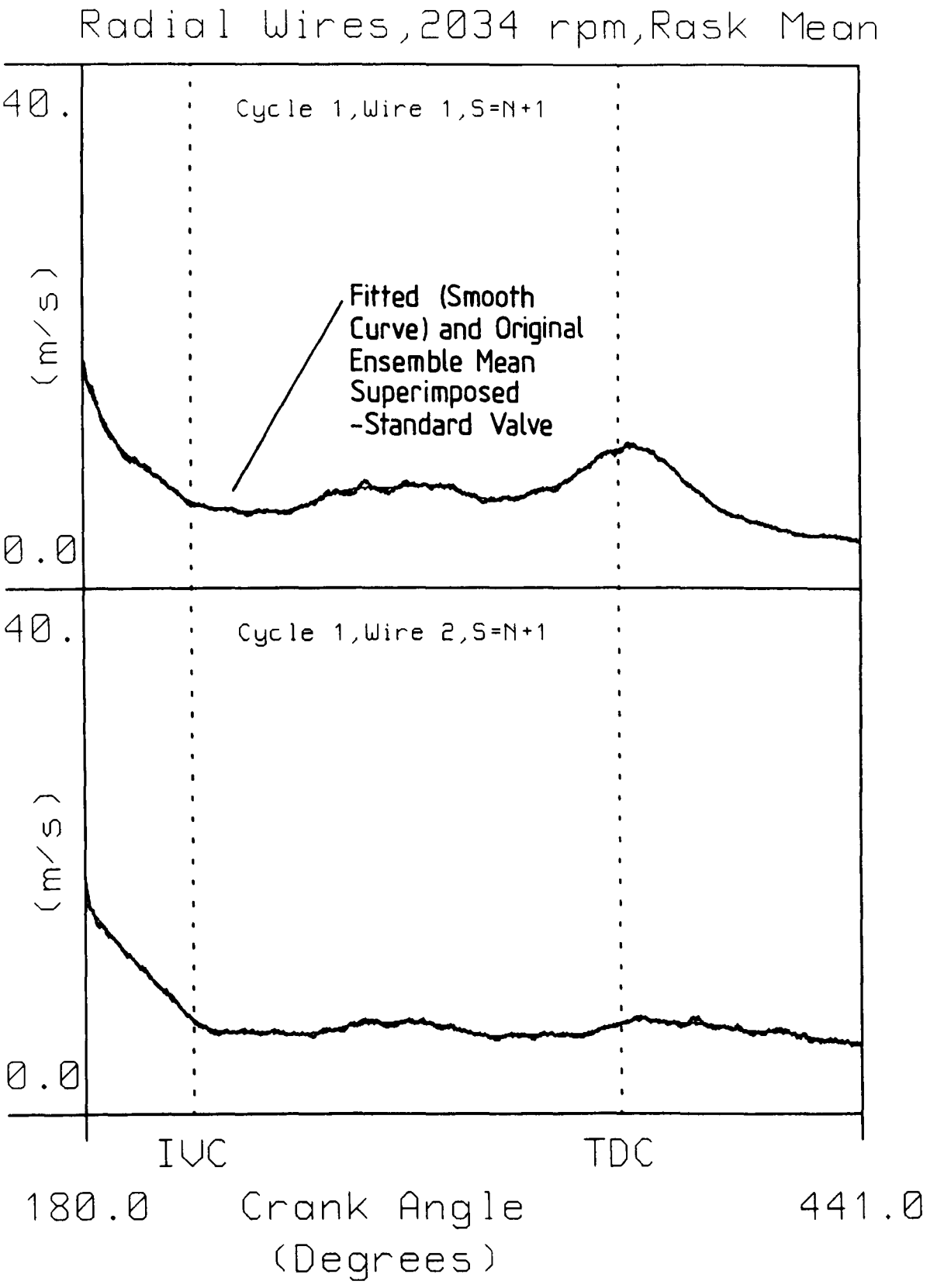

Figure 6.1 Comparison Between Phase Averaged and Spline Smoothed Ensemble Mean Velocity Plots.

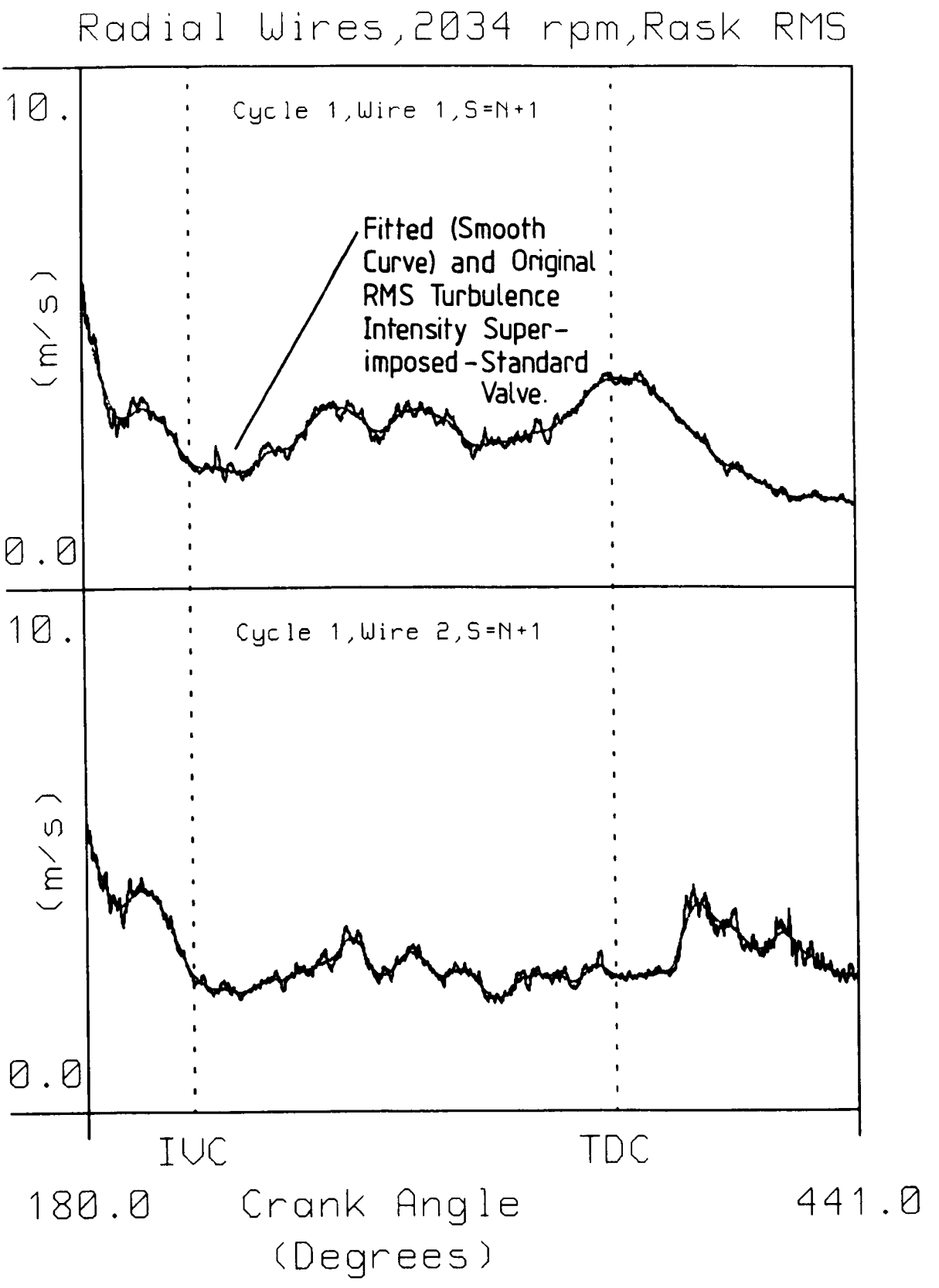

Figure 6.2 Comparison Between Phase Averaged and Spline Smoothed RMS Turbulence Intensity Plots.

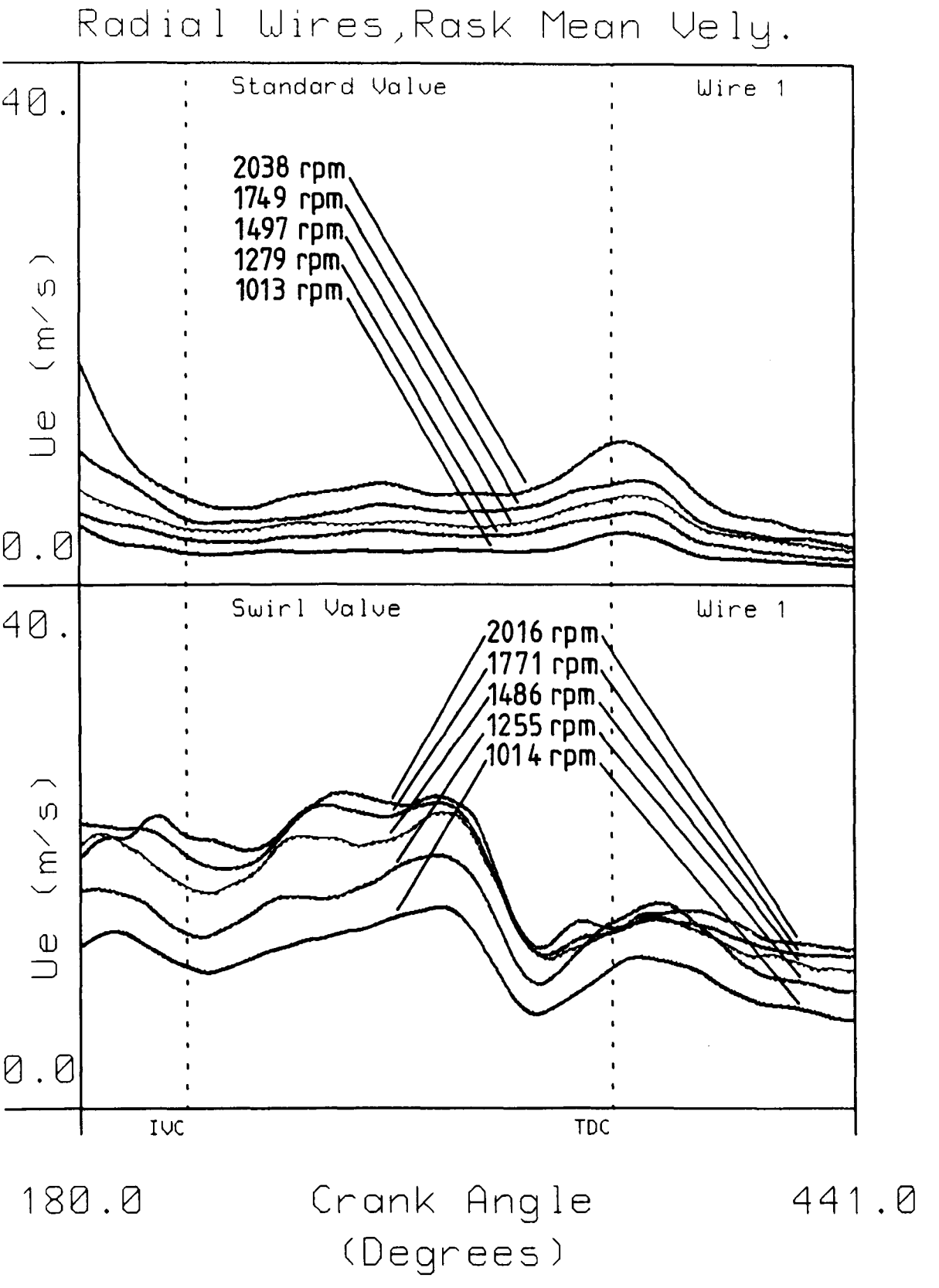

Figure 6.3 Smoothed Ensemble Mean Velocity Plots.

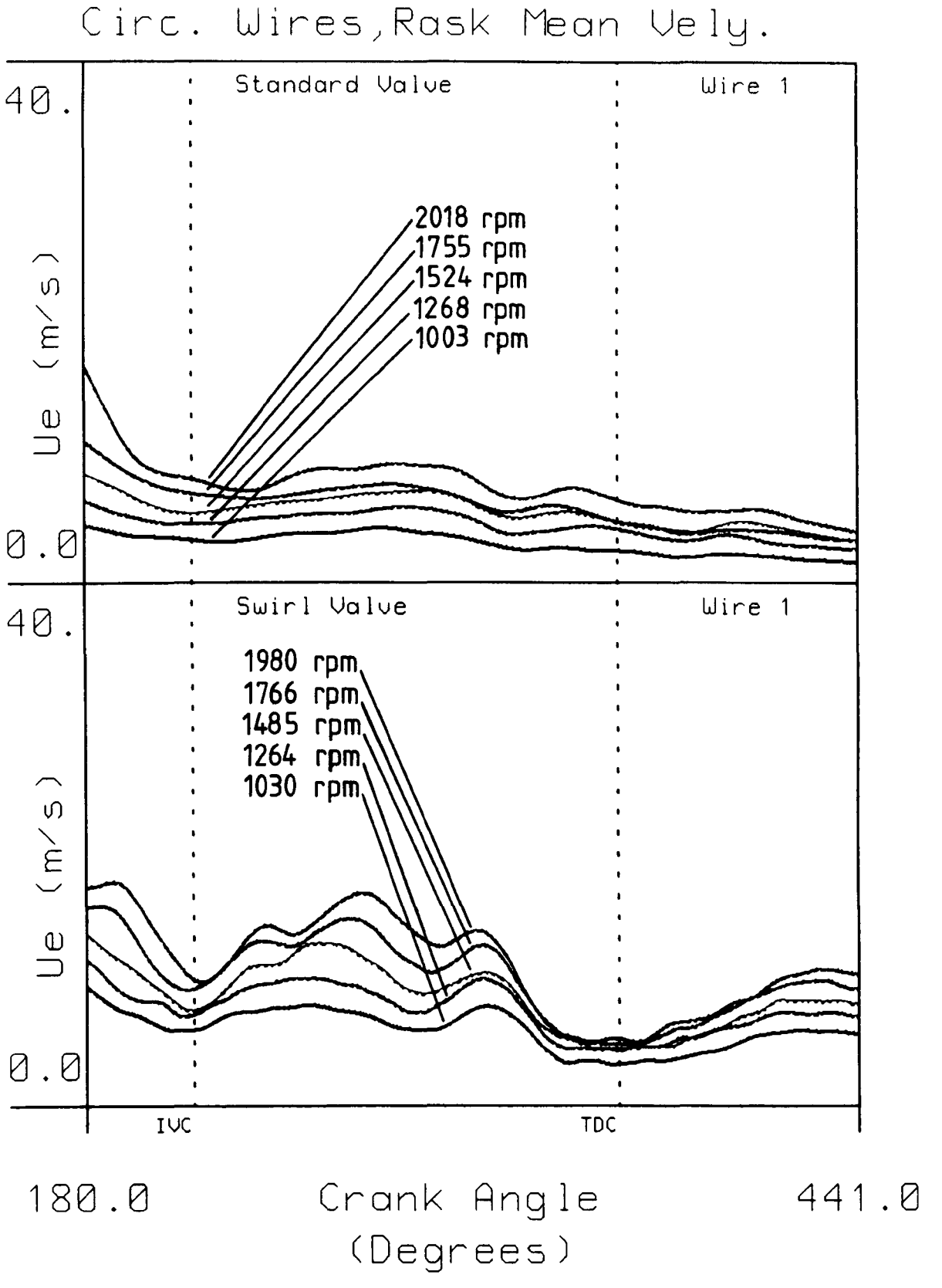

Figure 6.4 Smoothed Ensemble Mean Velocity Plots.

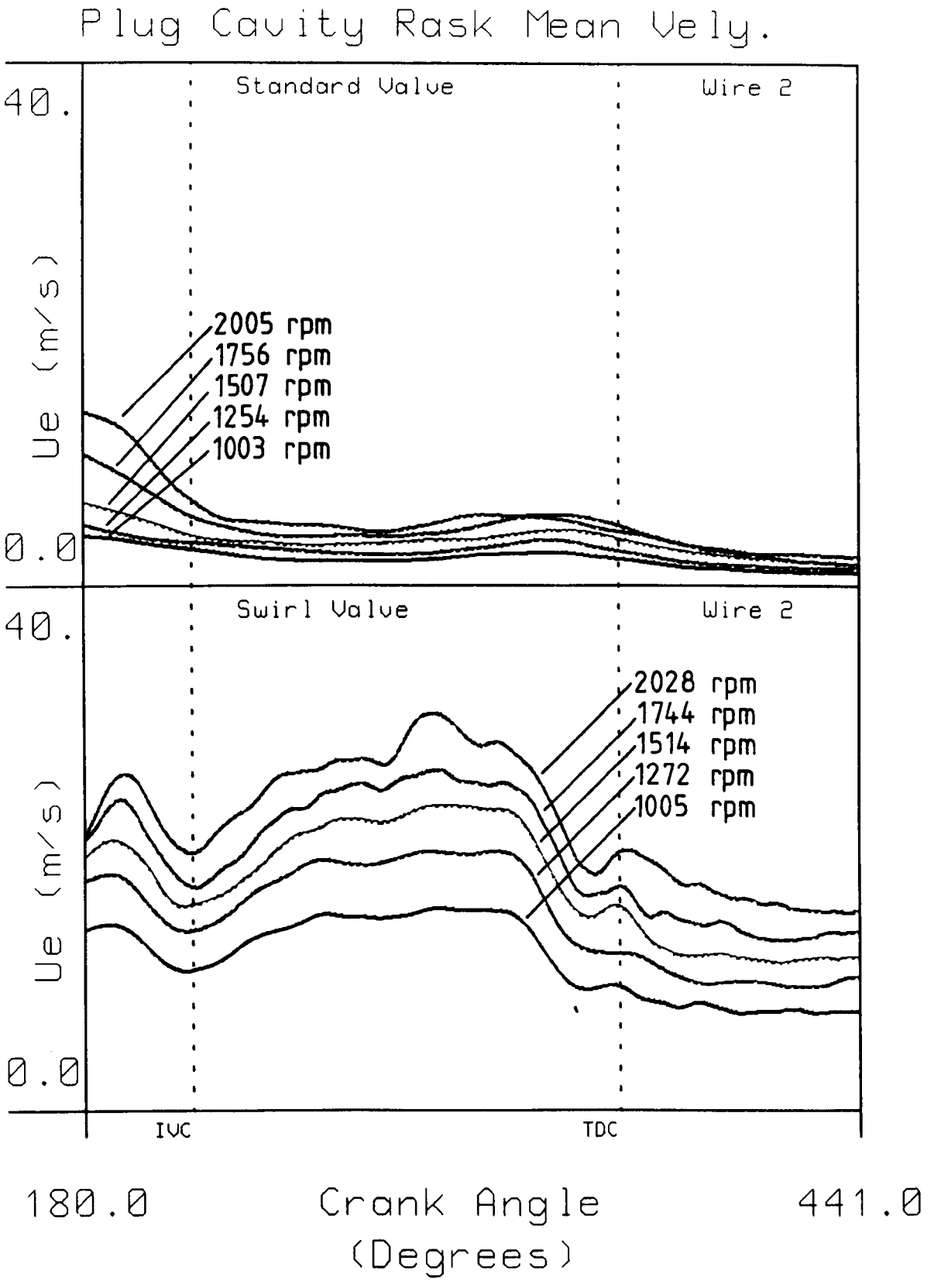

Figure 6.5 Smoothed Ensemble Mean Velocity Plots.

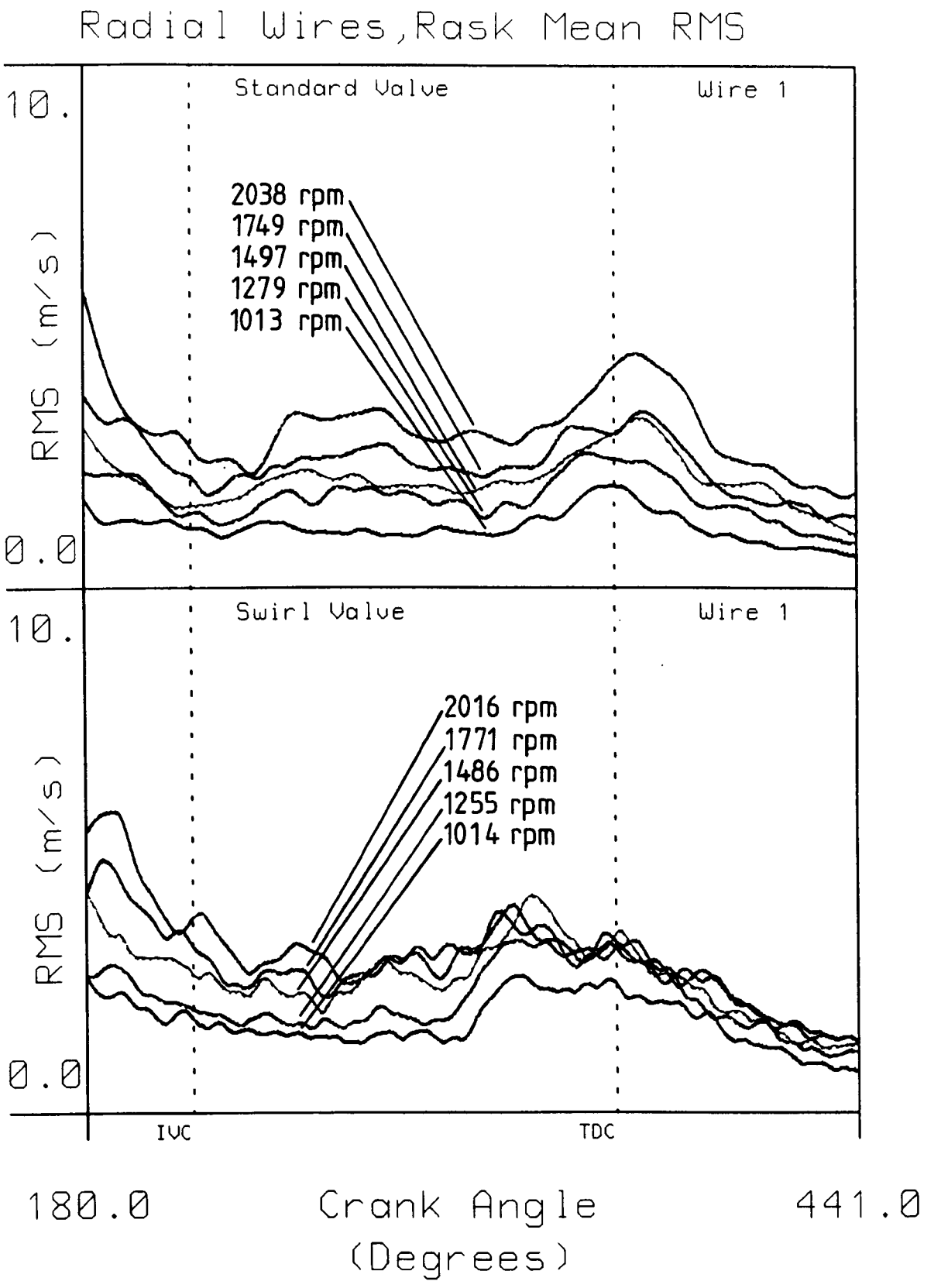

Figure 6.6 Smoothed RMS Turbulence Intensity Plots.

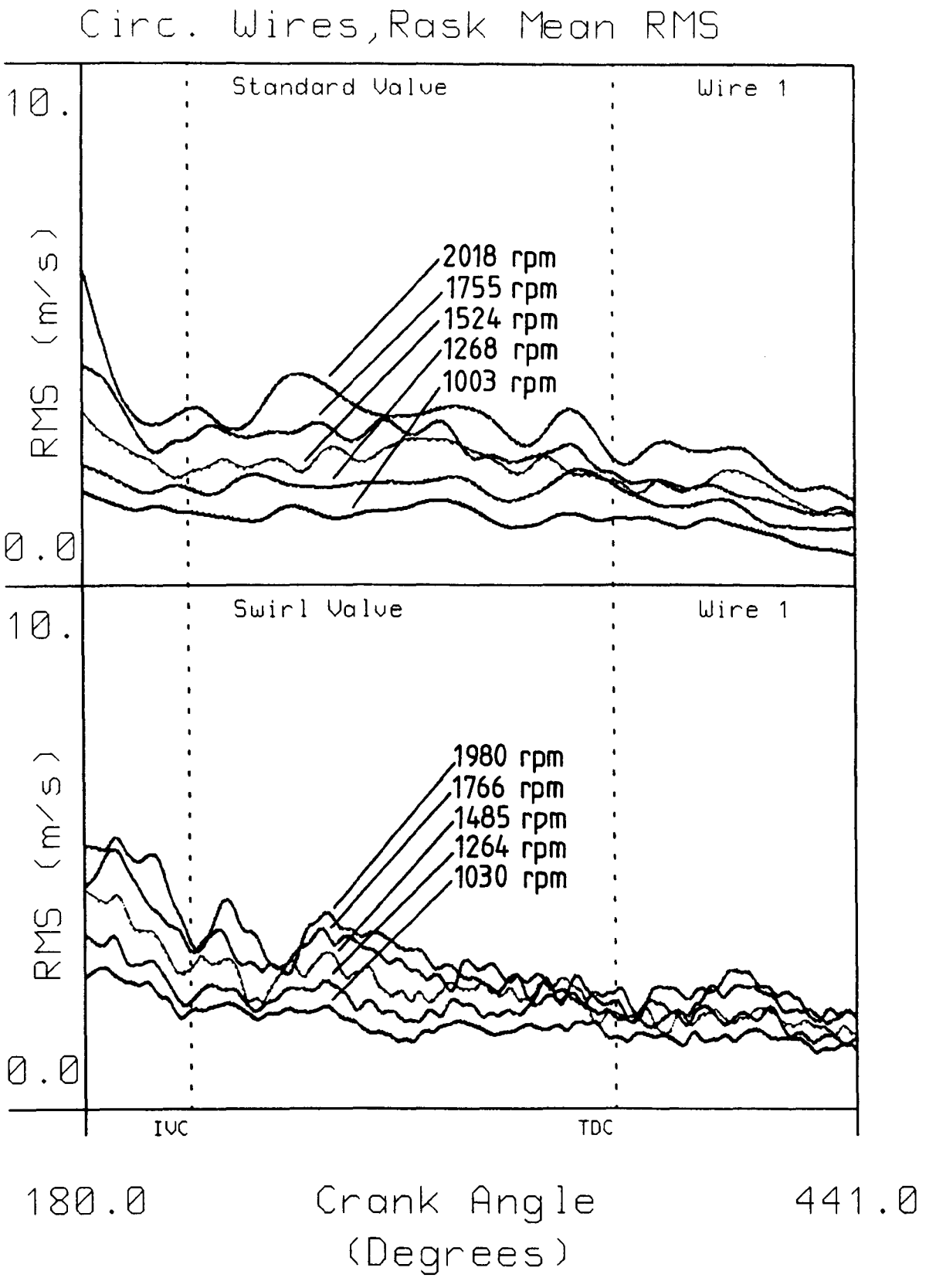

Figure 6.7 Smoothed RMS Turbulence Intensity Plots.

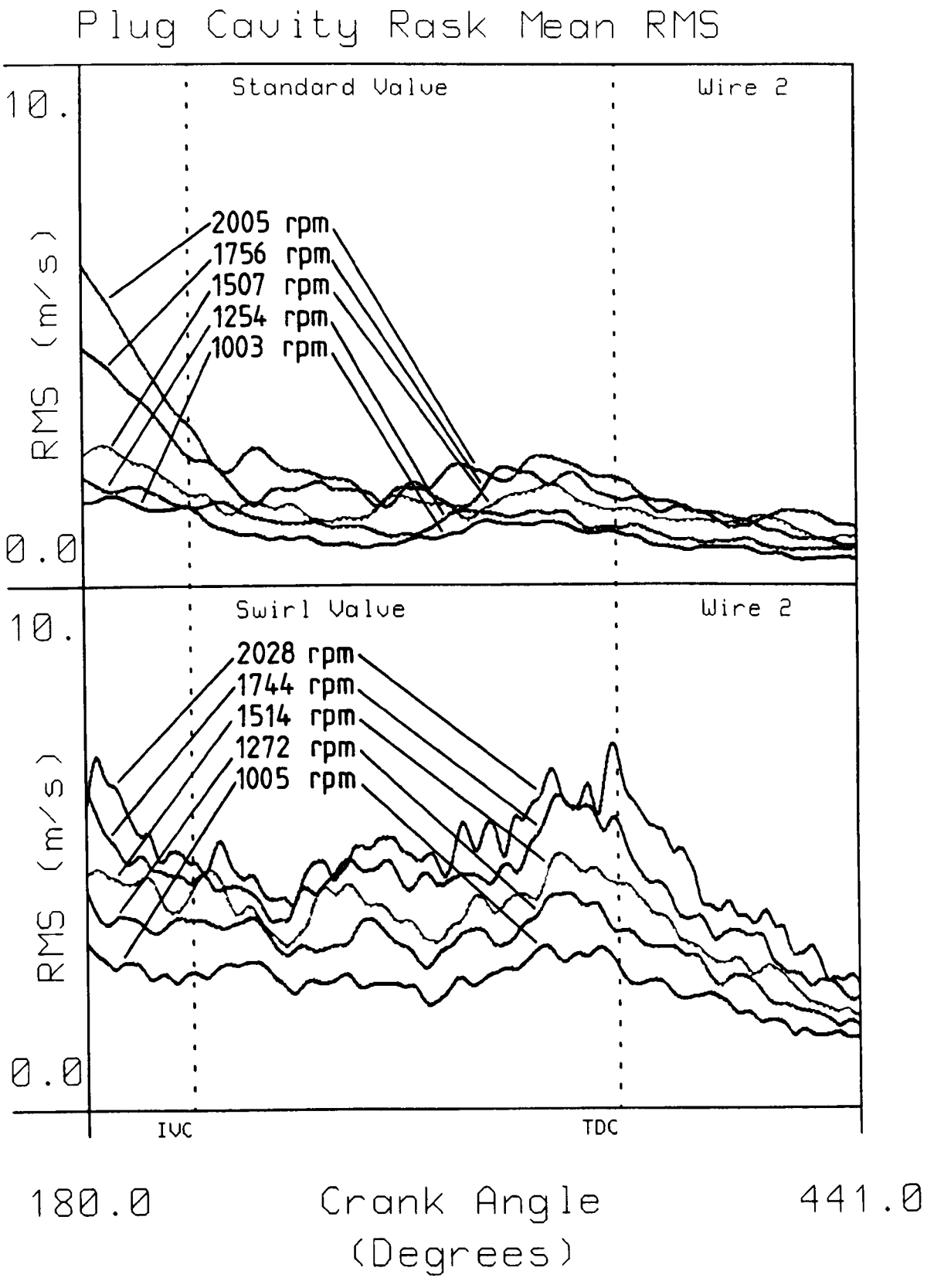

Figure 6.8 Smoothed RMS Turbulence Intensity Plots.

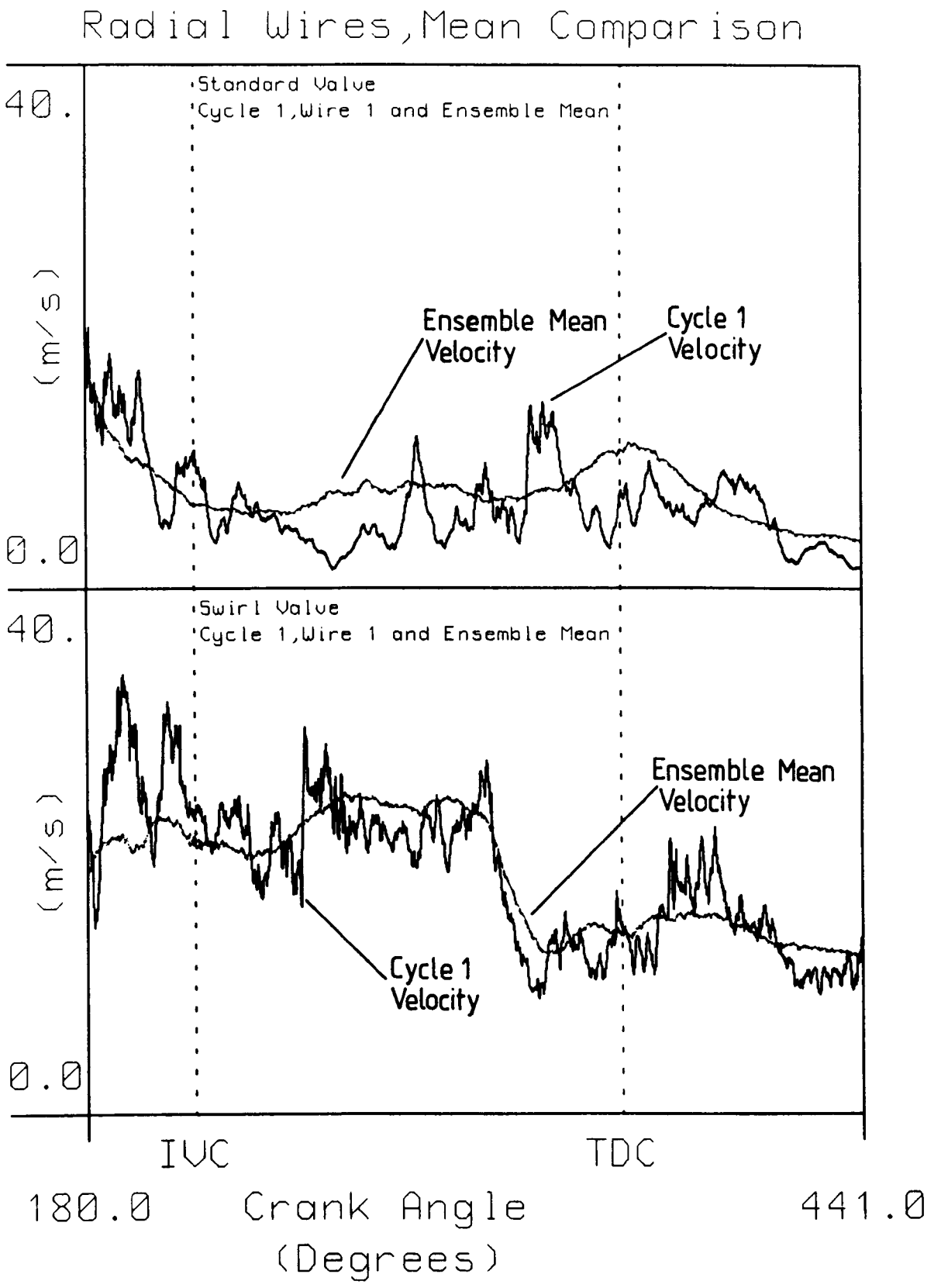

Figure 6.9 A Comparison Between Single Cycle and Ensemble Mean Velocity Plots.

Fourier Coefficients from Ensembled Mean Velocity DFT Curve Fits

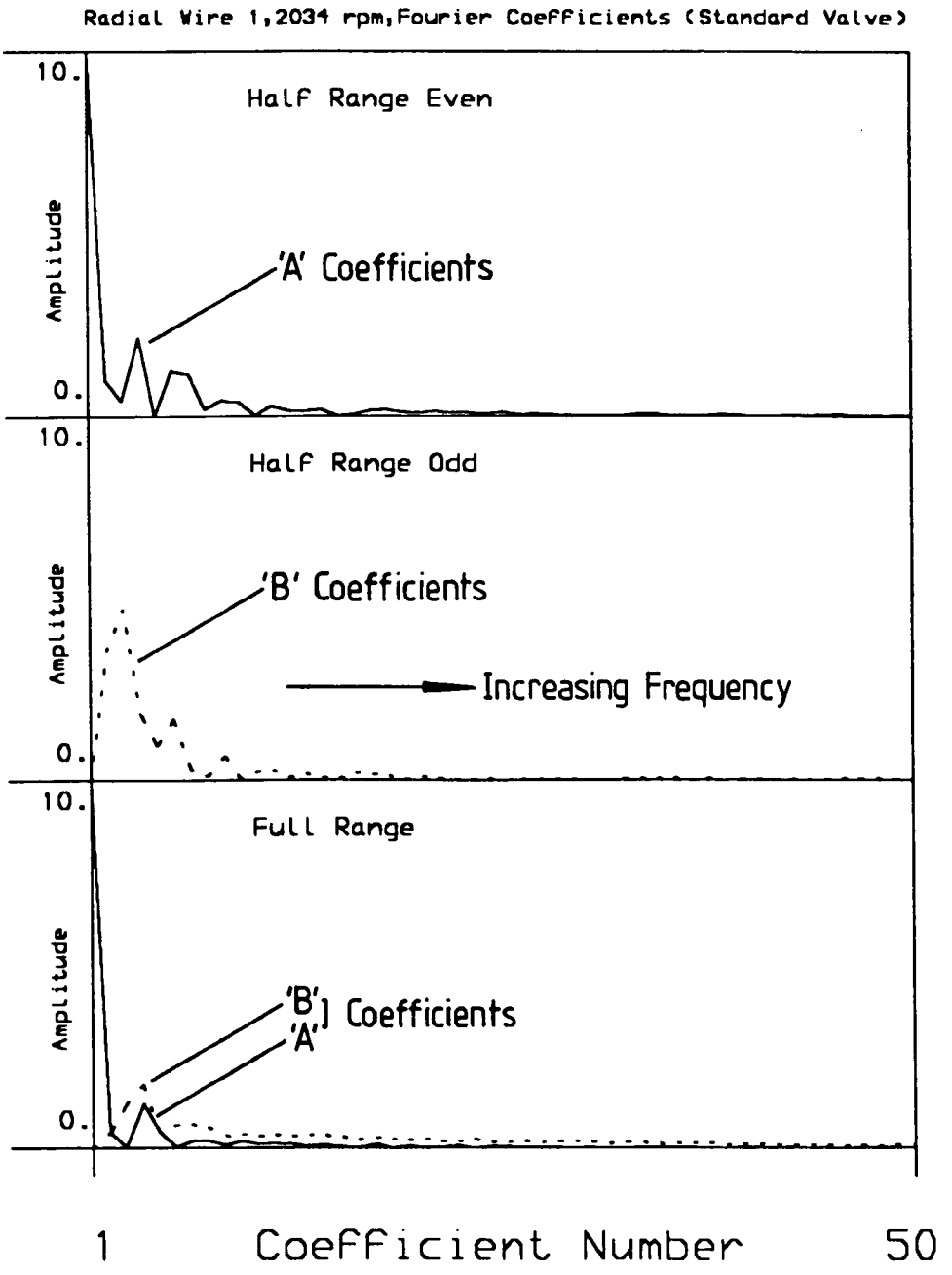

Figure 6.10

Fourier Coefficients from Ensembled Mean Velocity DFT Curve Fits

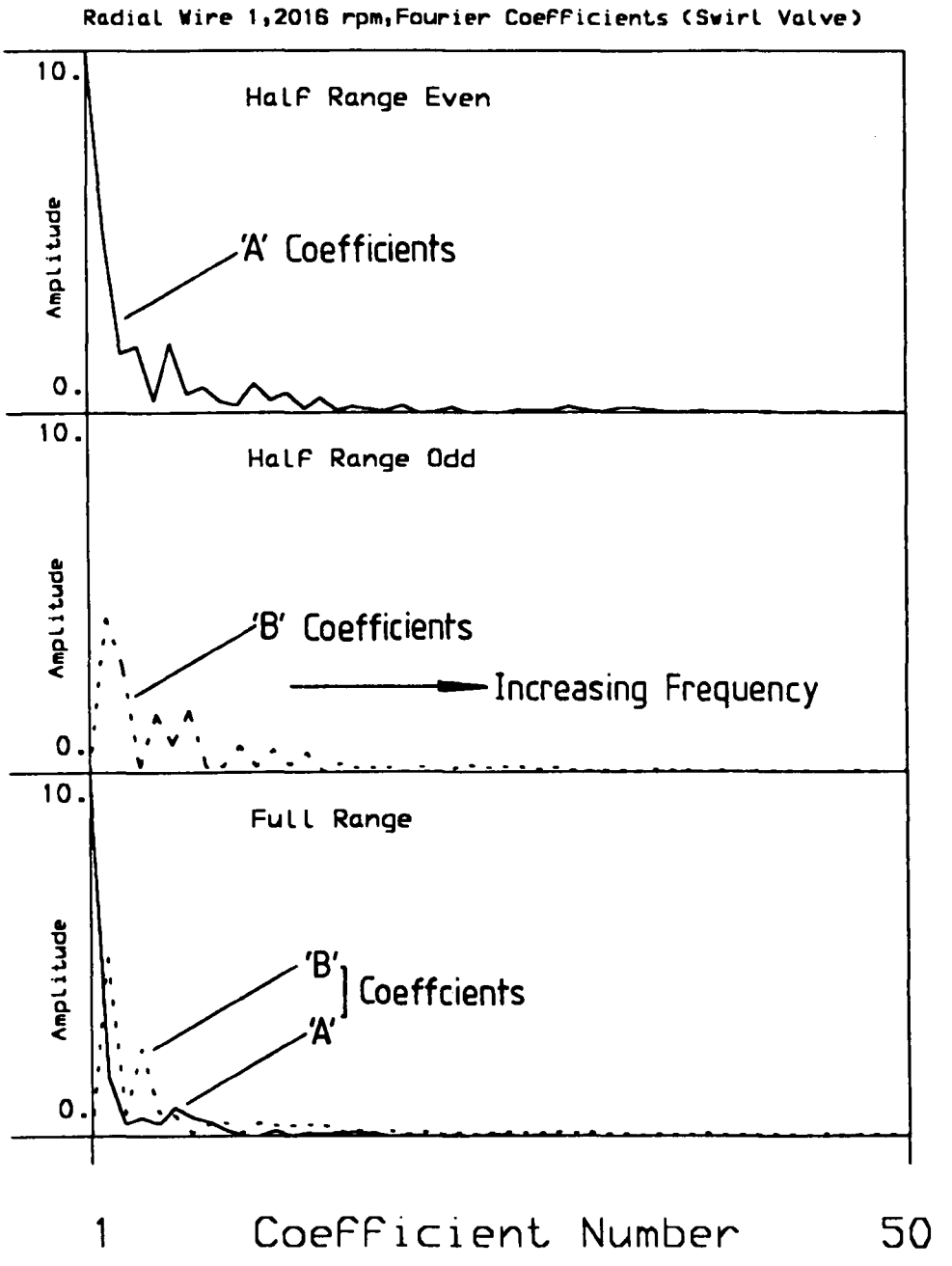

Figure 6.11

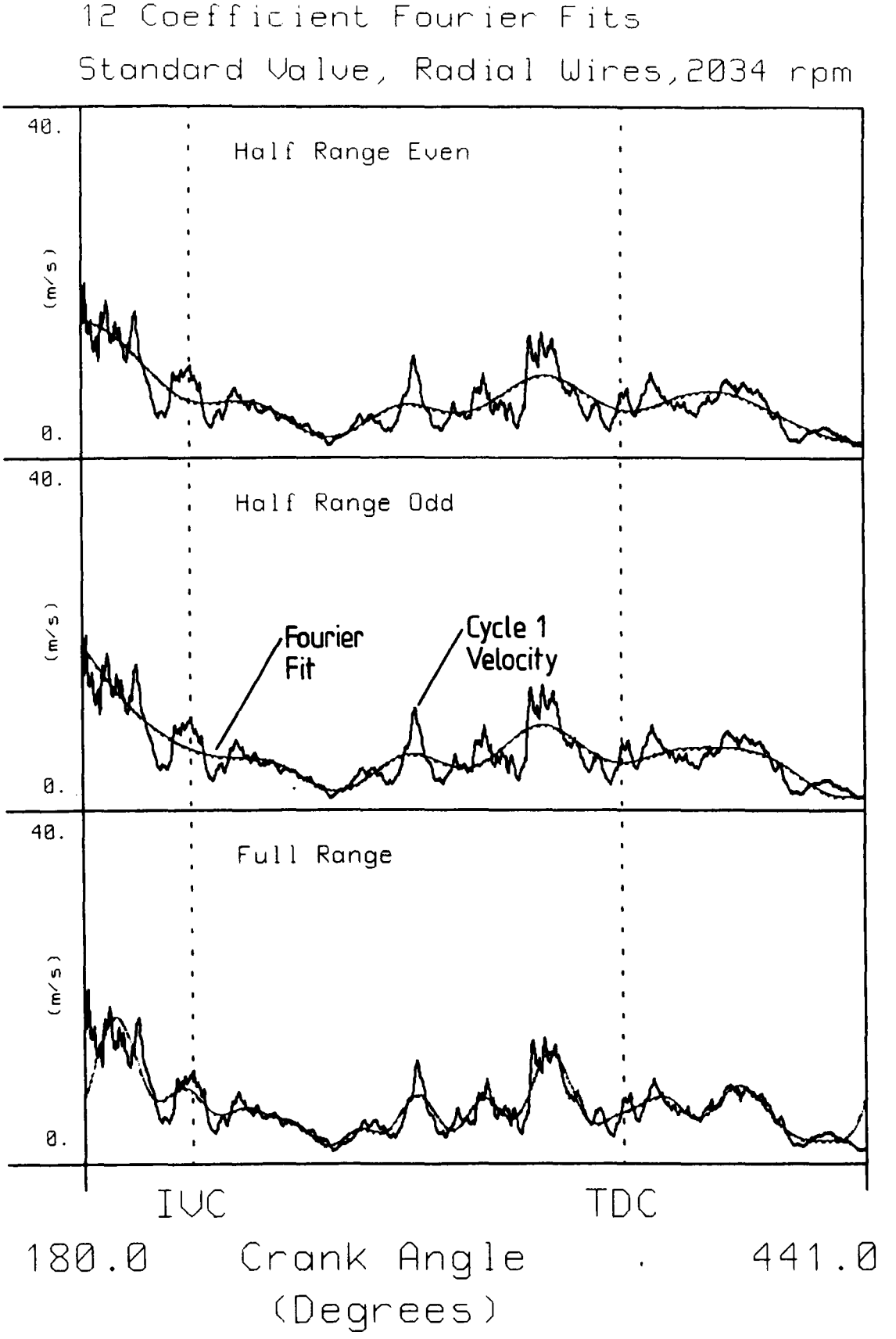
12 Coefficient Fourier Fits
Standard Valve, Radial Wires, 2034 rpm
40.
Half Range Even
(m/s)
0.
40.
Half Range Odd
(m/s)
Fourier Fit
Cycle 1 Velocity
0.
40.
Full Range
(m/s)
0.
IVC
TDC
180.0
Crank Angle
441.0
(Degrees)

Figure 6.12

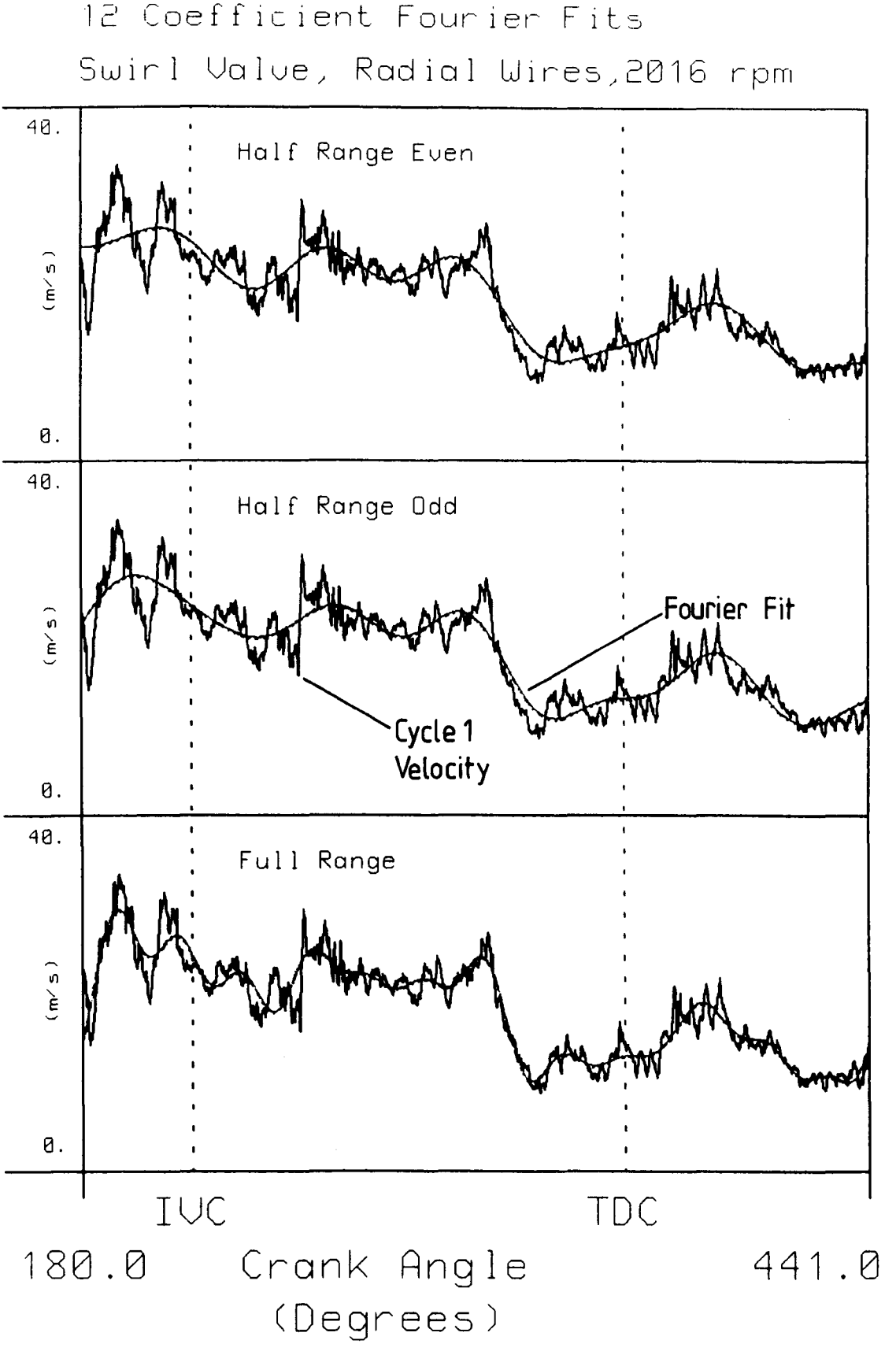
12 Coefficient Fourier Fits
Swirl Valve, Radial Wires, 2016 rpm
40.
(m/s)
0.
Half Range Even
40.
(m/s)
0.
Half Range Odd
Fourier Fit
Cycle 1
Velocity
40.
(m/s)
0.
Full Range
IVC
TDC
180.0
Crank Angle
(Degrees)
441.0

Figure 6.13

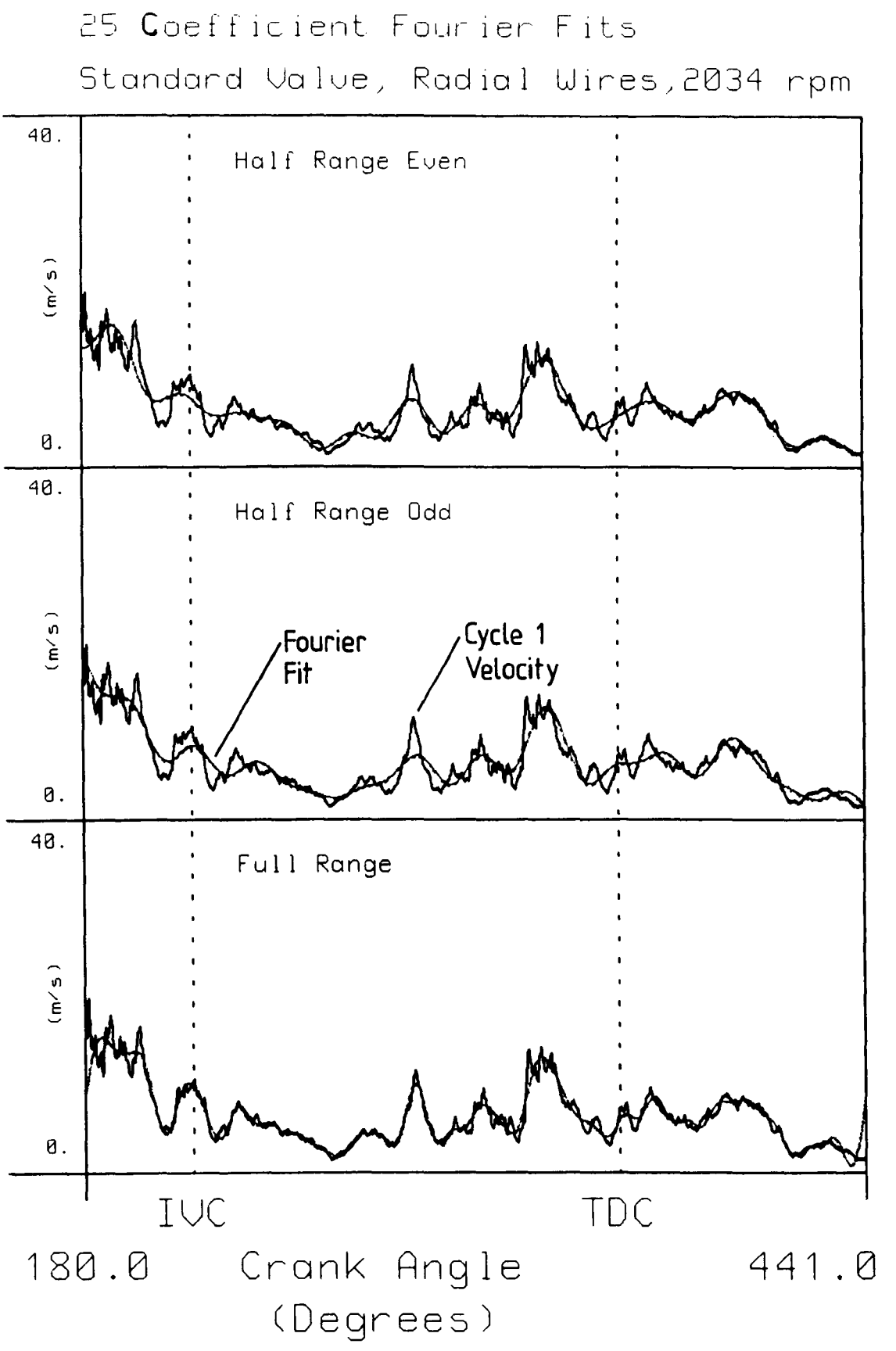
25 Coefficient Fourier Fits
Standard Valve, Radial Wires, 2034 rpm
40.
Half Range Even
(m/s)
0.
40.
Half Range Odd
(m/s)
Fourier Fit
Cycle 1 Velocity
0.
40.
Full Range
(m/s)
0.
IVC
TDC
180.0
Crank Angle
(Degrees)
441.0

Figure 6.14

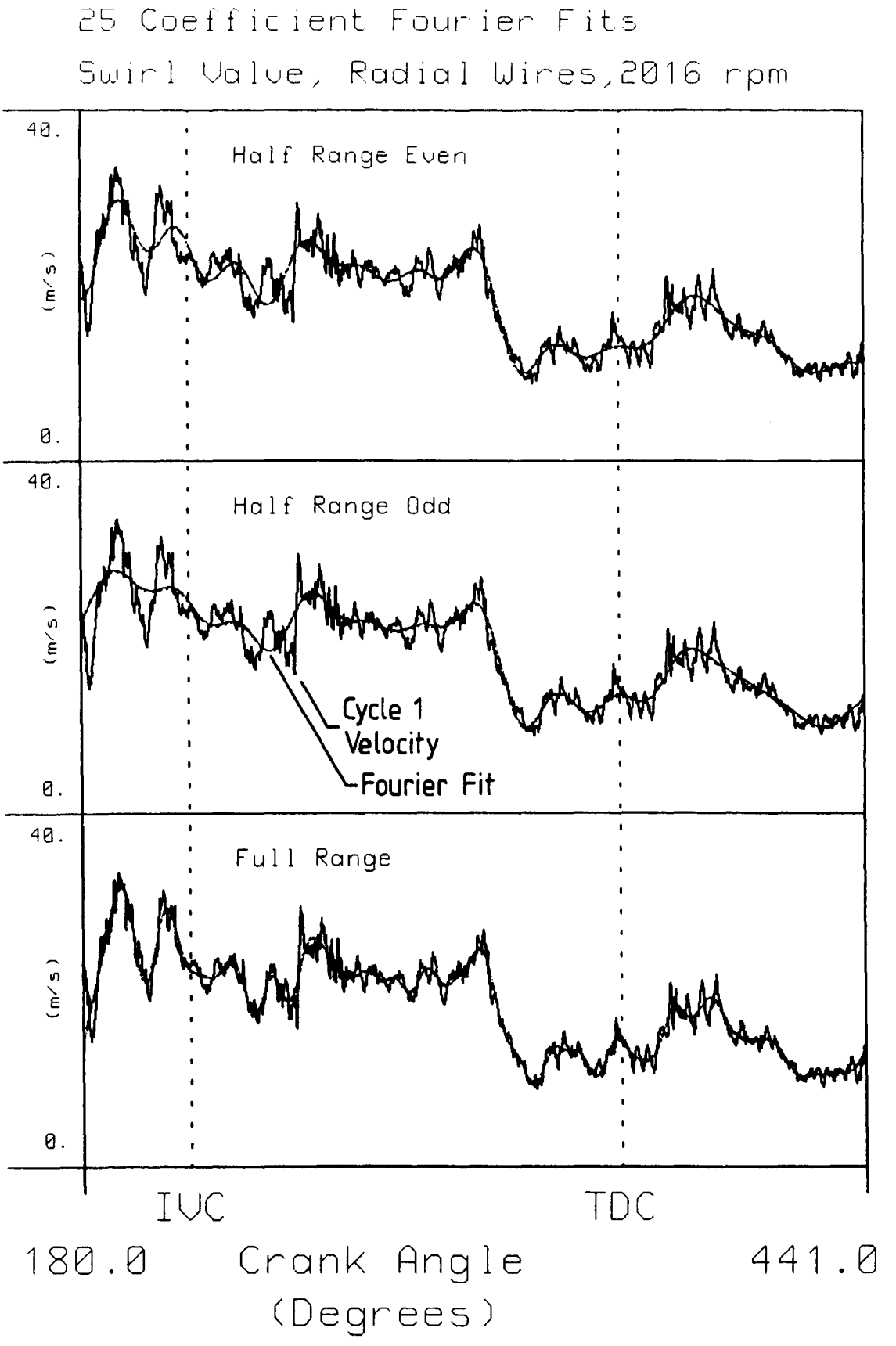
25 Coefficient Fourier Fits
Swirl Valve, Radial Wires, 2016 rpm
40.
Half Range Even
(m/s)
0.
40.
Half Range Odd
(m/s)
Cycle 1
Velocity
Fourier Fit
0.
40.
Full Range
(m/s)
0.
IVC
TDC
180.0
Crank Angle
(Degrees)
441.0

Figure 6.15

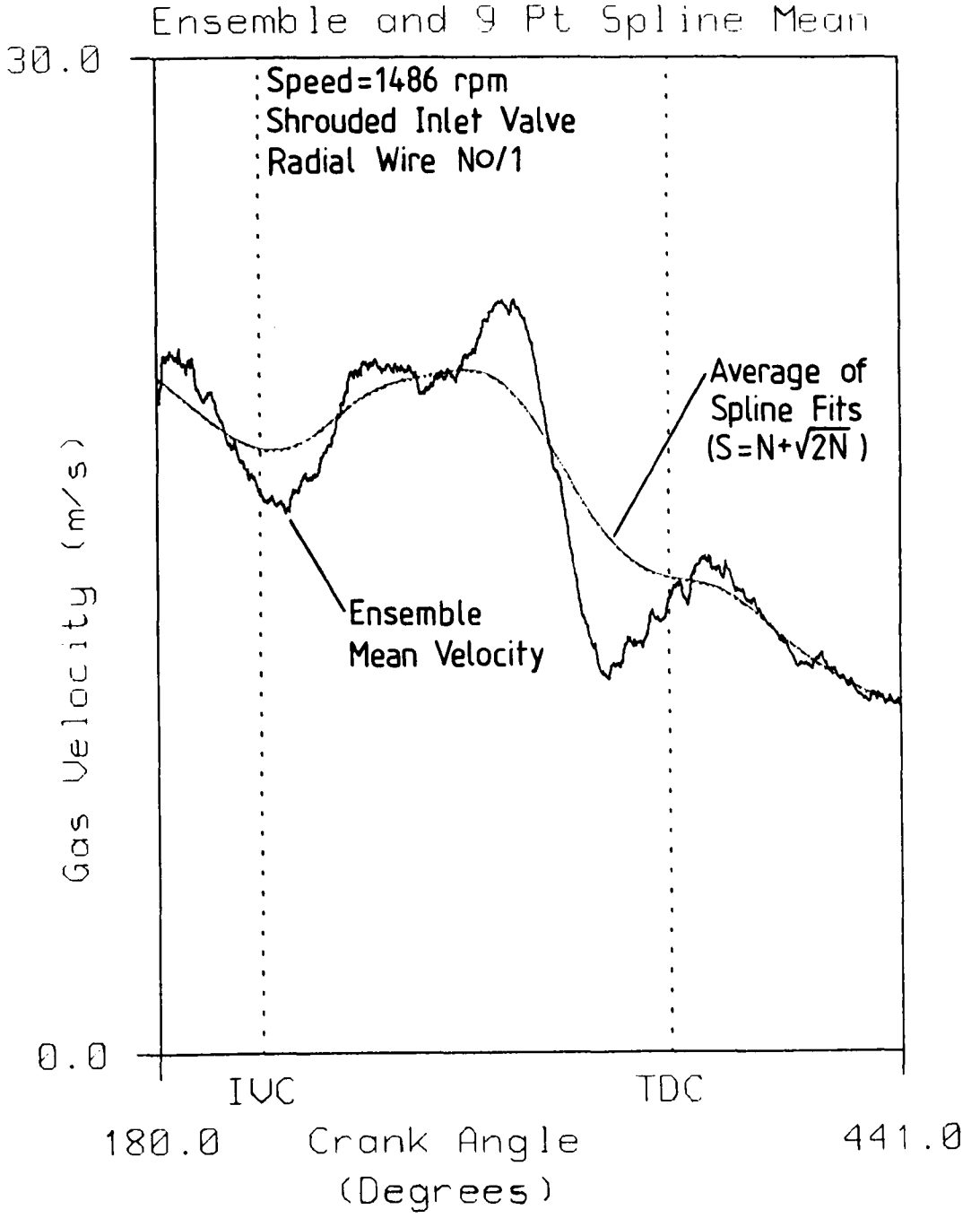

Figure 6.16 A Comparison Between Ensemble and Averaged CBC Mean Velocity Plots (Maximum Smoothing).

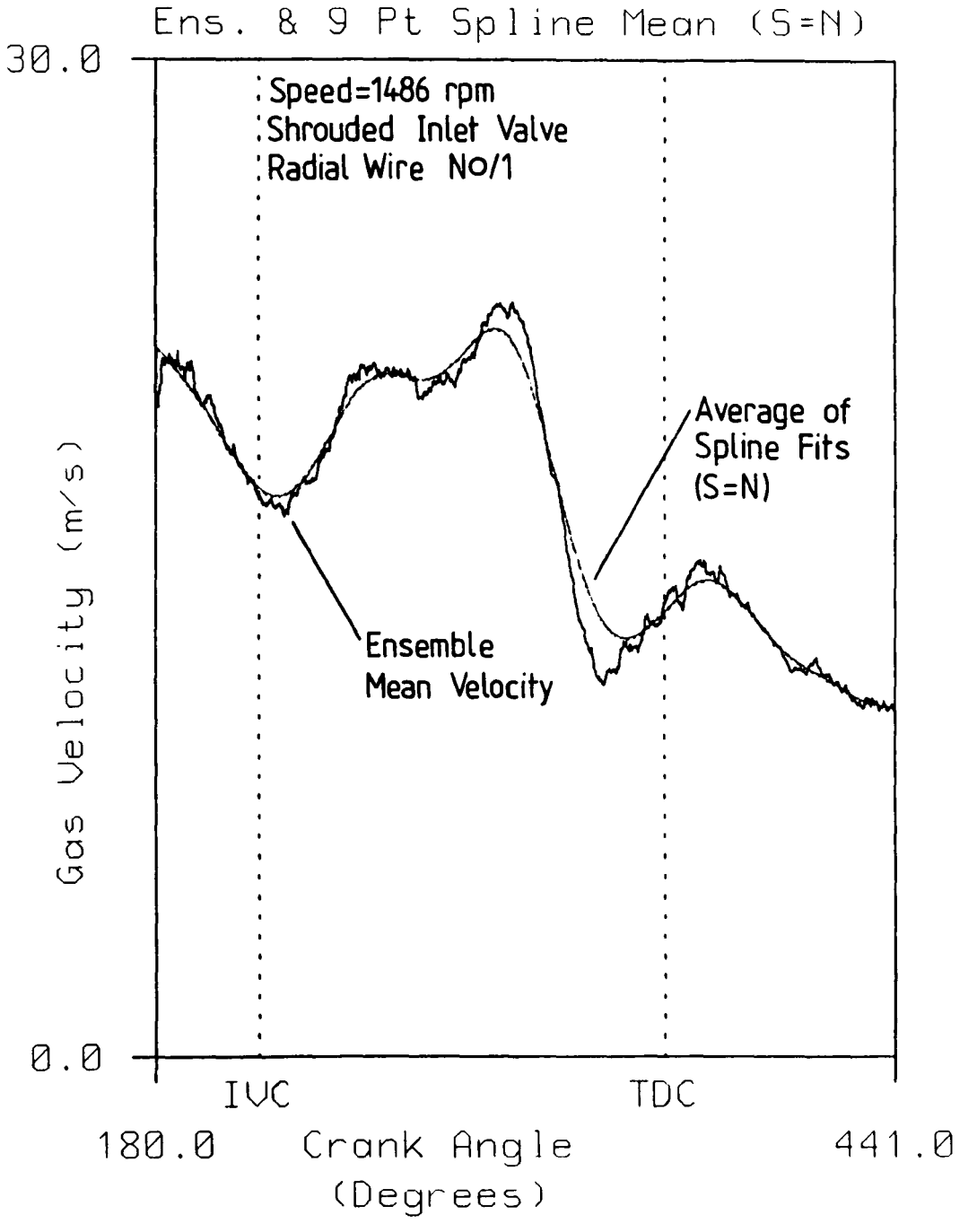

Figure 6.17 A Comparison Between Ensemble and Averaged CBC Mean Velocity Plots (Medium Smoothing).

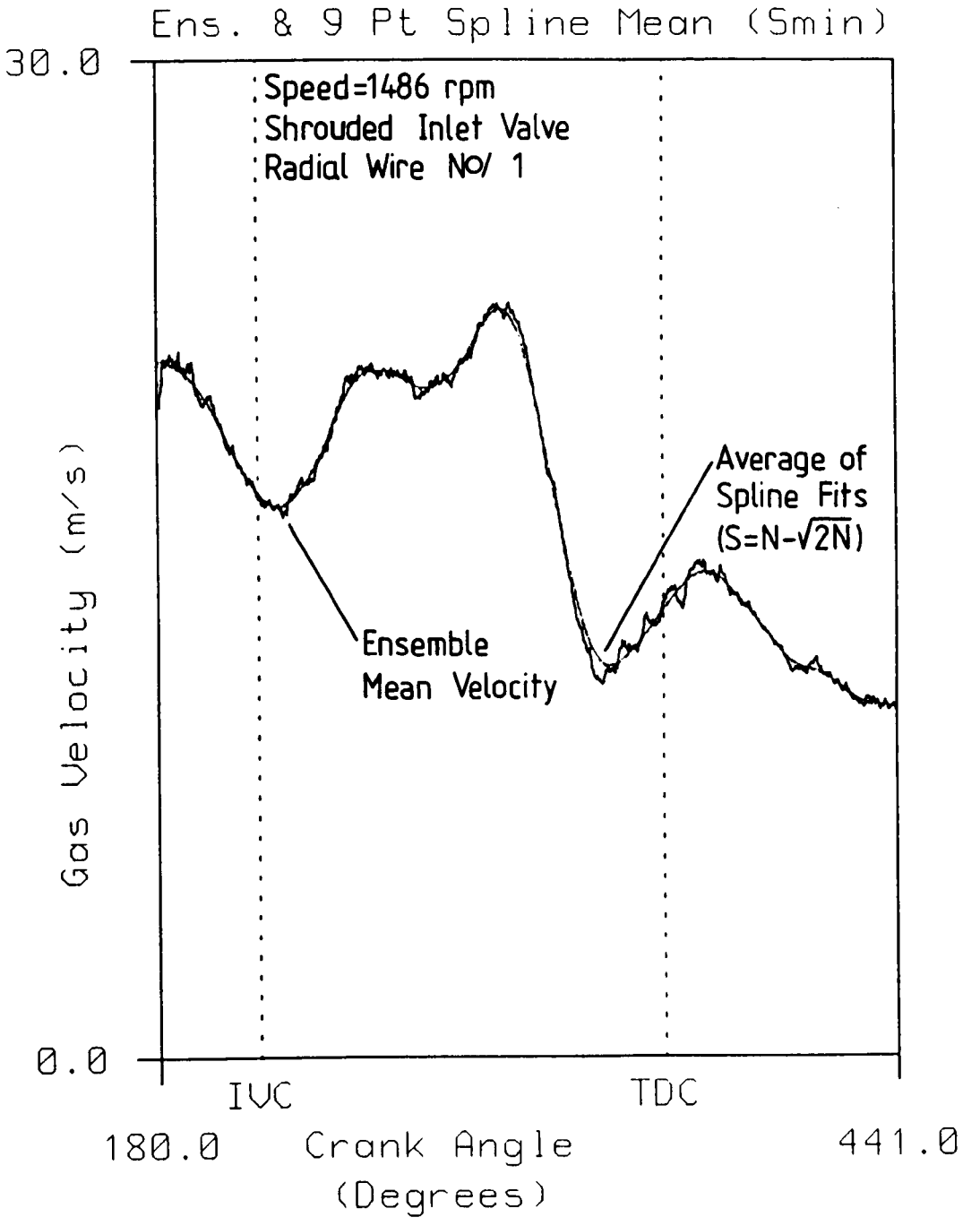

Figure 6.18 A Comparison Between Ensemble and Averaged CBC Mean Velocity Plots (Minimum Smoothing).

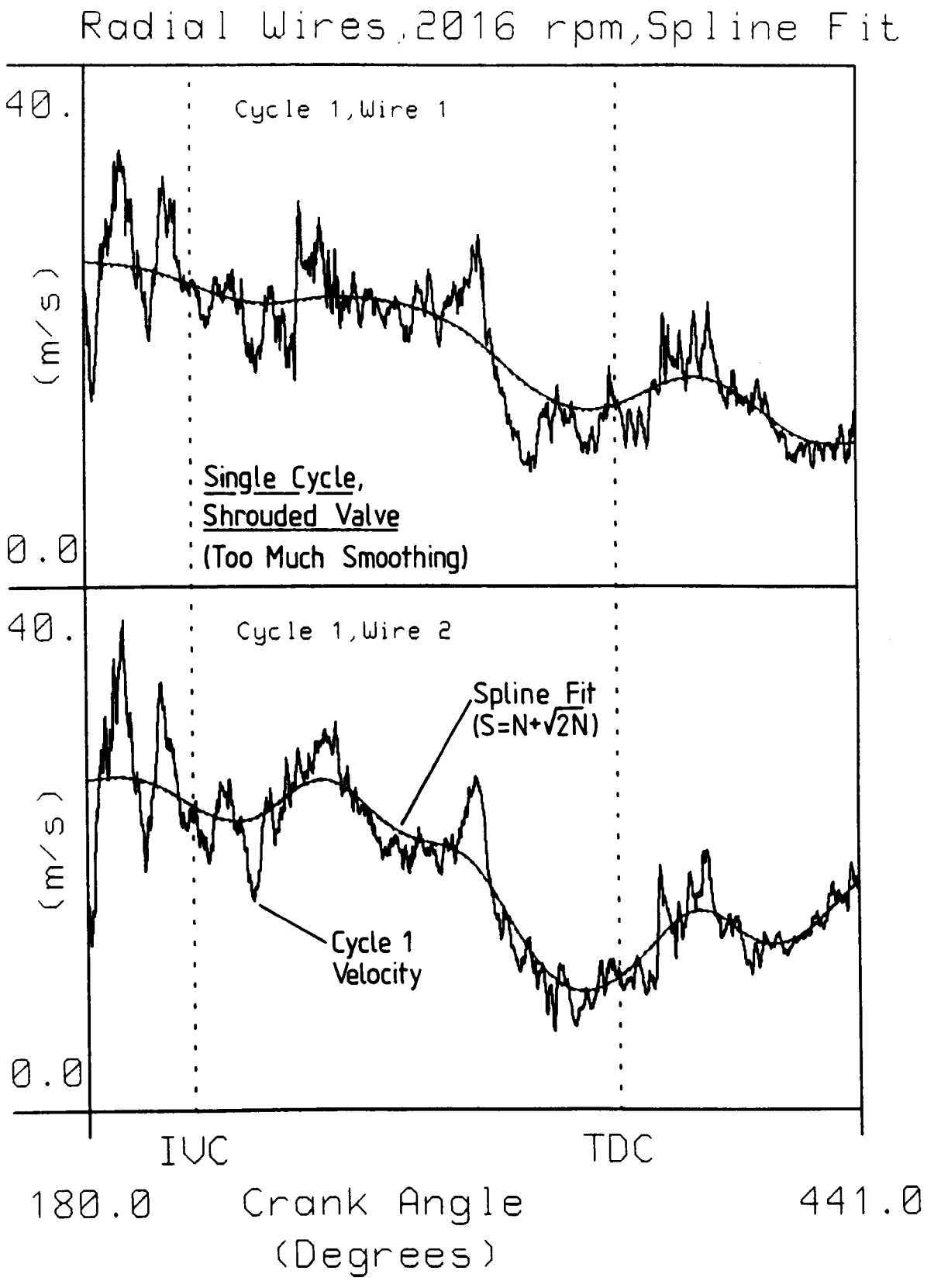
Radial Wires, 2016 rpm, Spline Fit
40.
Cycle 1, Wire 1
(m/s)
Single Cycle,
Shrouded Valve
(Too Much Smoothing)
0.0
40.
Cycle 1, Wire 2
Spline Fit
(S=N+√2N)
(m/s)
Cycle 1
Velocity
0.0
IVC
TDC
180.0
Crank Angle
(Degrees)
441.0

Figure 6.19

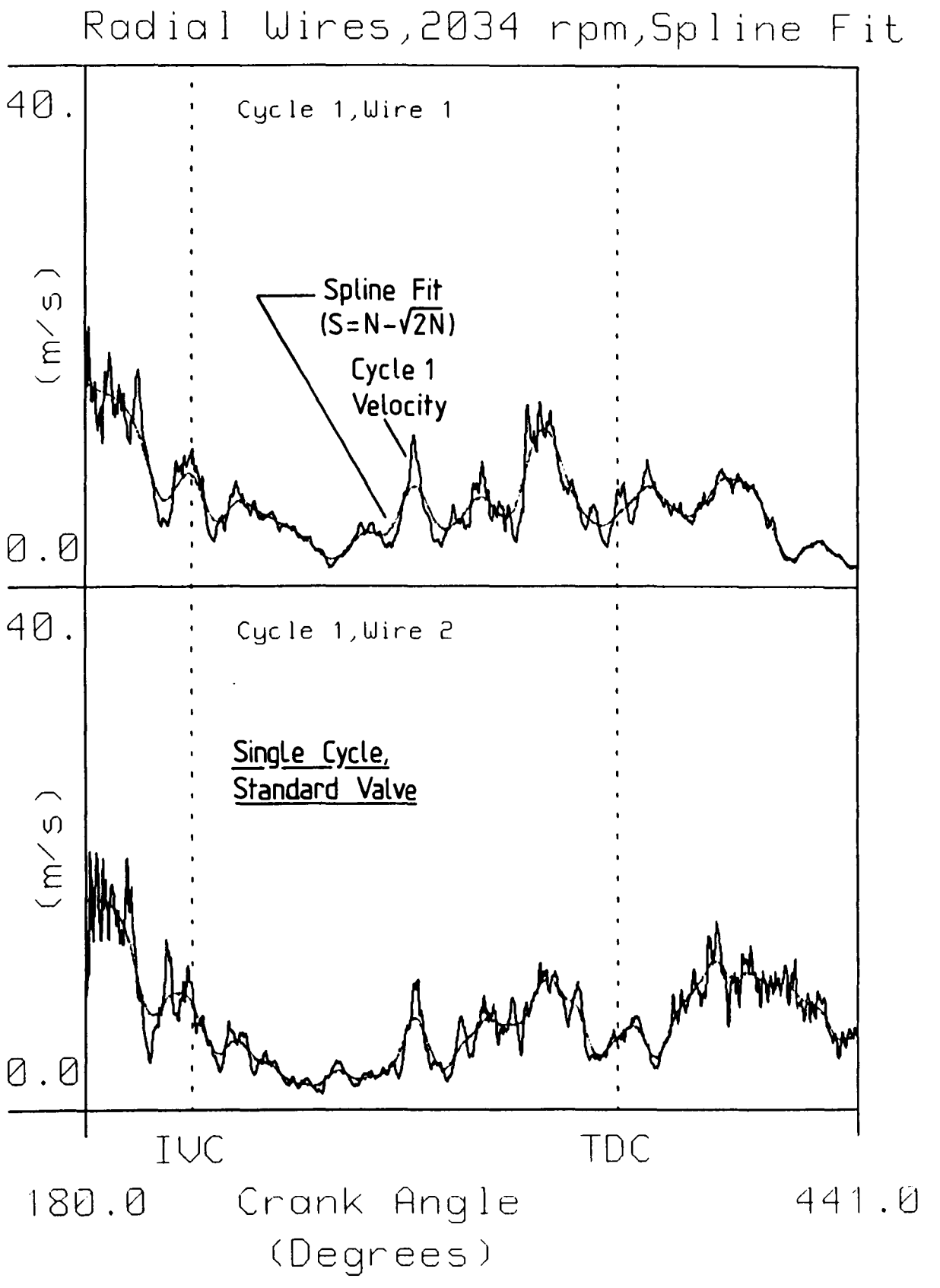
Radial Wires, 2034 rpm, Spline Fit
40.
Cycle 1, Wire 1
(m/s)
Spline Fit
(S=N-√2N)
Cycle 1
Velocity
0.0
40.
Cycle 1, Wire 2
Single Cycle,
Standard Valve
(m/s)
0.0
IVC
TDC
180.0
Crank Angle
(Degrees)
441.0

Figure 6.20

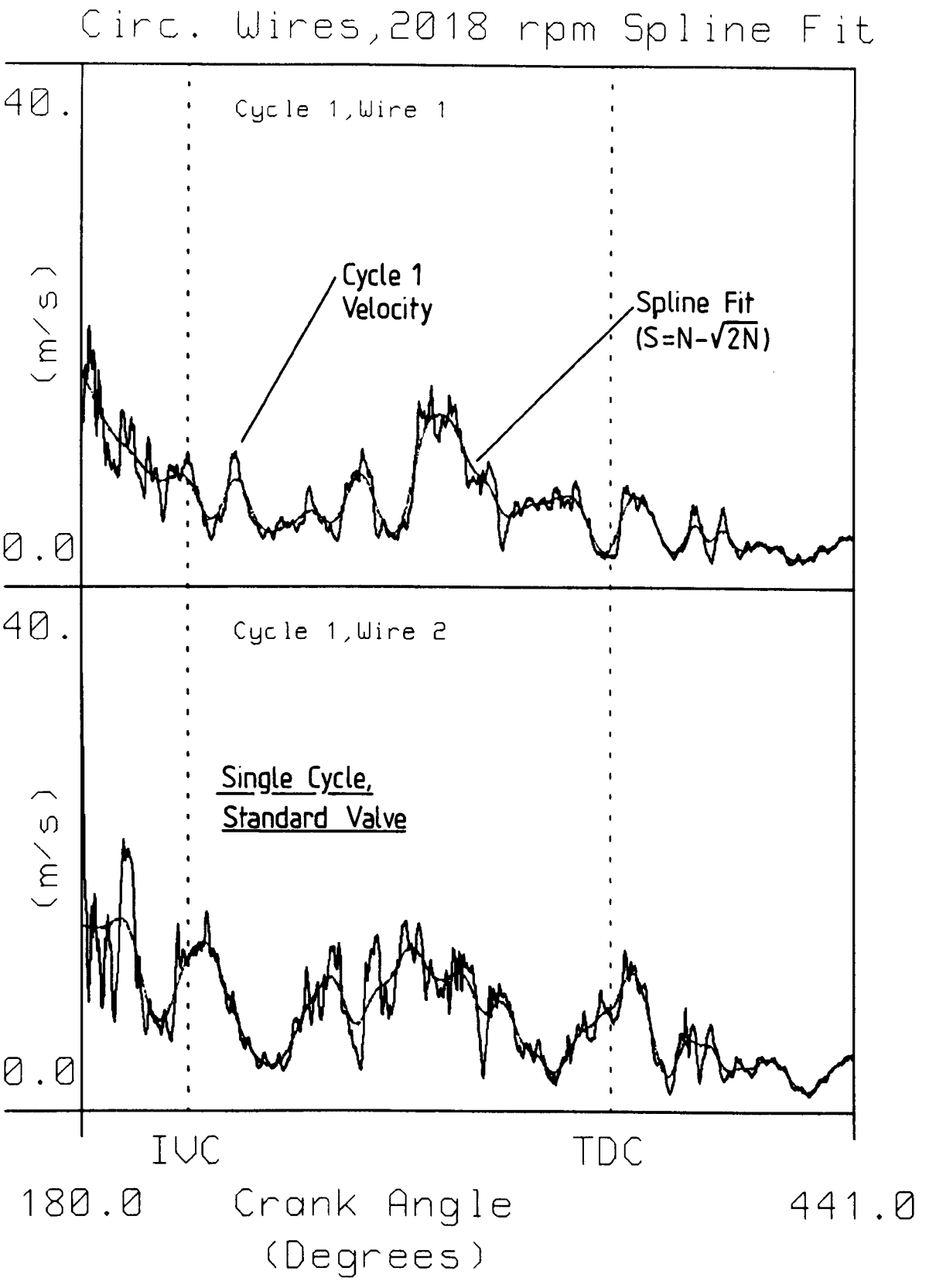
Circ. Wires, 2018 rpm Spline Fit
40.
Cycle 1, Wire 1
(m/s)
Cycle 1
Velocity
Spline Fit
(S=N-√2N)
0.0
40.
Cycle 1, Wire 2
Single Cycle,
Standard Valve
(m/s)
0.0
IVC
TDC
180.0
Crank Angle
(Degrees)
441.0

Figure 6.21

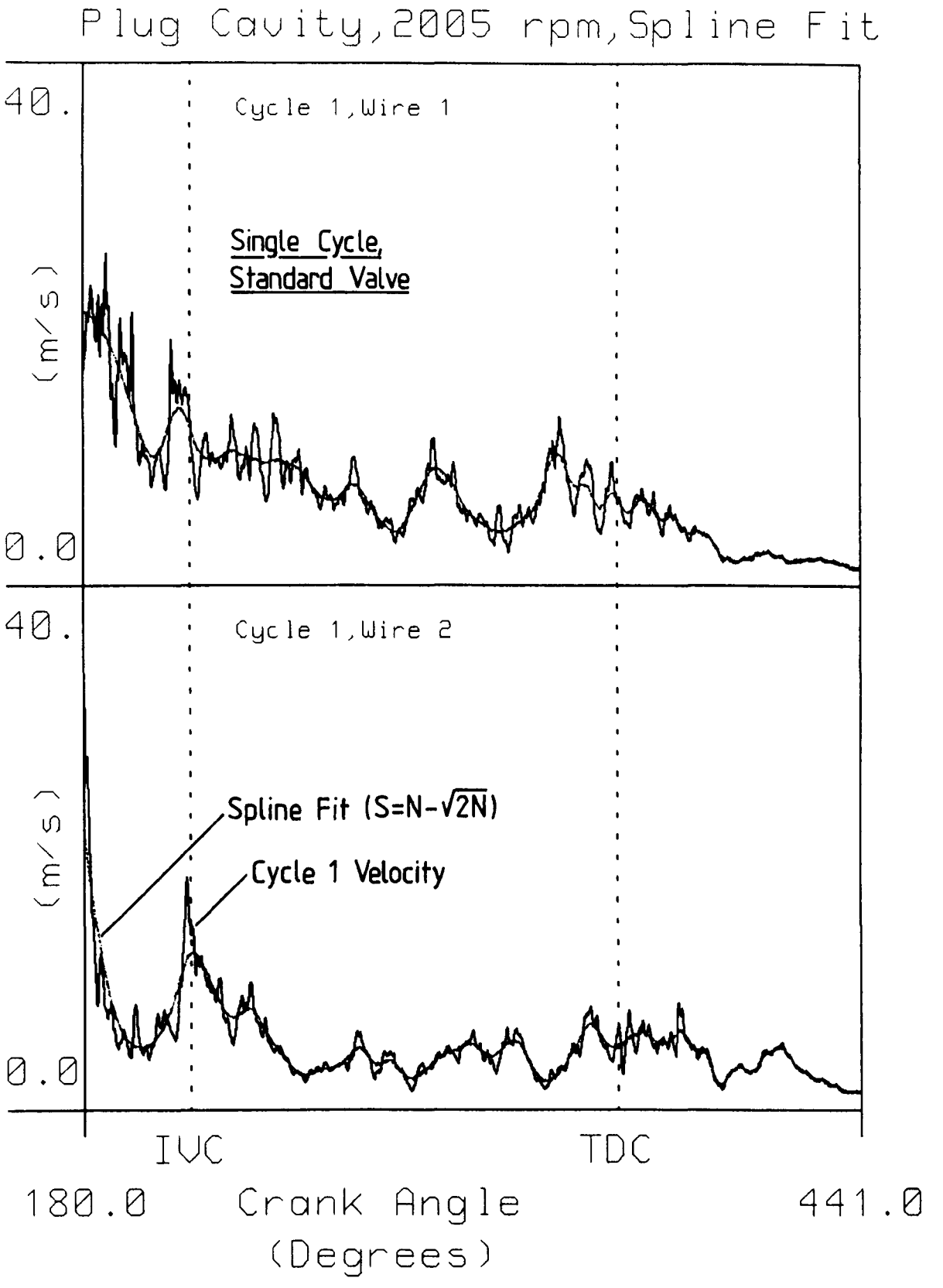
Plug Cavity, 2005 rpm, Spline Fit
40.
Cycle 1, Wire 1
Single Cycle,
Standard Valve
(m/s)
0.0
40.
Cycle 1, Wire 2
Spline Fit (S=N-√2N)
Cycle 1 Velocity
(m/s)
0.0
IVC
TDC
180.0
Crank Angle
(Degrees)
441.0

Figure 6.22

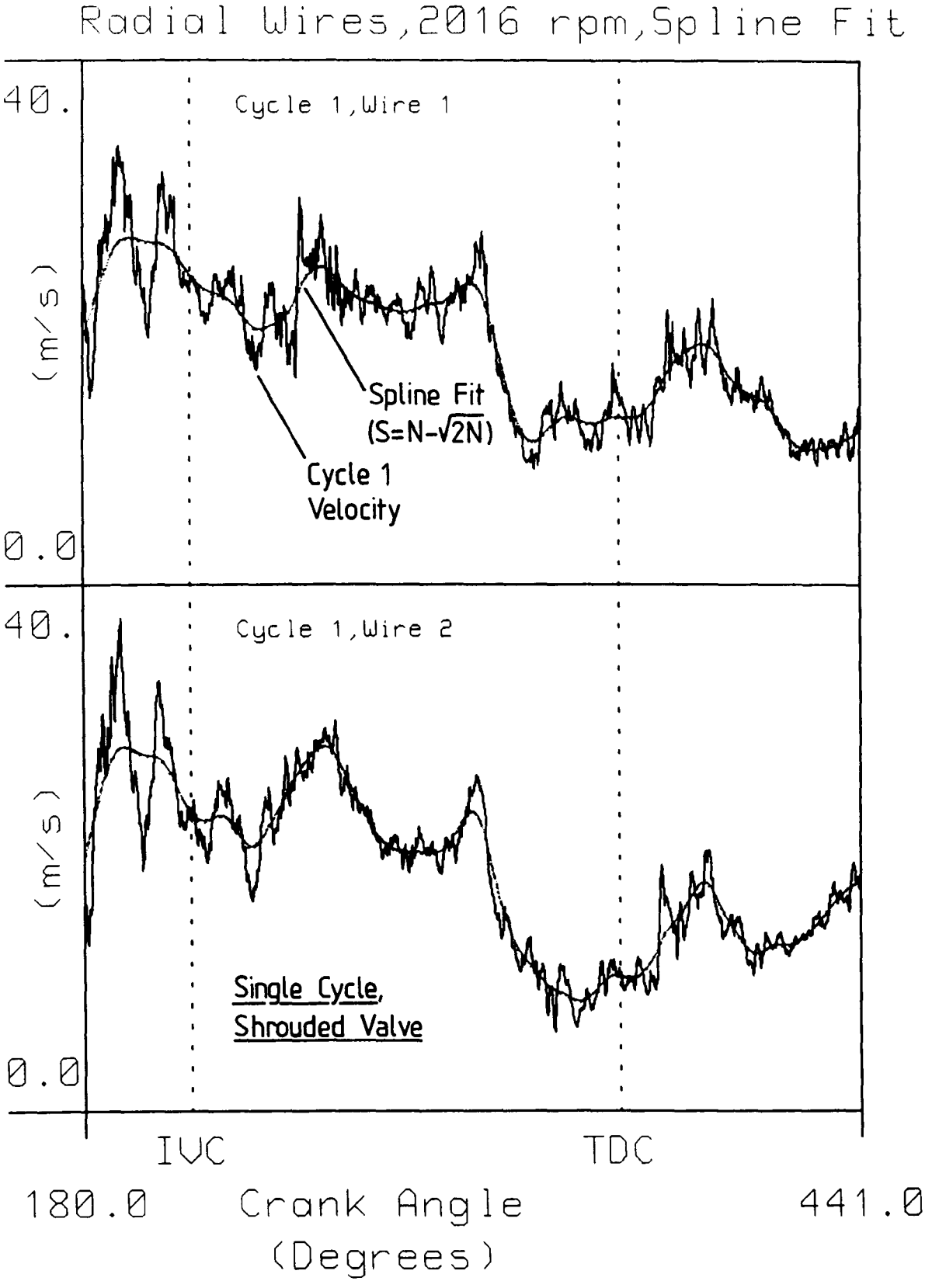
Radial Wires, 2016 rpm, Spline Fit
40.
Cycle 1, Wire 1
(m/s)
Spline Fit
(S=N-√2N)
Cycle 1
Velocity
0.0
40.
Cycle 1, Wire 2
(m/s)
Single Cycle,
Shrouded Valve
0.0
IVC
TDC
180.0
Crank Angle
(Degrees)
441.0

Figure 6.23

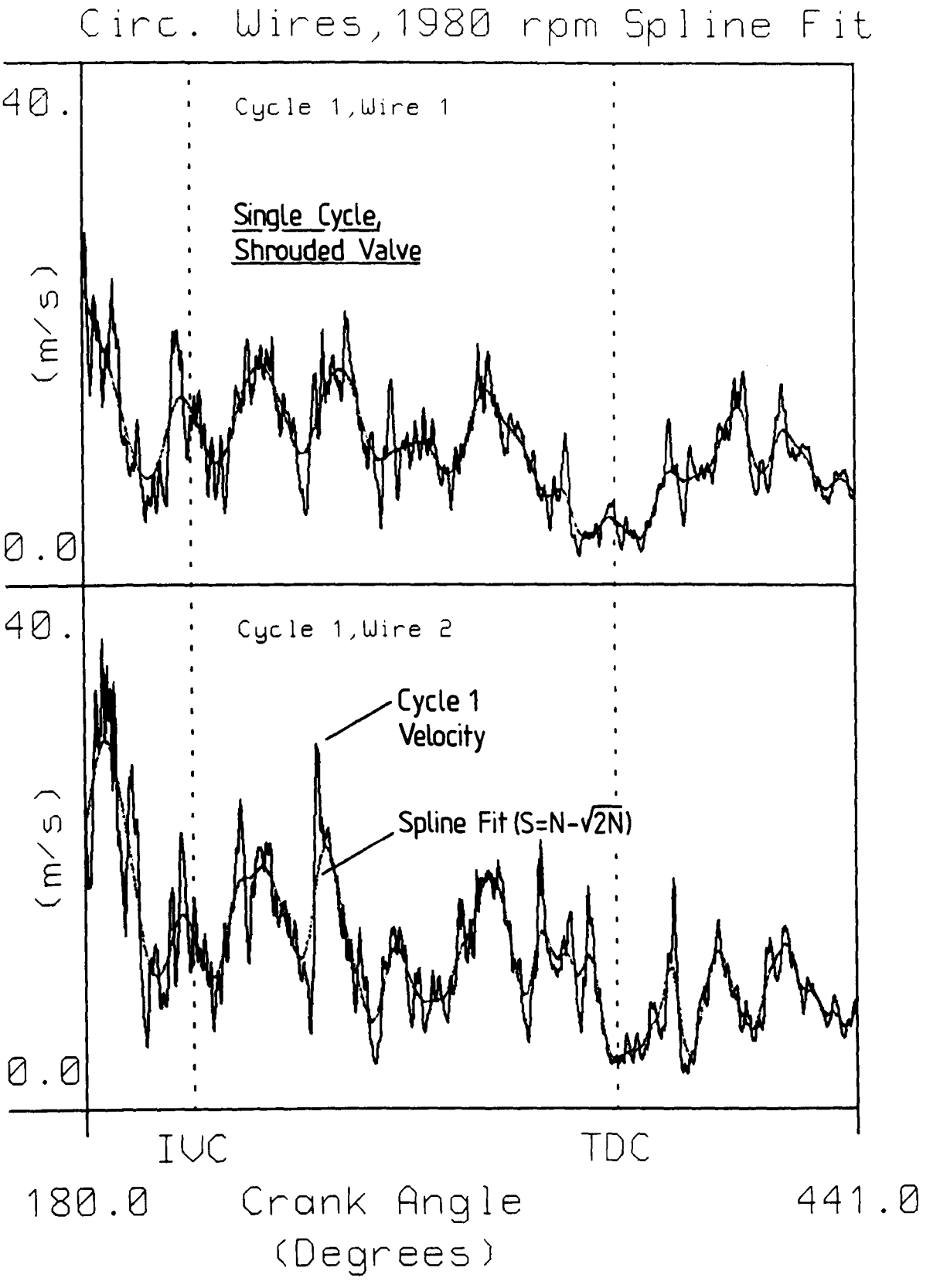
Circ. Wires, 1980 rpm Spline Fit
40.
Cycle 1, Wire 1
Single Cycle,
Shrouded Valve
(m/s)
0.0
40.
Cycle 1, Wire 2
Cycle 1
Velocity
Spline Fit (S=N-√2N)
(m/s)
0.0
IVC
TDC
180.0
Crank Angle
(Degrees)
441.0

Figure 6.24

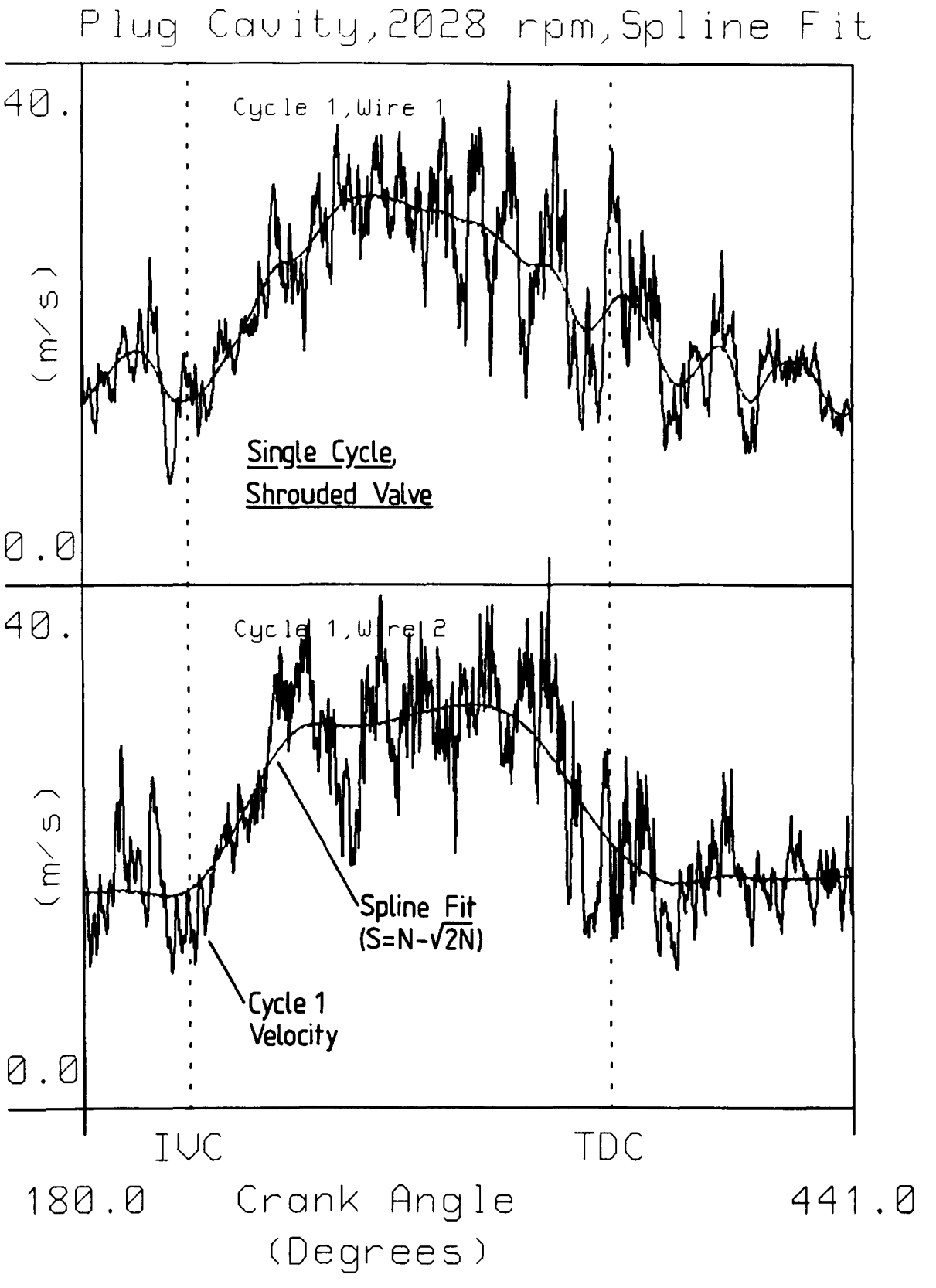
Plug Cavity, 2028 rpm, Spline Fit
40.
Cycle 1, Wire 1
(m/s)
Single Cycle,
Shrouded Valve
0.0
40.
Cycle 1, Wire 2
(m/s)
Spline Fit
(S=N-√2N)
Cycle 1
Velocity
0.0
IVC
TDC
180.0
Crank Angle
(Degrees)
441.0

Figure 6.25

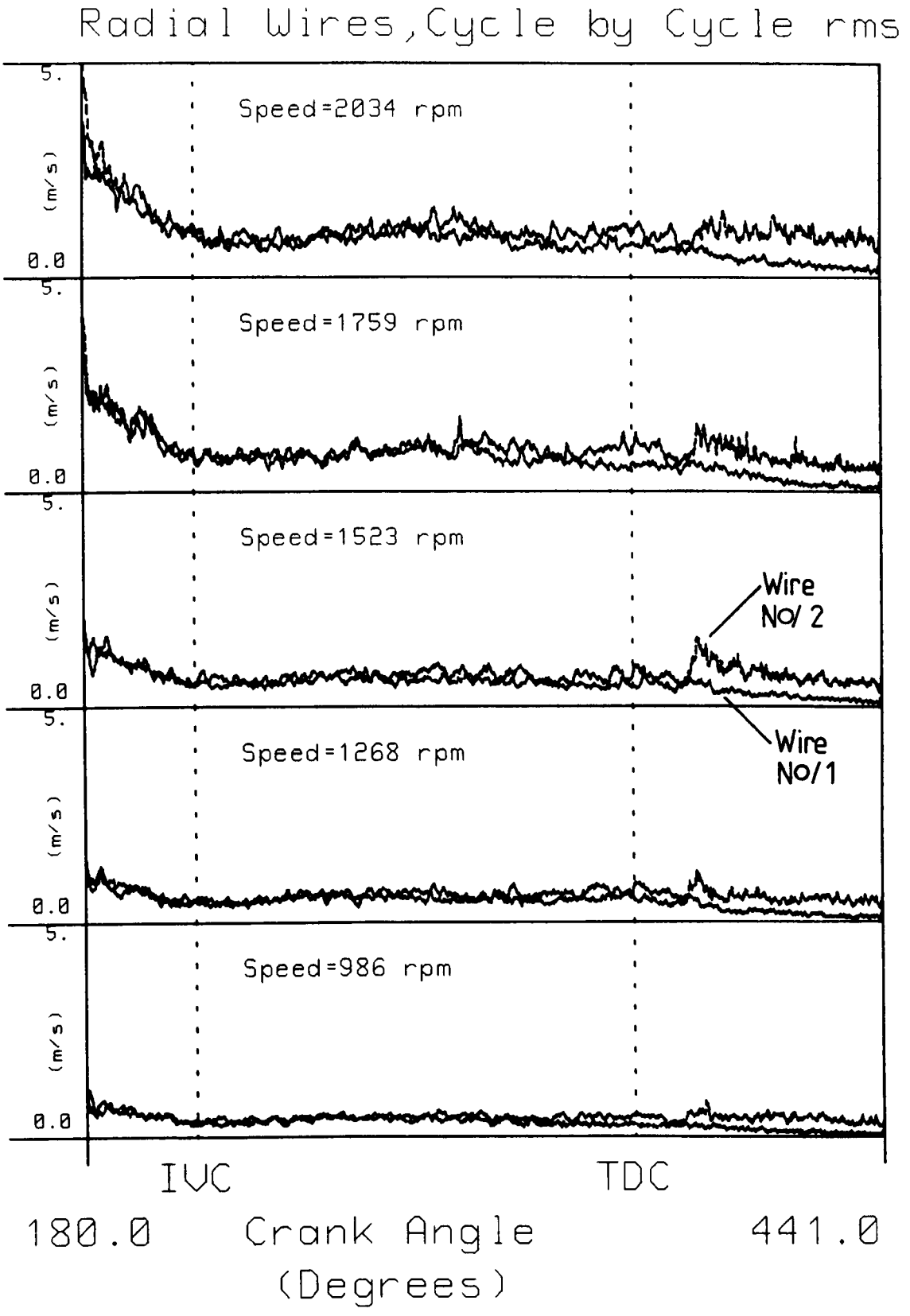

Figure 6.26 Phase Averaged CBC Turbulence Intensity Plots (Standard Valve)

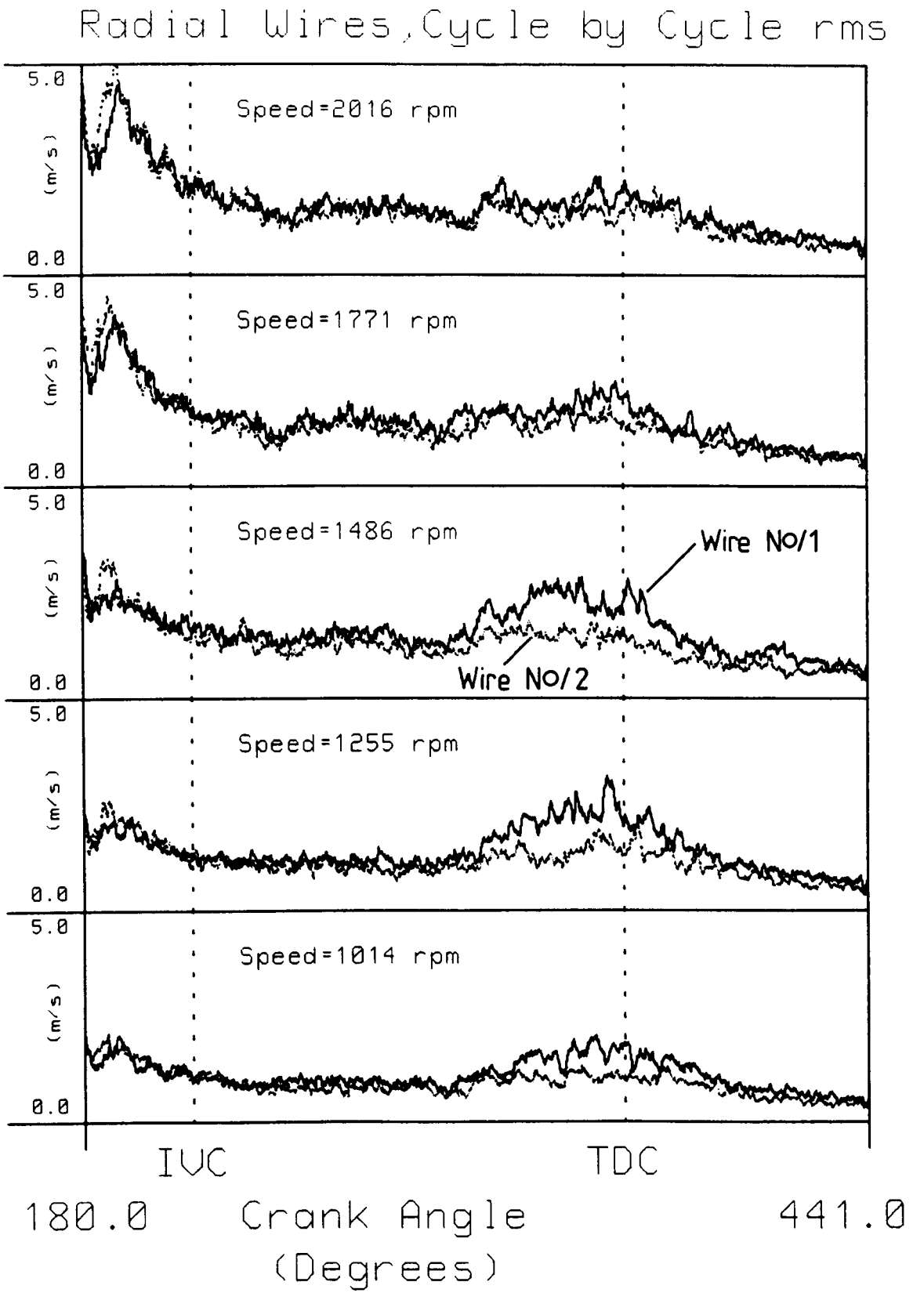

Figure 6.27 Phase Averaged CBC Turbulence Intensity Plots (Shrouded Valve)

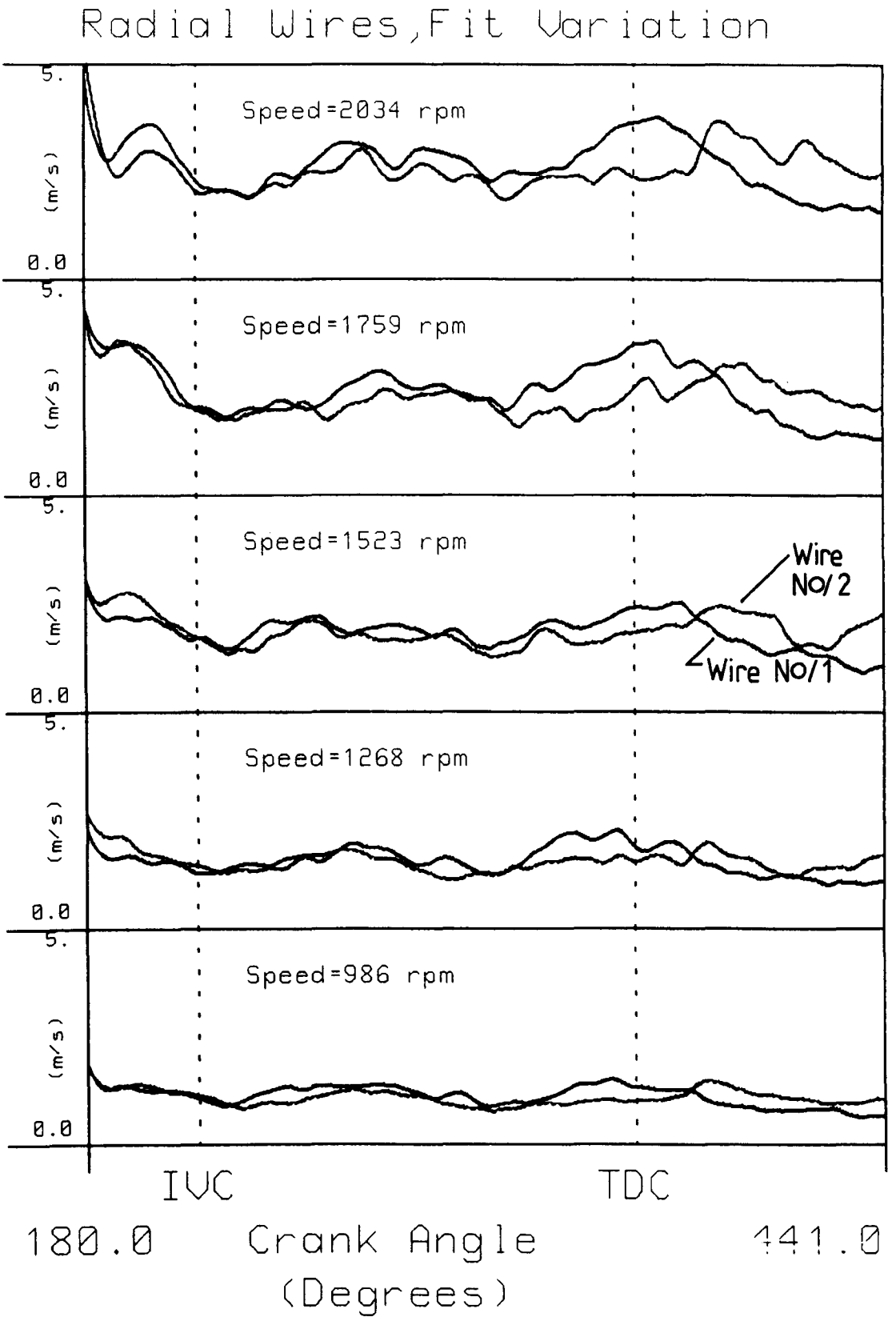

Figure 6.28 Phase Averaged CBC Mean Variation (Standard Valve)

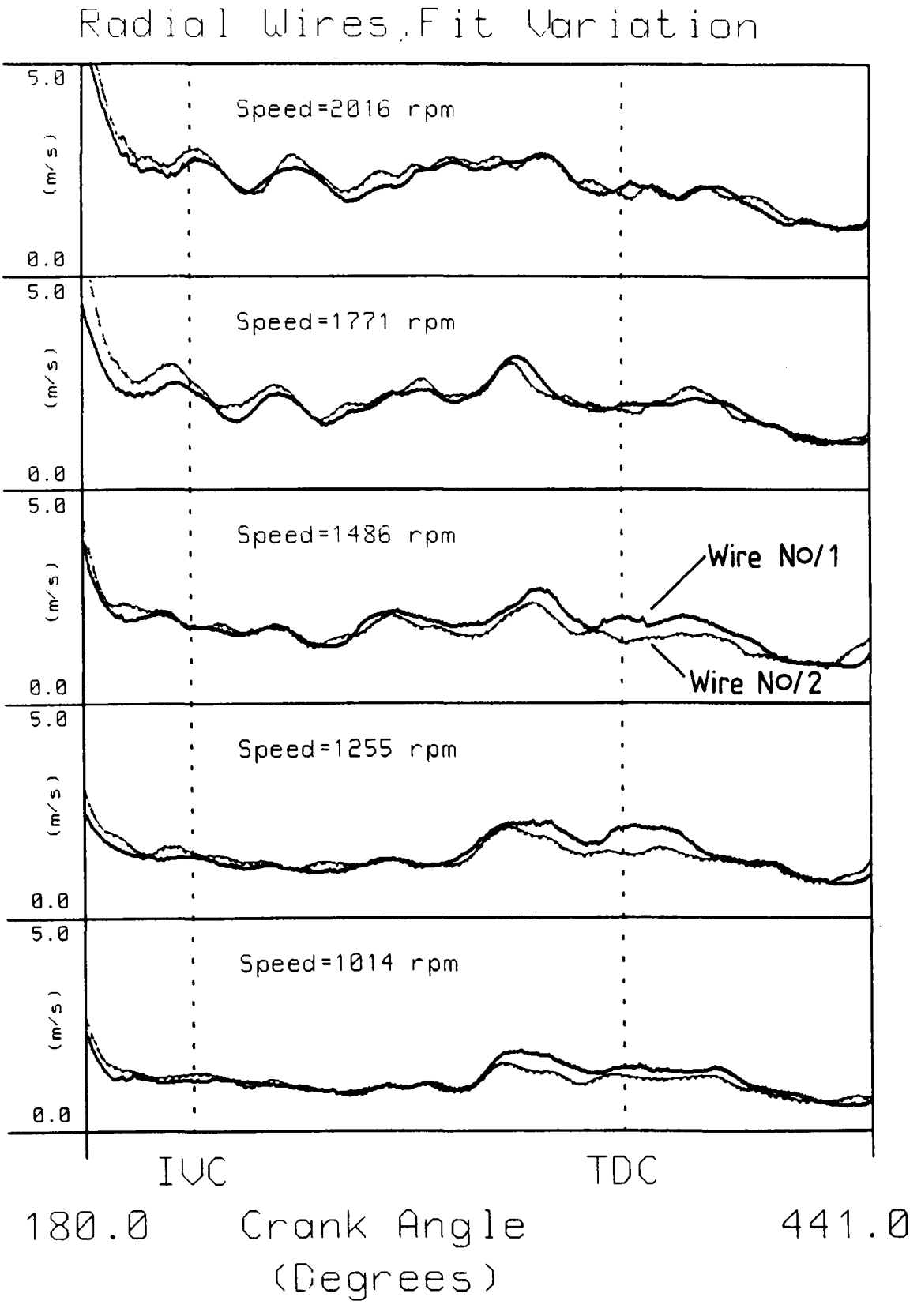

Figure 6.29 Phase Averaged CBC Mean Variation (Shrouded Valve)

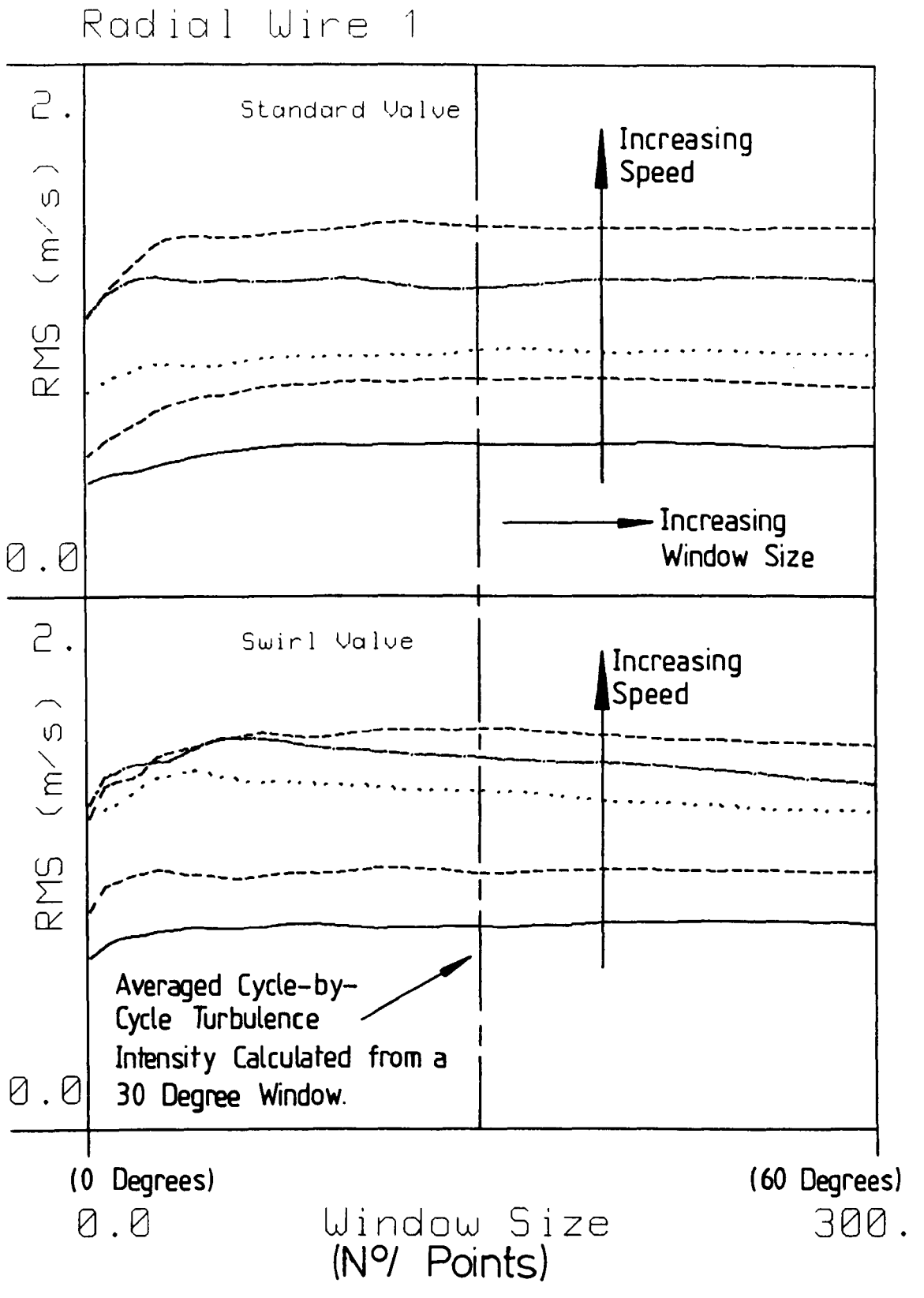

Figure 6.30 Time Averaged CBC Turbulence Intensities as a Function of Window Size (Centred 90° BTDC).

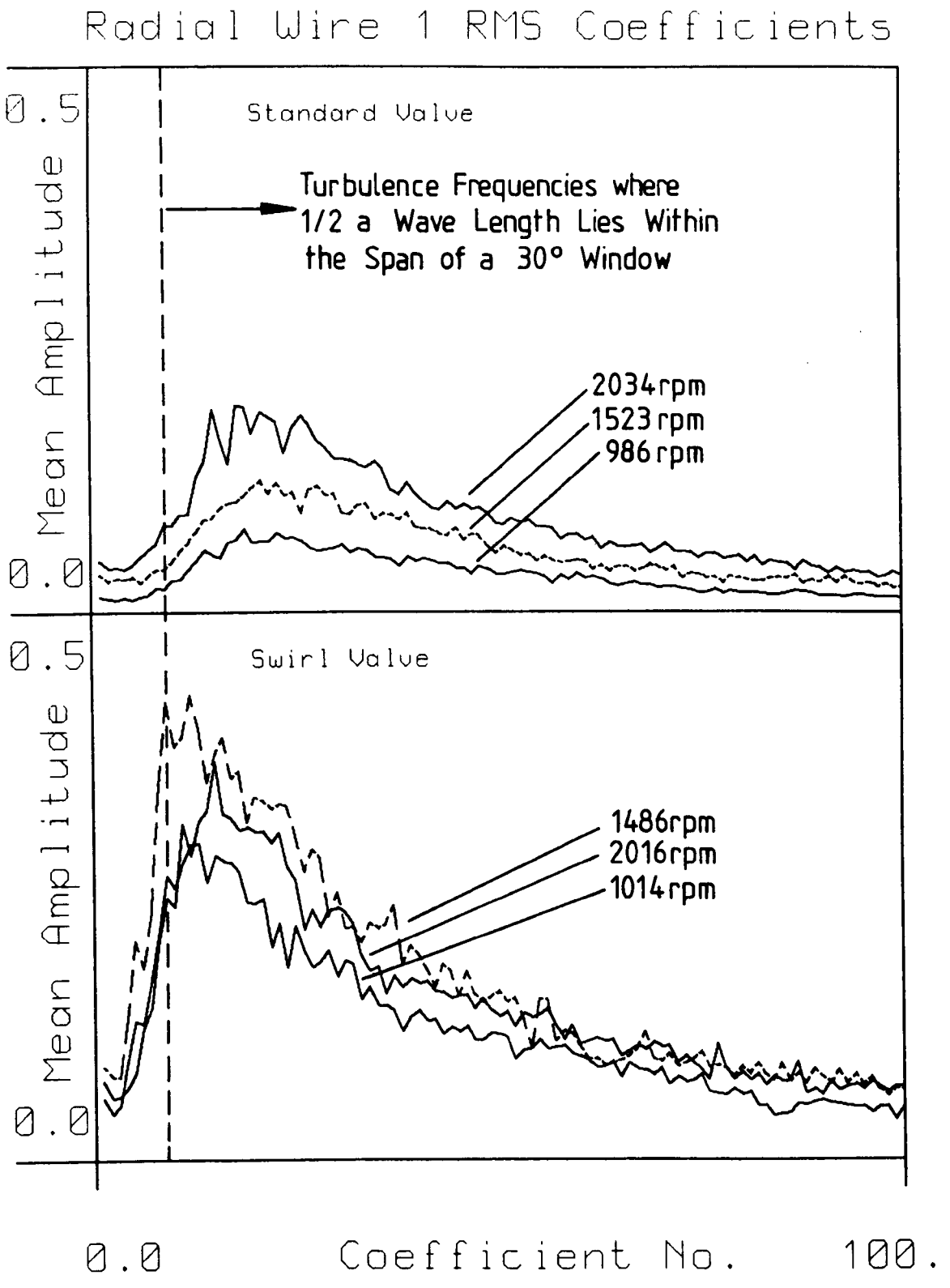

Figure 6.31 Fourier Analysis of CBC Turbulence Frequencies.

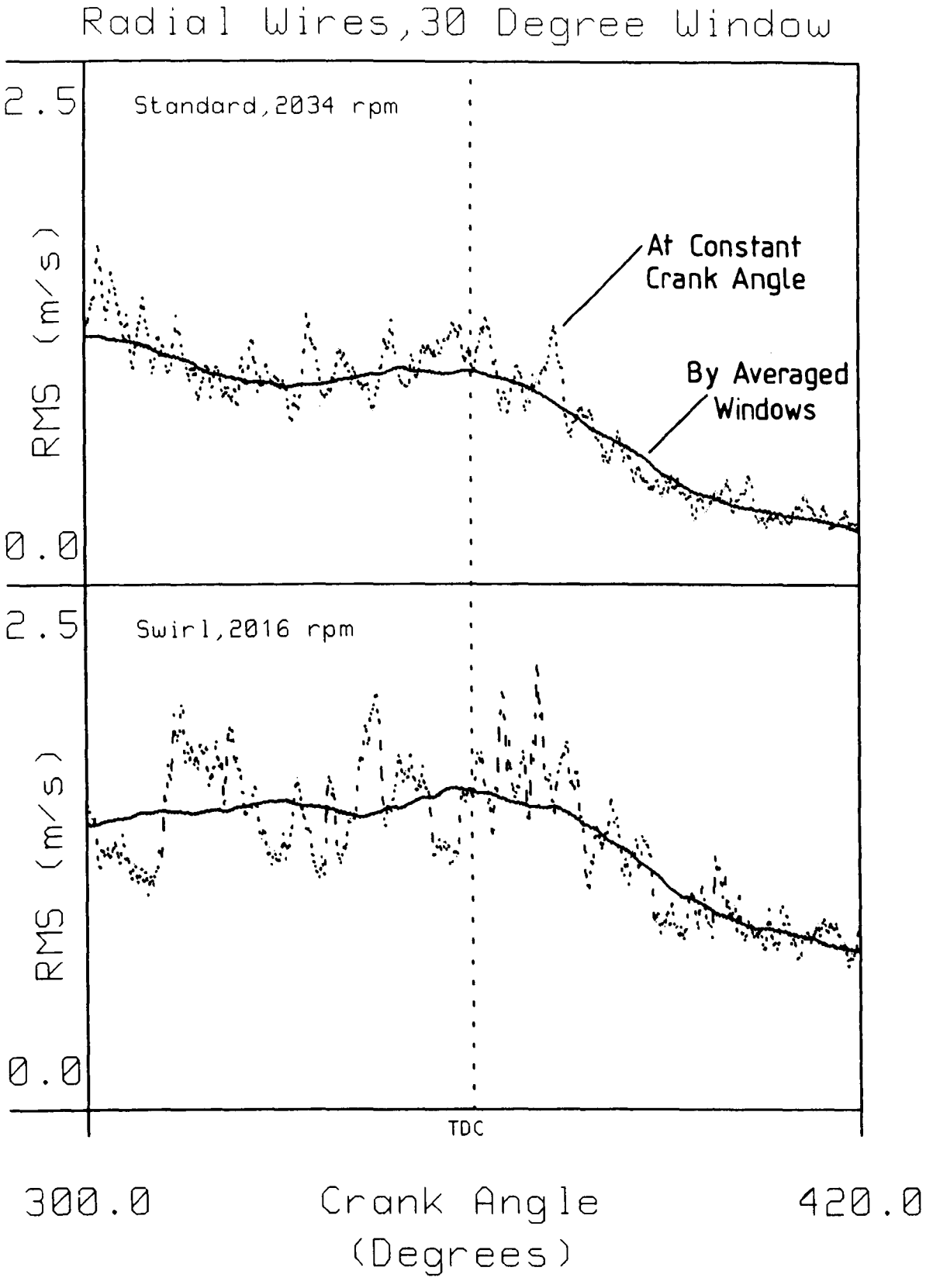

Figure 6.32 A Comparison Between Phase Averaged and Averaged Window CBC Intensity Plots.

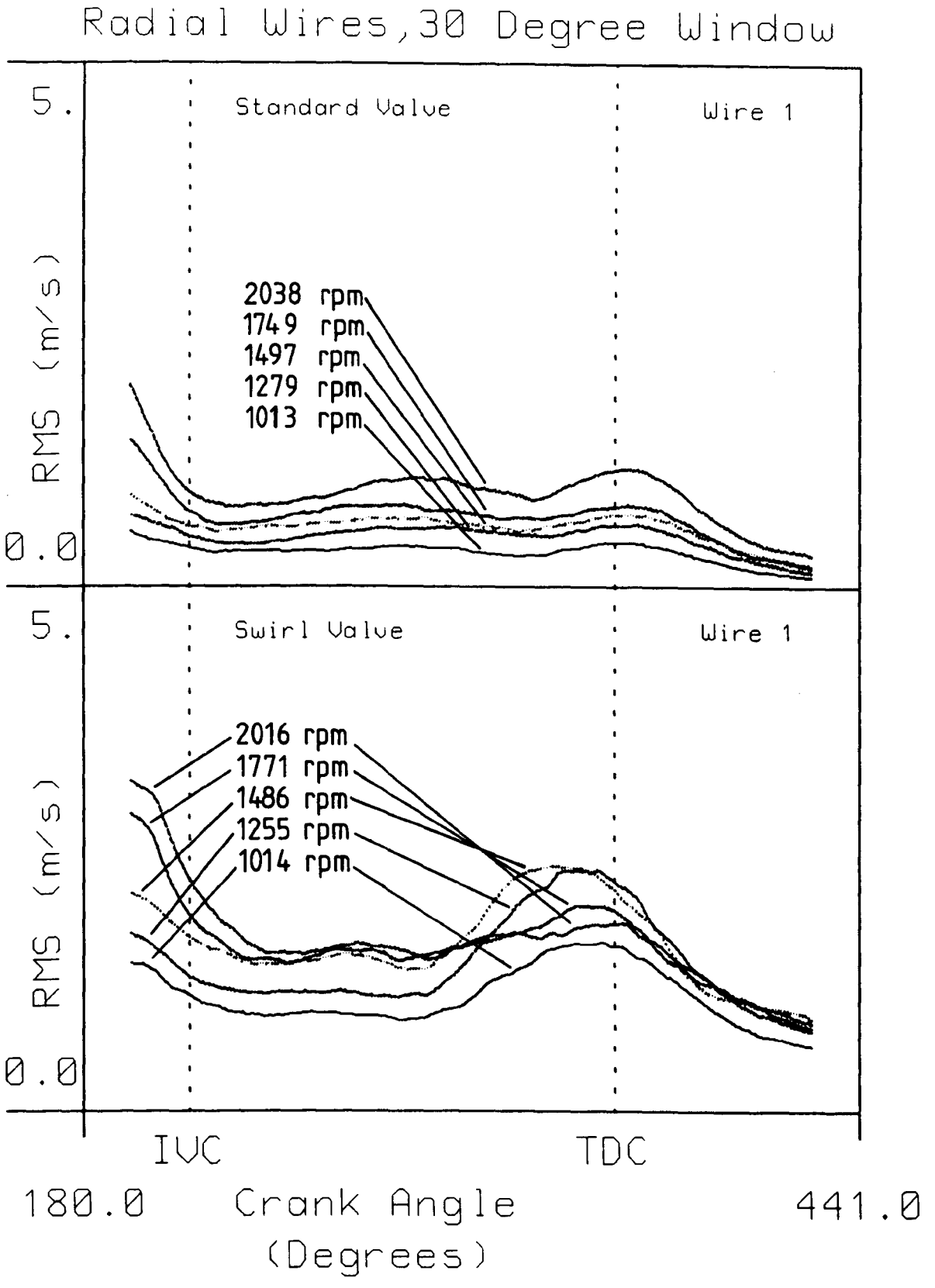

Figure 6.33 Averaged Window CBC Turbulence Intensity Plots.

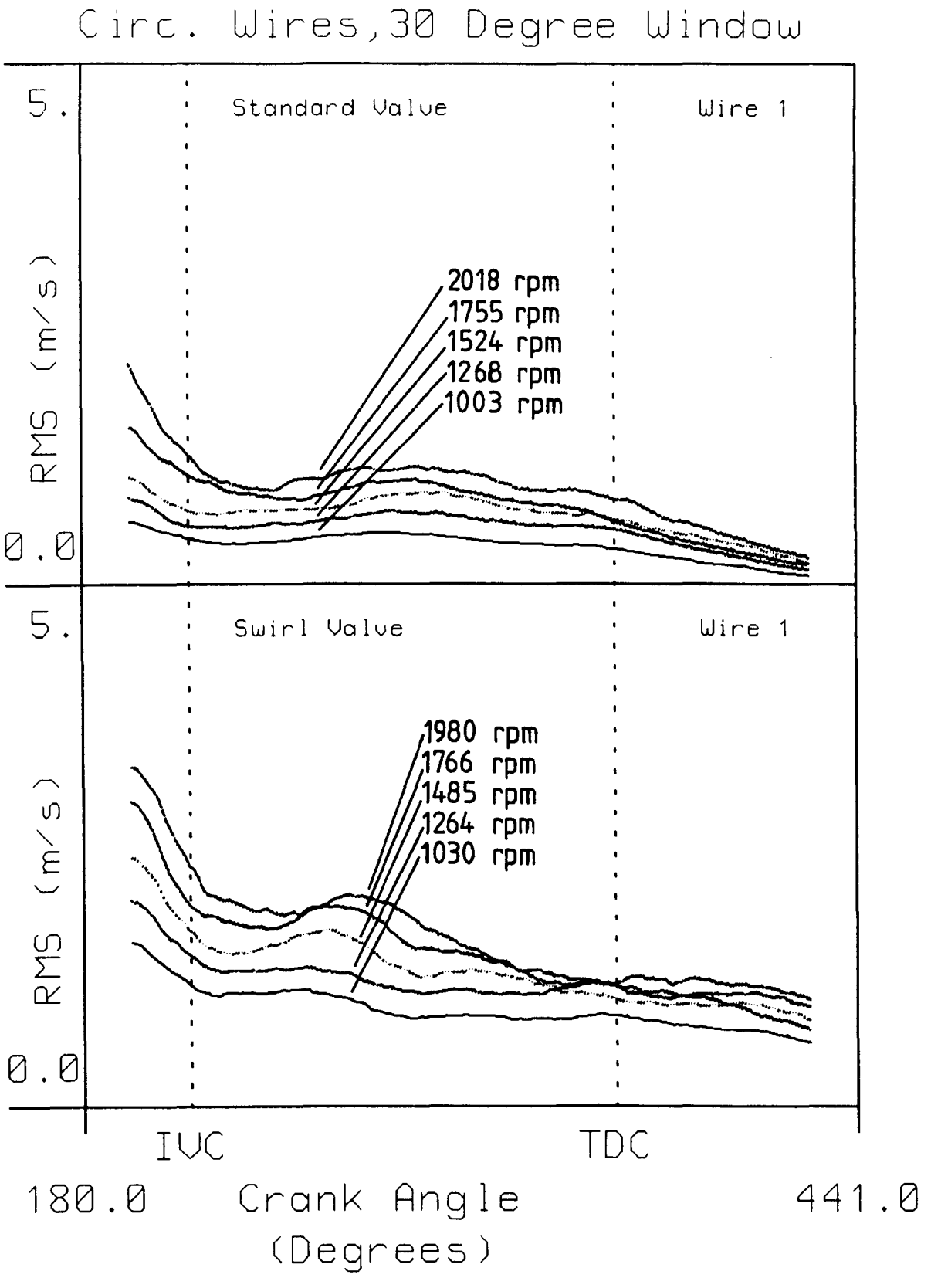

Figure 6.34 Averaged Window CBC Turbulence Intensity Plots.

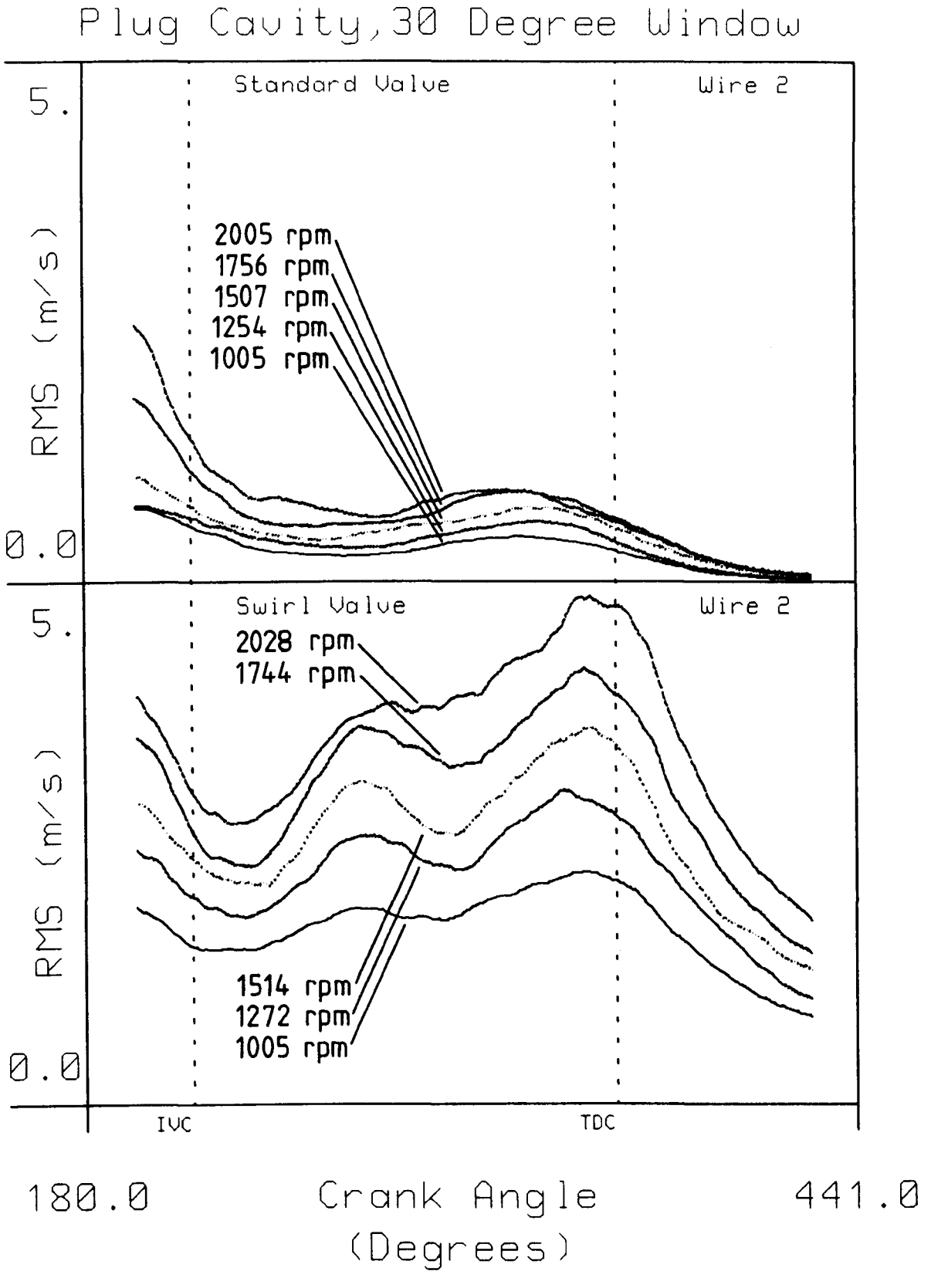

Figure 6.35 Averaged Window CBC Turbulence Intensity Plots.

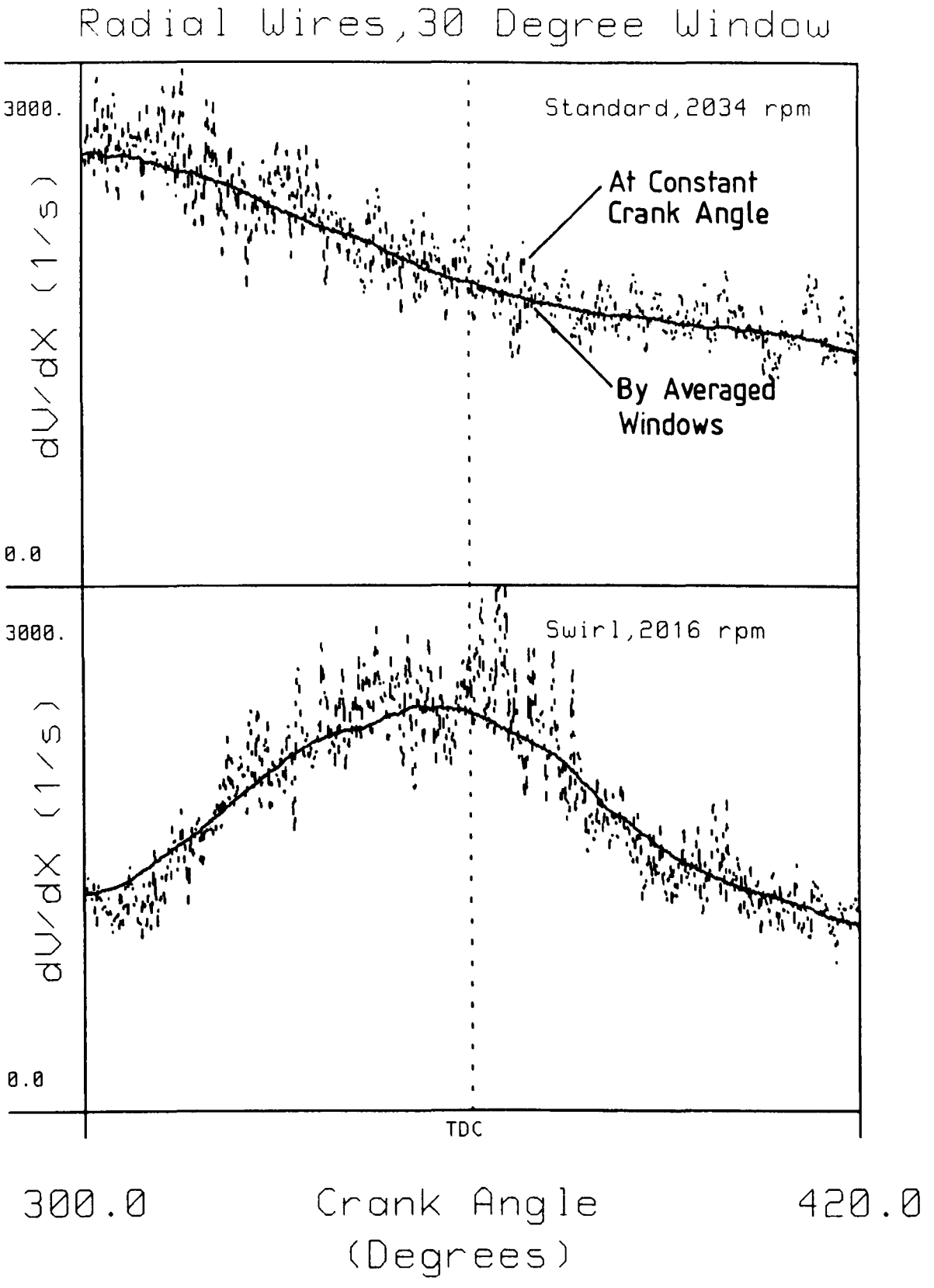

Figure 6.36 A Comparison Between Phase Averaged and Averaged Window CBC Velocity Gradient Plots.

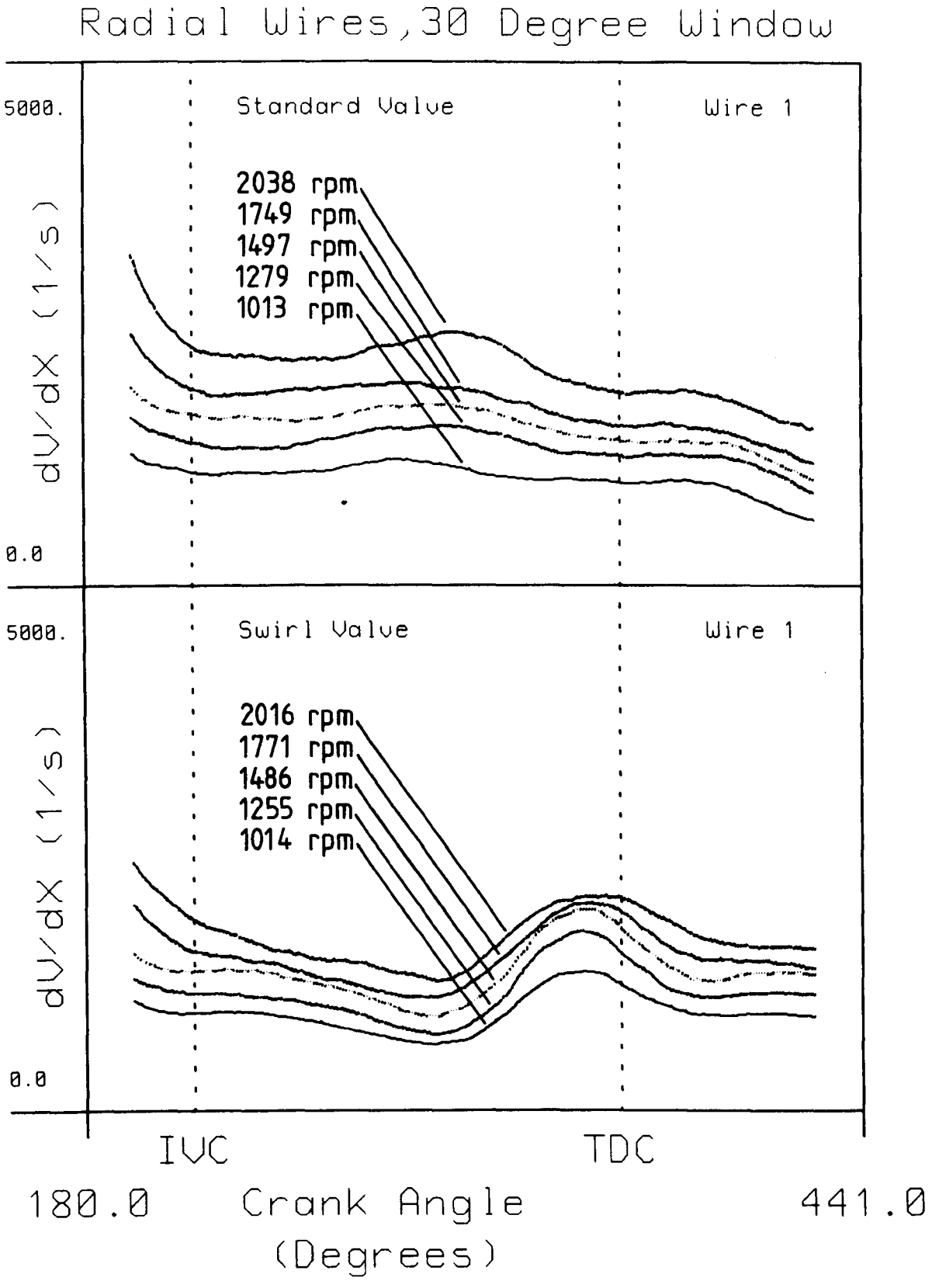

Figure 6.37 Averaged Window CBC Velocity Gradient Plots

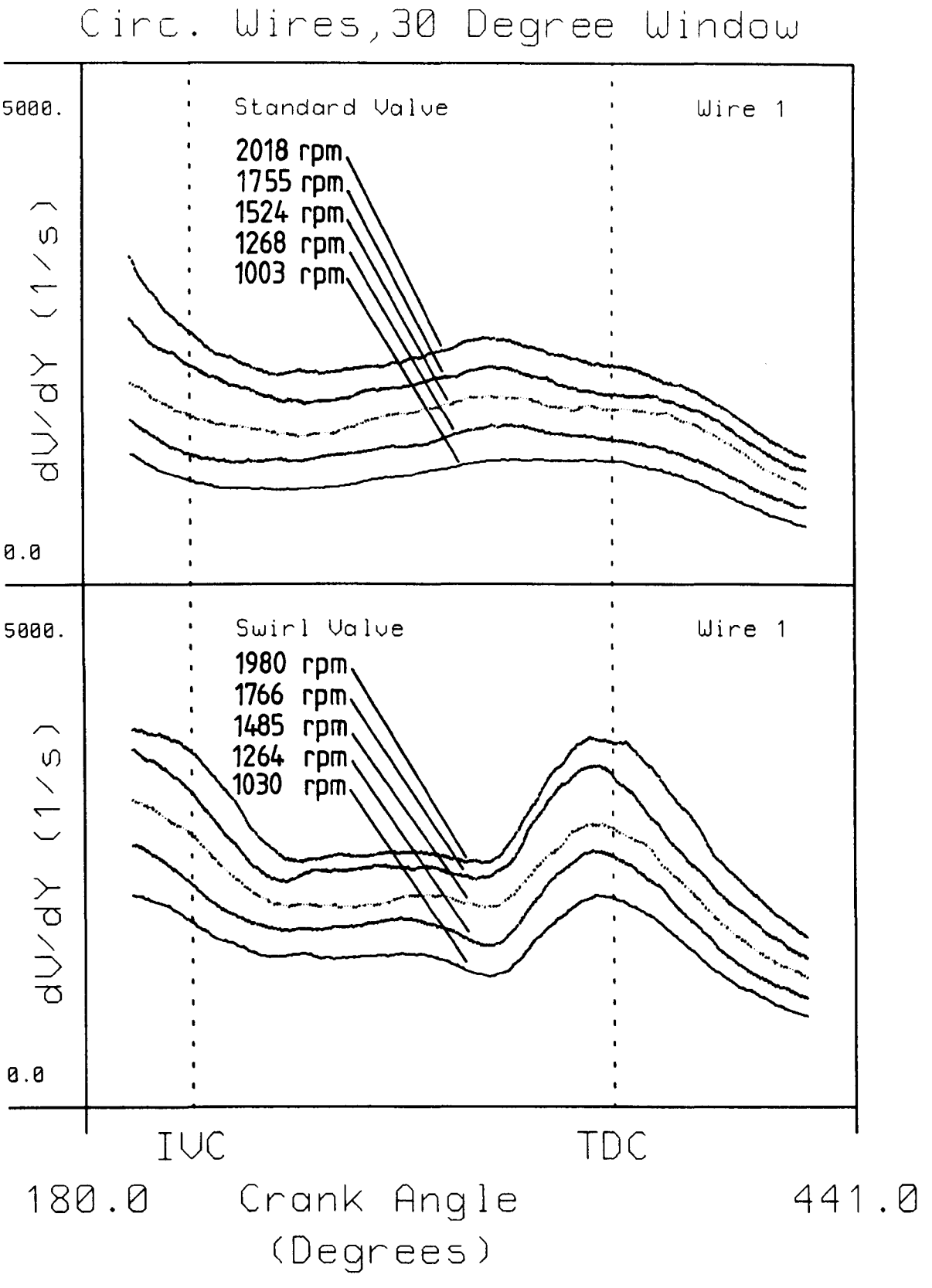

Figure 6.38 Averaged Window CBC Velocity Gradient Plots

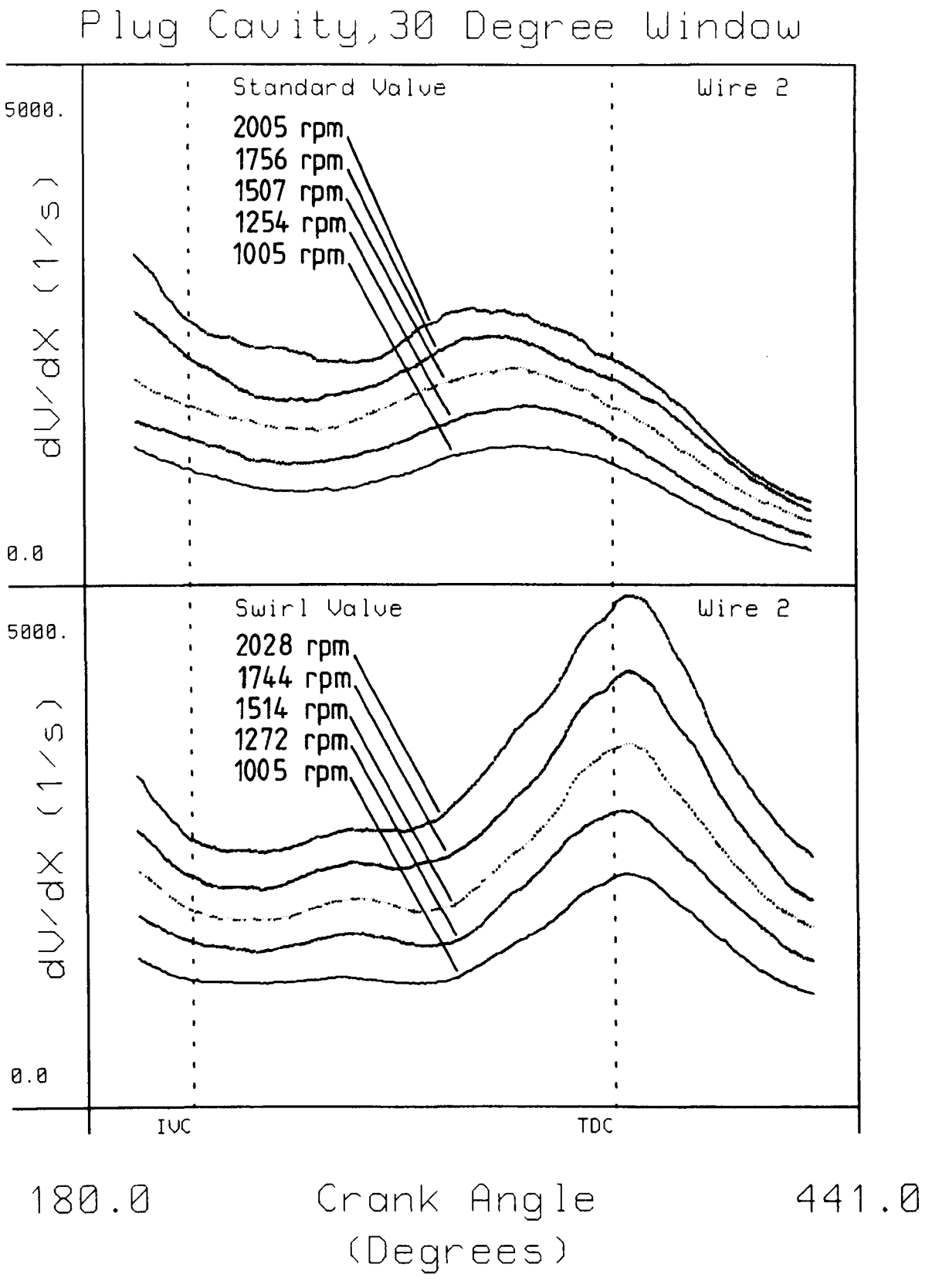

Figure 6.39 Averaged Window CBC Velocity Gradient Plots

The Estimated Spatial Velocity Gradient Intensity from Parallel Hot Wire Measurements (That are Weighted to Give Equal Ensembled Mean Velocities)

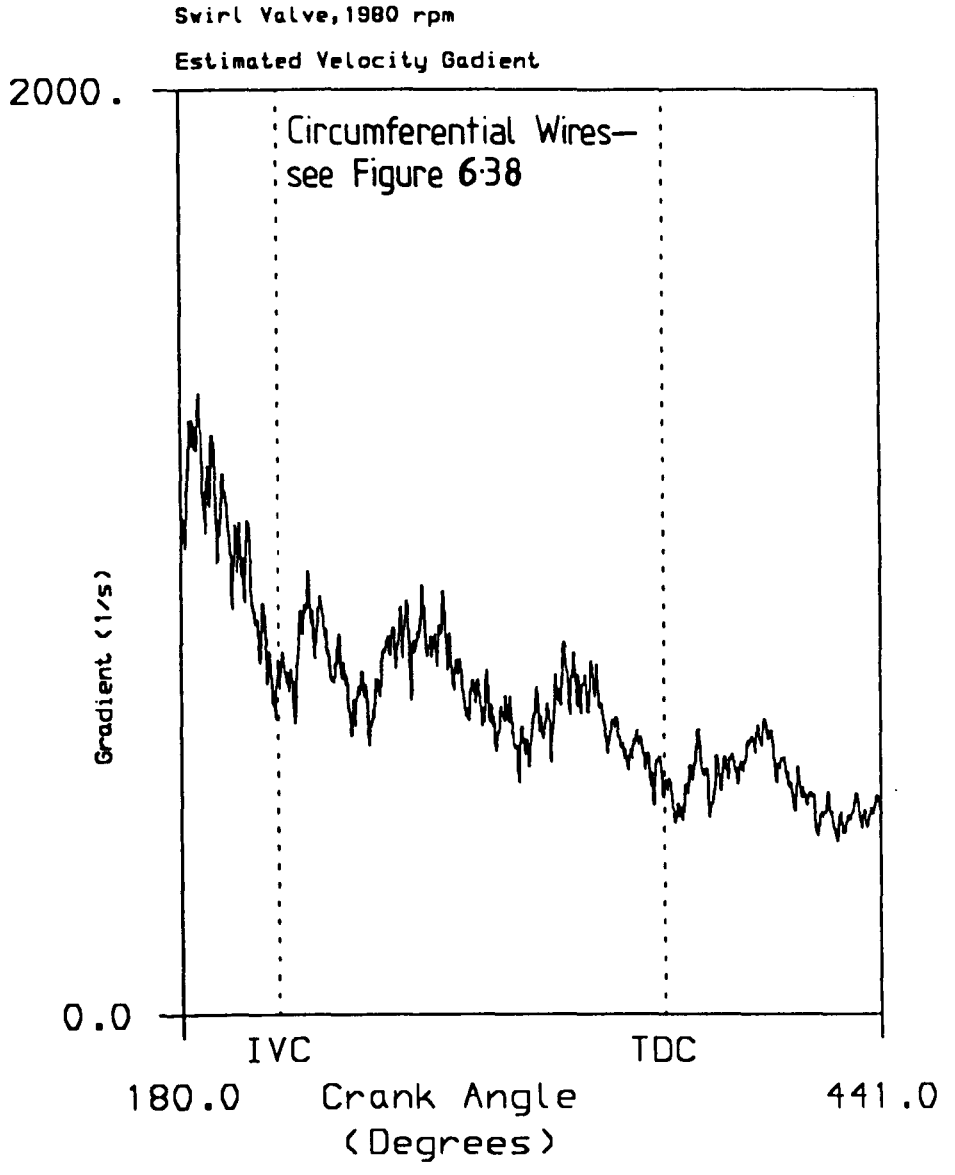

Figure 6.40 A Direct Estimate of Velocity Gradients

Mass Fraction Burnt Calculations for 182 Consequetive Cycles

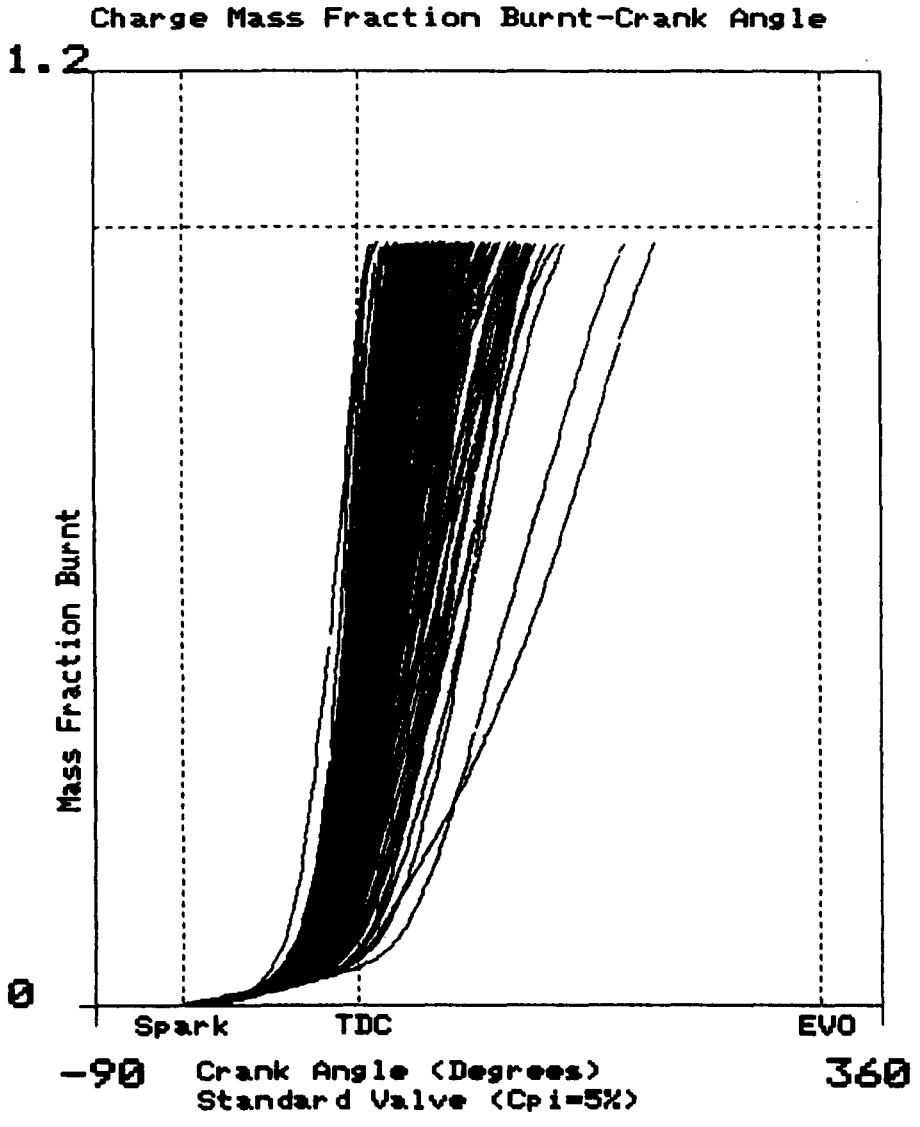

Figure 7.1

Mass Fraction Burnt Calculations for 182 Consequetive Cycles

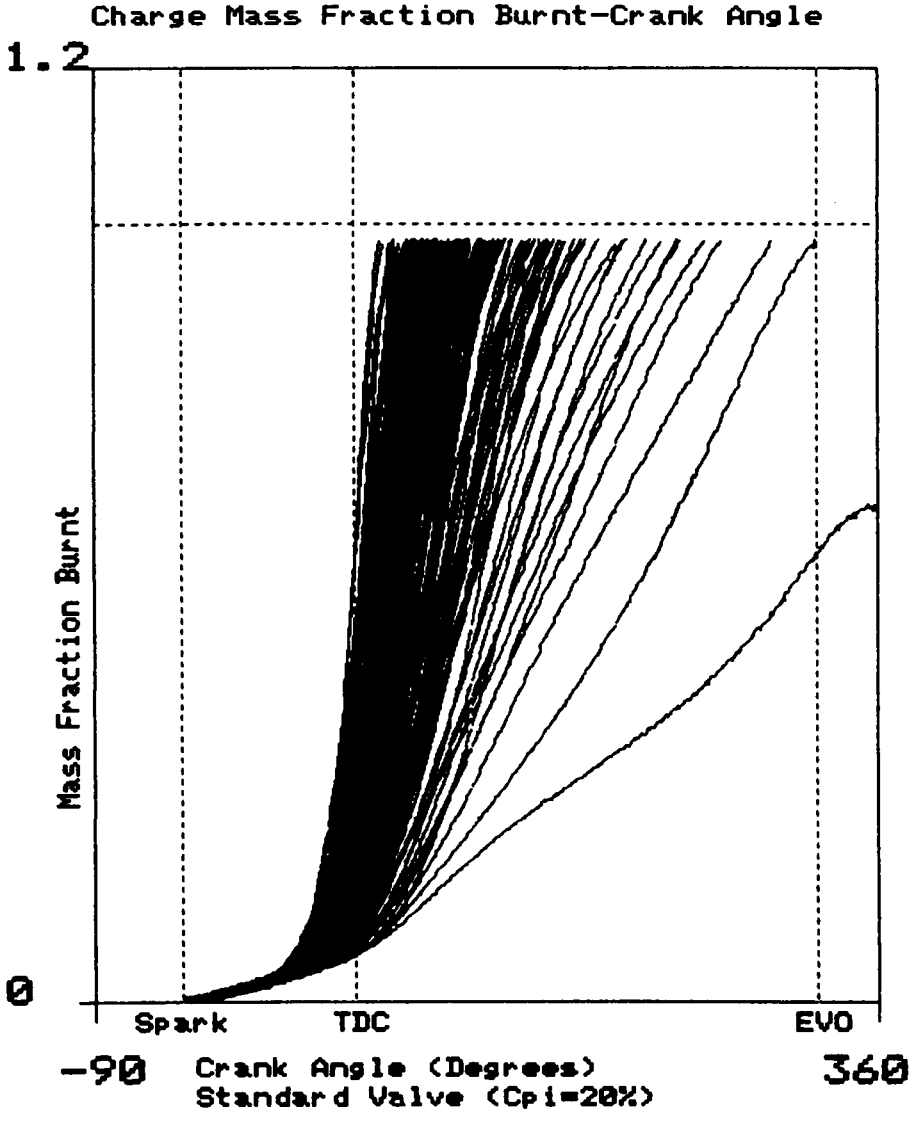

Figure 7.2

Delay to Burn a 2% Mass Fraction Plotted Against the Total Burn Time

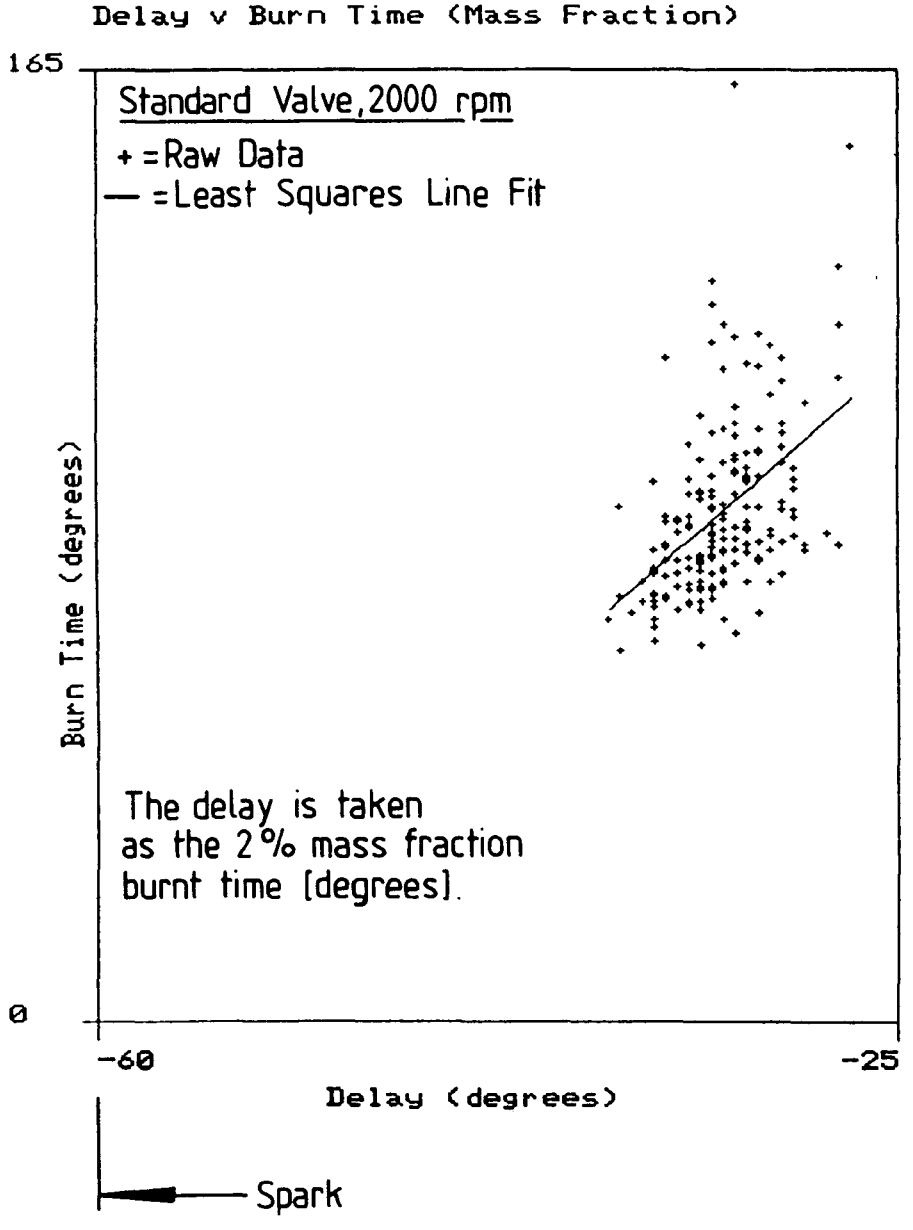

Figure 7.3

Delay to Burn a 5% Mass Fraction Plotted Against the Total Burn Time

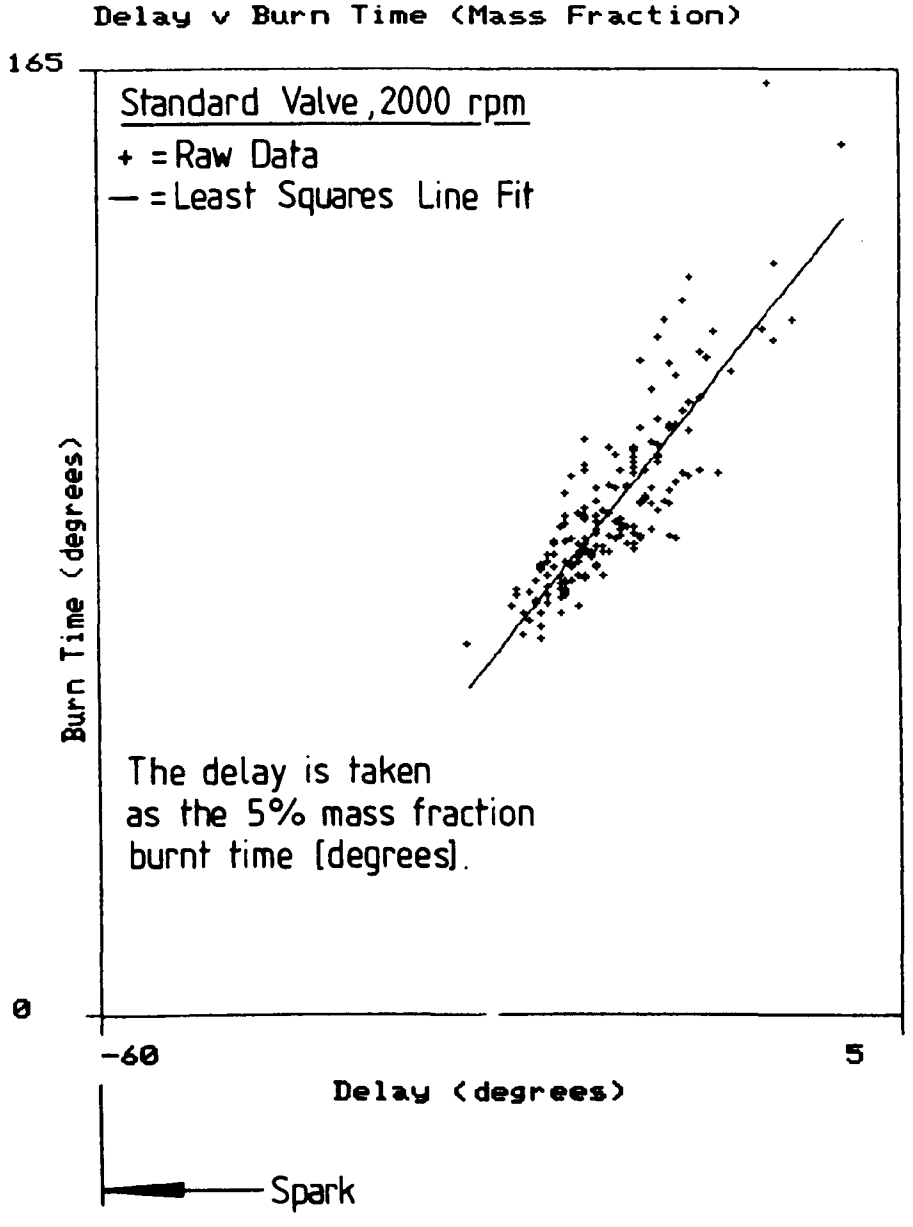

Figure 7.4

Delay to Burn a 10% Mass Fraction Plotted Against the Total Burn Time

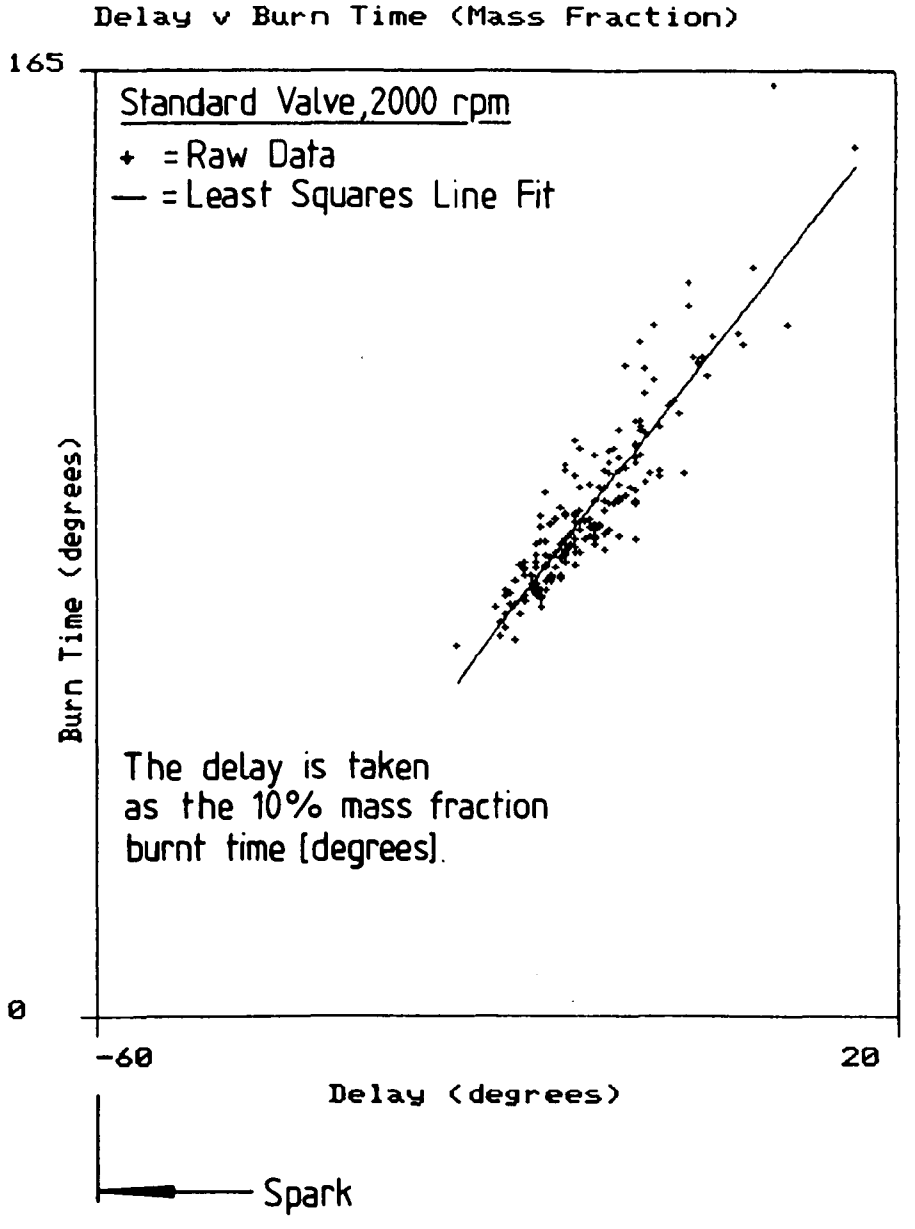

Figure 7.5

Sum of Squared Errors and Correlation Coefficient from Mass Fraction Defined 'Delay'-Total Burn Time Relationship.

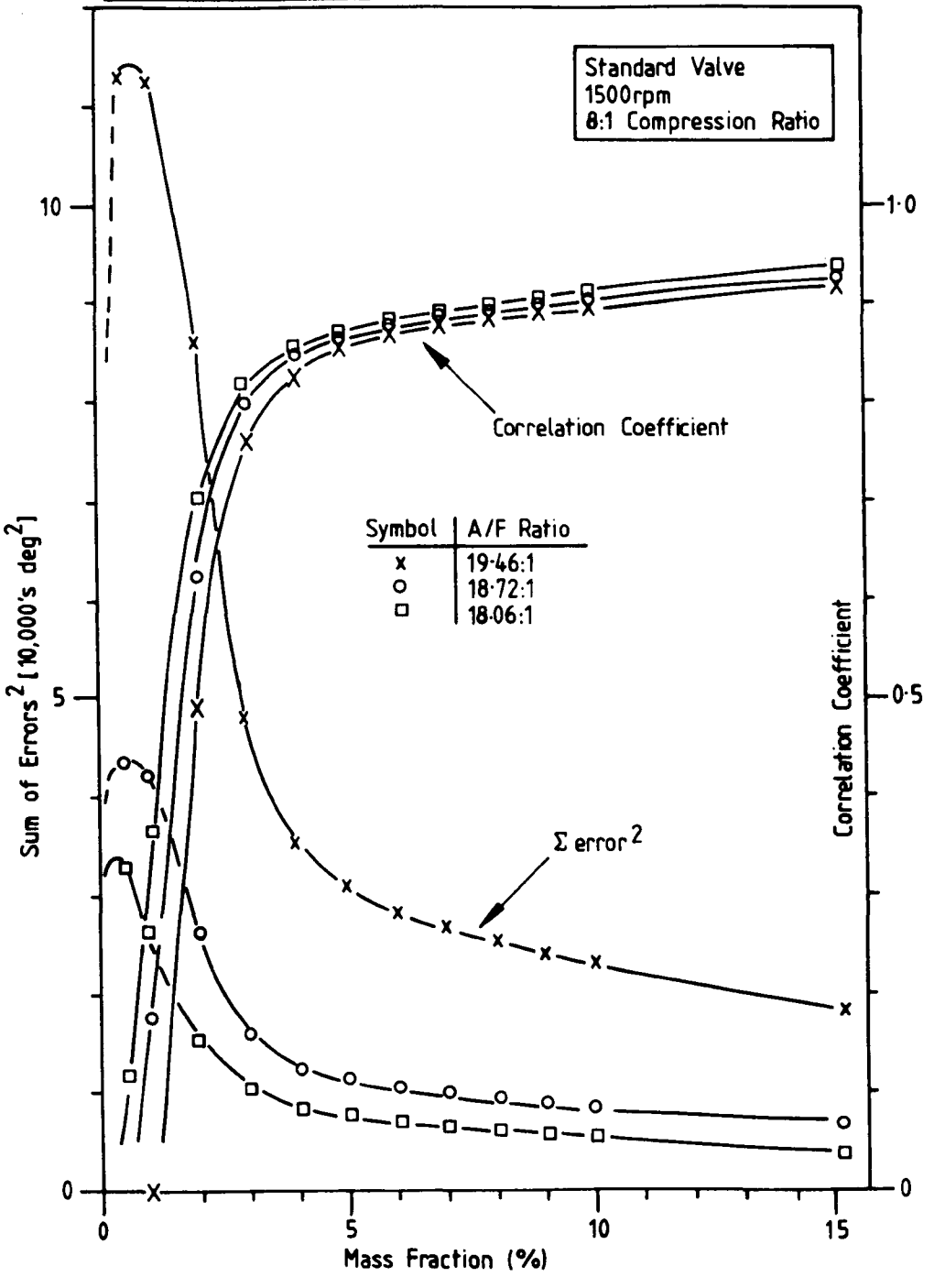

Figure 7.6

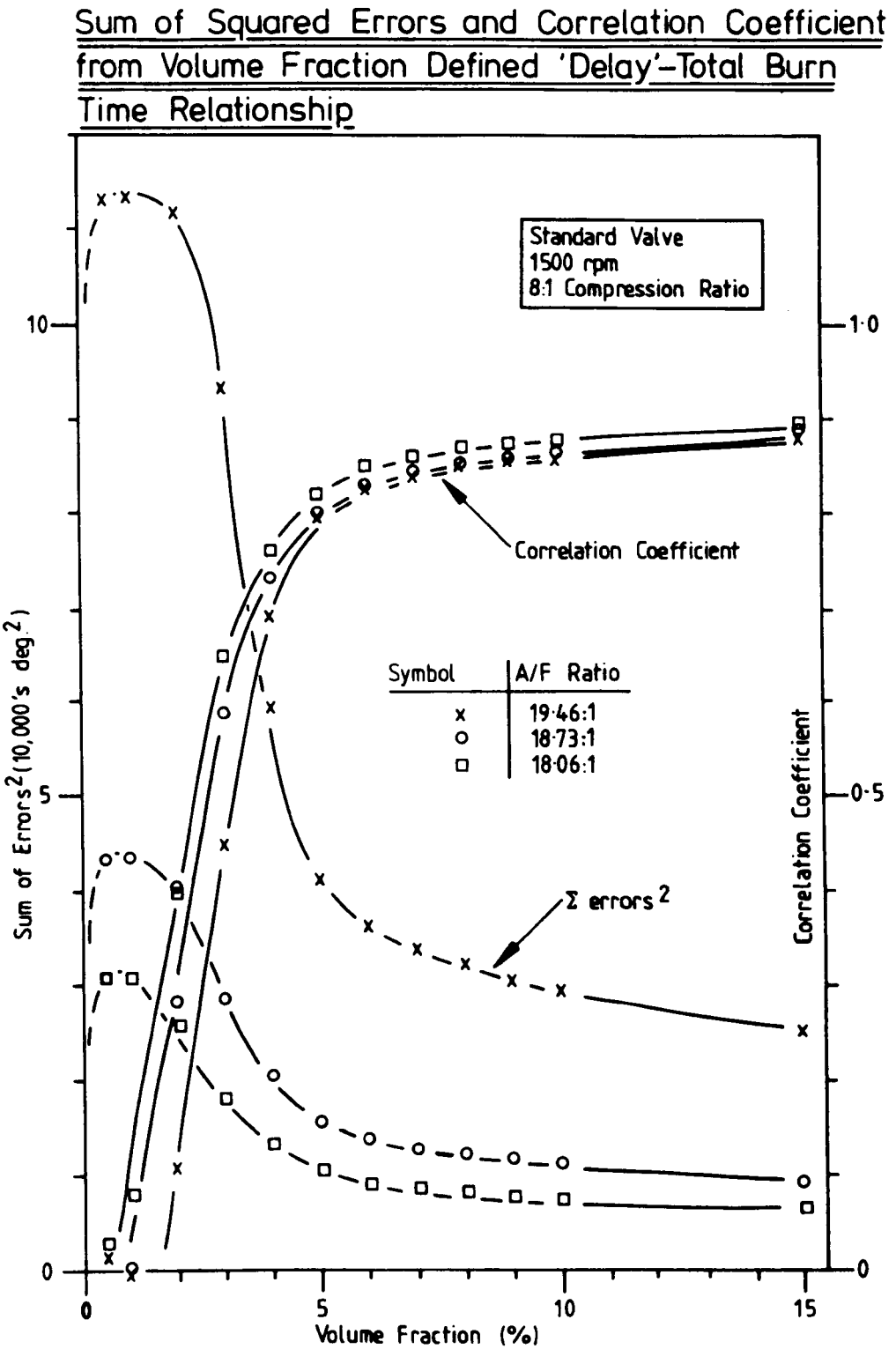
Sum of Squared Errors and Correlation Coefficient from Volume Fraction Defined 'Delay'–Total Burn Time Relationship
Standard Valve
1500 rpm
8:1 Compression Ratio
Correlation Coefficient
Symbol | A/F Ratio
x | 19·46:1
o | 18·73:1
□ | 18·06:1
Σ errors 2
Sum of Errors 2 (10,000's deg. 2)
Correlation Coefficient
Volume Fraction (%)
0
5
10
15
1·0
0·5

Figure 7.7

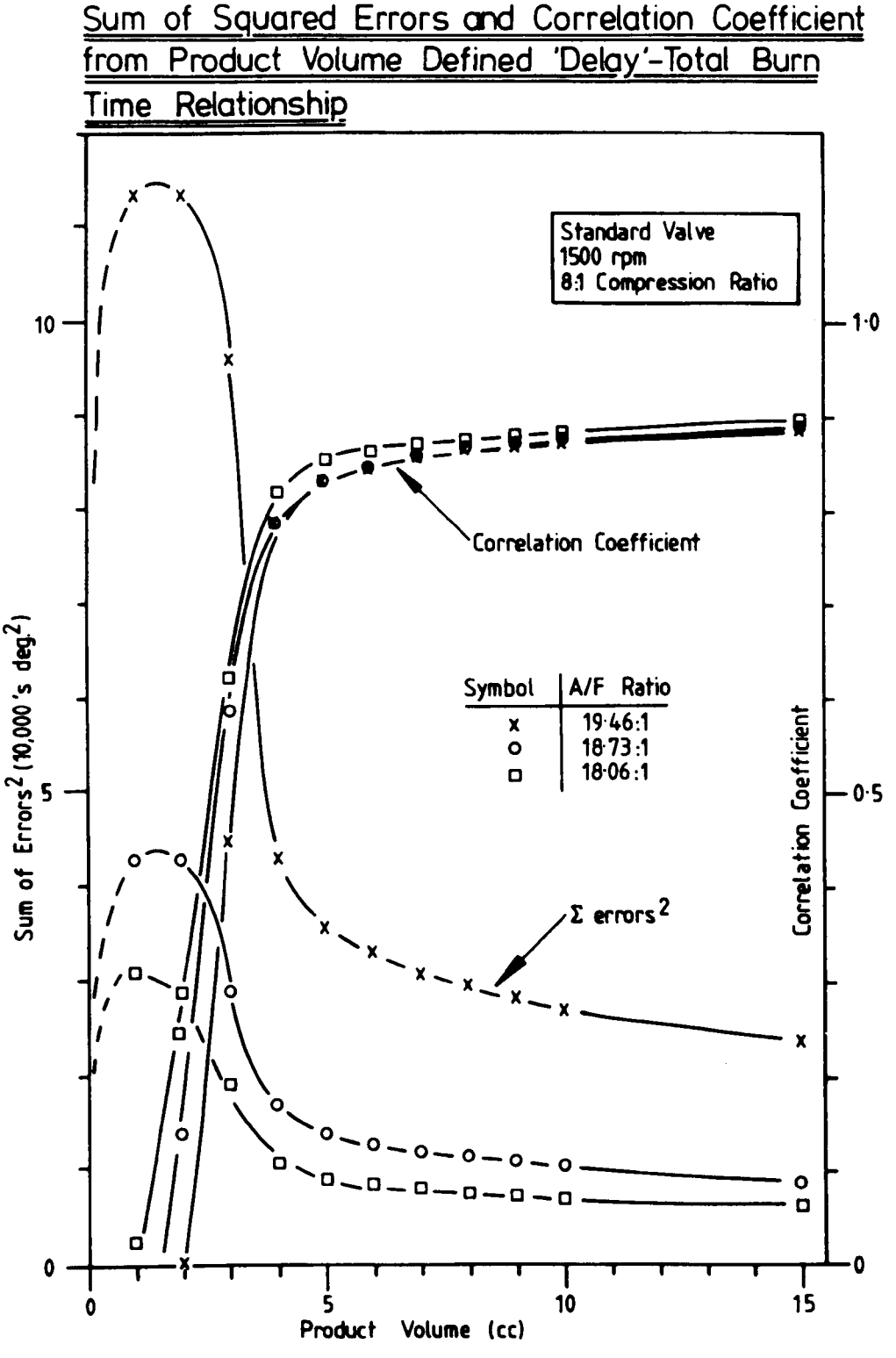
Sum of Squared Errors and Correlation Coefficient from Product Volume Defined 'Delay'-Total Burn Time Relationship
Standard Valve
1500 rpm
8:1 Compression Ratio
Correlation Coefficient
Symbol | A/F Ratio
x | 19·46:1
o | 18·73:1
□ | 18·06:1
Σ errors²
Sum of Errors² (10,000's deg.²)
Correlation Coefficient
Product Volume (cc)
0
5
10
15
0·5
1·0

Figure 7.8

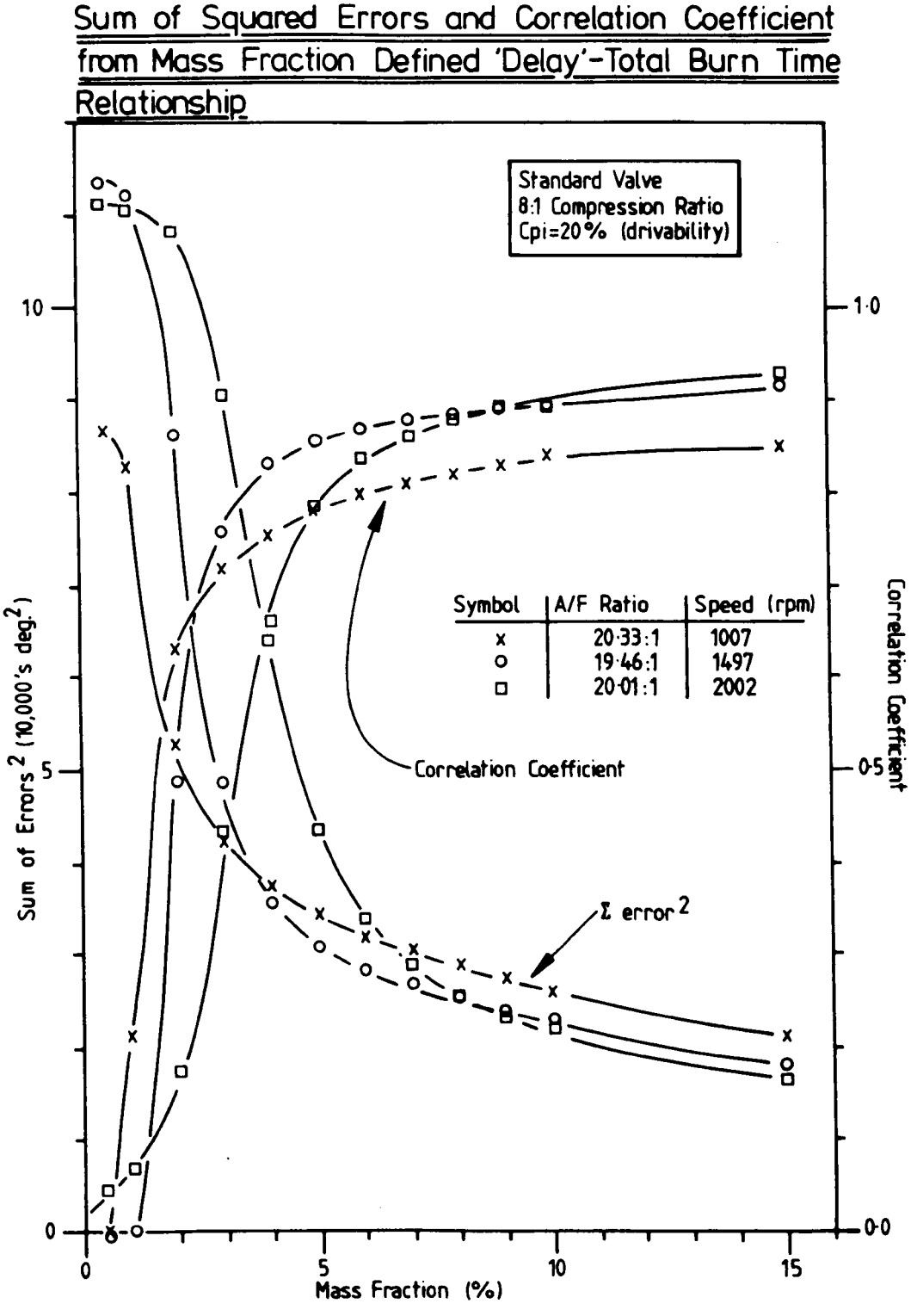
Sum of Squared Errors and Correlation Coefficient from Mass Fraction Defined 'Delay'-Total Burn Time Relationship
Standard Valve
8:1 Compression Ratio
Cpi=20% (drivability)
Symbol | A/F Ratio | Speed (rpm)
x | 20·33:1 | 1007
o | 19·46:1 | 1497
□ | 20·01:1 | 2002
Correlation Coefficient
Σ error 2
Sum of Errors 2 (10,000's deg.2)
Correlation Coefficient
Mass Fraction (%)
0
5
10
15
0·0
0·5
1·0

Figure 7.9

Mass Fraction Burnt Calculations for 182 Consequetive Cycles

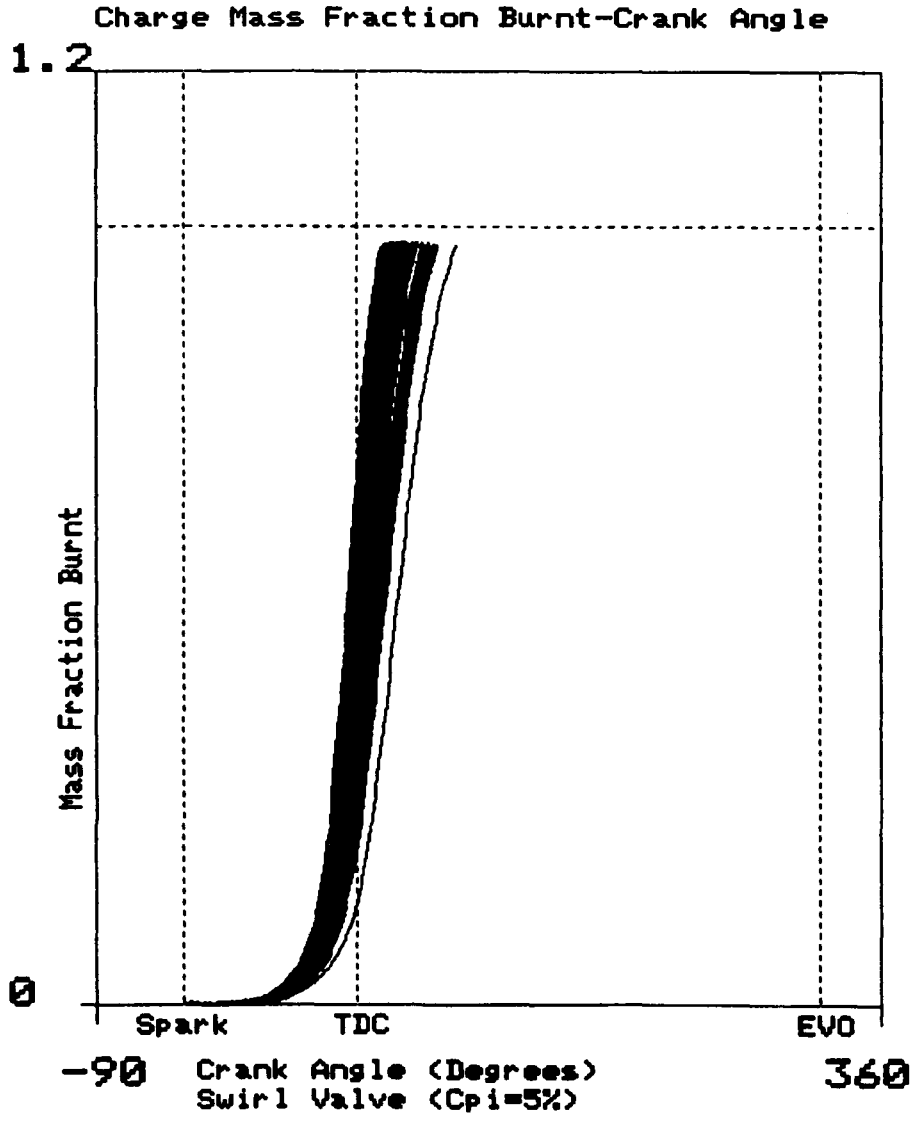

Figure 7.10

Delay to Burn a 5% Mass Fraction Plotted Against the Total Burn Time

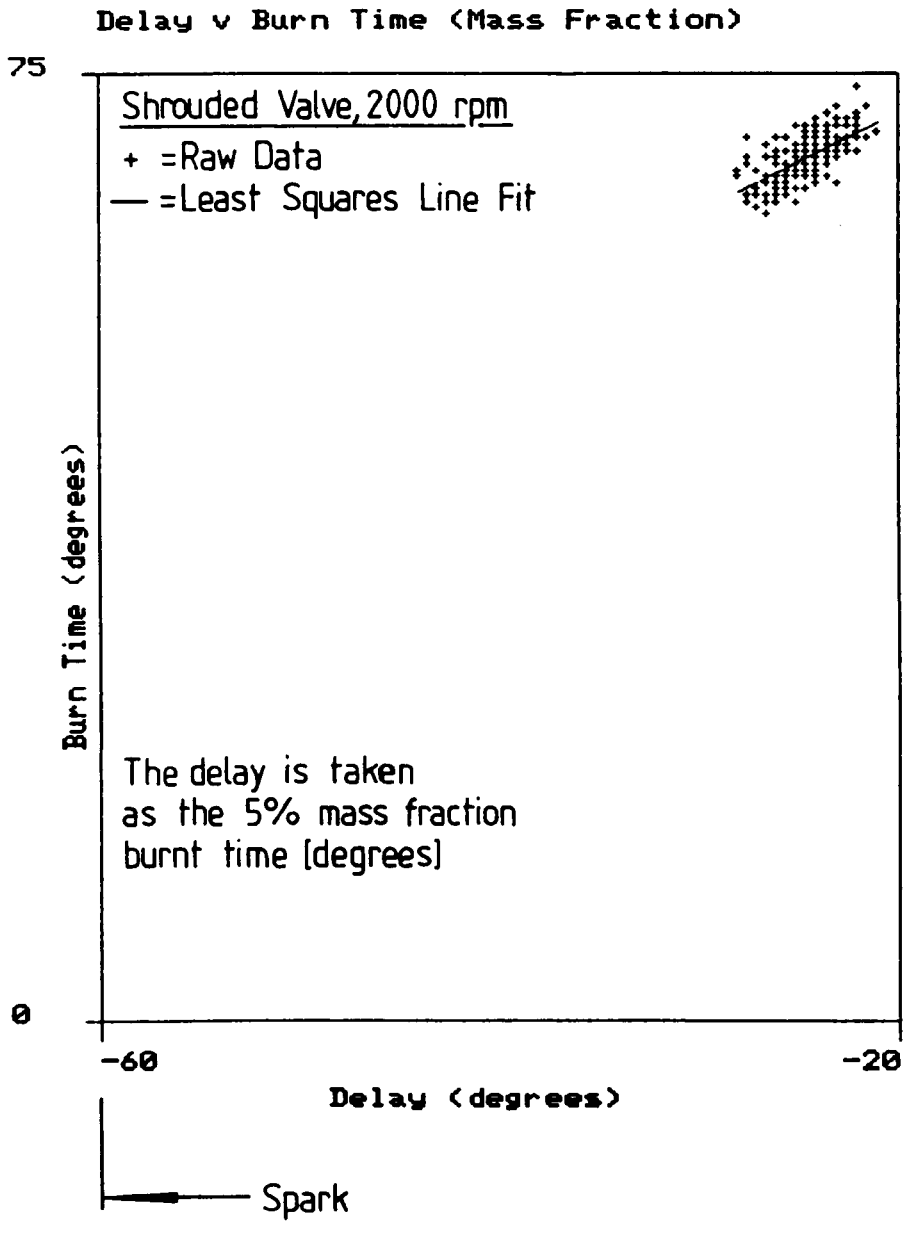

Figure 7.11

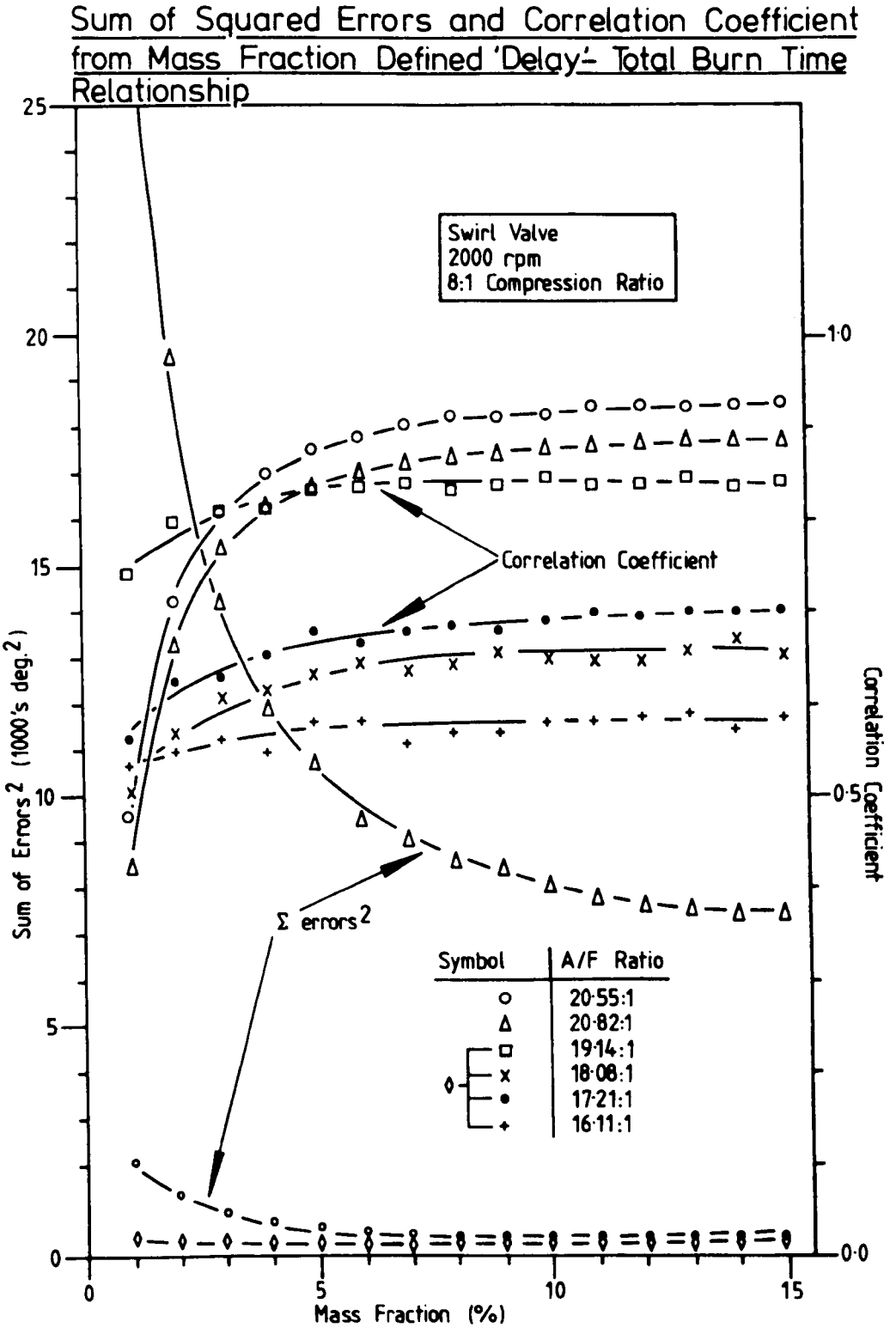
Sum of Squared Errors and Correlation Coefficient from Mass Fraction Defined 'Delay'- Total Burn Time Relationship
Swirl Valve
2000 rpm
8:1 Compression Ratio
Correlation Coefficient
Σ errors²
Symbol
A/F Ratio
20·55:1
20·82:1
19·14:1
18·08:1
17·21:1
16·11:1
Sum of Errors² (1000's deg.²)
Correlation Coefficient
Mass Fraction (%)
0
5
10
15
20
25
0·0
0·5
1·0

Figure 7.12

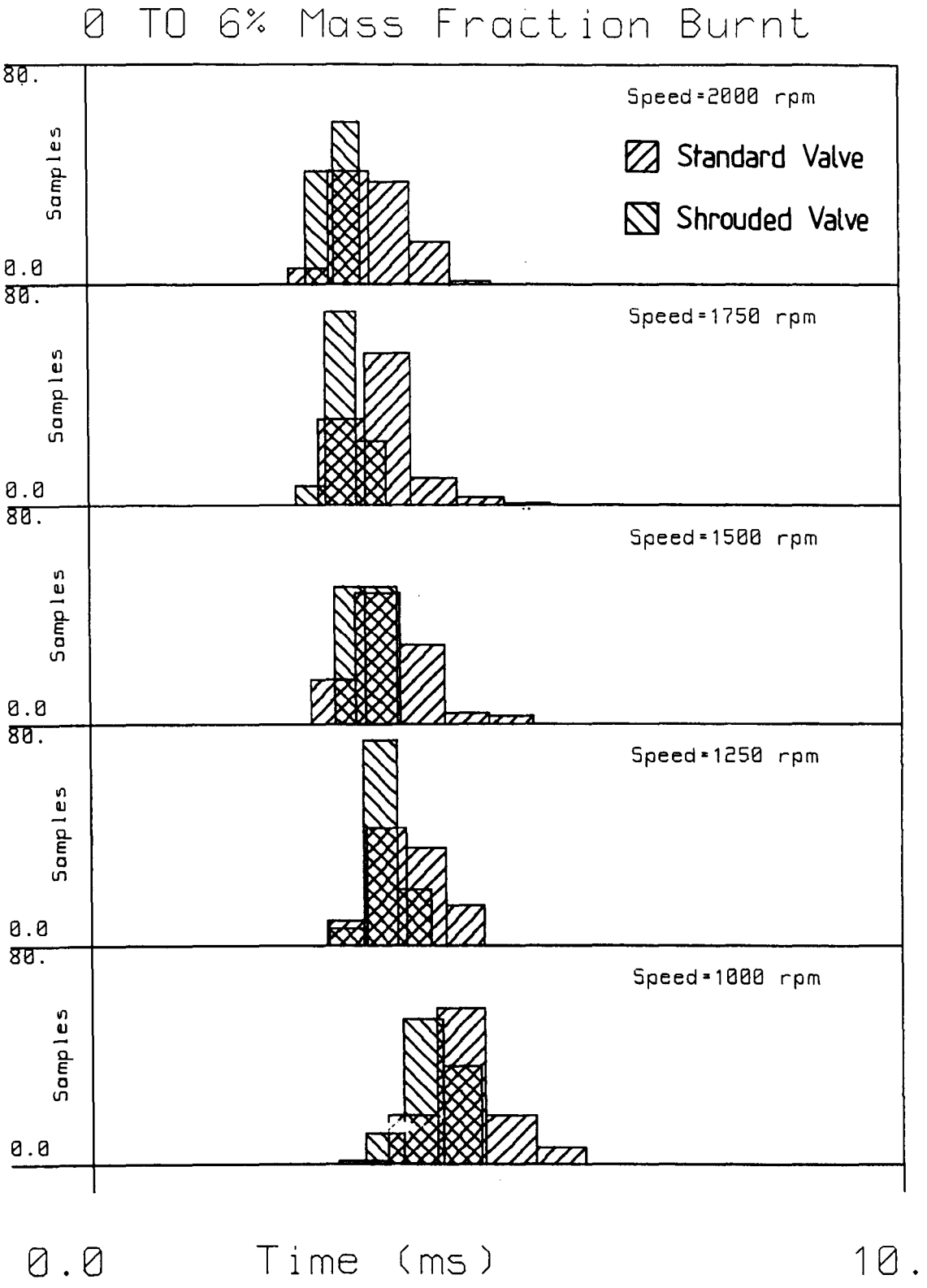
0 TO 6% Mass Fraction Burnt
80.
Samples
0.0
Speed=2000 rpm
Standard Valve
Shrouded Valve
Speed=1750 rpm
Speed=1500 rpm
Speed=1250 rpm
Speed=1000 rpm
0.0
Time (ms)
10.

Figure 7.13

Distributions of Instantaneous Velocities (at the Time of Sparking)

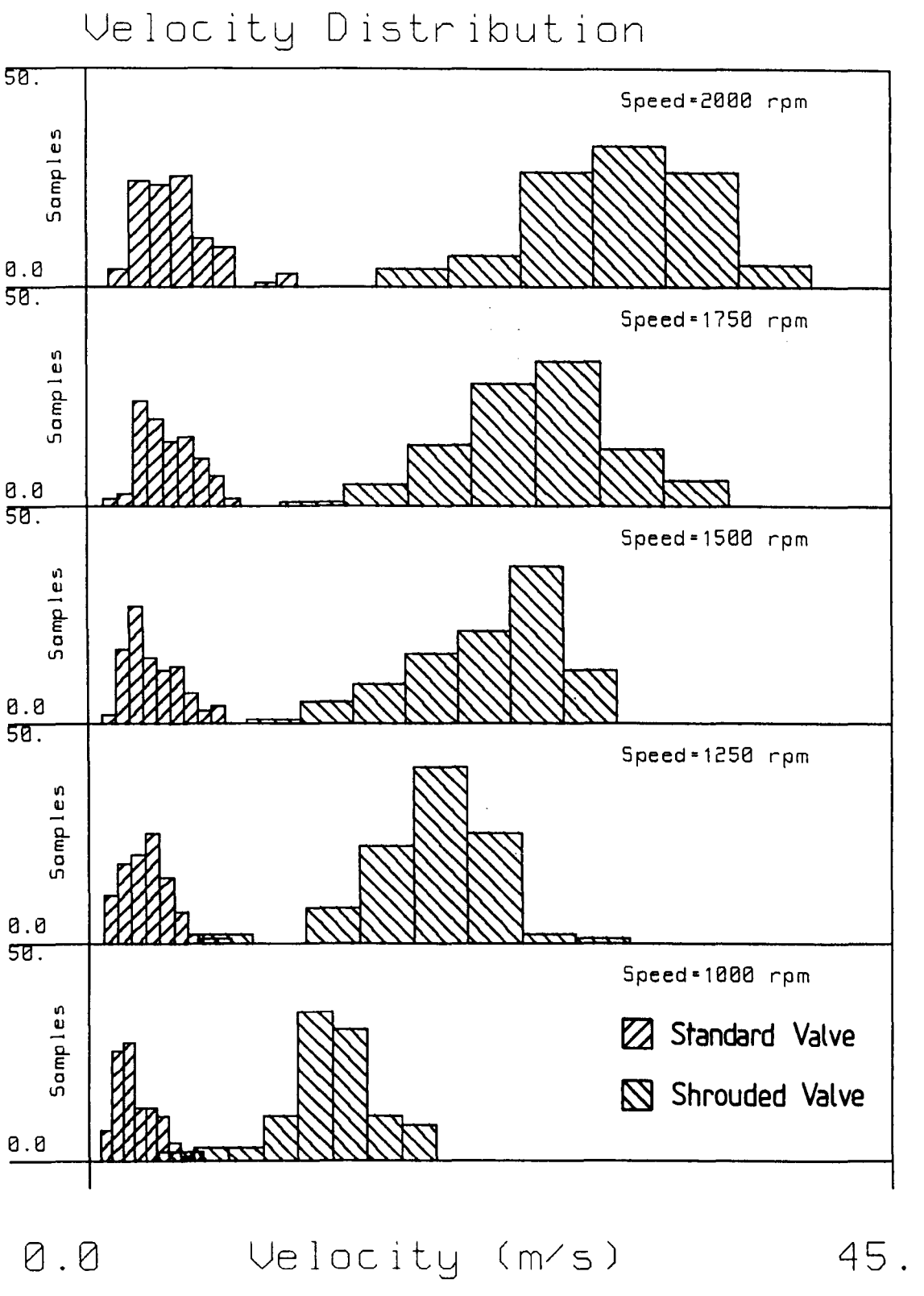

Figure 7.14

Distributions of CBC Turbulence Intensities (at the Time of Sparking)

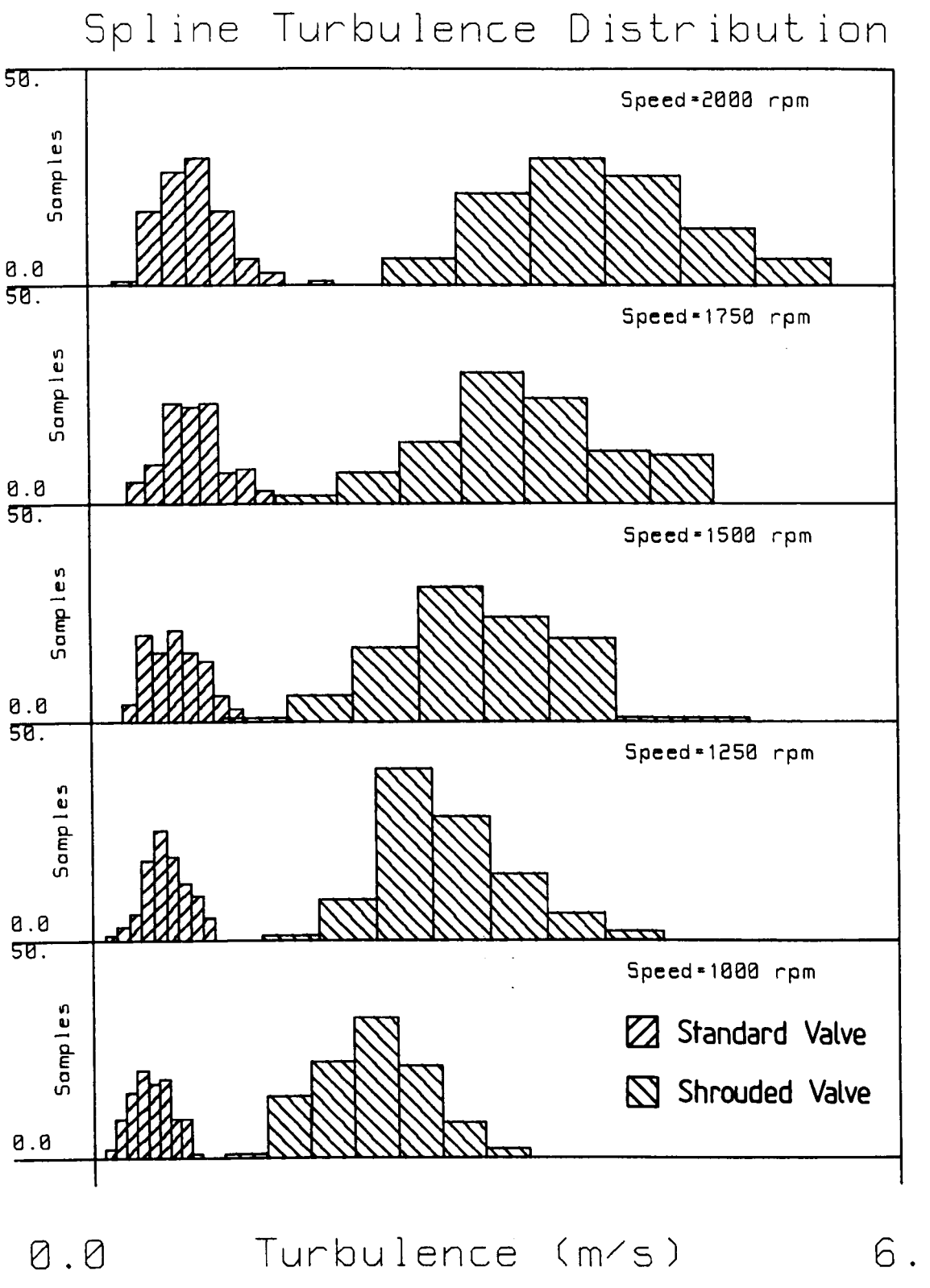

Figure 7.15

Distributions of CBC Mean Velocities (at the Time of Sparking)

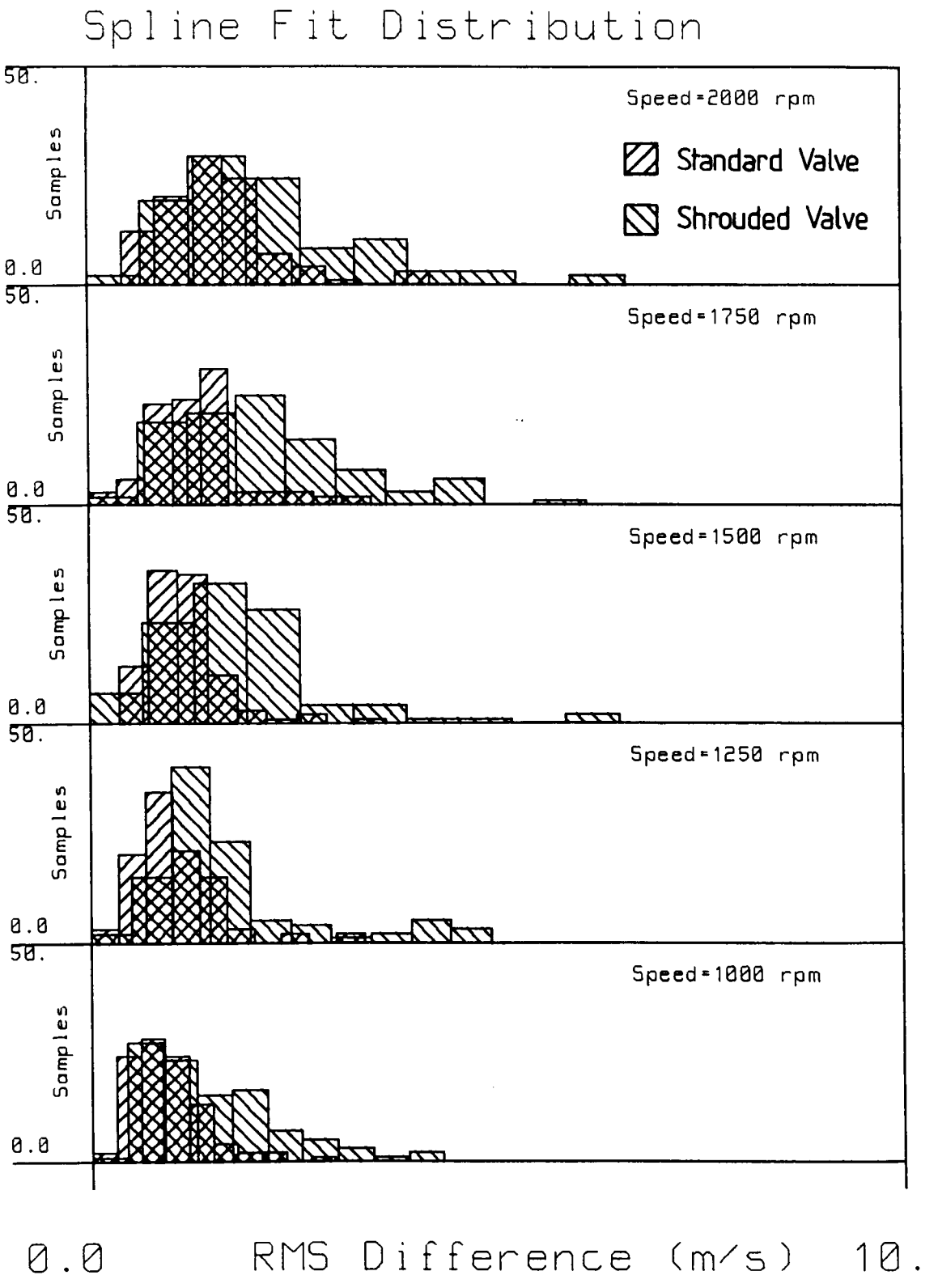

Figure 7.16

Distributions of CBC Velocity Gradient Intensities (at the Time of Sparking)

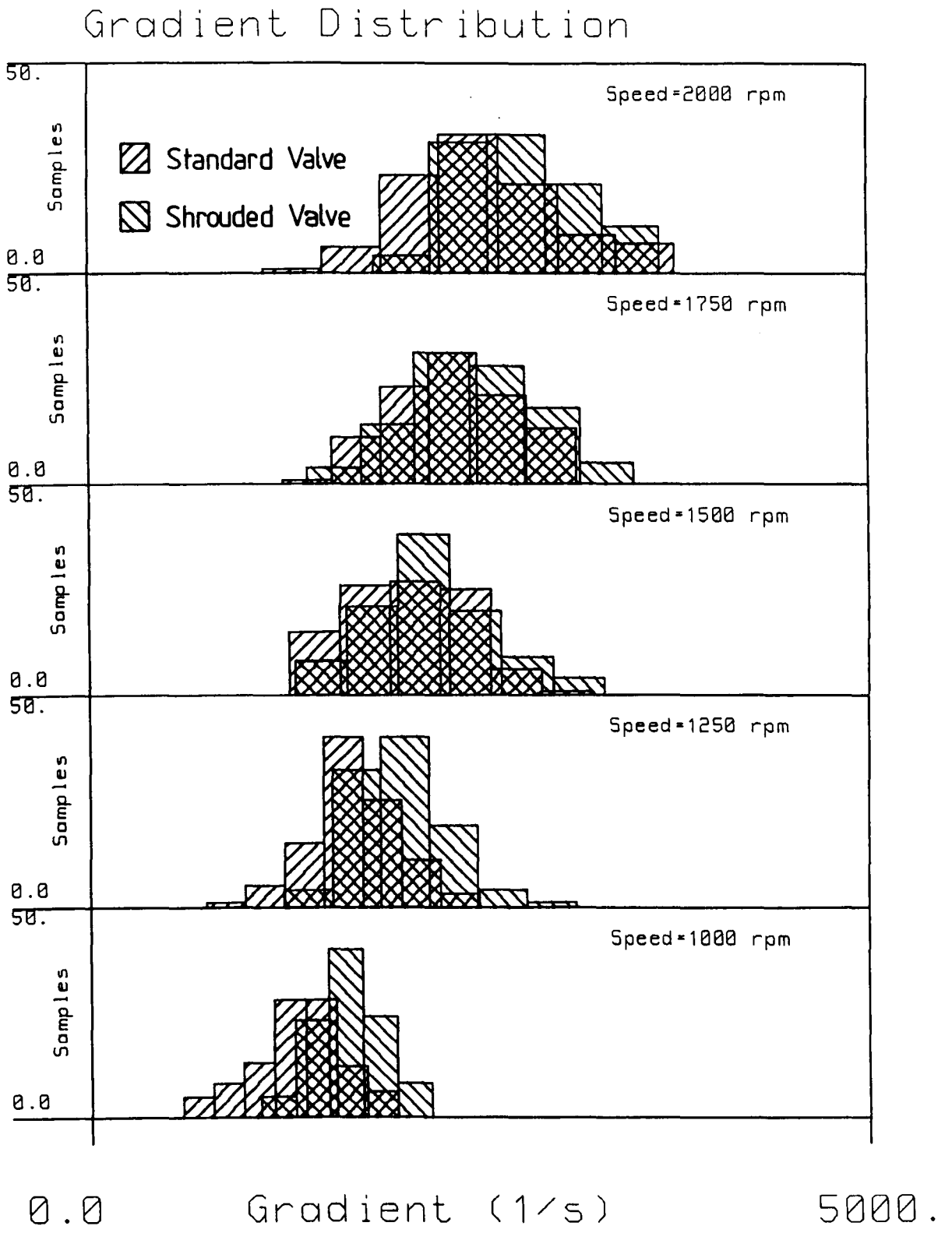

Figure 7.17

Ratios of Averaged Standard/Shrouded Valve Mass Fraction Burnt Times

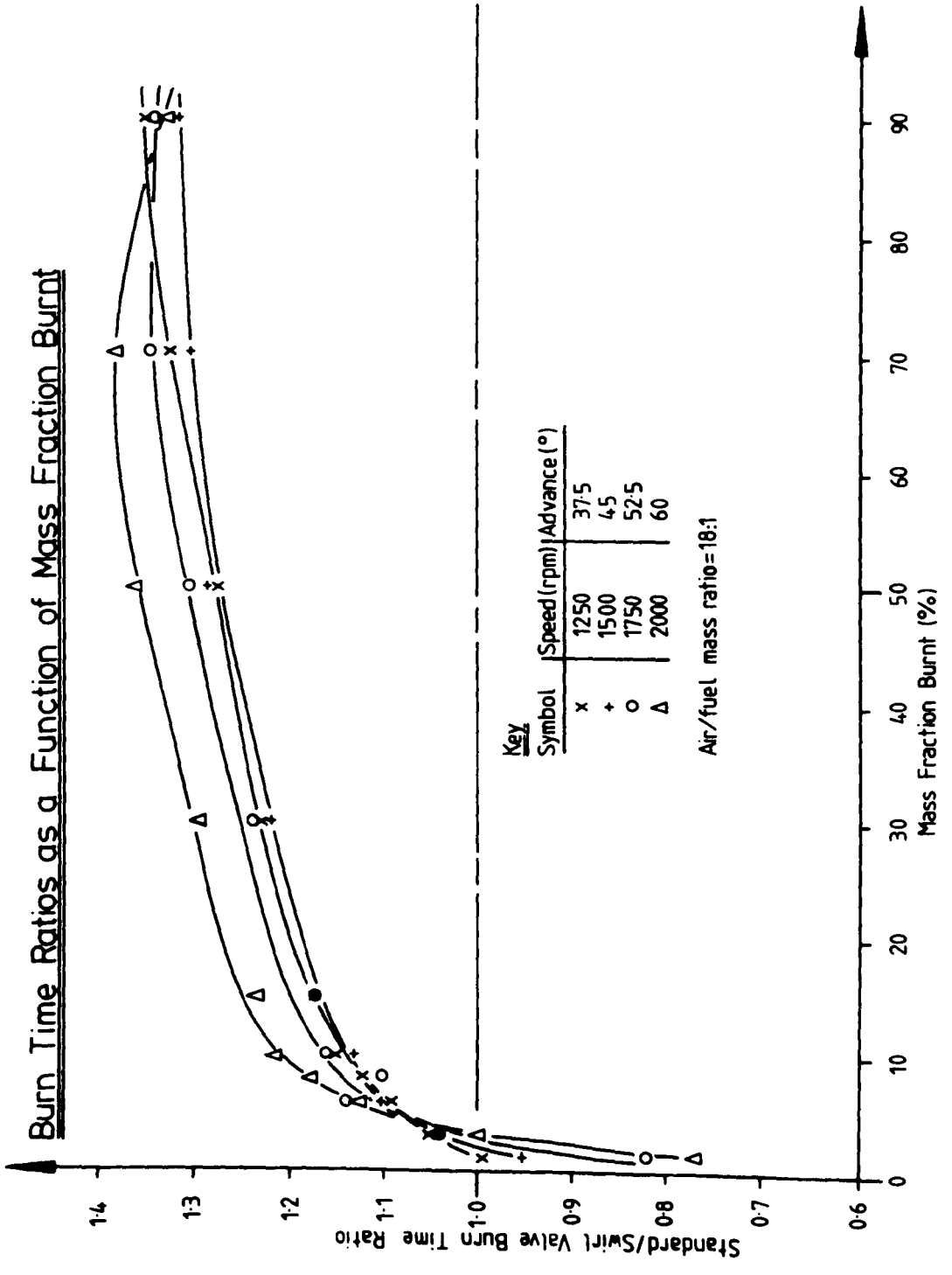

Figure 7.18

Averaged Mass Fraction Burnt Times for Changing Air/ Fuel Ratios

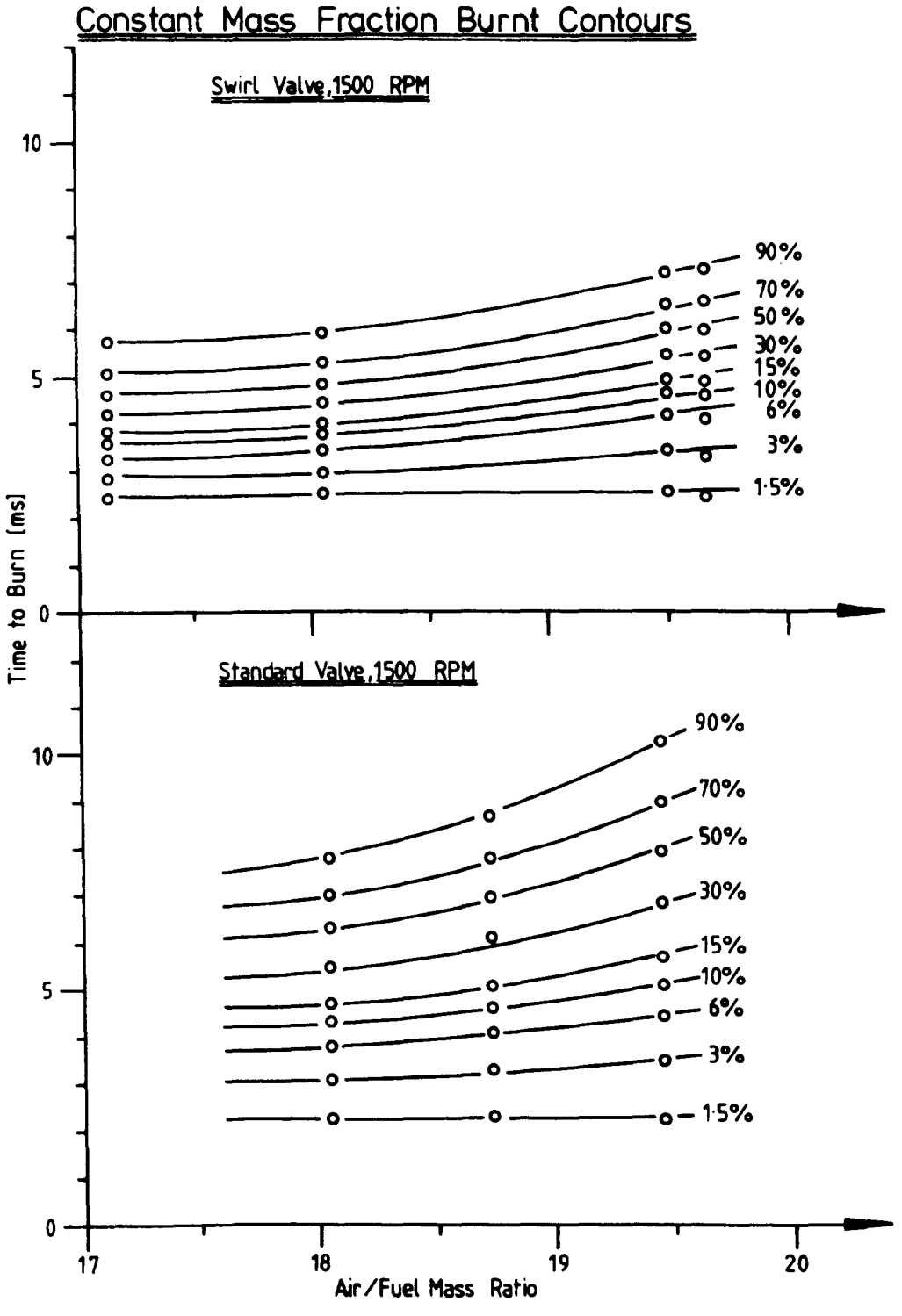

Figure 7.19

Averaged 0-6% Mass Fraction Burnt Times

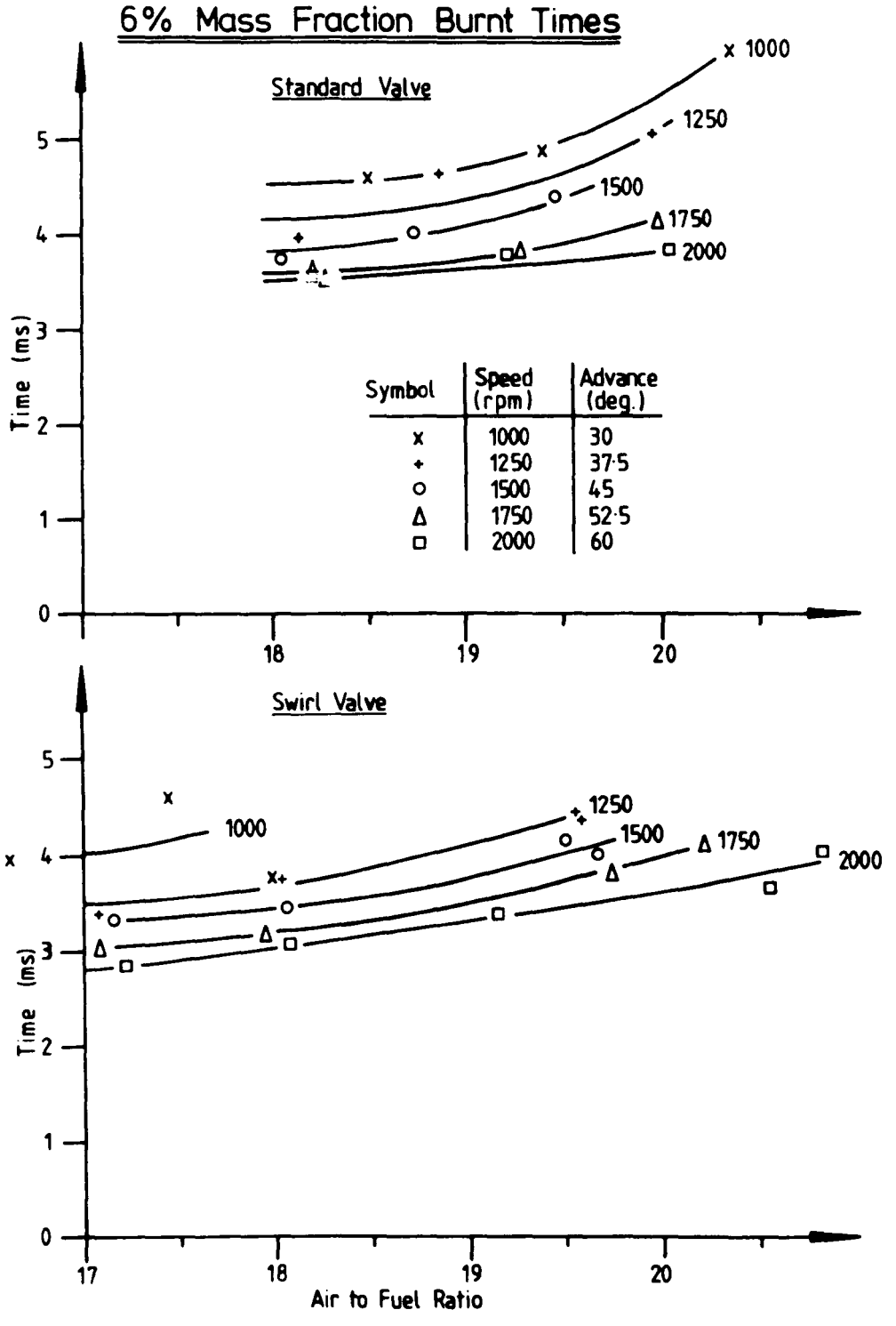

Figure 7.20

Averaged 6-90% Mass Fraction Burnt Times

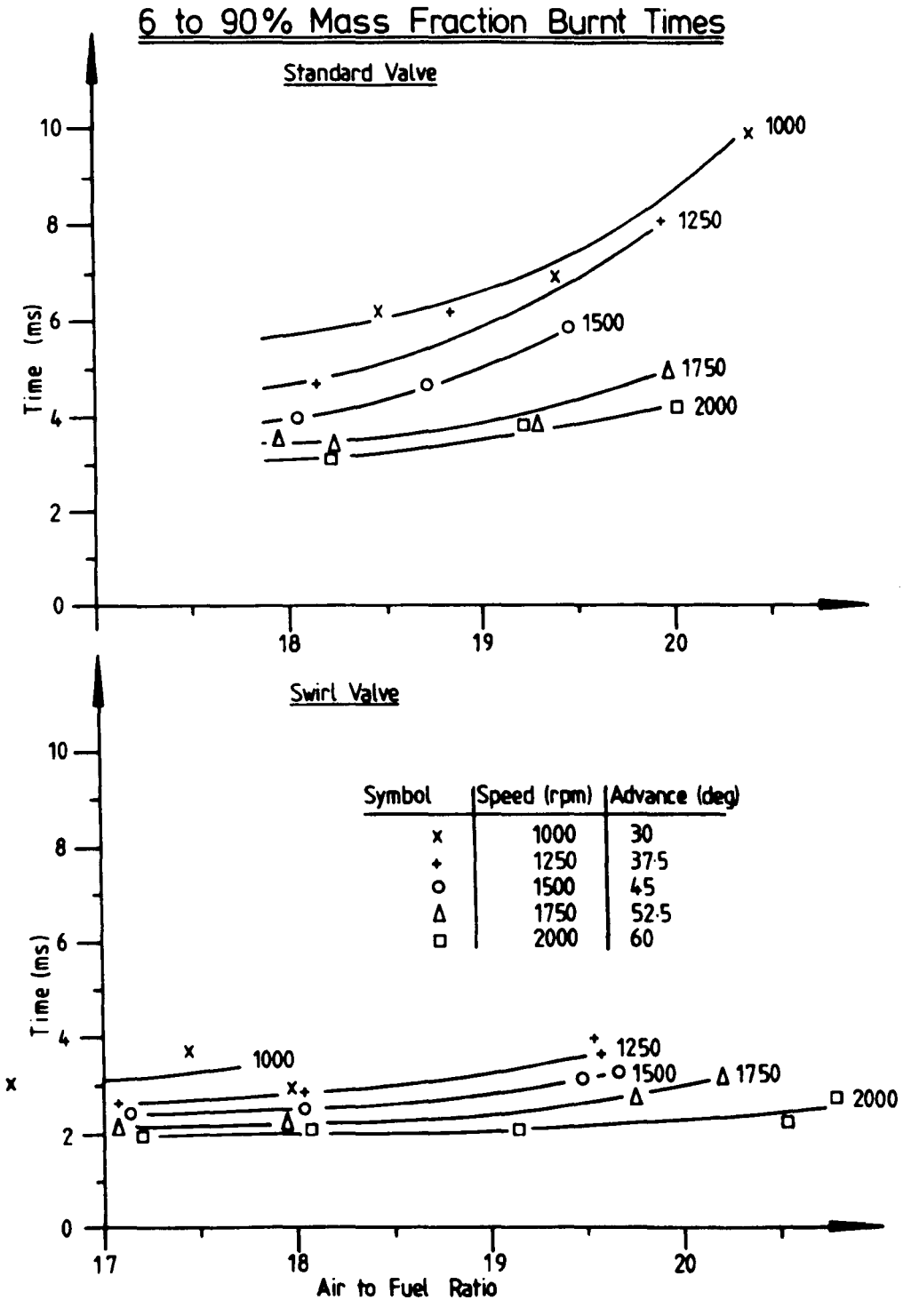

Figure 7.21

Averaged 0-90% Mass Fraction Burnt Times

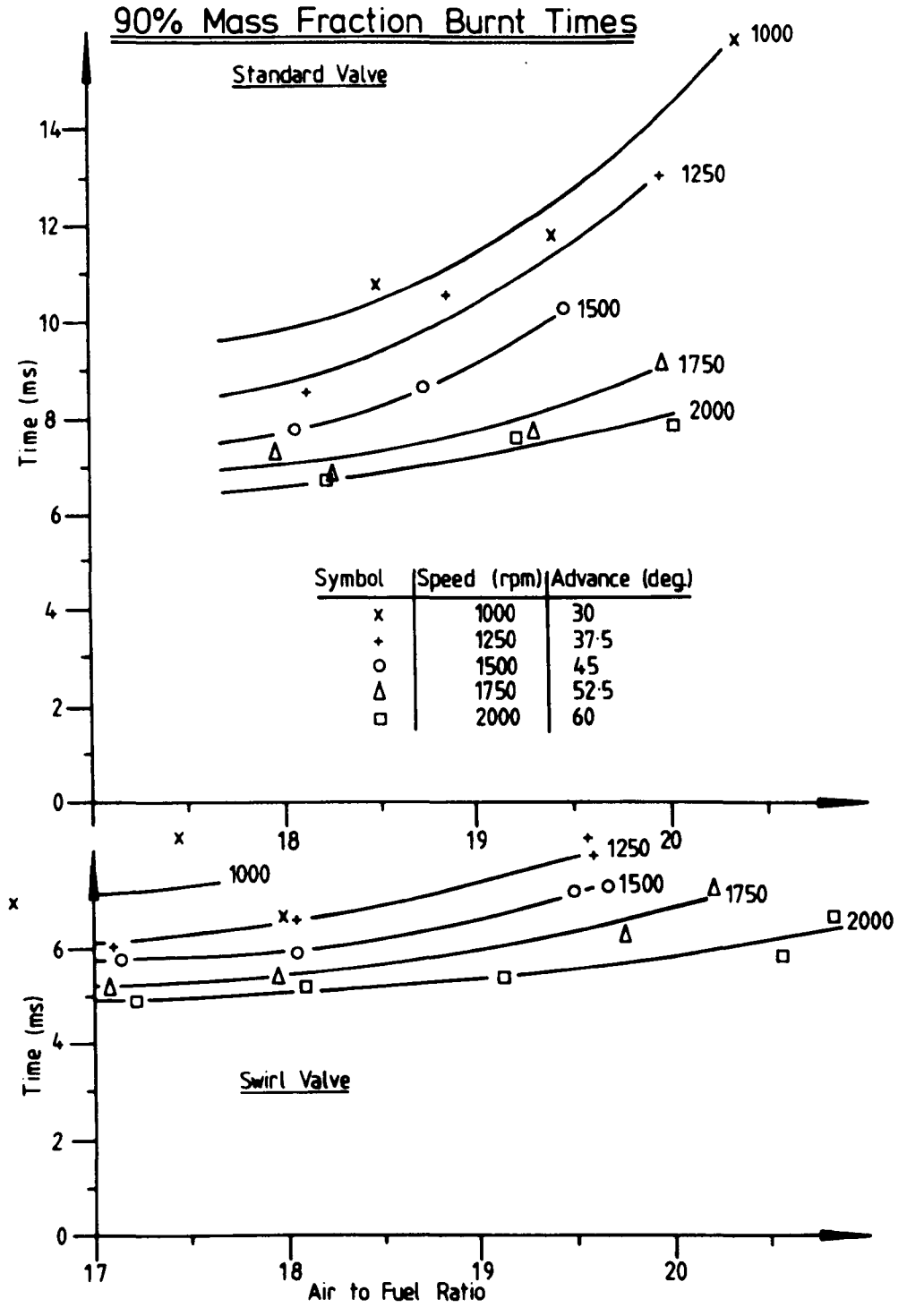

Figure 7.22

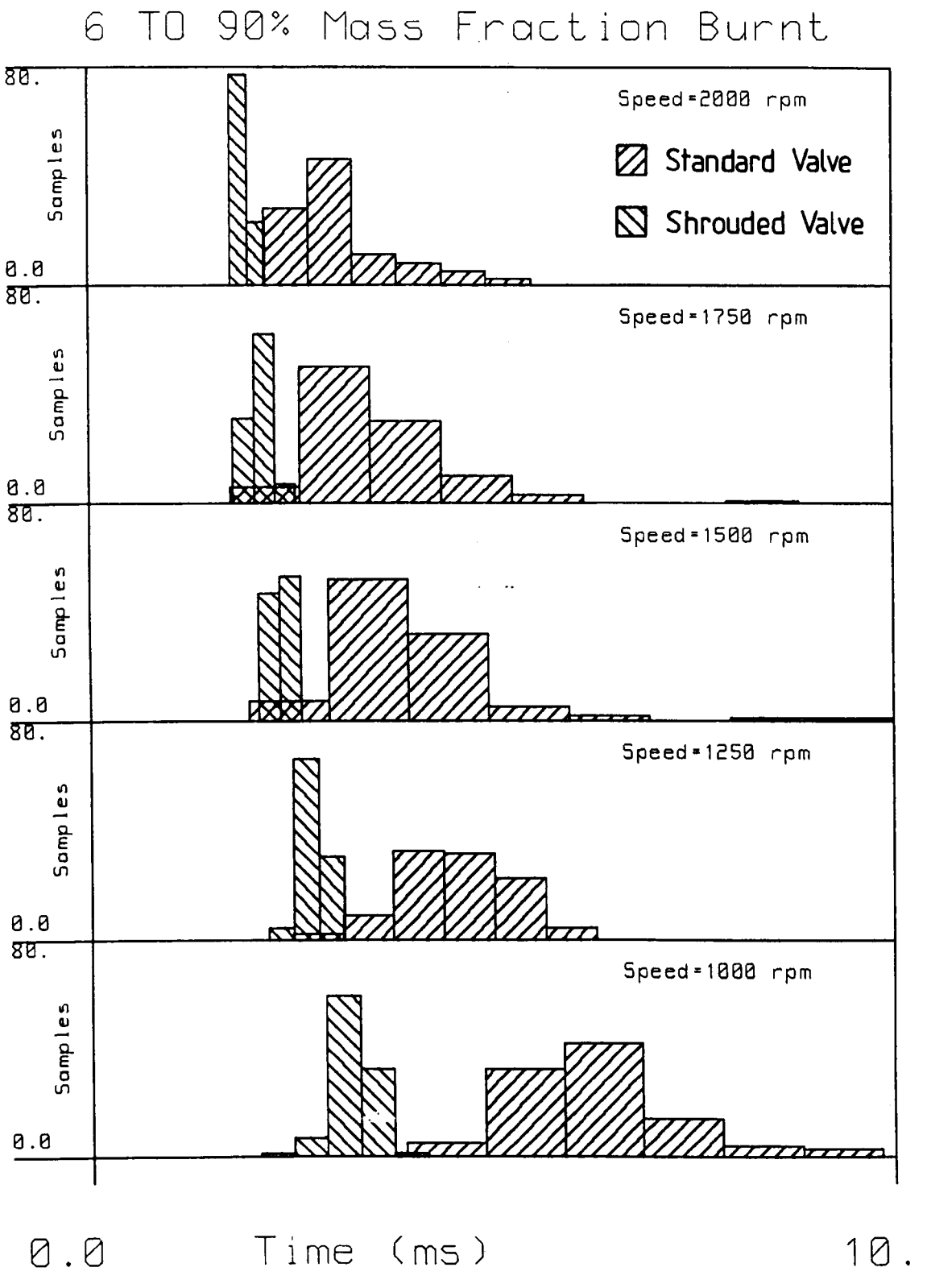
6 TO 90% Mass Fraction Burnt
80.
Samples
0.0
Speed=2000 rpm
Standard Valve
Shrouded Valve
Speed=1750 rpm
Speed=1500 rpm
Speed=1250 rpm
Speed=1000 rpm
0.0
Time (ms)
10.

Figure 7.23

Distributions of 0-90% Mass Fraction Burnt Times

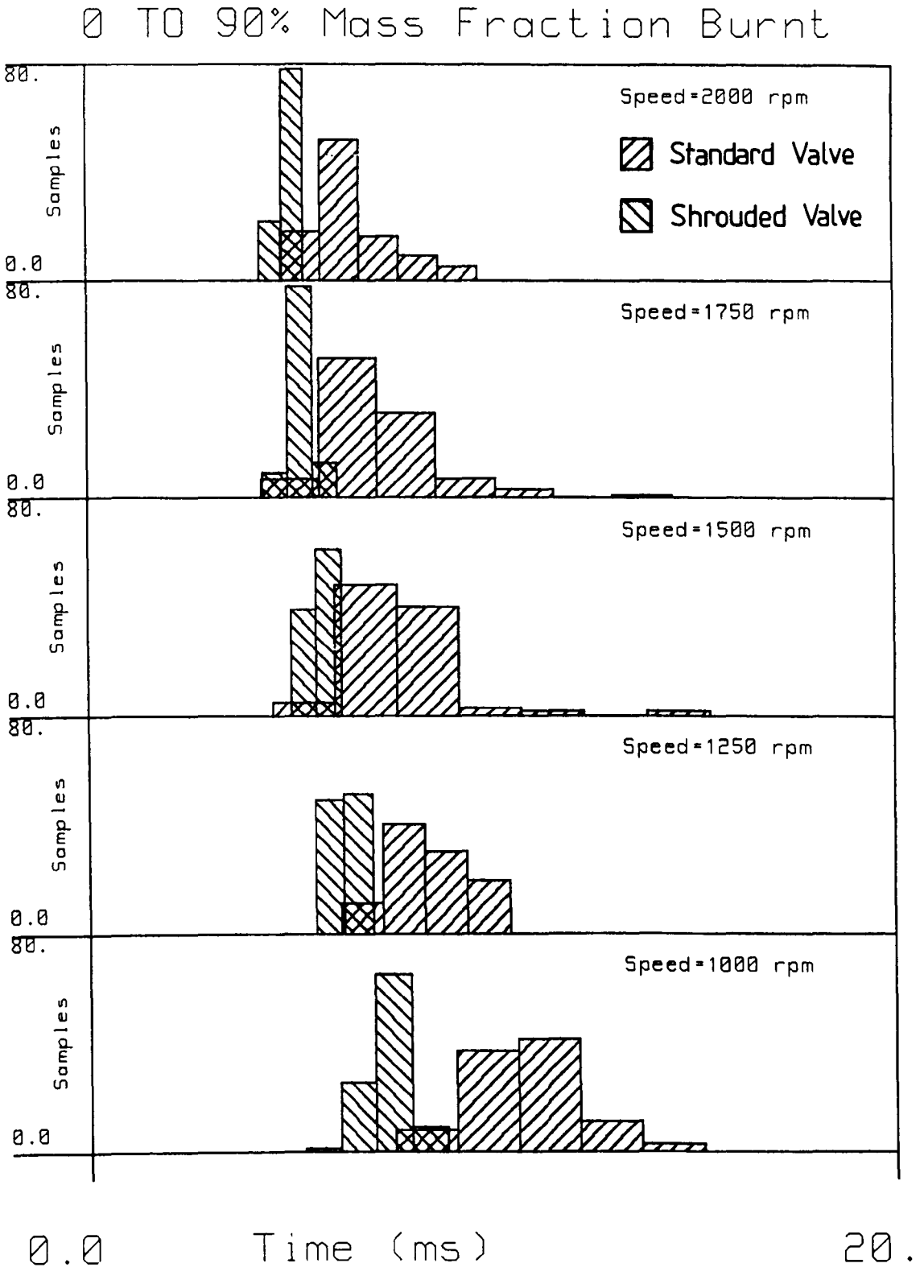

Figure 7.24

Averaged Model 1 Burning Velocity Ratios as a Function of Crank-Angle

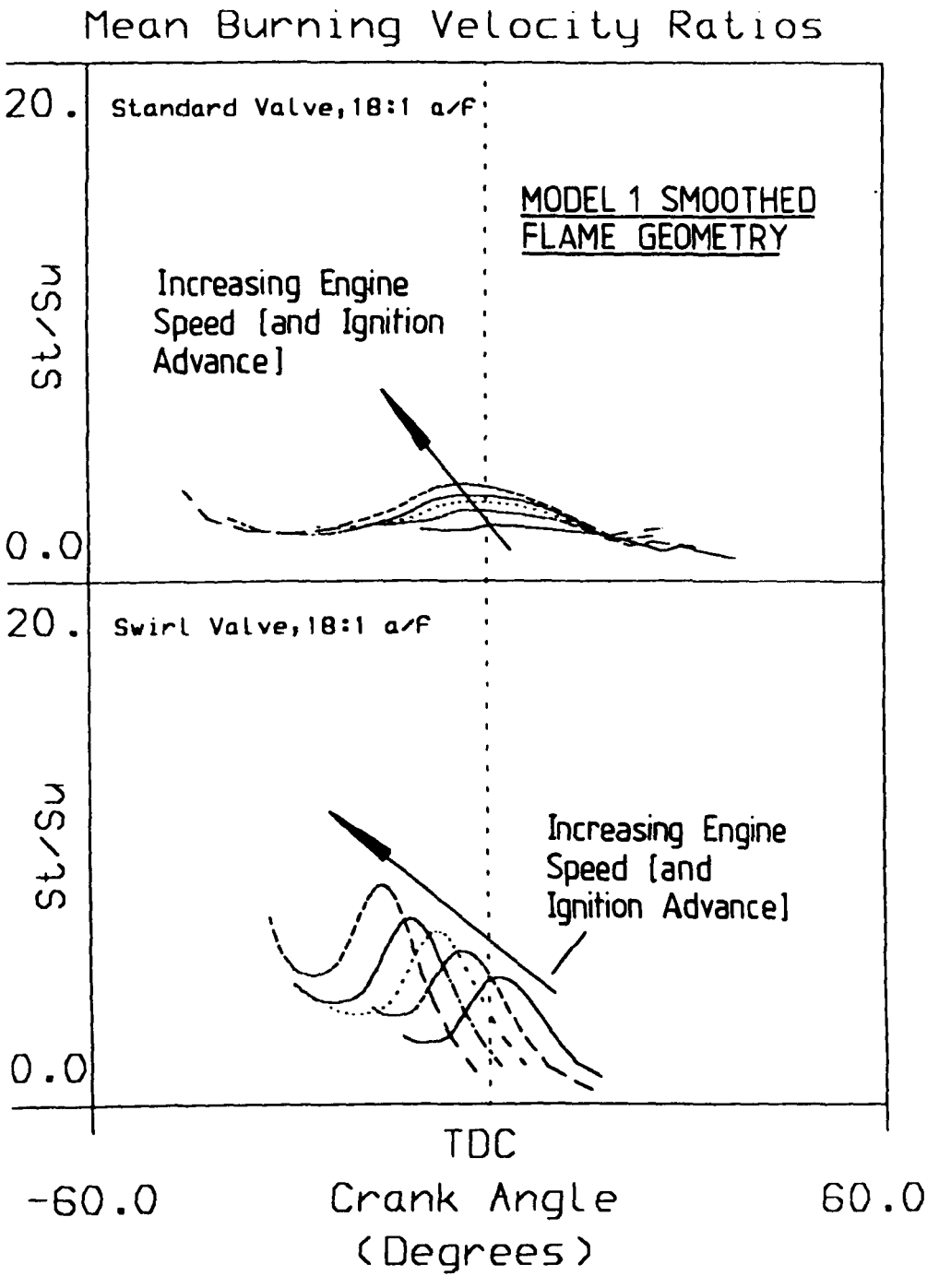

Figure 7.25

Averaged Model 2 Burning Velocity Ratios as a Function of Crank-Angle

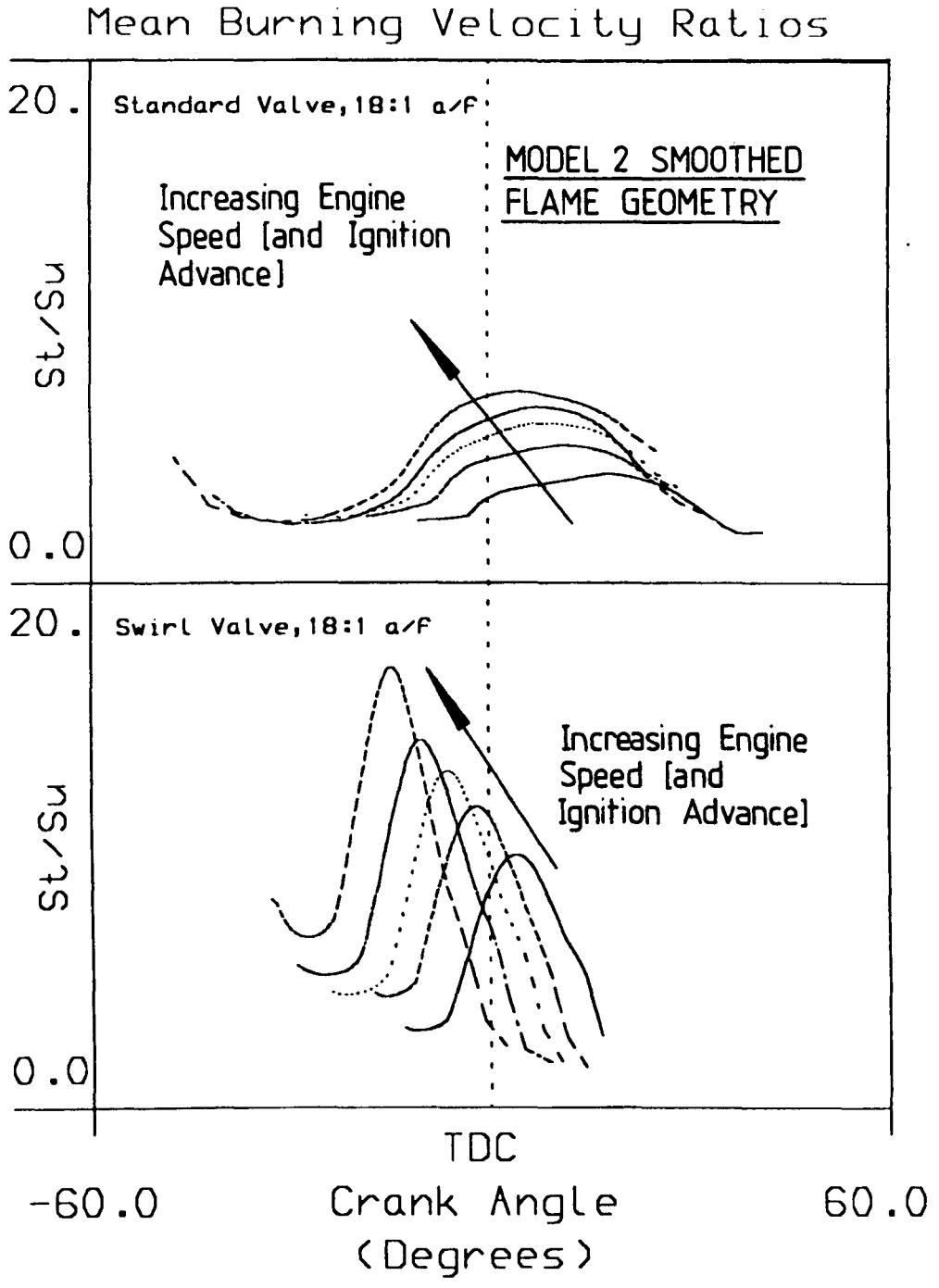

Figure 7.26

Averaged Model 2 Burning Velocity Ratios as a Function of Smoothed Flame Radius

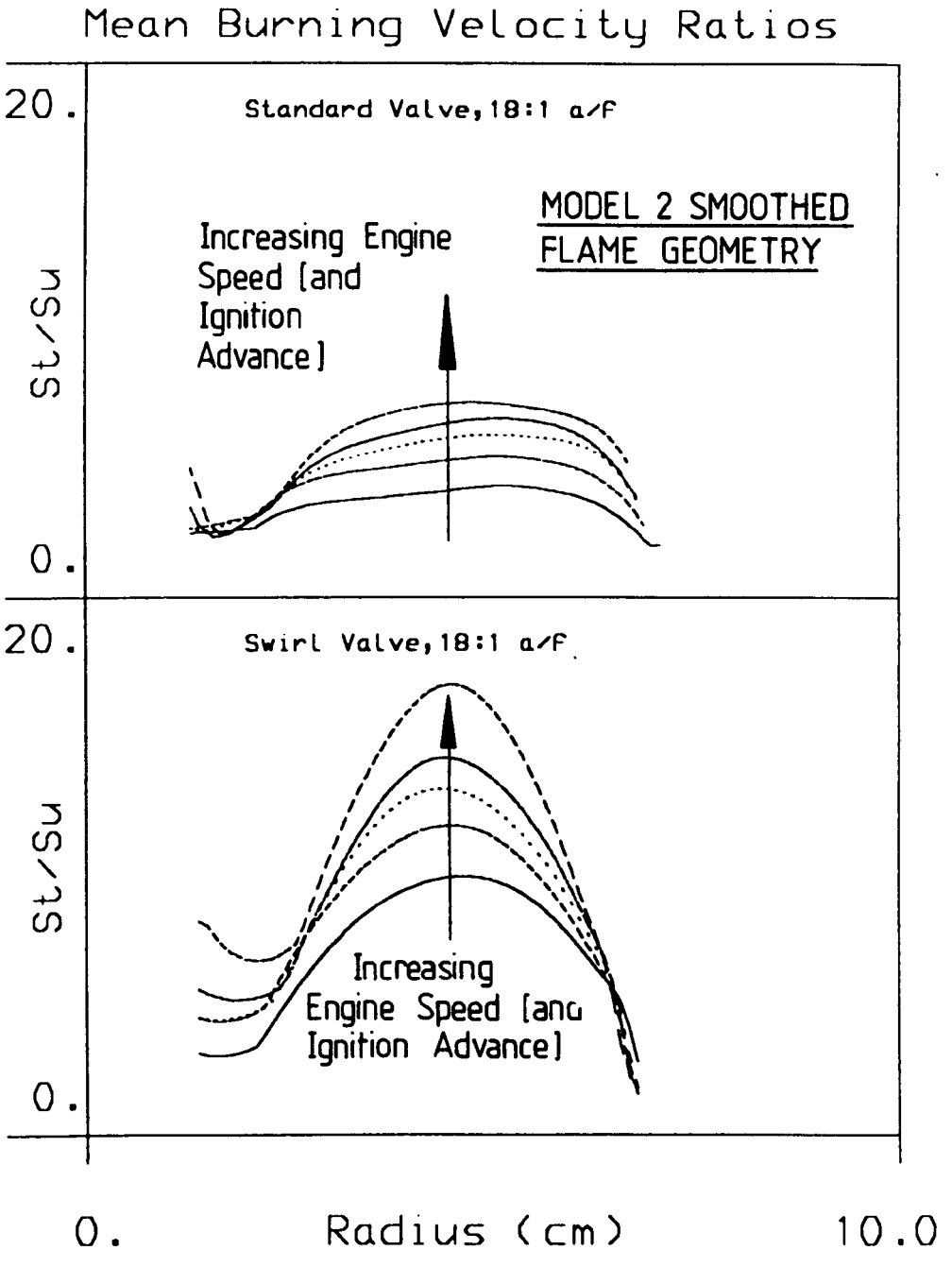

Figure 7.27

Averaged Model 2 Burning Velocity Ratios as a Function of Crank-Angle

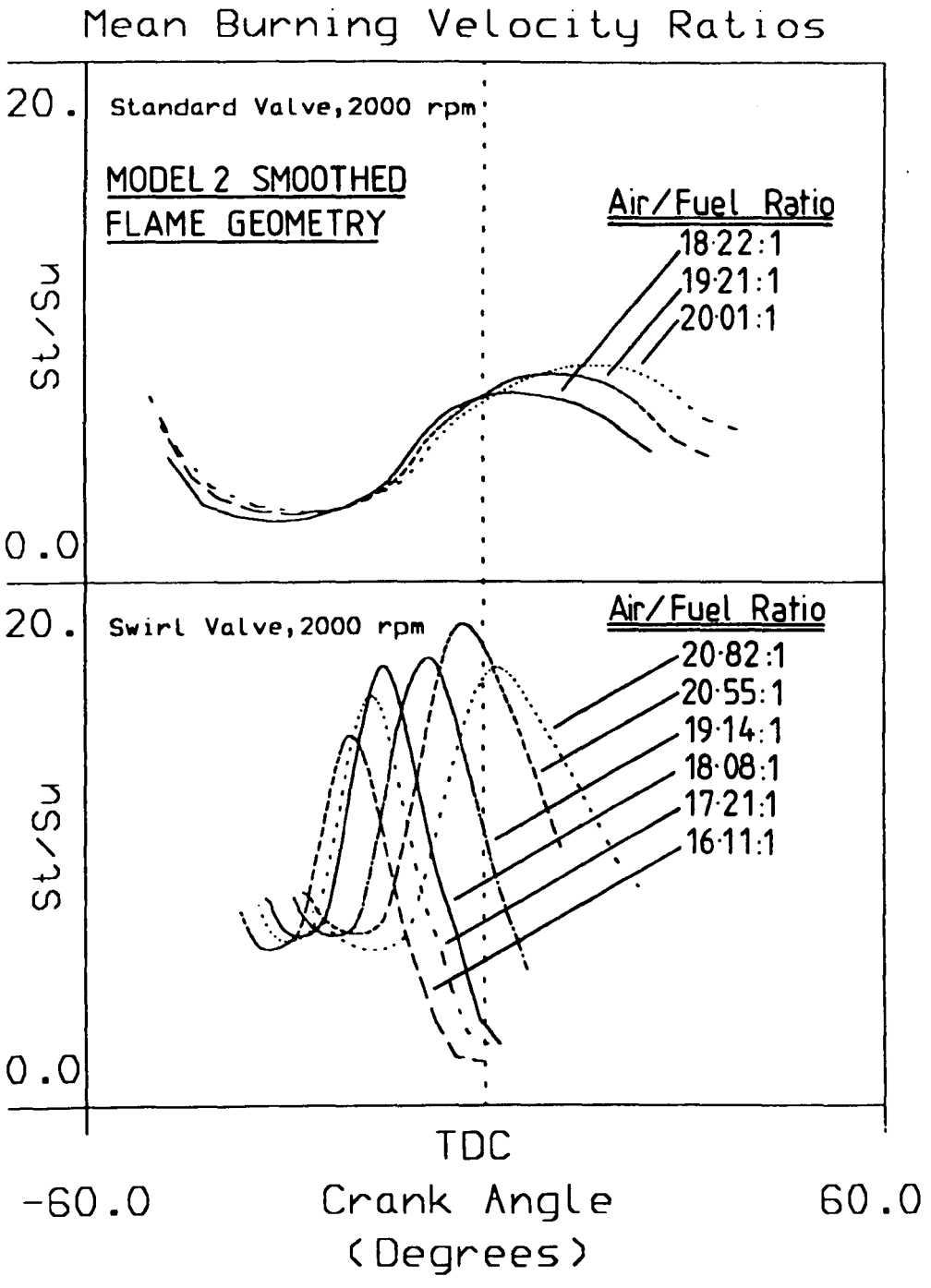

Figure 7.28

Averaged Model 2 Burning Velocity Ratios as a Function of Smoothed Flame Radius

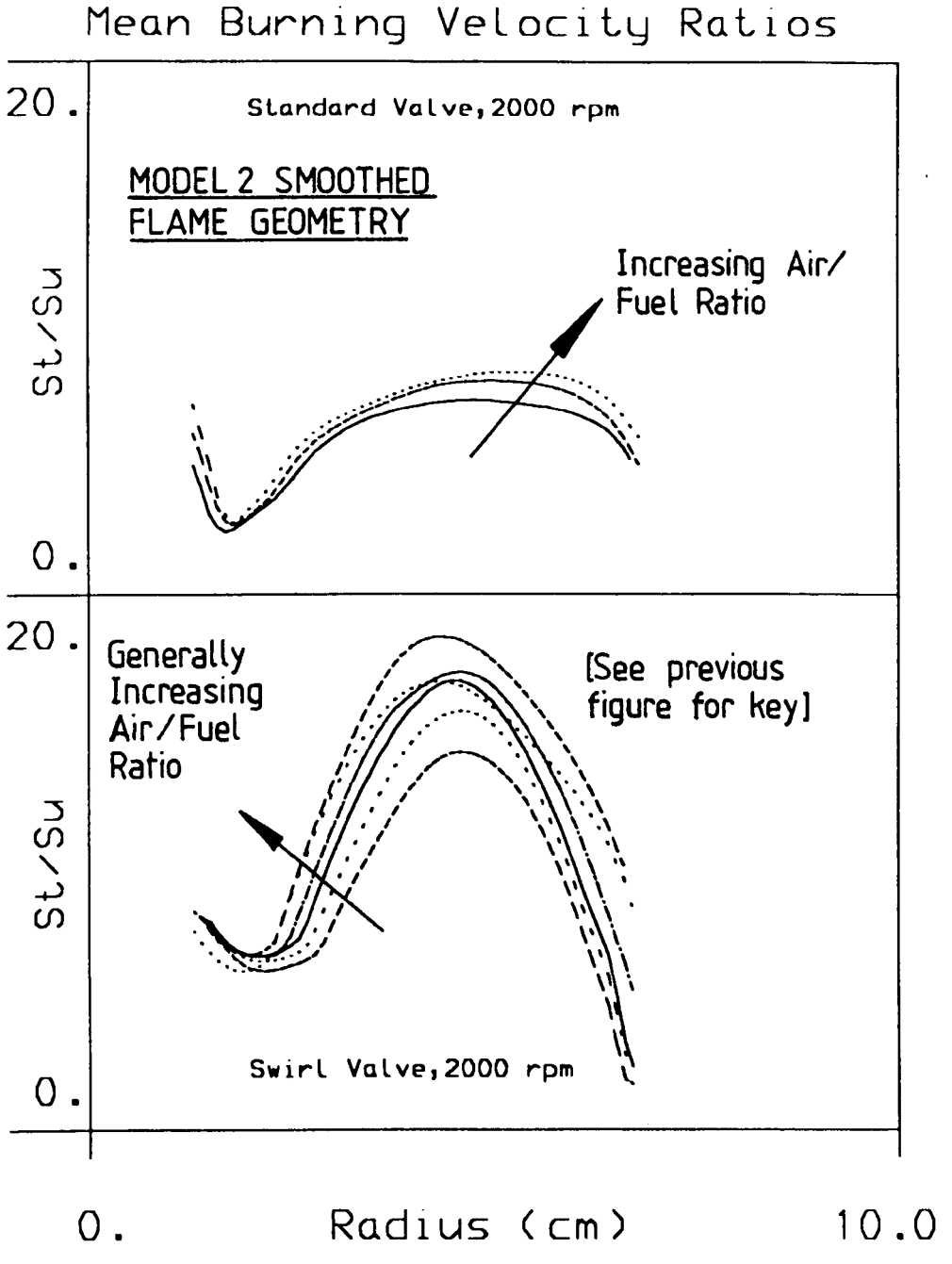

Figure 7.29

Averaged Model 2 Flame Speeds as a Function of Smoothed Flame Radius

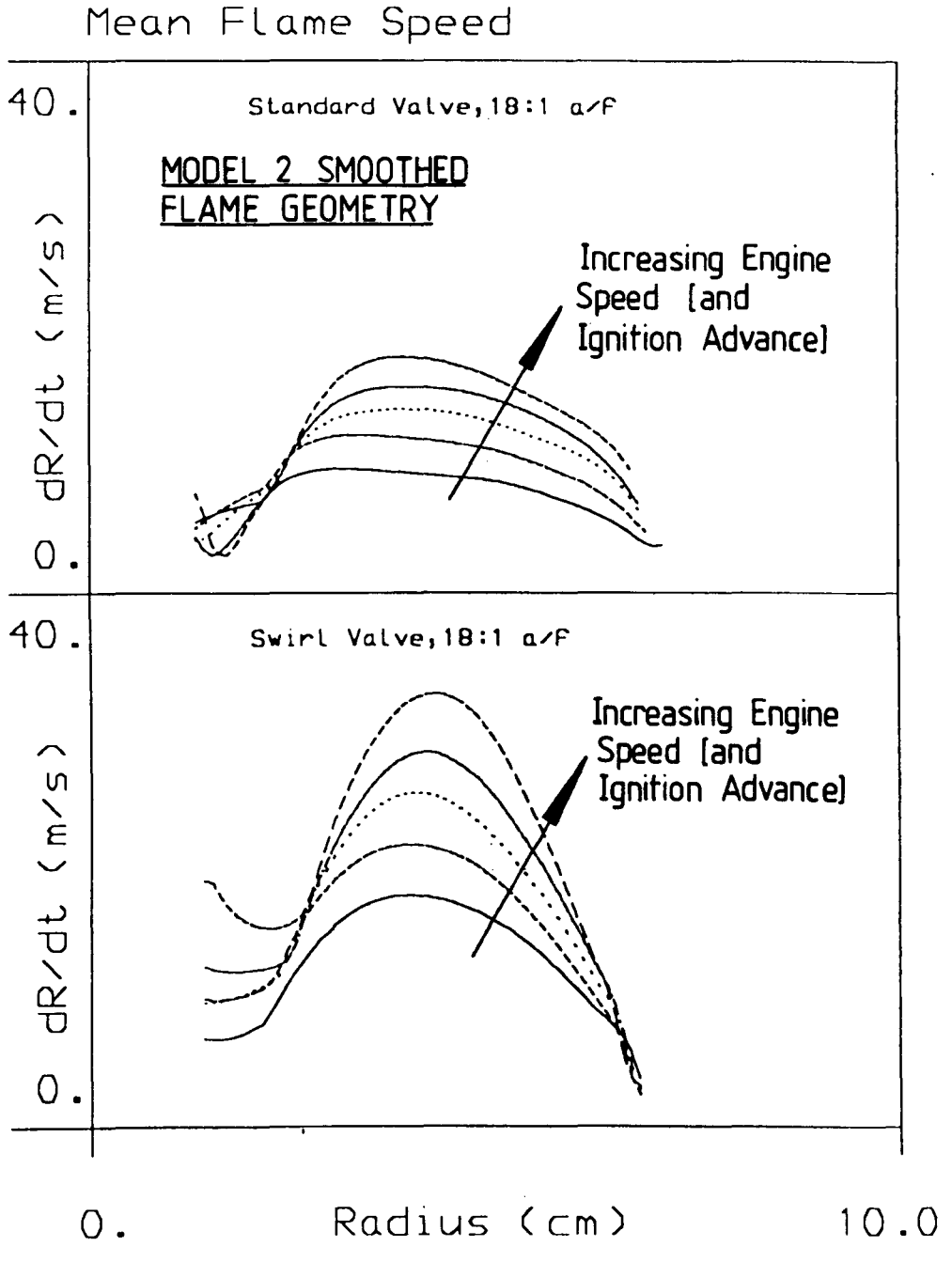

Figure 7.30

Model 1 Peak Burning Velocity Ratio/Radial Wire CBC Turbulence Intensity Correlation

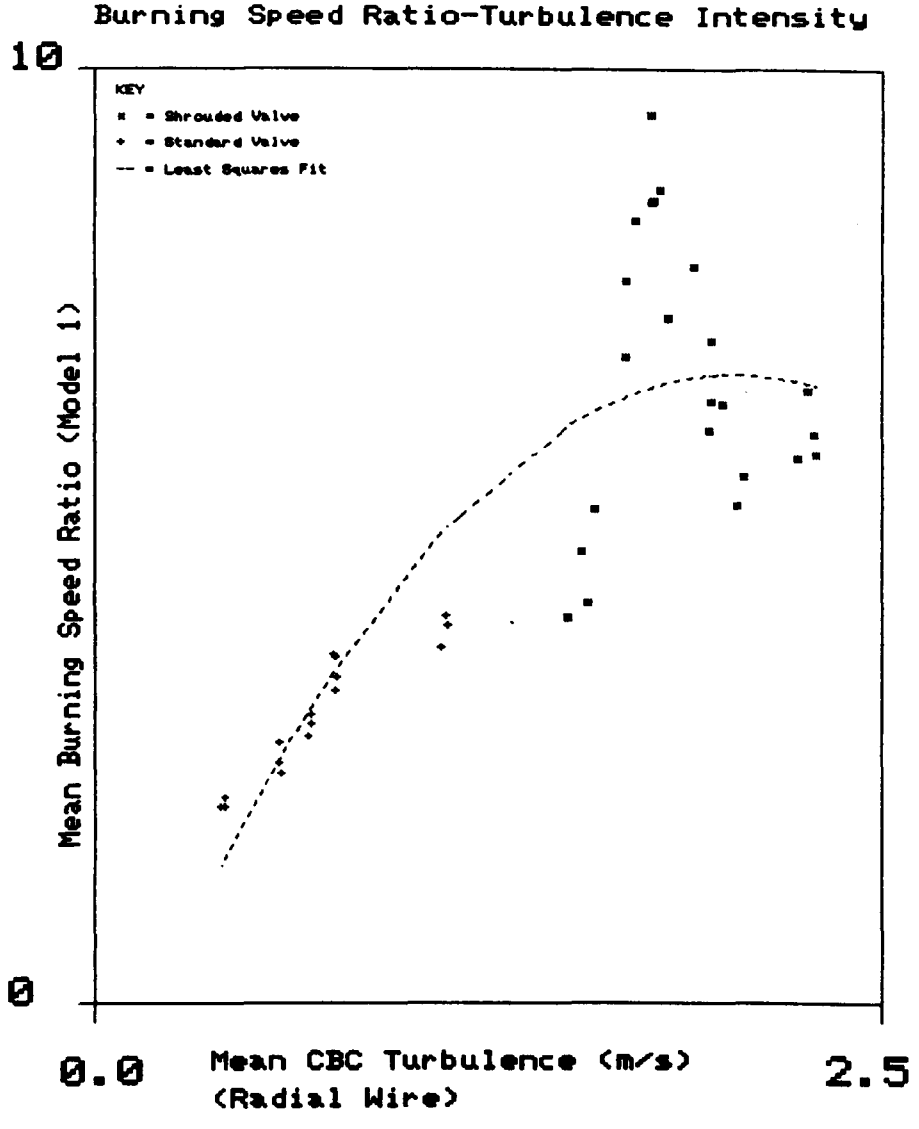

Figure 7.31

Model 1 Peak Burning Velocity Ratio/Circumferential Wire CBC Turbulence Intensity Correlation

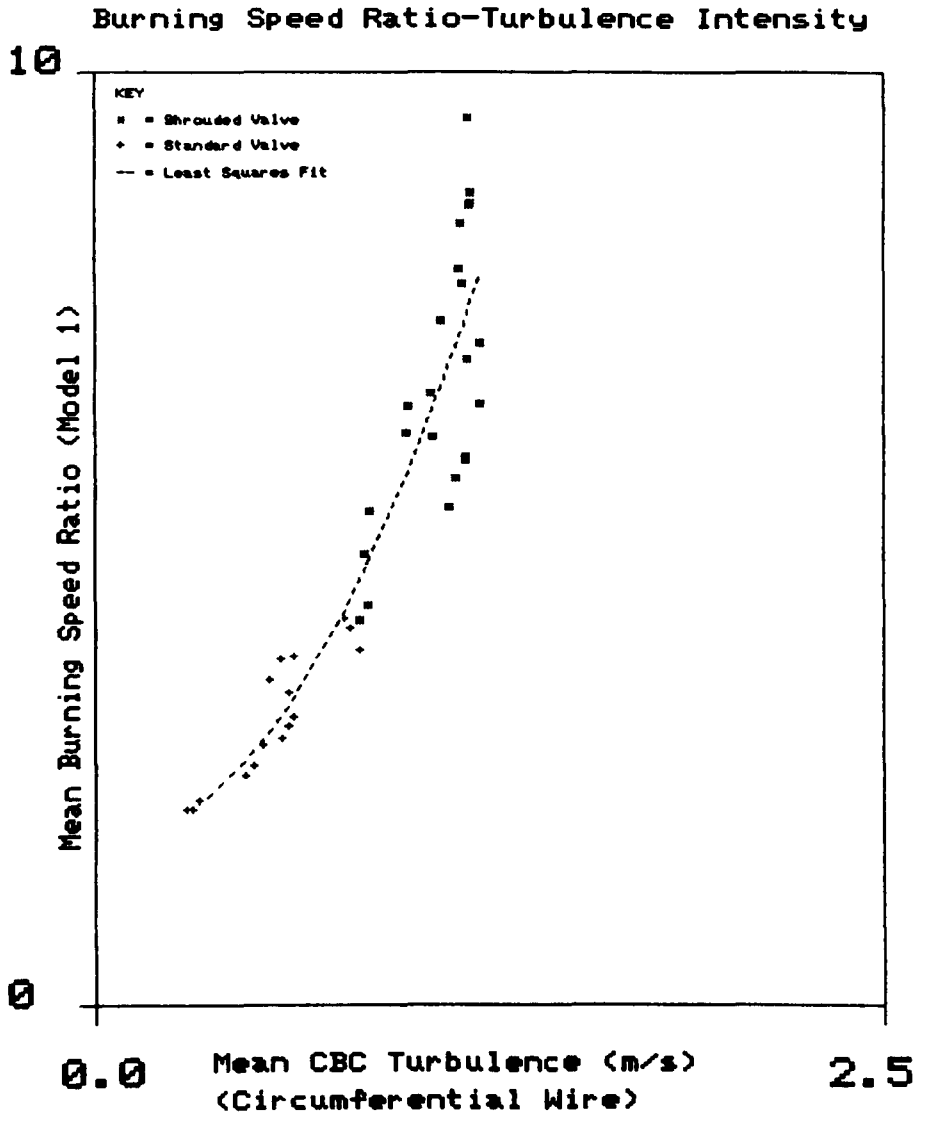

Figure 7.32

Model 1 Peak Burning Velocity Ratio/Radial Wire CBC Velocity Gradient Intensity Correlation

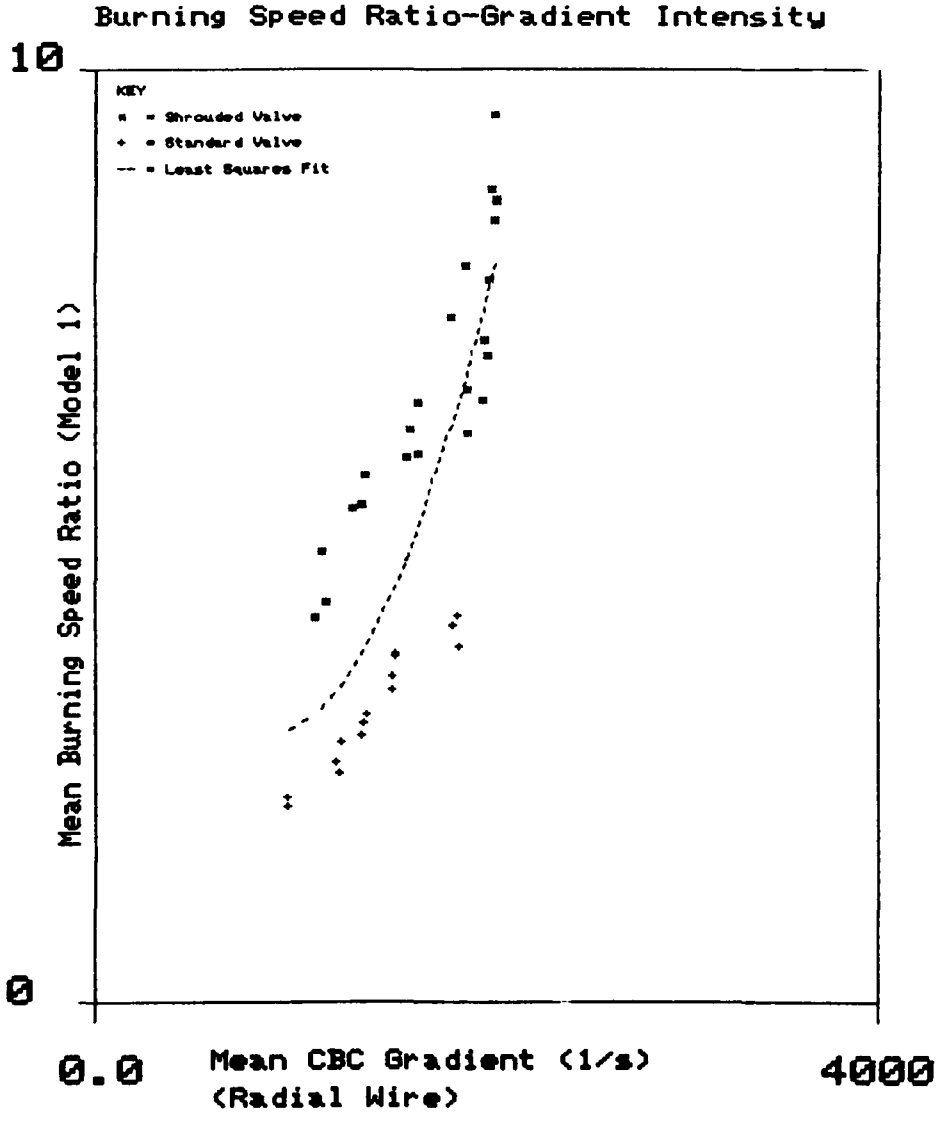

Figure 7.33

Model 1 Peak Burning Velocity Ratio/Circumferential Wire CBC Velocity Gradient Intensity Correlation

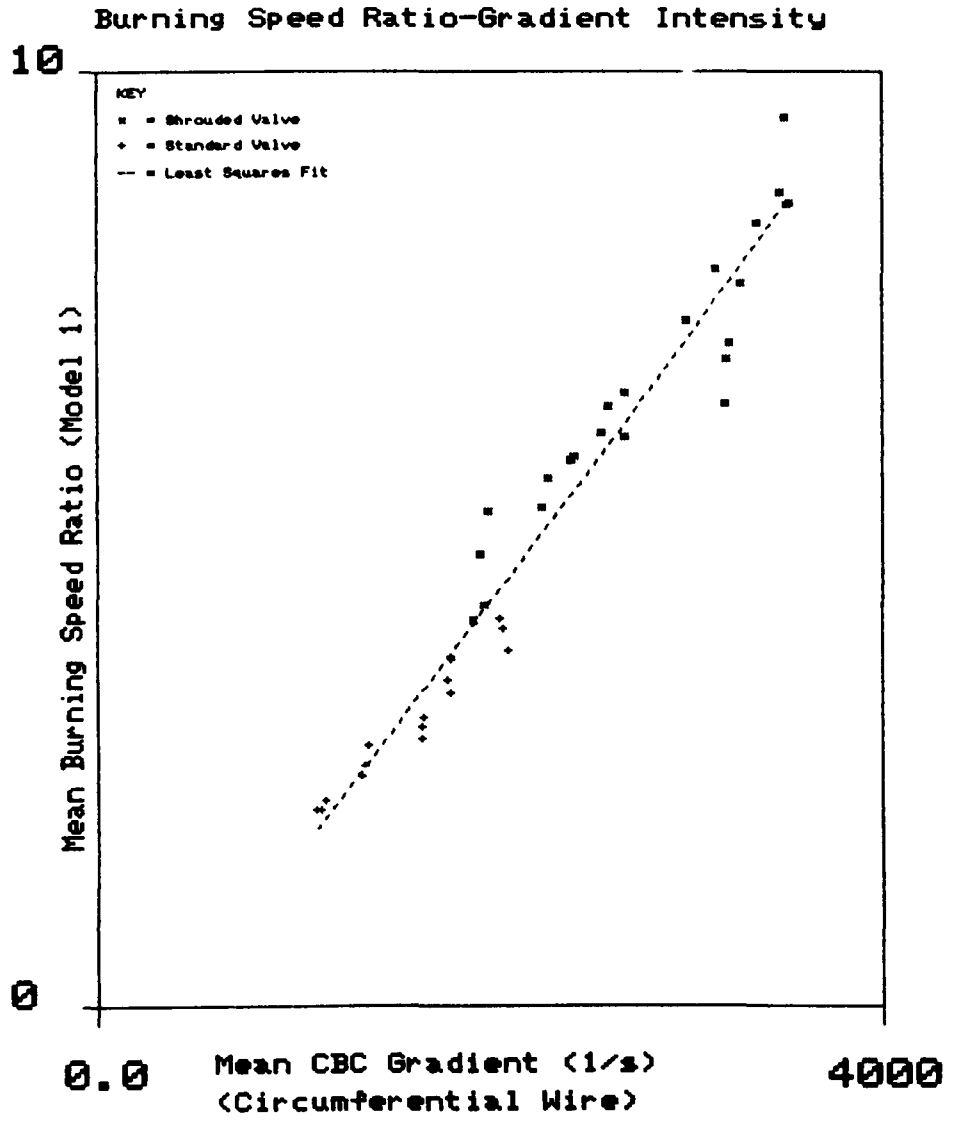

Figure 7.34

Model 2 Peak Burning Velocity Ratio/Radial wire CBC Turbulence Intensity Correlation

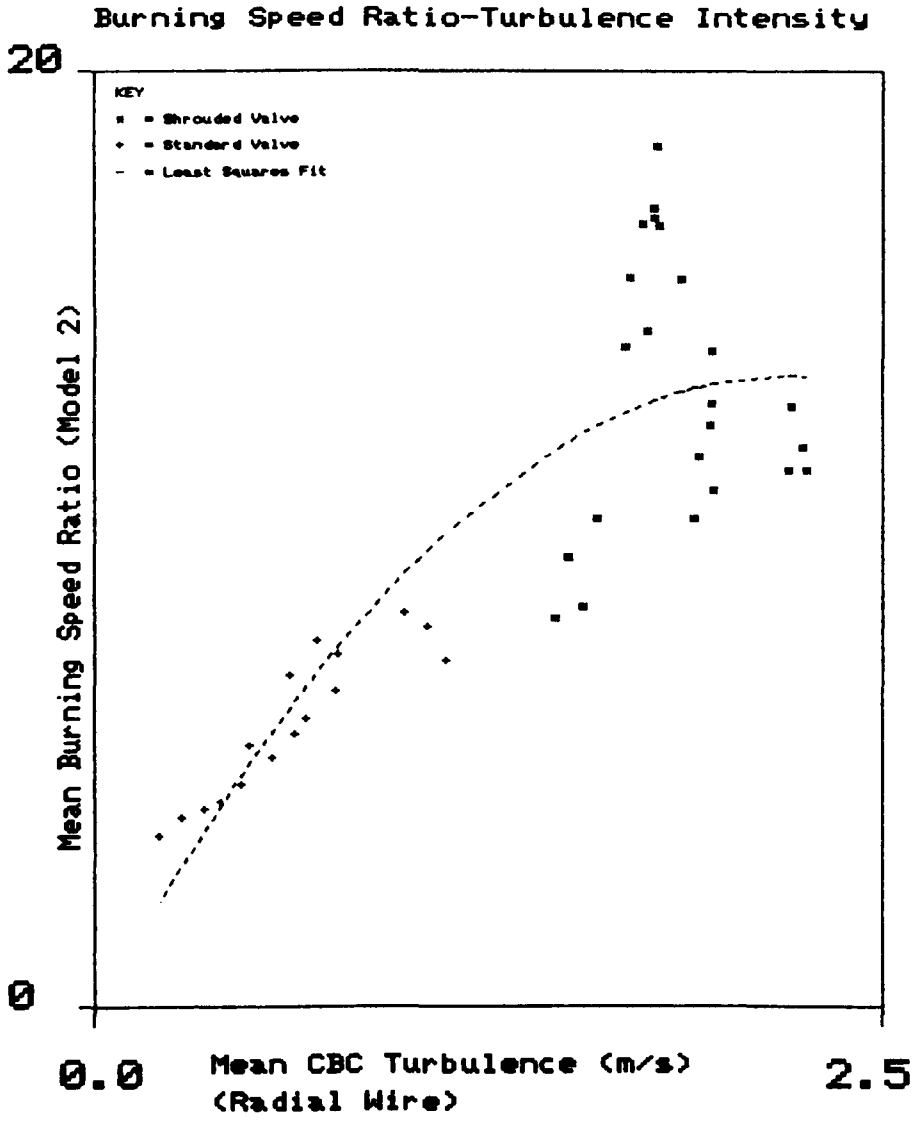

Figure 7.35

Model 2 Peak Burning Velocity Ratio/Circumferential Wire CBC Turbulence Intensity Correlation

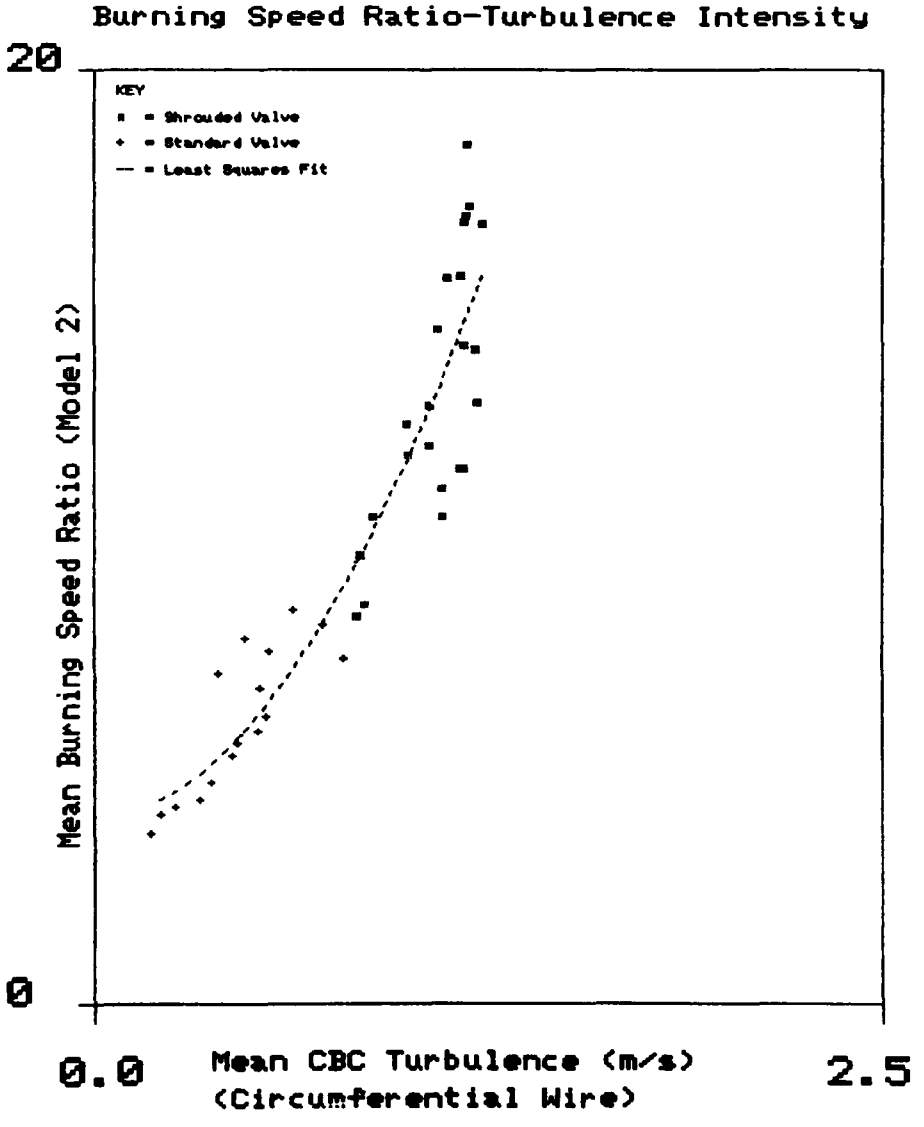

Figure 7.36

Model 2 Peak Burning Velocity Ratio/Radial Wire CBC Velocity Gradient Intensity Correlation

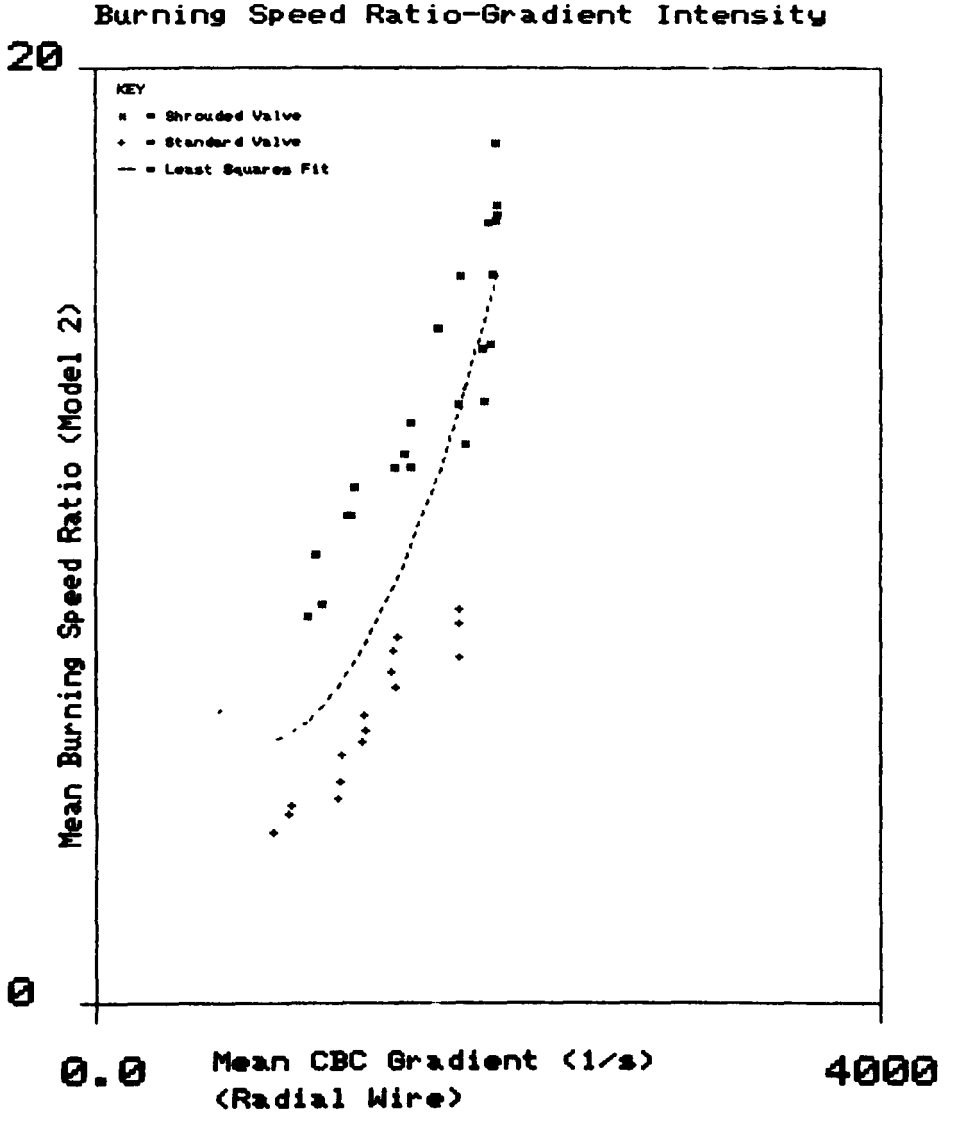

Figure 7.37

Model 2 Peak Burning Velocity Ratio/Circumferential Wire
CBC Velocity Gradient Intensity Correlation

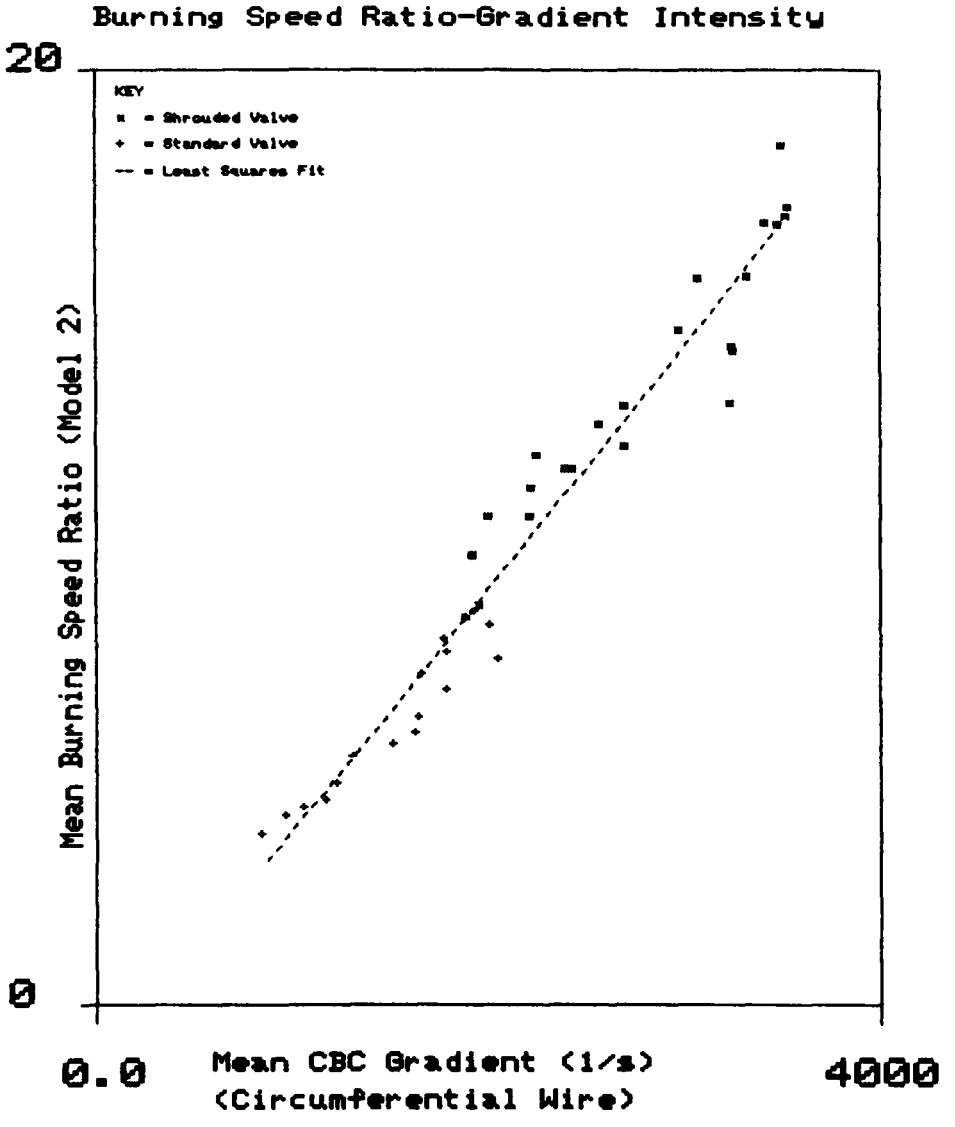

Figure 7.38

Models 1 and 2 Peak Burning Velocity Ratio/Radial Wire CBC Turbulence Intensity Correlation

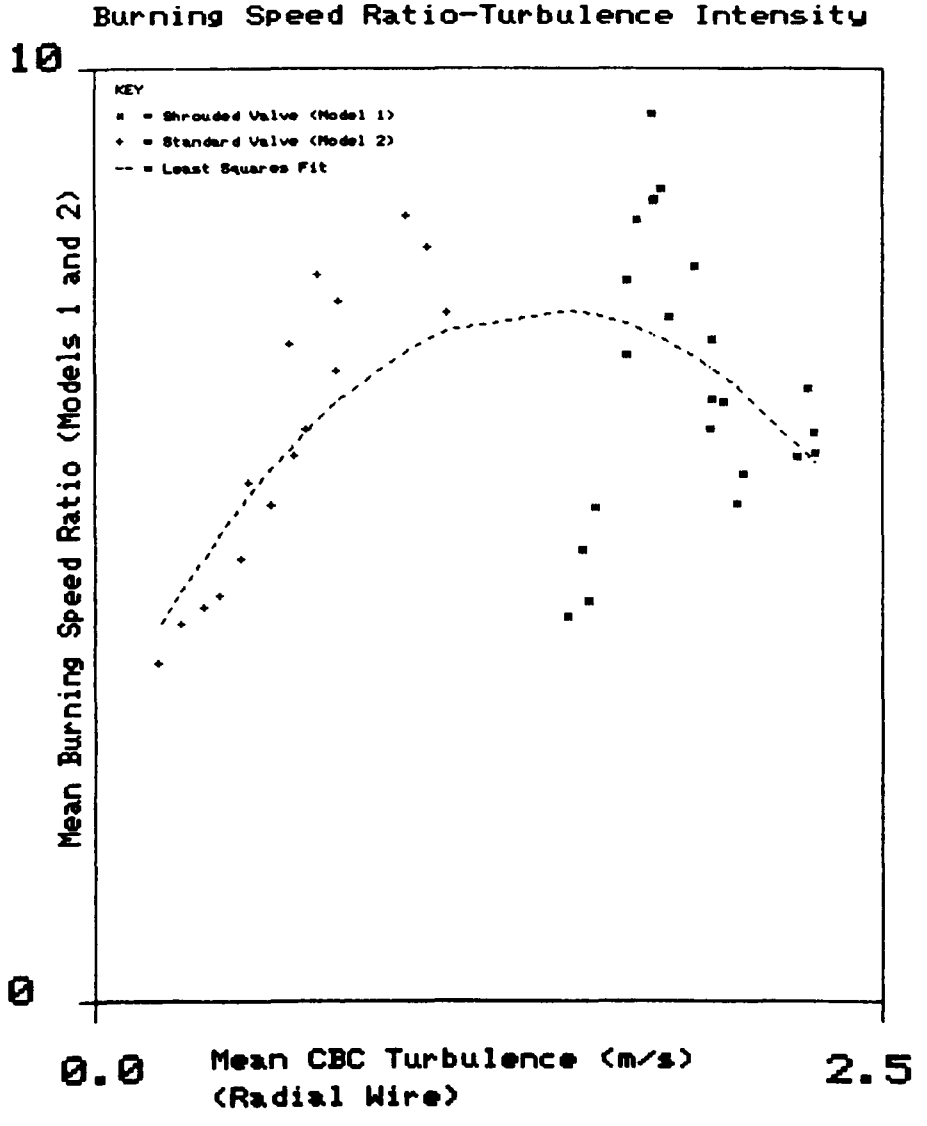

Figure 7.39

Models 1 and 2 Peak Burning Velocity Ratio/Circumferential Wire CBC Turbulence Intensity Correlation

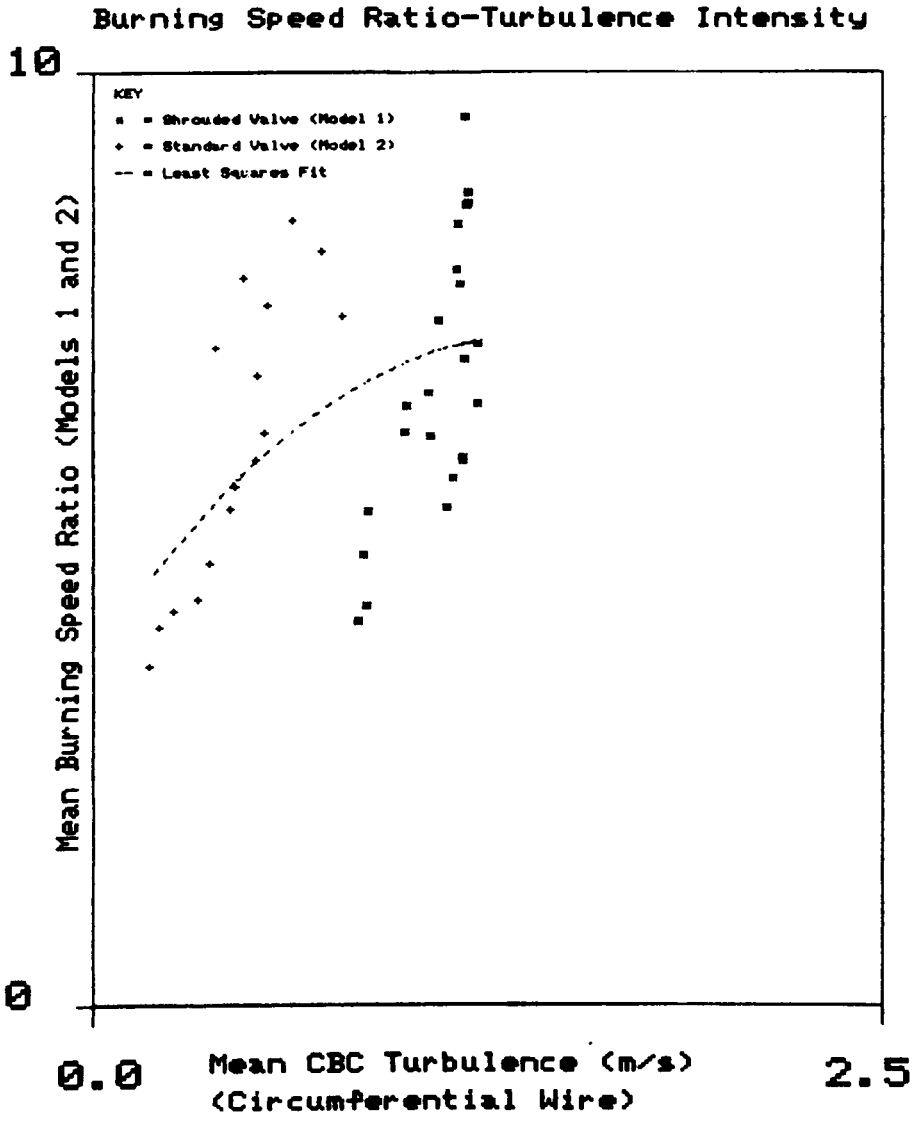

Figure 7.40

Models 1 and 2 Peak Burning Velocity Ratio/Radial Wire
CBC Spatial Velocity Gradient Intensity Correlation

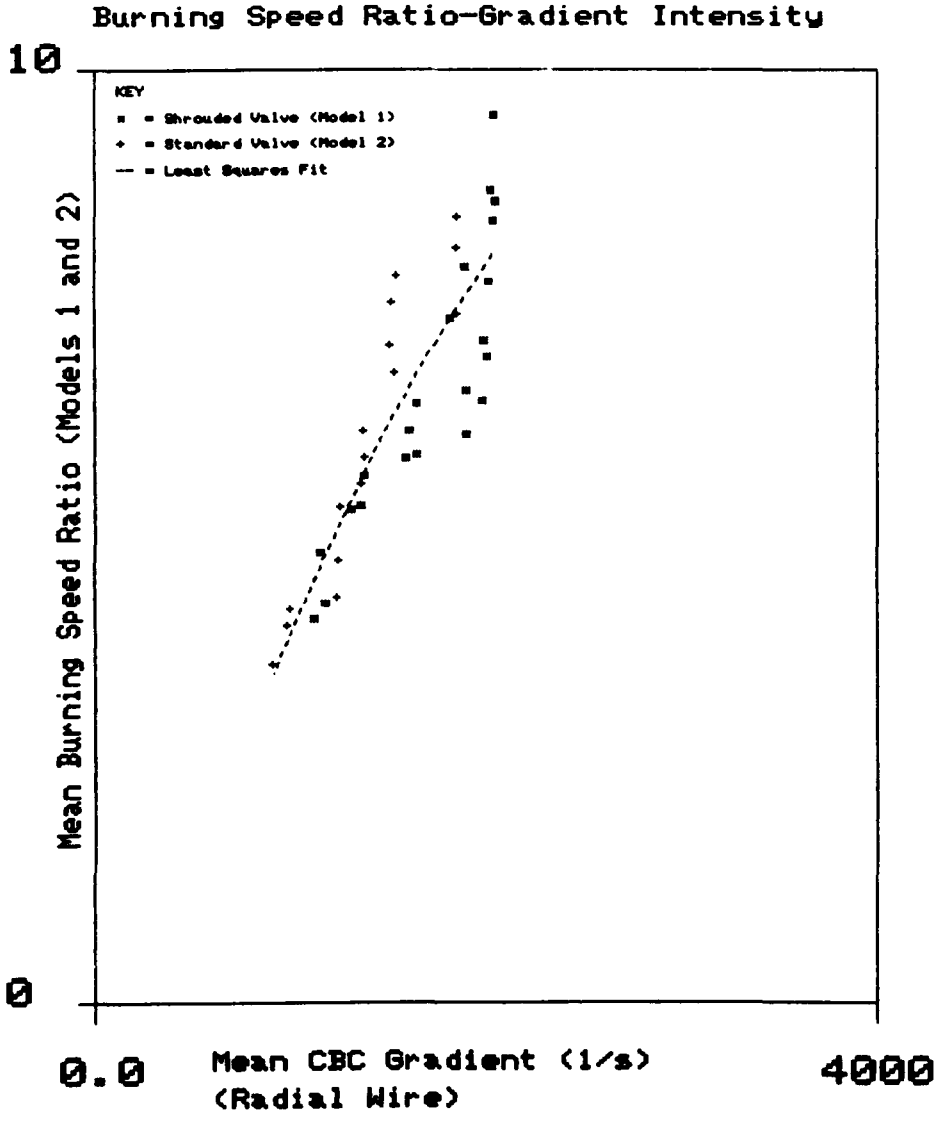

Figure 7.41

Models 1 and 2 Peak Burning Velocity Ratio/Circumferential Wire CBC Velocity Gradient Intensity Correlation

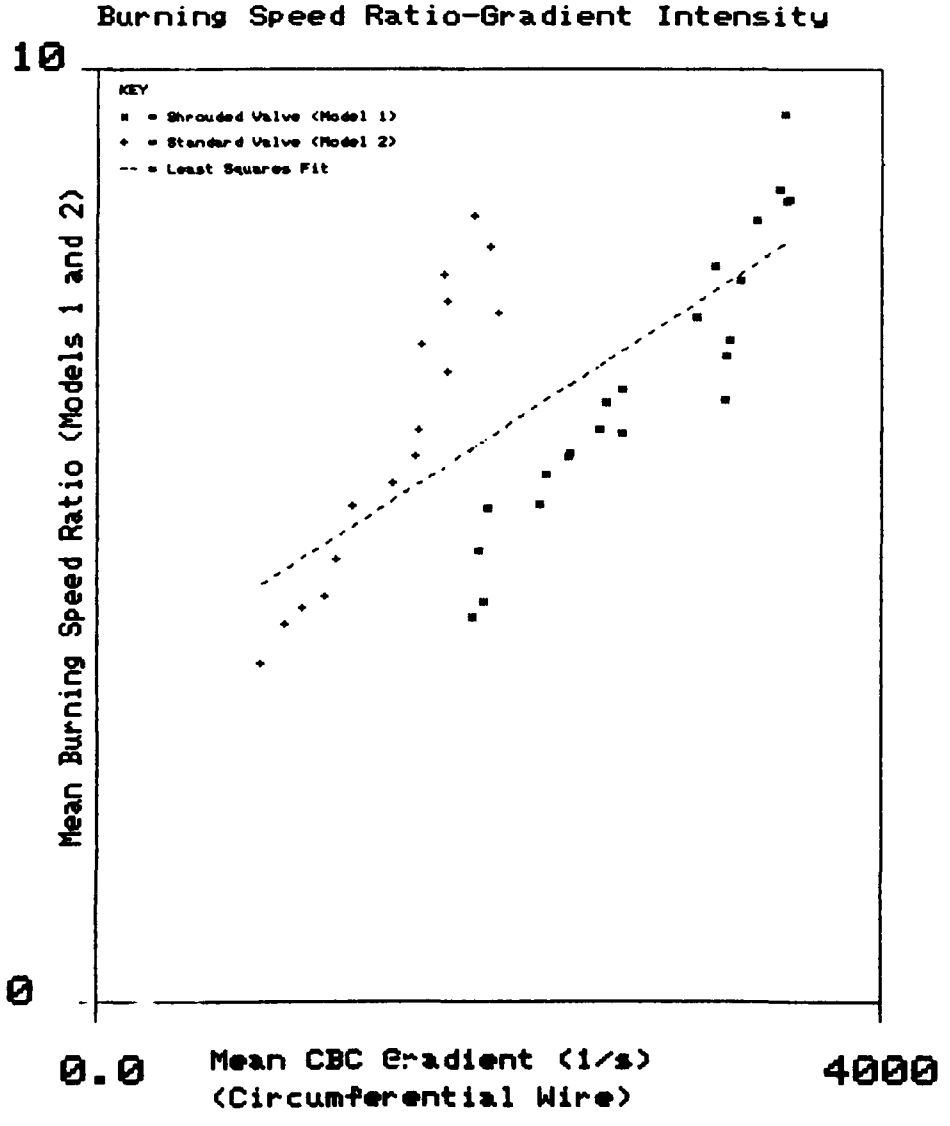

Figure 7.42

APPENDIX A

Proof of End-Loss Equations for Fine Wire Anenometers

The initial equations are taken from Davis and Fisher [28], and the final result is confirmed by Witze [87]. It is assumed that the anenometer is a perfect cylinder, attached to prongs that act as large heat sinks. Discontinuities caused by the weld that fixes the wire and local heating at the prong tips are ignored. Also the contribution of radiation to the overall heat balance is considered to be negligible.

Let Q_c = heat conduction/unit length (watts/m)

Q_e = ohmic heating/unit length (watts/m)

Q_h = convective heat transfer/unit length (watt/m)

$$Q_c = \frac{d}{dx}\left(- k(T)\, A \frac{dT}{dx} \right) \tag{A.1}$$

$$= - A \left(k(T) \frac{d^2T}{dx^2} + \frac{dk(T)}{dT} \left(\frac{dT}{dx} \right)^2 \right) \tag{A.2}$$

where x = distance along the wire (m)

T = absolute temperature (K)

k(T) = wire thermal conductivity as a function of T (W/mK)

A = wire cross-sectional area (m^2)

If the wire thermal conductivity is assumed to be relatively insensitive to temperature, then:

$$Q_c = - A k_w \frac{d^2T}{dx^2} \tag{A.3}$$

where k_w = overall thermal conductivity of wire (W/mK).

The ohmic heating is given by:

$$Q_e = i_p^2 \rho(T)/A \qquad (A.4)$$

where i_p = current through wire (amps)

$\rho(T)$ = resistivity of wire as a function of T (ohm metres).

Also,

$$\rho(T) = \rho_o (1 + \alpha (T_w - T_o)) \qquad (A.5)$$

where α = temperature coefficient of resistance (K^{-1})

ρ_o, T_o = resistivity and temperature reference values

T_w = wire temperature (K).

Finally, the convective component is given by,

$$Q_h = \pi dh (T_w - T_g) \qquad (A.6)$$

where d = wire diameter (m)

h = convective heat transfer coefficient (w/m^2K)

T_g = free stream gas temperature (K)

The overall balance gives,

$$Q_c + Q_h = Q_e \qquad (A.7)$$

Combining equations (A.3 - A.7) gives, with some rearrangement,

$$k_w A \frac{d^2T}{dx^2} + T_w \left(\frac{i_p^2 \alpha \rho_o}{A} - \pi dh \right) + \frac{i_p^2 \rho_o}{A} - \frac{i_p^2 \alpha \rho_o T_o}{A} + \pi dh T_g = 0 \qquad (A.8)$$

Let

$$K_1 = \frac{\pi dh}{k_w A} - \frac{i_p^2 \alpha \rho_o}{k_w A^2} \qquad (A.9)$$

$$K_2 = \frac{i_p^2 \rho_o}{k_w A^2} (1 - \alpha T_o) + \frac{\pi dh T_g}{k_w A}$$

$$T' = T_w - \frac{K_2}{K_1}$$

The differential equation hence becomes,

$$\frac{1}{K_1}\frac{d^2T'}{dx^2} - T' = 0 \qquad (A.10)$$

Boundary conditions: i) At $x = \ell/2$, $T_w = T_s$ = support temperature (K)

(see Figure A.1) ii) At $x = 0$, $\frac{dT_w}{dx} = 0$ (A.11)

Using the solution,

$$T' = P\, e^{\sqrt{K_1}x} + Q\, e^{-\sqrt{K_1}x} \qquad (A.12)$$

the wire temperature at ordinate x is found to be,

$$T_w = (T_s - K_2/K_1)\left(\frac{\cosh(\sqrt{K_1}x)}{\cosh(\sqrt{K_1}\ell/2)}\right) \qquad (A.13)$$

Integrating over the wire length to obtain a mean temperature value,

$$T_w' = \frac{2(T_s - K_2/K_1)}{\sqrt{K_1}\ell}\tanh(\sqrt{K_1}\ell/2) + \frac{K_2}{K_1} \qquad (A.14)$$

Let $$C_1 = \frac{K_2}{K_1} \qquad (A.15)$$

$$C_2 = K_1$$

and $$\rho_o = \frac{R_oA}{\ell} \qquad (A.16)$$

where R_o = wire resistance at T_o (ohms).

Thus, from (A.9)

$$C_2 = \frac{4}{k_w d}\left(h - \frac{i_p^2 \alpha R_o}{\pi d \ell}\right) \qquad (A.17)$$

$$C_1 = \frac{i_p^2 R_o (1 - \alpha T_o) + h T_g}{h - \frac{i_p^2 \alpha R_o}{\pi d \ell}} \qquad (A.18)$$

and from (A.14)

$$T_w' = \frac{2(T_s - C_1)}{\ell\sqrt{C_2}} \tanh(\sqrt{C_2}\,\ell/2) + C_1 \qquad (A.19)$$

Extracting C_1 from (A.19),

$$C_1 = \frac{2T_s \tanh(\sqrt{C_2}\,\ell/2) - T_w'\ell\sqrt{C_2}}{2\tanh(\sqrt{C_2}\,\ell/2) - \ell\sqrt{C_2}} \qquad (A.20)$$

Combining (A.17) and (A.18),

$$C_2 = \frac{4}{C_1 k_w d}\left[\frac{i_p^2 R_o(1 - \alpha T_o)}{\pi d \ell} + h T_g\right] \qquad (A.21)$$

Finally, from (A.17)

$$h = \frac{C_2 k_w d}{4} + \frac{i_p^2 \alpha R_o}{\pi d \ell} \qquad (A.22)$$

The iterative solution necessary takes the following form:

i) Guess h assuming no end loss by using,

$$h = \frac{i_p^2 R_w}{A_s(T_w - T_g)} \qquad (A.23)$$

where A_s = wire surface area (m^2)

ii) Estimate C_2 from (A.17).

iii) Find C_1 from (A.20).

iv) Find C_2 from (A.21).

v) Find h from (A.22).

vi) Seek convergence in h. If this is not the case, update h in (iii) and repeat steps (iii) - (vi).

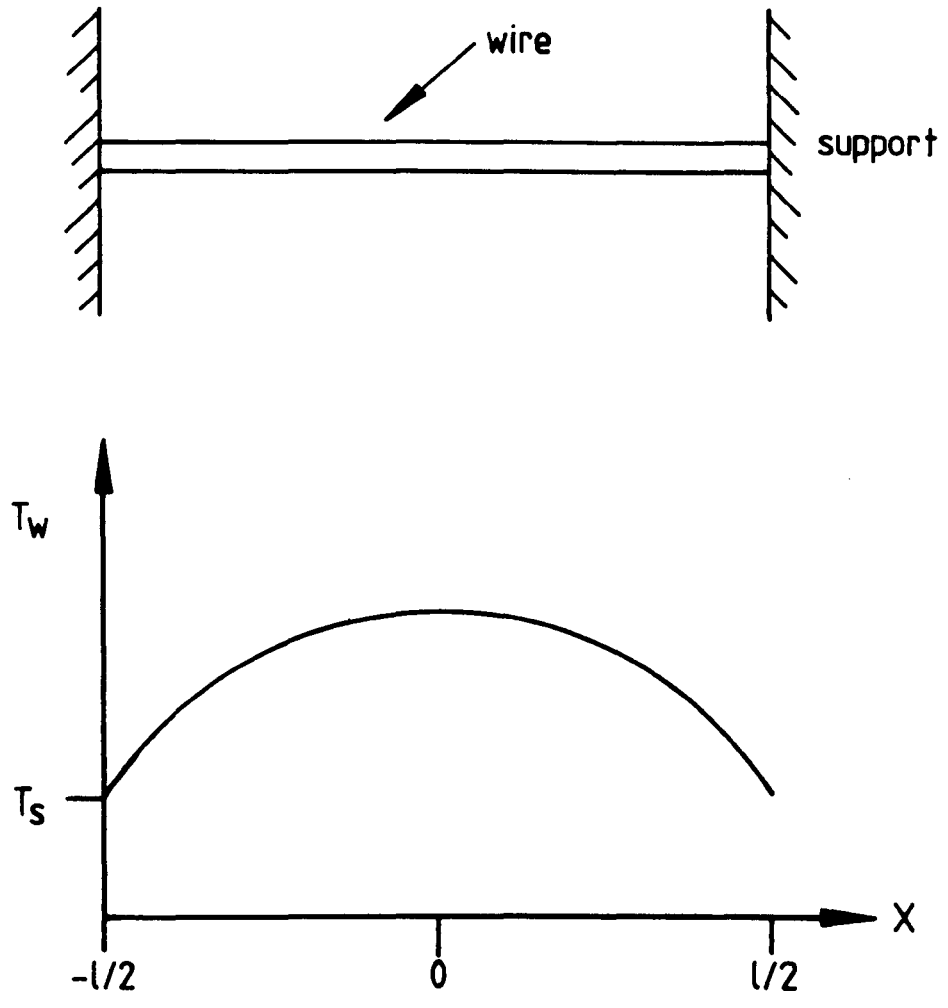

Figure A.1 Temperature Distribution Along Hot Wire Filament.

APPENDIX B

Parabolic Error Minimisation

In Section 3.3, a solution of the form $Nu' = A + B\ Re^c$ is sought to give the best fit to data obtained from the steady-flow hot wire calibration rig. Using a first-order least squares method (see Appendix C), it is possible to find 'A' and 'B', or 'B' and 'c', but one coefficient will remain unknown.

The sum of squared errors between the original raw data and the calculated fit gives a second source of information on the accuracy of the calibration. Of the three constants, a variation in 'c' is likely to give the most dramatic effect. To this end, three values of 'c' are guessed, and hence three values of A and B follow.

The sum of squared errors is found by:

$$E(j) = \sum_{i=1}^{NPTS} (Nu'_d(i) - Nu'_f(j,i)^2 \qquad (B.1)$$

where $E(j)$ = sum of squared errors from fit (j)

Nu'_d = Nu' calculated from logged data

Nu'_f = Nu' calculated from fit (j)

NPTS = number of points logged.

Hence,

$$E(j) = \sum_{i=1}^{NPTS} (Nu'_d(i) - A(j) - B(j)\ Re_d(i)^{c(j)})^2 \qquad (B.2)$$

where $A(j)$, $B(j)$ = coefficients from fit (j)

$c(j)$ = guessed 'c' value (j)

Re_d = Reynold's number calculated from data.

By plotting 'E' against 'c', a parabola can be fitted through the three calculated points. The value of 'c' that lies at the parabola minimum is sought. The possible outcomes are illustrated in Figure B.1.

i) Case 1

The general equation for this parabola is:

$$4a\ (E-f) = (c-g)^2 \tag{B.3}$$

Solving for the three co-ordinates (C_1, E_1), (C_2, E_2), (C_3, E_3):

$$g = \frac{(E_2-E_1)(E_3-E_2)^{-1}(C_3^2-C_2^2) - (C_2^2-C_1^2)}{2((E_2-E_1)(E_3-E_2)^{-1}(C_3-C_2) - (C_2-C_1))} \tag{B.4}$$

$$a = \frac{(C_2^2-C_1^2) + 2g(C_1-C_2)}{4(E_2-E_1)} \tag{B.5}$$

$$f = E_1 - \frac{(c_1-g)^2}{4a} \tag{B.6}$$

To check that g lies on a parabola minimum,

$$\frac{d^2E}{dc^2} = \frac{1}{2a} \tag{B.7}$$

If $a > 0$, then all is well. The value of 'c' that is most in error can be replaced by 'g', and the process repeated until the values converge.

Case 2

The error curve may be asymptotic, but a parabola maximum is predicted. The intercept with the x-axis, 'c_o', is used to replace the value most in error, where:

$$c_o = g - (4af)^{\frac{1}{2}} \tag{B.8}$$

The process is hence repeated in the hope that the case 1 is subsequently encountered.

Case 3

This is similar to case 2, but the 'c_o' value predicted above is negative. In this situation, a new value is found by:

$$c_o = g + (4af)^{\frac{1}{2}} \tag{B.9}$$

The process is repeated as before.

If reasonable initial values are set to c_1, c_2 and c_3, cases 2 and 3 will be rarely encountered in practice. This solution procedure converges rapidly and gives repeatable results.

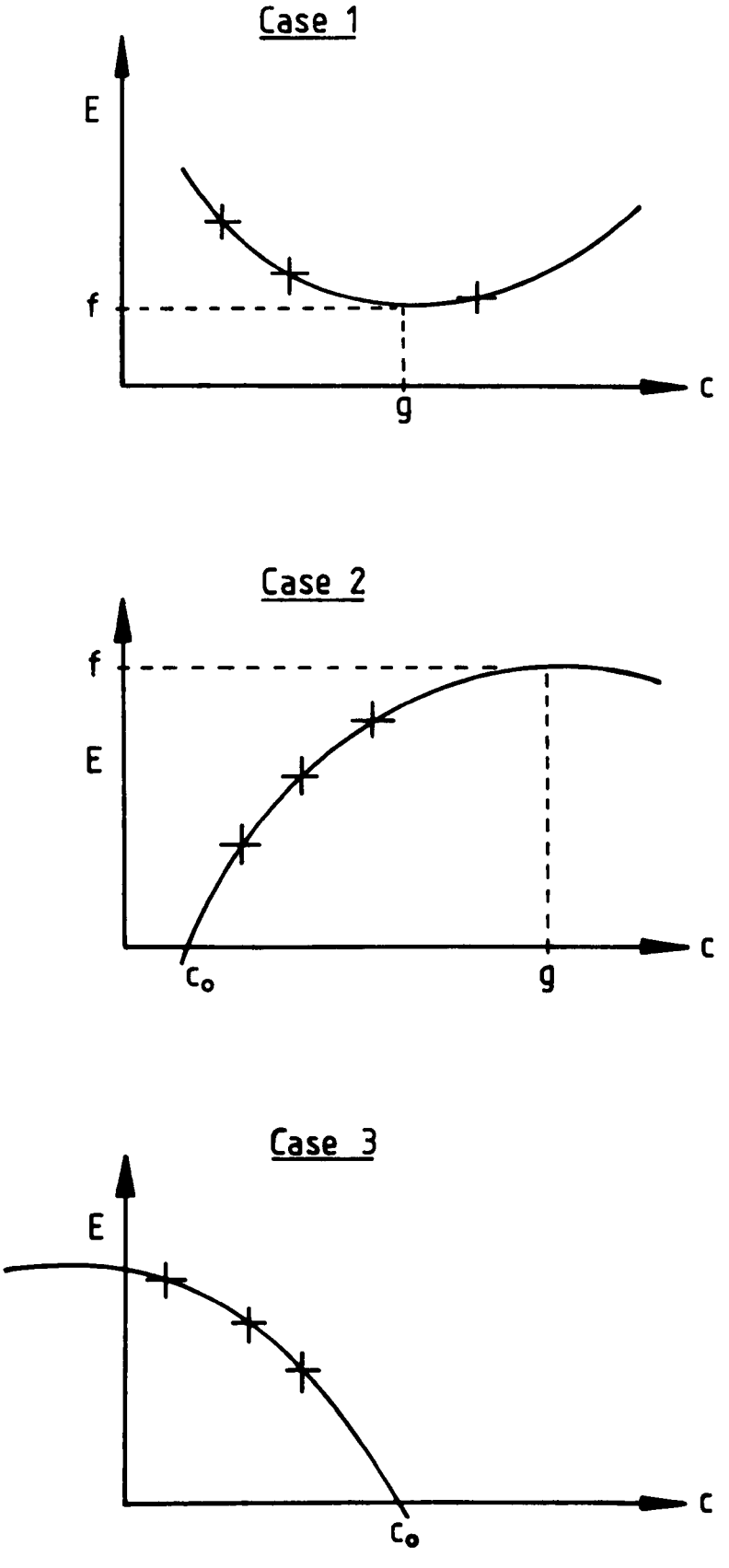

Figure B.1 Possible Error Versus Coefficient Plots.

APPENDIX C

Data Fitting by the Method of Least Squares

The aim is to find a set of coefficients describing a polynomial of given order such that the error between the original data and the computed curve is minimised. Considering a cubic equation as an example, the sum of the squared errors is given by:

$$E = \Sigma\ (y_i - (a + bx_i + cx_i^2 + dx_i^3))^2 \qquad (C.1)$$

where E = sum of squared errors

Σ = sum from i=1 to NPTS

NPTS = number of data points fitted

a,b,c,d = polynomial coefficients of fit

x_i, y_i = data ordinates (i)

'E' is hence minimised with respect to each of the coefficients. This is achieved as follows:

$$\frac{\partial E}{\partial a} = \Sigma(-\ 2(y_i - (a + bx_i + cx_i^2 + dx_i^2 + dx_i^3))) = 0 \qquad (C.2)$$

$$\frac{\partial E}{\partial b} = \Sigma(-\ 2x_i(y_i - (a + \ldots\ldots dx_i^3))) = 0 \qquad (C.3)$$

$$\frac{\partial E}{\partial c} = \Sigma\ (-\ 2x_i^2\ (y_i - (a + \ldots\ldots dx_i^3))) = 0 \qquad (C.4)$$

$$\frac{\partial E}{\partial d} = \Sigma\ (-2x_i^3\ (y_i - (a + \ldots\ldots\ldots dx_i^3))) = 0 \qquad (C.5)$$

With some rearrangement:

$$\begin{pmatrix} \Sigma y_i \\ \Sigma y_i x_i \\ \Sigma y_i x_i^2 \\ \Sigma y_i x_i^3 \end{pmatrix} - \begin{pmatrix} NPTS & \Sigma x_i & \Sigma x_i^2 & \Sigma x_i^3 \\ \Sigma x_i & \Sigma x_i^2 & \Sigma x_i^3 & \Sigma x_i^4 \\ \Sigma x_i^2 & \Sigma x_i^3 & \Sigma x_i^4 & \Sigma x_i^5 \\ \Sigma x_i^3 & \Sigma x_i^4 & \Sigma x_i^5 & \Sigma x_i^6 \end{pmatrix} * \begin{pmatrix} a \\ b \\ c \\ d \end{pmatrix} \qquad (C.6)$$

In the above matrix, the no. of rows = no. of columns = order + 1

the maximum exponent = order x 2.

The coefficients are found by Gaussian elimination. In the case of a first-order least squares fit, the number of elements in the above matrix is sufficiently small to make a direct solution approach preferable. Thus if:

$$y = a + bx \qquad (C.7)$$

then,

$$b = \frac{NPTS\ \Sigma x_i y_i - \Sigma x_i\ \Sigma y_i}{NPTS\ \Sigma x_i^2 - (\Sigma x_i)^2} \qquad (C.8)$$

$$a = \frac{\Sigma y_i - b\Sigma x_i}{NPTS} \qquad (C.9)$$

The first order least squares solution is used in the calibration of all linear transducers, whereas polynomial fits are applied to the smoothing of noisy data.

APPENDIX D

The Programming and Polling of the Microlink Transient Capture System

In this appendix a summary of the programming and polling codes and routines used to drive the Microlink transient capture system, discussed in Section 3.2, is presented. The hard- and software has since been updated by the manufacturers, hence the information in this section is specific to the Apricot P.C. microcomputer, the associated IEEE-488 interface card and the Microlink modules purchased for the present application.

The driving routines are contained within a package called ULINKB.COM, which must be loaded first when booting up the computer. Access to the commands, when writing a Basic applications program, is achieved by including the following lines of code:

i) DEF SEG = 0

ii) DEF SEG = PEEK(641)*256 + PEEK(640)

iii) NUI488 = &H103

iv) NUO488 = &H106

v) FAS488 = &H10F

The Apricot disk operating system has been modified many times, and thus line (ii) above is intended to 'self locate' the ULINKB routines in the computer memory stack. NUO488 is used for module programming, whereas NUI488 and FAS488 read data from the

CH12 units. FAS488 is the faster of the latter two, because no data transfer checking is performed.

To invoke the routines, taking NUI488 as an example, a command of the following form is used:

```
CALL NUI488 (TT%,ST%,FL%,NB%,X%(1),SC%,PA%)
```

Typical values of the enclosed arguments are given in the following tables.

Table D1 CH12 Programming (NU0488)

Variable	Value		Comments
	CH12BEM	CH12/16	
TT%	1000	1000	Time-out checking (arbitrary value)
ST%	0	0	Status. Set to zero, non-zero return indicates error.
FL%	16	16	8-bit data transfer, test for time-out.
NB%	1	1	One programming byte (X%(1)).
X%(1)	0 or 8	0 or 4	Unipolar (0-10) or bipolar (±5) voltage range.
SC%	2 or 3	4	Secondary address (of CH12s').
PA%	7	7	Primary address (of Microlink).

Table D2 Time Base (TB) Programming (NU0488)

Variable	Value	Comments
TT%	1000	As above
ST%	0	As above
FL%	16	As above
NB%	7	Seven programming bytes (X%(1)-X%(7))
X%(1)	0	Internal clock setting (not used)
X%(2)	0	Internal clock setting (not used)
X%(3)	0	Internal clock setting (not used)
X%(4)	8	8 x 16384 post trigger samples
X%(5)	3	Set 'RUN', set 'SYNC (SYNCed to trigger)
X%(6)	1	Set 'ARM'
X%(7)	1 or 0	Software or hardware trigger respectively
SC%	1	Secondary address (of TB)
PA%	7	Primary address (of Microlink)

Table D3 CH12 Polling (NUI488 or FAS488)

Variable	Value	Comments
TT%	1000	As above
ST%	0	As above
FL%	81	Wait until ready, test time-out, 16-bit transfer
NB%	N	Transfer N 16-bit words to array Y%( )
Y%(1)	-	First member of data array
SC%	2,3 or 4	As above
PA%	7	As above

When the data acquisition process is complete, the 'RUN' status set in Table D2, is reset and CH12 polling can commence. At this point data can be re-read as often as desired, the number of 16-bit words determining the position of the memory pointer. This feature is useful because the capacity of the CH12BEM units exceeds that of the computer.

APPENDIX E

Apricot Specific Programming of Non-Transient Data Logger MEE12030

1. Introduction

The aim of this Appendix is to briefly discuss the commands, codes and addresses required to program the steady state parameter data logger/interface, described in Chapter 4, that are specific to the Apricot P.C. operating system and architecture. A card is slotted into one of the three expansion slots on the computer mother board, and communication to each sub-unit of the logger is achieved by the use of port addresses. From this point the problem splits into two, that of eight and sixteen bit data exchange. The former is possible directly by the use of the MS-Basic programming language, however the latter requires a short assembler code routine to transfer the low and high bytes separately.

2. Programming and Polling

All of the programming, and some of the polling, is achieved by single byte transfers. Here the MS-Basic command used for programming is,

```
OUT ADR%,DAT%                    (E.1)
```

where ADR% = expansion port address

DAT% = data byte

The corresponding polling statement is,

```
DAT% = INP(ADR%)                 (E.2)
```

The assembler code routine used to receive 16-bit words is accessed by the command,

CALL MCODE (ADR%, DATL%, DATH%) (E.3)

where DATL% = low byte

DATH% = high byte

Figure (E.1) illustrates the code and the position of the parameters in the part of the computer memory used to this end. Essentially the Basic language references by address rather than value, and hence the variables contained in the above parentheses represent the associated stack data segment (ds) locations. The function of the routine is to find the expansion port address and input the 16-bit word, resolve the high and low bytes and store each as separate (low byte) numbers and hence to return the data segment addresses of the values that result.

3. Analogue to Digital Conversion

Three analogue to digital (A-D) converters are connected to expansion port addresses &HB2, &HB4 and &HB6. A further channel, &HB0, receives 'data ready' flags. To complete a successful conversion, the following steps are necessary,

i) Clear converter

ii) Configure for gain

iii) Trigger

iv) Read

The programming codes (8-bit transfer) are tabulated below.

Table E1 MEE12030 A - D Gain Codes

Function	Decimal Code (DAT%)
Set gain x 1000	12
Set gain x 100	8
Set gain x 10	4
Set gain x 1	0
Set gain x 0.5	1
Set gain x 0.1	2
Set gain x 0.01	3
Clear A-D	16
Trigger A-D	32 (+ gain code)

The investigation of the status of each converter requires the transfer of the 16-bit word from port address &HB0 using the MCODE routine. The required condition is met when,

$$VAL\% = DATL\% \text{ AND } VAL\% \qquad (E.4)$$

where VAL% = 2 for A-D converter number 1

VAL% = 4 for A-D converter number 2

VAL% = 8 for A-D converter number 3

The conversion is in the form of nine data plus one polarity bit. The former is complimentary to the latter, which is set high when the result is negative. Hence,

$$POL\% = DATH\% \text{ AND } 2 \qquad (E.5)$$

where POL% = polarity.

If POL% = 0 then,

$$CONV\% = (DATH\% \text{ AND } 1) \times 256 + DATL\% \qquad (E.6)$$

where CONV% = the A-D conversion result.

If POL% = 1 then,

$$CONV\% = -(511 - CONV\%) \qquad (E.7)$$

4. Thermocouple Input Selection and Polling

Two pyrometers, located at addresses &HB8 and &HBA, are connected in turn to a ten input scanning relay board. To read a temperature on a given channel, the following steps are taken:

i) Select channel

ii) Wait to allow reading to stabilise

iii) Inhibit auto update

iv) Read data

v) Reset auto update.

The programming codes may be summarised as follows:

Table E2 MEE12030 Thermocouple Programming Codes

Address	Data	Comments
&HB8	0-9	Pyrometer (1), select channel 0-9
&HBA	0-9	Pyrometer (2), select channel 0-9
&HBC	0	Enable auto update
&HBC	2	Pyrometer (1), inhibit auto update
&HBC	4	Pyrometer (2), inhibit auto update

The resolution of the first and second pyrometers is 0.1 and 1.0 degree C respectively. The 16-bit word, received in step (iv) above by using the MCODE routine, contains three decades in the form of four bit numbers, and a fourth decade and the polarity, occupying one bit each. If D1-D4 represent the four decades, then for the second pyrometer,

D1 = DATL% AND 15 (E.8)

D2 = (DATL% AND 240)/16 (E.9)

$$D3 = DATH\% \text{ AND } 15 \quad \text{(E.10)}$$

$$D4 = (DATH\% \text{ AND } 16)/16 \quad \text{(E.11)}$$

$$TEMP = D1 + (D2 \times 10) + (D3 \times 100) + (D4 \times 1000) \quad \text{(E.12)}$$

where TEMP = measured temperature (°C).

The polarity is hence sought by:

$$POL\% = DATH\% \text{ AND } 32 \quad \text{(E.13)}$$

If POL% = 0, then

$$TEMP = - TEMP \quad \text{(E.14)}$$

5. Tachometer Polling

The programming of this unit is restricted to the setting and resetting of the auto update facility. The inhibit is connected to bit 1 of address %HBC. To obtain a tachometer reading, the following steps are taken,

i) Inhibit auto update.

ii) Read data.

iii) Reset auto update.

The actual read address of the tachometer is also &HBC. The data is in the form of four decades, occupying four bits each. The polarity is always positive, and the decoding procedure is very similar to that of the thermocouple case, except that the fourth decade is found by:

$$D4 = (DATH\% \text{ AND } 240)/16 \quad \text{(E.15)}$$

6. TTL Input/Output and Relay Driver

Eight input and eight output lines share the same address, &HBE. These are divided into four relay drivers, four TTL outputs and eight TTL inputs. Programming and polling achieved by using the standard MS-Basic routines in Section (2), and the data range is 0-255.

```
DATA    SEGMENT WORD     PUBLIC 'DATA'
DATA    ENDS
DGROUP  GROUP   DATA

CODE SEGMENT    BYTE PUBLIC 'CODE'
        PUBLIC  mcode
        ASSUME  cs:CODE,ds:DGROUP
mcode   PROC    FAR
        push    bp
        mov     bp,sp
        mov     bx,10[bp]
        mov     dx,ds:[bx]
        in      ax,dx
        mov     dl,ah
        xor     dh,dh
        xor     ah,ah
        mov     bx,8[bp]
        mov     ds:[bx],ax
        mov     bx,6[bp]
        mov     ds:[bp],dx
        pop     bp
        ret     6
mcode   ENDP
CODE    ENDS
        end
```

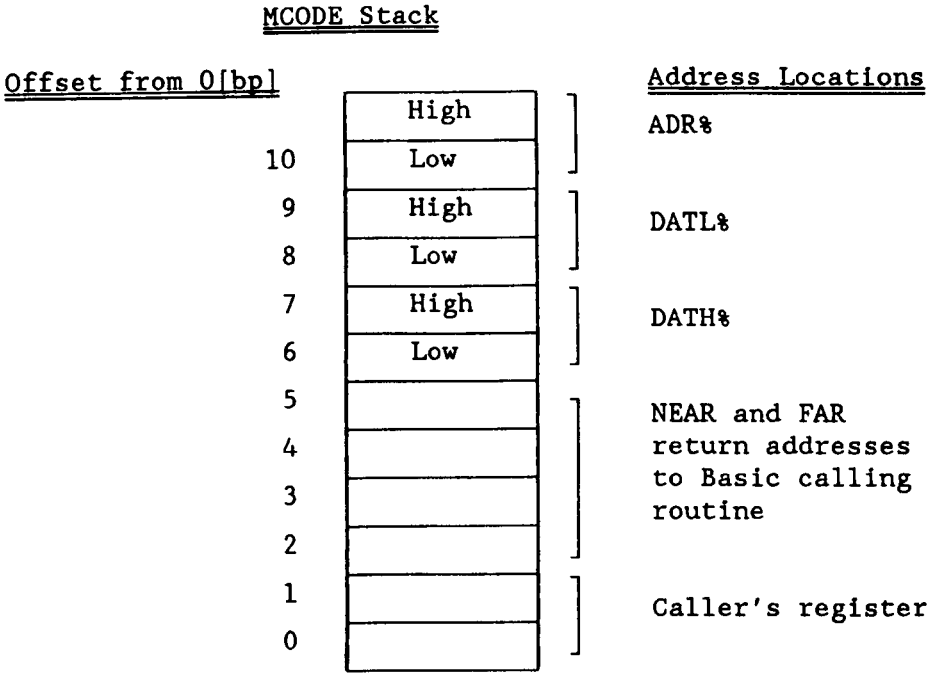

Figure E.1 Assembler Code Routine and Parameter Stack Positions

APPENDIX F

Smoothing by a Finite Fourier Series

1. Introduction

The underlying principle behind a Fourier analysis is that all functions of practical importance, which are defined on the interval $-\pi \leq x \leq \pi$, can be expressed in terms of a convergent trigonometric series of the form [45]:-

$$f(x) = \frac{A_o}{2} + \sum_{i=1}^{\infty} (A_i \cos(ix) + B_i \sin(ix)) \qquad (F.1)$$

where $f(x)$ = Fourier fit of data

A, B = Fourier coefficients.

The interval $\pm \pi$ is not important, as a change in the form of the product (ix) can modify any range to obey the above restriction.

If the data is resolved into a "true" function, with a high frequency "error" superimposed, the former can be extracted by truncating the series in Equation (Figure 1). It can be shown that the result thus obtained is actually at least squares trigonometric sum [45]. As the upper value of i is increased (an explicit mechanism for specifying a cut-off frequency), the sum of squares error tends to zero.

2. Fitting of Discrete Data

To evaluate the coefficients A_i and B_i, the following properties of orthogonality are exploited [75]:-

$$\text{a)} \quad \sum_{x=0}^{m} \sin\left(\frac{2\pi}{m+1} jx\right) \sin\left(\frac{2\pi}{m+1} kx\right) = \begin{cases} 0 \text{ if } j \neq k \\ (m+1/2 \text{ if } j = k \neq 0 \end{cases} \qquad (F.2)$$

$$\text{b)} \quad \sum_{x=0}^{m} \sin\left(\frac{2\pi}{m+1} jx\right) \cos\left(\frac{2\pi}{m+1} kx\right) = 0 \qquad (F.3)$$

$$\text{c)} \quad \sum_{x=0}^{m} \sin\left[\frac{2\pi}{m+1} jx\right] \cos\left[\frac{2\pi}{m+1} kx\right] = \begin{cases} 0 & \text{if } j \neq k \\ (m+1)/2 & \text{if } j = k \neq 0,\ m+1 \\ (m+1) & \text{if } j = k = 0,\ m+1 \end{cases} \quad \text{(F.4)}$$

If a series of the form of Equation (F.1) yields $y = f(x)$, then a sine and cosine multiplication of the original data should yield the B and A coefficients respectively.

Given a set of data points (x,y), which are equally spaced along the x-ordinate, and is in the form $x = 0, 1, 2 \ldots$ etc, the following permutations of (F.1) are available [43, 75]:-

a) Full-range, odd number of data points (2N+1)

$$f(x) = \frac{A_0}{2} + \sum_{k=1}^{J} \left(A_k \cos\left[\frac{2\pi}{2N+1} kx\right] + B_k \sin\left[\frac{2\pi}{2N+1} kx\right]\right) \quad \text{(F.5)}$$

where,

$$A_k = \frac{2}{2N+1} \sum_{x=0}^{2N} y \cos\left[\frac{2\pi}{2N+1} kx\right], \quad \begin{matrix} k = 0,1, \ldots,J \\ J \leq N \end{matrix} \quad \text{(F.6)}$$

and J = highest coefficient number chosen.

$$B_k = \frac{2}{2N+1} \sum_{x=0}^{2N} y \sin\left[\frac{2\pi}{2N-1} kx\right], \quad \begin{matrix} k = 1,2,\ldots,J \\ J \leq N-1 \end{matrix} \quad \text{(F.7)}$$

b. Full-range, even number of data points (2N)

$$f(x) = \frac{A_0}{2} + \sum_{k=1}^{J} \left[A_k \cos\left[\frac{\pi}{N} kx\right] + B_k \sin\left[\frac{\pi}{N} kx\right]\right] \quad \text{(F.8)}$$

where,

$$A_k = \frac{1}{N} \sum_{x=1}^{2N-1} y \cos\left[\frac{\pi}{N} kx\right], \quad \begin{matrix} k = 0,1,\ldots,J \\ J \leq N \end{matrix} \quad \text{(F.9)}$$

$$B_k = \frac{1}{N} \sum_{x=1}^{2N-1} y \sin \left(\frac{\pi}{N} kx \right), \quad \begin{matrix} k = 1,2,..,J \\ J \leq N-1 \end{matrix} \qquad (F.10)$$

If N terms of this Fourier series are required, then:-

$$f(x) = f(x) + A_N \cos (\pi x)$$

c) Half-range, even extension (N data points):-

$$f(x) = \frac{A_0}{2} + \sum_{k=1}^{J} A_k \cos \left(\frac{\pi}{N-1} kx \right) \qquad (F.11)$$

where,

$$A_k = \frac{1}{N-1} (y_o + y_N \cos (k\pi)) + \frac{2}{N-1} \sum_{x=1}^{N-1} y \cos \left(\frac{\pi}{N-1} kx \right) \qquad (F.12)$$

$k = 0,1,...J$

$J \leq N-2$

$$B_k = 0 \qquad (F.13)$$

If N-1 coefficients are required,

$$f(x) = f(x) + \frac{A_{(N-1)}}{2} \cos (\pi x) \qquad (F.14)$$

d) Half-range, odd extension (N data points)

$$f(x) = \frac{A_0}{2} + \sum_{k=1}^{J} \left(B_k \sin \left(\frac{\pi}{N-1} kx \right) \right) \qquad (F.15)$$

where,

$$A_k = 0 \qquad (F.16)$$

$$B_k = \frac{2}{N-1} \sum_{x=1}^{N-2} y \sin \left(\frac{\pi}{N-1} kx \right) \qquad (F.17)$$

$k = 1,2,...J$

$J \leq N-2$

In this final case, the data is modified to assist the fitting of the first harmonic by:-

$$y_i = y_i - y_o - \left[\frac{y_N - y_o}{N-1}\right] i \qquad (F.18)$$

and hence the scale of the final results is restored by:-

$$f(x_i) = f(x_i) + y_o + \left[\frac{y_N - y_o}{N-1}\right] i \qquad (F.19)$$

APPENDIX G

Smoothing by Cubic Splines

1. Introduction

The theory outlined here is taken from Reinsch [69] and Woodford [92]. The aim is to smooth a set of data points with no prior knowledge of the shape of the final curve, but with a good idea of the degree of confidence in the fitting of each point. The latter criterion is expressed in the form of a standard deviation, which is used as an inverse weighting function.

The main concepts behind the theory, rather than a total proof, are outlined here. Simplifications are achieved by using equally spaced, unit x-ordinate increments. Routines from the IBM 3083 mainframe NAG library [62] are used to solve the matrix algebra that finally results.

2. Objectives

Although the theory for the computation of higher orders is available, the use of cubic splines permits a direct algebraic solution [92]. Each spline is a discrete polynomial of the form

$$f(x) = a_i + b_i\,(x-x_i) + c_i\,(x-x_i)^2 + d_i\,(x-x_i)^3 \qquad (G.1)$$

where $a_i, \ldots, d_i$ = polynomial coefficients

$f(x)$ = discrete fit

and $x_{i+1} \geq x \geq x_i$.

The derivatives that result are:

$$f'(x) = b_i + 2c_i\,(x-x_i) + 3d_i\,(x-x_i)^2 \qquad (G.2)$$

$$f''(x) = 2c_i + 6d_i\ (x-x_i) \tag{G.3}$$

$$f'''(x) = 6d_i \tag{G.4}$$

$$f''''(x) = 0 \tag{G.5}$$

The following criteria are set:

1. The raw data is in co-ordinate pairs (x_i,y_i), i=1,...n

2. $x_1 < x_2 < ,....x_n$ i.e. the data must be in order.

3. The discrete curves are continuous in f(x), f'(x) and f"(x) at the nodes where one spline ends and another begins.

The basis of the technique is to formulate a continuous, smooth curve. To this end, the aim is to:

$$\text{minimise} \int_{x_1}^{x_n} (f''(x))^2\ dx \tag{G.6}$$

among all functions f, with the constraint that:

$$\sum_{i=1}^{N} \left[\frac{f(x_i) - y_i}{\delta y_i}\right]^2 \leq S \tag{G.7}$$

where δy_i = weight value for point i

S = smoothing parameter

and, $\delta y_i > 0$, i=1,...n
$S \geq 0$ } are input with the data

The parameter S permits the rescaling of the δy_i values. If the latter represents the standard deviation of the smaller in y_i, the magnitude of S for a 95% confidence interval [60,69,92] is given by:

$$S = N \pm \sqrt{(2N)} \tag{G.8}$$

where N = n + 2.

If S is zero, pure interpolation is achieved. If S is very large, the total fit reduces to a straight line.

Equality replace '≤' in (G.7) by introducing a z^2 term. The use of a Lagrangean parameter, p (see [38] for its application) enables the objective of (G.6) to be sought given the constraint imposed by (G.7). Now the minimum of a new function, g(pz), is to be found, where:

$$g\,(pz) = \int_{x_1}^{x_n} (f''(x))^2\,dx + p\left(\sum_{i=1}^{n} \left(\frac{f(x_i) - y_i}{\delta y_i}\right)^2 + z^2 - S\right) \qquad (G.9)$$

3. <u>Coefficient Evaluation and Matrix Manipulation</u>

The useful information that stems from equations (G.2), (G.3), (G.4) and (G.9), modified by setting $x_{i+1} - x_i = 1$, can be listed as follows (see [69,92]):

1) $C_1 = C_n = 0$ (G.10)

2) $d_i = {}^1/_3\,(C_{i+1} - C_i) \quad i = 1,\ldots.n-1$ (G.11)

3) $b_i = a_{i+1} - a_i - c_i - d_i$ (G.12)

4) $Tc = Q^T a$ (G.13)

where T = a positive, tri-diagonal matrix of order (n-2) with

elements $t_{ii} = {}^4/_3$, $t_{i,i+1} = t_{i+1,i} = {}^1/_3$.

Q = a tri-diagonal matrix with n rows and (n-2) columns with

elements $q_{i-1,i} = q_{i+1,i} = 1$, $q_{i,i} = -2$.

Q^T = transpose of Q.

c = a column matrix of length (n-2) where:

$$c^T = (c_2,\ c_3,\ldots,c_{n-1}).$$

a = a column matrix of length n, where:

$$a^T = (a_1,\ a_2,\ldots,a_n)$$

5) $$Q_c = p\, D^{-2}\, (y-a) \qquad (G.14)$$

where D = a diagonal matrix of order n, with non-zero elements

$$(\delta y_1,\ \delta y_2, \ldots, \delta y_n).$$

y = a column matrix of length n, where:

$$y^T = (y_1,\ y_2, \ldots, y_n)$$

Multiplying the left hand side of (G.9) by Q^TD^2, and using equation (G.13) yields:

$$(Q^TD^2Q + pT)c = pQ^Ty \qquad (G.15)$$

Also from (G.14).

$$a = y - p^{-1}D^2Qc \qquad (G.16)$$

Thus for a given value of p, obtain matrix c from (G.15), matrix a from (G.16), the d coefficients from (G.11) and the b values from (G.12).

4. Solution of the Lagrangean Parameter, p

The aim is to find the value of p that leads to the input S value. To this end, the minimum of (G.9) is sought with respect to p and z. Hence,

$$\frac{\partial g(pz)}{\partial z} = 0 = 2pz \qquad (G.17)$$

$$\frac{\partial g(pz)}{\partial p} = 0 = \sum_{i=1}^{n} \left(\frac{f(x_i) - y_i}{\delta y_i}\right)^2 + z^2 - S$$

The conclusions from (G.17) and (G.18) being,

1) $$pz = 0 \qquad (G.19)$$

2) $$\sum_{i=1}^{n} \left[\frac{f(x_i) - y_i}{\delta y_i}\right]^2 = S - z^2 \qquad (G.20)$$

The two possible outcomes of (G.19) are that either p or z equals zero. In seeking the correct root it is noted that at x_i, $f(x_i) = a_i$, and using equations (G.15) and (G.16), the following is found:

$$D^{-1}(a-y) = - D\,Q(Q^TD^2Q + pT)^{-1}Q^Ty \qquad (G.21)$$

Define a function F(p) such that,

$$F(p) = |DQ\,(Q^TD^2Q + pT)^{-1}Q^Ty| \qquad (G.22)$$

From (G.20):

$$F(p)^2 = S - z^2 \qquad (G.23)$$

Hence, if $p = 0$, $F(0) \leq \sqrt{S}$. From equation (G.15),

$$(Q^TD^2Q + pT)c = pQ^Ty = 0 \qquad (G.24)$$

Thus,

$$Q^TD^2Q\ c = 0 \qquad (G.25)$$

Q^T, D^2 and $Q \neq 0$, thus $c = 0$.

From (G.11) $d = 0$ and from (G.12), $b_i = a_{i+1} - a_i$. Hence each spline reduces to a straight line, which does not conform with the objective of the procedure. Therefore, the conclusion is,

$$p \neq 0,\ z = 0,\ F(p) = \sqrt{S} \qquad (G.26)$$

From equation (G.22) it is easy to see that if $p \geq 0$, F(p) tends to zero as p approaches infinity. Given than F(p) is convex, it is safe to use Newton's method to seek p.

5. Solution Procedure

The final steps to obtain the value of p for the input S are given in [69]. The essence of the method can be listed as follows:

1) Define a column matrix u such that:

$$u = p^{-1}c = (Q^TD^2Q + pT)^{-1}Q^Ty$$

2) Start by setting p = 0, then

3) Find the Cholesky decomposition R^TR of $Q^TD^2Q + pT$.

4) Compute u from $R^TRu = Q^Ty$, and v from $v = DQu$. Accumulate $e = v^Tv$.

5) If $e > S$ (approach doesn't oscillate):

Compute $f = u^TTu$ and $g = w^Tw$, where $R^Tw = Tu$.

Replace p by $p = (e + (Se)^{\frac{1}{2}})/(f - pg)$.

Restart from (3).

6) Otherwise, Compute $a = y - Dv$, $c = pu$ and hence the d and b values from (G.11) and (G.12) respectively.

6. NAG Routine Implementation

Of the two NAG routines on the IBM 3083 library designed to perform Cholesky factorisation, F01MCF is designed for symmetrical banded matrices, and only requires the input of the diagonal and lower diagonal band elements. This is important because the overall matrix dimensions in step (3) of the previous section are large. However it gives a solution in the form LdL^T. L is a lower triangular matrix, but is of unit diagonal form (d contains the necessary diagonal elements). Conversion to R^TR is achieved by exploiting the symmetry of the system such that $R^T = Ld^{\frac{1}{2}}$ and $R = d^{\frac{1}{2}}L^T$.
The compliment of F01MCF is F04MCF. This routine uses the Cholesky decomposition to solve the matrix equations. It is very flexible, and can solve various permutations of LdL^T by choosing a value of an integer ISELECT. In the present analysis, the column matrix in step (4) of the previous section is found from:

$$LdL^{T}u = Q^{T}y, \quad ISELECT = 1 \tag{G.27}$$

and for step (5), the column matrix w is found from:

$$Ld^{\frac{1}{2}}w = Tu, \quad ISELECT = 2 \tag{G.28}$$

F01MCF will fail if the input matrix is not positive definite. This can occur if the δy_i values are very close to zero.

7. Testing the Routine

As in Reinsch [69] and Woodford [92], the program is tested by plotting sin(x) data rounded to four decimal places. To determine the accuracy of the coefficients ai, bi, ci and di, the fitted function, and its first, second and third derivatives, are plotted separately in Figures (G.1) to (G.4). The choice of unit x-axis increments necessitates that for one degree, as opposed to one radian, steps, the data must be input in the form:

$$y_i = \text{INT}((\sin(x_i/57.2958)) \times 10{,}000)/10{,}000 \tag{G.29}$$

where INT() = integerise value in parentheses.

$$i = i,\ldots,180$$

From [69,92], $\delta y_i = 5 \times 10^{-5}/\sqrt{3}$.

The fit is reproduced by setting x = 0 for each spline. Hence,

$$\frac{d\, f(x_i)}{dx} = 57.2958\ b_i \tag{G.30}$$

$$\frac{d^2 f(x_i)}{dx^2} = (57.2958)^2 \times 2c_i \tag{G.31}$$

$$\frac{d^3 f(x_i)}{dx^3} = (57.2958)^3 \times 6d_i \tag{G.32}$$

and $S = 182 - (2 \times 182)^{\frac{1}{2}} = 162.9$ (G.33)

It can be seen that the fit, the first and second derivatives reproduce well. The anticipated shape of -cos(x) can be seen in Figure (G.4), but the scatter is high because the third derivative is free to float and the rounding errors in (G.32) are large.

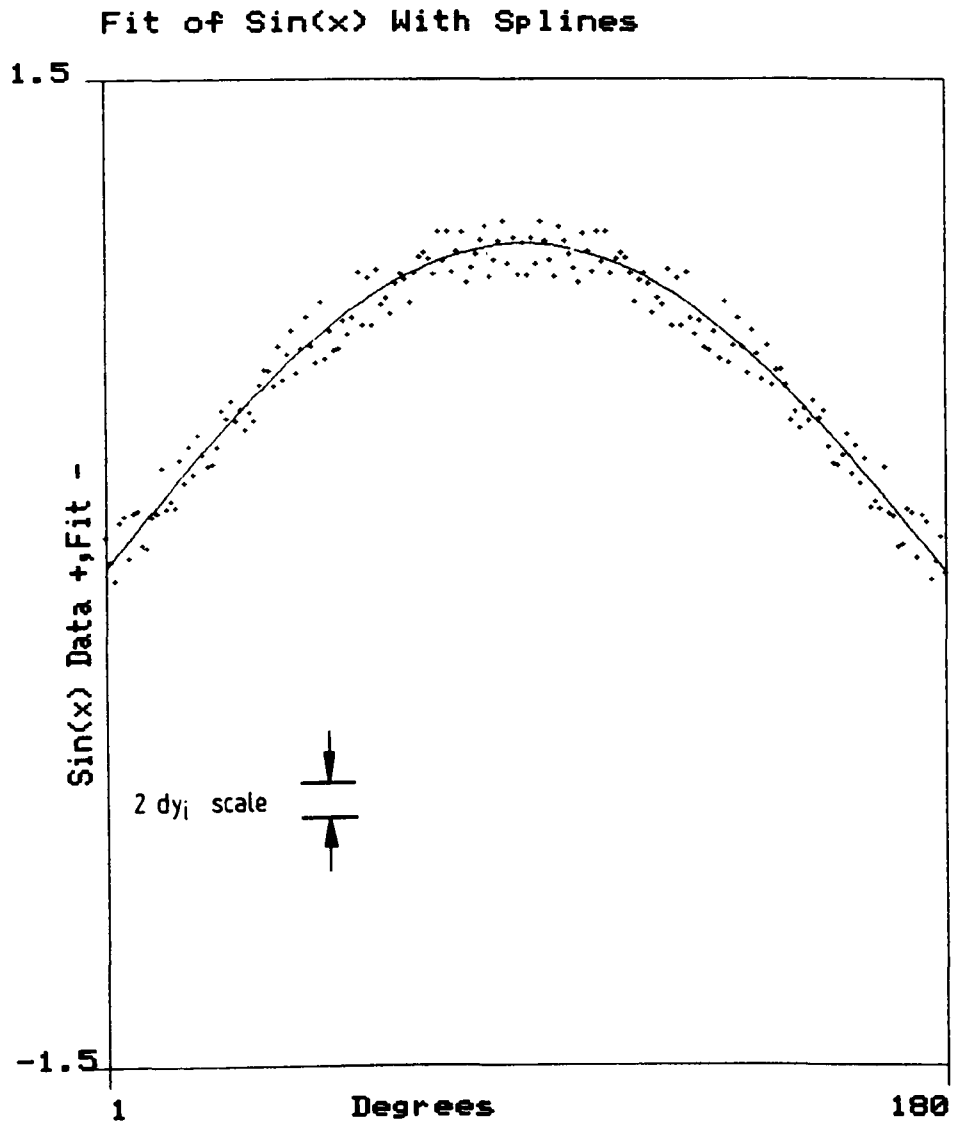

Figure G.1 Fit of Sin(x) and Input Data (Scatter Amplified).

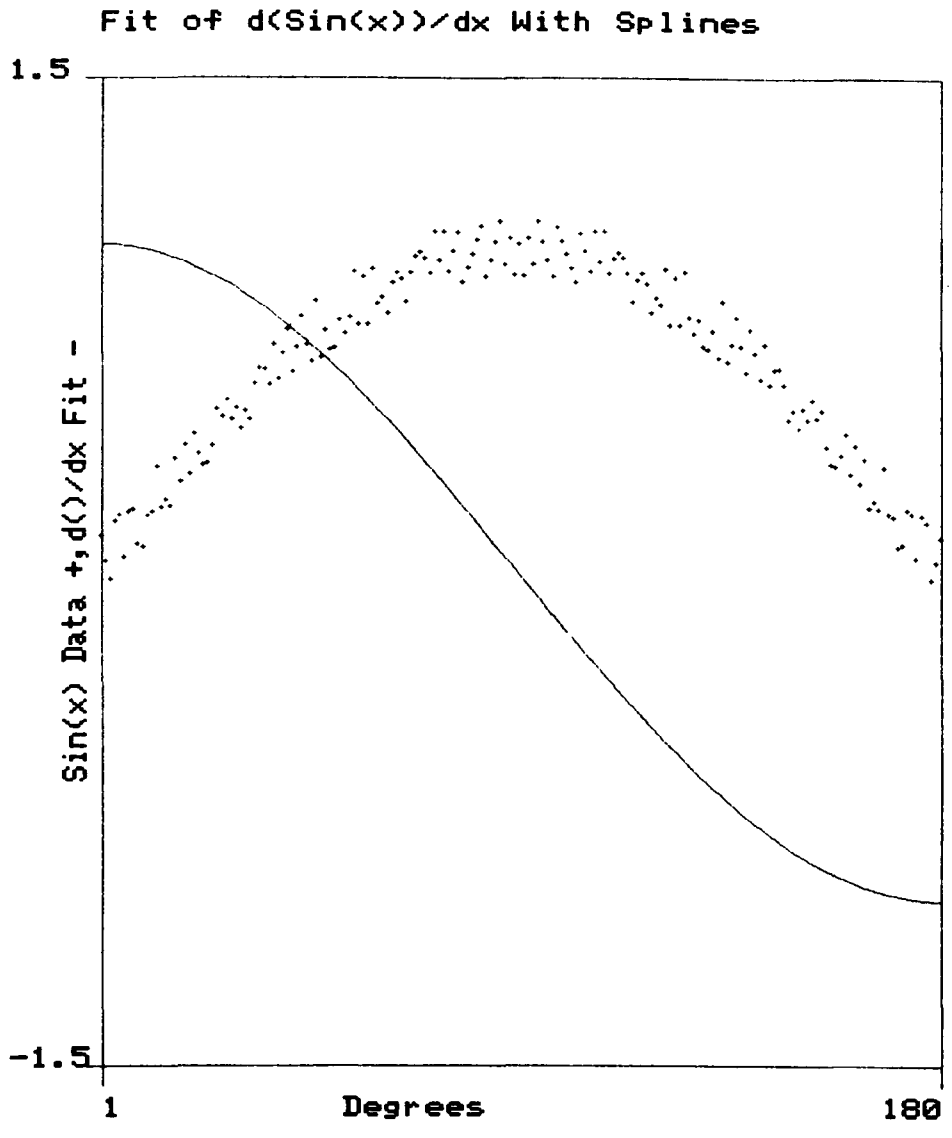

Figure G.2 Fit of ∂Sin(x)/∂x and Original Data

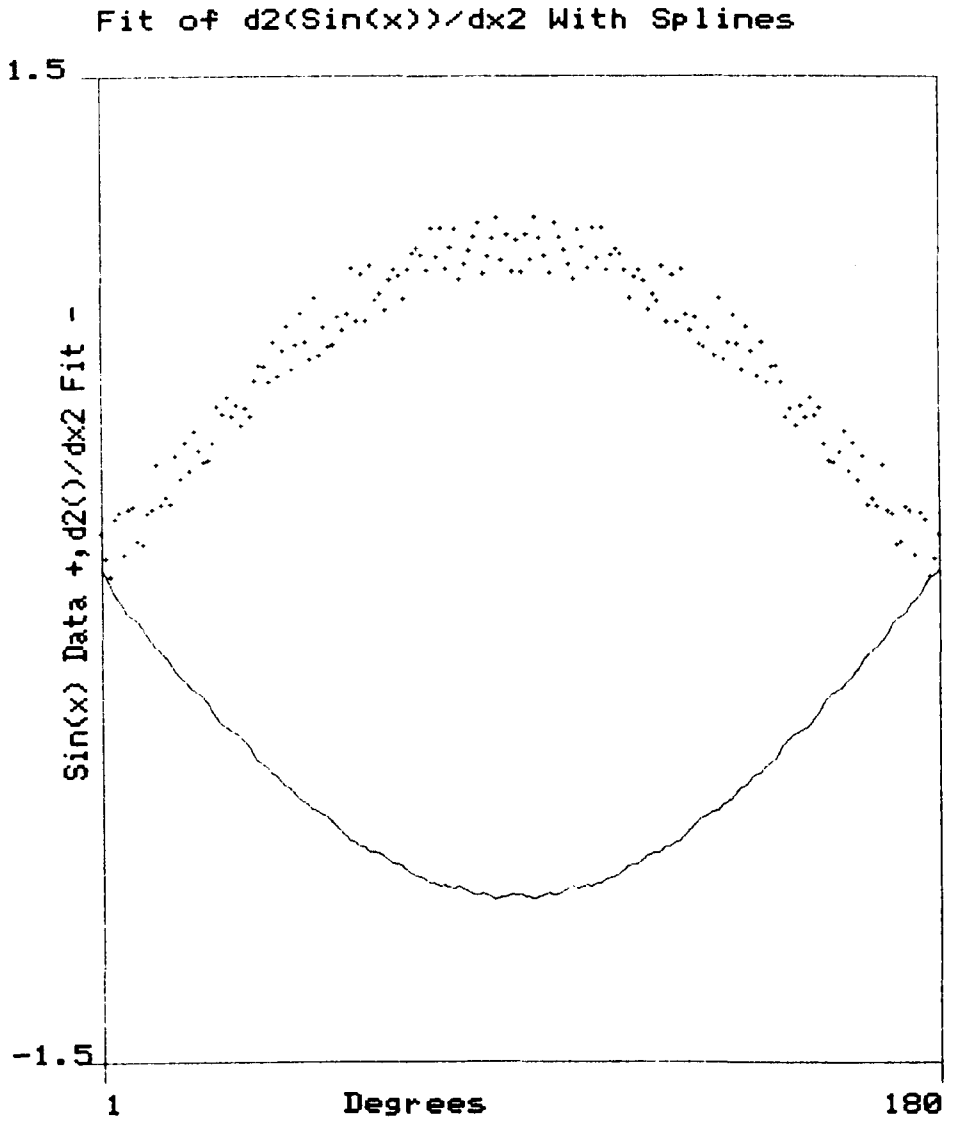

Figure G.3 Fit of $\partial^2 \mathrm{Sin}(x)/\partial x^2$ and Original Data.

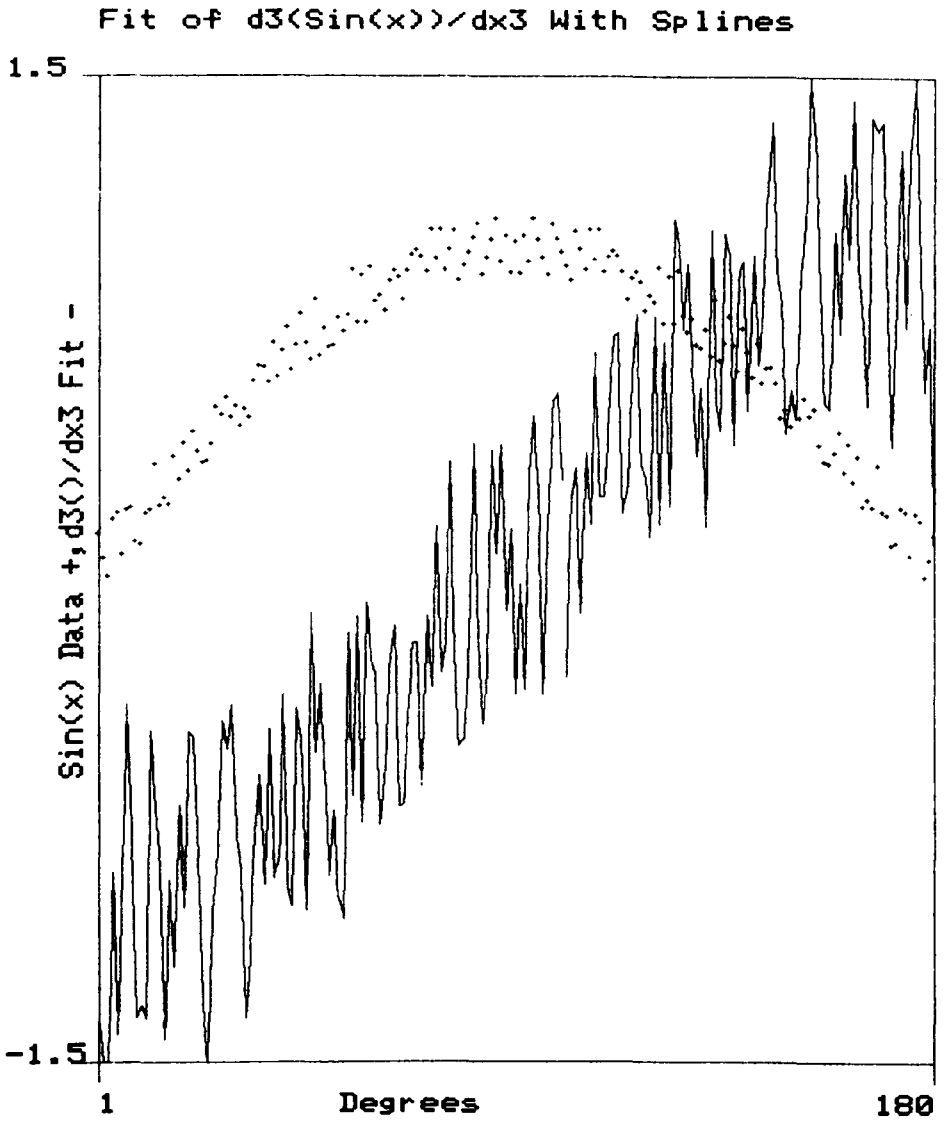

Figure G.4 Fit of $\partial^3 \mathrm{Sin}(x)/\partial x^3$ and Original Data.

APPENDIX H

Data File Formats, Contents and Locations

1. Introduction

This section is intended to serve as a record of the motored and firing engine test results processed in this study. It will hopefully be a useful document to the author's immediate successor, giving a summary of the contents, type and format of the data saved. However in five or ten years hence, when the computer systems have become outdated, the value of this appendix will correspondingly diminish.

2. Motored Engine Test Results

i) Velocity and Temperature Data

As discussed in Chapter 3, each logged data point is stored on micro-computer floppy disks (in Apricot MS-DOS format), as three character hexadecimal integers. Each test comprises of three files, which have been named chronologically (by date), and by the order in which they have been generated. In the early experiments the larger of these files (100 cycles each), namely the hot wire and resistance thermometer data, have been reduced to four smaller units (25 cycles each). This has facilitated the successful transfer from micro to main-frame computer. In the later tests, these larger files remain complete (100 cycles). The raw data has been 'archived' on the mainframe system until 31/12/1994.

The results hence calculated are stored on magnetic tape (6251 bits per inch, 2400 feet long). In reflecting the transfer problem mentioned above, the number of output files generated may be four or one. Each of these is headed by a reference number, as the sole means of identification. The subsequent records may be in the form of velocity (1), temperature (1),...velocity (n), temperature (n), or velocity (1,1), velocity (2,1),...velocity (1,n), velocity (2,n), depending upon the type of the associated experiment. The following format information applies:

Block size	=	6000
Record length	=	6
Reference number format	=	I6
Velocity format	=	F6.3
Temperature format	=	F6.2

Each file is separated by a single 'tape mark', a further three of which are used at the end of the last tape file. The velocity and temperature data generated can be found from the following sources:

Tape Name	Comments
USR351	Complete by 'ropey'
USR403	Backup (1)
USR390	Backup (2), LABEL NL (no IBM tape label)

Tables H.1a-c give a summary of the above data records. The FSF column indicates the number of tape marks which must be jumped to access a given result set.

ii) Probe Calibration Values

One cause of inconsistency in a given file of velocity and temperature results, is the details concerning the anenometer or resistance thermometer filament's heat transfer. Table H.2 is included to list the magnitude of the dominant calibration factors, and the corresponding result file test numbers (Table H1 a-c), where:

R_o = sensing element cold resistance (ohms)

A = heat transfer calibration constant 'A'

B = heat transfer calibration constant 'B'

3. Cycle-by-Cycle Velocity Curve Fitting

A further set of tape files has been generated in curve fitting (using smoothing splines - Chapter 6 and Appendix G) some of the velocity data sets found in Tables H.1 a-c. Each file contains 100 cycles of data in the form velocity (1), spline fit (1)...velocity (n), spline fit (n), and is headed by a reference number as before. The general rules that apply are similar to those

of section H.1, namely:

Block size	=	6000
Record length	=	6
Reference number format	=	I6
Velocity format	=	F6.3
Spline Fit format	=	F6.3

The records created are summarised in Table H.3, and the sources involved are listed below:

Tape Name	Comments
USR275	-
USR402	Backup (1), LABEL NL

In switching from the standard to the swirl valve data, it has been necessary to relax the smoothing parameter 'S' (Appendix G). In order to compare like-with-like, some of the results have been reprocessed, as documented in Table H.4. The tapes are listed below:

Tape Name	Comments
USR436	LABEL NL
USR439	Backup (1), LABEL NL

4. Firing Engine Pressure Records

As discussed in Chapter 4, the pressure histories logged from the firing engine are stored on floppy disks (Apricot MS-DOS format) in three character hexadecimal form. The tests recorded are documented in Tables H.5 and H.6. The data used in the subsequent mass fraction burnt calculations is also listed.

The original criterion used to classify each test is the coefficient of drivability (Cpi). However in the swirl valve case this has been found to be an impractical approach and the second set of tests listed in Table H.6, have been performed to provide a further source of information. The new data files are archived on the IBM 3083 system until 31/12/1994.

Table H.1a: Motored Test Results Tape Files

Tapes USR351, USR390, USR403

Test No	Speed (rpm)	Comp-ression Ratio	Raw Data Files	FSF	Ref No	Comments
1	1013	8.0	7MAR1-3	0-3	1-4	Standard valve.
2	1279	8.0	7MAR4-6	4-7	5-8	Flush probe.
3	1497	8.0	7MAR7-9	8-11	9-12	Velocity.
4	1749	8.0	9MAR1-3	12-15	13-16	Temperature data.
5	2038	8.0	9MAR4-6	16-19	17-20	Radial wires.
6	986	8.0	8MAR1-3	20-23	21-24	Standard valve.
7	1268	8.0	8MAR4-6	24-27	25-28	Flush probe.
8	1523	8.0	8MAR7-9	28-31	29-32	Velocity, velocity
9	1766 *	8.0	23MAR1-3	32-35	33-36	data.
10	2034	8.0	9MAR10-12	36-39	37-40	Radial wires.
11	1003	8.0	7MAR10-12	40-43	41-44	Standard valve.
12	1268	8.0	7MAR13-15	44-47	45-48	Flush probe.
13	1524	8.0	7MAR16-18	48-51	49-52	Velocity, velocity
14	1755	8.0	25MAR1-3	52-55	53-56	data.
15	2018	8.0	25MAR4-6	56-59	57-60	Circumferential wires.
16	1750	8.0	8APR1-3	60-63	61-64	Re-run of *
17	1534	7.0	15APR1-3	64-67	65-68	Standard value.
18	1517	7.5	18APR1-3	68-71	69-72	Flush probe.
19	1513	8.5	18APR4-6	72-75	73-76	Velocity,
20	1536	9.0	18APR7-9	76-79	77-80	temperature data. Radial wires.
21	1520	7.0	11APR10-12	80-83	81-84	Standard valve.
22	1520	8.5	11APR16-18	84-87	85-88	Flush probe.
23	1517	7.5	11APR13-15	88-91	89-92	Velocity, velocity
24	1514	9.0	11APR19-21	92-95	93-96	data. Radial wires.
25	1519	7.0	11APR22-24	96-99	97-100	Standard valve.
26	1518	7.5	11APR25-27	100-103	101-104	Flush probe.
27	1524	8.5	11APR28-30	104-107	105-108	Velocity, velocity
28	1536	9.0	11APR31-33	108-111	109-112	data. Circumferential wires.
29	1004	8.0	17MAY1-3	112-115	113-116	Standard valve.
30	1258	8.0	17MAY4-6	116-119	117-120	Plug cavity probe.
31	1508	8.0	17MAY7-9	120-123	121-124	Velocity,
32	1751	8.0	18MAY1,2,9	124-127	125-128	temperature data.
33	2027	8.0	18MAY3,4,10	128-131	129-132	

Table H.1a: Motored Test Results Tape Files

Tapes USR351, USR390, USR403

Test No	Speed (rpm)	Compression Ratio	Raw Data Files	FSF	Ref No	Comments
34	1003	8.0	17MAY10-12	132-135	133-136	Standard valve.
35	1254	8.0	17MAY13-15	136-139	137-140	Plug cavity probe.
36	1507	8.0	17MAY16-18	140-143	141-144	Velocity, velocity
37	1756	8.0	18MAY5,6,9	144-147	145-148	data.
38	2005	8.0	18MAY7,8,10	148-151	149-152	

Table H.1b: Motored Engine Test Results Tape Files

Tapes USR403, USR390

Test No	Speed (rpm)	Comp-ression Ratio	Raw Data Files	FSF	Ref No	Comments
39	997	8.0	13SEPT1-3	152	153	Swirl valve.
40	1254	8.0	13SEPT4-6	153	154	Flush probe.
41	1494	8.0	14SEPT1-3	154	155	Velocity, temperature
42	1724	8.0	14SEPT4-6	155	156	data.
43	1945	8.0	16SEPT1-3	156	157	Radial wires.
44	1005	8.0	7SEPT1-3	157	158	Swirl valve.
45	1257	8.0	7SEPT4-6	158	159	Flush probe.
46	1512	8.0	7SEPT7-9	159	160	Velocity, velocity data.
47	1771	8.0	16SEPT4-6	160	161	Radial wires.
48	2016	8.0	16SEPT7-9	161	162	
49	1014	8.0	23SEPT1-3	162	163	Repeats of above (tests
50	1255	8.0	23SEPT4-6	163	164	44-46)
51	1486	8.0	23SEPT7-9	164	165	
52	1030	8.0	27SEPT1-3	165	166	Swirl valve.
53	1264	8.0	27SEPT4-6	166	167	Flush probe.
54	1485	8.0	27SEPT7-9	167	168	Velocity, velocity data.
55	1766	8.0	27SEPT10-12	168	169	Circumferential wires.
56	1980	8.0	27SEPT13-15	169	170	

Table H.1c: Motored Engine Test Results Tape Files

Tape USR403

Test No	Speed (rpm)	Comp-ression Ratio	Raw Data Files	FSF	Ref No	Comments
57	1010	8.0	6OCT1-3	170	171	Swirl valve.
58	1258	8.0	6OCT4-6	171	172	Plug cavity probe.
59	1539	8.0	6OCT7-9	172	173	Velocity, temperature
60	1727	8.0	6OCT10-12	173	174	data.
61	2028	8.0	6OCT13-15	174	175	
62	1005	8.0	7OCT1-3	175	176	Swirl valve.
63	1272	8.0	7OCT4-6	176	177	Plug cavity probe.
64	1514	8.0	7OCT7-9	177	178	Velocity, velocity data.
65	1744	8.0	7OCT10-12	178	179	
66	2028	8.0	7OCT13-15	179	180	

Table H.2: Probe Cold Resistances and Calibration Constants A and B

	Wire 1			Wire 2			
Test Number	R_o	A	B	R_o	A	B	Probe Type
1-5	10.17	0.616	0.617	9.58	0.535	0.594	Radial
6,7,8,10	10.17	0.602	0.624	9.59	0.523	0.608	Radial
9,16	8.77	0.623	0.596	7.82	0.571	0.582	Radial
11,12,13	9.20	0.601	0.597	8.36	0.524	0.565	Circumferential
14,15	9.20	0.617	0.586	8.16	0.508	0.520	Circumferential
17-20	9.12	0.606	0.583	7.92	0.553	0.595	Radial
21-24	9.17	0.559	0.571	10.21	0.598	0.599	Radial
25-28	8.79	0.538	0.546	8.15	0.524	0.538	Circumferential
29-33	7.70	0.526	0.590	7.84	0.498	0.585	Plug
34-38	7.70	0.526	0.590	7.84	0.498	0.585	Plug
39,40	9.39	0.625	0.606	9.82	0.571	0.593	Radial
41,42	9.39	0.625	0.606	10.72	0.583	0.587	Radial
43	11.44	0.706	0.588	10.72	0.575	0.589	Radial
44-46	8.80	0.533	0.557	9.82	0.559	0.588	Radial
47,48	11.44	0.706	0.588	10.72	0.575	0.589	Radial
49-51	9.68	0.673	0.605	8.09	0.564	0.621	Radial
52-56	8.86	0.551	0.562	8.24	0.495	0.533	Circumferential
57-61	8.0	0.525	0.543	9.60	0.466	0.537	Plug
62-66	8.0	0.525	0.543	9.60	0.466	0.537	Plug

Table H.3: Velocity and Spline Fit Tape Files

Tapes USR 275, USR 402

Speed (rpm)	Comp-ression	Wire Number	FSF	Ref No	Comments
986	8.0	1	19	5	Standard valve.
986	8.0	2	20	6	Flush probe.
1268	8.0	1	21	7	Radial wires.
1268	8.0	2	22	8	$S = N + (2N)^{\frac{1}{2}}$
1523	8.0	1	23	9	
1523	8.0	2	24	10	
1759	8.0	2	25	11	
1759	8.0	1	26	12	
2034	8.0	1	27	13	
2034	8.0	2	28	14	
1003	8.0	1	29	15	Standard valve.
1003	8.0	2	30	16	Flush probe.
1268	8.0	1	31	17	Circumferential waves.
1268	8.0	2	32	18	$S = N + (2N)^{\frac{1}{2}}$
1524	8.0	1	33	19	
1524	8.0	2	34	20	
1755	8.0	1	35	21	
1755	8.0	2	36	22	
2018	8.0	1	37	23	
2018	8.0	2	38	24	
1003	8.0	1	39	25	Standard valve.
1003	8.0	2	40	26	Plug cavity probe.
1254	8.0	1	41	27	$S = N + (2N)^{\frac{1}{2}}$
1254	8.0	2	42	28	
1507	8.0	1	43	29	
1507	8.0	2	44	30	
1756	8.0	1	45	31	
1756	8.0	2	46	32	
2005	8.0	1	47	33	
2005	8.0	2	48	34	
1014	8.0	1	49	35	Swirl valve.
1014	8.0	2	50	36	Flush probe.
1255	8.0	1	51	37	Radial wires.
1255	8.0	2	52	38	$S = N - (2N)^{\frac{1}{2}}$
1486	8.0	1	53	39	
1486	8.0	2	54	40	
1771	8.0	1	55	41	
1771	8.0	2	56	42	
2016	8.0	1	57	43	
2016	8.0	2	58	44	

Table H.3: Velocity and Spline Fit Tape Files (Cont)

Speed (rpm)	Comp-ression	Wire Number	FSF	Ref No	Comments
1030	8.0	1	59	45	Swirl valve.
1030	8.0	2	60	46	Flush probe.
1264	8.0	1	61	47	Circumferential waves.
1264	8.0	2	62	48	$S = N - (2N)^{\frac{1}{2}}$
1485	8.0	1	63	49	
1485	8.0	2	64	50	
1766	8.0	1	65	51	
1766	8.0	2	66	52	
1980	8.0	1	67	53	
1980	8.0	2	68	54	
1005	8.0	1	69	55	Swirl valve.
1005	8.0	2	70	56	Plug cavity probe.
1272	8.0	1	71	57	$S = N - (2N)^{\frac{1}{2}}$
1272	8.0	2	72	57	
1514	8.0	1	73	58	
1514	8.0	2	74	59	
1744	8.0	1	75	60	
1744	8.0	2	76	61	
2028	8.0	1	77	62	
2028	8.0	2	78	63	

Table H.4: Further Velocity and Spline Fit Tape Files

Tapes USR 436, USR 439

Speed (rpm)	Comp-ression	Wire Number	FSF	Ref No	Comments
2034	8.0	1	0	65	Standard valve.
2034	8.0	2	1	65	Flush probe.
986	8.0	1	2	66	Radial wires.
986	8.0	2	3	67	$S = N - (2N)^{\frac{1}{2}}$
1268	8.0	1	4	68	
1268	8.0	2	5	69	
1523	8.0	1	6	70	
1523	8.0	2	7	71	
1759	8.0	1	8	72	
1759	8.0	2	9	73	
1003	8.0	1	10	75	Standard valve.
1003	8.0	2	11	76	Flush probe.
1268	8.0	1	12	77	Circumferential waves.
1268	8.0	2	13	78	$S = N - (2N)^{\frac{1}{2}}$
1524	8.0	1	14	79	
1524	8.0	2	15	80	
1755	8.0	1	16	81	
1755	8.0	2	17	82	
2018	8.0	1	18	83	
2018	8.0	2	19	84	
1003	8.0	1	20	84	Standard valve.
1003	8.0	2	21	84	Plug cavity probe.
1254	8.0	1	22	87	$S = N - (2N)^{\frac{1}{2}}$
1254	8.0	2	23	88	
1507	8.0	1	24	89	
1507	8.0	2	25	90	
1756	8.0	1	26	91	
1756	8.0	2	27	92	
2005	8.0	1	28	93	
2005	8.0	2	29	94	
1013	8.0	1	31	95	Standard valve.
1279	8.0	1	32	96	Flush probe.
1497	8.0	1	33	97	Radial wires.
1749	8.0	1	34	98	$S = N - (2N)^{\frac{1}{2}}$
2038	8.0	1	35	99	From Velocity, Temperature Data
997	8.0	1	36	99	Swirl valve.
1254	8.0	1	37	100	Flush probe.
1494	8.0	1	38	101	Radial wires.
1724	8.0	1	39	102	$S = N - (2N)^{\frac{1}{2}}$
1945	8.0	1	40	103	From Velocity, Temperature Data

Table H.5: Standard Valve Firing Engine Pressure Records

Data Disk Number	Ignition Advance (°)	Comp-ression Ratio	Speed (rpm)	Air/ Fuel Ratio	Fuel Flow (10^{-4}Kg/s)	Annand 'A'	Pref (N/m^2)	Cpi (%)
56	30	8.0	1000	18.483	2.267	0.45	99078	6
57	30	8.0	1035	19.390	2.171	0.23	99078	11
58	30	8.0	1007	20.329	2.085	0.36	99078	21
60	37.5	8.0	1251	18.132	2.198	0.58	98593	5
59	37.5	8.0	1249	18.850	2.828	0.36	98593	10
61	37.5	8.0	1252	19.942	2.683	0.28	98593	21
64	45	8.0	1498	18.056	3.411	0.51	98171	6
63	45	8.0	1496	18.728	3.317	0.45	98171	9
62	45	8.0	1497	19.457	3.229	0.44	98171	20
30	52.5	8.0	1747	18.253	3.882	0.43	97764	5
31	52.5	8.0	1751	17.955	3.967	0.51	97764	5
35	52.5	8.0	1751	19.281	3.723	0.41	97764	9
34	52.5	8.0	1753	19.976	3.612	0.24	97764	21
48	60	8.0	2035	18.22	4.451	0.36	97258	5
36	60	8.0	1996	19.206	4.243	0.34	97258	10
47	60	8.0	2002	20.005	4.099	0.48	97258	20
54	45	7.0	1506	17.613	3.509	0.48	98647	5
55	45	7.0	1502	18.021	3.411	0.5	98647	11
53	45	7.0	1503	18.997	3.287	0.32	98647	18
65	45	9.0	1501	18.696	3.288	0.51	98150	5
67	45	9.0	1498	19.160	3.288	0.58	98150	10
66	45	9.0	1499	19.860	3.145	0.43	98150	21

Table H.7 Swirl Valve Firing Engine Pressure Records

Data Disk Number	Ignition Advance (°)	Compression Ratio	Speed (rpm)	Air/ Fuel Ratio	Fuel Flow (10^{-4}Kg/s)	Annand 'A'	Pref (N/m^2)	Cpi (%)
10	30	8.0	1003	16.598	2.421	0.24	99293	7
9	30	8.0	976	17.440	2.313	0.395	99293	10
11	37.5	8.0	1251	19.558	2.629	0.16	98788	3
1	37.5	8.0	1255	19.578	2.629	0.16	98788	10
3	45	8.0	1500	19.49	3.045	0.15	98414	3
2	45	8.0	1504	19.65	3.021	0.24	98414	10
16	52.5	8.0	1750	19.748	3.4159	0.03	98053	3
17	52.5	8.0	1747	20.219	3.353	0.08	98053	11
19	60	8.0	1993	20.524	3.692	0.19	97641	2
18	60	8.0	2000	20.692	3.692	0.13	97641	11
20	30	8.0	1000	17.971	2.370	0.28	100840	1
37	45	8.0	1003	17.998	2.340	0.32	100840	1
43	37.5	8.0	1252	17.079	3.041	0.41	100420	1
38	37.5	8.0	1244	18.028	2.897	0.37	100376	1
44	45	8.0	1495	17.134	3.476	0.33	100046	2
24	45	8.0	1494	18.040	3.318	0.32	100074	1
45	52.5	8.0	1749	17.075	3.925	0.38	99697	2
50	52.5	8.0	1748	17.941	3.763	0.36	99644	2
52	60	8.0	2014	16.113	4.620	0.48	99295	2
21	60	8.0	2000	17.205	4.345	0.52	99295	2
23	60	8.0	2000	18.077	4.148	0.37	99270	2
22	60	8.0	2013	19.139	3.967	0.30	99273	2
51	45	8.0	2000	18.103	4.195	0.34	99233	1

APPENDIX I

Idealised Flame Geometry Modelling

1. Introduction

This section is intended to present mechanisms by which the surface area of a smoothed flame front can be evaluated by considering the volume occupied by the combustion products alone. In the absence of further information, in charting the flame deveopment history, one is forced to use a consistent set of geometric models to compare data obtained in different performance conditions.

The flame front is assumed to grow spherically from the point of ignition. However, in considering the complexities of the engine design, and the fact that the wall, head and piston crown boundary is a cylinder of crank angle dependent aspect ratio, two approaches are discussed. The first consists of simple cylinder centre line based hemispherical geometries, whereas the second tackles the problem by including the actual radial and axial offset of the point of ignition. In both cases the capacity of the pocket in which the spark plug is located (see Figure 2.1), estimated to be 0.9 cc, is subtracted from the product volume value used.

2. CYLINDER CENTRE LINE BASED MODELS

The geometries considered, and the notation used here, are illustrated in Figure I.1. A directly analytical volume to surface area calculation approach is permitted in most cases. The resulting procedure may be most appropriate in a strongly swirling flow, where the lighter burnt gases will tend to migrate to the cylinder centre line.

Table I.1 lists the volume, radius and surface area equations relating to each geometry. Model 1b is the most common, and is used

to calculate an initial radius estimate. Depending upon the relative magnitude of this vaue when compared to the enclosing dimensions, this geometry is either accepted, or is replaced by one which is more appropriate.

Models 1c and 1d require an iterative solution, since both R and z_2 are unknown. This is performed by using the method of false position on a radius versus error basis, where:-

i) Model 1c

$$z_2 = (R^2 - R_c^2)^{\frac{1}{2}} \qquad (I.1)$$

$$E = \frac{V}{\pi} - z_1 \left[R^2 - \frac{z_1^2}{3} \right] + \frac{2}{3} z_2^3 \qquad (I.2)$$

where E = error term.

ii) Model 1d

z_2 is found by Equation I.1 and:-

$$E = \frac{3V}{2\pi} - R^3 + z_2^3 \qquad (I.3)$$

3. SPARK PLUG ELECTRODE CENTRED MODELS

The point of ignition is actually closer to the cylinder wall than its centre line. The next order in analysis complexity would be to consider the flame growth from such a location. However in analytically seeking the radius for a given volume value, a triple integral is encountered for which no ready solution presents itself. A second approach is to solve the problem numerically. If this route is taken, there is little additional cost in tackling the full geometrical complexity caused by the spark plug's actual position.

The forms of geometry and the notation used are illustrated in Figure I.2.

The most general case consists of three components, namely a cylinder, a semi-quenched sphere and a cap. Depending upon the relative value of the flame radius to that of the cylinder and the piston clearance height, a combination of these elements will be used. Each is discussed in the sections below.

i) The Cylindrical Component

This component is included if:-

$$R > (R_c^2 + z_o^2) \qquad (I.4)$$

The volume enclosed hence follows from:-

$$V_1 = \pi z_1 R_c^2 \qquad (I.5)$$

where V_1 = cylinder component volume (m^3)

and $$z_1 = (R^2 - 4R_c^2) \qquad (I.6)$$

No contribution to the flame surface area is made at this point, hence

$$A_{s1} = 0 \qquad (I.7)$$

Where A_{s1} = the smoothed surface area (m^2)

ii) Semi-Quenched Sphere Component

This component is essentially a sphere constrained by the cylinder walls, and in cases 2c and 2d in Figure I.2 (top), by the piston crown. It is analysed numerically by summing the circumferential area and volume contributed by twenty elements of thickness Δz. Each of these elements is bound by cross-sectional surfaces of the form shown in Figure I.2 (bottom).

The elemental thickness is found by:-

$$\Delta z = (z_4 - z_2)/20 \qquad (I.8)$$

Hence the axial position of any cross-sectional area follows:-

$$z_{3i} = z_1 + i\Delta z \qquad (I.9)$$

where $i = 0,1,\ldots 20$

The cross-section radius, r_i, is:-

$$r_i = R \cos \phi_i \qquad (I.10)$$

where $$\phi_i = \sin^{-1} \left(\frac{Z_{3i}}{R} \right) \qquad (I.11)$$

Hence, $$A_{xi} = R_c^2 \left(\frac{\pi}{2} - \alpha_i - \sin \frac{2\alpha_i}{2} \right) + r_i^2 \left(\frac{\pi}{2} + \beta_i + \sin \frac{2\beta_i}{2} \right) \qquad (I.12)$$

where A_{xi} = cross-sectional area i (m^2)

and $$\alpha_i = \sin^{-1} \left(\frac{R_c^2 - r_i^2 + x_o^2}{2x_o r_i} \right) \qquad (I.13)$$

$$\beta_i = \sin^{-1} \left(\frac{R_c^2 - r_i^2 - x_o^2}{2x_o r_i} \right) \qquad (I.14)$$

The enclosed volume and smoothed suface area can now be found by numerical integration:-

$$V_2 = \frac{1}{2} \sum_{i=0}^{19} (A_{xi} + A_{xi+1})\, \Delta z \qquad (I.15)$$

where V_2 = semi-quenched sphere volume (m^3).

$$A_{s2} = \frac{R}{2} \sum_{i=0}^{19} (r_i + r_{i+1})\, (\pi + 2\beta_i)(\phi_{i+1} - \phi_i) \qquad (I.16)$$

where A_{s2} = semi-quenched sphere surface area (m^2).

iii) <u>The Cap Component</u>

This is the remaining small part of the flame geometry, which is unquenched by the cylinder wall, and is soluble analyticaly. Its inclusion may seem superfluous, when it is perfectly reasonable to

carry part (ii) into this region. However the numerical integration of this last element will be the least accurate, giving serious errors if the enclosed volume is small.

The associated equations are:-

$$z_2 = (R^2 - (R_c - x_o)^2)^{1/2} \text{ or } = z_p \qquad (I.17)$$

$$z_4 = R \text{ or } = z_p \qquad (I.18)$$

The second values listed above depend upon the piston clearance height. The volumes and surface areas that follow are:-

$$V_3 = \pi R^2 (z_4 - z_2) - \pi/3 (z_4^3 - z_2^3) \qquad (I.19)$$

where V_3 = cap volume (m^3)

$$A_{s3} = 2\pi R (z_4 - z_2) \qquad (I.20)$$

where A_{s3} = cap surface area (m^2).

iv) Solution Procedure

Model 2a is not used in the present analysis, simply because part of the surface is still emerging from the spark plug pocket (Figure 2.1), while another part is in contact with the cylinder walls. A simple hemispherical geometry is used however to make a first guess at the flame radius. From this appropriate values are assigned to z_1, z_2 and z_4. The enclosed volume and smoothed surface area are found by summing the contributions by the three components. An iterative procedure is hence used to adjust R to give the current enclosed volume value. From cylinder ead drawings the following dimensions have been evaluated for use in the above calculations:-

$$z_o = 5.14 \times 10^{-3} \text{ m}$$

$$x_o = 0.324 \text{ m}$$

$$(R_c = 0.762 \text{ m})$$

TABLE I.1

ANALYTICAL RELATIONSHIPS LINKING THE VOLUME, RADIUS AND SURFACE AREA FOR THE IDEALISED MODELS 1 a-d

Model	Enclosed Volume	Radius	Surface Area
1a	$\frac{2}{3}\pi^3 R$	$\left(\frac{3V}{2\pi}\right)^{1/3}$	$2\pi R^2$
1b	$\pi\left[R^2 z_1 - \frac{z_1^3}{3}\right]$	$\left(\frac{V}{z_1\pi} + \frac{z_1^2}{3}\right)^{1/2}$	$2\pi R z_1$
1c	$\pi\left[R^2 z_1 - \frac{z_1^3}{3}\frac{2}{3} - z_2^3\right]$	$\left(\frac{V}{z_1\pi} + \frac{z_1^2}{3} + \frac{2z_2^3}{3z}\right)^{1/2}$	$2\pi R(z_1 - z_2)$
1d	$\frac{2}{3}\pi(R^3 - z_2^3)$	$\left(\frac{3V}{2\pi} + z_2^3\right)^{1/3}$	$2\pi R(R - z_2)$

Cylinder ℄ Based Idealised Flame Geometries

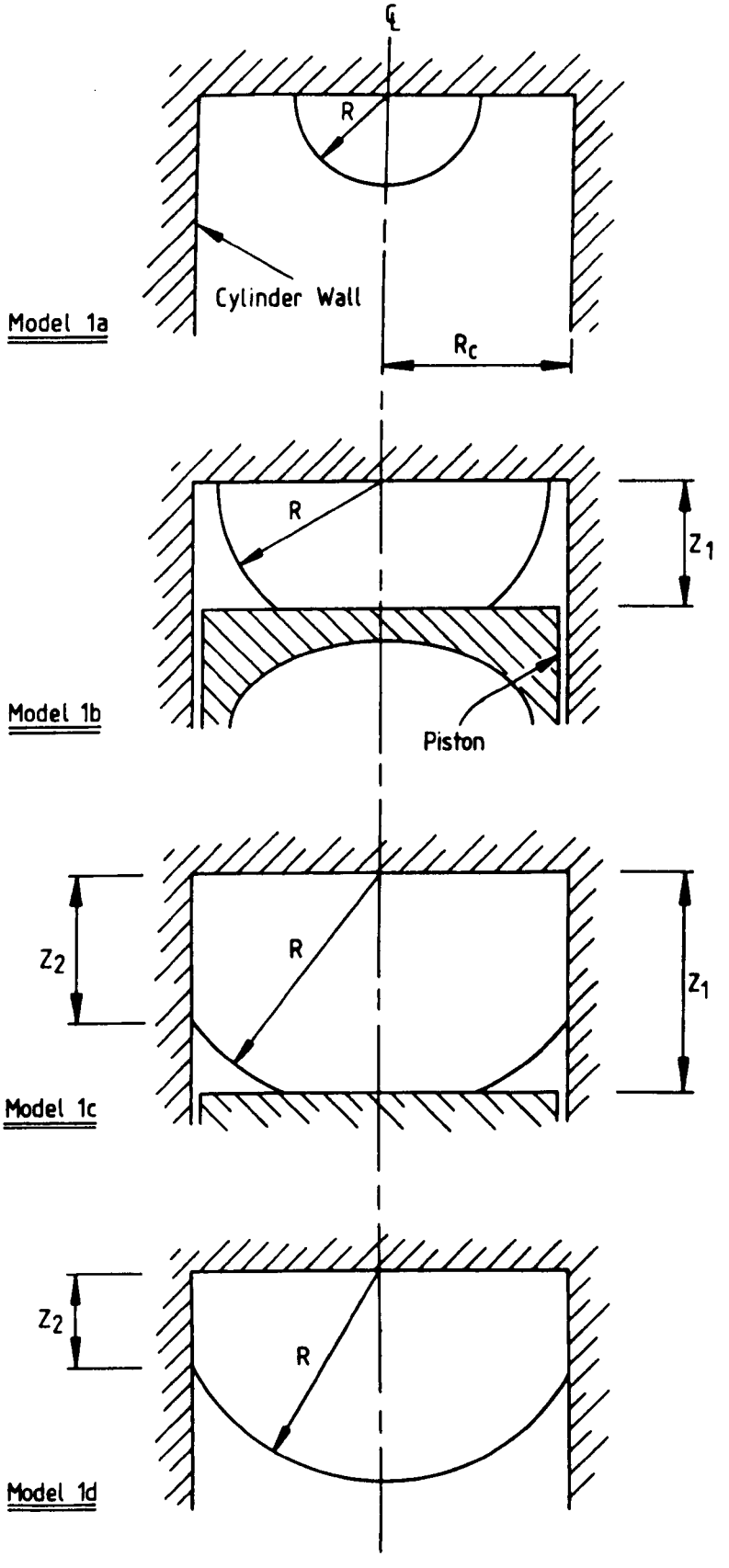

Figure I.1

Plug Centred Idealised Flame Geometries

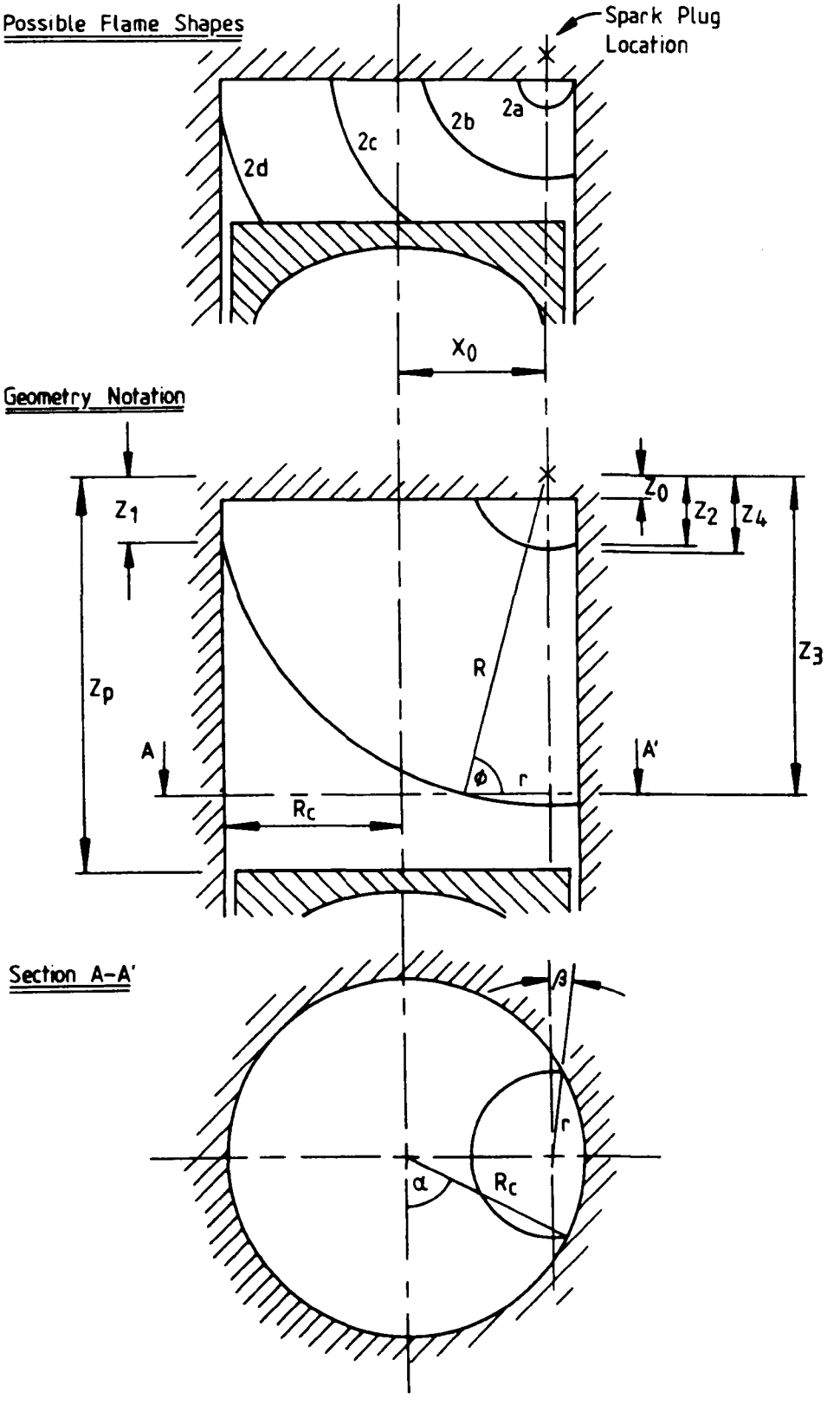

Figure I.2

Appendix J

Averaged Peak Burning Velocity Ratios and Associated Anemmetric and Combustion Data

In Section 7.4 averaged peak burning velocity ratios, based upon the idealised flame geometry models in Appendix I, are calculated from the test results documented in Appendix H. These are subsequently compared with averaged cycle-by-cycle (CBC) main chamber motored engine turbulence and velocity gradient intensities that are determined at corresponding crank-angle values from the results discussed in Chapter 6. The data used to this end is listed in Tables J.1 to J.6. Further results from the combustion and flame wrinkling analysis, in Tables J.7 and J.8, are also included to establish the context from which the burning velocity ratios are taken. The symbols, units and origin of the parameters documented in this Appendix are listed in Table J.0.

Table J.0; The Tabulated Parameter Names, Symbols, Units and Origins.

Parameter	Symbol	Units	Origin
Engine Speed	RPM	rpm	-
Ignition Advance	-	degrees	-
Air-Fuel Ratio	AFR	-	-
Crank-Angle	-	degrees after TDC	-
Burning Velocity Ratio	BSR	-	Equations 7.5
Averaged CBC Turbulence	$\overline{u_c}'$	m/s	Equations 6.15, 6.16
Averaged CBC Velocity Gradient Velocity	$\overline{\left[\frac{dV}{dx}\right]_c}'$	1/s	Equation 6.18
(Laminar) Burning Velocity	S_L	m/s	Equation 7.6
(Wrinkled) Flame Speed	dR/dt	m/s	Appendix I
Mass Fraction (Burnt)	-	%	Section 4.10
Volume Fraction (Burnt)	-	%	" "

Table J.1: Peak Burning Speed Ratios and the Corresponding Crank-Angles. Standard Inlet Valve.

Test Number	Engine Speed	Ignition Advance	Air-Fuel Ratio	BSR-Model 1	Crank-Angle	BSR-Model 2	Crank-Angle
1	1000	30	18.48	2.19	1.4	4.22	18.3
2	1000	30	19.39	2.09	5.4	4.05	27.2
3	1007	30	20.33	2.09	9.2	3.63	37.8
4	1251	37.5	18.13	2.78	-3.0	5.32	11.7
5	1249	37.5	18.85	2.57	3.3	4.74	21.8
6	1252	37.5	19.94	2.45	6.1	4.35	28.4
7	1498	45	18.06	3.08	-2.8	6.14	9.1
8	1496	45	18.73	2.99	0.3	5.84	14.8
9	1497	45	19.46	2.86	4.1	5.56	27.3
10	1751	52.5	17.96	3.35	-3.0	6.75	8.1
11	1747	52.5	18.25	3.73	-4.2	7.52	5.0
12	1751	52.5	19.28	3.70	0.5	7.80	15.5
13	1753	52.5	19.98	3.49	4.7	7.06	21.7
14	2035	60	18.22	3.80	-4.4	7.38	4.7
15	1996	60	19.21	4.03	1.7	8.09	10.5
16	2002	60	20.01	4.14	4.9	8.42	16.2

Table J.2: Peak Burning Speed Ratios and the Corresponding Crank-Angles. Shrouded Inlet Valve.

Test number	Engine Speed	Ignition Advance	Air-Fuel Ratio	BSR-Model 1	Crank Angle	BSR Model 2	Crank-Angle
17	1003	30	16.60	4.28	0.4	8.52	2.2
18	976	30	17.44	4.12	4.4	8.27	6.8
19	1000	30	17.97	4.82	2.1	9.59	4.3
20	1003	45	17.98	5.29	-9.0	10.42	-7.6
21	1252	37.5	17.08	5.87	-6.8	11.45	-4.8
22	1244	37.5	18.03	5.83	-4.1	11.46	-1.9
23	1251	37.5	19.56	5.33	6.0	10.44	9.0
24	1255	37.5	19.59	5.64	4.7	11.02	8.0
25	1495	45	17.13	6.09	-8.7	11.96	-7.5
26	1494	45	18.04	6.57	-8.2	12.80	-6.3
27	1500	45	19.49	6.42	1.8	12.42	4.0
28	1504	45	19.65	6.13	3.7	11.75	5.7
29	1749	52.5	17.08	6.45	-13.4	12.88	-11.3
30	1748	52.5	17.94	7.09	-11.9	13.98	-10.3
31	1750	52.5	19.75	7.89	-1.1	15.54	0.8
32	1747	52.5	20.22	7.34	2.8	14.41	6.0
33	2014	60	16.11	6.93	-20.06	14.07	-19.8
34	2000	60	17.21	7.73	-18.2	15.58	-16.8
35	2000	60	18.08	8.37	-16.0	16.73	-15.0
36	2013	60	19.14	8.57	-10.3	17.07	-8.1
37	1993	60	20.55	9.51	-5.0	18.38	-2.8
38	2000	60	20.82	8.71	0.0	16.69	2.1
39	20000	45	18.10	8.59	-8.8	16.86	-7.2

Table J.3; Averaged CBC Turbulence Intensity Corresponding to the Crank-Angles in Table J.1 (Standard Valve).

		Model 1		Model 2	
Test Number	Engine speed	Radial Wire	Circ' Wire	Radial Wire	Circ' Wire
1	1013,1003	0.420	0.331	0.351	0.259
2	1013,1003	0.421	0.313	0.283	0.213
3	1013,1003	0.402	0.291	0.210	0.184
4	1279,1268	0.592	0.539	0.567	0.440
5	1279,1268	0.594	0.509	0.469	0.372
6	1279,1268	0.599	0.482	0.404	0.336
7	1497,1524	0.695	0.635	0.678	0.548
8	1497,1524	0.695	0.618	0.641	0.524
9	1497,1524	0.688	0.599	0.497	0.457
10	1749,1755	0.771	0.621	0.774	0.528
11	1749,1755	0.769	0.636	0.779	0.558
12	1749,1755	0.773	0.594	0.714	0.482
13	1749,1755	0.779	0.558	0.622	0.395
14	2038,2018	1.110	0.884	1.124	0.792
15	2038,2018	1.129	0.816	1.064	0.727
16	2038,2018	1.124	0.792	0.992	0.663

Table J.4; Averaged CBC Spatial Velocity Gradient Itensity Corresponding to the Crank-Angles in Table J.1 (Standard Value)

		Model 1		Model 2	
Test Number	Engine Speed	Radial Wire	Circ' Wire	Radial Wire	Circ' Wire
1	1013,1003	979.8	1177.8	998.3	1065.4
2	1013,1003	979.7	1148.3	982.3	973.6
3	1013,1003	980.5	1124.2	910.6	855.6
4	1279,1268	1250.1	1392.5	1250.1	1316.4
5	1279,1268	1229.5	1376.9	1242.6	1235.1
6	1279,1268	1241.0	1356.8	1234.6	1177.8
7	1497,1524	1385.2	1679.2	1363.6	1654.6
8	1497,1524	1371.3	1674.9	1377.7	1638.3
9	1497,1524	1357.8	1672.5	1359.9	1522.2
10	1749,1755	1519.2	1820.4	1531.7	1799.5
11	1749,1755	1528.2	1822.3	1517.2	1801.4
12	1749,1755	1529.9	1815.5	1540.6	1783.3
13	1749,1755	1517.2	1801.4	1511.0	1668.0
14	2038,2018	1855.5	2101.5	1849.2	2068.0
15	2038,2018	1825.9	2084.4	1855.1	2021.1
16	2038,2018	1849.2	2068.2	1848.3	1941.9

Table J.5; Averaged CBC Turbulence Intensity Corresponding to the Crank-Angles in Table J.2 (Shrouded Valve).

		Model 1		Model 2	
Test Number	Engine Speed	Radial Wire	Circ' Wire	Radial Wire	Circ' Wire
17	1014,1030	1.573	0.864	1.553	0.854
18	1014,1030	1.506	0.841	1.464	0.831
19	1014,1030	1.553	0.854	1.506	0.841
20	1014,1030	1.593	0.872	1.596	0.880
21	1255,1264	2.286	1.173	2.257	1.169
22	1255,1264	2.234	1.170	2.202	1.159
23	1255,1264	2.043	1.123	1.906	1.099
24	1255,1264	2.064	1.140	1.965	1.100
25	1486,1485	2.283	1.070	2.249	1.061
26	1486,1485	2.263	1.065	2.212	1.062
27	1486,1485	1.998	0.992	1.955	0.986
28	1486,1485	1.955	1.918	1.918	0.992
29	1771,1766	1.961	1.218	1.962	1.210
30	1771,1766	1.962	1.217	1.961	1.205
31	1771,1766	1.905	1.151	1.862	1.116
32	1771,1766	1.822	1.095	1.755	1.084
33	2016,1980	1.687	1.179	1.683	1.165
34	2016,1980	1.691	1.160	1.700	1.159
35	2016,1980	1.718	1.156	1.740	1.166
36	2016,1980	1.185	1.185	1.779	1.183
37	2016,1980	1.768	1.175	1.786	1.177
38	2016,1980	1.795	1.188	1.794	1.225
39	2106,1980	1.778	1.189	1.779	1.173

TableJ.6; Averaged CBC Spatial Velocity Gradient Intensity Corresponding to the Crank-Angles In Table J.2 (Shrouded Value)

		Model 1		Model 2	
Test Number	Engine Speed	Radial Wire	Circ' Wire	Radial Wire	Circ' Wire
17	1014,1030	1173.0	1982.7	1142.8	1957.8
18	1014,1030	1112.2	1924.0	1069.9	1888.6
19	1014,1030	1142.8	1957.8	1112.2	1924.0
20	1014,1030	1304.2	2000.1	1295.7	2008.5
21	1255,1264	1639.0	2434.9	1601.0	2429.7
22	1255,1264	1577.0	2419.4	1515.1	2401.8
23	1255,1264	1350.4	2272.9	1280.9	2216.7
24	1255,1264	1369.1	2303.5	1307.6	2230.4
25	1486,1485	1890.5	2690.3	1876.9	2692.9
26	1486,1485	1888.4	2688.4	1843.6	2695.8
27	1486,1485	1640.0	2604.3	1601.0	2572.4
28	1486,1485	1601.0	2572.4	1560.4	2253.1
29	1771,1766	1973.3	3203.1	1975.7	3235.0
30	1771,1766	1978.3	3224.4	1968.5	3250.5
31	1771,1766	1883.0	3157.6	1854.4	3074.6
32	1771,1766	1810.5	3066.8	1733.2	2977.0
33	2016,1980	2001.5	3214.0	2006.2	3241.4
34	2016,1980	2007.9	3285.7	2013.1	3322.7
35	2016,1980	2030.6	3364.9	2027.8	3412.1
36	2016,1980	2039.4	3516.9	2039.0	3528.0
37	2016,1980	2031.6	3506.9	2031.8	3499.4
38	2016,1980	2011.6	3483.1	1989.5	3478.7
39	2016,1980	2036.3	3528.0	2039.7	3520.6

Table J.7; Further Combustion Parameters Corresponding to the Crank-Angles in Table J.1 (Standard Valve).

	Model 1				Model 2			
Test Number	Burning Velocity	Flame Speed	Mass Fraction	Volume Fraction	Burning Velocity	Flame Speed	Mass Fraction	Volume Fraction
1	1.06	5.90	9.8	22.9	1.20	8.30	45.2	70.3
2	1.03	5.45	10.2	22.6	1.11	7.37	50.9	74.3
3	0.82	4.64	79	16.8	0.81	5.88	44.0	68.6
4	1.07	7.26	11.0	25.6	1.24	10.72	43.8	69.1
5	0.99	6.43	11.2	25.4	1.09	8.89	44.0	69.3
6	0.86	5.51	9.1	19.6	0.87	7.77	36.3	61.2
7	1.14	7.88	15.8	34.8	1.30	12.76	43.9	69.2
8	1.06	7.33	14.6	31.6	1.18	11.43	43.8	68.5
9	0.97	6.61	13.4	28.2	1.04	9.47	53.3	75.7
10	1.21	8.68	18.1	38.1	1.36	14.54	44.4	69.3
11	1.17	9.04	20.0	41.6	1.32	15.51	44.5	69.4
12	1.03	8.21	18.7	38.0	1.16	13.51	53.9	76.2
13	0.94	7.46	17.2	34.5	1.01	11.85	47.8	71.2
14	1.23	9.87	18.1	37.9	1.36	16.79	38.2	63.3
15	1.06	8.72	23.3	45.1	1.14	15.22	42.3	66.9
16	0.99	8.28	24.3	44.8	1.05	14.23	47.3	70.0

Table J.8; Further Combustion Parameters Corresponding to the Crank-Angles in Table J.2 (Shrouded Valve).

	Model 1				Model 2			
Test Number	Burning Velocity	Flame Speed	Mass Fraction	Volume Fraction	Burning Velocity	Flame Speed	Mass Fraction	Volume Fraction
17	1.01	9.47	21.9	49.5	1.07	17.45	30.1	59.7
18	0.90	8.23	21.9	49.3	0.95	14.86	31.9	61.6
19	0.86	8.96	22.3	49.4	0.92	16.22	32.5	61.7
20	0.88	9.64	22.0	48.8	0.93	18.13	28.9	57.4
21	0.93	12.16	19.2	45.3	1.01	22.03	28.6	57.6
22	0.87	11.20	19.8	45.5	0.94	20.31	29.1	57.7
23	0.71	8.63	20.6	45.3	0.75	15.32	29.6	57.3
24	0.72	9.09	20.7	45.4	0.77	15.93	31.6	59.4
25	1.01	12.84	21.8	48.8	1.05	24.45	26.9	55.4
26	0.94	13.18	19.9	45.1	1.00	24.32	27.7	55.5
27	0.77	10.82	21.0	45.6	0.81	19.51	28.4	55.6
28	0.75	10.18	21.0	45.4	0.78	18.36	26.8	53.4
29	1.10	14.38	21.5	47.9	1.18	27.35	30.6	59.1
30	1.01	14.39	22.2	48.2	1.07	27.36	29.4	57.2
31	0.74	11.96	23.8	49.4	0.77	22.31	30.4	57.7
32	0.71	11.26	21.5	45.4	0.75	20.29	30.8	57.4
33	1.23	15.82	25.4	53.6	1.27	32.45	29.1	57.9
34	1.09	16.18	23.4	50.9	1.15	32.04	30.0	58.4
35	1.01	16.18	24.3	51.1	1.05	32.09	28.8	56.7
36	0.92	15.37	23.1	48.5	0.98	29.09	32.2	59.4
37	0.75	14.28	22.0	45.4	0.79	26.31	29.9	55.6
38	0.71	12.72	22.3	45.5	0.74	23.21	28.4	53.5
39	0.96	16.83	22.5	48.8	1.02	31.74	29.5	57.5